

Proceedings of
**First Conference for
Engineering Sciences and
Technology**
Vol. 1

Editor

M. A. Elalem



September 25–27, 2018, GARABOULLI, LIBYA

**First Conference for Engineering
Sciences and Technology
(CEST-2018)**

The Horizons of Engineering Sciences between Reality and Future Challenges

Organised by Garaboulli and Al-khoms Engineering Faculties



AIJR Publisher

Series: AIJR Proceedings

More information about this series at

<https://books.aijr.org/index.php/press/catalog/series/proceedings>

M. A. Elalem
(Editor)

Proceedings of
***First Conference for Engineering Sciences and
Technology***

CEST-2018 (25-27th September 2018)

Volume 1

Organized by
Garaboulli and Al-khoms Engineering Faculties,
Elmergib University (Libya)



Published by
AIJR Publisher, 73, Dhaurahra, Balrampur, India 271604



Proceedings of First Conference for Engineering Sciences and Technology (CEST-2018) 25-27th September 2018, Volume 1

Editor

Mohamed A. Elalem
Assistant Professor
Department: Electrical and Computer Engineering
Elmergib University, Libya

Conference Organizer

Garaboulli and Al-khoms Engineering Faculties, Elmergib University (Libya)

ISBN: 978-81-936820-5-0 (eBook)

Series

AIJR Proceedings
Series Volume: 2
DOI: [10.21467/proceedings.2](https://doi.org/10.21467/proceedings.2)

Series Editor

Dr. Adam A. Bahishti

Published

30 November 2018

Imprint

AIJR Books

© 2018 [Copyright](#) held by the author(s) of the individual articles. Abstracting is permitted with credit to the source. This is an open access book under [Creative Commons Attribution-NonCommercial 4.0 International](#) (CC BY-NC 4.0) license, which permits any non-commercial use, distribution, adaptation, and reproduction in any medium, as long as the original work is properly cited.

Published by



AIJR Publisher, 73, Dhaurahra, Balrampur, India 271604

Table of Contents

ABOUT CEST-2018	I
ABOUT THE EDITOR	III
REVIEW PROCESS	IV
THE COMMITTEE.....	V
PROGRAM SCHEDULE	VII

Track 1

FIBER-OPTIC TEMPERATURE SENSOR DESIGN ADAPTED FOR LIBYAN ENVIRONMENT	1
EMPLOYING VARIOUS DATA MINING TECHNIQUES TO FORECAST THE SUCCESS RATE OF INFORMATION TECHNOLOGY EDUCATION STUDENTS	13
MULTIPLE NOISES REMOVAL FROM COMPUTED TOMOGRAPHY (CT) IMAGES.....	23
A NEW TECHNIQUE TO ENCRYPT-DECRYPT DIGITAL COLOR IMAGES USING ONE-DIMENSIONAL MATRIX.....	30
THE PERFORMANCE OF SPACE TIME BLOCK CODING (STBC) IN MIMO RELAY NETWORK.....	36
BUILDING ENGLISH VOCABULARY SCHEMA AND WORDS RETENTION USING REVIEW VALUE CALCULATION FOR ENGLISH AS SECONDARY LANGUAGE STUDENTS.....	43
USING TRIPLE MODULAR REDUNDANT (TMR) TECHNIQUE IN CRITICAL SYSTEMS OPERATION	52
HANDWRITING ARABIC WORDS RECOGNITION BASED ON STRUCTURAL FEATURES	61
A NOVEL CHAOTIC UNIFORM QUANTIZER FOR SPEECH CODING.....	69
ITERATIVE TIME-VARYING FILTER ALGORITHM BASED ON DISCRETE LINEAR CHIRP TRANSFORM	75
COLOR IMAGE ENCRYPTION IN THE SPATIAL DOMAIN USING 3-D CHAOTIC SYSTEM.....	81
HEARING PROTECTION SYSTEM BY USING A SIMPLE NOISE REDUCTION STRATEGY	87
ENHANCEMENT OF BANDWIDTH OF U-SHAPE LOADED MICROSTRIP PATCH ANTENNA ACCORDING TO 802.11B STANDARD.....	95

BANDWIDTH OPTIMIZATION THROUGH HYBRID CODECS G.711 AND G.729 FOR VOIP ETHERNET, FR AND MP NETWORKS.....	104
MODELING AND PERFORMANCE EVALUATION OF MAPREDUCE IN CLOUD COMPUTING SYSTEMS USING QUEUEING NETWORK MODEL.....	111
COMBINED IMAGE ENCRYPTION AND STEGANOGRAPHY ALGORITHM IN THE SPATIAL DOMAIN	120
EXPERIMENTAL EVALUATION OF THE HUMANS' HEALTH HAZARDS' POTENTIAL DUE TO EXPOSURE TO THE MICROWAVES' RADIATIONS IN GARABOULLI CITY-LIBYA.....	126
CAPABILITY OF MODIFIED SIFT TO MATCH STEREO IMAGERY SYSTEM	132

Track 2

MICRO GAS TURBINE SIMULATION AND CONTROL	141
OPTIMAL POWER LOSS MINIMIZATION USING OPTIMAL SIZE AND LOCATION OF SHUNT CAPACITORS, AND DG	159
EXPERIMENTAL INVESTIGATION ON THE PERFORMANCE EVALUATION OF SOLAR TRACKING PHOTOVOLTAIC SYSTEM.....	166
COMPARATIVE ANALYSIS OF ELECTRIC FIELD AND POTENTIAL DISTRIBUTIONS OVER PORCELAIN AND GLASS INSULATORS USING FINITE ELEMENT METHOD	176
LONG TERM PEAK LOAD FORECASTING FOR THE LIBYAN NETWORK	185
THD INVESTIGATION OF HYBRID CASCADED MULTILEVEL INVERTER	194
IMPACT OF WIND GENERATION LOCATION ON POWER SYSTEM LOSSES	203
ANTENNA ELEVATION CONTROL USING MULTIPLE SWITCHED SELF-TUNING CONTROLLERS DESIGN.....	211
CONTROL OF A THREE-PHASE OFF-GRID INVERTER FOR PHOTOVOLTAIC SYSTEMS APPLICATIONS	223
EXCIMER LASER PROCESSING OF IGZO THIN FILMS FOR TRANSPARENT TFTS	233
LOSS OF LOAD EXPECTATION OF ALKHOMS GENERATING UNITS	244

Track 3

SYNTHESIS GAS PRODUCTION WITH HIGH HYDROGEN CONCENTRATION ASPEN SIMULATION	254
A STOCHASTIC OPTIMISATION TECHNIQUE FOR TUNING A CONTINUOUS STIRRED TANK REACTOR CONTROLLERS	263

CO₂ CORROSION INHIBITOR ASSESSMENT USING VARIOUS MEASUREMENT TECHNIQUES IN OILFIELD	270
VERIFICATION OF THE RESERVE OF AL-HAMADA OIL FIELD V-NC6 AREA BY APPLICATION OF WELL LOGS.	279
BOILERS PERFORMANCE EVALUATION OF ZUARA DESALINATION PLANT ...	290
ESTIMATION OF ORIGINAL OIL IN PLACE FOR BELHEDAN OIL FIELD BY USING VOLUMETRIC METHOD, MATERIAL BALANCE EQUATION METHOD, AND RESERVOIR SIMULATION METHOD	298
PRESSURE TRANSIENT ANALYSIS BY USING MS. EXCEL SHEET AND COMPUTER PROGRAMMING	310
EVALUATION OF CORROSION RESISTANCE OF MILD STEEL AND ALUMINIUM USING ANODIC INHIBITOR METHOD AND PASSIVITY	323
OPTIMUM DEPOSITION OF TUNGSTEN OXIDE ON TITANIA NANOTUBULAR ARRAYS AND STUDY THE PHOTOACTIVITY OF NANO-COMPOSITE PHOTOANODE	330
MODELING THE EFFECT OF CO₂ ON THERMODYNAMIC BEHAVIOR OF CO₂/LIBYAN NATURAL GAS MIXTURE	341

About CEST-2018

A scientific conference explores the developments of scientific research in the field of applied engineering sciences, technologies, material science, environmental and engineering management, in order to support inter-disciplinary work. The conference is being organized by Faculty of Engineering Garaboulli, and Faculty of Engineering, Al-khoms, Libya. The main objectives of this even are

- Focus on new developments in technical fields and display its key role in national development.
- Exchange ideas and experiences between the academics and technologists in engineering fields.
- Work among different engineering disciplines in design and implementation of projects.
- Role of engineering colleges and technical institutes in contributing effectively to development of Scientific research and link with related institutions.

A scientific conference explores the developments of scientific research in the field of applied engineering sciences, technologies, material science, environmental and engineering management, in order to support inter-disciplinary work. The following 43 but not limited to are the main tracks

1- Communication and Information Technology.

- Broad Band Communication
- Intelligent Communication.
- Mobile, Wireless and Optical Communication.
- Wireless Sensor Networks.
- Signal and Image Processing.
- Software Engineering and Cloud Computing.
- Computer Networks and Security.
- E-Government and E-Commerce.
- Education and Information Technology.

2- Electrical and Electronics Engineering

- Smart Grid Systems and Applications.
- Power Quality Improvement Techniques.
- Control System Technologies.
- Power System Modeling and Simulation.
- Power System Generation.

3- Oil and Chemical Engineering.

- Oil Exploration and Production Operations.
- Polymer Engineering and Technology
- Oil Refining Processes.
- Corrosion and Method of Prevention and treatment.

- Membrane science and Water Desalination.
- Modeling and Design in Chemical Processing.
- Separation processes and Petrochemical Production.

4- Industrial, Structural Technologies and Science Material

- Concrete and Building Technologies.
- Roads Engineering and survey.
- Design and Analysis of Mechanical and Structural.
- Production Processes, Welding Techniques and Heat Treatment.
- Rehabilitation of Engineering Facilities.
- Destructive and Non-destructive Tests.
- Engineering Materials and their Applications.
- Nano Technology in Engineering fields.

5- Engineering Systems and Sustainable Development

- Renewable and Alternative Energies.
- Water Purification and Water Distribution Networks.
- Feedback and Optimal Control Systems.
- Air Conditioning and Refrigeration Systems.
- Power System Generation.
- Hydraulic and Pneumatic Systems.
- Environmental waste management.
- Auditory and visual pollution.
- Auditory and visual pollution.
- Any other Topics on Architecture & Urban Planning

6- Engineering Management

- Risk Management.
- Design and Implementation Management.
- Quality Management Systems.
- Natural Resource Management.

Among about 145 contributed submissions, there were two keynote addresses, and 92 accepted research papers. The Conference started with reciting Quran and national anthem "Beladi" sung followed by inaugural speech delivered by Dr. Salhin Alaud, the organizing committee chair, faculty of Engineering, Elmergib University, Libya. The welcome speech was delivered by Dr. Mohamed Elalem, the scientific committee chair, Elmerghib university, followed by the Dean of the faculty of Engineering Dr. Farag Alsool. The Plenary talks were delivered by distinguished scientists; the details of which are available in the Scientific Program which is downloadable from the conference website <http://cest2018.elmergib.edu.ly>.

The Libya Iron and Steel Company, The Melleta Oil and Gas, Libya Export Promotion Center, Engineering Academy Tajoora, Zajel Libya and Elmergib University were the main Cosponsors of the CEST-2018.

About the Editor



Mohamed A. Elalem obtained his B.Sc. and M.Sc. in Electrical and Electronic Engineering (with specialization in Telecommunications) degrees in 1990 and 2006 respectively, and his Ph.D. in Electrical and Computer Engineering, Ryerson University, Toronto, Canada in wireless communications 2013. He is currently an assistant professor at telecommunications branch, faculty of Engineering, Elmergib University. He has contributed in a lot of conferences and committees (national and international). His main interesting areas are digital modulations schemes, cognitive radio, spectrum sharing, optimization techniques and RF design and evolution. Elmergib University, Faculty of Engineering, Khoms, Libya.

Review Process

Authors were invited to submit abstracts which were peer reviewed by two specialists. The committee has received about (250) abstracts. The committee rejected about (40) abstracts. Then the authors were motivated to send their full-length papers for peer-review. CFP is managed by EasyChair System. Each manuscript was peer-reviewed by two (2) technical specialists in fully blind base (the names and affiliation of the authors were hidden to the reviewers) The review process is conducted anonymously. To be published both reviewers were to agree separately that the manuscript met the standard required for publication in these proceedings.

Ignoring withdrawn papers, there were (160) papers submitted and (90) accepted for oral presentations. Three (3) papers were excluded from the proceedings according to their authors request. The committee and technical chairs would like to thank all the reviewers for their diligence and for contributing their time, effort and technical expertise to the review process.

The Committee

1	Dr. Mohamed A. Elalem	Libya	Elmergib University	Assistant prof	Chair
2	Dr. Meftah Alfatni	Libya	Elmergib University	Lecturer	Track 1 Coordinator
3	Dr. Adnan S. Krzma	Libya	Elmergib University	Lecturer	Track 2 Coordinator
4	Dr. Ali Ebshish	Libya	Elmergib University	Assistant prof	Track 3 Coordinator
5	Dr. Hosen Jawan	Libya	Elmergib University	Professor	Track 4 Coordinator
6	Dr. Hatem Hadia	Libya	Elmergib University	Lecturer	Track 5 Coordinator
7	Dr. Mohamed A. Alaalam	Libya	Elmergib University	Professor	Track 6 Coordinator
8	Dr. Abdullah Masrub	Libya	Elmergib University	Assistant prof	
9	Dr. Osama Alkishriwo	Libya	University of Tripoli	Assistant prof	
10	Dr. Khalid Alajel	Libya	Elmergib University	Assistant prof	
11	Eng. Ali Tamtum	Libya	Elmergib University	Assistant prof	
12	Dr. Ibrahim El Aziz	UK	University of Sheffield	Associate prof	
13	Dr. Bashir Saleh Younise	Libya	Elmergib University	Assistant prof	
14	Dr. Salah Aburawe	Libya	Elmergib University	Lecturer	
15	Dr. Ahmed Mohamed Hamruni	Libya	Elmergib University	Assistant prof	
16	Dr. Khaled Abdusamad	Libya	Elmergib University	Lecturer	
17	Dr. Ausama Hadi Ahmed	Libya	Elmergib University	Lecturer	
18	Dr. Mohamed K. Zambri	Libya	Elmergib University	Assistant prof	
19	Dr. Ali El Sharif	Libya	Elmergib University	Assistant prof	
20	Dr. Abdussalam M. Rifai	Libya	Elmergib University	Professor	
21	Dr. Faraj Farhat Eldabee	Libya	Elmergib University	Lecturer	
22	Dr. Abduel Majid K. Najjar	Libya	Elmergib University	Professor	
23	Dr. Mahmoud Y. Khamaira	Libya	Elmergib University	Lecturer	
24	Dr. Ali Elkais	Libya	Elmergib University	Assistant prof	
25	Dr. Ahmed Bshish	Libya	Elmergib University	Assistant prof	
26	Dr. Abubaker Alshuiref	Libya	Elmergib University	Assistant prof	
27	Dr. Abdussalam Addeeb	Libya	Elmergib University	Associate prof	
28	Dr. Ali Elghariani	Libya	University of Tripoli	Lecturer	

29	Dr. Ahmed Mohamed Goma	Libya	Elmergib University	Associate prof	
30	Eng. Abdulmajid Ferh	Libya	Elmergib University	Lecturer	
31	Dr. Abubkr Abdelsadiq	Libya	Elmergib University	Assistant prof	
32	Dr. Izziddien Alsogkier	Libya	Elmergib University	Lecturer	
33	Dr. Salem M. Sharif	Libya	Elmergib University	Assistant prof	
34	Dr. Abdelhamed I. Ganaw	Libya	Elmergib University	Assistant prof	
35	Dr. Mohamed El-Abboud	Libya	Elmergib University	Associate prof	
36	Dr. Mohamed S. Elforgani	Libya	Elmergib University	Assistant prof	
37	Dr. Bashir Ashhuby	UK	University of Sheffield	Lecturer	
38	Dr. Abdelrazak Ben Jaber	Libya	Nat. Standriz. Center	Assistant prof	
39	Dr. Sallin M. Alaud	Libya	Elmergib University	Lecturer	
40	Dr. Matouk M. Elamari	Libya	Engineering Academy	Assistant prof	
41	Dr. Khaled M. Dadesh	Libya	University of Tripoli	Assistant prof	

Program Schedule

Day 1: Tuesday, September 25, 2018			
Time	Tuesday	Wednesday	Thursday
09:00 - 10:00	Registration	Invited Speaker	Invited Speaker
10:00 - 10:30	Coffee Break		
10:30 - 11:45	Open Ceremony	Oral Sessions	Oral Sessions
11:45 - 13:00	Oral Sessions		
13:00 - 14:30	Lunch Time		
14:30 - 15:45	Oral Sessions	Oral Sessions	Oral Sessions
15:45-16:15	Coffee Break		
16:15 - 17:30	Oral Sessions	Oral Sessions	Close Ceremony

Tuesday, September 25, 2018 (11:45 – 13:00)

Room 1

Session: Communication and Information Technology				
	Chair	Dr. Meftah Salem Alfatni and Dr. Khalid Mohamed Alajel		
Time	Paper ID	Paper		Author(s)
11:45-12:00	CEST_013	Fiber-Optic Temperature Sensor Design Adapted for Libyan Environment		Mohamed Bin Saeed Mohamed Otman Twati
12:00-12:15	CEST_070	The performance of Space Time Block Coding (STBC) in MIMO Relay Network		Hamza Ali Jamal Elbergali
12:15-12:30	CEST_129	Hearing Protection System by Using a Simple Noise Reduction Strategy		Izziddien Alsogkier
12:30-12:45	CEST_136	Enhancement of Bandwidth of U-shape Loaded Microstrip Patch Antenna According to 802.11b Standard		Mohamed A. S. Alshushan Fadel A. M. Alaswad Marai M. Abousetta
12:45-13:00	CEST_185	Experimental Evaluation of the Humans' Health Hazards' Potential Due to Exposure to the Microwaves' Radiations in Garabouli City-Libya.		Abdurahman Altawil Mohamed Youssef Abdelbaset Karem Omran Majdi Masoud Alrajhi

Room 2

Session: Electrical and Electronics Engineering			
Chair	Dr. Adnan S. Krzma and Dr. Mohmoud Y. Khamaira		
Time	Paper ID	Paper	Author(s)
11:45-12:00	CEST_058	Micro Gas Turbine Simulation and Control	Ibrahim Sharif Mahmoud Mansour El-
12:00-12:15	CEST_217	Antenna Elevation Control using Multiple Switched Self-tuning Controllers Design	Othman E. Aburas Ahmed M. Alnajeh Youssef Amer Arebi
12:15-12:30	CEST_220	Control of a Three-phase Off-Grid Inverter for Renewable Energy Systems Applications	Ali M A Almaktoof Abdulslam M Ashoor Shaouf
12:30-12:45	CEST_111	Optimal Power Loss Minimization using Optimal Size and Location of Shunt	Hesain Milad Alfrd
12:45-13:00	CEST_114	Experimental Investigation on the Performance Evaluation of Solar Tracking Photovoltaic System	A.Kagilik S. Mousa I.Enageem

Tuesday, September 25, 2018 (14:30 – 15:45)

Room 1

Session: Oil and Chemical Engineering			
Chair	Dr. Mohamed K. Zambri and Dr. Ali Elkaish		
Time	Paper	Paper	Author(s)
14:30-14:45	CEST_025	Synthesis gas Production with High Hydrogen Concentration Aspen Simulation.	Abdalhamed A. E. Musbah Salah.M.Algoul Abdalbaset M.R. Algish Eisa A. abdalaslam
14:45-15:00	CEST_040	A Stochastic Optimisation Technique for Tuning a Continuous Stirred Tank Reactor Controllers	Yousif Alsadiq
15:00-15:15	CEST_060	Verification of the reserves of Al-Hamada Oil Field V-NC6 Area by Application of Well Logs	Tariq Basher Essa Tabar Ali Omran
15:15-15:30	CEST_077	Boilers Performance Evaluation of Zuara Desalination Plant	Ali Muftah Mabruk M. Abugderah Hakem S. Dakhel
15:30-15:45	CEST_116	Estimation of Original Oil in Place for Belhedan Oil Field by Using Volumetric Method, Material Balance Equation Method, and Reservoir Simulation Method	Ali Nasar Jibriel Abusaleem Essa M. Tabar

Room 2

Session: Industrial, Structural Technologies and Science Material				
Chair	Dr. Hosen A. Jawan and Dr. Salem M. Sharif			
Ti	Paper		Paper	Author(s)
14:30-14:45	CEST_015	The Effect of Using Ash Residues of Olive Fruits on the Properties of Cement Mortar		Hamza Almadani Mukhtar Muammar Aburawi
14:45-15:00	CEST_017	Study the Performance of Solar Water Heater with Various Loads		Ghassan Almasri Mustafa El-Musbahi Benur Maatug
15:00-15:15	CEST_024	Effects of Reduction in Construction Temperature on Workability of Warm Mix Asphalt Incorporating Rh-Wma Additive		Bashir M. Aburawi
15:15-15:30	CEST_032	Seismic Response of Reinforced Concrete Buildings as Predicated by the Draft of Libyan Standard (DSLS-1977) and (IBC-2009)		Issa. A. Mohammed Suleiman. A. Khatrush
15:30-15:45	CEST_035	Nonlinear Structural Dynamic Response of Multi-Story Buildings Under Seismic Loading		Awatif Twil

Tuesday, September 25, 2018 (16:15 – 17:30)

Room 1

Session: Engineering Systems and Sustainable Development				
Chair	Dr. Hatem Hadia and Dr. Khaled Abdusamad			
Tim	Paper		Paper	Author(s)
16:15-16:30	CEST_062	Exergy Analysis Of A Brine Mixing Othrough MSF Distillation Plant		Usama Ezzeghni Mohamed Abduljawad
16:30-16:45	CEST_064	The Optimal Membrane Type for the Next Membrane Replacement of Tajoura SWRO Desalination Plant		Usama Ezzeghni
16:45-17:00	CEST_072	Feasibility Study of Cardboard Waste Recycling		Mahdi Esmieo Moad Shaklawon Omar Sheneb
17:00-17:15	CEST_103	Designing and Optimizing 10,000 M3/Day Conventional SWRO Desalination Plant		Usama Ahmed
17:15-17:30	CEST_120	Finite Element Modeling and Simulation of A Microstructure Silicon Beam Resonant		Mohamed Shaglouf Elharoshi Diryak Ahmed Abugalia

Room 2

Session: Industrial, Structural Technologies and Science Material			
Chair	Dr. Hosen A. Jawan and Dr. Abdelhamed I. Ganaw		
Tim	Paper	Paper	Author(s)
16:15-16:30	CEST_0 38	Investigations of Kaolin Clay Collapse Behavior Using an Oedometer Apparatus	Musbah Hasan Gumaa Abdelazizi Hasan
16:30-16:45	CEST_0 59	Design of Reinforced Concrete Beams using Two Different Methods	Gumaa Hasan Mohammed A. Elsageer
16:45-17:00	CEST_0 82	High Density Polyethylene/Libyan Kaolin Clay Nanocomposites: Effect of Clay Particle Size on Rheological, Surface aMechanical Properties	Abdalbary Rhab Anour Shebani Abdalah Klash Abdelkader Aswei
17:00-17:15	CEST_0 98	كيفية الاستفادة من مخلفات الخرسانة في حالتها الطازجة	م. علي عثمان مسعود م. محمد ميلاد الأستتر
17:15-17:30	CEST_1 67	A Review Study of The Effects of Air Voids on Asphalt Pavement Life	Ali Zaltuom

End of the 1st day

Day 2: Wednesday, September 26, 2018

Day 2: Wednesday, September 26, 2018		
Room 1	09:00-10:00	Invited Speaker [Dr. Hamid H Sherwali]
	10:00-10:30	Coffee Break
	10:30-13:00	Oral Session [Communication and Information Technology]
	13:00-14:30	Lunch Break
	14:30-15:45	Oral Session [Electrical and Electronics Engineering]
	15:45-16:15	Coffee Break
	16:15-17:30	Oral Session [Engineering Systems and Sustainable Development + Engineering Management]
Room 2	09:00-10:00	
	10:00-10:30	Coffee Break
	10:30-13:00	Oral Session [Industrial, Structural Technologies and Science Material]
	13:00-14:30	Lunch Break
	14:30-15:45	Oral Session [Engineering Systems and Sustainable Development]
	15:45-16:15	Coffee Break
	16:15-17:30	Oral Session [Industrial, Structural Technologies and Science Material]

Wednesday September 26, 2018 (10:30 – 13:00)

Room 1

Session: Industrial, Structural Technologies and Science Material			
Chairs:	Dr. Abdussalam M. Rifai, Dr. Moamer Hmead and Dr. Bashir S. Younise		
Time	Paper ID	Paper Title	Author(s)
10:30-10:45	CEST_170	Modeling and Finite Element Analysis of Leaf Spring Using Pro-Engineer and ANSYS Softwares	Salem Fathi Elsheltat Abdulbaset Alshara
10:45-11:00	CEST_197	Influence of Plastic Bottles Fibre on Self Compacting Concrete	Abdelhamed Ganaw Basel Meghari Abdulnasir Alkourm
11:00-11:15	CEST_212	Prediction of local concretes compressive strength using the maturity method	Mohammed Elsageer Wisam Elhmali Mansour Hamad Suliman Abulaaaj

11:15-11:30	CEST_225	Design of Vertical Pressure Vessel Using ASME Codes	Najeeb A. Yahya Othman M. Daas Nureddin O. Fahel Albourn
11:30-11:45	CEST_226	Design Methodology for Supply Water Distribution Network; Case Study: Al-Hadeka District, Garaboulli-Libya	Abdulghani Ramadan Khairi Algrad
11:45-12:00	CEST_158	Static and Dynamic Analysis of Multistory RC Building with Various Heights in High Seismic Zone	Md. Shahnewaz Sarkar Ghusen Al-Kafri Md. Shaizuddin Sarkar
12:00-12:15	CEST_140	Influence of Surface Roughness on Adhesion between the Existing and new plain concretes	Nurdeen Altwair Saad Jaber Abu Jarir
12:15-12:30	CEST_021	Thermal performance of a heat pipe with different working fluids	Ayad Alwaer Jasson Gryzagaridis
12:30-12:45	CEST_026	Effect of Corrugation Geometry And Shape On Energy Absorption of composite plate.	Fathi A.al ssahly Khalid A. Elbkory
12:45-13:00	CEST_132	Analysis of the Failure of Cylindrical Pressure Vessels	Osama Terfas Arwa M. Elambrouk Ahlam Y. Elraqiq

Room 2

Session: Communication and Information Technology			
Chair	Dr. Ahmed M. Goma, Dr. Khaled M. Dadesh and Dr. Abdullah A. Masrub		
Time	Paper ID	Paper Title	Author(s)
10:30-10:45	CEST_12 4	A Novel Chaotic Uniform Quantizer for Speech Coding	Osama Alkishriwo
10:45-11:00	CEST_12 5	Iterative Time--Varying Filter Algorithm Based on Discrete Linear Chirp Transform	Osama Alkishriwo Ali A. Elghariani Aydin Akan
11:00-11:15	CEST_13 1	Fast Efficient Transforms for Contour Extraction from Encrypted Medical Image	Ali Ukasha Ali Ahmed Ganoun
11:15-11:30	CEST_04 7	Employing Various Data Mining Techniques to Forecast the Success Rate of Information Technology Education Students	Mosbah Mohamed Elssaedi

11:30-11:45	CEST_18 7	Capability of Modified SIFT to Match Stereo Imagery System	Omar Abusaeeda Salah Naas Nasar Aldian Shashoa
11:45-12:00	CEST_14 4	Fast Efficient Transforms for Contours Extraction and Image Compression using Zonal Sampling Methods	Ali Ukasha Abdolhameed Ali Madi
12:00-12:15	CEST_04 9	Multiple Noises Removal from Computed Tomography (CT) Images	Abdelkader Salama Alrabaie Marwan M M El marmuri Emhimed Saffor
12:15-12:30	CEST_05 4	A New Technique to Encrypt-Decrypt Digital Color Images Using One-Dimensional Matrix	Khdega A.Yosef Galala
12:30-12:45	CEST_08 5	Using Triple Modular Redundant (TMR) Technique in Critical Systems Operation	Ali A. Tamtum Samira Abu Shernta
12:45-13:00	CEST_08 4	Building English Vocabulary Schema and Words Retention Using Review Value Calculation for English as Secondary Language Students	Mosbah Mohamed Elssaedi Burnhan Mustafa Tanis Melvin A. Ballera

Wednesday, September 26, 2018(14:30 – 15:45)

Room 1

Session: Electrical and Electronics Engineering			
Chair	Dr. Adnan S. Krzma and Dr. Ali Tamtum		
Tim	Paper	Paper	Author(s)
14:30-14:45	CEST_16 8	Comparative Analysis of Electric Field and Potential Distributions over Porcelain and Glass Insulators Using Finite Element Method	Adnan S. Krzma Mahmoud Y. Khamaira Maruwan Abdulsamad
14:45-15:00	CEST_18 2	Long Term Peak Load Forecasting for the Libyan Network	Mahmoud Y. Khamaira Adnan S. Krzma
15:00-15:15	CEST_18 4	THD Investigation of Hybrid Cascaded Multilevel Inverter	A.Elzowawi Islam Saad Mustafa Elsherif

15:15-15:30	CEST_20 6	Impact of Wind Generation Location on Power System Losses	Ibrahim Naser
15:30-15:45	CEST_22 3	Excimer Laser Processing of IGZO Thin Films for Transparent TFTs	Khairi Abusabee Khalid .M. Alajel Salem .O. Elhamali

Room 2

Session: Engineering Systems and Sustainable Development			
Chair		Dr. Mohamed A. Alaalam and Dr. Mohamed S. Elforqani	
Tim	Paper	Paper	Author(s)
14:30-14:45	CEST_15 7	Zero Energy and Low Water Schools: Case Study Building of Garaboulli Engineering Faculty-Libya	Salhin Alaud Khalid M. H. Jaballa Abdulghani M. Ramadan
14:45-15:00	CEST_15 5	Wind Energy Reliability Analysis based on the Monte Carlo Simulation Method	Khaled Abdusamad
15:00-15:15	CEST_17 4	Synthesis and characterization of magnetic CoFe _{1.9} Cr _{0.1} O ₄ nanoparticles by sol-gel method and their applications as an adsorbent for water treatment	Ibrahim Amar Abubaker Sharif Najat A. Omer Naght E. Akale Fatima Altohami
15:15-15:30	CEST_17 8	To What Extent Do Nursery Group Rooms Match with The Architectural Design Considerations?	Mustafa Zarigan Lutfi Senan Muftah Omran
15:30-15:45	CEST_19 0	Solar Hydrogen Production System Simulation using Pscad	Matouk M. Elamari

Wednesday, September 26, 2018(16:15 – 17:30)

Room 1

Session: Engineering Systems and Sustainable Development + Engineering Management			
Chair		Dr. Mohamed A. Alaalam and Dr. Abdulghani M. Ramadan	
Time	Paper ID	Paper Title	Author(s)
16:15-16:30	CEST_19 3	Performance Analysis of a Solar Driven Single Stage LiBr/H ₂ O Absorption Refrigiration System	Islam Shahboun Salem Omran Adeilla

16:30-16:45	CEST_20 5	Preserving. Architectural Heritage within the International Covenants and its Reflection in the Libyan Case	Hussein Ali Ashraf Laswad Latefa Wafa
16:45-17:00	CEST_21 9	Measuring urban clarity of the built environment	Fawzi Mohamed Agael
17:00-17:15	CEST_17 9	Key Performance Indicators in Libyan Oil and Gas Projects	Mahmoud Matoug Abdulbaset Frefer Haleema Omer
17:15-17:30	CEST_19 9	An Investigation of Corrosion Risks in the Oil and Gas Pipelines Using Analytical Hierarchy Process and Fuzzy Analytical Hierarchy Process	Abdulbaset Frefer Mahmoud M. Matoug Fatma L. Haddada

Room 2

Session Industrial, Structural Technologies and Science Material			
Chair	Dr. Bashir S. Younise and Ahmed M. Hamruni		
Tim	Paper	Paper	Author(s)
16:15-16:30	CEST_02 9	Effects of Spring Stiffness on Suspension Performances Using Full Vehicle Models	Moamar Hamed M. Elrawemi
16:30-16:45	CEST_03 0	Influence of Coolant Concentration on Surface Roughness during Turning of Steel C-6	Abdulaziz Abodena Muhannad Alrzage Ibrahim K. Husain
16:45-17:00	CEST_03 9	Effects of outlet nozzle geometry on Swirling Flows in gas turbine	Hesham Baej Adel Akair Adel Diyaf Salem Adeilla
17:00-17:15	CEST_02 7	Mapping of Sea Water Intrusion in the Westren Libyan Coast using Geoelectric Method: Case Study	Abdel Hameed M. Salem Magdi A. Mountasir Husam Abdussalam R. Shames
17:15-17:30	CEST_02 8	Effects of Different Fluids Properties on Cavitation Performance in Centrifugal Pump	Saad Ghidhan Moamar Hamed Mansor Benaros

End of 2nd day

Day 3: Thursday, September 27, 2018

Room 1	09:00-10:00	Invited Speaker [Dr. Tammam Ben Mousa] (apologized for coming)
	10:00-10:30	Coffee Break
	10:30-13:00	Oral Session [Industrial, Structural Technologies and Science Material]
	13:00-14:30	Lunch Break
	14:30-15:30	Oral Session [Communication and Information Technology + Electrical and Electronics Engineering]
	15:30-16:30	Close Ceremony
Room 2	09:00-10:00	
	10:00-10:30	Coffee Break
	10:30-12:45	Oral Session [Oil and Chemical Engineering]
	13:00-14:30	Lunch Break

Thursday, September 27, 2018 (10:30 – 13:00)

Room 1

Session: Industrial, Structural Technologies and Science Material			
Chair	Dr. Matouk M. Elamari, Dr. Mustafa A. Almusbahi and Dr. Salhin Alaud		
Tim	Paper	Paper	Author(s)
10:30-10:45	CEST_12 2	The Effect of Adding Steel Slag and Lime on the Engineering Properties of a Sandy Soil	Mohammed Elsageer Ayad Abdelmoula Mohammed
10:45-11:00	CEST_15 9	Capablity of Designing a Novel Smart Fluid Damper using a Mckibben Actuator	Haithem Elderrat Elganidi Elsaghier
11:00-11:15	CEST_05 0	Theoretical Invistigation Of An Indirect Evaporation Air Cooling System	Mohamed Alowa Gassem A. Azzain

11:15-11:30	CEST_04 1	Aerodynamic Effects Of Blade Positive Sweep In Axial Flow Cascades	Ali Kwedikha Abdul Azeam A. Elgayed Abelmalek N. Algaoud
11:30-11:45	CEST_01 9	Built to Code Building Envelop Versus Sustainability of High-Rise Building Performance	Mohamed Ali Karim
11:45-12:00	CEST_02 0	Simple and Sustainable Constipate to Save Cost and Time for Constructions Structure	Abdualraouf Mohamed Mohamed Ali Karim
12:00-12:15	CEST_05 7	Monitoring Mis-Operating Conditions of Journal Bearings based on Modulation Signal Bispectrum Analysis of Vibration Signals	Osama Hassin Usama Haba Fengshou Gu A. J. Bell
12:15-12:30	CEST_08 3	Particle Size Dependence of MnO Reduction for Fabrication of $[(Al-AlMnO)]_X$ Composite vir Stir Casting	Khalid Almadhoni Sabah Khan
12:30-12:45	CEST_11 5	Nanotechnology: Concepts, Importance and the Current State of Scientific Research	Samieh Abu Saad Amani Elmahjubi
12:45-13:00	CEST_16 2	Investigation into Accuracy of LGD2006 for Medium-elevation Areas	Ahmed Hamruni Adel Alkilani

Room 2

Session: Oil and Chemical Engineering			
Chair		Dr. Abduel Majid K. Najjar, Dr. Ali S. Ebshish and Dr. Ibrahim M. El Aziz	
Time	Paper ID	Paper Title	Author(s)
10:30-10:45	CEST_04 5	CO ₂ Corrosion Inhibitor Assessment Using Various Measurement Techniques in oilfield	Abdelrazag Aziz
10:45-11:00	CEST_13 9	Pressure Transient Analysis by Using MS. Excel Sheet and Computer Programming	Essa M. Tabar Ali Omran Nasar Tariq Basher
11:00-11:15	CEST_14 1	Evaluation of Corrosion Resistance of Mild Steel and Aluminium Using Anodic Inhibitor Method and Passivity.	Ali Elkais Mohamed K Zambri
11:15-11:30	CEST_20 0	Optimum deposition of Tungsten Oxide on Titania Nanotubular and study Photoactivity of Nano-Composite Photoanode	Asma M. Husin Milad Soud Saad Awitil Mohammad B. Kassim Wan Ramli Wan Daud
11:30-11:45	CEST_20 8	Modeling the Effect of CO ₂ on Thermodynamic Behavior of CO ₂ /Libyan Natural Gas Mixture	Almahdi Alhwaige Ali S. Bshish Salem M. Abdusalam Ahmed M. Ebshish

11:45-12:00	CEST_21 4	Novel Green Sorbents Derived from Mesembryanthemum-based Biomass for Wastewater Treatment Applications	Almaki Abushaina Abdelrahman Sultan Wael Elhrari Almahdi A. Alhwaige
12:00-12:15	CEST_21 5	Novel Green Photocatalysts Derived from Date-based biomass/TiO ₂ for Photocatalytic Oxidation of Methylene Blue Dye in Aqueous Solutions	Almahdi Alhwaige Mohammed A. El-Ghweil Wael Elhrari
12:15-12:30	CEST_08 3	Particle Size Dependence of MnO Reduction for Fabrication of [(Al-AlMnO)] _x Composite via Stir Casting	Khalid Almadhoni Sabah Khan
12:30-12:45	CEST_22 7	Estimation of Empennage Design Weight in Conceptual Design Phase for Tactical Uavs	Abdulahkim Muhammad Essari

Thursday, September 27, 2018 (14:30 – 16:00)

Room 1

Session: Communication and Information Technology + Electrical and Electronics Engineering			
Chair	Dr. Izziddien Alsogkier and Dr. Ausama H. Ahmed		
Tim	Paper	Paper	Author(s)
14:30-14:45	CEST_15 1	Bandwidth Optimization Through Hybrid Codecs G.711 and G.729 for VoIP Ethernet, FR and MP Networks	Abdullah Masrub Mohamed Alahemar AbdulSalam Addeeb
14:45-15:00	CEST_16 4	Modeling and Performance Evaluation of MapReduce in Cloud Computing Systems Using Queueing Network Model	Guzlan Miskeen
15:00-15:15	CEST_10 9	Handwriting Arabic Words Recognition Based on Structural Features	Salim Aloud
15:15-15:30	CEST_12 8	Color Image Encryption in the Spatial Domain Using 3-D Chaotic System	Osama Alkishriwo Hanan Salem Alzregghi
15:30-15:45	CEST_17 1	Combined Image Encryption and Steganography Algorithm in the Spatial Domain	Osama Alkishriwo Aya H. S. Abdelgader Raneem A. Aboughalia
15:45-16:00	CEST_22 4	Loss of Load Expectation of Alkhoms Generating Units	Mohamed Altaher Ben Mouhsen Ali A. Tamtum

Track 1

Communication and Information Technology

Fiber-Optic Temperature Sensor Design Adapted for Libyan Environment

Mohammed Bin Saeed*, Mohamed Otman Twati

Department of Electrical and Electronic Engineering, University of Tripoli, Libya

DOI: <https://doi.org/10.21467/proceedings.2.1>

* Corresponding author email: bin703m@gmail.com

ABSTRACT

In this work, the design of the Fiber optic Temperature Sensor has been performed using two different techniques aimed at determining the optimum design parameters of the fiber optic sensor that should work properly in the Libyan environment (temperature: -13 to 57.8 degrees Celsius). The first technique is based on Fabry-Perot Interferometer that tracks the phase change of the received light by the interferometer due to the sensitivity of the Fabry-Perot's cavity to the surrounding temperature changes. Three different substances (GaAs, Ge and Si) were used in determining the optimum design parameters of the fiber optic sensor. The optical wavelength used is 1550nm with line width of 40nm. The material selected is Si where the optimum Fabry-Perot length was found to be 20.7 μ m. The second technique studied is based on Fiber Coupling Actuated by a Bimetal Strip to read the change in temperature with respect to coupling power loss. Three different standard Bimetal types were used for the design of the strip, (KANTAL 200 TB20110 Ni/MnNiCu), (KANTAL 135 Ni/NiMn-steel) and (KANTAL100 TB0965 Ni/NiMn-steel). The (KANTAL 200 TB20110 Ni/MnNiCu) Bimetal material was selected for the optimal sensor design. The optimum design length, delta deflection and thickness for the strip were found to be 5.6 μ m, 35 μ m and 1.3 μ m respectively.

Keywords: optical fiber; temperature sensor design; fabry-perot interferometer.

1 Introduction

Over the last few decades, optical fibers have been widely deployed in telecommunication industries owing to their special performance as the best light guidance. Optical fibers have been intensively investigated at various sensor fields, owing to their unique characteristics such as multiplexing, remote sensing, high flexibility, low propagating loss, high sensitivity and low fabrication cost. Temperature is one of the most widely measured parameters within safety industry and science. In many applications, sensors are required, because of their immunity to electromagnetic interference, small in size, suitability for remoting and having lightweight. In addition, they allow operation in harsh environments to replace conventional electronic sensors due to their possibility of performing measurements in environments suffering from



© 2018 Copyright held by the author(s). Published by AIJR Publisher in Proceedings of First Conference for Engineering Sciences and Technology (CEST-2018), September 25-27, 2018, vol. 1.

This is an open access article under [Creative Commons Attribution-NonCommercial 4.0 International](https://creativecommons.org/licenses/by-nc/4.0/) (CC BY-NC 4.0) license, which permits any non-commercial use, distribution, adaptation, and reproduction in any medium, as long as the original work is properly cited. ISBN: 978-81-936820-5-0

electromagnetic disturbance, or in environments where electronics cannot survive. Fiber optic sensors can survive offer an excellent solution to many of these challenges. Different fiber optic sensor techniques have been designed and many researches are focused on developing reliable and cost-effective fiber temperature sensors. In this work, we first describes Fabry-Perot interferometer temperature sensor that uses a reflective etalon. The etalon's optical path difference (OPD) is a temperature dependent. This is due, primarily, to the dependence of its refractive index to the temperature variations. The sensed temperature can then be determined from the positions of the minima in the sensor's output spectrum by several simple types of spectrum analyzers, other type of sensing devices that use power coupling loss between two fibers to determine the temperature, will be described next. The designed fiber-optic temperature sensors would be used highly in high power generation rooms.

2 Materials and Methods

2.1 Fabry-Perot Interferometer

Basically, the Fabry-Perot temperature sensor (FPI) is a thin platelet of a material that has a temperature-dependent refractive index [1]. It is composed of two parallel reflecting surfaces separated by a certain distance called etalon and are classified into two categories: one is extrinsic and the other is intrinsic [2], [3]. The extrinsic FPI sensor uses the reflections from an external cavity formed out of the interesting fiber [4]. Figure 1 (a) shows an extrinsic FPI sensor, in which the air cavity is formed by a supporting structure. Since it can utilize high reflecting mirrors, the temperature-sensitive interferometer is constructed from thin films that are deposited directly onto the end of an optical fiber [5]. In other sense, when the cavity material is not the fiber itself, it is called extrinsic and it is shown in Figure 1 (b). Figure 2 shows a more detailed Fiber-optic temperature sensor using a thin-film Fabry-Perot interferometer.

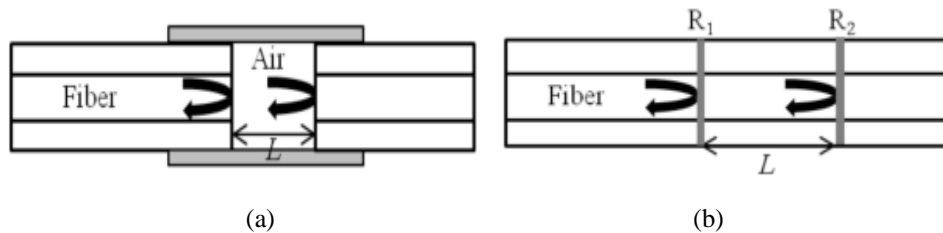


Figure 1: (a) Extrinsic FPI sensor made by forming an external air cavity, and (b) intrinsic FPI sensor formed by two reflecting components, R1 and R2, along a fiber.

2.2 Fiber Coupling Actuated by a Bimetal Strip

Coupling based intensity modulated fiber-optic sensors can be configured in basically two ways: either in a reflective arrangement as shown in Figure 3 (a), or in a transmissive arrangement, using straightforward transmission from one fiber to the other, as in Figure 3 (b).

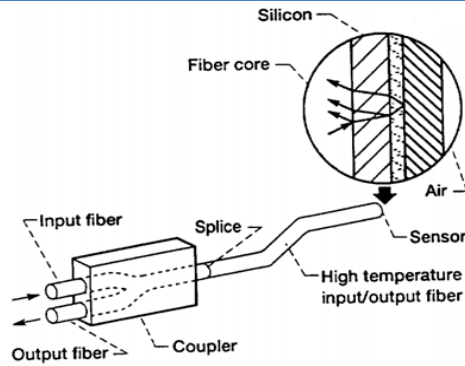


Figure 2: Fiber-optic temperature sensor using a thin-film Fabry-Perot interferometer.

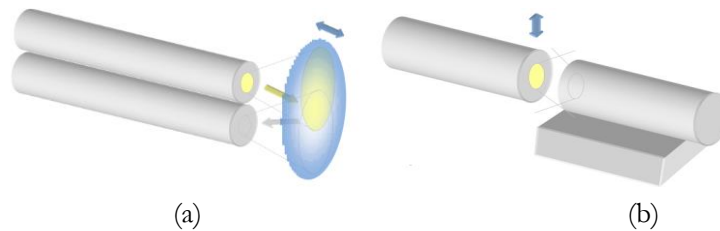


Figure 3: (a) Schematic view of a coupling based intensity modulated fiber-optic sensor using a reflective configuration (b) using a transmissive configuration.

The bimetal strip Consists of different metals expand at different rates as they warm up, behave in different manner when exposed to temperature variation owing to their different thermal expansion rates. One end of straight bimetallic strip is fixed in place as the strip is heated the other end tends to curve away from, the side that has the greater coefficient of linear expansion as shown in Figure 4.

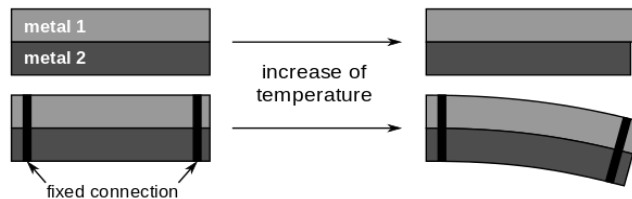


Figure 4: Shows the bimetal strip.

This part should contain sufficient detail to reproduce reported data. It can be divided into subsections if several methods are described. Methods already published should be indicated by a reference [4], only relevant modifications should be described.

3 Theory and Calculation

3.1 Fabry-Perot Interferometer

Here, the interferometer’s optical path difference (OPD) is given by:

$$\Lambda_{OPD} = 2n_1L \cos \theta_1 \quad (1)$$

And:

$$\Phi = \frac{2\pi}{\lambda} \Lambda_{OPD} \quad (2)$$

As shown if the length, L , of the cavity increases the phase shift, Φ , between two reflected light increases as well as refractive index of the material n_1 . the reflectivity can be rewritten as:

$$R_F = \frac{F \sin^2 \Phi}{1 + F \sin^2 \Phi} \quad (3)$$

Where:

$$F = \frac{4R}{(1 - R)^2} \quad (4)$$

With:

$$R = \frac{(n_1 - n_2)^2}{(n_1 + n_2)^2} \quad (5)$$

The transmissivity of the ideal Fabry-Perot interferometer is given by:

$$T_F = \frac{1}{1 + F \sin^2 \Phi} \quad (6)$$

As expected, for zero loss, $T_F + R_F = 1$, Figure 5 shows that for (GaAs) for designed length as function of (Φ) [7].

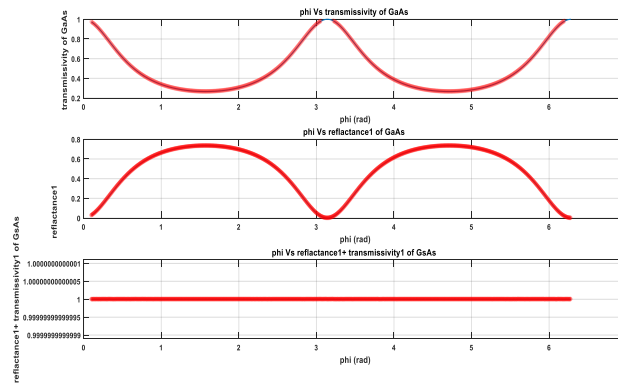


Figure 5: (Reflectance + Transmissivity) GaAs for designed length as function of (Φ) .

3.2 Fiber Coupling Actuated by a Bimetal Strip

The temperature dependent deflection δ of a bimetal strip clamped at one end is given by:

$$\delta = \alpha_d \cdot (T - T_0) \frac{L_0^2}{t} \quad (7)$$

Where α_d is the specific deflection, T represents the variable the temperature, L_0 is the free strip length at room temperature T_0 and t represents the strip thickness. For a fiber sensor configuration according to Figure 6

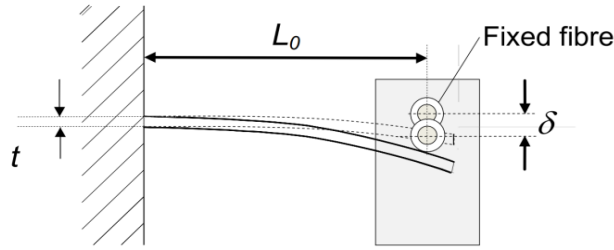


Figure 6: Temperature sensor operation principle.

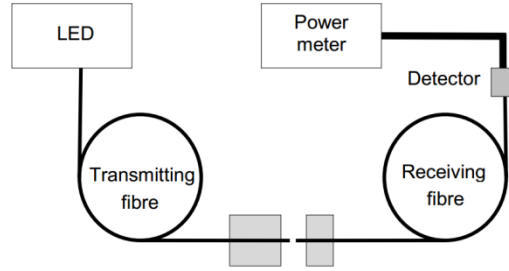


Figure 7: Temperature sensor operation principle.

In the linear temperature region of the bimetal strip , the deflection can be counted from any reference temperature T_0 , which means that the reference temperature could be chosen when the moveable fiber has a zero offset to the fixed fiber . The coupled power P between two fibers as a function of temperature T [8], can thus be written as:

$$P(T) = P_0 \cdot e^{-k(T-T_0)^2} \quad (8)$$

A Theory section should extend, not repeat, the background to the article already dealt with in the Introduction and lay the foundation for further work. In contrast, a Calculation section represents a practical development from a theoretical basis.

4 Results and Discussion

4.1 Fabry-Perot Interferometer

The design consists of the selection of a material (GaAs, Ge, Si) and the determination of the optimum thickness at for the Libyan environment range, the interferometer's reflectance is minimized at resonance, or $\Phi = \pi m$, where m is an integer. For the ideal Fabry-Perot interferometer, the minimum reflectance $[R_F]_{\min} = 0$. In terms of wavelength, the resonance condition is at $\lambda = \lambda_m$ where:

$$m\lambda_m = \Lambda_{OPD} \quad (9)$$

The maximum reflectance, which occurs at $\Phi = \pi(m+1/2)$ and is given by:

$$[R_F]_{\max} = \frac{F}{1 + F} \quad (10)$$

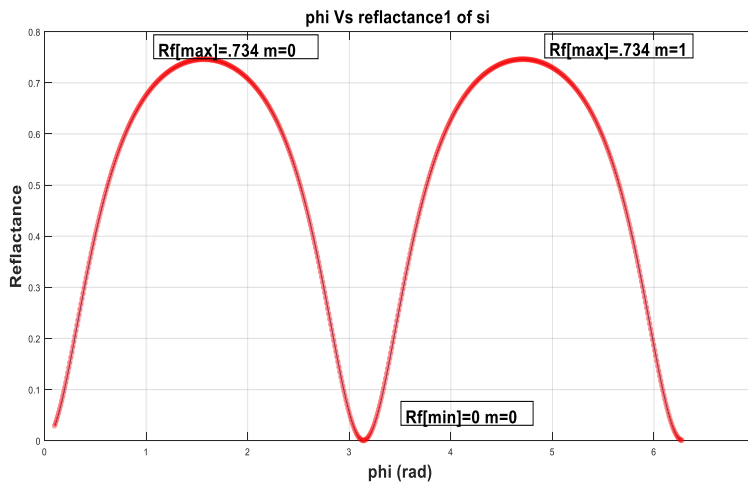


Figure 8: Shows the reflectance of (GaAs) for designed length (20.7 μm).

The maximum reflectance obtained for the designed length, $L=20.7 \mu\text{m}$, is equal 0.734, for the integers $m=0, 1, 2$ as shown in Figure 8. The phase sensitivity is obtained by differentiating equation (3), which gives:

$$\frac{dR_F}{d\Phi} = \frac{F \sin 2\Phi}{(1 + F \sin^2 \Phi)^2} \quad (11)$$

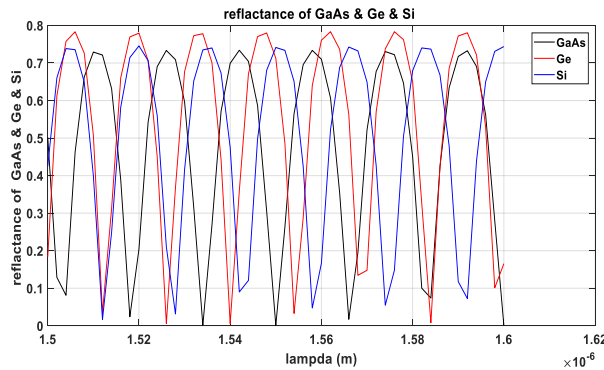


Figure 9: Comparison of phase sensitivity of (GaAs) & (Ge) & (Si) as function of (λ).

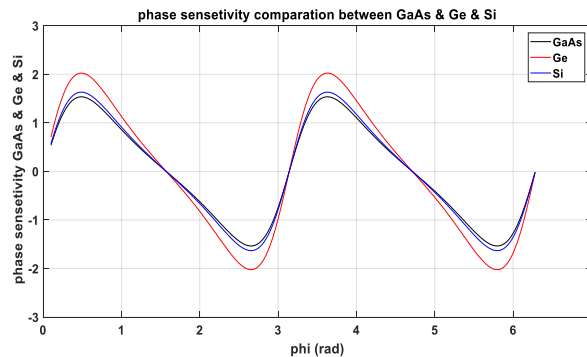


Figure 10: Comparison of phase sensitivity of (GaAs) & (Ge) & (Si) as function of Φ .

The temperature sensitivity of the Fabry-Perot's phase shift is given by:

$$\frac{d\Phi}{dT} = \pi \frac{\Delta_{OPD}}{\lambda} \kappa_{\Phi} \quad (12)$$

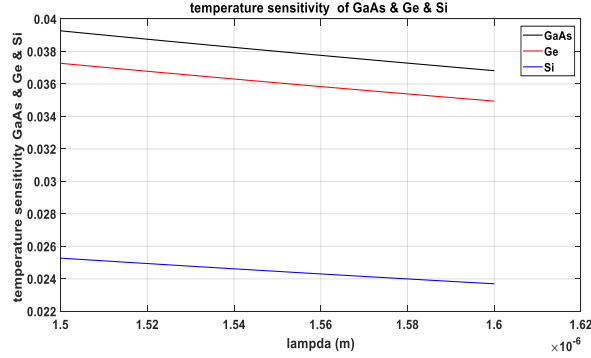


Figure 11: Comparison of temperature sensitivity of the Fabry-Perot's phase shift of (GaAs) & (Ge) & (Si) as function of λ and $L=20.7\mu\text{m}$.

By integrating both sides $\int d\Phi = \int \pi \frac{\Delta_{OPD}}{\lambda} \kappa_{\Phi} \cdot dT, \Phi = \pi \frac{\Delta_{OPD}}{\lambda} \kappa_{\Phi} \cdot T$

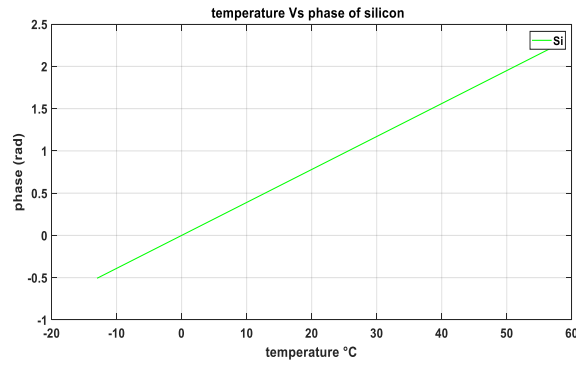


Figure 12: Phase vs. Temperature.

Where:

$$\kappa_{\Phi} = \kappa_n + \kappa_L \quad (13)$$

Here, κ_n is the thermo-optic coefficient

$$\kappa_n = \frac{1}{n_1} \frac{dn_1}{dT} \quad (14)$$

And κ_L is the thermal expansion coefficient,

$$\kappa_L = \frac{1}{L} \frac{dL}{dT} \quad (15)$$

The temperature sensitivity of the Fabry-Perot's reflectance can be determined by substituting from equations (11) and (12) into:

$$\frac{dR_F}{dT} = \left(\frac{dR_F}{d\Phi} \right) \left(\frac{d\Phi}{dT} \right) \quad (16)$$

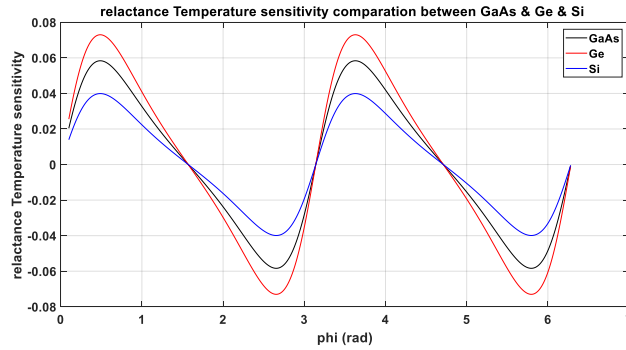


Figure 13: Comparison of temperature sensitivity of the Fabry-Perot’s reflectance of (GaAs) & (Ge) & (Si) as function of(Φ).

(Ge) gave us best results for temperature sensitivity of the Fabry-Perot’s reflectance because it has the largest refractive index [7].

4.2 Selection of Temperature Sensitive Material

G. Beheim has previously summarized a comparison of candidate materials for a thin-film temperature sensor. The temperature sensitivity of various candidate materials requires that sensitivity figure-of-merit be independent of the film thickness, Table1 tabulates the candidate materials in descending order of κ_{Φ} . This table provides n , κ_n , and κ_L , together with the wavelengths at which the optical properties were measured, all data.

Table 1: Properties of candidate Fabry-Perot materials. Units of κ_n , κ_L , and κ_{Φ} are $10^{-6}/0C$.

<i>Material</i>	λ (μm)	n	κ_n	κ_L	κ_{Φ}
<i>GaAs</i>	0.9	3.6[7]	120[7]	5.7[5]	126
<i>Ge</i>	2.55	4.06[7]	100[7]	5.7[7]	106
<i>Si</i>	2.5	3.44	46[7]	2.6[7]	
	1.5	3.5	53[7]		
	1.26	3.51[7]	59[7]		
	0.78	3.695[7]	76[7]		79

So the temperature induced phase change is almost entirely caused by the change in refractive index. Of the three materials with the largest values of κ_{Φ} , silicon is best suited for this range application and available almost everywhere, however, it is highly absorbing at the emission wavelengths of AlGaAs LEDs. At 830nm, the absorption coefficient of germanium is $4.5 \times 10^4 \text{ cm}^{-1}$, so that transmission through 1 μm produces a 20-dB loss. At 1.3 μm , is much lower, $0.68 \times 10^4 \text{ cm}^{-1}$, but this wavelength is outside the range of inexpensive silicon photodiodes, Silicon is preferred to germanium for this application, because its absorption coefficient is much lower at the AlGaAs emission wavelengths. At 830nm, $\alpha = 0.19 \times 10^4 \text{ cm}^{-1}$, which causes a 17% absorption in 1.0 μm [6].

4.3 Determination of Fabry-Perot Sensor's Thickness

For a typical AlGaAs's LED we can choose any LED, $\frac{\Delta\lambda_{LED}}{\lambda_m} \geq \frac{\lambda_m}{2\Lambda_{OPD}}$, $\Lambda_{OPD} = m \times \lambda_m$, $\lambda=1550\text{nm}$ and $\Delta\lambda_{LED}= 40\text{nm}$, which gives $m \geq 19.3$. For silicon, this corresponds to $L1 \geq 4 \mu\text{m}$.

$$m \leq \frac{1}{\kappa_{\Phi}(T_{\max}-T_{\min})} \quad (17)$$

For a silicon sensor with a -13 to 57.80 °C.

$$\Lambda_{OPD}/\lambda_m \leq \frac{1}{79 \times 10^{-6}(57.8 - (-13))} = \frac{2 \times 3.695 \times L \times \cos(3.1)}{1550 \times 10^{-9}} \leq \frac{1}{79 \times 10^{-6}(57.8 - (-13))}$$

$$L \leq \frac{1550 \times 10^{-9}}{2 \times 3.695 \times \cos(3.1) \times 79 \times 10^{-6}(57.8 - (-13))} = 37.55 \mu\text{m}, \text{ must be less than } 178.7 \mu\text{m}, \text{ which gives}$$

$L < 37.55 \mu\text{m}$. In this case we chose $L1 = 20.7 \mu\text{m}$, so that $L1$ is within the above limiting cases so the optimization length is $20.7 \mu\text{m}$.

4.4 Fiber Coupling Actuated by a Bimetal Strip

First we should measure P_0 , the coupled power, at temperature T_0 , i.e., at zero offset (deflection), the moveable fiber at zero position, the design factor k is given by :

$$k = \left(\frac{\alpha_d}{w} \cdot \frac{L_0^2}{t} \right)^2 \quad (18)$$

where w is the characteristic radius of the modulation function of the sensor and typically $25 \mu\text{m}$, the temperature dependent loss A of the sensor, quoted in decibels (dB), can be derived as

$$A(T) = 10 \cdot \log \frac{p(T_0)}{p(T)} = K \cdot (T - T_0)^2 \quad (19)$$

Using equations (18) and (19) the design constant K can be written as:

$$K = \left(\frac{\alpha_d}{w} \cdot \frac{L_0^2}{t} \right)^2 \cdot 10 \log e \quad (20)$$

Using formulas (7), (19) and (20) a temperature sensor for any temperature range in the linear region of the bimetal can be designed, The sensitivity of such a sensor can be adjusted by choosing a suitable bimetal (parameters α_d and t) and by adjusting the free strip length L_0 , T_0 should therefore be chosen to be a bit lower than the minimum temperature T_{\min} to be measured, or a bit larger than the maximum temperature T_{\max} also to be measured. The deflection range Δ is given by:

$$\Delta = \delta_m - \delta_{\min} = \frac{\alpha_d L_0^2}{t} \cdot (T_{\max} - T_{\min}) \quad (21)$$

Where δ_m is the desired maximum deflection and T_{\max} and T_{\min} are the maximum and minimum temperatures of the measurement range, corresponding to the desired deflection

range. From equation (21) the fiber position L_0 can be calculated, and using this value together with $\delta = \delta_{\min}$ and $T = T_{\min}$, equation (7) gives the zero deflection temperature T_0 for the right slope of the modulation curve. First we take three material with linear range that can measure our Libyan environment with specific deflection (20.8×10^{-6} , 13.9×10^{-6} , 10×10^{-6}), as shown in Table 2. In designing and calculating sensor's parameters we take the larger deflection range to increase the sensitivity, this is because our temperature range is large.

Table 2: Some details of standard bimetal types

Thermostatic Bimetal type DIN designation added	Specific deflection [$10^{-6} K^{-1}$]	Specific curvature [$10^{-6} K^{-1}$]	Linearity range [$^{\circ}C$]	Max operating temperature [$^{\circ}C$]	Resistivity [$\Omega mm^2 m^{-1}$] at temperature $^{\circ}C$						Thermal conductivity [$Wm^{-1} ^{\circ}C^{-1}$]	Modulus of elasticity [$10^3 N mm^{-2}$]		Standard hardness [HV]		Density [$g cm^{-3}$]
					0	20	100	200	300	400		low exp. side	high exp. side			
230	22.7	43.0	-20-+230	330	1.04	1.05	1.15	1.22	1.28		6	135	210	200	7.8	
200	TB20110	20.8	-20-+175	330	1.09	1.10	1.20	1.27	1.33		6	135	210	250	7.8	
155	TB1577A	15.6	-20-+250	450	0.77	0.78	0.86	0.94	1.00	1.07	13	170	210	260	8.1	
145		14.8	-20-+250	450	0.78	0.79	0.85	0.93	0.99	1.06	12	170	210	240	8.1	
135		13.9	-20-+200	450	0.78	0.79	0.85	0.93	0.99	1.06	12	170	210	240	8.1	
130		13.2	-20-+325	450	0.72	0.74	0.82	0.89	0.95	1.02	12	170	210	240	8.1	
115	TB1170	11.7	-20-+380	450	0.68	0.70	0.78	0.86	0.93	0.99	13	170	210	240	8.1	
100	TB0965	10.0	-20-+425	450	0.62	0.65	0.75	0.86	0.94	1.00	15	175	210	240	8.2	
94S		9.5	-0-+200	450	0.84	0.85	0.90	0.95			12	190	210	250	8.1	
60		6.0	-20-+450	450	0.19	0.21	0.28	0.37	0.47	0.59	44	190	230	240	8.0	
50HT		5.0	-20-+500	550	0.635	0.66	0.72	0.78	0.83		20	200	240	340	7.8	

Table 3: Bimetal data and calculated sensor design parameters for minimum deflection = 5 μm , $T_{\min} = -13 ^{\circ}C$ and $T_{\max} = 57.8 ^{\circ}C$ using a fiber coupling with a typical characteristic radius of $w = 25 \mu m$.

Type	α_d ($10^{-4} K^{-1}$)	r (mm)	Δ (μm)	L_0 (mm)	T_0 ($^{\circ}C$)	K ($10^{-3} dB K^{-1}$)	$A(T_{\min})$ ($10^{-2} dB$)	$A(T_{\max})$ (dB)
200	20.8	1.3	20	4.2	-15	0.55	2.2	2.938
			25	4.7	-18	0.86	21.7	4.978
			35	5.6	-20	1.7	83.2	10.278
			40	5.9	60	2.2	11819.6	.0107
135	13.9	0.8	20	4	-15	0.55	2.2	2.938
			25	4.5	-18	0.86	21.7	4.978
			35	5.3	-20	1.7	83.2	10.278
100	10	1.0	10	5.3	-15	0.55	2.2	2.938
			16	5.9	-18	.86	21.7	4.978
			25	7	-20	1.7	83.2	10.278

The sensitivity of the sensor in terms of the loss change in dB per temperature degree is given by the derivative of:

$$s(T) = \frac{d(A)}{d(T)} = 2 \cdot K \cdot (T - T_0) \tag{22}$$

By integrate both sides $\int d(A) = \int 2KTd(T) - \int 2KT_0d(T)$

$A = KT^2 - 2KT_0T$. Fig.14 shows the sensitivity versus the temperature at different deltas, whereas the comparison between the two devices is shown in Fig. 15.

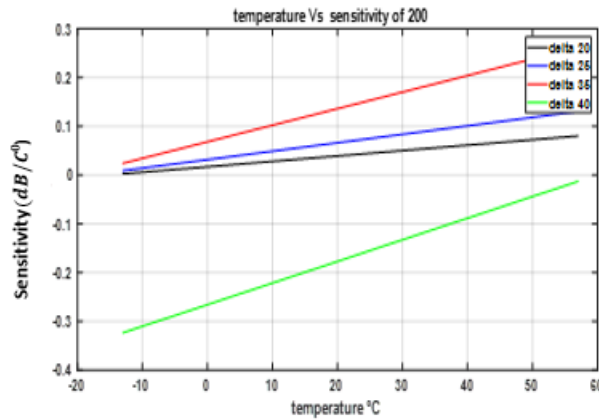


Figure 14: Sensitivity as a function of temperature for the sensor designs based on type200 bimetal listed in Table 3.

Table 3 shows the different material and the different design parameters, where the best design parameters obtained are at length of 5.6 mm and at $\Delta=35\mu\text{m}$.

Clearly, Fabry-Perot technique sensor is more accurate than Intensity-type Fiber Optic Sensor, because the Fabry-Perot changing linearly with phase of silicon, so it is more suitable for our design purpose in the desired range of measurements than the other one.

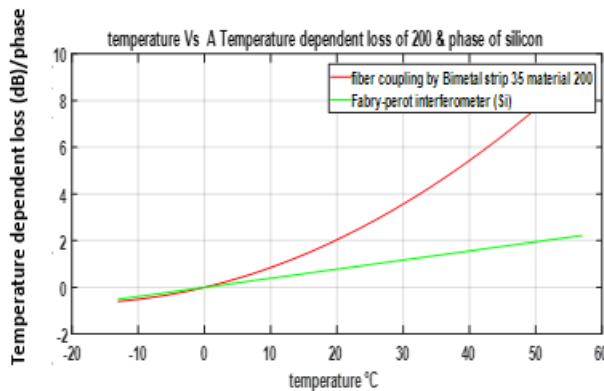


Figure 15: Comparison between two devices.

5 Conclusions

Two different types of fiber optic temperature sensors have been designed and studied. The two sensors were specially designed to be able to measure the temperature range (-13 °C to 57.8 °C) that is well suited for Libyan environment. These types of fiber optics sensor are usually used in high power generators rooms, where the explosion risk factor is very high with

the using of regular electric sensors. The first device is based on the Fabry-Perot interferometer with the material of silicon. The optimum designed length obtained is 20.7 μm for the operating wavelength of 1550nm. The second device designed is based on fiber coupling actuated by a bimetal strip. The designed length, delta deflection and thickness for the strip were found to be 5.6 μm , 35 μm and 1.3 μm respectively.

From the simulation results, it is clear that the Fabry-Perot temperature sensor of silicon material changes linearly with phase while the sensor based fiber coupling by bimetal strip is not changing linearly with power loss, which would give less measuring accuracy and it is also more difficult to calibrate, however, it is more cheaper than Fabry-Perot sensor.

References

- [1] G. Beheim, "Fiber-Optic Thermometer Using Semiconductor-Etalon Sensor," *Electron. Lett.* 22, 238-239 (1985).
- [2] Fabry-Pérot Interferometer. Available online:
http://en.wikipedia.org/wiki/Fabry%E2%80%93P%C3%A9rot_interferometer,22/8/2017.
- [3] K. Kyuma, S. Tai, T. Sawada and M. Nunoshita, "Fiber-Optic Instrument for Temperature Measurement," *IEEE J. Quantum Electron.* QE-18, 676 (1982).
- [4] Kim, S.H.; Lee, J.J., Lee, D.C., Kwon, I.B. A study on the development of transmission-type extrinsic Fabry-Perot interferometric optical fiber sensor. *J. Lightw. Technol.* 1999, 17, 1869-1874.
- [5] L. Schultheis, H. Amstutz, and M. Kaufmann, "Fiber-Optic Temperature Sensing With Ultrathin Silicon Etalons," *Opt. Lett.* 13, 782 (1988).
- [6] Fu, H.Y.; Tam, H.Y.; Shao, L.Y.; Dong, X.; Wai, P.K.A.; Lu, C.; Khijwania, S.K. Pressure sensor realized with polarization-maintaining photonic crystal fiber-based Sagnac interferometer. *Appl. Opt.* 2008, 47, 2835-2839.
- [7] Glenn Beheim, *Fiber-Optic Temperature Sensor Using a Thin-film Fabry-Perot Interferometer*, Ph.D. thesis, Case Western Reserve University, Cleveland, Ohio, May 1996.
- [8] Johan Jason, "Theory and Applications of Coupling Based Intensity Modulated Fibre-Optic Sensors", Mid Sweden University, 2008.

Employing Various Data Mining Techniques to Forecast the Success Rate of Information Technology Education Students

Mosbah Mohamed Elssaedi

Department of Computer Science, Faculty of Science, Sirte University - Libya

DOI: <https://doi.org/10.21467/proceedings.2.2>

* Corresponding author email: mosbah_us@hotmail.com

ABSTRACT

This study was designed to investigate the factors that affect the success rate of Information Technology Education students which composed of Computer Science and Information Technology. Several variables such as years of graduation, entrance exams, and other variables have been used for the investigation. Several data mining techniques such as linear regression, neural network, and decision tree have employed to determine the valid predictors and acceptability of the data mining technique. The results show that the best predictor taken from the entrance exams is non-verbal ability while the best forecasting using data mining is decision tree analysis with 99.19 percent accuracy. If the results taken from the system will be incorporated in entrance examinations results, admission office will be able to identify students that can graduate on-time and whose students should be taken as probationary in the program. It can also identify students not to be taken in the program to avoid waste of time in studying at the University.

Keyword— Neural network, linear regression, decision tree, forecasting, data mining.

1 Introduction

Technology is the application of scientific knowledge for practical purposes especially in industry, engineering and applied sciences. Technology can be used at work to extract materials, transportation, learning, manufacturing, creating artefacts, securing data, scaling business and more [1]. The benefits of technology in education have been a gateway to the new learning environment. Assistive technology that helps children with special needs such as an e-reader, adaptive voice software are a few good examples. The use of computers and innovation in classrooms has opened up an entirely new system for showing and successful learning. Computers generate huge amounts of information and can benefit the field of education, like helping students learn faster or make learning more interesting to some extent. With technology's rapid development, no surprise that there is an abundant of courses related to technology that is offered by different university worldwide.

The major problem is that at there is a big percentage of the unemployed with an average of 17% of college graduate came from Bachelor of Science in Computer Science and Bachelor of Science in Information Technology [2]. This sort of measurement is disturbing; it implies



© 2018 Copyright held by the author(s). Published by AIJR Publisher in Proceedings of First Conference for Engineering Sciences and Technology (CEST-2018), September 25-27, 2018, vol. 1.

This is an open access article under [Creative Commons Attribution-NonCommercial 4.0 International](https://creativecommons.org/licenses/by-nc/4.0/) (CC BY-NC 4.0) license, which permits any non-commercial use, distribution, adaptation, and reproduction in any medium, as long as the original work is properly cited. ISBN: 978-81-936820-5-0

that colleges are delivering graduates with lacking abilities with the connection to Computer Science and IT which add to the unemployment rate. National development is every nation's goal throughout the world. A country is seen to be developed when underemployment and unemployment rates decrease if not eliminated. One of the probable reasons for this is the mismatch between education and employment.

Admission Examination or University Entrance Examination is believed to help students to select an appropriate course in college matching their aptitude and maintains a quality of education thereby, bringing national development in the country. Among the objectives of the creation of admission, examinations are to minimize aimless wastage of labour and different assets which generally could be coordinated towards more beneficial endeavours. It also assesses the capabilities and skills the students develop in their early studies which are necessary to be successful in college or even becoming an entrepreneur [3]. It can be very beneficial for students if followed but many students choose to deviate from the recommendations made by Admission by choosing another program in college. The huge amount of information and data, when analyzed can help in decision making and help to create a model that determines the success rate of Computer Science and IT student deviating their admission exams results using data mining. Data mining uses sophisticated mathematical algorithms to segment the data and evaluate the probability of future events and outputs useful information while reducing the quantity of data [4]. This study aims to develop a model that determines the success rate of computer science and IT student that deviated from a recommendation from Admission result. Furthermore, to find out the field of interest that should be improved to pass computer science or IT degree and help the academe reduce drop-outs and shifters of the program offered.

This study was designed to investigate the factors that affect the success rate of Computer Science and IT student that deviates from the recommendation of admission examination. It will also correlate to the abilities of students in the result of admission examinations to the date of graduation of Computer Science and IT students and to develop a model that determines the success rate of students. Specifically the research will be guided by the following questions: what are the predictors to be considered to determine the success rate of Computer Science and IT student that deviate from the recommendation of admission examinations?, what are the correlations of the predictors in passing On – Time the Computer Science degree? and what are the data mining techniques and algorithms will be used in the forecasting model?

2 Related Literature

Career assessment is the first step in career planning. Admission Test or College Entrance Examination is one of the career assessments given by the any University to entrants students. There is a study that aims student's performance base on information's like attendance, class test, name, age, course, and topographic location or address. In this research, they used the classification method of data mining using a decision tree. A forecasting system model was

developed in a study in which the main goal is to analyze the learning behaviour of the higher education students[5]. They used the decision tree, a popular classification method of data mining that results in a flowchart-like a tree structure where each node denotes a test on an attribute value. Another forecasting system model was developed which the main goal is to understand student data such as name, age, address, student's grades and course for career selection and job absorption rate after graduation[6]. There is research that finds out whether natural talents and interest of 116 students based on admission exams result match the program that the students have enrolled in. In this study, the researcher employed a qualitative research design. There are eight potentials/inclinations of students measured: scientific ability, reading comprehension, verbal ability, mathematical ability, clerical ability, manipulative skills, nonverbal ability and entrepreneurial skills[7]. In the conducted study, the results show that the respondents have varied occupational interest based on an admission exam. Based on this research, most of the respondents choose not to enrol in the program that matches respondent's field of interest that leads to the respondent's failure on some of the respondent's subject while the respondents that enrol in the program that matches the respondent's field of interest were seen to have become successful.

3 Methods

In building the forecasting model, student data such as admission examination field of interest, occupational Interests and the student's date of graduation were used to find the relationship by feeding to the data mining analyzing tool. The data sets that were used to develop the forecasting model are the records of these students of Computer Science and IT degree. The data of Computer Science and IT student batch 2011–2015 served as the training data of the forecasting model and the Computer Science student batch 2016 served as the test data that evaluate the model. The data used were combined data from the admission office of one University in the Philippines and compared to the data of Sirte University. The data was labelled according to the data to conform with Sirte University. Rapidminer, a data mining tool is used to process data and create a forecasting model. Certain algorithms are used in creating the forecasting model and to find out the best ability in admission exams that best affect the performance of the Computer Science and IT students.

Descriptive Correlation. The correlation measures the strength and direction of a linear relationship between two variables. The value correlation is always between +1 and -1. The following are an interpretation of values in correlation:

- Exactly -1. A perfect downhill linear relationship.
- - 0.70. A strong downhill linear relationship.
- - 0.50. A moderate downhill linear relationship.
- - 0.30. A weak downhill linear relationship.
- 0. No linear relationship.
- + 0.30. A weak uphill linear relationship.
- + 0.50. A moderate uphill linear relationship

- + 0.70. A strong uphill linear relationship.
- Exactly +1. A perfect uphill linear relationship.

3.1 Conceptual Framework

A conceptual framework was used by the researchers to outline the courses of action or to present a preferred approach to the developed system. As shown in Figure 1, there are five phases in the proposed forecasting model:

1. *Data Gathering* – this is the first phase of the model where data such as the admission examination result were extracted which contains the different fields of interest, the occupational interest of the student and the student graduation date. This data will be saved in the repository.
2. *Data Pre-Processing* – the second phase of the model this is where the data cleansing, estimating of missing values and normalization of database takes place.
3. *Modelling* – the third phase of the model is where the building of the model takes place. The data mining tool will analyze all the data and outputs all data mining algorithms results for each technique.
4. *Determine the Success Rate* – the fourth phase of the model is the entry point of the test data to evaluate the model's accuracy.
5. *Result* – the last phase of the model is where the output will be displayed in a dashboard which is the success rate of computer science and IT students that deviates from the admission results.

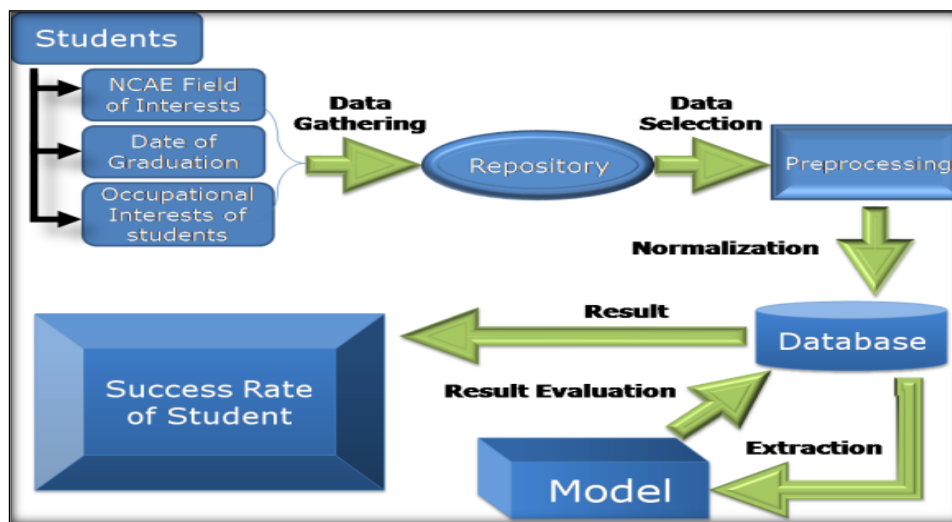


Figure 1: Phases of the model

4 Results and Analysis

4.1 Predictors for Success Rate

The variables used in the study are the data of Computer Science and IT students from the school year 2011–2015 with 368. The data set is put in the outlier detection to minimize the noise of the actual datasets and to increase the accuracy of the forecasting model before measuring the significance of each predictor.

Table 1: *Predictors and variables*

Dependent Variable	Independent Variable	Optimize Selection
Date of graduation	Clerical Ability	Clerical Ability
	Nonverbal ability	Nonverbal ability
	Scientific Ability	Scientific Ability
	Mathematical Ability	Mathematical Ability
	Manipulative skills	Manipulative skills
	Verbal ability	Reading Comprehension
	Reading Comprehension	Entrepreneurial Skills
	Entrepreneurial Skills	

Table 1 shows the predictors and the variables used in the study. The researcher used the date of graduation of the students as the dependent variable because the student's date of graduation defines if the student is successful in the course that the students take during college. After the detection of outliers, the researchers used the optimize selection operator in RapidMiner. It selects the most relevant attributes of the given datasets. Two deterministic greedy feature selection algorithms (forward selection and backward elimination) are used for feature selection. It eliminated the Verbal Ability using backward elimination from the seven dependent variables.

4.2 Correlation of Predictors to Graduate On-Time in Computer Science Degree

The researchers used the correlation of RapidMiner to measure the relationship and strengths of the variables after feeding and using correlation in the tool. Table 2 shows the correlation between On-Time graduations of a student with Abilities extracted from admission exams. The scientific ability has a moderate uphill linear relationship with On-Time graduations of Computer Science and IT student with 0.430, meaning it has a moderate effect on the success rate of passing the degree. Table 3 shows that the most important ability in admission exam to pass Computer Science and IT program is the Non Verbal Ability.

4.3 Data Mining Techniques and Algorithms

The researcher used three data mining techniques and compared each result to find out what are the best data mining techniques that best suits the data sets that the researchers gathered namely regression, neural network, and decision tree analysis.

4.3.1 Regression

The researcher used linear regression to be able to forecast the success rate of computer science student in passing the computer science degree using the abilities presenting NCAE. After applying the model to the RapidMiner tool, the researcher came up and produced the following output:

Table 2: Correlation predictors

First Attribute	SecondAttribute	Correlation
On-Time	ScientificAbility	0.430
On-Time	Manipulative Ability	0.057
On-Time	VerbalAbility	0.034
On-Time	NonVerbalAbility	1
On-Time	ReadingComprehension	0.024
On-Time	ClericalAbility	0
On-Time	MathematicalAbility	0.172
On-Time	EntrepreneurialSkills	0.083

Table 3: Linear regression output

Attribute	Coefficient
Clerical Ability	-0.002
ScientificAbility	0.005
Non-VerbalAbility	0.031
MathematicalAbility	0.005
Intercept	-2.383

Table 3 was the result after using the linear regression from the RapidMiner tool, the coefficients are used for Linear Regression Model which is:

$$Y = -2.383 + (-0.002) (\text{Clerical Ability}) + (0.005) (\text{Scientific Ability}) + (0.031) (\text{Non Verbal Ability}) + (0.005) (\text{Mathematical Ability})$$

To get the forecasted value, the intercept should be subtracted to the sum of products of abilities in admission exams to their respective coefficient values. If the value is equal to 1, the student will pass, and if it is 0, the student will not pass the CS degree.

4.3.2 Neutral Network

The researcher used a neural network for the next test and Table 4 shows the three layers under Multilayer Perception of the neural network. In able to map the following input, The researcher uses the predictors as the input layer or factors consists of Non-Verbal Ability, Clerical Ability, Mathematical Ability, Scientific Ability, Manipulative Skills, Verbal Ability, Reading Comprehension and Entrepreneurial skill. The hidden layer consists of Number of units, Number of Hidden Layers, Number of Units in the hidden layer, Activation Function, Dependent Variables and Number of Units. The last year or the output layer consists of Rescaling Method for Scale Dependents, Activation Function, and Error Function. The

neural network normalized the data and was used to map and get the input layer, hidden layer, and output layer. It was developed to measure the frequency of action potentials.

Table 4: *Neural network analysis*

Neural Network Information			
Network Information			
Input Layer	Factors	1	Non Verbal Ability
		2	Clerical Ability
		3	Mathematical Ability
		4	Scientific Ability
		5	Verbal Ability
		6	Manipulative Skill
		7	Reading Comprehension
		8	Entrepreneurial Skills
Number of Units		2913	
Hidden Layers	Number of Hidden Layers		1
	Number of Units Hidden Layers		7
	Activation Function		Hyperbolic Tangent
Output Layers	Dependent Variable		1 On-Time
	Number of units		
	Rescaling Method for Scale Dependents		Standardized
	Activation Function		Identity

4.3.3 Decision Tree Algorithm

Figure 2 shows the result of the decision tree using CHAID algorithm with the predictors are the child and the dependent variable was the parent. The researchers used a classification tree to classify the nodes of the predictors according to the data. The Node 0 which is Non Verbal ability is the highest factor or the best predictor to determine if the student will pass the Computer Science or IT degree. The node of the Non-Verbal Ability was the computed quantitative measurement of the data of graduates of computer science and IT program in the University.

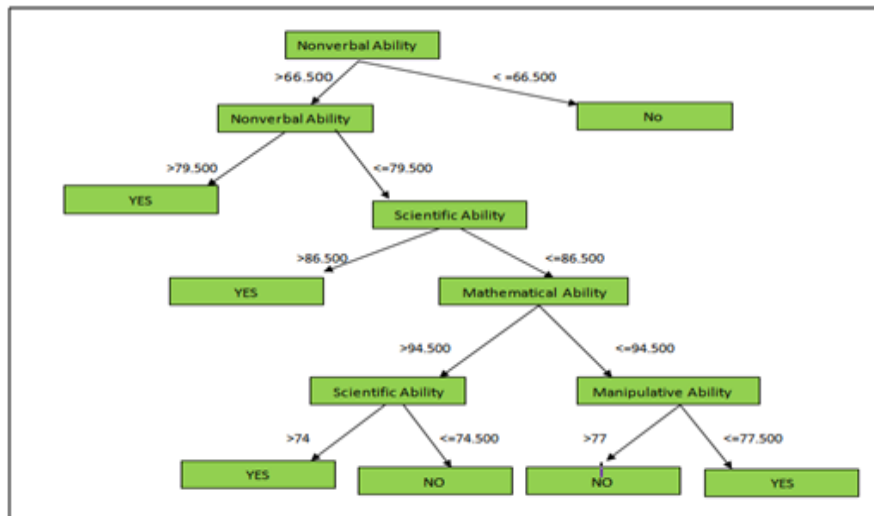


Figure 2: *Decision tree analysis*

4.4 Level of Acceptability of the Forecasting Model.

Accuracy or decision effectiveness is the main factors in evaluating a forecasting model[8]. The RapidMiner tool has a performance evaluator who can display the accuracy, precision, and area of the curve in each model created using the tool.

Table 5: Sample measure of forecasted result: linear regression

(A) Student	(B) Actual	(C) Forecasted	(D) (A-F) Error	(E) Error	(F) Error ²	[A/B] *100
A	1	1.078	-0.078	0.078	0.006	7.8
B	1	0.845	0.155	0.155	0.024	15.5
C	1	0.815	0.185	0.185	0.034	18.5
D	1	1.147	-0.147	0.147	0.021	14.7
E	1	1.076	-0.076	0.076	0.005	7.6
F	1	1.044	-0.044	0.044	0.001	4.4
G	0	0.4	-0.4	0.4	0.16	0
			%Error		8.81428%	
			Accuracy		91.18572%	

Table 5 shows the actual and forecasted value in the batch 2011 of Computer Science and IT student of the University, the percentage of error of student's actual value and the accuracy of the predicted value. The research used different measures such as MAD (|Error|) which weights all errors evenly, MSE (|Error|²) which weights errors according to their squared values, and MAPE (|Error|/Actual)*100 which weights according to relative error. The percent error computed is 8.81428%, almost equal to 91.18572%, which means that the result for the model is accurate and therefore the admission exams occupational interest was relative in the success rate of the students.

Table 6: Sample measure of forecasted result: decision tree

Student	AV	PV	CA	SA	MS	VA	NVA	RC	MA	EA
A	YES	YES	75	81	91	83	91	81	77	83
B	YES	YES	78	81	92	83	84	77	75	78
C	YES	YES	93	76	82	92	88	80	80	75
D	NO	NO	85	78	78	87	79	76	76	78
E	YES	YES	82	88	76	94	88	95	91	92
F	YES	YES	98	83	87	75	88	92	96	78
G	YES	YES	96	85	94	79	72	94	99	93
% error	123/124	=	0.81							
Accuracy	100-0.81	=	99.193%							

From the given table, the accuracy of decision tree mode is the difference of the percent error which is 0.81 and 100 percent as shown in Table 6. After solving the level of acceptability, the result is 99.193%, which means that the result for the decision tree was accurate and can be used as evidence of relevance to the study.

The accuracy of the neural network model is the difference of the percent error which is 3.225 and 100 percent. After solving the level of acceptability, the result is 96.774%, which means that the success rate of the students is valid with the help of admission exams occupational

interest. Based on the result and observations from the model together with data that was being gathered, here are the findings of the researcher.

Table 7: Sample measure of forecasted result: decision tree

Student	AV	PV	CA	SA	MS	VA	NVA	RC	MA	EA
A	YES	YES	75	81	91	83	91	81	77	83
B	YES	YES	78	81	92	83	84	77	75	78
C	YES	YES	93	76	82	92	88	80	80	75
D	YES	YES	82	88	76	94	88	95	91	92
E	YES	YES	98	83	87	75	88	92	96	78
F	NO	NO	85	78	78	87	79	76	76	78
G	YES	YES	96	85	94	79	72	94	99	93
% Error		120/124		=	3.225					
Accuracy		100-3.225		=	96.774%					

1. *Predictors that are considered to determine the success rate of Computer Science student from the recommendation of Admission Exams.* Based on the gathered data the predictors that are considered in predicting the success rate of Computer Science students are Non-Verbal Ability, Verbal Ability, Clerical Ability, Reading Comprehension, Manipulative Skills, Mathematical Ability, Scientific Ability and Entrepreneurial Skills. The abilities that are present in NCAE results are used as a dependent variable or the input to forecast the outcome or independent variable. The researcher used the date of graduation of Computer Science students as the independent variable because this will determine if the student is successful in the Computer Science degree if the student was able to finish the degree within four years, then the student is said to be successful.

2. *Relationship of the predictors in passing Computer Science degree.* The researcher used the RapidMiner tool to be able to find the value of correlation of the predictors to the success rate of Computer Science student. After feeding the data in the tool, the researcher found out that the Non-Verbal Ability is the best predictor to determine the success rate because it has a perfect linear relationship with the success rate of Computer Science student in passing the degree. Followed by the Scientific Ability which has a moderate uphill linear relationship with the success rate.

3. *Data mining techniques and algorithms that were used in the forecasting model.* The data mining techniques that were used by the researcher during the study are Linear Regression, Neutral Network, and Decision Tree. Linear regression estimates the value of the target as a function of the predictors for each case. The neutral network which consists of an interconnected group of artificial neurons, and it process information using a connectionist approach to computation. Decision tree shows how one choice leads to the next, and the use of branches shows that every alternative or option is mutually exclusive. The researcher used the different measures such as MAD($|\text{Error}|$) which weights all errors evenly, MSE($|\text{Error}|$) which weights errors according to their squared values, and Physical Education [$|\text{Error}|/\text{Actual}$]*100 which weights according to relative error. The researcher used Physical Education or Linear

Regression; the researchers found out that physical education is the most popular aggregate measure of forecasting accuracy. The percent error computed is 8.81428% or equal to 91.18572% accurate. For the remaining models which are the neural network and decision tree, the researcher used the performance evaluator of Rapid miter. The neural network got an accuracy of 96.774% while the decision tree got an accuracy of 99.193%.

5 Conclusion and Recommendation

1. The proposed study could be a great help to the Admission Office or Registrar of the University students in enhancing their basic forecasting skills especially using Data Mining.
2. The researcher considered that the forecasting model that was made efficient if it will be used to determine the success rate of Computer Science and IT student in passing the degree.
3. There is a significant relationship between the date of graduation of Computer Science and IT student and predictors in forecasting the success rate of the students in passing the Computer Science degree.

The researcher recommends that there should be a separate section for students that have a low score on Non-verbal ability to give more attention or supervision in teaching them because these students have a high chance in failing the Computer Science degree.

References

- [1] Fildes, R. and Kourentzes, N. (2010). Validation and Forecasting Accuracy in Models of Climate Change.
- [2] Ramey. (2012). Use of Technology.
- [3] Mallorca, R. (2008). Student's Natural Aptitudes and the Required Skills in their Chosen Program."
- [4] Gupta, S., Adhay Bnasal, and Retish Rastogi. (2012). Learning Behaviour of Analysis of Higher Studies Using Data Mining.
- [5] Saurab Pal. (2012). "Mining Educational Data to Reduce Drop-out Rates of Engineering Students.
- [6] Torres, T. (2015). I8 percent of unemployed college graduates – NSO.
- [7] TuffreyStephane (2011). Data Mining and Statistics for Decision Making Statistic for Dummies.
- [8] Wilma L. Labrador. (2009). National Career Assessment Examination (NCAE) As It Influences The TV System.

Multiple Noises Removal from Computed Tomography (CT) Images

Abdelkader Salama Alrabaie^{1*}, Marwan M M El marmuri², Emhimed Saffor³

¹Department of Physics, College of Education /Brack, Sebha University, Libya

²Department of X-ray Diagnostic & Radiotherapy, College of Medical Technology, Zawia University, Libya

³Department of Physics, College of Sciences, Sebha University, Libya

DOI: <https://doi.org/10.21467/proceedings.2.3>

* Corresponding author email: kadersalama1@gmail.com

ABSTRACT

Noise is seen in images during image acquisition and transmission. This is characterized by noise model. Image enhancement through noise reduction is a fundamental problem in image processing. Noise filtering is a necessary action and has become one of the indispensable components of image processing operation. In this work, we have applied different filtering techniques (arithmetic mean filtering, median, and Weiner) to remove multiple mixed noises such as; (speckle, Gaussian, salt and pepper) from Computed Tomography (CT) images. Performance metrics such as; Peak Signal to Noise Ratio (PSNR), and Mean Square Error (MSE) were used to evaluate filtering techniques. The results showed that the median filter had worked more effectively to remove these noises. All the above mentioned techniques were implemented using MATLAB environment. It should give some results showing the values of PSNR and MSE for these filters to indicate the differences between them.

Keywords: *CT, MATLAB, MSE, Noise, PSNR.*

1 Introduction

Medical images such as magnetic resonance imaging (MRI), computed tomography (CT), ultrasound (US), and X-ray images are subject to a wide variety of distortions, during acquisition, processing, compression, storage, transmission and reproduction, any of which may result in a degradation of visual quality. Medical images are collected by different types of sensors and they are contaminated by different types of noises. Generally speckle; Gaussian, salt and pepper noises mostly occurred in the MRI, CT, and US images.[1] Noise tells unwanted information in digital images. Noise produces undesirable effects such as artifacts, unrealistic edges, unseen lines, corners, blurred objects and disturbs background scenes. In medical image processing many methods are used for noise reduction.[2] Noise filters generally attempt to smooth the corrupted image by neighbourhood operations. To measure the performance and image quality of the noise removal techniques several parameters are available for the comparison. Common parameters are Peak Signal Noise Ratio (PSNR), Root Mean Squared Error (RMSE), Mean Squared Error (MSE) etc.[1][3]



© 2018 Copyright held by the author(s). Published by Aijr Publisher in Proceedings of First Conference for Engineering Sciences and Technology (CEST-2018), September 25-27, 2018, vol. 1.

This is an open access article under [Creative Commons Attribution-NonCommercial 4.0 International](https://creativecommons.org/licenses/by-nc/4.0/) (CC BY-NC 4.0) license, which permits any non-commercial use, distribution, adaptation, and reproduction in any medium, as long as the original work is properly cited. ISBN: 978-81-936820-5-0

A). Noise Models:

i) Gaussian Noise: Gaussian noise caused by natural sources such as thermal vibration of atoms and discrete nature of radiation of warm objects. Gaussian noise generally disturbs the gray values in digital images. That is why Gaussian noise model essentially designed and a characteristic by its probability density function (PDF) or normalizes histogram with respect to gray value and it is given as:[2][4]

$$P(g) = \sqrt{\frac{1}{2\pi\sigma^2}} e^{-\frac{(g-\mu)^2}{2\sigma^2}} \quad (1)$$

Where: g = gray value, σ = standard deviation and μ = mean

ii). Speckle Noise: This noise is multiplicative noise. Their appearance is seen in a coherent imaging system such as laser, radar and acoustics etc. Speckle noise can exist similar in an image as Gaussian noise. Its probability density function follows gamma distribution, and given as:[2]

$$F(g) = \frac{g^{\alpha-1} e^{-\frac{g}{a}}}{(\alpha-1)! a^\alpha} \quad (2)$$

Where a^2 is the variance, α is the shape parameter of gamma distribution and g is the gray level.

iii). Impulse Valued Noise (Salt and Pepper Noise): Salt and pepper noise is represents itself as randomly occurring white and black pixels. Salt and pepper noise creeps into images in situations where a quick transient, such as faulty switching, takes place.[5] Image pixel values are replaced by corrupted pixel values either maximum or minimum pixel value i.e., 255 or 0 respectively. Although in noisy image, there are possibilities of some neighbours do not changed as shown in Figure 1 for an example.



Figure 1: the central pixel value is corrupted by Pepper noise

$$p(g) = \begin{cases} pa & \text{for } g = a \\ pb & \text{for } g = b \\ 0 & \text{otherwise} \end{cases} \quad (3)$$

Salt and Pepper noise generally corrupted the digital image by malfunctioning of pixel elements in camera sensors, faulty memory space in storage, errors in digitization process and many more.[2]

The (PDF) of this noise is shown in the Figure 2.

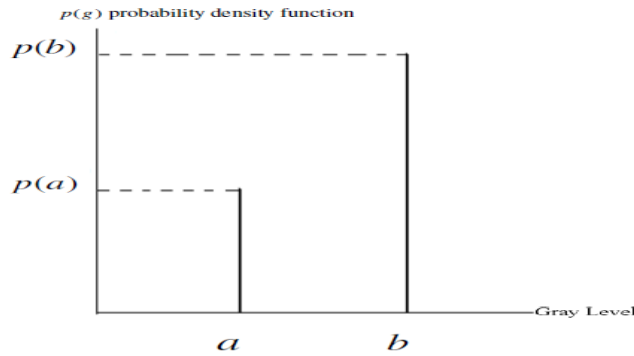


Figure 2: PDF of Salt and Pepper noise

(B) Filters:

i). Arithmetic Mean Filtering (AMF): This is one of the simplest of the mean filtering techniques. It expressed as AMF by the equation (4).[6]

$$f(x, y) = \frac{1}{mn} \sum_{(s,t) \in S_{xy}} g(s, t) \quad (4)$$

S_{xy} represent the set of coordinates in a rectangular space that is image window of size $m \times n$ centred at given point (x,y) . The AMF technique calculates the average value of the corrupted image $g(x,y)$ in the area defined by S_{xy} . The value of restored image f at any point (x,y) is Arithmetic Mean computed using the pixels values in the image that is in the region defined by S_{xy} .

ii). Median Filter: the median filter replaces the value of the pixel by the median of the gray levels in the neighbourhood of that pixel [1] i.e.

$$Z_{(x,y)} = \text{median}_{(s,t) \in S_{xy}} \{g(x, y)\} \quad (5)$$

The value of the pixel at (x, y) is included in the computation of the median.[7-9]

iii). Wiener filter: It is an adaptive low-pass filter which uses a pixel-wise adaptive Wiener method based on statistics estimated from a local neighbourhood of each pixel.[7] Adaptive filters are a class of filters which change their characteristics according to the values of the grey scales under the mask. Such a filter can be used to clean Gaussian noise by using local statistical properties of the values under the mask. One such filter is the minimum mean-square error filter; this is a non-linear spatial filter; and as with all spatial filters, is implemented by applying a function to the grey values under the mask. The output value can be calculated by following equation.[6]

$$m_f + \frac{\sigma_f^2}{\sigma_f^2 + \sigma_g^2} (g - m_f) \quad (6)$$

Where; g is the current value of the pixel in the noise affected image, m_f is the mean, σ_f^2 is the variance in the mask and σ_g^2 is the variance of the noise over the entire image. The wiener2

function applies a Wiener filter which is a type of linear filter to an image adaptively, tailoring itself to local image variance. Where the variance is large, wiener2 performs little smoothing. Where the variance is small, wiener2 performs more smoothing. This approach often produces better result than linear filtering.[8] The technique that is implemented in MATLAB is Weiner filter. It is an adaptive low-pass filter which uses a pixel-wise adaptive Wiener method based on statistics estimated from a local neighbourhood of each pixel.[7]

2 Materials and Methods

Brian and Chest Computed Tomography (CT) images of sizes (225x225) pixels are used in this study. These images are corrupted by multiple and different noises (speckle, Gaussian, salt and pepper). Filtering techniques (AMF, Median, and Weiner) are used to remove these noises. To evaluate filtering techniques quality metrics like Mean Squared Error (MSE), and Peak Signal to Noise Ratio (PSNR) were used. Algorithms were implemented in MATLAB with default setup parameters. The structure of methodology used in this study can be shown in Figure (3).

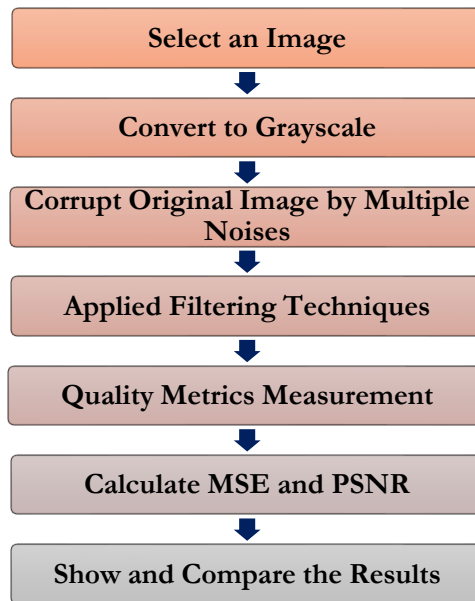


Figure 3: Methodology Structure

The (PSNR) is evaluated in decibels and is inversely proportional the Mean Squared Error. The PSNR can be calculated form equation (7) :[1]

$$PSNR (dB) = 10 \log \left(\frac{(255)^2}{MSE} \right) \quad (7)$$

Where (MSE) used to calculate by taking difference between two images pixel by pixel, and it is defined as :[3]

$$MSE = \frac{1}{MN} \sum_{i=1}^M \sum_{j=1}^N (x(i, j) - y(i, j))^2 \quad (8)$$

Where $x(i,j)$ represents the original (reference) image and $y(i,j)$ represents the distorted (modified) image and i and j are the pixel position of the $M \times N$ image. MSE is zero when $x(i, j) = y(i,j)$.

3 Results and Discussion

The visualization results of MATLAB simulation are shown in Figure (4).

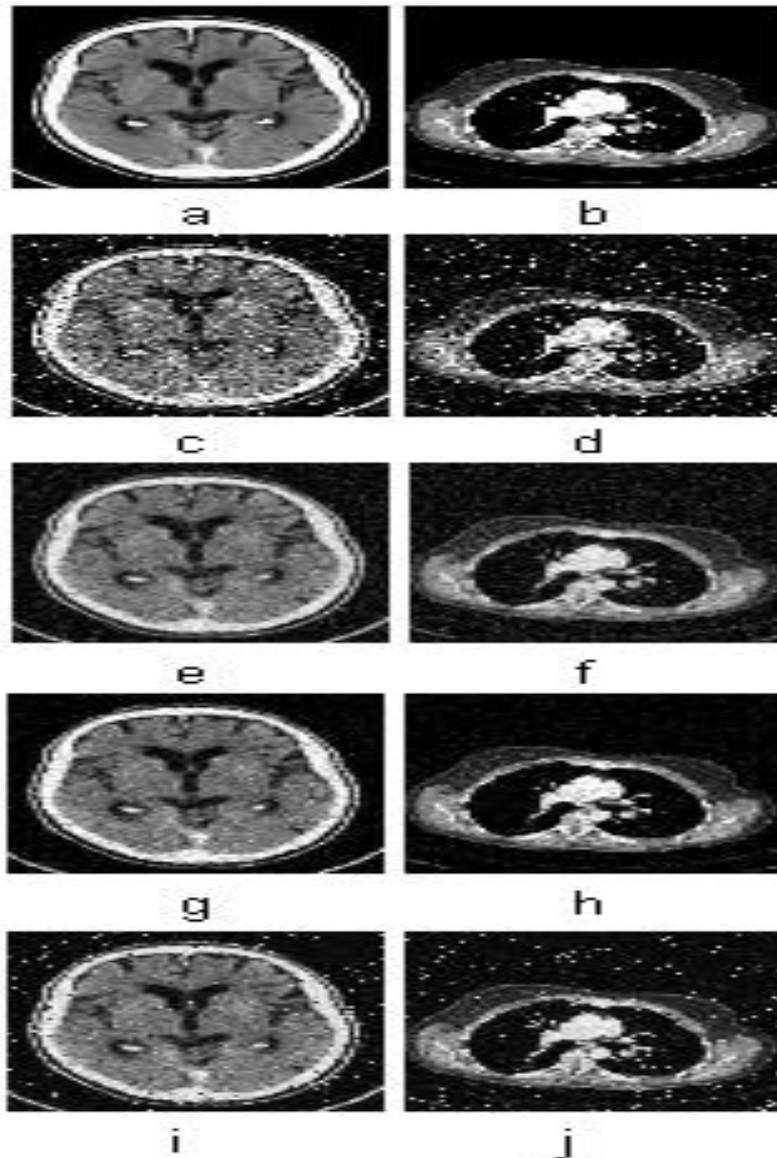


Figure 4: Filtering noisy (CT) images (a) and (b) original images (Brain & Chest) (c) and (d) noisy images (e) and (f) Average filter applied (g) and (h) Median filtering applied (i) and (j) Wiener filtering applied

The values of (MSE & PSNR) for applied filter techniques are tabulated in Table (1) to evaluate and compare the filtered (CT) images. The comparison has been made amongst (AMF, Median, and Weiner) filters. Table (1), Figure (4), and Figure (5). show the experimental results and illustrate a thorough comparison of all the filtering techniques for brain and chest (CT) image used in this study.

Table 1: MSE and PSNR values

Image	Brain		Chest	
	MSE	PSNR	MSE	PSNR
Average	572.77	20.55	742.16	19.42
Median	412.41	21.97	435.38	21.74
Weiner	886.03	18.65	1.10 x10 ³	17.69

Through finding the noises (speckle, Gaussian, salt and pepper) noises in both (CT) images by filtering techniques it is found that the median filter works better for the removing multiple noises from (CT) images. The highest values of (PSNR) are given by Median filter 21.97 and 21.74 for Brain and Chest (CT) images respectively. Therefore the output images is greater denoised. The median filter is more effective in removing different noises (speckle noise, Gaussian noise, salt and pepper). Whereas the Weiner filter can be used to clean Gaussian noise by using local statistical properties of the values under the mask, and it fails for salt and pepper noise. The median is much less sensitive than the mean to extreme values. Since the median value must actually be the value of one of the pixels in the neighbourhood, the median filter does not create new unrealistic pixel values when the filter straddles an edge. These advantages aid median filters in suppressing the uniform noise as well as other noises. Median filtering is therefore better able to remove this outlier without reducing the sharpness of the image.[7-9]

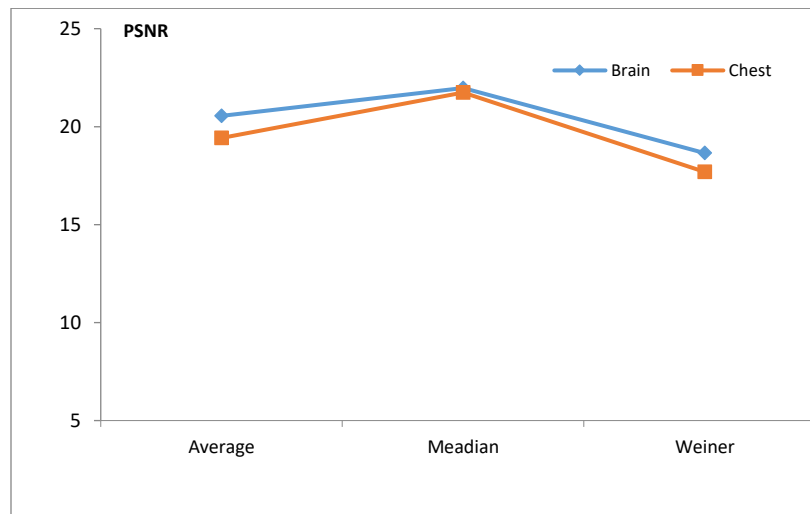


Figure 5: PSNR values

4 Conclusions

During image acquisition and transmission, noise is seen in images. This is characterized by noise model. Image denoising is necessary action in image processing operation. Noise models also designed by probability density function using mean, variance and mainly gray levels in digital images. In this work, we have applied different filtering techniques (AMF, Median, and Weiner) to remove multiple noises (speckle noise, Gaussian noise, salt and pepper). The simulation results found that the median filter is more effective in removing different noises. Through this work we have observed that the choice of filters for denoising the medical images depends on the type of noise and type of filtering technique, which are used. These filters are very useful in many applications. These results are more useful for medical diagnostic.

References

- [1] S.Senthilraja, P.Suresh, and M.Suganthi, "Noise Reduction in Computed Tomography Image Using WB – Filter", *International Journal of Scientific & Engineering Research*, Volume 5, Issue 3, pp. 243-247, March-2014.
- [2] Ajay Kumar Boyat, and Brijendra Kumar Joshi, "A Review Paper: Noise Models in Digital Image Processing", *Signal & Image Processing : An International Journal, SIPIJ*, Vol. 6, No. 2, pp. 63-75, April- 2015.
- [3] C.Sasi varnan, et al, "Image Quality Assessment Techniques on Spatial Domain", *International Journal of Computer Science and Technology*, Vol. 2, Issue 3, pp. 177-184, September 2011
- [4] K. Somasundaram, and P. Kalavathi, "Medical Image Denoising using Non-Linear Spatial Mean Filters for Edge Detection", *National Conference of Signal and Image Processing, (NCSIP)*, pp.149-153, 2012.
- [5] SONALI R. MAHAKALE & NILESHSINGH V. THAKUR "A Comparative Study of Image Filtering on Various Noisy Pixels", *International Journal of Image Processing and Vision Sciences*, Vol. 1, Issue 2, pp. 69-77, 2012.
- [6] Gururaj P.Surampalli et al, "Adaptive Approach to Retrieve Image Affected by Impulse Noise", *International Journal of Research in Engineering and Technology*, Vol. 3, Special Issue 3, pp. 218-221, May- 2014.
- [7] Ajay Kumar Nain, et al "A Comparative Study of Mixed Noise Removal Techniques", *International Journal of Signal Processing*, Vol. 7, No. 1, pp.405-414, 2014.
- [8] Bhausahab Shinde, Dnyandeo Mhaske, and A.R. Dani, "Study of Noise Detection and Noise Removal Techniques in Medical Images", *I.J. Image, Graphics and Signal Processing*, pp. 51-60, 2012.
- [9] Sukhwinder Singh, and Neelam Rup Prakash, "Modified Adaptive Median Filter for Salt & Pepper Noise" *International Journal of Advanced Research in Computer and Communication Engineering*, Vol. 3, Issue 1, pp. 5067-5071, January 2014.

A New Technique to Encrypt-Decrypt Digital Color Images Using One-Dimensional Matrix

Khdega A.Yosef Galala

Department of Computer Science, College of Education, Al Jufrah University, Libya

DOI: <https://doi.org/10.21467/proceedings.2.4>

* Corresponding author email: kdebh@yahoo.com

ABSTRACT

Due to digital technologies, the usage of images in modern industrial life is increasing rapidly. Therefore, the security of digital image has been a major issue in the modern digital world. Image encryption methods are one of the strong techniques recommended in this domain. These techniques try to convert an image to another image that is difficult to recognize and to understand. This art aims fundamentally to achieve the storage and transmission of image securely over the network. In this study a new image security technique is presented. As first step, the new technique extracts the red, green, and blue (RGB) components from the original color image. Then the XOR operation is used to change the RGB values of each pixel and then the RGB pixel positions are also changed randomly according to the key matrix. MATLAB R2012a was used to get the experimental results. The evaluation of this technique was done using some color images which differ in size and type. Simulation results show that, the performance of the proposed technique is high, and the original image was retrieved without any distortion.

Keywords: image encryption; image decryption; color images; network security.

1 Introduction

In recent years, with the explosive growth of both computer and internet technology, a huge amount of sensitive and valuable data is being exchanged over unsecured networks. Data not just text it also includes digital images, video, graphical objects, audio and other the multimedia data [1]. Digital image is the most important multimedia data, it is widely used for many aspects of our daily life such as online personal photograph album, internet communication, pay-per-view TV, digital signatures legal, medical imaging systems, military image systems, etc [2]. Digital images are sent, treated automatically and shared across the internet. So the protection of these images from unauthorized access is offering a great challenge to governments, individuals and companies alike [3].

To meet this challenge, various image security techniques such as encryption, steganography, secret sharing, watermarking, etc were proposed. Among these all, image encryption (IE) become one of eminent technique especially using over the internet. These techniques try to convert an image to another image that is difficult to recognize and to understand; while the image decryption is the result of retrieving original image from the encrypted one [4].



© 2018 Copyright held by the author(s). Published by AIJR Publisher in Proceedings of First Conference for Engineering Sciences and Technology (CEST-2018), September 25-27, 2018, vol. 1.

This is an open access article under [Creative Commons Attribution-NonCommercial 4.0 International](https://creativecommons.org/licenses/by-nc/4.0/) (CC BY-NC 4.0) license, which permits any non-commercial use, distribution, adaptation, and reproduction in any medium, as long as the original work is properly cited. ISBN: 978-81-936820-5-0

Generally, the image encryption applies two basic methods: replacement methods or scrambling methods [5]. Digital image scrambling is a useful method for providing high protection to image data by scrambling image into an unintelligible format [6].

Since 1990s, many existing image encryption techniques have been developed based on scrambling techniques like key based scrambling techniques, Rubik Cube matrix transformation, image scrambling based on 2D, etc [7]. One of them was proposed by [8] to encrypt image by generate random key sequence. Then the rows and columns of the image are scrambled using this key and then circular shifting of the rows and columns are done using the same key. The authors of [5] also uses scrambling method to encrypt the grey level image based on random number generation as matrix. In [9], a new technique based on one-dimensional random scrambling and combined with XOR operation is developed.

Although, there are various image encryption techniques available for executing images encryption but, there is still a lack of appropriate techniques for images encryption [10]. So we still need to develop more and more powerful techniques. Therefore, the main goal of this paper is to propose a new image encryption technique based on one-dimensional scrambling method. Thus, the rest of the paper is organized as follows: in section 2 the proposed technique is discussed in details; section 3 focuses on the experimental results of the new technique; section 4 gives explains the features of proposed technique and conclusion is presented in section 5.

2 The Proposed Technique

The new image encryption technique is based mainly on true color images, free from image size and type. It consists of two main phases which are encryption and decryption phase as shown in figure 1 below. The first phase can be described as follows:

2.1 Encryption phase

The proposed method of encryption consists of ten main steps as shown below:

Step 1. Input original color image and get its size.

Step 2. Based on the size of the original image, generate a random single array with unique values varies from 1 to the original image size (i.e. If an image is 150×120 then the array will have 18000 elements). Save it as the secret key matrix 'SKM' which will be used later for image scrambling.

Step 3. Extract red 'R', green 'G', and blue 'B' components of the original image.

Step 4. Apply the XOR operation between the red matrix 'R' and the green matrix 'G' to get the new green matrix 'G1', ' $G1 = R \oplus G$ '.

Step 5. Apply the XOR operation between the red matrix 'R' and the blue matrix 'B' to get the new blue matrix 'B1', ' $B1 = R \oplus B$ '.

Step 6. Apply the XOR operation between the red matrix 'R' and the matrix obtained in the previous step to get the new red matrix 'R1', ' $R1 = R \oplus B1$ '.

Step 7. Reshape the three matrices obtained in steps (4,5,6) to three one-dimensional arrays.

Step 8. Scrambling the pixel position in each matrix obtained in the previous step in the order of randomness of SKM key.

Step 9. Reshape each matrix obtained in the previous step to 2-dimensional array which is the same size as the original one.

Step 10. Finally re-combine separate color channels obtained in step 9 into a single RGB color image to get encrypted image.

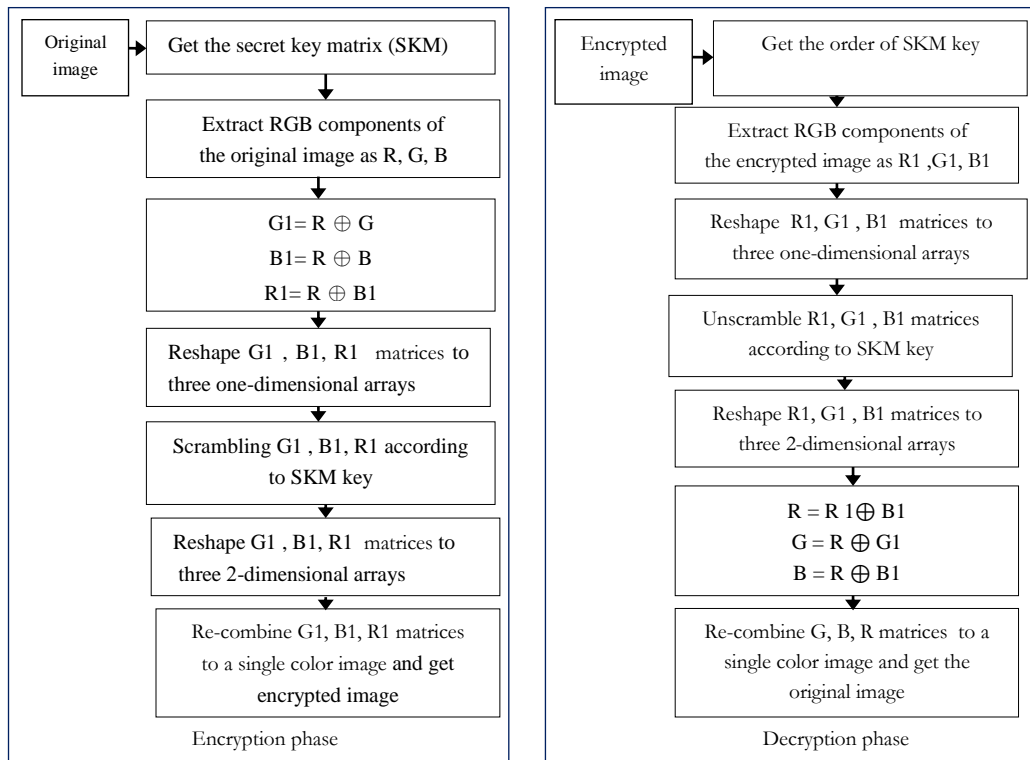


Figure 1: The proposed technique phases

2.2 Decryption phase

The decryption stage can be performed according to following steps:

Step 1. Load the encrypted image and get its size.

Step 2. Get the random matrix, sort its elements in ascending order. Get the order of the key matrix by comparing elements of matrix before and after sorting. According to the obtained order of the key matrix 'SKM', we change positions of pixels in the input image to get back the original image.

Step 3. Extract red 'R1', green 'G1', and blue 'B1' components of the encrypted image.

Step 4. Reshape each matrix obtained in the previous step to three one-dimensional arrays.

- Step 5. Unscrambling pixels in each matrix obtained in the previous step using SKM key.
- Step 6. Convert each matrix obtained in the previous step to 2-dimensional array which is the same size as the original one.
- Step 7. Apply the XOR operation between the red matrix ‘R1’ and the blue matrix ‘B1’ obtained in the previous step to get the original red matrix ‘R’, ‘ $R = R1 \oplus B1$ ’.
- Step 8. Apply the XOR operation between the red matrix obtained in the previous step and the green matrix obtained in step 6 to get the original green matrix ‘G’, ‘ $G = R \oplus G1$ ’.
- Step 9. Apply the XOR operation between the red matrix obtained in step7 and the blue matrix obtained in step 6 to get the original blue matrix ‘B’, ‘ $B = R \oplus B1$ ’.
- Step 10. Finally re-combine separate color channels obtained in steps (7,8,9) to a single RGB color image to get back the original image.

3 Experimental Results

The simulation of the above technique has been achieved by using MATLAB R2012a. The test images applied in this work was analyzed using histogram and operational speed of technique. The details of those processes as described below:

3.1 Histogram

At this stage, two images were used in this performed analysis. They are 300 * 300 RGB image named ‘Ahmed Al Bashir’ and 600 * 450 RGB image named ‘Tree’. Figure 2 and figure 5 show the original images with the histogram of each channel of the original color image. Figure 3 and figure 6 show encrypted images with the histogram of each channel of the encrypted color image while figure 4 and figure 7 show the decrypted images with the histogram of each channel of the decrypted color image.

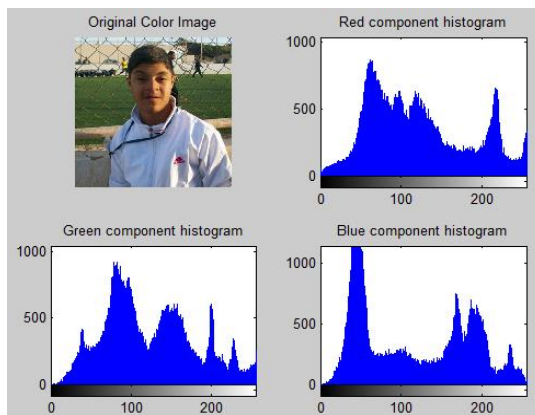


Figure 2: *Original image of Ahmed*

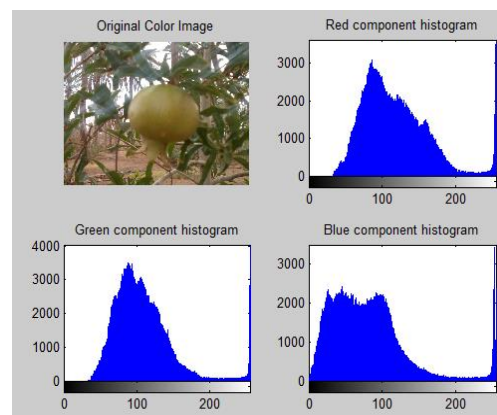


Figure 5: *Original image of tree*

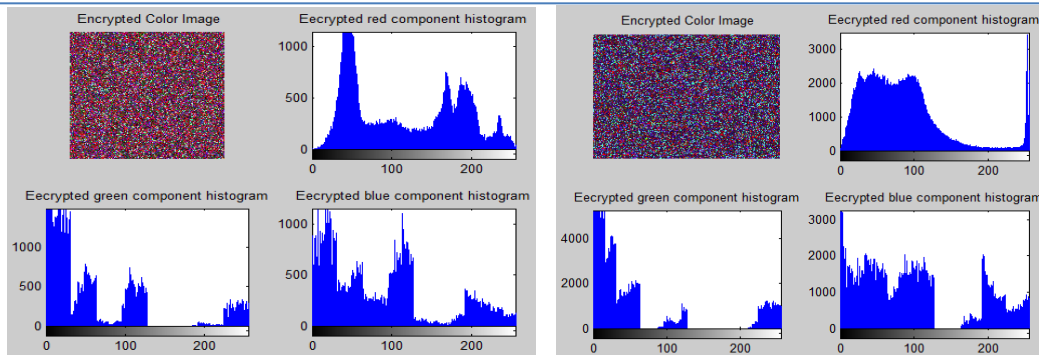


Figure 3: Encrypted image of Ahmed

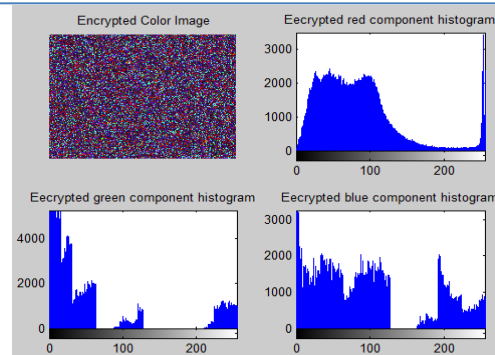


Figure 6: Encrypted image of tree

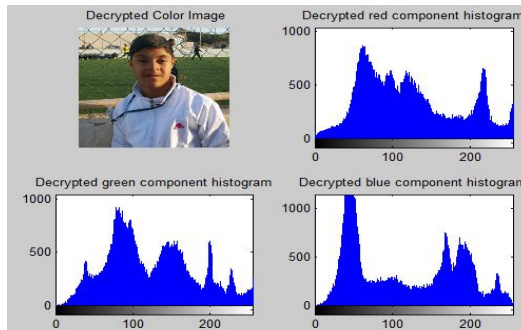


Figure 4: Decrypted image of Ahmed

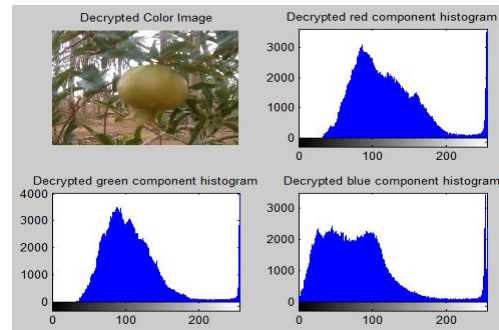


Figure 7: Decrypted image of tree

The histogram analysis indicates that, for both images the original image and its encrypted image has different statistics. As we see, the histograms of encrypted images are great different from the histograms of the original images, which will make it difficult to apply any statistical attack on the image encrypted.

3.2 Operational Speed Analysis

This work also measures the CPU time taken by the new technique to encrypt and decrypt color images. Seven different image sizes are selected to be used in this test. Table 1 shows the results of compared the CPU time to encrypt and its decryption for each image.

Table 1: Consumed time for encryption and decryption processes

Image size	Encryption time (sec.)	Decryption time (sec.)	Total time (sec.)
259*194*3	0.003495	0.013511	0.017006
276*182*3	0.003214	0.012671	0.015885
299*168*3	0.003232	0.014378	0.01761
300*200*3	0.004063	0.014976	0.019039
300*300*3	0.005545	0.027047	0.032592
600*450*3	0.018416	0.083314	0.10173
940*627*3	0.040704	0.188611	0.229315

As can be seen in the table 1 above, the proposed technique gives the best speed to encrypt and decrypt color images and has been observed a slight increase in execution time of technique with the increase in image size.

The consequences disclose that, the proposed technique was implemented successfully and all original images were recovered without any loss. So it could be used effectively to encrypt any color image.

4 Features

A prominent feature of the new technique are:

1. The proposed technique is a very effective and simple technique to encrypt color images.
2. It is adaptable to encrypt images differ in size and type.
3. It has high operation speed to execute both encryption and decryption processes.

5 Conclusions

In this work, a new technique to encrypt digital color images has been introduced. Statistical analysis was done using histograms and operational speed analysis to get the experimental results. Simulation results confirmed that the new technique has been successfully implemented and it could be used effectively for encryption purposes. For the future work the proposed technique could be used to encrypt other images types such as binary images and gray images.

References

- [1] W. Lee, T. Chen and C. Chieh Lee, "Improvement of an encryption scheme for binary images," *Pakistan Journal of Information and Technology*, Vol. 2, pp. 191-200, 2003.
- [2] Rojo, M.G., G.B. García, C.P. Mateos, J.G. García and M.C. Vicente, "Critical comparison of 31 commercially available digital slide systems in pathology," *International journal of surgical pathology*, Vol. 14, pp. 285-305, 4 October 2006.
- [3] A. Mitra, Y V. Subba Rao and S. R. M. Prasanna, "A new image encryption approach using combinational permutation techniques," *Journal of computer Science*, Vol. 1, pp.127, 2006.
- [4] Madhu B., Ganga Holi and Srikanta Murthy K., "An overview of image security techniques," *International Journal of Computer Applications*, Vol.154, pp. 37- 46, November 2016.
- [5] Makera M Aziz and Dena Rafea Ahmed, "Simple image scrambling algorithm based on random numbers generation," *International Journal of Advanced Research in Computer Science and Software Engineering*, Vol. 5, pp. 434 - 438, September 2015.
- [6] Prarthana Madan Modak and Vijaykumar Pawar, " A comprehensive survey on image scrambling techniques," *International Journal of Science and Research (IJSR)*, Vol. 4, pp.814 -818, December 2015.
- [7] Sandeep Kaur and Sumeet Kaur, "Four level image encryption using scrambling and key based methods," *IJCSC*, Vol. 3, pp. 187-190, 2012.
- [8] P. Premaratne and M. Premaratne, "Key-based scrambling for secure image communication," *Emerging Intelligent Computing Technology and Applications*, P. Gupta, D. Huang, P. Premaratne & X. Zhang, Ed. Berlin: Springer, Vol. 304, pp.259-263, 2012.
- [9] Quidong Sun, Ping Guan, Yongping Qiu and Yunfeng Xue, "A Novel digital image encryption method based on one-dimensional random scrambling," *9th International Conference on Fuzzy Systems and Knowledge Discovery*, pp. 1669-1672, May 2012.
- [10] T. Bhaskara Reddy, Hema Suresh Yaragunti, T. Sri Harish Reddy and S. Kiran, "An effective algorithm of encryption and decryption of images using random number generation technique," *International Journal of Computer Technology & Applications*, Vol. 4, pp. 883-891, 2013.

The performance of Space Time Block Coding (STBC) in MIMO relay network

Hamza Eldenferia^{1*}, Jamal Elbergali²

1,2 Electronic Engineering Department- College of Industrial Technology Misurat- Libya

DOI: <https://doi.org/10.21467/proceedings.2.5>

* Corresponding author email: hamza.ham1985@gmail.com

ABSTRACT

This paper is presenting the performance analysis of a cooperative MIMO (Multiple-Input-Multiple-Output) relaying system with a single relay based on Alamouti scheme. It examines the Space Time Codes (STC) techniques where the focus is on the Space Time Block Coding (STBC). The MIMO system is built on Alamouti Space Time Block Coding (STBC) over Rayleigh flat fading channels. The source and destination nodes are equipped with two transmit antennas while the relay node is equipped with multiple antennas and Amplifiers-and-Forwards (AF). In addition the receiver uses the Zero Forcing (ZF) equalizer. The system reliability will be evaluated by using of bit error rate (BER) performance.

Keywords: MIMO relay network; Alamouti scheme; Space Time Block Coding (STBC); Zero Forcing (ZF) equalizer; bit error rate (BER)

1 Introduction

Wireless communications have recently turned to a technique known as Multiple Input Multiple Output (MIMO) to improve the quality (bit-error rate) and data rate (bits/sec). MIMO technology has attracted attention in wireless communications, because it offers significant increases in data throughput and link range without additional bandwidth or increasing transmit power [1]. This is done by using multiple transmit and receive antennas, as well as suitable coding techniques. They take benefit of spatial and temporal diversity to combat the random fading induced by multi-path propagation of the signal and maximize efficient use of bandwidth. There is also a fundamental gain in transmitting data over a matrix rather than vector channel. Transmission of data over MIMO channels has traditionally focused on data rate maximization or diversity maximization [2]. Recently, Cooperative communication [3] has attracted a lot of attention because of its ability to enhance the system performance. Cooperative communication concerns a system where users share and organize their resources to improve the transmission quality and enhance the power allocation. The combination of MIMO processing with cooperative relaying helps to improve the capacity of the overall cooperative system [4]. In recent times, it has been revealed that cooperation based on Space-Time Block Codes (STBC) gives an effective method to present spatial diversity in various wireless scenarios [5][6].

1.1 Multi - Antenna Transmission Methods

To transmit information over a single wireless link, different transmission and reception strategies can be applied. Which one of them should be used depends on the knowledge of the instantaneous MIMO



© 2018 Copyright held by the author(s). Published by AIJR Publisher in Proceedings of First Conference for Engineering Sciences and Technology (CEST-2018), September 25-27, 2018, vol. 1.

This is an open access article under [Creative Commons Attribution-NonCommercial 4.0 International](https://creativecommons.org/licenses/by-nc/4.0/) (CC BY-NC 4.0) license, which permits any non-commercial use, distribution, adaptation, and reproduction in any medium, as long as the original work is properly cited. ISBN: 978-81-936820-5-0

channel parameters at the transmitter side. If the Channel State Information (CSI) is not available at the transmitter, Spatial Multiplexing (SM) or Space-Time Coding (STC) can be used for transmission. If the CSI is available at the transmitter, beamforming can be used to transmit a single data stream over the wireless link. In this way, spectral efficiency and robustness of the system can be improved [1]. It can be concluded that the choice of the transmission model depends on three entities important for wireless link design, namely bit rate, system complexity and reliability. STC has low complexity and promises high diversity, but the bit rate is moderate. SM provides high bit rate, but is less reliable. Beamforming exploits array gain, is robust with respect to channel fading, but it requires CSI at both transmitter and receiver. In this research only STC transmission has been considered.

Let us consider a point-to-point MIMO system with n_t transmit and n_r receive antennas. The block diagram is given in Figure 1. Let $h_{i,j}$ be a complex number corresponding to the channel gain between transmit antenna j and receive antenna i [2][3].

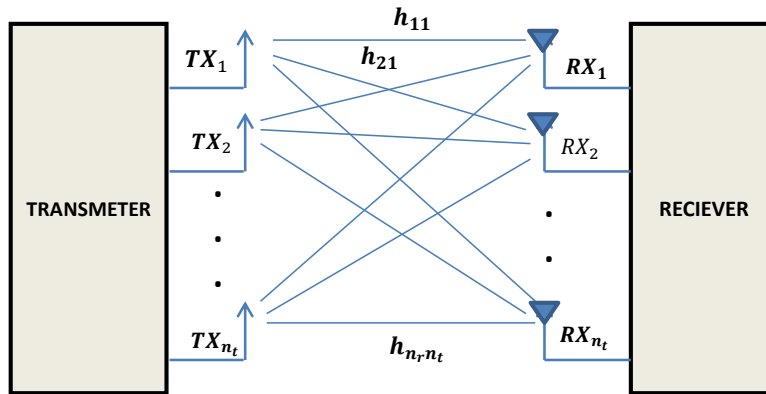


Figure 1. MIMO model with n_t transmit antennas and n_r receive antennas.

If at a certain time instant the complex signals $\{x_1, x_2, \dots, x_{n_t}\}$ are transmitted via n_t transmit antennas, the received signal at antenna i can be expressed as [7]:

$$y_i = \sum_{j=1}^{n_t} h_{i,j} x_j + n_i \quad (1)$$

Where n_i is a noise term. Combining all receive signals in a vector Y , this equation can be easily expressed in matrix form [7]:

$$Y = Hx + n \quad (2)$$

Y is the $n_r \times 1$ receive symbol vector, H is the $n_r \times n_t$ MIMO channel transfer matrix, x is the $n_t \times 1$ transmit symbol vector and n is the $n_r \times 1$ additive noise vector.

1.2 Wireless Relaying Systems

The main advantages of using relay are to increase coverage and decrease the need to use high power at the transmitter [8][9][10]. Essentially, in relaying systems the source terminal uses other terminals or relays to forward its information to the destination terminal. Generally, there are two types of relaying

systems, Decode-and-Forward (DF) relaying systems, and Amplify-and-Forward (AF) systems. In this paper AF system is used to implement the Model. Recently, with a good understanding of the benefits of MIMO systems, scientists have suggested some methods that could help to achieve the advantages of both MIMO and wireless relaying systems.

2 System Model

In this paper, we present performance analysis of a MIMO relaying system based on Alamouti scheme. As shown in Figure 2, the system considered two antennas at source and destination and one relay centred exactly between the source and destination. BPSK signal modulation is used to generate equal probability of ‘0’s and ‘1’s at the transmitter side.

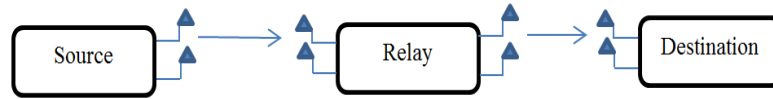


Figure 2. 2x2 MIMO relaying system.

At the relay node, we have used AF algorithm. The system channel between source, relay and relay destination are simply used as Rayleigh flat-fading channel with Additive White Gaussian Noise (AWGN) with zero mean. Also the Zero Forcing (ZF) technique has been used as equalizer at the receiver side.

2.1 Space Time Block Coding scheme

In this paper, two transmit and receive antennas is used. The input information stream $\mathbf{x}(t)$ is encoded by STBC encoder. Alamouti suggested that group the symbols into groups of two. In the first time slot, send \mathbf{x}_1 and \mathbf{x}_2 from the first and second antenna. In second time slot send \mathbf{x}_1^* and $-\mathbf{x}_2^*$ from the first and second antenna. Where $(.)^*$ denoted to complex conjugate function. Thus, at two time slots the input symbols are given by [10]:

$$\mathbf{x}(t) = \begin{pmatrix} x_1 & -x_2^* \\ x_2 & x_1^* \end{pmatrix} \quad (3)$$

The encoded information is transmitted through Rayleigh fading channel and AWGN as addition noise. The received signal vector at the receiver can be given like:

In the first time slot, the received signal is [7]:

$$\begin{pmatrix} y_1^1 \\ y_2^1 \end{pmatrix} = \begin{pmatrix} h_{11} & h_{12} \\ h_{21} & h_{22} \end{pmatrix} \begin{pmatrix} x_1 \\ x_2 \end{pmatrix} + \begin{pmatrix} n_1^1 \\ n_2^1 \end{pmatrix} \quad (4)$$

In the second time slot, the received signal is:

$$\begin{pmatrix} y_1^2 \\ y_2^2 \end{pmatrix} = \begin{pmatrix} h_{11} & h_{12} \\ h_{21} & h_{22} \end{pmatrix} \begin{pmatrix} -x_2^* \\ x_1^* \end{pmatrix} + \begin{pmatrix} n_1^2 \\ n_2^2 \end{pmatrix} \quad (5)$$

Combining the equations at time slot 1 and 2.

$$\begin{pmatrix} y_1^1 \\ y_2^1 \\ y_1^{2*} \\ y_2^{2*} \end{pmatrix} = \begin{pmatrix} h_{11} & h_{12} \\ h_{21} & h_{22} \\ h_{12}^* & -h_{11}^* \\ h_{22}^* & -h_{21}^* \end{pmatrix} \begin{pmatrix} x_1 \\ x_2 \end{pmatrix} + \begin{pmatrix} n_1^1 \\ n_2^1 \\ n_1^{2*} \\ n_2^{2*} \end{pmatrix} \quad (6)$$

2.2 Relay Procedure

The received signal y_r at relay node is amplified by matrix F and retransmitted to the destination node. The relaying matrix F can be expressed by [10][11][12]:

$$F = \beta_r I_{N_r} \quad (7)$$

Where β_r is the amplifying factor of the relay and I_{N_r} is the $N_r \times N_r$ identity matrix. The amplifying factor is calculated by [11][12]:

$$P_a = \beta_r^2 \text{tr}\{F(H_r H_r^H + I_{N_r})F^H\} \quad (8)$$

Where P_a is the transmit power in relay node, $(\cdot)^H$ represent the Hermitian complex conjugate transpose and $\text{tr}(\cdot)$ denotes to trace of a matrix[9][8].

2.3 Zero Forcing (ZF) Algorithm

The ZF equalizer is used in receivers to alleviate the effects of ISI. Therefore, to reach reasonable system performance and to decrease the complexity of the equalizer, ZF equalization technique has been used in this research [7]. The equivalent channel matrix with noise given by [11][12]:

$$H = H_{r,d} F H_r \quad (9)$$

$$n = H_{r,d} F n_r + n_{r,d} \quad (10)$$

Where H_r is the channel between source and relay and $H_{r,d}$ is the channel between relay and destination.

The estimated received signal \hat{x} can be determined as following:

$$\hat{x} = W_{ZF} Y \quad (11)$$

Where $W_{ZF} = H(H^H H)^{-1}$, is known as the ZF pseudo-inverse for a general $m \times n$ matrix and $(\cdot)^{-1}$ indicates simple matrix inversion.

3 Results and Discussion

In this research two-hops MIMO relay network with STBC is simulated by MATLAB software. The MATLAB program used to highlight the performance of STBC MIMO relay compared with STBC MIMO without using relay (Direct connection). In addition, we have examined the optimum location of the relay, by fixing the Signal to Noise Ratio (SNR) at 20dB and make the distance varied.

In this program the BPSK modulation is used to modulate the information, and also STBC encoder and decoder is used at the source and destination sides. The backward channel (source to relay) and the forward channel (relay to destination) are Rayleigh fading channel with zero mean complex circular AWGN. In addition, the ZF relay scheme is used at the receiver side as equalizer to alleviate the effects of ISI. At the relay node the AF technique has been used because it's easy to implement and the results near to practice one. The results have been divided to two sections:**Section I:** The performance is

measured by means of calculating the Bit Error Rate (BER) and plotting against the SNR between the source and destination, where the SNR is varied between 0 to 30dB. The MIMO network is used, with and without using relay. The distance in this section has been fixed as D for source-relay and relay destination, and $2D$ for direct connection (without aid of relay) as shown in Figure 3.

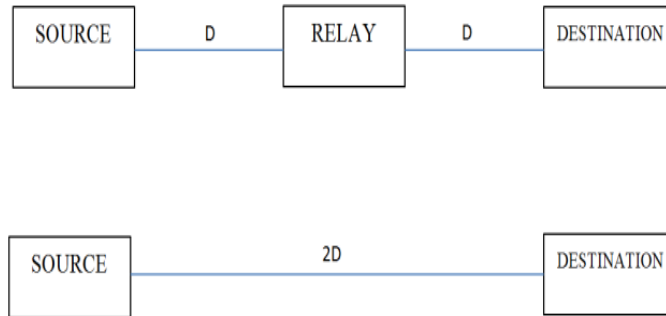


Figure 3. The distance considerations.

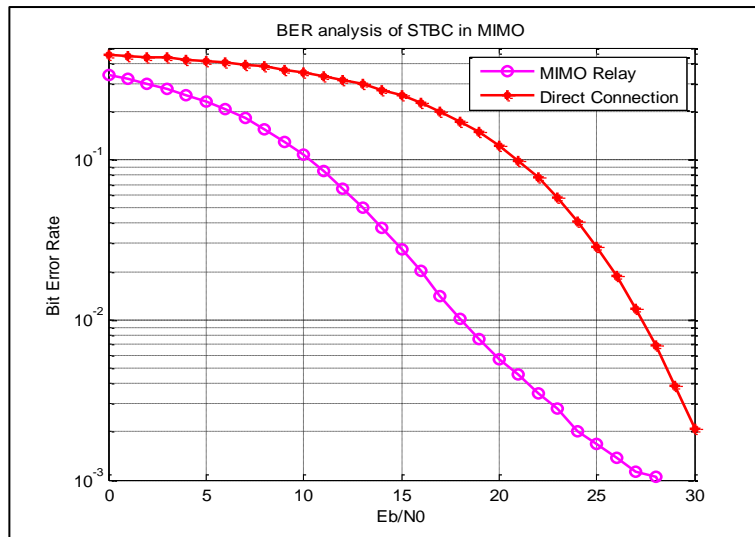


Figure 4. BER for MIMO using relay (MIMO relay) and MIMO without relay (Direct Connection).

As can be seen from Figure 4, the curves show the performance of MIMO using relay (MIMO relay) and MIMO without using relay (Direct Connection) between the source and destination using ZF algorithm for both. It can be observed that the BER performance for (MIMO relay) network is much better than the performance of MIMO (Direct Connection) network that's because the relay amplify and forward the information at distance D and retransmitted it again while in direct connection the source transmit the information directly over distance $2D$ with the same transmitted power. So, when we compare the BER plot, we can see that (Direct Connection) network has around 3dB poorer performance than (MIMO relay) network. That's introducing the relay network in the MIMO system minimize the BER which is more constructive in practical communication systems.

Section II: In this section the SNR has been fixed at 20dB and the distance between the source and relay is varied. This step has been taken to find out the optimum location for the relay between the

source and destination. In this part, we estimate the distance between the source and destination as unit function equal to 1, so the distance between source to relay is D and relay destination $B=(1-D)$. Therefore, the relay location starts at 0.1 and ends at 0.9.

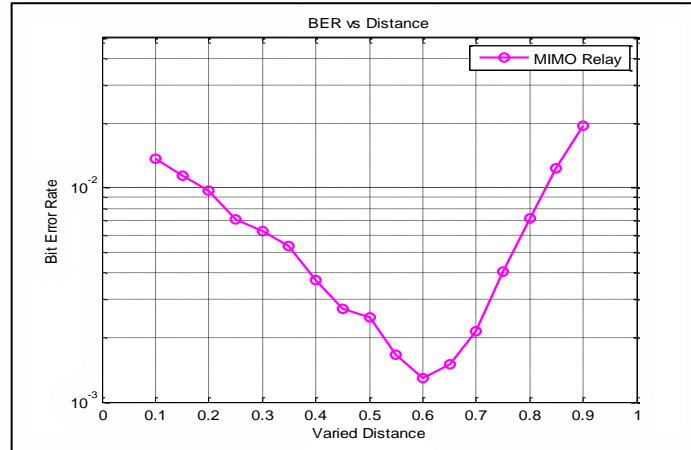


Figure 5. Find out the optimum location of the relay between the source and destination.

As can be seen from Figure 5 the curve shows optimum location of the relay between source and destination and the effects of changing the relay location. The curve shows the best location for the relay between source and destination. As can be seen from output performance the best place for relay is almost in the middle distance between source and destination. In addition, the worst case when the relay was near to the destination.

4 Conclusion

In conclusion, the aim of this paper was the performance of Space Time Block Codes (STBC) in MIMO relay communication systems. The research showed the relevant theories for MIMO relay network and STBC coding in order to get the appreciation for the theoretical predictions of the performance of the MIMO relay network systems. The simulation used the STBC based on multi-antenna cooperative systems and provided the corresponding simulated performance under Rayleigh fading channel AF algorithm and ZF equalizer. The system performance is improved more with the (MIMO relay) network than the MIMO system without the aid of relay network (Direct connection). In addition, to get the best performance of the MIMO relay network the relay has to be at the middle distance between the sources and destination.

References

- [1] M. Alamouti, "A Simple Transmit Diversity Technique for wireless communications", *IEEE Journal on selected areas in communications*, Vol. 16, No. 8, October 1998.
- [2] D.Gesbert, M.Shafi, D.S.Shui, P.Smith and A.Naguib, "From Theory to Practice: An Overview of MIMO space-time coded wireless systems".
- [3] A. Stefanov, E. Erkip, On the performance analysis of cooperative space-time coded systems, in: *IEEE Wireless Communications and Networking*, 16–20 March 2003, vol. 2, pp. 729–734.

- [4] Y.Wang, F.Liu, S. Xu, X.Wang, Y. Qian and P.Wang, "Performance Analysis of Multi-hop MIMO Relay Network", *IEEE Communications society*, ICC 2008 workshop proceedings.
- [5] A.Nosratinia, E.Hunter and A.Hedayat, "Cooperative Communications in Wireless Networks", *Adaptive Antennas and MIMO Systems for Wireless Communications*, *IEEE Communications Magazine*, October 2004.
- [6] J. N. Laneman, D. Tse, and G. W. Wornell, "Cooperative diversity in wireless networks: Efficient protocol and outage behavior," *IEEE Trans. on Information Theory*, vol. 50, no. 12, pp. 3062–3080, Dec 2004.
- [7] N.Ngajikin, W.N.Ahmad, N.Fisal and S.K.Yusof, "Simulation on Performance of Space time Block Code", *RF and Microwave Conference*, October 2004.
- [8] Y.fan and J.Thompson, "MIMO Configurations for Relay Channels: Theory and Practice", *IEEE Transactions on wireless communications*, Vol. 6, No. 5, May 2007,
- [9] S.Behbahani and R.Merched, M. Eltawil, "Optimizations of a MIMO Relay Network", *IEEE transactions on signal processing*, Vol. 56, No. 10, October 2008,
- [10] S. Atapattu and N. Rajatheva, "Exact SER of Alamouti code transmission through amplify-forward cooperative relay over Nakagami-m fading channels," in *Proc. IEEE International Symposium on Communications and Information Technologies ISCIT '07*, 2007, pp. 1429–1433.
- [11] Y. Song, H. Shin, and E. Hong, "MIMO cooperative diversity with scalar-gain amplify-and-forward relaying," *IEEE Trans. Commun.*, vol. 57, no. 7, pp. 1932–1938, Jull 2009.
- [12] Y. Ding, J. K. Zhang and K. M. Wong, "The Amplify and Forward Half Duplex Cooperative System: Pairwise Error Probability And Precoder Design", *IEEE Transaction on Signal Processing*, Vol. 55, No. 2, pp. 605-617, February 2007.

Building English Vocabulary Schema and Words Retention using Review Value Calculation for English as Secondary Language Students

Burnhan Mustafa Tanis^{1*}, Melvin A. Ballera², Mosbah Mohamed Elssaedi³

¹ AMA University - School of Graduate Studies, Philippines

² Technological Institute of the Philippines - Manila, Philippines

³ Faculty of Science - Computer Science, Sirte University, Libya

DOI: <https://doi.org/10.21467/proceedings.2.6>

* Corresponding author email: burnhanmt@outlook.com

ABSTRACT

Vocabularies, the core of any language, is probably the most challenging and time consuming part of learning a foreign language in a diverse and disperse community of learners. This study proposes an approach that can help a learner build up his/her English vocabulary volume by intensive article reading, the inclusion of Google Cloud Natural Language API and Glosbe Dictionary API, the use of review value calculation computing technique. The review vale calculation were able to determine the number of days were the new words should be reviewed and be part of the long-term memory. Result shows that students were able to increase their words acquisition skills by applying technology and computing. Students were able to retain words fast and understand better, by employing an interactive monitoring process. If the system will be implemented carefully, it is hypothetically produce a faster technique in acquiring new vocabularies for foreign students.

Keywords: Vocabulary schema, review value calculation, short term memory, long term memory, assessment interval

1 Introduction

E-learning has been used to help students learn the English language in their own convenient time and place [1]. It has become a large industry offering online lessons to students with the use of video-conference system. Video conferencing fosters communication and collaboration and trainee-teachers and can jointly dissect the newly acquired knowledge [2][3]. The author [4] concluded that video conferencing is a “powerful tool” to give students confidence in innovative teaching practices. More students view it as a great alternative to learning the English language outside the classroom. They see it as new age education systems that can bring knowledge in an updated form. Vocabulary is one of the critical part of learning English language. It is a fundamental way to comprehend whatever the student hears, reads



© 2018 Copyright held by the author(s). Published by AIJR Publisher in Proceedings of First Conference for Engineering Sciences and Technology (CEST-2018), September 25-27, 2018, vol. 1.

This is an open access article under [Creative Commons Attribution-NonCommercial 4.0 International](https://creativecommons.org/licenses/by-nc/4.0/) (CC BY-NC 4.0) license, which permits any non-commercial use, distribution, adaptation, and reproduction in any medium, as long as the original work is properly cited. ISBN: 978-81-936820-5-0

and most importantly, how the person communicates to the world. It is known to be one of the hardest of acquiring the knowledge to speak the English language, but it is often overlooked. With more teachers and learners giving priorities to Grammar and Reading Skills, students have a hard time learning and retaining the words that they have learned. They immediately forget the words after the teacher has given them the meaning or even after looking at the dictionary. A lot of studies suggested on how students can improve their vocabulary. One of the best would be through reading.

A long-term habit of extensively reading articles that are appropriate for a learner's English ability can greatly improve the vocabulary and command of a learner of English. However, this strategy may be difficult to implement for a learner with no extensive vocabulary because the learner may have problems either in choosing appropriate levels of articles in accordance with her/his needs and interests or in figuring out the meaning of unknown words using the semantics of familiar words in an article that is obtained. Dictionaries are always helpful; however, the need to continually look up unknown words, which once learned may be forgotten in a few days as per learning curve theory, might also easily discourage a learner. Several studies have also developed language tutoring systems in order to assist learners in learning language and have also proposed different personalization strategies [5]. With regard to an e-learning system, it is also hard to select appropriate articles for such learners if details on or precise profiles of learners are never established.

This study proposes an approach that can help a learner build up his/her English vocabulary volume by intensive article reading, during which meanings of unknown words are understood in the context of articles, assessment test and the used of evolutionary computer science technique, the review value calculation for determining vocabulary memory retention. The intention is to obtain the vocabulary from articles more affective, so learners will not easily forget the words.

2 Related Literature

Vocabulary learning is the area in which learners use learning strategies most frequently [6]. Oxford defines learning strategies as "operations employed by the learner to aid the acquisition, storage, retrieval and use of information". Vocabulary learning has been classified into two ways the traditional vocabulary learning and technology savvy vocabulary learning. Traditional vocabulary learning prepare selected vocabulary lists to assist learners and claim that such lists can reinforce students' memories and understanding of the words. However, it is impossible to compile a vocabulary list that is appropriate for all the students in a class with different English levels [7]. Another study used keyword method as the best memory technique for learning concrete words but not abstract words [8]. Another suggests that the use of vocabulary notebook/index cards can be an effective shortcut to achieve [9]. Ideally, the words recorded in the notebook/index cards are chosen according to the need of individual learners, thus learner autonomy is raised. As a matter of fact, learner autonomy and

its effectiveness have been widely recognized. One way to aid vocabulary acquisition is through the use of technology in pedagogically sound manner [10]. Semantic mapping is a popular strategy used in classrooms. Learners are encouraged to use concepts and relationships to create a semantic map in which keywords are highlighted. Linkage is formed between the above information and the new word so as to reinforce the memory of the new word. Researchers have both positive and negative comment toward this method [11]. It is also interesting to note that both traditional and technology savvy technique is worthy to mention however there still a need to address and develop new innovative ways to improve learning in vocabulary acquisition using deterministic peer review calculation that deals with words retention and acquisitions.

3 Vocabulary Architecture and Methods

Figure 1 shows the English vocabulary schema building processes which are composed of four phases: assessment phase, practicing phase, vocabulary acquisition phase, and the actual acquisition phase. During assessment phase, the level and interest of the learner will be initially assessed to create learner's vocabulary schema, profiles and a personalized learning process. The establishment of interest and level of the student (based on European standard), the system is capable of rendering 25 – 40 articles, depending on the information taken during the initial assessment. As the learning process progress, short quizzes will be given based on the learner's vocabulary schema to determine learner's comprehension.

Practicing phase on the other hand is capable of helping learners through human English native speakers subject to the availability of online Instructor. Usually, learners will request an online instructor for actual mentoring and tutoring. Results will then be recorded for profiling the learner's vocabulary schema. When the user requested to speak to a native speaker, the system will find a teacher that is available at that time in the system. The native speaker will then be given enough time to review the student's level and vocabulary schema before speaking to the student.

Vocabulary acquisition phase is a stage where an article will be presented based on learner's level, interest and profiles. The article is directly link to the Google Cloud Natural Language Application Programming Interface (API) to determine parts of speech and grammars rules, lemmatization and stemming while Instructor define vocabularies that needs to be learned by the learners. Actual acquisition stage define the meaning of the vocabularies, employing Glospe Dictionary API to define the vocabulary according to the localized definition of words and language conversion from language to another e. g. English to Spanish and to other recognized languages.

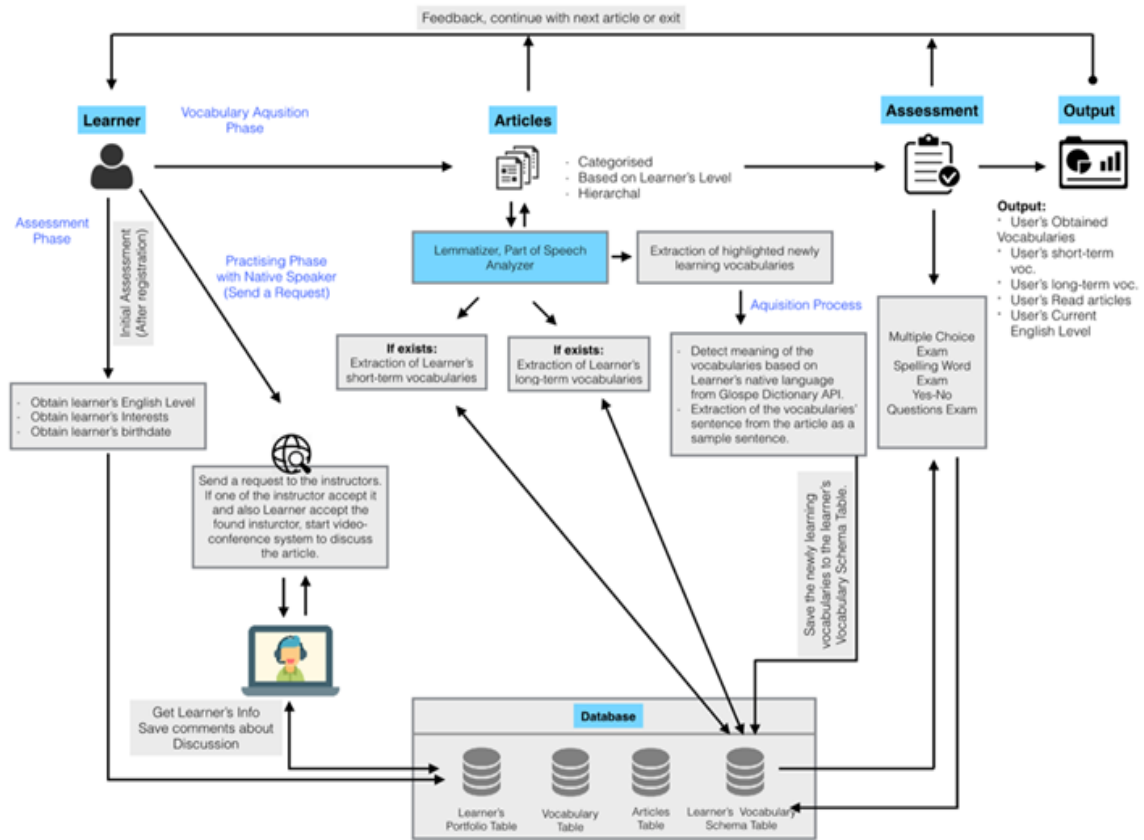


Figure 1: The vocabulary learning processes of the system

In the learning process and acquiring new words, the review value calculation will dynamically computed to determine reinforcement (reading related articles), adjustment (quizzes) to make sure that new vocabularies will be learned. The higher the value of review value calculation the higher its memory retention. There are four essential table that will keep the progress and assessment of the learner: learner's portfolio table, learner's vocabulary schema table, general vocabulary table and article table. These tables will contain the entire learner's information such as interest, level and articles which will be saved automatically. This is where Review Value Calculation Module will get all the information before giving the user the appropriate articles to read, vocabulary to use in the articles and quizzes to give.

Looking at the conditions, if the learner gets lower than 3 out of the given 4 questions, learner stays in the same level, but on the other hand, if the learner gets 3 or more he would then move on to the next succeeding questions until the system finds his rightful level. To determine the acquisition of a new vocabulary, short-term and long-term should be determined using the concepts of review value calculation or *rv*. Short-term refers to any newly obtained vocabulary in the system. When user obtains a new vocabulary it will be marked as a default short-term. Each newly obtained vocabulary is ranked as 1 in the user's vocabulary schema. As the words continuously appearing in the quizzes its rank increases. The system will compute

the assessment interval or A_i as shown in (1). The lower the rank of the word, the more it would appear in assessment so the learner could master that particular word. If the words reaches rank 4 then it will be transferred to long term memory.

$$A_i = (\text{round}(0.5 * rc) + (2 * sp) + (2 * riec)) * rg \quad (1)$$

The assessment interval, A_i is computed in terms of days. The next assessment for that particular vocabulary is after 36 days. A quiz containing that word would then appear and if the learner gets it correctly, a new assessment interval would then take places and it could appear – depending on the system’s calculation, a month, a year or so. Nevertheless, after 36 days interval and an assessment happen, if the user got it wrong, it would be degraded again into short-term.

4 Results And Discussion

For brevity, figures and tables have been restructured; only 20 out of 50 learners have been used for discussion. A total of 50 students were extracted from 1000 possible learners of the company. Table 1 shows the initial level of learners from different countries doing online courses of English Communication, mostly from Turkish, Russian, European and Central Asian. The age average is 24.5 with standard deviation of 1.25. The area of interest is adventure while English level is ranging from beginners level A1 to B1.

Table 1: Users’ profile and initial assessment result

#	Name	Family Name	Initial Level	Vocabulary Area	Age	User’s Native Lang.
1	Kubilay	Künç	A2	Adventure	34	Turkish
2	Numan	Numan	A1	Adventure	42	Turkish
3	Mücella	Çelik	A2	Adventure	20	Turkish
4	Zeynep	Pampal	A1	Adventure	17	Turkish
5	Ömer	Mindivanli	B1	Adventure	22	Turkish
6	Ahmet Turan	Bakır	A2	Adventure	23	Turkish
7	Furkan	Pehlivan	A1	Adventure	21	Turkish
8	Selman Kasim	BAĞIRICI	A2	Adventure	17	Turkish
9	İbrahim	Özsürücü	B1	Adventure	19	Turkish
10	Adalet	Arikanoglu	B1	Adventure	20	Turkish
11	Uğur	Özdemir	A2	Adventure	25	Turkish
12	Ahmet	Söyler	A2	Adventure	26	Turkish
13	Öznur	Karakılıç	A1	Adventure	30	Turkish
14	Яна	Елфимова	A1	Adventure	24	Russian
15	Bariş KARSLI	KARSLI	A1	Adventure	22	Turkish
16	Леша	ЯН	A2	Adventure	21	Czec Rep.
17	Mustafa	Onat	A1	Adventure	19	Turkish
18	Leopoldo	Datuin	B1	Adventure	33	Moldova
19	Orxan	Ismayilov	A1	Adventure	19	Azerbaijan
20	EMRE	ULAKÇI	A2	Adventure	32	Turkish

It has shown that the participants have almost the same level considering their age and nationalities. This may be probable due to less exposure of English language on these

countries. The development process of vocabulary schema was divided into three parts, namely: will be obtained, newly obtained and obtained vocabulary words.

Table 2 shows the status of the 20 learners with their corresponding records given the articles in the area of adventures. The third column corresponds to the target vocabulary or will be obtained vocabularies. For student number 1 for example, it requires to have a 110 to be obtained vocabularies but 78 were obtained with rendered 10 articles out of 15 articles and etc. All these are all part of showing the students' progress throughout their journey in enhancing their vocabulary schema and learning English.

Table 2: Learners profile on target vocabulary and number of articles

#	Name	Family Name	Target Vocabulary	Vocabulary Area*	Obtained Vocabulary	User's Native Lang.	Article Level	Total Article	Finished Article
1	Kubilay	Künç	110	Adventure	78	Turkish	A2	15	10
2	Numan	Numan	100	Adventure	80	Turkish	A1	22	18
3	Mücella	Çelik	110	Adventure	80	Turkish	A2	15	18
4	Zeynep	Pampal	100	Adventure	50	Turkish	A1	20	10
5	Ömer	Mindivanlı	113	Adventure	45	Turkish	B1	20	7
6	Ahmet Turan	Bakır	115	Adventure	45	Turkish	A2	15	8
7	Furkan	Pehlivan	100	Adventure	45	Turkish	A1	20	12
8	Selman Kasım	BAĞIRICI	115	Adventure	70	Turkish	A2	15	11
9	İbrahim	Özsürücü	113	Adventure	50	Turkish	B1	20	7
10	Adalet	Arikanoglu	113	Adventure	60	Turkish	B1	20	9
11	Uğur	Özdemir	115	Adventure	70	Turkish	A2	15	13
12	Ahmet	Söyler	115	Adventure	50	Turkish	A2	15	9
13	Öznur	Karakiliç	100	Adventure	40	Turkish	A1	25	12
14	Яна	Елфимова	100	Adventure	40	Russian	A1	22	12
15	Barış KARSLI	KARSLI	100	Adventure	60	Turkish	A1	22	15
16	Лёва	ЯН	115	Adventure	80	Czec Rep.	A2	22	18
17	Mustafa	Onat	100	Adventure	90	Turkish	A1	22	20
18	Leopoldo	Datuin	113	Adventure	50	Moldova	B1	20	10
19	Orxan	Ismayilov	100	Adventure	70	Azerbaijan	A1	22	17
20	EMRE	ULAKÇI	115	Adventure	60	Turkish	A2	22	11

Apart from the front-end of the system, another major component to consider as to how review value calculation algorithm is implemented to support improving the learner's vocabulary schema is considering the back-end, formula used in finding the assessment of interval. Assessment interval defines the schedule on when that particular vocabulary should appear in the quiz. Considering the performance during exam counter, how many times the word appeared in the articles and did the learner conduct a speaking practice with the lecturer online, are the components of finding the assessment interval. For discussion, student number 2 were taken and extracted for discussion.

Applying the formula discussed in previous section, Table 3 derived the attributes of *vocabulary_id* 62, and the assessment interval of the vocabulary will be assessed after 4 days. Looking at the *created_at* entry, this shows when the vocabulary was first seen and if it appears in other articles *updated_at* will be refreshed. But based on the assessment interval, if the particular word was created last 2017-11-29, a quiz will be given to the learner four days later (2017-12-03) regarding the vocabulary.

This approach is actually seen in General English Proficiency Test, GEPT, in Taiwan as early as 2000. Same vocabulary and articles used in different levels of GEPT for different levels of

English abilities. In addition to adjusting memory cycles of vocabulary (Wang, 2012), it also infers the relationships between words in an article and intelligently adjusts the memory cycles of those words that do not appear in the after-reading quizzes but are known to a learner. This approach does not only enhance the learner's vocabulary schema but also checks the learnt word from time-to-time with assessment interval.

Table 3: *The assessment interval of a particular student*

id	user_id	av_id	vocabulary_id	ranking	review_counter	review_in_exam_counter	speaking_practice_counter	assessment_interval	next_assessment_dt	created_at	updated_at
85	2	66	62	1	3	1	0	4	2017-12-03	2017-11-29 18:46	2017-11-29 18:46
87	2	65	61	1	1	1	0	3	2017-12-02	2017-11-29 18:46	2017-11-29 18:46
88	2	64	60	2	1	2	0	5	2017-12-04	2017-08-10 18:19	2017-11-29 18:46
89	2	63	59	1	1	1	1	5	2017-12-04	2017-11-29 18:46	2017-11-29 18:46
84	2	58	55	1	5	1	1	7	2017-12-06	2017-11-29 18:46	2017-11-29 18:46
86	2	57	54	2	3	2	1	8	2017-12-07	2017-08-10 18:19	2017-11-29 18:46
83	2	56	53	1	3	1	1	6	2017-12-05	2017-08-10 18:19	2017-11-29 18:46
78	2	55	52	1	2	1	1	5	2017-12-04	2017-08-10 18:19	2017-11-29 18:46
82	2	53	50	3	1	3	1	9	2017-12-08	2017-08-10 18:19	2017-11-29 18:46
81	2	52	49	1	2	1	0	4	2017-12-03	2017-08-10 18:19	2017-11-29 18:46
80	2	51	48	1	3	1	0	4	2017-12-03	2017-11-29 18:46	2017-11-29 18:46
77	2	50	47	3	1	3	0	7	2017-12-06	2017-11-29 18:46	2017-11-29 18:46
79	2	49	46	1	1	1	0	3	2017-12-02	2017-11-29 18:46	2017-11-29 18:46
76	2	48	45	1	1	1	0	3	2017-12-02	2017-11-29 18:46	2017-11-29 18:46

Figure 2 shows the monitoring of individual progress of the user in terms of his/her vocabulary schema. It includes the number of gained short-term and long-term vocabularies. This graphic illustration is presented for visual and vivid purposes. Out of 67 new acquired vocabularies 10 of which were converted into long-term while the other is currently active based on read articles. Clicking the show button in Figure 2 will show all the new vocabularies learnt by the learner. The vocabulary, type of figure of speech and its translation are all shown to serve as if a dictionary of its own and refer as the vocabulary schema. Learners can easily track his/her own progress with a click in his/her most convenient time. The used of review value calculation provide essential factor to support improving the learner's vocabulary schema is through the promotion of the learner from one level to another. For instance, the system can shows and monitor students who makes progress by increasing its level. For example student 2 was able to obtain 100 new vocabularies and after taking a handful of quizzes; he would be promoted to A2.

Vocabulary, the core of any language, is probably the most challenging and time consuming part of learning a foreign language. It takes time and flows like a continuous process, once you have settled the fundamentals of a language (pronunciation, orthography and basic grammar). Throughout this process, learners become familiarized with the words they come across. It is the frequency of usage and the number of encounters in different forms and contexts that determine the acquisition of new vocabulary. When teaching vocabulary, the context is really

important that is why some authors underlines the important words that can be used for real communication [12].

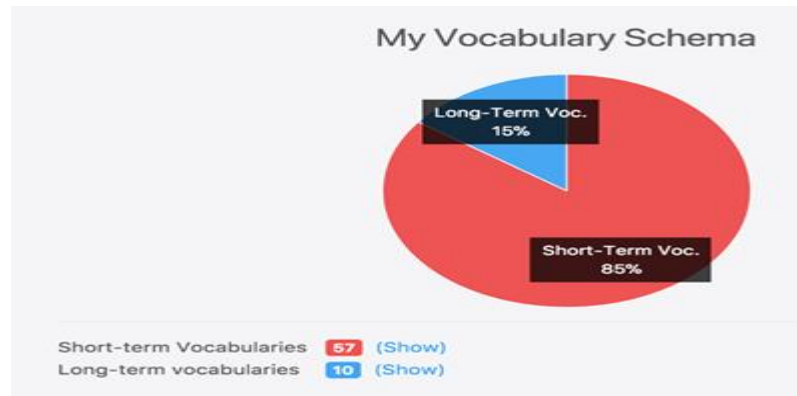


Figure 2: Long-term vs. short-term vocabulary

The great challenge for teachers to design individual and group activities using the Internet resources is how to explore different cultures more directly and effectively [13]. University language learners studying English as additional subject, still have problems in acquiring vocabulary. The assumption is that this might be due to the strategies used in teaching vocabulary. Thus, language teachers and researchers started considering technology as an option to teach more effectively. It seems that learners show very little effort to deal with their problems about newly learned words when technology is involved. During the lesson teachers often assume that students will deal with this problem of vocabulary building outside the class on their own. However, learners do not have enough knowledge about the vocabulary learning techniques and they have difficulty in dealing with this problem themselves [14].

5 Conclusion

Learning new vocabulary is one of the most challenging and time eating processes of foreign learners. Several vocabulary type of researches have navigated this area of tutoring and successfully implemented in different manners. The study focus on learning new vocabulary by rendering articles for reading based on the user interest and entry level thereby progressing in due time. To make sure that the acquisition of vocabulary will happen, a computing mechanism has been incorporated into the system using review value calculation. By it used, learners were able to monitor their progress and vocabulary acquisition by transferring to long-term memory from short term memory. Based on the results many foreign students were able to demonstrate fast comprehension and understanding. Almost all the student increased their English level according to European English Level Framework. Although the study is successfully implement, computing mechanism in words acquisition, there is a need to have an intelligent system to help the learners to advance in words acquisition. For example, a presence of an artificial intelligence to teach the student and encourage them to continue is

needed for faster words acquisition. Another proposal is to transform the learning process into a game based tutoring system in acquiring new vocabularies.

References

- [1] Kritikou, Yioli (2013).Cognitive Web-Based Vocabulary Learning System: The Results Of A Pilot Test Of Learning Greek As A Second Or Foreign Language. *Procedia - Social and Behavioral Sciences* 141 (2014) 1339 – 1345.
- [2] Johnson, T.E, Maring, G.H., Doty, J.H., & Fickle, M. (2006). Cybermentoring: Evolving High-End Video Conferencing Practices to Support Preservice Teacher Training. *Journal of Interactive Online Learning* 5(1), 59-74.
- [3] Hu, C. & Wong, A. F. L. (2006). Video Conferencing by Student Teachers: Does it Make Any Difference? *New Horizons in Education*, (53), 42-56.
- [4] Kent, A. M., Simpson, J. L. (2010). Interactive videoconferencing: Connecting theory to practice for pre-service teachers. *Journal of Digital Learning in Teacher Education*, 27(1), 12–21.
- [5] Atkinson J. (2009). Designing a feedback component of an intelligent tutoring system for foreign language. *Knowledge-Based Systems*, 22(7), 496-501.
- [6] Klapper, J. (2008) ‘Deliberate and incidental: vocabulary learning strategies in independent second language learning’, in Hurd, S. and Lewis, T.,(eds.) (2008) *Language Learning Strategies in Independent Settings*, vol. 33, Clevedon, Multilingual Matters.
- [7] Graham, S.,Harris, K.R., and Loynachan, C. (1993). *Journal of Educational Research* 86 (6): 363-368.
- [8] Stoller, F.L., &Grabe, W. (1993). Implications for L2 vocabulary acquisition and instruction from L1 vocabulary research in Huckin T., Haynes, M., and Coady, J. (eds.), *Second language reading and vocabulary learning*, pp.24-45. Norwood, New Jersey: Ablex.
- [9] Schmitt, N. & Schmitt, D. (1995). Vocabulary notebooks: theoretical underpinnings and practical suggestions.*ESL Journal* 49(2): 133-143.
- [10] Sahin, Mehmet. (2009). Computer Assisted Instruction in Aiding Second- Language Learners. *Eurasian Journal of Educational Research*. Issue 34. Pp. 115-132.
- [11] Nation, I.S.P. (1990). *Teaching and learning vocabulary*. Boston. Heinle and Heinle Publishers.
- [12] Warschauer, M. (1995). *E. Mail for English Teaching*. Alexandria, VA: TESOL Publications. The role of using Facebook in improving English, *TOJSAT : The Online Journal of Science and Technology*- July 2013, 3 (1).
- [13] Nadar, R. (1996) Digital democracy in action, *Forbes*. 2 December: 49, The role of using Facebook in improving English *TOJSAT : The Online Journal of Science and Technology*- July 2013, Volume 3, Issue 1
- [14] Monica S., &Mirabela P. A. (2014). The Impact of Social Media on Vocabulary Learning Case Study Facebook. <http://steconomicuoradea.ro/anale/volume/2014/n2/013.pdf>

Using Triple Modular Redundant (TMR) Technique in Critical Systems Operation

Samira Abu Shernta, Ali A. Tamtum

Department of Electrical and Computer Engineering, Elmergib University, Libya

DOI: <https://doi.org/10.21467/proceedings.2.7>

* Corresponding author email: aamtatum@yahoo.com

ABSTRACT

Many computing systems used in applications of critical systems utilize fault tolerance criteria for normally continuing to operate. Operating in the presence of faults is required in many applications for safety and reliability such as in electric power distribution systems, telecommunications, medical life-support, nuclear reactor control, transportation, automotive, aircraft, and space vehicles. Such systems require continuity and reliability of service. One of the used techniques for meeting the severe reliability requirements inherent in certain future computer application is the use of Triple Modular Redundant (TMR) configuration. Essentially, this technique depends on voting two out of three system output levels. In this paper a fault-tolerant system is proposed using TMR configuration for processors and memory modules with spare model for - line self - reconfiguration. A voter is designed to pass reliable data and signals between processors and memory modules. The voter has the capability to analyze the error and stop the system on the proper time. The proposed system is designed at register level and tested using MATLAB simulation. A set of different faults are injected in different modules of the system in different data pater. The simulation results present the accuracy and capability of the proposed system with respect to faults as well as the ability of errors handling.

Keywords: Triple Modular Redundant (TMR); Critical systems; Voter; Computing systems.

1 Introduction

Many systems require continuity and reliability of service while operating in the presence of limited faults. The ability to deliver highest quality of service for which it is intended is very important criteria in critical systems. To fulfil these primary requirements, fault tolerant techniques are necessary to make sure these systems are fault-tolerant systems which continue to operate satisfactory in the presence of faults [1]. One of the used techniques for meeting the severe reliability requirements inherent in certain future computer application is the use of Triple Modular Redundant (TMR) configuration. The author in [2] stated that the TMR technique required tight synchronization between different units which achieved by using a single and very reliable clock to insure continuity of operation in fault tolerant systems. A fault tolerant system is a system that its behaviour is compatible with its specification in presence of



© 2018 Copyright held by the author(s). Published by Aijr Publisher in Proceedings of First Conference for Engineering Sciences and Technology (CEST-2018), September 25-27, 2018, vol. 1.

This is an open access article under [Creative Commons Attribution-NonCommercial 4.0 International](https://creativecommons.org/licenses/by-nc/4.0/) (CC BY-NC 4.0) license, which permits any non-commercial use, distribution, adaptation, and reproduction in any medium, as long as the original work is properly cited. ISBN: 978-81-936820-5-0

faults in some of its components [3]. Faults in different operating systems are presented in many publications such as in [4] and [5] which represent detailed information regarding fault time latency and transient faults. The choice of error detection, fault handling techniques and their implementation as well as the classes of faults are presented in [6].

Multi-Version techniques based on the use of two or more versions or “variants” of a piece of software, executed either in sequence or in parallel are presented in [7]. Dynamic recovery is generally more hardware-efficient than voted systems, and it is, therefore, the approach of choice in resource-constrained systems especially in high performance scalable systems.. Its disadvantage is that computational delays occur during fault recovery where fault coverage is often low and special operating systems may be required [8]. Error detection checks that are employed in computer systems can be of different types, depending on the system and the fault of interest. Most error detection mechanisms are presented in [9]. Error coverage and mechanisms of error prediction and of latent errors are presented in [5, 10, 11]. Error detection methods such as Watchdog timers have been used since the early days of digital systems especially in embedded systems [12, 13].

The concept of redundancy implies the addition of information, resources, or time beyond what is needed for normal system operation. The redundancy can take one of four forms, including hardware redundancy, time redundancy, software redundancy, and information redundancy. The concept of hardware redundancy became more common and more practical, the cost of replicating hardware within a system is decreasing simply because the cost of hardware are decreasing. The Hardware redundancy means the addition of extra hardware, usually for the purpose either detecting errors or tolerating faults[14]. The most known hardware fault tolerance technique is triple modularity redundancy (TMR), which has been used in many fault tolerant systems. The use of TMR technique and its advantages as well as the use of multistage TMR with replicate voters are presented in [15] and [16]. In [17], a commodity chip multiprocessors (CMP) design with features for providing system-level soft error protection, is described with dual modular redundant (DMR) and triple modular redundant (TMR) systems. In [18], A hypothetical triple-modular redundant computer is subjected to a Monte Carlo program on the IBM 704, which simulates component failures. Two types of namely duplex and triple modular redundancy (TMR) systems are presented in [19]. More application and representations of TMR are presented in [20-22]. In this paper a fault-tolerant system is proposed using TMR configuration for processors and memory modules with spare model for –line self- reconfiguration. A voter is designed to pass reliable data and signals between processors and memory modules.

2 The Proposed TNR System

2.1 TMR Technique Review

The most known hardware fault tolerance technique is triple modularity redundancy (TMR), which has been used in many fault tolerant systems. The hardware unit (M) represented in Figure 1 is triplicated and all three units work in parallel. The outputs of these three units are given to the voting element (V). The voting element accepts the outputs from the three modular and delivers the majority vote as output.

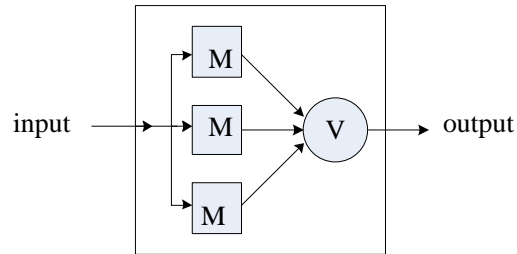


Figure 1: Triple Modularity Redundancy (TMR) organization

Clearly, the TMR organization can completely mask the failure of the one hardware unit. One of the features of TMR is that no explicit actions need to be performed for error detection, recovery, etc. TMR is particularly suitable for transient faults, since in the basic TMR the voter does not "remove" the faulty unit after an error occurs. This scheme cannot handle the failure of two units. In fact, once one unit fails, it is essential that both units should work correctly (so that the voter can get a majority voted output). Due to this, the reliability of the TMR system becomes lower than a simplex system once a failure occurs.

The TMR scheme depends on the voting element. However, the voting element is typically a simple and highly reliable circuits. Another implementation aspect of TMR is that it requires tight synchronization between the different units. This has been frequently achieved by using a single clock. This requires the clock to be very reliable.

2.2 The Proposed System

Triple Modular Redundancy (TMR) configuration is the most efficient method to tolerate many types of faults and masking many types of errors at the system level. It is suitable for real time applications and online system reconfiguration where instant maintenance is not possible such as in Autopilot and unmanned space vehicles. This configuration tolerates the following set of faults:

- Faults effecting the operation of processors, memory modules and system buses.
- Faults produced from programs, compilers used to produce those programs
- Design and manufacturing faults in processors modules and memory modules.

Whereas the set of occurred errors that can be masked by this configuration includes the following classes:

- Processors internal transient errors.
- Processors internal intermittent errors.

- Data bus errors.
- Address bus Errors.
- Control and timing bus errors.
- Memory transient errors.
- Memory intermittent errors.
- Memory buses errors.

In a TMR configuration permanent errors caused by any faulty module are detected but not tolerated. Therefore the faulty module has to be replaced by a good one in order to resume system functions. Real-Time applications cause long down-time and increases Mean Time To Repair MTTR. In such a system the MTTR should be zero in order to recover from those errors and to continue system operations to achieve a high reliability.

To overcome a wide range of those errors and to tolerate that set of faults, a good configuration is proposed for a high reliable and available system with Self-Reconfiguration. In this proposed configuration, processors modules are treated separately from memory modules and the memory modules form also TMR subsystem. Another feature of this configuration is that voting is done at the signals level (data, address and control signals) between the processors modules and the memory modules.

According to this proposed configuration, the three processors (1,2,3) work in parallel and execute the same code and perform the same task. All signals outgoing from these processors are passed through a voter that compares these signals and passes the majority matched ones. If one processor does not match with the other two then the selected majority output from the voter is passed to the memory modules (or to the external I/O devices). Then that processor or its system bus is considered faulty and is given a time to recover from transient faults. If the same processors shows faulty outputs for more than a pre-specified attempts, it is considered as permanent faulty module and the whole system enters a reconfiguration procedure by bringing the spare processor to replace the faulty one.

The same process is done with the memory modules when data is read from memory to the processors. The voter is introduced with two sides: one side for the processors modules and the other side for the memories modules. The voter should also be designed in such a way to work as a comparator and by pass buffer. The voter should also have the mechanism to reconfigure the system by isolating (disconnecting) a faulty module and invoking (connecting) the spare module. The other task of the voter is to load the invoked processor with the current state of the other two processors by a roll-forward recovery procedure and resuming the system operation.

2.3 System Operation

The following assumptions are considered for the proposed system:

- 1 System is at start state.
- 2 All named model are loaded with the same copy of the program.
- 3 All three processors are ready to execute the same program.

- 4 The spare processor is physically connected but logically and electorally disconnected.
 - 5 Give all general block diagram to used voter, three processors and three memories.
- The block diagram of the voter are shown in Figure 2 which represents the composition of the Voter.

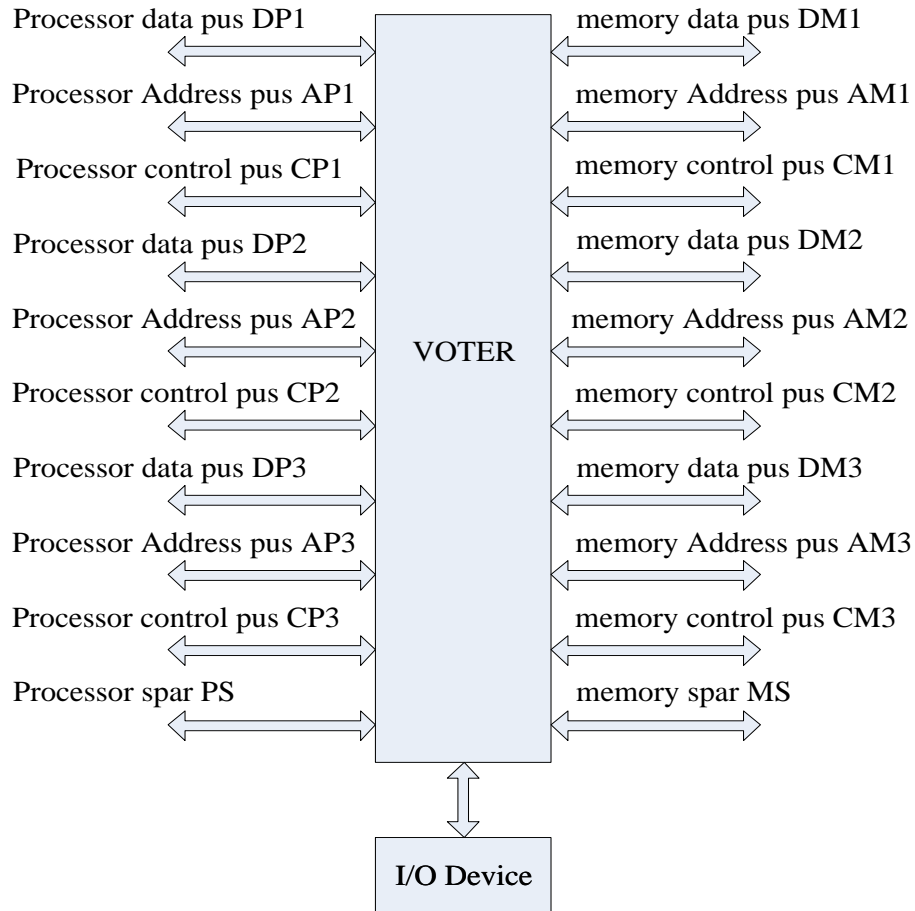


Figure 2: Block Diagram of the voter

In the input side of the Voter there are three processors (Data, Address, and Control) as well as a spare processor. Similarly, in the output of the Voter there are three memories (Data, Address, and Control) as well as a spare memory. Data will be transferred to the I/O devices in case of data saving fail.

Figure 3 represents operating flow chart in which the system starts working by applying either Read or Write command. The system is then tested whether it is working or not. If the system working, a check is made on Address, Control and Data. If not, processors are added to the system and the system is tested again. Then, the three processors are tested. In case of error detection, the damaged processor is specified and repaired and the system continues working. Then data writing and saving in the memory is done. On the other side the process of reading

data from the memory is running. Then a test is made. In case of an error is detected, error is located and repaired. This process continues until finishing the desired job. The operation starts in "write cycle" by entering data to pr1,pr2 and pr3. After that ,the operation is tested to know if there is an error or not?

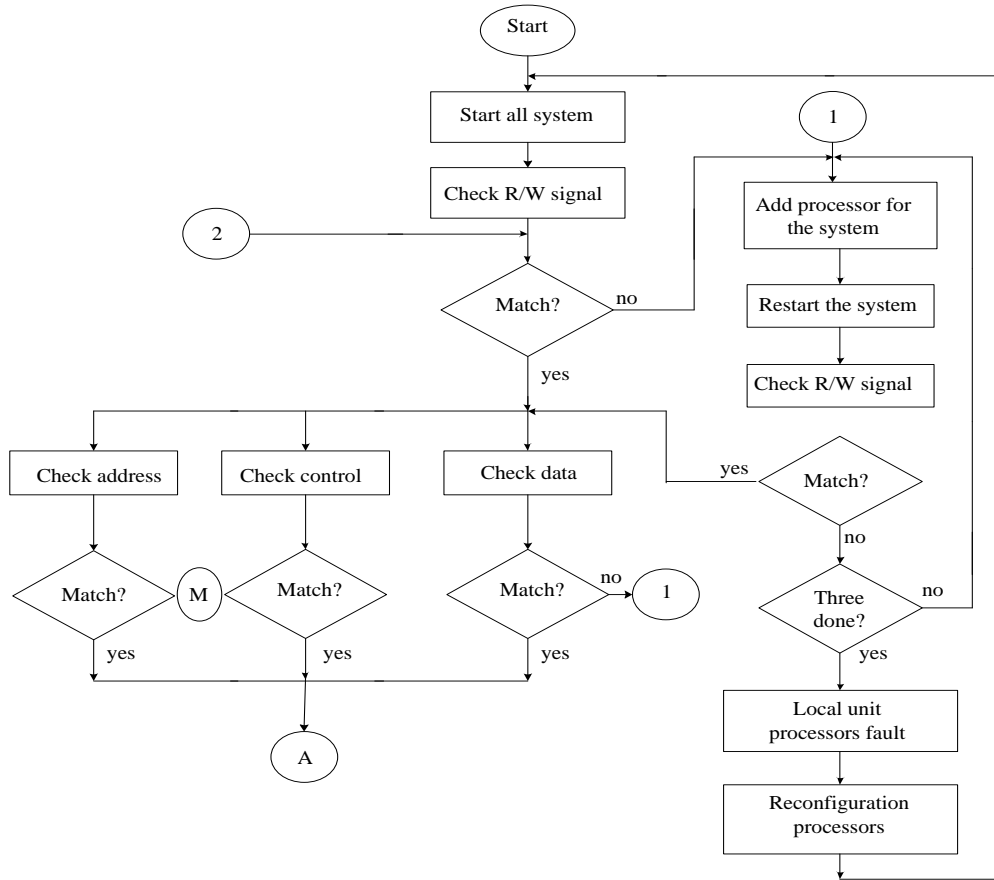


Figure 3: Operating flow chart

There are two cases "Yes" or "No".

"yes" means there is an error and another test will start to know whether the error is permanent or not. The voter will know in which process the error occurs.

"no" means that the error is transient and it may be regained by doing the operation again. Once the faulty process is known, it will be changed by a spare process to continues the operation

Case II: If "NO" we need to know where the results will be sent. There are two options. Either the results will be sent to the memory and the data will be saved into "me1,me2 and me3" or the data will be sent into the input ,output devices.

Regarding read cycle, the data will be read from the memory and the operation will continue to the end of the cycle in similar manner.

3 Numerical results

The results can be summarized in Tables 1, 2, 3, 4, 5 and 6 which represent Processor Data Bus, Memory Data Bus, processor address Bus, memory address Bus, Control processor Bus and Control memory Bus including total time latency.

Table 1: Processor Data Bus

Module	Injected faults	Detected faults	Time Latency (Second)	Coverage	System Recovery (Y,N)
Dp1	0	0	2.7375e-005	0	N
Dp2	0	0	2.7375e-005	0	N
Dp3	4	3	2.7375e-005	75%	Y
Total	4	3	8.3991e-005	75%	Y

The system considered healthy when DP3 recorded failure two consecutive times. When number of errors =3, a permanent error in DP3 is recorded and changed with the spare one (DPs).

Table 2: Memory Data Bus

Module	Injected faults	Detected faults	Latency (Second)	Coverage	System Recovery (Y,N)
DM1	2	2	2.9241e-005	100%	Y
DM2	0	0	2.9241e-005	0	N
DM3	0	0	2.9241e-005	0	N
Total	2	2	8.7724e-005	100%	Y

A permanent error in DM1 is recorded with latency time = 2.9241e-005 sec; and total latency time = 8.7724e-005 sec; The error in DM1 is temporary and a 100% recovered.

Table 3: processor address Bus

Module	Injected faults	Detected faults	Latency (Second)	Coverage	System Recovery (Y,N)
Ap1	0	0	3.2352e-005	0	N
Ap2	3	3	3.2352e-005	100%=100%	Y
Ap3	0	0	3.2352e-005	0	N
Total	3	3	9.7055e-005	100%	Y

The number of injected errors equal to 3, and the error in AP2 is permanent and changed with the spare one (Aps).

Table 4: memory address Bus

Module	Injected faults	Detected faults	Latency (Second)	Coverage	System Recovery (Y,N)
AM1	0	0	2.8152e-005	0	N
AM2	0	0	2.8152e-005	0	N
AM3	6	3	2.8152e-005	3/6*100%=50%	Y
Total	6	3	8.4457e-005	50%	Y

Number of errors =3 and permanent error in AM3. The spare AMs replaces the mean AM3 with 50% coverage.

Table 5: Control processor Bus

Module	Injected faults	Detected faults	Latency (Second)	Coverage	System Recovery (Y,N)
Cp1	2	2	2.8774e-005	2/2*100%=100%	Y
Cp2	0	0	2.8774e-005	0	N
Cp3	0	0	2.8774e-005	0	N
Total	2	2	8.6323e-005	100%	Y

The error in CP1 is temporary with 100% coverage.

Table 6: Control memory Bus

Module	Injected faults	Detected faults	Latency (Second)	Coverage	System Recovery (Y,N)
CM1	0	0	2.9863e-005	0	N
CM2	3	3	2.9863e-005	3/3*100%=100%	Y
CM3	0	0	2.9863e-005	0	N
Total	3	3	8.9589e-005	100%	Y

The number of errors = 3 and the error in CM2 is permanent. The spare CMs is utilized instead of using the mean CM2.

4 Conclusions

The principles and concepts of fault tolerance were introduced and investigated. The analysis was devoted to the online error detection and mainly focused on the use triplication techniques. According to the outcome from the survey of the online error detection techniques and investigation of some previous systems, a TMR system configuration was proposed to increase system reliability and availability for self – reconfigurable application. In this system both the processor and memory module are triplicated with one spare module. A voter was designed to pass reliable data and singles between processors module and memory modules. The voter has the capability to stop the system and analysis the error. It enters the system for roll- back procedure in case of transient error or it replaces the faulty

module with the spare one in case of permanent error. Thus system is recovered and resumes its operation on line which achieves the target objective. To verify the capabilities and the behaviour of proposed system and voter design, the system is simulated using MATLAB package. A set of faults are injected in different information paths and the response of the system was monitored.

References

- [1] N. Kim and S. Gupta "Testing of Digital Systems", *Cambridge University press* 2003.
- [2] Chris Weaver , Todd Austin, "A Fault Tolerant Approach to Microprocessor Design" *Advanced Computer Architecture Laboratory University of Michigan*, July 2001.
- [3] Teijo Lehtonen , Juha Plosila, Jouni Isoaho , "On Fault Tolerance Techniques towards Nanoscale Circuits and Systems " *Turku Center for Computer Science, TUCS Technical Report*, August2005..
- [4] Ali H. Maamar , Asma y. Elhawadi, "Self Checking Register file" *Computer Department Higher Institute of Electronics, Beni- Waled*, APRIL 1999.
- [5] Lisboa,C.A. Erigson, M.I. and Carro, l.and carro ,L, "System level approaches for mitigation of long duration transient faults in future technologies", *12th IEEE European Tcst Symposium (ETS,07)*, 2007.
- [6] Januu Sosnowski, "Transient fault Tolerance in Digital System", *Warsaw University of technology, IEEE* , 1994.
- [7] Subhashish Mitra, "Diversity Techniques for Concurrent Error Detection" *Technical Report , Center for Reliable Computing* , may 2000.
- [8] Parg K Lala "Self- checking and fault –Tolerance Digital Design", *Morgan Kaufmann Publisher*,2001.
- [9] Manoj Franklin , "A Study of Time Redundant Fault Tolerance Techniques for Superscalar processors", *Department of Electrical &computer Engineering , Clemson Universty ,Clemson, USA*, 1995 IEEE.
- [10] Stanislaw J.Piestrak," Design of fast self -testing checkers a Class of Berger Codes", *IEEE Transaction on Computer*, MAY 1987.
- [11] Kim and K. G. Shin , "Evaluation of Fault Tolerance Latency from Real -Time Application 's Perspectives", *IEEE Transactions on Computers*, vol . 49 No 1, Jan. 2000.
- [12] Robert Redinbo, " Generalized Algorithm-Based Fault Tolerance: Error Correction via Kalman Estimation", *IEEE Transactions on Computers*, Vol. 47, No. 6, June 1998.
- [13] Robert Redinbo, " Generalized Algorithm-Based Fault Tolerance: Error Correction via Kalman Estimation", *IEEE Transactions on Computers*, Vol. 47, No. 6, June 1998.
- [14] Constantinescu, "Teraflops Supercomputer : Architecture and Validation of the Fault Tolerance Mechanisms", *IEEE Transactions on Computers*, Sep 2000.
- [15] Karri, K. Kim, and M. Potkonjak, " Computer Aided Design of Fault-Tolerant Application Specific Programmable Processors", *IEEE Transactions on Computers*, Nov 2000.
- [16] Dutt and N. R. Mahapatra, "Node-Covering, Error Correcting Codes and Multiprocessors With Very High Average Fault Tolerance", *IEEE Transactions on Computers*, Sept 1997.
- [17] James E. Smith, " Motivating Commodity Multi-Core Processor Design For System-Level Error Protection", *Kewal K. Saluja* 2006.
- [18] George W. Grosline, "The Use of Triple-Modular Redundancy to Improve Computer Reliability", *IBM Journal*, April 1962.
- [19] Rami Melhem, "Energy-Efficient Duplex and TMR Real-Time Systems Appeared in the IEEE Real-Time Systems Symposium", *Computer Science Department, University of Pittsburgh*, Dec 2002.
- [20] Dmitry Burlyaev, Pascal Fradet, Alain Girault, "Verification-guided voter minimization in triple-modular redundant circuits", *Automatin & Test in Europe Conference & Exhibition (DATE)*, Year: 2014.
- [21] Jeffrey Prinzie, Michiel Steyaert, Paul Leroux, Jorgen Christiansen, Paulo Moreira, "A single-event upset robust, 2.2 GHz, to 3.2 GHz, 345fs jitter PLL with triple-modular redundant phase detector in 65 nm CMOS", *IEEE Asian Solid-State Circuits Conference (A-SSCC)*, Year: 2016..
- [22] Pang Zh, Qi Zheng, Zhankui Zeng, Liman Yaung, "The single integrity design and simulation of triple-modular redundant (TMR) computer", *IEEE International Conference on Cybernetics and Intelligent Systems (CIS) and , IEEE Conference on Robotics, Automation and Mechatronics (RAM)*, Year: 2017.

Handwriting Arabic Words Recognition Based on Structural Features

Salim Aloud

Department of Computer Science, College of Sciences, Azzaytuna University, Libya

DOI: <https://doi.org/10.21467/proceedings.2.8>

* Corresponding author email: salemali416@yahoo.com

ABSTRACT

Handwriting recognition technology is the ability of a computer to recognize characters, words and other symbols that have been written by hand in natural handwriting. This study presents a method for recognition of Handwritten Arabic Words (HAW) through expanding in the way of structural features extraction by relying on geometrical information (straight lines, loops, points, and curve). The input to the system is binary images written by hand by number of people. The features are to convert the image from two dimensional into one dimensional as a vector that is to be used as a signature for the image the experiments have been conducted on a database of a thousand words representing names of a hundred Libyan cities at a rate of ten patterns for each city. Classification of the words was dependence on Artificial Neural Networks (ANN) of Multiple Layers Perceptron (MLP) type. Wherein half of the words were used to train the network and the other half to test the network. The ratio of recognition was 80.4 %.

Keywords: recognition, features extraction, structural information.

1 Introduction

Words and characters recognition methods have been improved since many years. These methods used for printed or handwritten scripts and used two different approaches of processing which are online and offline. It has been gaining more interest lately due to the increasing popularity of handheld computers, digital notebooks, and advanced cellular phones. These devices nowadays are commonly used worldwide that encouraged companies to improve their products to support multi languages. These devices can deal with many languages spoken by billions of people around the world. Arabic language is the main language of all Arabic countries with more than 280 million people are speaking this language as a first language and by 250 million as a second language. Arabic language comes as the fifth rank of most commonly used languages in the world. There are some other languages related to Arabic language. These languages have some similarities with Arabic language whence from the characters shapes or from the pronunciation [1]. the progress in Arabic language is slower than the progress in developing solutions for Latin and Asian languages [7]. There are many other applications for analysis of human handwriting such as writer recognition and verification,



© 2018 Copyright held by the author(s). Published by AIJR Publisher in Proceedings of First Conference for Engineering Sciences and Technology (CEST-2018), September 25-27, 2018, vol. 1.

This is an open access article under [Creative Commons Attribution-NonCommercial 4.0 International](https://creativecommons.org/licenses/by-nc/4.0/) (CC BY-NC 4.0) license, which permits any non-commercial use, distribution, adaptation, and reproduction in any medium, as long as the original work is properly cited. ISBN: 978-81-936820-5-0

form processing, interpreting handwritten postal addresses on envelopes and reading currency amounts on bank checks etc. The main problem encountered when dealing with handwritten Arabic characters is that characters written by different persons representing the same character are not identical but can vary in both size and shape. unlimited variation in human handwriting styles similarities of distinct character shapes, character overlaps, and interconnections of neighboring characters. In addition, the mood of the writer and the writing situation can have an effect on writing styles [2][4][6] Handwritten recognition starts with image preparation stage by transforming it from a color image into grayscale image. Then convert it into a binary image. . The preparation stage is followed by features extraction stage during which the image is converted into a group of features in order to change them from two dimension data to one dimension data or a vector of the features. In general the features come in three main parts statistical features, structural features and global transformation. [1]. In this study the structural features are used which depend on the word's geometrical information as ratio of the length to the width, the loops, branching points, straight lines and the curve or slopes in the various directions. The process of separation of the features of each word connected with it, occurs by relying on the ANN of the MLP type. The training process takes place by allowing the network to practice on half of the number of patterns at a rate of 5 models, or patterns for each word. The training algorithm place by way of back propagation (BP) which is used to train the MLP type network [8]. The testing process was conducted on the other half of the patterns which amount to 500 words. The recognition rate was over 80%. This paper is organized as follows: Section 1 gives a brief description of Arabic Alphabet Characteristics. Section 2 explained Features extraction stage. Section 3 explaining classification stage by ANN. Section 4 gives Experiments and results.

2 Arabic Language Alphabet Characteristics

The Arabic language has a lot of advantages which make it different from the other ones in terms of shape, and way of writing and direction of the writing and which are clarified as follows:

1. Arabic text (machine printed or handwritten) is written cursively and in general from right to left.
2. Arabic writing uses letters, punctuation marks, spaces, and special symbols.
3. An Arabic letter might have up to four different shapes, depending on its relative position in the word: 1: isolated, 2: connected from the left, 3: connected from the right and 4: connected from both right and left according to its place in the word like the letter (ع).
Table 1.
4. Some letters exist as a combination of two letters in some certain situations, like the letter (lamelif لآ) which is created by combining two letters , the letter(lam ل) and (alif ا).
5. Sixteen Arabic letters have from one to three secondary components. The type and position of the secondary components are very important features of Arabic letters. For

example, Tah (ط) and Thah (ظ) differ only by the number of dots above the main body, Seen (س) and Sheen (ش), Sad (ص) and Dad (ض).

Table 1: show four different shapes for letter (ع)

(a) isolated	(b)connected from the left	(c)connected from the right	(d)connected from both right and left
ع	ع	ع	ع

6. Arabic writing contains many fonts and writing styles. The letters are overlaid in some of these fonts and styles.
7. Ligatures are combinations of two and sometimes three letters into a single shape [4].
In general, the Arabic writing is written by using different writing techniques, or styles which result in letters and words having different shapes which in turn cause obscurity in any recognition system.

In general the Arabic writing may be classified into three different styles:

Typewritten: This style is generated by computer. It is the simplest one because the characters are written without overlaps or ligature.

Typeset: This style is more difficult than the typewritten because it has many ligatures and overlaps. It is used to write newspapers and books. Nowadays, this style may also be generated using computers.

Handwritten: This style is the most difficult because of the variation of writing the Arabic alphabets from one writer to another [3].

3 Features Extraction

The first step in features extraction stage is preprocessing stage. In this step the image convert from gray scale into binary image which means it has only two levels zero (0) level which represents a background, and level (1) which represents foreground. The change process occurs by using the threshold technique. And then extract connected components through convert it into labeled image [9]. Then the features extraction stage comes. The features extraction stage is considered as the most important stage of the study and the capability of any recognition system to differentiate any writing depends to a large degree on the exactness of the features extracted from the image. In this study the structural features are used.

Structural features describe the geometrical and topological characteristics of a pattern by describing its global and local properties. The structural features depend on the kind of pattern to be classified. For Arabic characters, the features consist of (ratio of the length to the width, the loops, branching points, straight lines and the curve or slopes in the various directions). In this study; the structural features have been used where a word is divided as in the Figure 1. Features of each area are extracted by analyzing the connected components existing in each area.

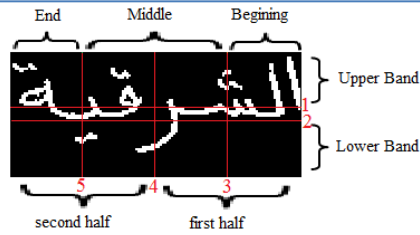


Figure 1: show sample of the name (الشرفية)

The letter alif (ا) usually appears in the upper part of a word and its height is twice as large as its width or more Figure 2. And the loops: each part of the binary image that has the color of the background, and whose edges have the color of the foreground, and falls within the connected components is regarded as a loop Figure 3.



Figure 2: detect letter alif



Figure 3: detect loop

The calculation of one point is found out through calculation of the area, of each component, and case where the area is less than the threshold, it is considered as a point Figure 4. And in case where the width of the component is bigger or equal to twice its length (-) then the component is considered as two points Figure 5. And in case there is a curve in the point falling above a word, the component is then regarded as three points (∩) Figure 6.



Figure 4: detect one point



Figure 5: detect two points



Figure 6: detect three points

The features that are possible to obtain in the lower part of the image are:

The letters of Arabic language that may appear underneath a word are

(ج خ ز س ش ص ض ع غ ل ن و ي) detect this features by tracing the number of crossings from the background to the foreground horizontally (h) and vertically (v) at middle connected component if $h = 1$ and $v = 1$ return (curve ج) Figure 7. If $h = 2$ and $v = 1$ return (curve ن) Figure 8. if $h = 1$ and $v = 2$ return (curve ح) Figure 9.



Figure 7: detect curve ج



Figure 8: detect curve ن



Figure 9: detect curve ح

Table 2: shows details of features vector

element	Description
1	Number of straight lines(1) in beginning of word
2	Number of straight lines(1) in middle of word
3	Number of straight lines(1) in end of word
4	Number of loops in beginning of word
5	Number of loops in middle of word
6	Number of loops in end of word
7	Number of points(•) up the word
8	Number of points(•) down the word
9	Number of (curve ٲ)in first half of word
10	Number of (curve ٲ) in second half of word
11	Number of (curve ٲ)in first half of word
12	Number of (curve ٲ) in second half of word
13	Number of (curve ٲ)in first half of word
14	Number of (curve ٲ) in second half of word
15	Number of (letters kaf ك) in the word

The letter kaf calculated either by calculating the width of the component Figure 10. Or by tracing the number of crossings from the background to the foreground vertically Figure 11.

**Figure 10:** detect character kaf**Figure 11:** detect character kaf

In this study a features vector containing 15 elements has been set up each of which expresses a feature of the word in a way that each image is represented by a vector containing 15 elements. This vector is the one that is used in the process of training and testing of the ANN. This vector is shown in Table 2.

For example the word (توكرة) Figure 12 its features vector was as follows:
Features vector = [0 0 0 1 0 1 4 0 1 1 0 0 0 0 1]

**Figure 12:** word (توكرة)

The first, second and third elements are 0, 0, 0 and they mean that they don't contain the straight lines neither on the beginning of the word nor the middle or end of the word. The fourth component (1) means existence of a loop at the beginning of the word, the fifth nonexistence of a loop in the middle of the word, the sixth which is (1) existence of one loop at the end of the word, the seventh (4) meaning existence of four points over the word, the eight (0) nonexistence of points under the word and the ninth which is (1) meaning existence of a (curve ٺ) in the first half of the word and the tenth (1) which means existence of an (curve ٺ) in the second half of the word. The eleventh and twelfth which are (0), mean nonexistence of (curve ٺ) in the first nor second half of the word. The thirteenth and fourteenth which are (0) mean the) curve ٺ) without its curve in the first half or the second one. The fifteenth (1) means existence of the letter (Kaf ڪ) in the word.

4 Classification Stage

The process of separation of the features of each word connected with it occurs by relying on the ANN of the MLP type which is used to separate any data even if they are not linear. The MPL network contains three layers input, hidden and output layer and in each layer there is a number of nodes Figure 13 [4]. The number of nodes in the input layer is equal to the number of elements in the features vector (15 elements). But the number of the nodes in the output layer depends on the number of the words which are to be separated (100 words). The hidden layer lies between the input and output layers. The training algorithm place by way of back propagation (BP) which is used to train the feed forward network MLP type network with supervised learning [8].

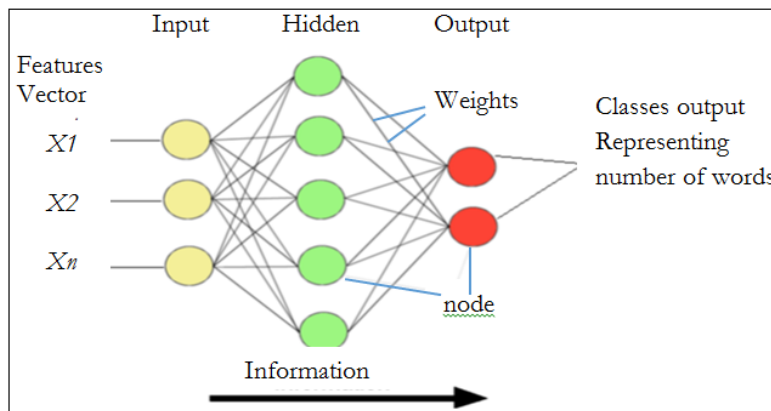


Figure 13: ANN of the MLP type

5 Experiments

5.1 Training Mode

In the training mode the first half of the data was selected and such a half represents 500 words at a rate of 5 forms for each word .The number of the names is 100 which requires to be 100 classes. And as the features vector includes 15 components, the number of the input layer nodes becomes 15. The number of the hidden layer's nodes was 22. As the required number of the classes is 100, the number of the output layer's nodes was 7. And the learning rate was 0.2 the network has been trained by counting on iteration in a way that the number of the iteration was determined to be at 30000, a number that reached to $8.222 * 10^{-5}$ by the average of the errors.

5.2 Recall Mode

In this mode the values of the weights are fixed. The neural network works to determine only the input data in each class. The values of the weights are not changed nor there a calculation for the error. In the recall mode, the other half of the patterns, totaling 500 words and representing an extra 5 models for each word, have been used.

6 Results

Out of the 500 words, the result was that the ANN classified, 402 correct words while 98 words were identified incorrectly, which means the rate of recognition was 80.40 % as in the Table 3.

Table 3: shows the results of study

Number of words	Correct words	Incorrect words	rate of recognition
500	402	98	80.4%

7 Conclusion

In this research, the way the features are extracted has been expanded upon to involve more details on the geometrical features connected with the word written by hand, which is to discover the curve, underneath the word which appears to lean to the left or to the bottom, thereby leading to more accurate features which in turn contributed in the enhancing rate. It remains a difficult task to try to recognition of Arabic handwriting due to difference in writing styles from one person to another and to various kinds of handwriting and what accompany them in terms of overlapping and interconnection. As such, the main concern is to upgrade the capability to recognition to the maximum extent possible. And the enhancing relies in the main on the way the features are extracted, that is to say, the more exact, or accurate the features are the more better the capability to recognition becomes.

In addition, the recognition enhancing rate depends on the separation method. Through the findings of this research it was found that some errors were attributed to the network not being trained on some patterns, thus not being capable to recognition those patterns. The solution lies in increasing the patterns, or in other words, in training the network on as much patterns as possible. In the future work, the same methods connected with the findings of this research will be employed in recognizing texts written by hand.

References

- [1] M.A Abuzaraida and A.M Zeki and A. M Zeki " Feature Extraction Techniques of Online Handwriting Arabic Text Recognition " 5th International Conference on Information and Communication Technology for the Muslim Word 2013.
- [2] H.EL Moubtahij, A.Halli and K.Satori " Review of Feature Extraction Techniques for Offline Handwriting Arabic Text Recognition " International Journal of Advances in Engineering & Technology, Mar.2014. Vol.7,Issue 1,pp.50-58.
- [3] A. Lawgali, A. Bouridane, M. Angelova, Z. Ghassemlooy "Handwritten Arabic Character Recognition: Which Feature Extraction Method? " International Journal of Advanced Science and Technology Vol.34,September, 2011.
- [4] Rafael M. O. Cruz, George D. C. Cavalcanti and Tsang Ing Ren "Handwritten Digit Recognition Using Multiple Feature Extraction Techniques and Classifier Ensemble "IWSSIP 2010 - 17th International Conference on Systems, Signals and Image Processing.
- [5] Ashoka H.N. , Manjaiah D.H. , Rabin dranath Bera " Feature Extraction Technique for Neural Network Based Pattern Recognition" International Journal on Computer Science and Engineering , Vol. 4 No. 03 March 2012.
- [6] Fenwa Olusayo Deborah, Omidiora Elijah Olusayo , Fakolujo Olaosebikan Alade," Development of a Feature Extraction Technique for Online Character Recognition System" Innovative Systems Design and Engineering , ISSN 2222-1727 (Paper) ISSN 2222-2871 (Online)Vol 3, No 3, 2012.
- [7] G. Abandah, K. Younis, M. Khedher " HANDWRITTEN ARABIC CHARACTER RECOGNITION USING MULTIPLE CLASSIFIERS BASED ON LETTER FORM" In Proc. 5th IASTED Int'l Conf. on Signal Processing, Pattern Recognition, & Applications (SPPRA 2008), Feb 13-15, Innsbruck, Austria.
- [8] A. Lawgali, A. Bouridane, M. Angelova, Z. Ghassemlooy "Handwritten Arabic Character Recognition: Which Feature Extraction Method? " International Journal of Advanced Science and Technology Vol.34,September, 2011.
- [9] Rafael C. Gonzalez and Richard E. Woods "Digital Image Processing " Second Edition. Prentice Hall 2002.

A Novel Chaotic Uniform Quantizer for Speech Coding

Osama A. S. Alkishriwo

Department of Electrical and Electronic Eng., College of Eng., University of Tripoli, Libya

DOI: <https://doi.org/10.21467/proceedings.2.9>

* Corresponding author email: alkishriwo@yahoo.com

ABSTRACT

Quantization is an essential step in the analog-to-digital conversion process and it is very important in all modern telecommunication systems. In this paper, a novel chaotic uniform quantizer is proposed and its application for speech coding is presented. The proposed system consists of three stages: two PCM coders separated by an XOR operation with a chaotic sequence, where the first step is used for continuous signal sampling and second stage performs data encryption, while the third stage provides additional data compression. The performance of the presented quantizer for Laplacian distributed signals and real speech signals is investigated and compared with that of the well-known uniform and non-uniform quantizers. Simulation results show that the proposed quantizer provides secured data with higher levels of SQNR compared to others.

Keywords: Quantization; Uniform quantization; Non-uniform quantization; Source coding; Encryption; Chaotic systems.

1 Introduction

In all modern telecommunication systems, the analog-to-digital conversion is very important phase in the way of processing analog signals. It consists of two main steps which are quantization and coding. Quantization provides a means to represent signals efficiently with acceptable fidelity for signal compression, while coding decides exactly which code-words to assign to each distinct quantization level [1].

Existing quantization schemes can be classified into two categories, namely, uniform quantization and nonuniform quantization [2]. Uniform quantization is widely used due to its simplicity of implementation, but not optimal for signals with nonuniform distribution in terms of mean square error. While nonuniform quantization is much more complex, it is in general causes less information loss than uniform quantization, especially for small quantization resolutions. Lloyd–Max quantization is a major type of nonuniform quantization [3, 4]. It is optimal in the sense of mean squared error (MSE), but it is computationally intensive. Companding, which consists of nonlinear transformation and uniform quantization, is a technique capable of trading off quantization performance with complexity for nonuniform quantization [5].



© 2018 Copyright held by the author(s). Published by AIJR Publisher in Proceedings of First Conference for Engineering Sciences and Technology (CEST-2018), September 25-27, 2018, vol. 1.

This is an open access article under [Creative Commons Attribution-NonCommercial 4.0 International](https://creativecommons.org/licenses/by-nc/4.0/) (CC BY-NC 4.0) license, which permits any non-commercial use, distribution, adaptation, and reproduction in any medium, as long as the original work is properly cited. ISBN: 978-81-936820-5-0

In literature, many nonuniform quantizers have been developed to meet the challenge of designing a low complexity and high signal-to-quantization noise ratio (SQNR). In [6, 7] sophisticated compression models based on fixed-rate scalar quantizer for Laplacian probability density function have been recently proposed. The problem of support region optimization has been extensively considered in the field of scalar quantization [8]. The optimization of the support region of the product polar companded quantizer is presented in [9]. This resulted in SQNR increase, but in a more complex encoding/decoding procedure. Although a great number of quantizers have been developed to provide an additional enhancement of the quantized signal quality, there is still a need to continue the research in this field.

In this paper, a novel chaotic uniform quantizer is proposed. It consists of three stages: two PCM coders separated by an XOR operation with a chaotic sequence. The first step is used for continuous signal sampling using rough quantization with a large number of quantization levels. After that, encoded data are XORed with a uniformly distributed random sequence which is generated from chaotic dynamic system to perform data encryption. The encrypted data are decoded to obtain discrete samples, which are further quantized using a quantizer with a small number of quantization levels in order to provide additional compression. The proposed quantizer is evaluated by means of a computer simulation using synthetic Laplacian source signals and real speech signals. The presented quantizer provides gain in the signal to quantisation noise ratio, encryption of the quantized samples, and compression over the conventional uniform quantizer as well as companding quantizer. This indicates the possibility of practical application of the chaotic proposed quantizer in the contemporary transmission of speech signals.

The rest of the paper is organized as below. Section II presents the preliminaries of chaotic uniform quantizer. Section III describes the proposed chaotic uniform quantizer. Simulation results, comparison and discussion are given in Section IV. Finally, conclusions are summarized in Section V.

2 Preliminaries of Chaotic Uniform Quantizer

2.1 Chaotic Dynamic System

Chaos systems are considered suitable for practical use because of its complex dynamic behaviors. They provide a good combination of speed and high security. They have many excellent intrinsic properties, such as high sensitivity to initial conditions and control parameters, which are the desired properties in the application of encryption. The three dimensional discrete chaotic system, which are presented in [10], is defined as follows

$$\begin{aligned} x_{n+1} \\ = \left[\frac{\alpha \times (x_n - x_n^2)}{(y_n - y_n^2)} \right] \text{ mod } 1 \end{aligned}$$

$$\begin{aligned}
& y_{n+1} \\
&= \left[\frac{\beta \times (y_n - y_n^2)}{(z_n - z_n^2)} \right] \text{ mod } 1 \tag{1} \\
& z_{n+1} \\
&= \left[\frac{\gamma \times (z_n - z_n^2)}{(x_n - x_n^2)} \right] \text{ mod } 1
\end{aligned}$$

The chaotic behaviour of the system is observed when the control parameters are chosen as $0.5 < \alpha, \beta, \gamma < 4$ with the initial conditions x_n, y_n , and $z_n \in [0, 1]$.

Uniform Quantizer

A uniform quantizer splits the mapped input signal into quantization steps of equal size. If X is a random variable with the probability density function $p_X(x)$ at input of the quantizer is converted to one of Q allowable levels, m_1, m_2, \dots, m_Q and Y is a discrete random variable at output of the quantizer. Then, the quantizer q maps X to Y as follows:

$$Y = q(X) = m_i, \quad i = 1, 2, 3, \dots, Q \tag{2}$$

Thus the quantization error, $e_q = x - y$, is a random variable with pdf $p_{e_q}(e_q)$ and the average distortion is,

$$D = E\{e_q^2\} = \int_{-\infty}^{+\infty} (X - Y)^2 p_X(x) dx \tag{3}$$

where $E\{\cdot\}$ is the expectation value. The signal to quantization noise ratio ($SQNR$) is obtained by dividing the input source variance σ^2 over the average distortion (D) as follows:

$$SQNR = 10 \log_{10} \left(\frac{\sigma^2}{D} \right) \tag{4}$$

Proposed Chaotic Uniform Quantizer

The configuration of the proposed chaotic uniform quantizer is shown in Figure 1. The quantization process can be achieved using three main steps. In the first step, analog-to digital (A/D) conversion is performed using a quantizer with a high number of quantization levels Q_1 , whose purpose is to convert analog signal to discrete samples. Then, the quantized samples are encoded and XORed with a uniform random sequence generated from chaotic system. The resulted data are decoded to obtain an encrypted discrete time signal which has a uniform probability density function. The aim of the second stage is to provide additional signal compression by using a low number of quantization levels Q_2 where ($Q_2 < Q_1$). The key stream in the chaotic system is composed of control parameters α, β, γ and initial values x_0, y_0, z_0 .

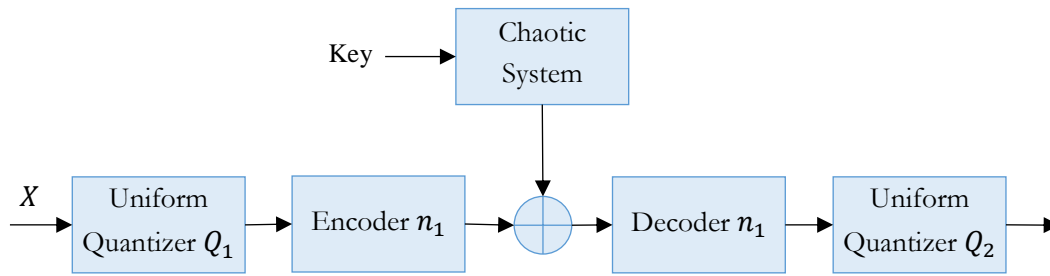


Figure 1: Proposed chaotic uniform quantizer.

3 Simulation Results

The input–output characteristics of uniform quantizer, nonuniform quantizer, and chaotic quantizer are shown in Figure 2. It is known that uniform quantizer has fixed step size and fixed output level as given in Figure 2(a), while nonuniform quantizer has variable step size and fixed output level as illustrated in Figure 2(b). However, chaotic quantizer has fixed step size and variable output level as shown in Figure 2(c).

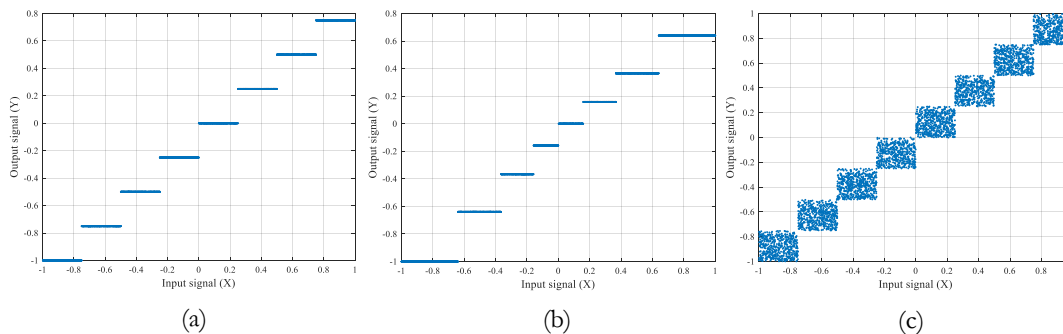


Figure 2: Quantizer characteristics : (a) Uniform quantizer, (b) Nonuniform quantizer, (c) Chaotic quantizer.

The performance of the proposed chaotic quantizer in quantization of signals having Laplacian probability density function is shown in Figure 3(a). The choice of Laplacian distribution is made so as to match the data typically found in speech coding problem. The results of chaotic quantizer are compared with the results presented by conventional uniform and nonuniform quantizers. As a direct application of the proposed chaotic quantizer for speech coding, it has been applied to a speech signal and the results are reported in Figure 3(b). In both cases, the performance of chaotic quantizer in terms of SQNR is superior to the performances of traditional uniform and nonuniform quantizers. For instance, for the case of Laplacian source, the chaotic quantizer produces 3 dB and 1 dB SQNR on average higher than uniform and nonuniform quantizers, respectively. Similarly, for the case of speech signal the improvement on the values of SQNR are 2.5 dB and 0.8 dB.

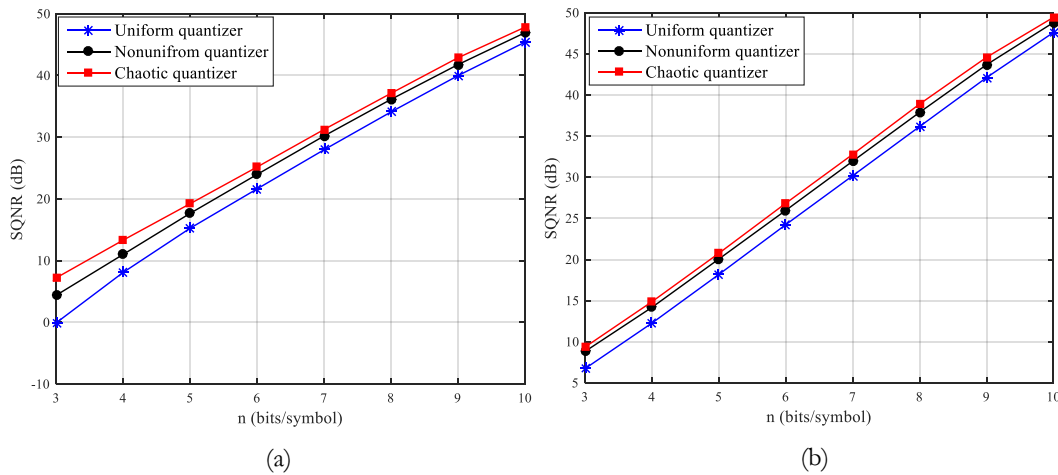


Figure 2: Signal to quantization noise ratio versus number bits per symbol for, (a) Source with Laplacian probability density function, (b) Speech signal.

An important advantage of the proposed chaotic quantizer is the quantization of samples and encrypting them at the same time. The used chaotic system given in (1) has three initial values and three control parameters. Thus, if the precision is set to be 10^{-15} , the key space can reach $10^{6 \times 15} \approx 2^{299}$, which can efficiently resist the brute-force attack.

4 Conclusions

In this paper, the chaotic uniform quantizer is proposed and its performance for input signal with Laplacian distribution and its application for speech signal processing are explored. Experimental results demonstrate that the chaotic uniform quantizer is superior to the conventional uniform and nonuniform quantizers at all bit per symbol region. It has been shown that the proposed chaotic quantizer provides more constant and higher level of SQNR, which can be considered via the gains in the SQNR that range up to 3 dB as illustrated in the results section. Finally, the quantized samples are encrypted with a chaotic sequence which has a key space of 2^{299} .

References

- [1] N. S. Jayant and P. Noll, *Digital Coding of Waveforms*, Prentice Hall, Upper Saddle River, N. J., 1984.
- [2] R. M. Gray and D. L. Neuhoff, "Quantization," *IEEE Transactions on Information Theory*, vol. 44, no. 6, pp. 2325-2383, Oct. 1998.
- [3] S. P. Lloyd, "Least squares quantization in PCM," *IEEE Transactions on Information Theory*, vol. IT-28, no. 2, pp. 129-137, Mar. 1982.
- [4] J. Max, "Quantizing for minimum distortion," *IRE Transactions on Information Theory*, vol. IT-6, pp. 7-12, Mar. 1960.
- [5] ITU-T, Recommendation G.711, Pulse Code Modulation (PCM) of Voice Frequencies, International Telecommunication Union, 1972.

- [6] Z. Peric and J. Nikolic, "An adaptive waveform coding algorithm and its application in speech coding," *Digital Signal Processing*, vol. 22, no. 1, pp. 199-209, Jan. 2012.
- [7] Z. Peric and J. Nikolic, "High-quality Laplacian source quantization using a combination of restricted and unrestricted logarithmic quantizers," *IET Signal Processing*, vol. 6, no. 7, pp. 633-640, Nov. 2012.
- [8] J. Nikolic, Z. Peric, and A. Jovanovic, "Two forward adaptive dual-mode companding scalar quantizers for Gaussian source," *Signal Processing*, vol. 120, no. 3, pp. 129-140, Mar. 2016.
- [9] Z. Peric, M. D. Petkovic, J. Nikolic, and A. Jovanovic, "Support region estimation of the product polar companded quantizer for Gaussian source," *Signal Processing*, vol. 143, pp. 140-145, Feb. 2018.
- [10] M. Y. Valandar, P. Ayubi, M.J. Barani, "A new transform domain steganography based on modified logistic chaotic map for color images," *Journal of Information Security and Applications*, vol. 34, no. 2, pp. 142-151, Jun. 2017.

Iterative Time-Varying Filter Algorithm Based on Discrete Linear Chirp Transform

Osama A. S. Alkishriwo^{1*}, Ali A. Elghariani², Aydin Akan³

^{1,2} Department of Electrical and Electronic Eng., College of Eng., University of Tripoli, Libya

³ Department of Electrical and Electronic Engineering, Istanbul University, Turkey

DOI: <https://doi.org/10.21467/proceedings.2.10>

* Corresponding author email: alkishriwo@yahoo.com

ABSTRACT

Denoising of broadband non-stationary signals is a challenging problem in communication systems. In this paper, we introduce a time-varying filter algorithm based on the discrete linear chirp transform (DLCT), which provides local signal decomposition in terms of linear chirps. The method relies on the ability of the DLCT for providing a sparse representation to a wide class of broadband signals. The performance of the proposed algorithm is compared with the discrete fractional Fourier transform (DFrFT) filtering algorithm. Simulation results show that the DLCT algorithm provides better performance than the DFrFT algorithm and consequently achieves high quality filtering.

Keywords: Discrete linear chirp transform, Filtering, Discrete fractional Fourier transform, Sparse signals.

1 Introduction

Non-stationary relates to the time-dependence of the statistics of a random process. As such, non-stationary signals display either time-varying mean, variance or evolving spectra, or a combination of some or all of these. It is thus why more sophisticated filtering approaches are needed for the representation and processing of non-stationary signals. Noise is an unwanted component which acts as a source of error in the signal analysis and should be suppressed before data processing and interpretation. In many cases, therefore, noise mitigation is essential in order to extract useful information from the signal contaminated in noise.

The Fourier transform is one conventional signal denoising technique. However, due to the nonlinear and non-stationary properties of signals, this method is limited in the denoising capability to this kind of signals [1]. To overcome this shortcoming, several new approaches have been proposed in literature. In [2, 3] the least mean square adaptive algorithms are presented, but these algorithm are not able to track the rapidly varying non-stationary signals. Moreover, the wavelet transform (WT) based methods are widely used because of their abilities to remove Gaussian noise. However, the performance of the WT-based denoising methods depends on their selected mother wavelets [4].



© 2018 Copyright held by the author(s). Published by AIJR Publisher in Proceedings of First Conference for Engineering Sciences and Technology (CEST-2018), September 25-27, 2018, vol. 1.

This is an open access article under [Creative Commons Attribution-NonCommercial 4.0 International](https://creativecommons.org/licenses/by-nc/4.0/) (CC BY-NC 4.0) license, which permits any non-commercial use, distribution, adaptation, and reproduction in any medium, as long as the original work is properly cited. ISBN: 978-81-936820-5-0

To capture the variability with time of the non-stationary signal parameters, it is necessary to consider extensions of the Fourier-based representations capable of providing instantaneous-frequency information for multi-component signals. Although this can be achieved by considering polynomial-phase transforms [5], second-order polynomial transforms [6, 7] are preferable due to computational viability. In [7] the discrete linear chirp transform (DLCT) is introduced to represent a signal as a combination of linear chirps. The DLCT is an extension of the discrete Fourier transform (DFT) and provides a parametric modelling of the instantaneous frequencies of the components. Rather than joint time-frequency, the DLCT is a joint chirp-rate frequency transformation. It can be implemented efficiently using the fast Fourier transform (FFT) algorithm [7].

In this paper, a time-varying filtering algorithm based on the DLCT is proposed. The algorithm relies on the ability of the DLCT to decompose a signal iteratively into its components locally. Each of these components is filtered separately and then synthesized with the other filtered components to estimate the desired signal. Since each segment of the signal has different components with different bandwidths, the filter has to be time-varying. The performance of the proposed algorithm is compared with the discrete fractional Fourier transform (DFrFT) based filtering method [8, 9]. Simulation results of the proposed method show better performance on the denoising in comparing with major denoising schemes based on the DFrFT.

The paper is organized as follows. Section 2 shows how to obtain the DLCT and presents some of its properties. In section 3, we introduce the DLCT filtering algorithm. Simulation results are given in section 4, where we compare the DFrFT with the DLCT. In particular, we consider which of these two transforms is more efficient in transforming a non-sparse signal into a sparse-signal in time or in frequency, the resolution of the transforms, and the computational time required. Then, we evaluate the capability of the DLCT in filtering nonstationary signals. Finally, conclusions are summarized in section 5.

2 The Discrete Linear Chirp Transform (DLCT)

For a discrete-time signal $x(n)$, $0 \leq n \leq N - 1$, its discrete linear chirp transform (DLCT) and its inverse are given by [7]

$$x(k, m) = \sum_{n=0}^{N-1} x(n) \exp\left(-j \frac{2\pi}{N} (c m n^2 + k n)\right) \tag{1}$$

$$x(n) = \sum_{m=-L/2}^{L/2-1} \sum_{k=0}^{N-1} \frac{X(k, m)}{LN} \exp\left(j \frac{2\pi}{N} (c m n^2 + k n)\right) \tag{2}$$

where c is the resolution of the transform, L and N are the number of samples in the chirp-rate, and in the frequency domain, respectively. The DLCT is a joint chirp-rate frequency transformation that generalizes the discrete Fourier transform (DFT): indeed

$$X(k, m) = \frac{1}{N} X(k) \odot DFT \left\{ \exp \left(j \frac{2\pi}{N} c m \right) \right\} \quad (3)$$

where \odot is the circular convolution. Hence, If $m = 0$, then $X(k, 0)$ is the DFT of $x(n)$. Thus, the DLCT can be used to represent signals that are locally combinations of sinusoids, chirps or both.

3 The Proposed DLCT-Based Filtering Algorithm

For a signal $x(n)$ we can identify from its DLCT $X(k, m)$ the number of components Q , the chirp-rates $\beta_i = c m_i$, and frequency parameters k_i . The energy concentration is indicated by the peak values of $|X(k, m)|^2$ as a function of k and m . Considering the region in the joint chirp-rate frequency plane where these peak values occur, we should find the values of the chirp-rates and frequencies that can be used to approximate the given signal locally as a sum of linear chirp components

$$x(n) = \sum_{i=1}^Q x_i(n) \quad (4)$$

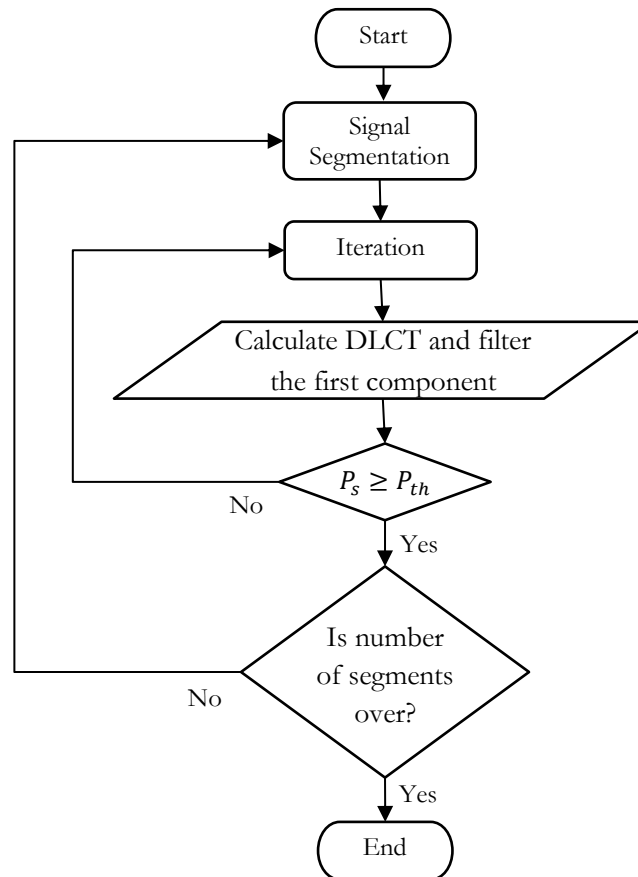


Figure 1: Filtering algorithm flowchart.

If we consider the case of a linear chirp contaminated in white Gaussian noise, filtering it directly without processing will permit for a large amount of noise to stay with the chirp since it has a broad bandwidth. However, if we implement the filtering process in the DLCT domain where the linear chirp has narrow bandwidth, then most of the noise will be removed.

The proposed DLCT filtering algorithm is performed over multiple iterations. Flowchart given in Figure 1 shows the step by step operation of the algorithm. The stopping criterion for the sub-iteration can be set manually by the expected number of components or adaptively based on a threshold P_{th} of the remaining energy P_s in the residual.

4 Simulation Results and Discussion

To evaluate the performance of the proposed algorithm, a simulation is performed to observe and compare the mean absolute error of the filtered signals with the DFrFT filtering algorithm. Both algorithms are applied to a synthetic signal as well as a real world signal. The synthetic signal is generated as follows,

$$x(n) = \exp\left(j \frac{\pi}{256} (0.1 n^2 + 10 n)\right)$$

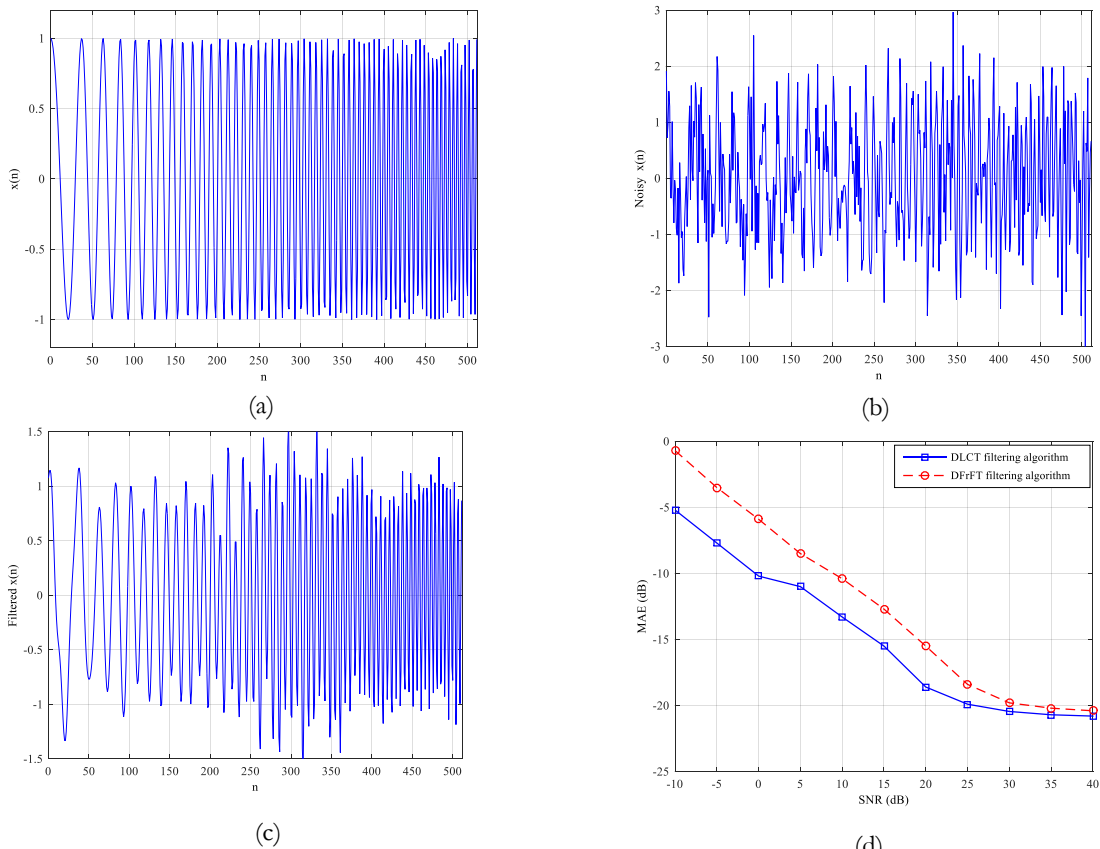


Figure 2: Linear chirp signal, (a) the chirp signal, (b) the noisy chirp signal with SNR= 0 dB, (c) the filtered chirp signal using DLCT filtering algorithm, and (d) mean absolute error for the two algorithms.

If the noiseless signal is denoted by $x(n)$ and $\hat{x}(n)$ is the filtered signal, then the mean absolute error can be calculated as follows,

$$MAE = \frac{1}{N} \sum_{n=0}^{N-1} |x(n) - \hat{x}(n)| \tag{5}$$

Figures 2(a), (b), and (c) show the chirp signal, the noisy chirp signal, and the filtered chirp signal using the DLCT filtering algorithm, respectively. In Figure 2(d), we provide the mean absolute error (MAE) for the two algorithms against signal-to-noise ratio (SNR). It can be seen that the DLCT filtering algorithm outperforms the performance of the DFrFT filtering algorithm, especially at low SNR. For instance, at 0 dB SNR, DLCT has a 5 dB improvement, while at 25 dB SNR, it has only about a 1 dB improvement over DFrFT.

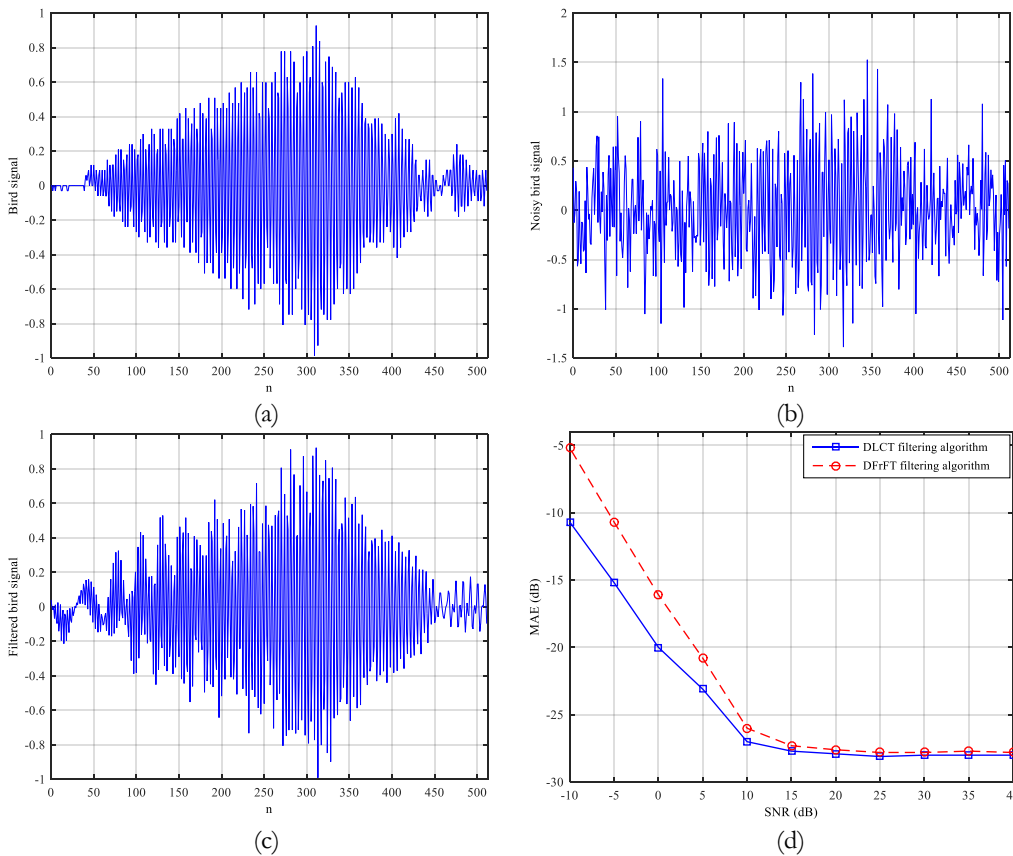


Figure 3: Real-world signal: (a) the bird chirping signal, (b) the noisy bird chirping signal with SNR= 0 dB, (c) the filtered bird chirping signal using DLCT filtering algorithm, and (d) the mean absolute error for the two algorithms.

To quantify the MAE improvement, a real-world signal (Bird chirping signal) with varying noise level is also simulated. The noiseless and noisy bird chirping signals are presented in Figures. 3(a) and (b). The denoised bird chirping signal based on the DLCT filtering algorithm

is shown in Figure 3(c) at SNR=0 dB. Similar to the previous case, Figure 3(d) depicts the MAE for the two algorithms as a function of the input SNR, where input SNR is varied from -10 dB (severely poor SNR) to 40 dB (high SNR). The DLCT filtering algorithm greatly enhances the MAE by simply employing few iterations in the simulation. This gain occurs because the DLCT algorithm gives sparser signals than the DFrFT algorithm.

5 Conclusion

In this paper, an iterative time-varying filtering algorithm based on the DLCT transform is proposed. The method exploits sparsity structure of signals to improve denoising performance of non-stationary signals. The performance of the proposed algorithm is analysed and compared with the performance of the (DFrFT) based method. Simulation results show that the DLCT filtering algorithm gives lower mean absolute error results than the DFrFT filtering algorithm in both synthetic and real-world signals. For instance, at SNR=0 dB, the proposed algorithm has a 5 dB improvement over the DFrFT filtering algorithm.

References

- [1] M. Alfaouri and K. Daqrouq, "ECG Signal Denoising By Wavelet Transform Thresholding," *American Journal of Applied Sciences*, vol. 5, no. 3, pp. 276-281, 2008.
- [2] V. Almenar and A. Albiol, "A new adaptive scheme for ECG enhancement," *Signal Processing*, Vol. 75, no. 3, pp. 253-263, Jun. 1999.
- [3] L. Durak and S. Aldirmaz, "Adaptive fractional Fourier domain filtering," *Signal Processing*, vol. 90, no. 4, pp. 1188-1196, Apr. 2010.
- [4] J. P. Amezquita-Sanchez and H. Adeli, "A new MUSIC-empirical wavelet transform methodology for time-frequency analysis of noisy nonlinear and non-stationary signals," *Digital Signal Processing*, vol.45, pp. 55-68, Oct 2015.
- [5] S. Peleg and B. Friedlander, "The discrete polynomial-phase transform," *IEEE Transactions on Signal Processing*, vol. 43, no. 8, pp. 1901-1914, Aug. 1995.
- [6] C. Candan, M. Kutay, and H. Ozaktas, "The discrete fractional Fourier transform," *IEEE Trans. on Signal Processing*, vol. 48, no. 5, pp. 1329-1337, May 2000.
- [7] O. A. Alkishriwo and L. F. Chaparro, "A Discrete Linear Chirp Transform (DLCT) for Data Compression," in *Proc. of the IEEE International Conf. on Information Science, Signal Processing and their Applications*, Montreal, Canada, Jul. 2012, pp. 1283-1288.
- [8] O. A. Alkishriwo, L. F. Chaparro, and A. Akan, "Signal separation in the Wigner distribution using fractional Fourier transform," *European Signal Processing Conf., EUSIPCO*, Spain, Sep. 2011, pp. 1879-1883.
- [9] P. Kumar and S. Kansal, "Noise removal in speech signal using fractional Fourier transform," *2017 International Conference on Information, Communication, Instrumentation and Control, ICICIC*, Indore, India, Aug. 2017.

Color Image Encryption in the Spatial Domain Using 3-D Chaotic System

Hanan Salem Alzreghi, Osama A S Alkishriwo*

Department of Electrical and Electronic Eng., Faculty of Eng., University of Tripoli, Libya

DOI: <https://doi.org/10.21467/proceedings.2.11>

* Corresponding author email: alkishriwo@yahoo.com

ABSTRACT

Users of Internet daily send and receive many images through social media. These images are vulnerable to hack by attackers. Therefore, it is necessary to develop methods to protect these images against attackers. A nontraditional encryption method for encrypting color images in the spatial domain is proposed. The main idea in this work is based on building strong encryption algorithm through implementing the permutation and diffusion operations on the pixels, where every pixel composed of three values red, green and blue. These operations are implemented depending on extracting three chaotic sequences from the 3-D chaotic system, where each chaotic sequence is used to shuffle and diffuse each color in the plaintext image. The proposed system is tested on well-known images like Lena and Mandrill. Experiments and security analysis prove that the algorithm has an excellent performance in image encryption.

Keywords: Color image encryption, spatial domain, 3-D chaotic system, permutation, diffusion.

1 Introduction

Nowadays information security is a vital problem in information communication. With the advancements of information technology, lots of digital contents are being stored and transmitted in various forms. As a result, the protection of digital contents data against irregular phenomena, such as illegal copying, and guarantee of their secure utility has become an important issue. In particular, compared to text data, some intrinsic features of image data, such as big size, high redundancy of data and strong correlation among neighbouring pixels are different with ordinary information. Therefore, an encryption method with fast speed and high security is needed. But the traditional block encryption being widely used now is found to be inefficient for real-time communication. Hence a lot of image encryption methods using chaotic maps with high sensitivity to their initial conditions and system parameter values and simple structures are proposed [1, 2].

2 Proposed Algorithm

The aim of this work is to design and implement a novel and highly secure method which is essential for confidentiality and to solve the problems of some previous chaotic image



encryption schemes. Figure 1 depicts the main algorithm executed in this paper and includes three operations which are permutation, diffusion, and linear transformation.

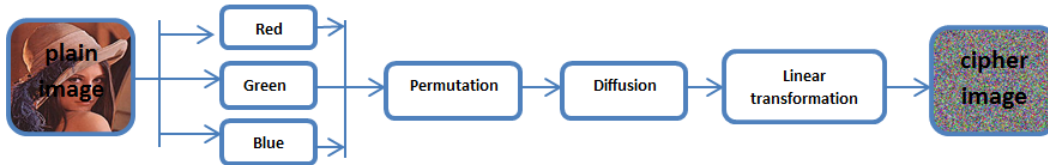


Figure 1: Block diagram of proposed image encryption scheme.

The original color images is divided into three images with Red ,Green and Blue channels, respectively. The encryption steps can be summarized as follows:

(1) permutation process by scrambling operation on all pixels in the image with chaotic sequence. (2) diffusion process by a sequential XOR operation on all the bits of pixels in the image. (3) linear transformation process by rotated the image to the left by amount of ℓ_p , where ℓ_p using as a security key, then we decrypte the image using inverse these process. These operations are implemented depending on extracting three chaotic sequences from the 3-D chaotic system, where each chaotic sequence is used to shuffle and diffuse each color in the plaintext image.

3 Chaotic System

The 3-D chaotic system used in this paper can be expressed as follows:

3.1 Logistic-Logistic map

$$x_{n+1} = u \times x_n \times (1 - x_n) \times 2^{14} - \text{floor}(u \times x_n \times (1 - x_n) \times 2^{14}) \quad (1)$$

3.2 Sine-Sine map

$$x_{n+1} = u \times \sin(\pi \times x_n) \times 2^{14} - \text{floor}(u \times \sin(\pi \times x_n) \times 2^{14}) \quad (2)$$

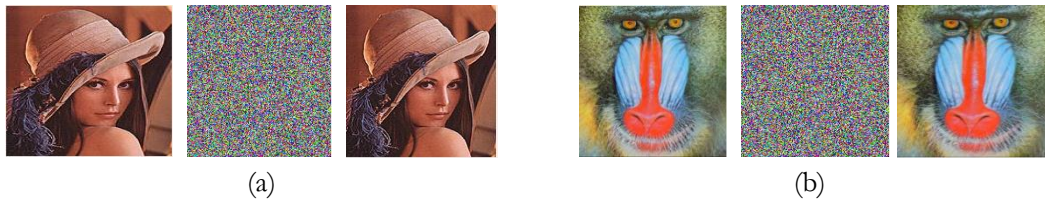
3.3 Chebyshev-Chebyshev map

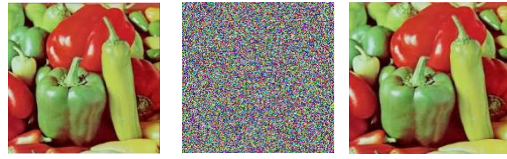
$$x_{n+1} = \cos((u + 1) \cos^{-1}(x_n)) \times 2^{14} - \text{floor}(\cos((u + 1) \cos^{-1}(x_n)) \times 2^{14}) \quad (3)$$

where the control parameter $u \in (0, 10)$ and x_n is the initial value of the sequence.

4 Experimental Results and Performance Analysis

A good quality encryption scheme should be robust against all types of attack, involves security attack and statistical attack. The proposed procedure is implemented in some color images to demonstrate its efficiency. The results of encryption and decryption are shown in Figure 2. This shows that all encrypted images are noise-like ones and can be efficiently applied to images of various forms such as grayscale images, color images and binary images [3].



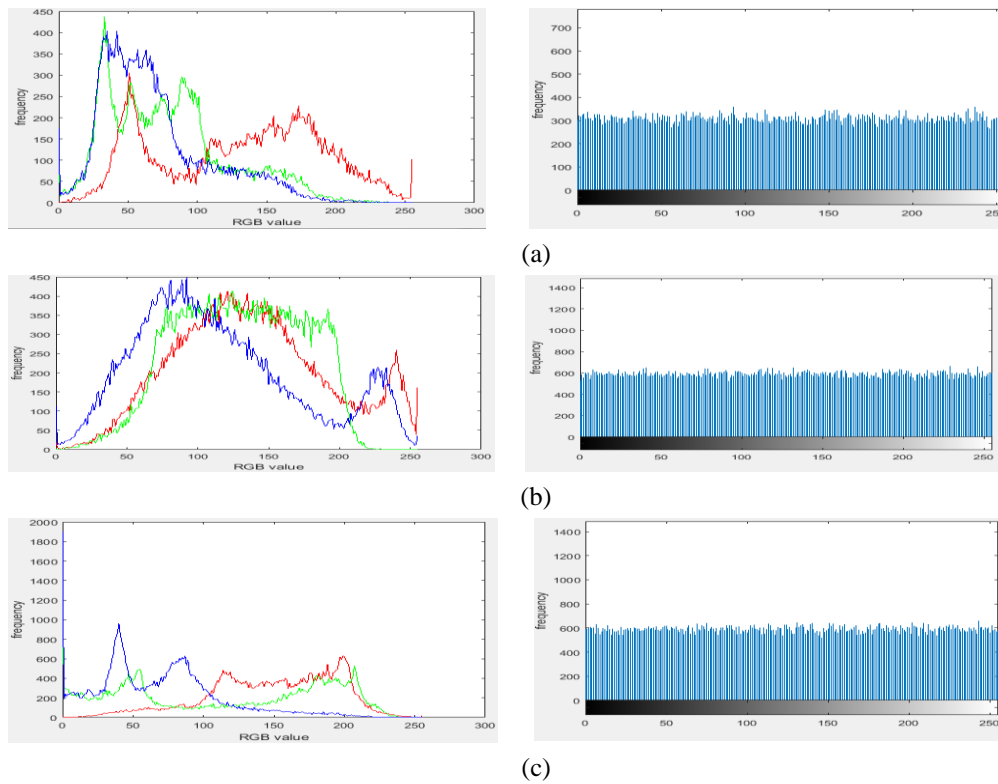


(c)

Figure 2: Encryption result of some images.

4.1 Histogram Analysis

Image histogram reflects the distribution of pixel values of an image. To resist statistic attacks, the image histogram should be flat. Figure 3 shows the histograms of the some images and the histograms of their encrypted images. The histogram of the encrypted image has a good uniform distribution, so that it is enough to resist statistical attacks [4].



(c)

Figure 3: (a) the histogram of the original and encrypted Lena images; (b) the histogram of the original and encrypted Mandril images; (c) the histogram of the original and encrypted Pepper images.

4.2 Correlation of Two Adjacent Pixels

Image data generally has some intrinsic features. We analysed the correlations between two adjoining pixels of the plain-image and the cipher image at horizontal, vertical and diagonal

directions for original and encrypted images [5]. The correlation coefficient is calculated by the following equations:

$$r_{xy} = \frac{cov(x, y)}{\sqrt{D(x) \times D(y)}}$$

where $cov(x, y) = \frac{1}{N} \sum_{i=1}^N (x_i - E(x))(y_i - E(y))$

$D(x) = \frac{1}{N} \sum_{i=1}^N (x_i - E(x))^2$ and $E(x) = \frac{1}{N} \sum_{i=1}^N x_i$

where x and y are color values of two adjacent pixels in the images. Figure 4 shows the correlation analysis of Lena image.

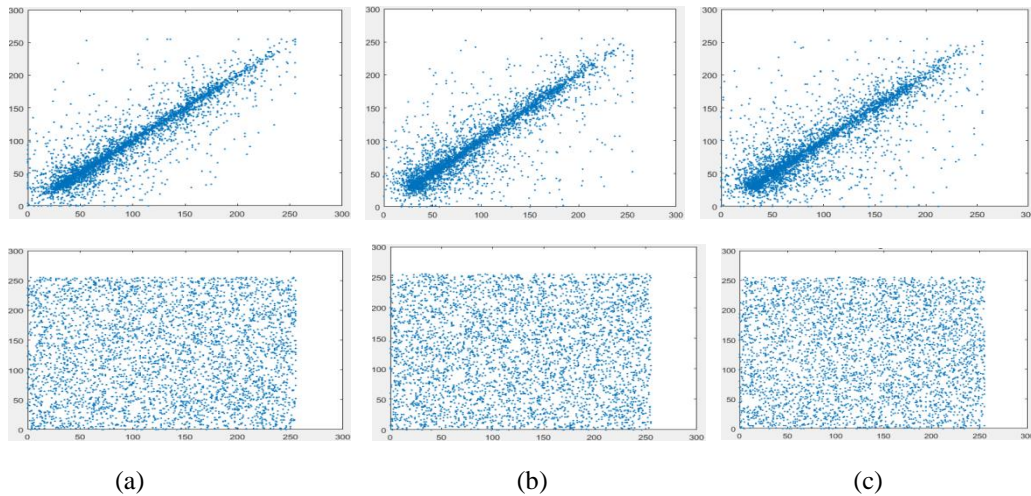


Figure 4: Correlation analysis of Lena image. (a) horizontal correlation of original and encrypted images; (b) vertical correlation of original and encrypted images; (c) diagonal correlation of original and encrypted images.

Table 1: Correlation coefficients of original Lena, Koala, Mandrill and Pepper images.

Image	Original image			Encrypted image		
	Vertical	Horizontal	Diagonal	Vertical	Horizontal	Diagonal
Lena	0.9062	0.8722	0.8387	0.0036	0.0012	0.00032
Mandrill	0.8592	0.8876	0.8360	0.00075	0.0016	0.0017
Pepper	0.9767	0.9696	0.9551	0.0004	0.0016	0.0025

As seen in Table 1, the correlation coefficient of the original images comes near to 1, but the correlation coefficient of the encrypted images comes near to 0. This means that the encrypted image has no correlation property with original image.

4.3 Data Loss and Noise Attack

Digital images can be easily influenced by noise and data loss during transmission through the network and storage in physical media. An image encryption algorithm should have an ability of resisting these abnormal phenomena. To test the ability of resisting the attack, we did some experiments on a data loss and a noise attack as shown in Figures 5 and 6. An original image is first encrypted by our proposed algorithm. The encrypted image is attacked by a data cut of size 15%, 30% and 40% and with 3%, 10% and 20% "salt & pepper" noise, respectively. The decryption process is then applied to these encrypted images.

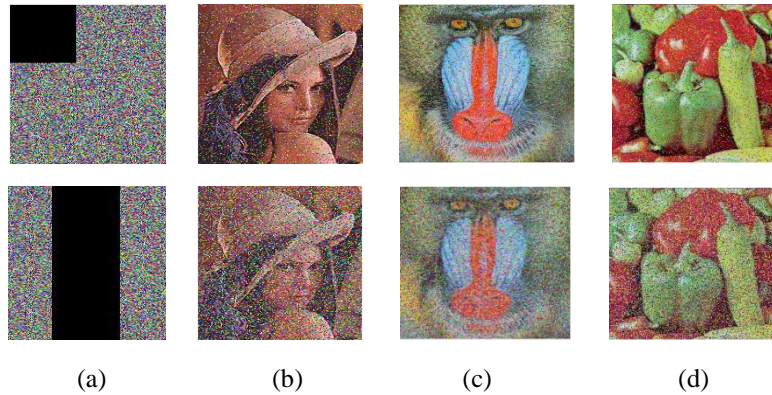


Figure 5: Data loss. (a) The encrypted images with data loss; (b) the decrypted Lena image with different data loss; (c) the decrypted Mandrill image with different data loss; (d) the decrypted Pepper image with different data loss.

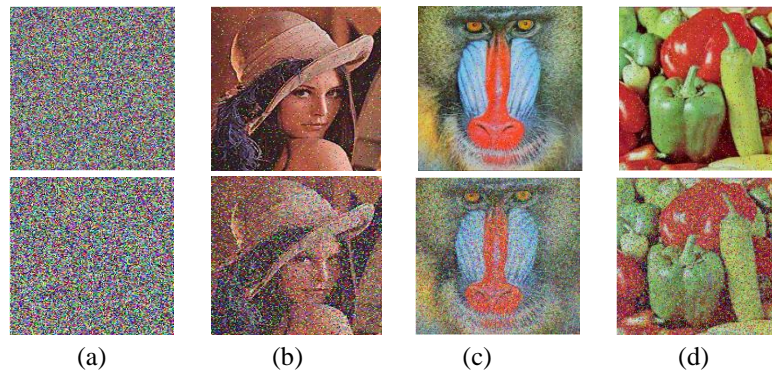


Figure 6: Noise attack. (a) the encrypted images added with 'salt & pepper' noise; (b) the decrypted Lena image of (a); (c) the decrypted Mandrill image of (a); (d) the decrypted Pepper image of (a).

The restoring ability of an image is evaluated by peak signal to noise ratio (PSNR) as expressed in the following equation.

$$PSNR = 10 \times \log \left(\frac{255}{MSE} \right) \quad (dB)$$

$$\text{where } MSE = \frac{1}{W \times H} \sum_{i=1}^H \sum_{j=1}^W (OI(i, j) - DI(i, j))^2$$

where $W \times H$ is the size of image, $OI(i, j)$ a pixel of the original image and $DI(i, j)$ a pixel of the decrypted image. Table 2 shows the PSNR values for some images.

Table 2: The peak signal to noise ratio of some encrypted images.

Image	Lena			Mandrill			Pepper		
	Red Blue	Green		Red	Green	Blue	Red	Green	Blue
loss 15%	35.3900	37.7780	38.4302	35.2594	35.6046	36.2049	34.9495	36.1639	38.7565
loss 40%	31.0203	33.4110	34.2228	30.7908	31.0408	31.7175	30.3950	31.5676	34.2500
Noise 3%	39.5836	42.2247	42.3936	39.3673	39.8392	40.1186	38.9030	39.9778	42.5033
Noise 20%	31.7474	34.2945	34.8950	31.4815	31.8250	32.3980	31.2189	32.4015	35.0655

5 Conclusions

In this paper, a scheme for image encryption using 3D chaotic system is presented. The encryption method involves scrambling, diffusion, and linear transformation techniques to make it more confident. The experimental analysis and results of the proposed system includes histogram analysis, correlation analysis, and peak signal to noise ratio. The results show that the graphical shape of histogram for cipher image is uniformly distributed, so the proposed algorithm is protected from frequency analysis attack. Also, the low correlation coefficient of encrypted image is near to the ideal value zero. Thus the experimental results and statistical analysis demonstrate the security, flexibility, correctness, effectiveness, and robustness of the proposed cryptosystem.

References

- [1] C. Pak and L. Huang, "A new color image encryption using combination of the 1D chaotic map," *Signal Processing*, vol. 138, pp. 129-137, Sep. 2017.
- [2] O. A. Alkishiwo, "An image encryption algorithm based on chaotic maps and discrete linear chirp transform," *Almadar Journal for Communications Information Technology and Applications*, vol. 5, no. 1, pp. 14-19, Jun. 2018.
- [3] A.B. Abugharsa, A. Basari, and H. Almagush, "A New Image Scrambling Approach using Block-Based on Shifted Algorithm," *Australian Journal of Basic and Applied Sciences*, vol. 7, no. 7, pp. 570-579, 2013.
- [4] Y. Zhang and X. Wang, "A symmetric image encryption algorithm based on mixed linear–nonlinear coupled map lattice," *Information Science*, vol. 273, pp. 329–351, Jul. 2014.
- [5] H. Huang and S. Yang, "Colour image encryption based on logistic mapping and double random-phase encoding," *IET Image Processing*, vol. 11, no. 4, pp. 211-216, Mar. 2017.

Hearing Protection System by Using a Simple Noise Reduction Strategy

Izziddien Alsogkier

Department of Electrical and Computer Engineering, College of Engineering, Elmergib University, Libya

DOI: <https://doi.org/10.21467/proceedings.2.12>

* Corresponding author email: izziddien@yahoo.de

ABSTRACT

In this paper, a very brief discussion and analysis of the noise problem are given particularly at the work environment, where the workers hearing system needs to be protected from an excessively loud noise source but at the same time the workers need to communicate with each other. Therefore, a simple strategy of noise reduction is introduced by means of isolation plus a noise filtered communication channel to keep the worker in contact with the work environment as well as the other co-workers with a minimum noise intervention as possible.

Keywords: Noise Reduction, Noise Isolation, Noise Filtering, Passive and Active Noise Control.

1 Introduction

There are a lot of noise sources that disturb the workers in the work environment, for example, machines driven by internal combustion engines such as cars, trucks and tractors also tool machines like generators, air compressors, drilling, cutting machines ... etc. Moreover, heavy machineries in industrial fabrics generate very loud noise so that the workers or the operators need to be isolated but at the same time they need to communicate with each other. The same instance can be found in civil and military aviation like jet engine aircrafts particularly with propellers as helicopters, where the pilot, copilot and the passengers need to be protected and isolated from the excessive noise so that they can easily communicate with each other.

Therefore, the strategy is mainly to protect the workers or the operators' hearing system from the loud noise generated in the workplace, as well as, providing a communication channel with a minimum possible noise intervention. This, in most circumstances, is a very critical and fatal safety issue. Usually, the noise problem take place or can be defined, whenever there are a *noise source*, which generates the noise, *noise transmission* or *propagation medium*, where the noise travels and expands, and *noise sink*, which is the target element that gets affected or disturbed by the noise. Therefore, the noise problem can primarily be solved from the very beginning at the noise source which gives a very general and global solution to the problem, but this can be in some circumstances the most expensive solution (e.g. internal combustion engine exhaust system). Furthermore, a secondary solution can be done by preventing the noise to reach the



© 2018 Copyright held by the author(s). Published by AIJR Publisher in Proceedings of First Conference for Engineering Sciences and Technology (CEST-2018), September 25-27, 2018, vol. 1.

This is an open access article under [Creative Commons Attribution-NonCommercial 4.0 International](https://creativecommons.org/licenses/by-nc/4.0/) (CC BY-NC 4.0) license, which permits any non-commercial use, distribution, adaptation, and reproduction in any medium, as long as the original work is properly cited. ISBN: 978-81-936820-5-0

noise sink by isolating the noise source from the noise sink this gives more local solution to the problem, but this can be in some circumstances the less expensive one.

Generally in the literature, there are two distinct classifications of noise control algorithms, which are passive and active noise control algorithms, passive is by implementing passive elements like isolating or absorbing materials to reduce the impact of the noise on the medium [1], active is by using active elements to generate an anti-noise to counteract the noise and reduce its impact on the targeted medium [2]. Moreover, sometimes in order to get maximum results, hybrid algorithms, a combination of passive and active methods can also be applied simultaneously [2].

In the following, a brief introduction to passive and active noise control techniques is given in Section 2, then the problem formulation of this paper and the experimental setup are given in Section 3. Experimental examples are presented in Subsection 3.2. Moreover, results analysis of the experiments and comments are given in section 4. Finally, conclusions and further work suggestions are given in Section 5.

2 Passive and Active Noise Control Techniques

Passive noise control technique is usually applied by using passive isolating and filtering elements. For example, noise isolation can be done by using sound isolating and absorbing (soundproof) materials like in civil buildings or an isolation compartment (as the case of cars, helicopter, bulldozer like machine) or at very smaller scale by implementing an isolating ear plugs, muffler headset or helmet, see Figure 1.

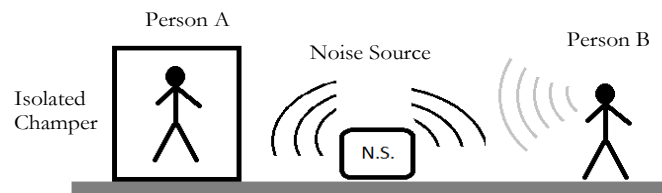


Figure 1: Passive noise control by using isolation.

The positive thing about this way of fighting the noise is that, it is very simple technically. On the other hand, apart from using intensive materials that leads to heavy weight solutions, which makes a big crucial problem particularly in the case of light weight applications like airplanes where the weight is an important factor. The negative thing about this technique is that the perfect isolation of an operator at a working place means that he will no longer receives information form the surrounding working place, which could be very fatal in most circumstances.

For example, in the case of helicopter where the pilot and the copilot need to be isolated from the excessive noise generated from the engine and the rotating blades but at the same time they need to communicate with each other without noise. This problem can be solved by

using the setup shown in Figure 2 where both persons A and B are completely isolated from the noise and talk to each other via an isolated communication channel. This can be implemented also by using a soundproof helmet for each person with an electronic communication channel, as shown in Figure 3. Much simpler is by using ear protection system (ear muffs plus a communication system).

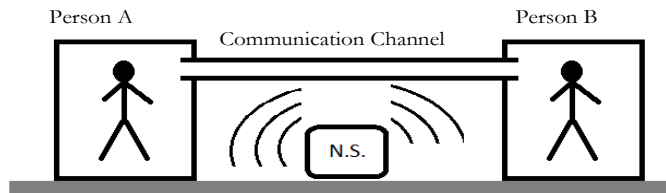


Figure 2: Two persons passive noise isolation with communication channel.

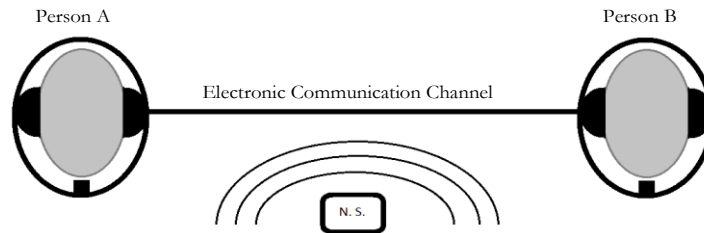


Figure 3: Two persons with head passive noise isolation and electronic communication channel.

Another example is the case of operators work beside a very loud noisy machine like an air compressor, internal combustion engine generator or any type of noisy rotational tool machines. Where, the communication channel could also be wireless based system so that the persons can move freely in their working area without any constant wire connection between them.

More specific situation regarded in this paper is when the workers need to be isolated but at the same time they need to communicate with each other. This can be done as in the helicopter case but with less expensive and simple technology by placing the operator in an isolated compartment, as shown in Figure 4, but still he receives noise filtered information from outside the isolated compartment, the communication channel is not noise isolated. Further simplification can also be achieved by using helmet or a headset ear protection system with noise filter set up as shown in Figure 5.

Alternatively, Active Noise and Control (ANC) is a technique that fights back the noise source by generating a counter action (anti-noise) against the noise actively [2]. In other words, it generates a counter action against the noise that cancels completely or partially the impact of the noise on the targeted environment. For example, in case of Figure 1, first the passive

vibration control methods can be used to reduce the vibration generated at the source, where these vibrations are the source of the noise. Moreover, the ANC methods can be applied to cancel the noise generated from the noise source. Furthermore, ANC methods can be used to cancel actively the rest noise that penetrates the non-perfect isolation compartment as demonstrated in Figure 6 and the headset stereo active noise control as shown in Figure 7. There are a lot of robust and adaptive algorithms developed for active noise and vibration control applications, see for example [3-6].

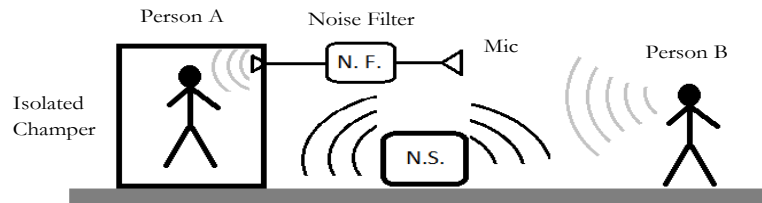


Figure 4: Passive and active noise isolation.

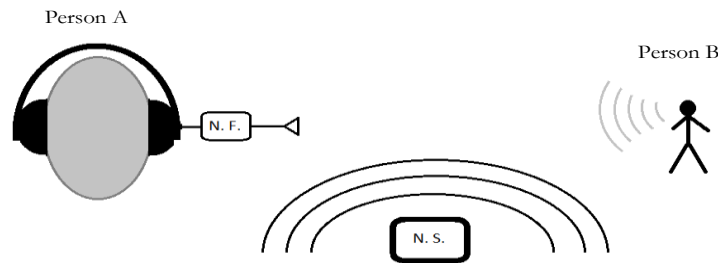


Figure 5: Passive and active noise control by using headset.

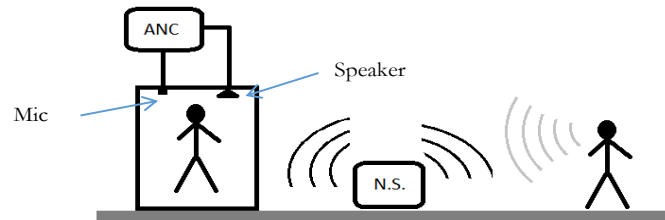


Figure 6: Active noise control system.

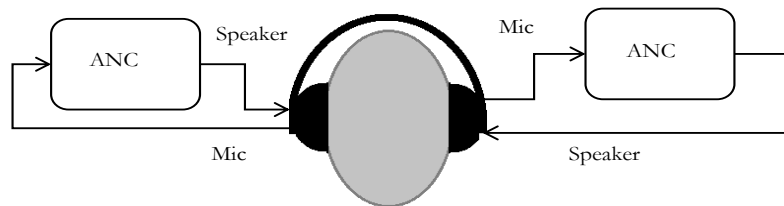


Figure 7: Stereo active noise control headset system.

3 Problem Formulation and Experimental Setup

As explained in sections (1 and 2), it is assumed that there is a noise source that disturbs the operators or the workers in the workplace, the goal is to reduce the effect of the noise by using passive isolation as well as keeping the worker in contact with the other coworkers but with the possible minimum noise intervention. Therefore, the experiment setup will be as presented in Figure 4 and Figure 5. Moreover, the noise source considered in this experiment is assumed to be a single harmonic (sinusoidal) function. Therefore, a narrow band stop filter can be used as a noise filter to reduce the noise in the communication channel.

In this experiment, a notch filter will be designed and applied as narrow band stop filter. The notch filter can be implemented by using analog passive elements, a combination of R, L and C circuits, or active filters by using some sort of linear amplifiers with RLC elements. Furthermore, a digital filter can also be designed and implemented by utilizing a digital signal processor.

3.1 Notch Filter

In this work, an analog notch filter in form of second order transfer function is designed and applied to filter out a single harmonic noise source. Hence, the notch filter transfer function is defined by

$$G_N(s) = \frac{s^2 + 2\xi_N \omega_N s + \omega_N^2}{s^2 + 2\xi_D \omega_D s + \omega_D^2}, \quad (1)$$

where $\omega_N = \omega_D = \omega_{\text{Notch}}$ is the notch angular frequency, $\xi_N = 0$, or ≈ 0 and $\xi_D \geq 1$.

Therefore, the notch filter transfer function becomes

$$G_N(s) = \frac{s^2 + \omega_N^2}{s^2 + 2\xi_D \omega_D s + \omega_D^2}, \quad (2)$$

The following Figure 8 shows the frequency response of the notch filter for the parameters $\omega_{\text{Notch}} = 100$ [rad/s], $\xi_N = 0, 0.1, 0.01$ and $\xi_D = 1$.

3.2 Notch Filter Experiment

The experimental setup as mentioned earlier is as shown in Figure 4 and Figure 5, where the noise source is a 100 Hz single harmonic (sinusoidal) function. Therefore the noise filter is an analog notch filter in form of second order transfer function, which is designed and applied to filter out noise from voice in the communication channel.

The experiment data is gathered and presented in Figure 9, where the voice signal without noise is plotted by a blue line, while the voice signal with 100Hz noise is plotted by a green line and the filtered voice with noise signal is plotted by a red line.

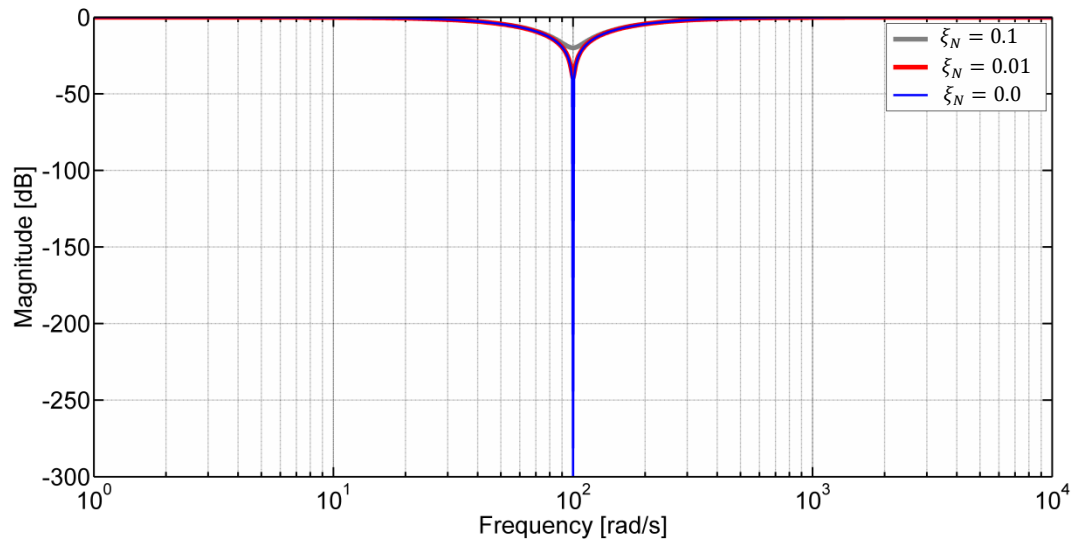


Figure 8: Notch filter frequency response.

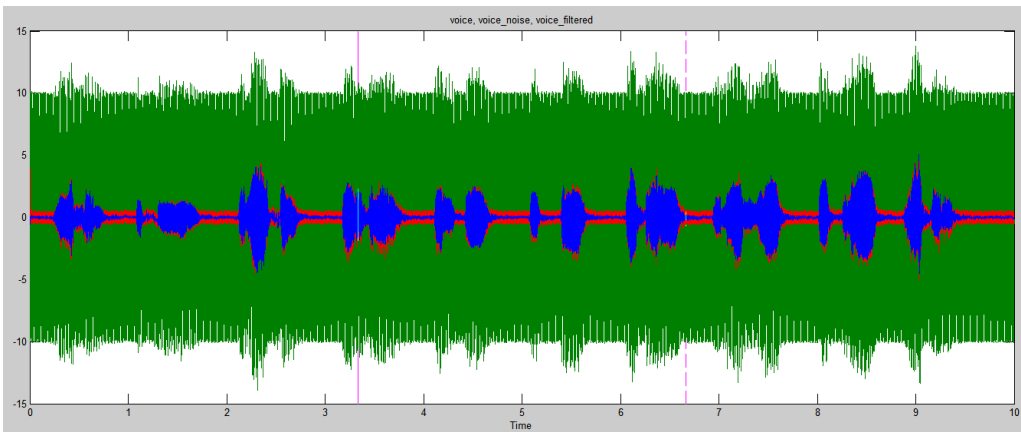


Figure 9: Original voice without noise (Blue), voice with noise (green) and filtered voice with noise (red).

4 Results Analysis and Discussion

Figure 9 shows the time plot of the original voice signal without noise, represented by the blue line, where the voice signal is simply a record of counting from one to ten in ten seconds. The green line is the plot of the voice signal corrupted with single harmonic noise at 100Hz frequency. Moreover, Figure 10 is time axis zoom in of Figure 9 between less than 3.9 and more than 4.4 seconds, where it shows clearly the filtered voice signal still has a rest noise component but it is much better than the voice signal with noise, in fact, the filtered signal became almost like the noise free voice signal. Furthermore, Figure 11 shows the plot of the frequency spectrum of corresponding signals in Figure 9 and Figure 10 with the same

respective colors as well. Also this graph shows that the notch filter has managed to reduce the noise component at the frequency 100 Hz.

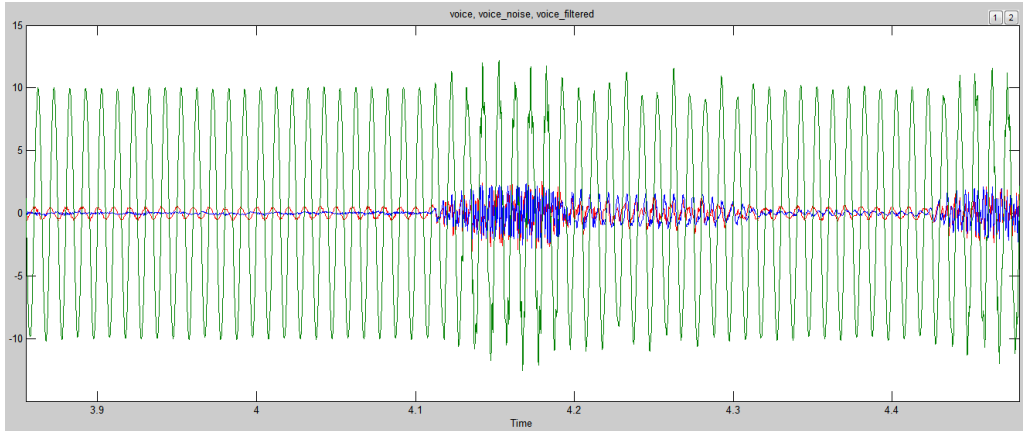


Figure 10: Original voice without noise (Blue), voice with noise (green) and filtered voice with noise (red).

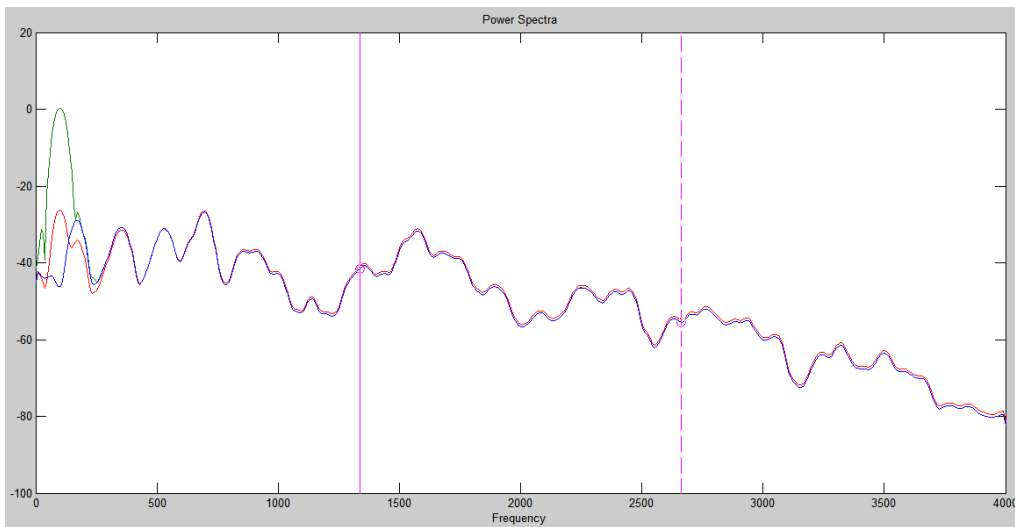


Figure 11: Frequency spectrum of original voice without noise (Blue), voice with noise (green) and filtered voice with noise (red).

5 Conclusions and Further Works

In this paper, instead of using isolation only to protect the workers or the operators against a very loud noise, which make them completely deaf in their working environment, a communication channel between the environment and the worker is applied with a band stop filter in form of a notch filter to reject or filter out the single harmonic noise, so that the worker can keep in contact with the work environment, this can improve the communication

with the other coworkers as well as the environment which, in consequence, is a very important safety factor.

The application of this technique can be at its simplest, by adding (to a head set muffler) a communication channel microphone, low power audio amplifier with noise filter and very small speaker embedded in the head set muffler.

The noise filter can be designed as RLC band stop notch filter, or just an analog transfer function filter that can be built by using operational amplifiers or can be built by using a digital signal processor utilizing a digital computer system. For small scale implementations, a suitable microcontroller-based system can also be used to realize this strategy.

References

- [1] I. L. Ver and L. L. Beranek, "Noise and vibration control engineering principles and applications," *John Wiley & Sons*, 2006.
- [2] C. H. Hansen, "Understanding active noise cancellation," *Taylor & Francis e-Library*, 2003.
- [3] B. Widrow and S. D. Stearns, "Adaptive signal processing," *Prentice-Hall PTR*, 1985.
- [4] C. R. Fuller, S. J. Elliott and P. A. Nelson, "Active control of vibrations," *Academic Press*, 1996.
- [5] S. Elliott, "Signal processing for Active Control," *Academic Press*, 2001.
- [6] B. Widrow and E. Walach, "Adaptive inverse control a signal processing approach," *John Wiley & Sons*, 2008.

Enhancement of Bandwidth of U-shape Loaded Microstrip Patch Antenna According to 802.11b Standard

Fadel A. M. Alaswad ^{1*}, Marai M. Abousetta ^{2*}, Mohamed A. S. Alshushan ^{3*}

¹ Department of Communication, Collage of electronic technology, Bani Walid, Libya

² Libyan Academy, Tripoli , Libya

³ Department of Electric and Electronics, College of engineering, Sabratha University, Libya

DOI: <https://doi.org/10.21467/proceedings.2.13>

* Corresponding author email: fadel.abu83@gmail.com

ABSTRACT

The bandwidth of microstrip antennas is proportional to the thickness of the substrate that used. Since most substrates are very thin in terms of wavelengths, the bandwidth is usually small. To enhance the bandwidth, a new design of rectangular microstrip patch antenna is presented. The proposed geometry consists of a rectangular shaped ground plane structure with a U- slot loaded patch layer. The aim of this is to design a single, double and triple U slotted rectangular patch antenna and compare its performance with non-slotted rectangular microstrip patch antenna. The antennas were designed and simulated using advanced design software. The design has been worked out according to 802.11b IEEE standard.

Keywords: Microstrip antenna, Feed point, Bandwidth, return loss.

1 Introduction

Microstrip antennas were first proposed in 1952. This concept had to wait until 1974 when that microstrip antenna got a lot of attention and began being used for military applications. So far, these antennas have mainly been used on aircraft, missiles, and rockets. Just recently, they have been expanded to commercial areas such as mobile satellite communication, the direct broadcast satellite (DBS), and the global position system (GPS) [1]. With the wide spread proliferation of communication technology in recent years, the demand for compact, low profile and broadband antennas has increased significantly. A number of new developed techniques to support high data rate wireless communication for the next generation technologies have been rapidly increasing.

802.11b is one of many Institute of Electrical and Electronics Engineers (IEEE) standards that govern wireless networking transmission methods. They are commonly used today to provide wireless connectivity in the home, office and some commercial. It operates on a 2.4 GHz band and allows for wireless data transfers up to 11 Mbps. Several techniques have been proposed to enhance the bandwidth in the state-of-the art antenna research for microstrip



© 2018 Copyright held by the author(s). Published by AIJR Publisher in Proceedings of First Conference for Engineering Sciences and Technology (CEST-2018), September 25-27, 2018, vol. 1.
This is an open access article under [Creative Commons Attribution-NonCommercial 4.0 International](https://creativecommons.org/licenses/by-nc/4.0/) (CC BY-NC 4.0) license, which permits any non-commercial use, distribution, adaptation, and reproduction in any medium, as long as the original work is properly cited. ISBN: 978-81-936820-5-0

patch antenna. In this research, our design is forwarded a rectangular shape that contains a single, double and triples U, centered accordingly.

2 Design procedure

The basic design uses a rectangular U-slot microstrip patch antenna on suitable microwave substrates [1]. The new antenna is a probe-fed rectangular microstrip patch antenna on a permittivity substrate with an internal U- slot as shown in Figure 1. In the second design, Another U –slot is added, and the dimension of the second U-solt will be the half length of the first U-solt as shown in Figure 2. In the final design, a third U -slot is formed and its dimension will be the half length of the second U-solt see Figure 3.

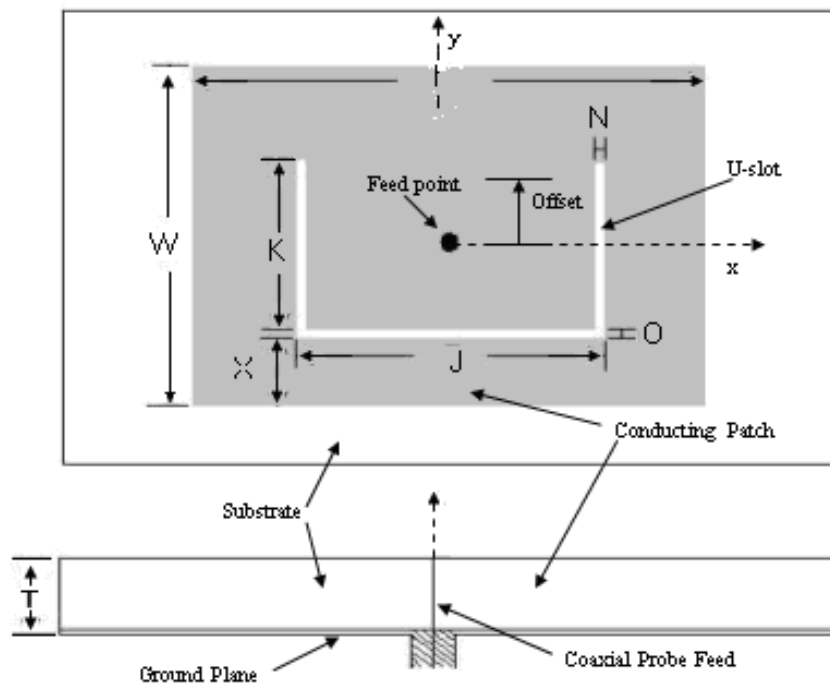


Figure 1: Geometry of the rectangular U-slot microstrip patch antenna

This design procedure is a set of steps for the rectangular U-slot microstrip patch antenna. Specify the center frequency and 2:1 VSWR bandwidth of the desire antenna. Approximate the center frequency as (f_{res3}) and the lower and upper frequency bounds of the bandwidth as (f_{res2}) and (f_{res4}) respectively. Select a substrate permittivity (ϵ_r) and a substrate thickness h . According to the following relationship [2]:

$$h \geq 0.06 \frac{\lambda_{res3}}{\sqrt{\epsilon_r}} \quad (1)$$

where λ_{res3} wavelength at the center frequency in air.

Calculate the width of the patch W as:

$$W = \frac{c}{2.f_{r3}} \sqrt{\frac{2}{\epsilon_r+1}} \quad (2)$$

where c speed of light in free space.

Calculate the effective permittivity ϵ_{eff} as:

$$\epsilon_{eff} = \frac{\epsilon_r+1}{2} + \frac{\epsilon_r-1}{2} \left(1 + \frac{12h}{W}\right)^{-1/2} \quad (3)$$

Then the length due to the fringing field ΔL

$$\Delta L = 0.824h \frac{(\epsilon_r+0.3)\left(\frac{W}{h}+0.262\right)}{(\epsilon_r-0.258)\left(\frac{W}{h}+0.813\right)} \quad (4)$$

Calculate the length of the patch L as:

$$L = \frac{c}{2f_{r3}\sqrt{\epsilon_{eff}}} - 2\Delta_L \quad (5)$$

Select a starting value of slot thickness E,F using following:

$$E = F = \frac{\lambda_{res3}}{60} \quad (6)$$

7) Calculate the Slot width J as:

$$J = \frac{c}{f_{r2}\sqrt{\epsilon_{eff}}} - 2(L + 2\Delta_L - E) \quad (7)$$

8) Select the Slot height K such that

$$\frac{K}{J} \geq 0.7 \text{ and } \frac{K}{W} \geq 0.3 \quad (8)$$

Calculate the effective permittivity and effective length extension of the pseudo patch $\epsilon_{eff(pp)}$ of the fourth resonance with the effective patch width $J - 2F$

$$\epsilon_{eff(pp)} = \frac{\epsilon_r+1}{2} + \frac{\epsilon_r-1}{2} \left(1 + \frac{12h}{J-2F}\right)^{-1/2} \quad (9)$$

$$2\Delta_{L-E-H} = 0.824H \frac{(\epsilon_{eff(pp)}+0.3)\left(\frac{J-2F}{h}+0.262\right)}{(\epsilon_{eff(pp)}+0.258)\left(\frac{J-2F}{h}+0.813\right)}$$

(10)

Calculate the Height of slot from base H as:

$$H \approx L - E + 2\Delta_{L-E-H} - \frac{1}{\sqrt{\epsilon_{eff(pp)}}} \left(\frac{c}{f_{res4}} - (2K + J)\right) \quad (11)$$

When The optimized lower band frequency, $f_{res2}= 1.8$ GHz, upper bound frequency, $f_{res4}=3.1$ GHz , Resonant Frequency $f_{res3}=2.45$ GHz, $\epsilon_r = 4.2$, and substrate Height = 10 mm are selected, The computed results are shown in Table 1 as:

Table 1: *Dimensions of single U slot antenna*

L (mm)	W (mm)	K (mm)	J (mm)	O (mm)	N (mm)	X (mm)	H (mm)	T (mm)	Offset (mm)	ϵ_r	f_3 (GHz)	f_2 (GHz)	f_4 (GHz)
24.7	37.9	13.4	28.1	2.0	2.0	10.0	7.6	10	0.0	4.2	2.45	1.8	3.1

The second design” the double U–slot patch microstrip antenna” is depended on the first design and the dimensions of the second U shape J', K', H' are the half length of first design. The next Table 2 summarizes the dimensions of the double U –slot patch microstrip antenna.

Table 2: Dimensions of double U slot antenna

L (mm)	W (mm)	K' (mm)	J' (mm)	O (mm)	N (mm)	X (mm)	H' (mm)	T (mm)	Offset (mm)	ϵ_r	f_3 (GHz)	f_2 (GHz)	f_4 (GHz)
24.7	37.9	6.7	14.05	2.0	2.0	10.0	3.8	10	0.0	4.2	2.45	1.8	3.1

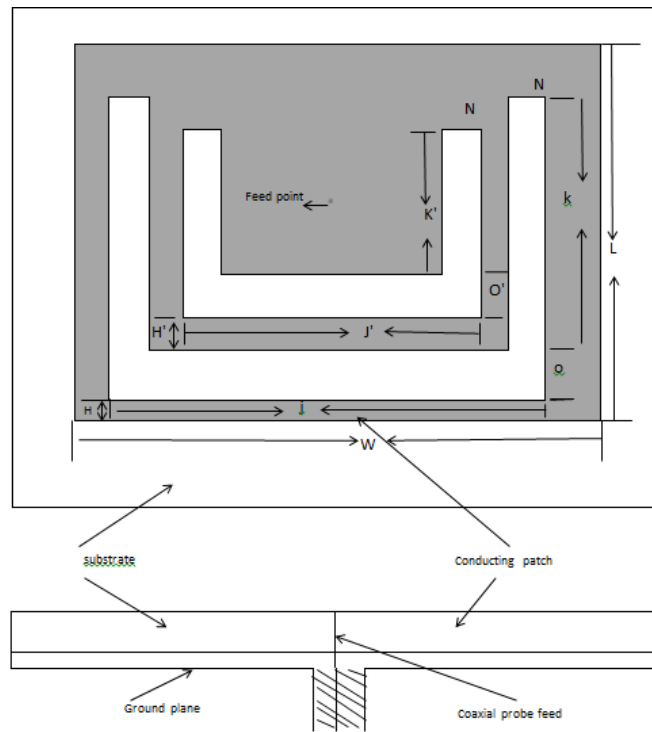


Figure 2: Geometry of the rectangular double U-slot microstrip patch antenna

In the same manner, the third design” the triple U–slot patch microstrip antenna “is depended on the second design and the dimensions of the third U shape J'', K'', H'' are the half length of second design. The next Table 3 summarizes the dimensions of the triple U –slot patch microstrip antenna.

Table 3: Dimensions of triple U slot antenna

L (mm)	W (mm)	K'' (mm)	J'' (mm)	O (mm)	N (mm)	X (mm)	H'' (mm)	T (mm)	Offset (mm)	ϵ_r	f_3 (GHz)	f_2 (GHz)	f_4 (GHz)
24.7	37.9	3.35	7.02	2.0	2.0	10.0	1.9	10	0.0	4.2	2.45	1.8	3.1

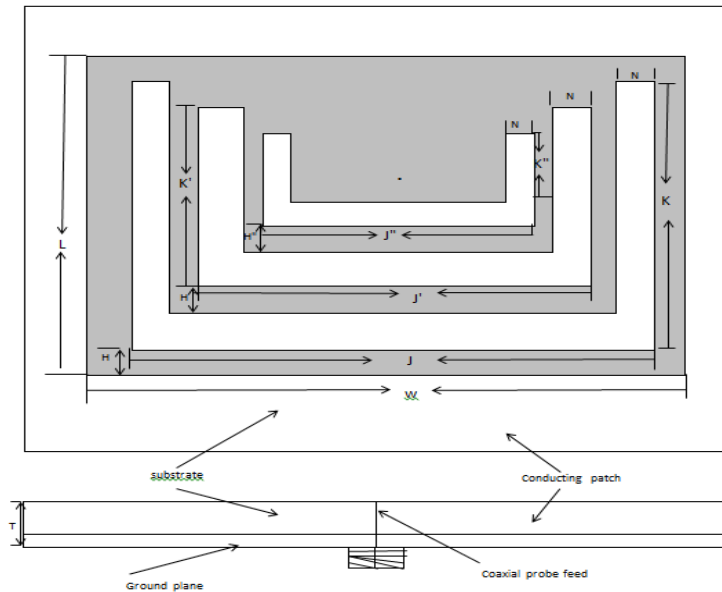


Figure 3: Geometry of the rectangular triple U-slot microstrip patch antenna

3 Result and discussion

3.1 Design of a rectangular patch microstrip antenna

Figure 4 illustrates a rectangle patch microstrip antenna which does not contain any slot in order to compare these results with the other designs to see how much improvement in the bandwidth. Figure 5 shows simulated results of the variation of return loss versus the frequency of the proposed antenna. There is a resonant frequency which is located at the desired values of 2.45 GHz with return loss of (-22) dB and 13% bandwidth. The Bandwidth (BW) % can be calculated as follow:

$$BW(\%) = \frac{f_h - f_l}{f_c} * 100 \tag{12}$$

Where f_h , f_l are the upper and lower frequency at the point -10dB, f_c is the resonant frequency .

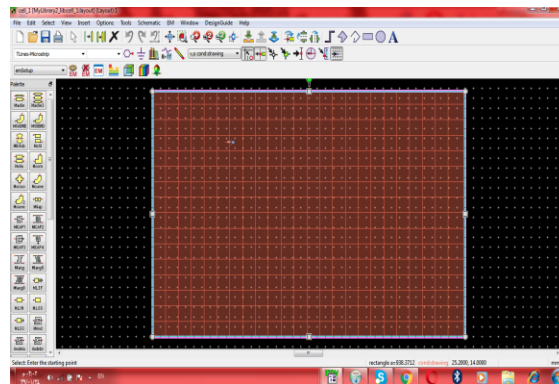


Figure 4: Rectangular patch microstrip antenna

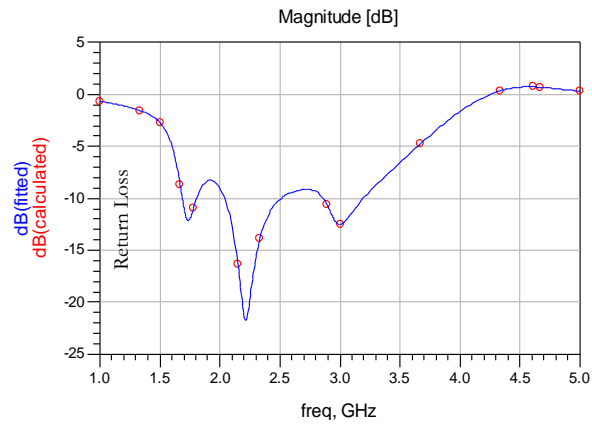


Figure 5: Return loss of the rectangular patch microstrip antenna

3.2 Design of a rectangular U-slot patch microstrip antenna.

Figure 6 shows a rectangle U-slot patch microstrip antenna. Figure 7 shows the resonant frequency at 2.2 GHz with return loss of -21dB. In addition, a bandwidth of 51.36% was achieved.

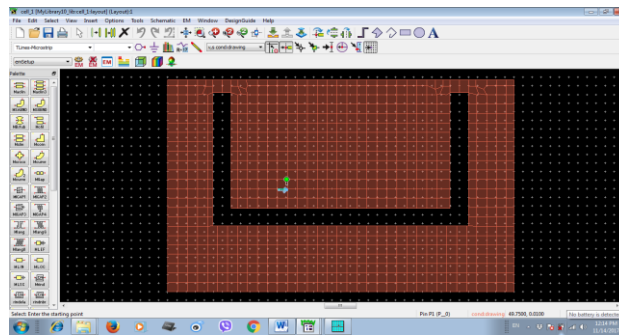


Figure 6: Design of the rectangle U-slot patch micro strip antenna

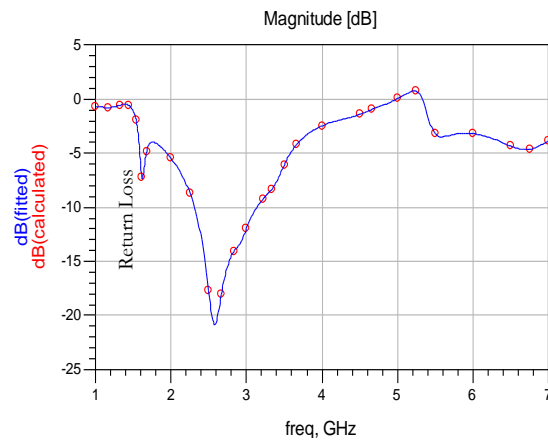


Figure 7: Return loss of the rectangle U-slot patch micro strip antenna

3.3 Design of a rectangle double U –slot patch microstrip antenna.

A rectangle double U-slot patch microstrip antenna is illustrated in Figure 8. From Figure 9, the antenna was found to be resonating at 2.47GHz with a return loss of -26 dB, and a bandwidth of 52.63% was achieved.

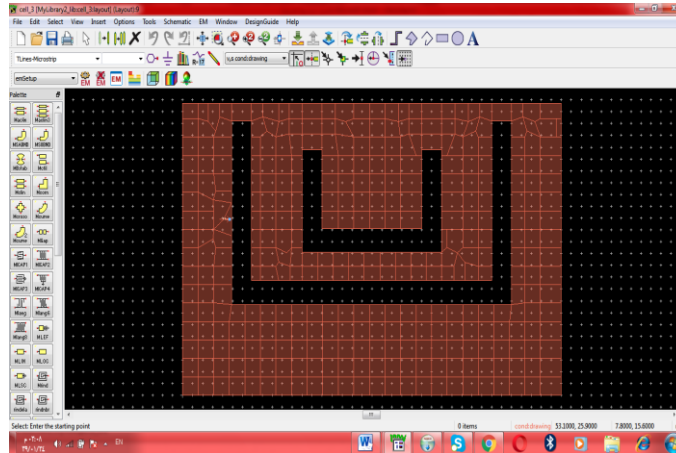


Figure 8: Design of the rectangle double U-slot patch microstrip antenna,

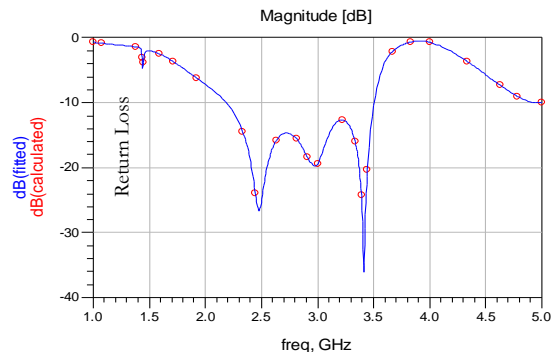


Figure 9: Return loss of the rectangle double U-slot patch microstrip antenna,

3.4 Design of a rectangular triple U –slot patch microstrip antenna.

Figure 10 shows a rectangle Triple U-slot patch microstrip antenna. Figure 11 shows a resonant frequency at 2.47GHz with a return loss of -22 dB. a bandwidth was found 52.63%, which is approximately the same as in a rectangle double U-slot patch microstrip antenna.

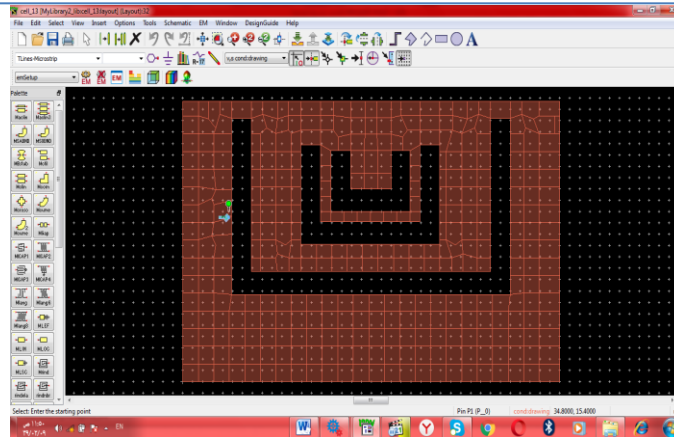


Figure 10: Design of the rectangle triple U-slot patch microstrip antenna,

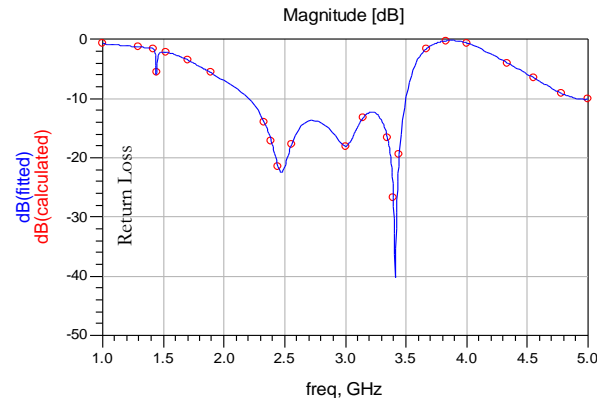


Figure 11: return loss of the rectangle triple U-slot patch microstrip antenna,

Table 4 summarizes the data from all designs. The three designs give bandwidth enhancement above 50%.The double U-solt and Triple U-slotpatch micro-strip give slightly higher bandwidth enhancement of 52.63% covering from 2.2 to 3.50 GHz frequency. It should be considered that the bandwidth specification changes according to the feed point location.

Table 4: summarizes the data from all designs

	$f_c(\text{GHz}_z)$	$f_u(\text{GHz}_z)$	$f_l(\text{GHz}_z)$	dB_i	Feed point position	bandwidth
Rectangular patch antenna	2.2	2.5	2.05	-26	(9.80,19.60)	13%
Single U-slot	2.2	3.13	2	-21	(7.60,20.00)	51.36%
Double U- slot	2.47	3.50	2.2	-26	(4.70,14.90)	52.63%
Triple U-slot	2.47	3.50	2.2	-22	(4.60,14.50)	52.63%

4 Conclusion

In this research, a rectangular shaped microstrip antenna has been designed that contains a single, double and triple U shape using ADS software. A single U shape has been designed and tested for the sake of increasing bandwidth at operating frequency 2.45 GHz. The achieved bandwidth was 51.36% at return loss equal to 21dB. A double U shape microstrip antenna has also been tested with bandwidth equal to 52.63% at return loss equal to -26 dB. In addition, a triple U shape has also been undertaken to give bandwidth equal to 52.63% at return loss equal -22 dB. In general, the results are considered very satisfactory where most designs give bandwidth enhancements above 50% at very acceptable levels of return loss.

Reference

- [1] P. Bhattacharjee, V. Hanumante, S. Roy, "Design of U-Slot Rectangular Patch Antenna for Wireless LAN at 2.45GHz", 9th International Conference on Microwaves, Antenna, Propagation and Remote Sensing, 2013.
- [2] Aruna Rani, R.K. Dawre, "Design and Analysis of Rectangular and U Slotted Patch for Satellite Communication", International Journal of Computer Applications, Volume 12– No.7, December 2010
- [3] Runa Rai, A. K. Gautam, "improvement in gain and bandwidth of rectangular and U slot loaded patch", International Journal of Computer Science Issues, Vol. 8, Issue 6, No 2, November 2011
- [4] H. Khidre, [Kai-Fong Lee](#), [A. Z. Elsherbini](#), [F. Yang](#), "Wide Band Dual –Beam U-Slot Microstrip Antenna", IEEE, Vol. 61, No. 3, March 2013.
- [5] J. Bahl, P. Bhartia , " [Design and Performance Evaluation of Microstrip Antenna for Ultra-Wideband Applications Using Microstrip Feed](#)", [American Journal of Electrical and Electronic Engineering](#), Vol. 3 No. 4, 93-99, 2015

Bandwidth Optimization Through Hybrid Codecs G.711 and G.729 for VoIP Ethernet, FR and MP Networks

Mohamed Alahemar, Abdullah Masrub, AbdulSalam Addeeb

Department of Electrical & Computer Engineering, Elmergib University, Libya

DOI: <https://doi.org/10.21467/proceedings.2.14>

* Corresponding author email: mohammed13111992@gmail.com

ABSTRACT

With the rapid growth in both internet and telecommunication technologies, VoIP has become more and more popular and expected to replace the traditional telephony services. The main issues in communication of real time application on IP networks, however, are providing high Quality of Service (QoS), security and appropriate capacity of transmission medium. Therefore, one of the most important factors to consider when designing packet voice networks is the capacity. This paper focuses on the capacity problem and attempts to determine the minimum bandwidth (BW) that can support in each transmission rate based on different speech codecs. In precise, this paper discusses an overhead problem in VoIP transmission and studies the extent of which the required BW is affected by the type of used network and the dependency on the codec type used for the VoIP encoders. The study devises the variation payload size in two codec techniques (G.711 and G.729) to optimize the BW utilization. The study concluded that increasing the payload size and using the cRTP protocol would reduce bandwidth requirements to more than 50%.

Keywords: VoIP; Overhead Problem; Codec Techniques; Capacity.

1 Introduction

Voice over Internet Protocol (VoIP) is a technology that used widely in both internet and telecommunication fields to make voice calls and expected to replace the traditional telephony services. Nowadays, using VoIP services users are not only allowed to call other users using the same service, but they may allow to call anyone who has a subscribe number connected to a VoIP adapter. The idea of this technology is to convert the user voice into a digital signal to be transmitted using the Internet connection. The idea behind such technology is a number of protocols that organize and control connection establishment over different network layers. As the voice packet is moved over different network layers, some additional information needs to be added to the packet. Real-time Protocol (RTP), Datagram Protocol (UDP), and Internet Protocol (IP) header address represent more than 70% of the added information to such packets. The formed (RTP/UDP/IP) packet represent about 54 bytes of information. The main components of a VoIP system are CODEC (Coder-Decoder), Packetizer and playout buffer [1].



© 2018 Copyright held by the author(s). Published by AIJR Publisher in Proceedings of First Conference for Engineering Sciences and Technology (CEST-2018), September 25-27, 2018, vol. 1.

This is an open access article under [Creative Commons Attribution-NonCommercial 4.0 International](https://creativecommons.org/licenses/by-nc/4.0/) (CC BY-NC 4.0) license, which permits any non-commercial use, distribution, adaptation, and reproduction in any medium, as long as the original work is properly cited. ISBN: 978-81-936820-5-0

The most critical components of a VoIP system is the voice codec. It is the process of converting the speech signal into digital form, transmit it through the medium to the receiver and reconstruct the received information to form the original signal. different algorithms are run on both sides, the sender and the receiver sides, to ensure the success deliver of the packetized voice data. Different codecs have different bit-rate, packet length, speech quality, algorithmic delay, complexity are used to enable optimization of bandwidth utilization. Bit rate is a very important parameter of codec which affects the quality of encoded speech. Therefore, to obtain the best quality of voice with the lowest bandwidth requirements, it is important to select the appropriate codec for a particular voice network [2] [3][4].

However, the main issues in communication of real time application on IP networks are providing high Quality of Service (QoS), security and appropriate capacity of transmission medium. Choosing the appropriate codec for a particular bandwidth of the network is also a little difficult. Using other internet application such as web browsing, file transfer, ... etc in the same time with VoIP service is affect the performance of the connection of the VoIP session because it is affecting the network bandwidth. Due to popularity of both the common hybrid codecs (G.711 and G.729), they have been studied in this paper to optimize the bandwidth utilization.

2 Background

2.1 Voice Codecs

With VoIP, the voice traffic is carried through the transport medium over an IP network, requiring a source, destination, User headers. Voice codec samples the waveform at regular intervals and generates a value. Samples are taken 8000 times/s (i.e. 8 kHz sampling rate) or 16000 times/s (i.e. 16 kHz sampling rate). The values are quantized in order to map it into discrete-finite value which can be represented using digital bits, which forms the voice data frame being transmitted over the network. To achieve such process, codec provides compression capabilities to save network bandwidth. The rapid development of VoIP technology has driven to deep advancement in designing of voice codecs which provide better QoS management capabilities. As mentioned above, choosing a proper codec is an important factor because it can affect the voice quality and bandwidth utilization together. Then the philosophy is, having higher compression codecs leads to lower bit rate which means lower bandwidth. From another point of view, high-quality voice codecs with high degree of compression require very low bandwidths for transmission, and thus have better performance in network congestion situations [2][5][6].

Formally, voice codecs are standardized by the International Telecommunication Union (ITU-T). The most common voice codecs specified by ITU-T include G.711 with 64 kbps and G.729 with 8 kbps bit rate. Both versions are widely used. G.729 utilizes one eighth of the bandwidth compared to G.711. This means that G.729 supports more calls but they have less

quality. G.711 codec doesn't have licensing fee so it can be used in VoIP applications freely. In contrary, G.729 is a licensed codec. Most phones that support VoIP have implemented this codec in their chipset. G.711 codec use Pulse Code Modulation (PCM) of voice frequencies at a standard bit rate of 64 Kbps. Typically 12..14 bit samples, sampled at 8 KHz sample rate, are compounded to 8 bit for transmission over a 64 Kbps data channel. This codec requires low computation complexity and provides very good voice quality with negligible delay. However, it consumes 64 Kbps of audio bandwidth per direction, which is high in comparison to other codecs. On the other hand, G.729 codec samples the voice band at 8 KHz with a 16 bit resolution. This codec provides significant bandwidth savings. It has 8:1 compression and requires just 8 Kbps of audio bandwidth [2][4]. Main characteristics of both codecs are shown in Table 1.

Table 1: Main characteristics of the G711, G729

Codec	Data Rate (kbps)	Coding Type	Comments
G.711	64	PCM	Delivers precise speech transmission. produces audio uncompressed
G.729	8	CS-ACELP	Excellent bandwidth utilization. produces audio compressed

2.2 Related Work

The issue of voice performance are widely studied and the most research have been done in this area focus on codec selection. The aim is to select the appropriate sampling method for suitable codec to provide better voice performance. The Quality of Service (QoS), network traffic, and bandwidth requirement are topics of interest in the research field [5]. However, not many work have been done on specific type of network and bandwidth optimization. For example, different voice codecs were employed to investigate VoIP traffic with silence suppression technique where no packets are generated in silence period [6]. Simulation methods were also used to investigate the performance of VoIP using different coding schemes [7]. As multi rate make different transmission rate and hence, different bandwidths possible. In this context, if the number of calls exceed the allocated bandwidth, the quality of perceived voice can be affected by packet loss, jitter and delay [8].

While Constant Bit Rate (CBR) traffic with different codec schemes were considered by many researchers, others suggest that G.729 codec generates smaller packets and is more error resilient than G.711 [9][10]. In such case, G.729 codec with Voice Activity Detection (VAD) enabled was used to produce the Variable Bit Rate (VBR) characteristics. Accordingly, it is more suitable for use in wireless network where there are higher channel errors [11]. Both codecs G.711 and G.729 were compared over 802.11 Distributed Coordination Function (DCF) protocol in infrastructure mode. Results have shown that the output bit rate of the G.729 encoder being eight times less than that of the G.711 encoder [12]. Moreover, to improve quality of service capabilities, it have shown that the header overhead for voice traffic

can be reduced [13] and can also be compressed during multiplexing to increase the bandwidth efficiency [14].

3 Bandwidth Calculation

In order to be moved over the IP network layers, the IP packet is wrapped by the physical transmission medium. The overhead introduced in VoIP communication links by the RTP/UDP/IP headers is quite high: Consider a scenario where a G.729 codec operating at a rate of 8Kbps, sending frames every 20 msec. This will result in a voice payloads of 20 bytes for each packet. However, to transfer these voice payloads using RTP/UDP/IP, the following headers must be added: an Ethernet header of 14 bytes (18 bytes if VLAN is used), IP header of 20 bytes, UDP header of 8 bytes and an additional 12 bytes for RTP. This is a whopping total of 54 bytes (58 with VLAN) overhead to transmit a 20-byte payload. Transmission of IP over other mediums will result in different overhead calculations. These protocol header assumptions can be summarized as follows:

- 40 bytes for: IP (20 bytes) / User Datagram Protocol (UDP) (8 bytes) / Real-Time Transport Protocol (RTP) (12 bytes) headers.
- Compressed Real-Time Protocol (cRTP) reduces the IP/UDP/RTP headers to 2 or 4 bytes (cRTP is not available over Ethernet).
- 6 bytes for Multilink Point-to-Point Protocol (MP) or Frame Relay Forum (FRF).
- 1 byte for the end-of-frame flag on MP and Frame Relay frames.

18 bytes for Ethernet L2 headers, including 4 bytes of Frame Check Sequence (FCS) or Cyclic Redundancy Check (CRC).

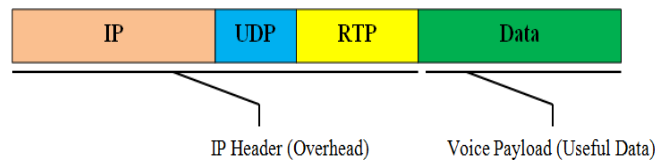


Figure 1: IP header forms a significant part of small Voice over IP packets

The amount of bandwidth required to carry voice over an IP network is dependent upon a number of factors such as Codec (coder/decoder) and sample period, IP header, Transmission medium, Silence suppression. The term 'IP header' is used to refer to the combined IP, UDP and RTP information placed in the packet, see fig. 1. The payload generated by the codec is wrapped in successive layers of information in order to deliver it to its destination. RTP is the first, or innermost, layer added. This is 12 octets. RTP allows the samples to be reconstructed in the correct order and provides a mechanism for measuring delay and jitter. UDP adds 8 octets, and routes the data to the correct destination port. It is a connectionless protocol and does not provide any sequence information or guarantee of delivery. IP adds 20 octets, and is

responsible for delivering the data to the destination host. It is connectionless and does not guarantee delivery of packets [4][5].

Overall, the IP/UDP/RTP headers add a fixed 40 octets to the payload. With a sample period of 20 ms, the IP headers will generate an additional fixed 16 kbps to whatever codec is being used. The payload for the G.711 codec and 20 ms sample period calculated above is 160 octets, the IP header adds 40 octets. This means 200 octets, or 1,600 bits are sent 50 times per second resulting in 80,000 bits per second. This is the bandwidth needed to transport the VoIP only, it does not take into account the physical transmission medium.

There are other factors, which can reduce the overhead incurred by the IP headers, such as compressed RTP (cRTP). This can be implemented on point-to-point links and reduces the IP header from 40 to just 2 or 4 octets. The codec determines the actual amount of bandwidth that the voice data will occupy. It also determines the rate at which the voice is sampled. The IP/UDP/RTP header can generally be thought of as a fixed overhead of 40 octets per packet, though on point-to-point links RTP header compression can reduce this to 2 to 4 octets (RFC 2508). The transmission medium, such as Ethernet, will add its own headers, checksums and spacers to the packet. Finally, some codecs employ silence suppression, which can reduce the required bandwidth by as much as 50 percent [2] [15].

$$\text{Total packet size} = (\text{layer 2 header: MP or FR or Ethernet}) + (\text{IP/UDP/RTP header}) + (\text{voice payload size}) \quad (1)$$

$$\text{Packet Per Second (PPS)} = (\text{codec bit rate}) / (\text{voice payload size}) \quad (2)$$

$$\text{Bandwidth} = \text{total packet size} * \text{PPS} \quad (3)$$

4 Results and Discussion

The programming language used in this work is the Matlab, for its speed of data processing and ease of use, and the possibility of displaying the results in graphical form so that it can be easily understood. Bandwidth requirement for transmission VoIP is calculated using codecs G711, G729. We examine the effect of the used network type and the variation payload size on bandwidth requirement. In this work, we consider the types of networks (Ethernet, Frame Relay (FR), Multilink Point-to-Point Protocol (MP)), and for Payload size when using the codec G711 it was (5, 10, 20, 30, 40) ms while when using the codec G729 it was (10, 20, 30, 40, 50, 60) ms.

From Fig. 2 and Fig. 3, it is noticed that as payload size increases the BW decreases. The network that requires the widest bandwidth is clearly the Ethernet network. This is due to not utilizing cRTP protocol which responsible for decreasing the header. On the other hand, the type of network system that requires less bandwidth is the Frame Relay (FR) and Multilink point-to-point (MP) networks. Again, this is due to cRTP function that is reducing the header and therefore condensing the bandwidth requirements. Fig. 4 and Fig. 5 show the percentage of the header size with respect to the total load size. When increasing the voice payload size the VoIP bandwidth reduces and the overall delay increases.

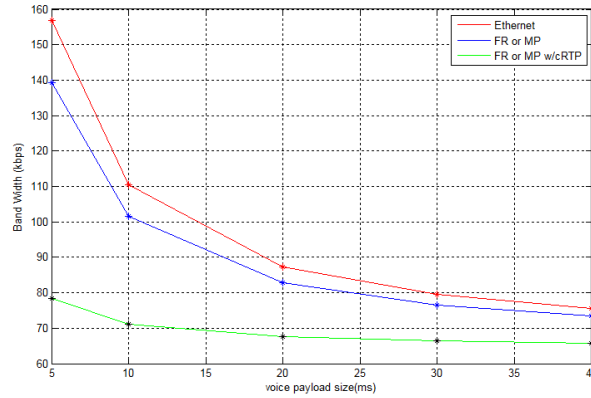


Figure 2: Bandwidth Requirement of Codec G711

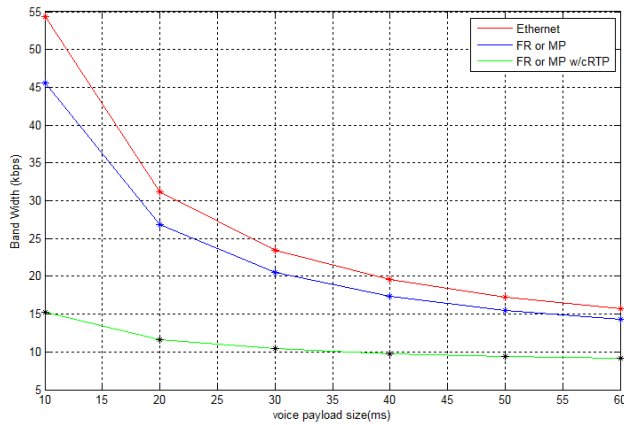


Figure 3: Bandwidth Requirement of Codec G729

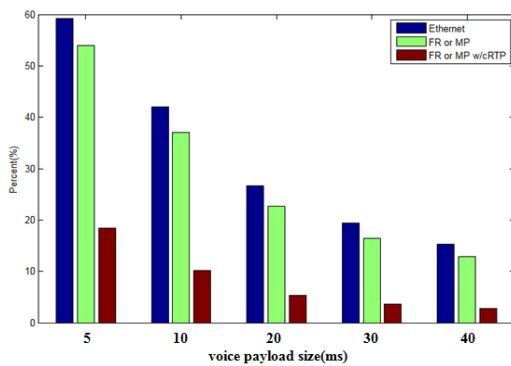


Figure 4: Packet Overhead of Codec G711

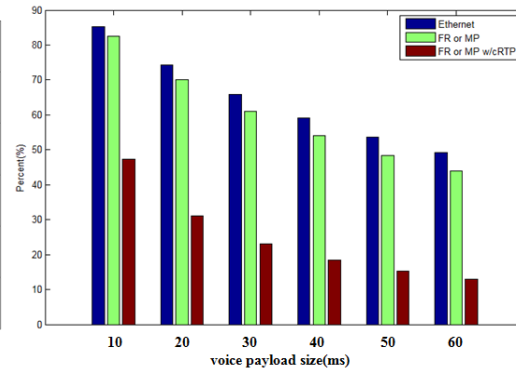


Figure 5: Packet Overhead of Codec G729

5 Conclusions

All VoIP packets are made up of two components: voice samples and IP/UDP/RTP headers. Although the voice samples are compressed by the Digital Signal Processor (DSP) and can vary in size based on the codec used, the headers are a constant of 40 bytes in length. With

cRTP, these headers can be compressed into two or four bytes. This compression offers significant VoIP bandwidth savings. When increasing the voice payload size the VoIP bandwidth reduces and the overall delay increases.

There are many factors that influence the amount of bandwidth required to transmit a voice call over an IP network. By approaching the problem one element at a time, the final calculation becomes relatively feasible. Other factors may influence the use of the actual bandwidth, such as RTP header compression, silence suppression and other techniques are still under development. The study concluded that increasing the payload size and using the cRTP protocol would reduce bandwidth requirements to more than 50%.

References

- [1] H. Kazemitabar, S. Ahmed, K. Nisar, A.Said, and H. Hasbullah, "A Comprehensive review on VoIP over Wireless LAN networks," *ISSR Journal*, Vol. 2, No. 2, September 2010, pp. 1-16.
- [2] Haniyeh Kazemitabar and Abas Md. Said, "Capacity Analysis of G.711 and G.729 Codec for VoIP over 802.11b WLANs" International Conference, ICIEIS 2011, November 14-16, 2011, Kuala Lumpur, Malaysia.
- [3] S. Rattal, A. Badri, M. Moughit, "Performance Analysis of Hybrid Codecs G.711 and G.729 over Signaling Protocols H.323 and SIP" international journal of Computer Applications, Vol. 72, No. 3, May 2013.
- [4] M. Sulovic, D.Raca, M.Hadqialic and N. Hadziahmetovic "Dynamic codec selection algorithm for VoIP". The sixth international conference on digital telecommunications, ICDT 2011
- [5] H.A. Ifijeh, F.E. Idachaba, and I.B. Oluwafemi, "Performance Evaluation of The Quality of VoIP Over WLAN Codecs" Proceedings of the World Congress on Engineering , July 1 – 3, 2015, London, UK.
- [6] Broadcom Corporation, "Critical Steps for Successful VoIP Deployment" available at <http://www.broadcom.com/> (April 2005) last visited February 2013.
- [7] J K. Salah & A. Alkhoraidly, "An OPNET-based Simulation Approach for Deploying VoIP" *International Journal of Network Management*, Volume 16 Issue 3, Pages 159-183, John Wiley & Sons, Inc. New York, NY, USA, (May 2006).
- [8] M. Meeran, P. Annus, M. Alam, Y. Moullec, "Evaluation of VoIP QoS Performance in wirelessMesh Networks" *Journal of information*, **2017**, 8, 88; doi:10.3390/info8030088.
- [9] Jiango Cao & Mark Gregory, "Performance Evaluation of VoIP Services Using Different CODECs Over A UMTS Network" Telecommunication Networks and Applications Conference, 2008. ATNAC 2008. Australasian ISBN: 978-1-4244-2602-7 pp 67 –71.
- [10] Abu Sayed Chowdkery, Mark Gregory "Performance Evaluation of Heterogeneous Network for Next Generation Mobile" 2009 12th International Conference on Computers and Information Technology (ICIT 2009) Dhaka, Bangladesh, IEEE Catalog Number: CFP0917D-PRT ISBN: 978-1-4244-6281-0 pp 100-104.
- [11] Bawei Xi, Hui Chen, William S. Cleveland, Thomas Telkamp, "Statistical Analysis and Modeling Of Internet VoIP Traffic for Network Engineering" *Electronic Journal of Statistics Vol. 4 (2010) pp58–116 ISSN: 1935-7524 DOI: 10.1214/09-EJS473*
- [12] Carlos Ign´acio de Mattos, Eduardo ParenteRibeiro and Carlos Marcelo Pedroso, "A New Model For VoIP Traffic Generation" *The 7th International Telecommunications Symposium (ITS 2010)*
- [13] AT & T, "Critical Steps for Successful VoIP Deployment" (2005).
- [14] Di Wu, "Performance Studies of VoIP over Ethernet LANs" A Master Degree dissertation submitted to Auckland University of Technology (2008).
- [15] R. Dimova, G.Georgiev, Z. Stanshev "Performance Analysis of QoS Parameters for Voice over IP Applications in a LAN Segment" International Scientific Conference Computer Science'2008

Modeling and Performance Evaluation of MapReduce in Cloud Computing Systems Using Queueing Network Model

Guzlan Miskeen

Dept of Computing, Faculty of Education Brack, University of Sebha, Sebha, Libya

DOI: <https://doi.org/10.21467/proceedings.2.15>

* Corresponding author email: guz.miskeen@sebhau.edu.ly

ABSTRACT

MapReduce is a two -stage information processing technique and it is common concept for big data. Map and Reduce procedures are distributed among some processors within a cluster in the cloud. The performance modeling and analysis of MapReduce execution times has been a challenging task. Analytic performance models provide reasonably accurate job response time estimation with significantly lower cost compared with experimental experiments. Queueing theory is one the modeling and analysis tools of such systems since it enables efficient analysis of the performance, availability and some other key metrics of a data processing system. In this paper, an M/G/1/K performance model with first come first serviced (FCFS) discipline of MapReduce is proposed. More specifically, it will present a queueing model with two stages hypoexponential service time and finite queue. This model has a cloud server with two stages to investigate the performance of the MapReduce technique subject to heavy traffic conditions. The system is analyzed via discrete-event simulation (DES). Key numerical examples are presented for varying number of mappers, reducers and the mean arrival rates to assess their effect on the system mean response time, loss probability and mean queue length. The results are expected to be useful for predicting MapReduce under various workloads and operating conditions of big data processing.

Keywords: Cloud computing, MapReduce, Performance Modeling, Queueing Theory, Hypoexponential distribution

1 Introduction

MapReduce is a well- known programming model that process in parallel large data on cloud clusters [1]. This model is composed of map and reduce functions, “Map” function processes a key/value pair to generate a set of intermediate key/value and a “Reduce” function merges all intermediate values associated with the same intermediate key [2]. In big data cluster, a MapReduce job is divided into several tasks that are executed on parallel on multiple virtual machines (VMs), which significantly reduce the job execution time. The operating concept of a MapReduce is depicted in Figure 1. The Hadoop Distributed File System (HDFS) is an open



© 2018 Copyright held by the author(s). Published by AIJR Publisher in Proceedings of First Conference for Engineering Sciences and Technology (CEST-2018), September 25-27, 2018, vol. 1.

This is an open access article under [Creative Commons Attribution-NonCommercial 4.0 International](https://creativecommons.org/licenses/by-nc/4.0/) (CC BY-NC 4.0) license, which permits any non-commercial use, distribution, adaptation, and reproduction in any medium, as long as the original work is properly cited. ISBN: 978-81-936820-5-0

source System that is responsible for storing replicated data fashion and run in a distributed way on a cluster of servers [1].

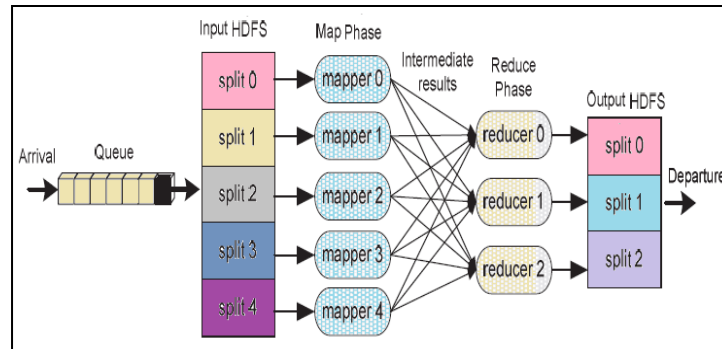


Figure 1: The operating concept of MapReduce process (adopted from [1])

For a cloud MapReduce cluster, a cloud node is a VM which can have several mappers and reducers [1]. MapReduce functionality can be described as following: upon arrival, MapReduce jobs are queued for processing at the cloud cluster which has hundreds of nodes. The job is scheduled by the load balancer which plays an important role in dispatching, monitoring, and tracking the availability of nodes at the cloud datacenter. Then, the input data of a MapReduce job is split into multiple data set. As a result, the map phase is initiated where each data set is processed by one mapper node to produce intermediate key/value pairs or results. After all data sets have received the required service, the reduce phase starts where each reducer can process and aggregate the intermediate results to form the final output results [3].

The ratio of the total mappers to reducers can be specified by the user and the job tracker, with additional controlling functionality, is responsible for provisioning the correct number of slave nodes (which host the mappers and reducers) to meet the QoS conditions. There is a tradeoff between cloud cluster's performance and the cloud usage cost since allocating fewer resources than required will affect the cloud's performance while allocating more nodes will increase the cost to the cloud user due to the over-provisioning[1]. Therefore, knowing the correct number of nodes can be implicitly made via determining the number of mappers and reducers needed to execute a MapReduce job and then resolving the cloud MapReduce performance-cost tradeoff.

The rest of the paper is organized as follows. Section 2 reviews the key studies on the performance evaluation of map reduce technique. Section 3 presents the proposed queueing mode to capture the MapReduce node's behaviour. Section 4 presents DES and numerical examples to show how to utilize the proposed model in predicting the performance of the node. Feasible extension of the proposed model is presented in Section 5 and finally Section 6 concludes the study and suggests directions for future work.

2 Related work

There has been some prior work on the performance of MapReduce node. A queueing network model with hypoexponential service time and finite queue was proposed to study and analysis the performance of MapReduce and multi-stage big data processing [4]. In [5] MapReduce model behaviour was captured via a Triple-Queue Scheduler based where MapReduce workloads were classified into three types based on their CPU and I/O utilization under heterogeneous workloads. A network of queues model was proposed in [6] to model MapReduce and it was evaluated via simulation. Only the execution time of MapReduce jobs with varying cluster size was estimated. While a closed queueing networks model was proposed in [7] to model the map phase. More specifically, a mathematical model was constructed for predicting the execution time of the map phase of MapReduce single class jobs. The model results were validated by experiments on a single as well as a 2-node Hadoop environment.

The work in [3] presented an analytical model based on finite queueing system M/G/1/K to model MapReduce algorithm and to determine, at any time and under current workload conditions, the minimal number of cloud resources needed to satisfy the Service Level Objective SLO response time. The queueing model server has three stages in tandem, namely: “job scheduling” delay centre, parallel n delay centre “VMs worker”, and “result aggregating” delay centre. An analytic solution and a DES were developed to solve the system and the work considered only light- to- medium traffic. The work in [3] was extended in [1] where the model has a three- phase service time namely: delay centre scheduler (load balancer), parallel m delay centre mappers and parallel n delay centre reducers. An analytic solution and a DES were developed to solve the system that has three phases where the second and third phases are with m and n servers with exponential service rate respectively. The above mentioned studies did not take into consideration the MapReduce operation under heavy traffic conditions. Moreover, to the best of the author’s knowledge, the heavy traffic approximation for multiple server queueing system was not utilized to simplify the queueing model analysis. The paper aims to simplify a model similar to those proposed in [1] and [3] according to this theory. In this context, i.e., at heavy traffic, multiple server queueing systems can be approximated by single server queues with total mean service rate, $\mu_t = C\mu$. Using a heavy traffic approximation, multiple server systems can be approximated to single server queueing systems, as approved in [8],[9].

3 The Proposed Model

3.1 The Queueing Model

A queueing model for executing big data MapReduce tasks is proposed, as depicted in Figure 2. Three performance metrics are considered for the mean service time, mean queue length and the loss probability. In order to simplify the simulation of the MapReduce node model

proposed in [1], the approximation based on the theory of heavy traffic condition is adopted where both parallel m and n delay centres were replaced in the proposed model by single delay server with $n\mu$ and $m\mu$ rates respectively.

The model assumptions and the analysis methods are justified as following: arrivals are assumed to have Poisson distribution, since it was shown that arrival of HTTP requests for documents under a heavy load closely follow the Poisson process (According to [1] and [3]). Service times are hyperexponentially distributed, as in reality, service times are not always exponential, but they are generally distributed. In this case, these models become difficult to be analytically solved when considering bursty traffic and non- Poisson arrivals. Therefore, simulation is an effective alternative to capture the system behaviour.

It is worth mentioning that the impact of buffer size variation on the node’s performance was not taken into consideration in this study.

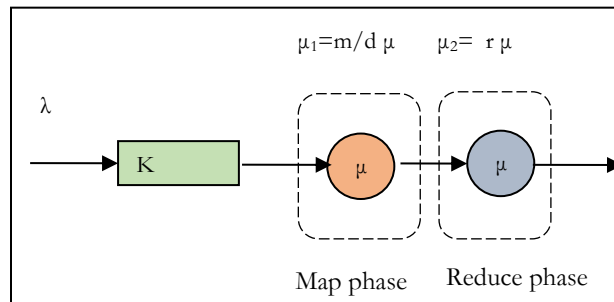


Figure 2: $M/G/1/K$ model for a big data server running m mappers and r reducers

3.2 Performance Metrics

The performance metrics adopted in this study are briefly described below[10]:

1. Mean Response time (W)

It is the time a server takes to process a job (i.e., it is the time between receiving a job at the server node and its departure from the node).

2. Loss Probability (LP)

This is the percentage of jobs that get lost on arrival when they found the server queue full.

3. Mean queue length (Wq)

It is the number of jobs waiting in the queue to be served by the server.

These performance metrics are chosen to explicitly reflect the system behaviour when the MapReduce is overloaded in the event of queue saturation (at heavy traffic conditions).

4 Simulation and Numerical Results

4.1 Simulation Analysis

Discrete-event simulation was implemented using a java package to simulate M/G/1/K /FCFS for MapReduce process with m mappers and r reducers where $m > r$. The performance was assessed in terms of the MapReduce node's mean response time, mean queue length and loss probability. These performance metrics were compared to assess the effect of increasing the number of m and r on the performance. where the service time has hypoexponential distribution. The simulation is implemented according to [11]. The built-in pseudorandom number generator was used to generate uniformly distributed random variables, U on $[0,1]$ interval. (RVs) which were employed to generate exponential and hypoexponential RVs, are expressed in equations 1 and 2:

$$\text{Exponential RV} = \frac{-1}{\lambda} \cdot \ln(U) \quad (1)$$

$$\text{Hypoexponential} = \sum_{i=1}^n \frac{-1}{\mu_i} \ln(U_i) \quad (2)$$

where λ is the mean rate of the exponential RV, μ_i is the mean rates for the hypoexponential stages of the RVs and U is a uniform RV. Since hypoexponential RVs are the sum of n exponential RVs. The rates of exponential RVs can be equal or different from each other. In the context of this work, the rates are assumed to be different and the simulation algorithm of 2-stages hypoexponential RV is depicted in Figure 3.

Algorithm:

Generating 2-stages hypoexponential RV, X , using the inverse transform method to generate two exponential RVs, the following steps as followed:

Begin

Step 1: Input the value of the mean rate λ_1, λ_2 of the Exponential RV;

Step 2: Generate two uniform RVs $U_1[0,1], U_2[0,1]$ and

Step 3: Let $X = \sum_{i=1}^2 [-\frac{1}{\lambda_i} \ln(U_i[0,1])]$;

End.

Figure 3: Algorithm of generating 2-stages hypoexponential RV

In order to improve the accuracy of simulation output, the number of the simulated events was made 10^6 . The values of the simulation parameters are listed in Table 1.

Table 1: The Parameters of The Simulation Experiments

<i>Parameter</i>	<i>Value</i>
K	100
Λ	200-1400 job /sec
μ	1200 job /sec
μ_1	$\mu_1 = m/d \mu$
μ_2	$\mu_2 = r \mu$
D	5
M	6,9,12,15
R	2,3,4,5

4.2 Numerical Results

Figures 4-7 show the relations between the adopted performance metrics for the MapReduce as a function of the mean arrival rate in order to check the effect of increasing of mappers and reducers subject to heavy traffic conditions. While Figures 6 and 7 show mean response time and loss probability against the number of both mappers and reducers. Figure 4 to 6 illustrate the effect of the number of mappers and reducers on the MapReduce performance metrics.

Figure 4 depicts the mean response time. The higher the mappers and reducers the better the performance will be (with the lowest mean response time). Clearly, this improvement is achieved because more workers operate in parallel so that any incoming job that finds the first CPU core is busy will be more probably to receive service by other workers. Figure 5 shows the performance comparison in terms of loss probability. It is verified that the loss probability for $m=15$ and $r=5$ is much smaller than that of a $m=6$ and $r=2$. This is expected as the server capacity is around twice as the original one. As a result, the queue will have less number of jobs and this will reduce the possibility of being full that causing job loss. Figure 6 illustrates the mean queue length. It is obvious that the increase of m and r will delay the full occupation of the queue till the moment when the mean arrival rate = 800 job/sec and this is almost close to the theoretical value when the server utilization $\rho=1$. On the contrary, when $m=6$ and $r=2$ the queue is more probable to be full. Due to the low service rate which is a function of both m and r .

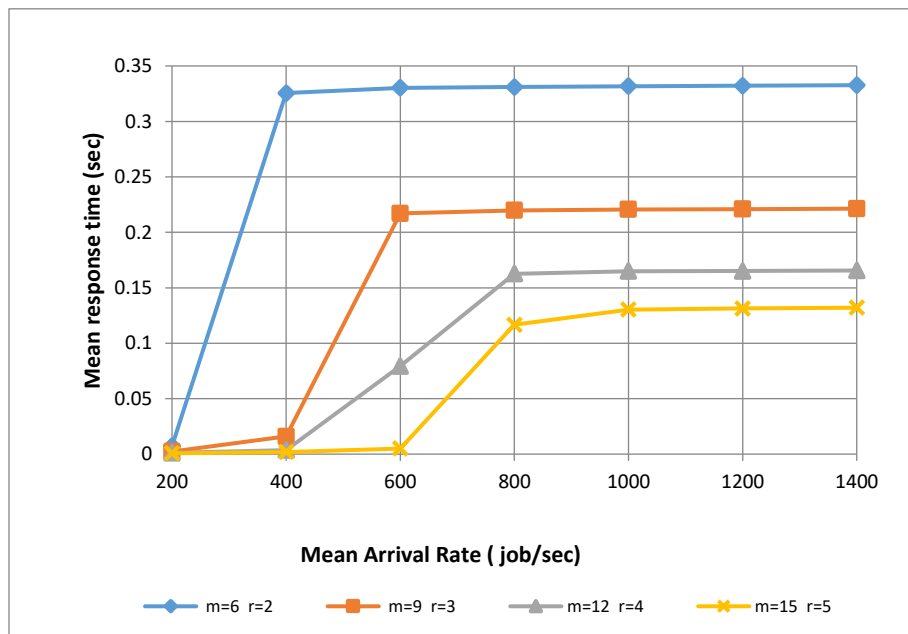


Figure 4: Mean response time V s mean arrival rate with varying mappers(m) and reducers (r)

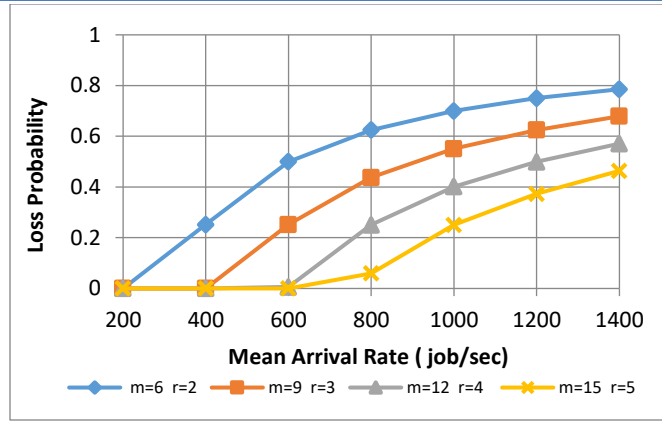


Figure 5: Loss probability Vs mean arrival rate with varying mappers(m) and reducers (r)

In order to make a decision on the number of mappers and reducers according to specific workload conditions, Figure 7 can be employed for this purpose by taking the mean response time as a key performance metric. When the sum of m and r are equal to 12, for example, the corresponding mean response time is around 0.22 sec.

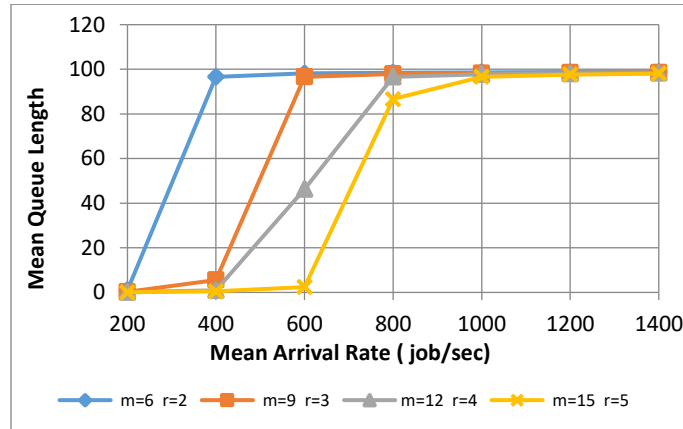


Figure 6: Mean queue length Vs mean arrival rate with varying mappers(m) and reducers (r)

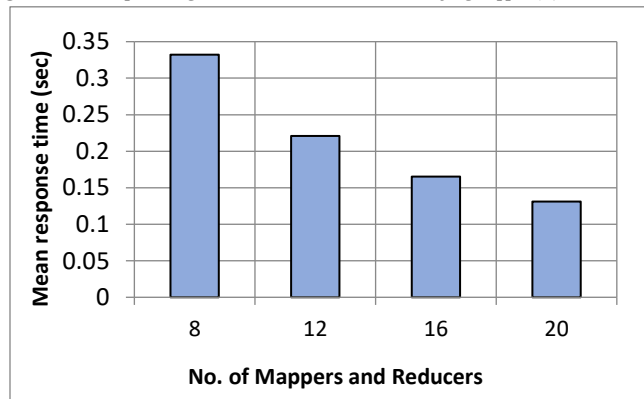


Figure 7: Mean response time Vs. the sum of mappers and reducers (m+r) (when $\lambda = 1200$ jobs/ sec)

5 A Model Extension Employing a QNM with Multiple Servers

In this section, a more general queueing model, depicted in Figure 8, is suggested to examine the performance of Map-reduces algorithm for a cluster has N servers utilizing the model proposed in [12]. This involves the use of the universal maximum entropy (ME) algorithm for arbitrary open QNMs with finite capacity (c.f., [8],[9]).

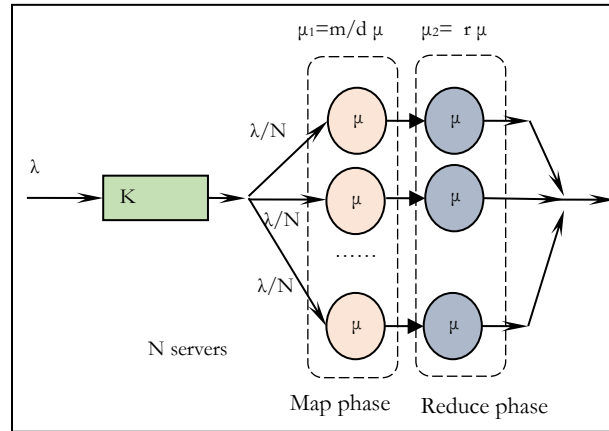


Figure. 8: Possible extension of the proposed model

6 Conclusions

The performance for big data map reduce process is investigated by assessing the impact of the number of mappers and reduces on the MapReduce system performance, in terms of the node mean response time, mean queue length and the loss probability, when fixing the buffer size. The results showed that the increase of the mappers and reducers in big data cluster node improve the overall performance. This improvement was quantified via DES. The proposed model can be used as an effective tool to determine the number of mappers and reducers to meet specific operating conditions. This study is an attempt towards investigating the performance of MapReduce procedure using a simple QNM as a quantitative tool for the design and possible development of MapReduce process under heavy traffic workloads.

Extensions of the work may address the modeling of a big data cluster that composed of N servers running MapReduce on parallel. In this context, one or more classes can be taken into consideration to reflect realistic operating conditions. The accuracy of the proposed queueing model can be improved by taking into account the scheduling delay at the load balancer, as suggested in [1],[3].

References

- [1] K. Salah, J. M. A. Calero, "Achieving Elasticity for Cloud MapReduce Jobs", IEEE International Conference on Cloud Networking (CloudNet 2013), 2013, pp 195-199.
- [2] J. Dean and S. Ghemawat, "MapReduce: Simplified Data Processing on Large Clusters", 2004, pp. 1-13.
- [3] K. Salah, "A Queueing Model to Achieve Proper Elasticity for Cloud Cluster Jobs," Proceedings of the 2013 IEEE Cloud Conference, Santa Clara, CA, June 27, 2013, pp. 755-761.
- [4] S. Zapechnikov, N. Miloslavskaya and A. Tolstoy "Analysis of Hypoexponential Computing Services for Big Data Processing", 2015 3rd International Conference on Future Internet of Things and Cloud, pp 579-584.

-
- [5] C. Tian, H.Zhou,Y. He , L. Zha, “A *Dynamic MapReduce Scheduler for Heterogeneous Workloads*”, 2009 Eighth International Conference on Grid and Cooperative Computing
 - [6] S. Ahn and S. Park, “An *Analytical Approach to Evaluation of SSD Effects under MapReduce Workloads*”, Journal of Semiconductor Technology And Science, Vol.15, No.5, October, 2015 Issn(Print) 1598-1657.
 - [7] S. Bardhan, D. A. Menasce, “Queuing Network Models to Predict the Completion Time of the Map Phase of MapReduce Jobs”, In the Proc. of International Computer Measurmenr Group Conference, Las Viga, NV, 3-4th of December 2012, PP. 146-153.
 - [8] D. D. Kouvatso, I. U Awan, “*Entropy Maximization and Open Queueing Networks with Priorities and Blocking*”, Elsevier, Performance Evaluation, 51, 2003,pp.191-227.
 - [9] Y. Li, “*Performance Modelling and Evaluation of Cellular Networks*”, Phd thesis, University of Bradford, UK (2005)
 - [10] D. D., Chowdhury, “*High Speed LAN Technology Handbook*”, Springer, USA (2000).
 - [11] A. M. Law , W. D. Kelton, “*Simulation Modelling and Analysis*”, Mc Grow-Hill , 3rd ed., 2000
 - [12] S. El Kafhali, K. Salah Stochastic,” *Modelling and Analysis of Cloud Computing Data Cente*”, IEEE, 2017.

Combined Image Encryption and Steganography Algorithm in the Spatial Domain

Aya H. S. Abdelgader, Raneem A. Aboughalia, Osama A. S. Alkishriwo *

Department of Electrical and Electronic Eng., College of Eng., University of Tripoli, Libya

DOI: <https://doi.org/10.21467/proceedings.2.16>

* Corresponding author email: alkishriwo@yahoo.com

ABSTRACT

In recent years, steganography has emerged as one of the main research areas in information security. Least significant bit (LSB) steganography is one of the fundamental and conventional spatial domain methods, which is capable of hiding larger secret information in a cover image without noticeable visual distortions. In this paper, a combined algorithm based on LSB steganography and chaotic encryption is proposed. Experimental results show the feasibility of the proposed method. In comparison with existing steganographic spatial domain-based algorithms, the suggested algorithm is shown to have some advantages over existing ones, namely, larger key space and a higher level of security against some existing attacks.

Keywords: Steganography, data hiding, cover image, stego image.

1 Introduction

The growing of digital communication technologies has caused a substantial increment in data transmission. When sensitive information such as bank account numbers is being shared between two communicating parties over a public channel, security of such data becomes necessary. Cryptography and steganography are two important tools for providing security and protecting sensitive information. Cryptography provides features such as confidentiality and integrity of data. For instance, confidentiality is achieved via an encryption algorithm which scrambles/mixes the private information so that it becomes unreadable to any party other than the intended recipient. However, steganography provides data security by hiding the information in a cover medium so that even the existence of a hidden message is not known to an intruder. Secret messages are embedded in cover objects to form stego objects. These stego objects are transmitted through the insecure channel. Cover objects may take the form of any digital image, audio, video and other computer files. Digital images are widely used as cover object of hidden information because of the high level of redundancy in them which is caused by the low sensitivity of the human visual system to details. The success of steganography lies in transmission of stego objects without suspicion [1].

A large number of image steganographic techniques have appeared in the literature, for example [2-7]. These techniques can be classified into two main classes: spatial domain and



© 2018 Copyright held by the author(s). Published by AIJR Publisher in Proceedings of First Conference for Engineering Sciences and Technology (CEST-2018), September 25-27, 2018, vol. 1.

This is an open access article under [Creative Commons Attribution-NonCommercial 4.0 International](https://creativecommons.org/licenses/by-nc/4.0/) (CC BY-NC 4.0) license, which permits any non-commercial use, distribution, adaptation, and reproduction in any medium, as long as the original work is properly cited. ISBN: 978-81-936820-5-0

transform domain techniques. In spatial domain techniques, private message is embedded in the intensity of image pixels directly [2-4]. In transform domain techniques, the private message is embedded in the cover by modifying coefficients in a transform domain such as discrete cosine transform (DCT) and integer discrete wavelet transform [5-6].

Although transform domain based algorithms are more robust to steganalytic attacks, the spatial domain based algorithms such as least significant bit (LSB) algorithms are much simpler and faster. Several versions of the LSBs embedding algorithms have appeared in the literature. However, many steganalysis tools that reveal the insecurity of some LSBs replacement algorithms have been reported. For example, in [7] authors suggested a steganalytic attack that can estimate the length of information embedded in a host image for various LSBs algorithms. Nevertheless, the high embedding capacity and low computational complexity of these algorithms have encouraged researchers to further participate in this area. Chaotic maps are well known for their sensitivity to initial conditions and control parameters. These properties make them suitable for building blocks in the design of many cryptographic and steganographic algorithms [3, 8]. In this paper, we propose a new LSBs spatial domain algorithm that is based on mixing two 2-D chaotic maps. The proposed algorithm encrypts the secret message using mixed chaotic map and uses LSB for data hiding.

The rest of the paper is organized as follow: Section 2 presents the used 2-D chaotic maps. In Section 3, we give a detailed description of the proposed algorithm and a flowchart. In Section 4, simulation results are presented and discussed. The conclusions are given in Section 5.

2 Two Dimensional Chaotic Maps

In the proposed steganography method, we have used a combination of two 2D chaotic systems which are logistic and duffing maps defined in [8, 9] as given in (1) and (2).

$$\begin{aligned}x_{n+1} &= \mu x_n (1 - x_n) \\y_{n+1} &= \lambda y_n (1 - y_n)\end{aligned}\quad (1)$$

where, μ , λ , x and y are the control parameters and state values, respectively. When μ and $\lambda \in [3.57, 4]$, the system is chaotic. The Duffing map depends on the two constants a and b . These are usually set to $a = 2.75$ and $b = 0.2$ to produce chaotic behaviour. It is a discrete version of the Duffing equation.

$$\begin{aligned}z_{n+1} &= w_n \\w_{n+1} &= -b z_n + a w_n - w_{n+1}^3\end{aligned}\quad (2)$$

3 The Proposed Steganographic Algorithm

The steganographic scheme proposed in this article embeds a binary message according to the least significant bit technique as shown in Figure 1. This helps imperceptibility since the more

significant bits of the cover image are not altered. Data embedded is done using the following steps:

- Step 2: Read both of cover image and secret image, the cover image must be equal or larger than the secret image.
- Step 3: use chaotic maps to encrypt secret image.
- Step 3: Select the block size for the encryption algorithm and generate random initial conditions for the chaotic maps.
- Step 4: Using the initial conditions to generate chaotic maps key streams X and Y .
- Step 5: Secret image is divided into blocks of same size ($m \times m$), scrambled using the encryption key stream and recombined into a single image.
- Step 6: Pixel wise XOR operation is done on the scrambled image using the key stream to get the encrypted image.
- Step 7: Extract the pixels of the cover image and encrypted secret image.
- Step 8: Choose first pixel of the cover image and pick first pixel of the encrypted secret image then place it using LSB algorithm, one pixel of the encrypted secret image have 8 bits, using for example 8bpp all this bits will be hidden inside one pixel of the color image.
- Step 10: Repeat step 9 till all the pixels of the encrypted secret image has been embedded.

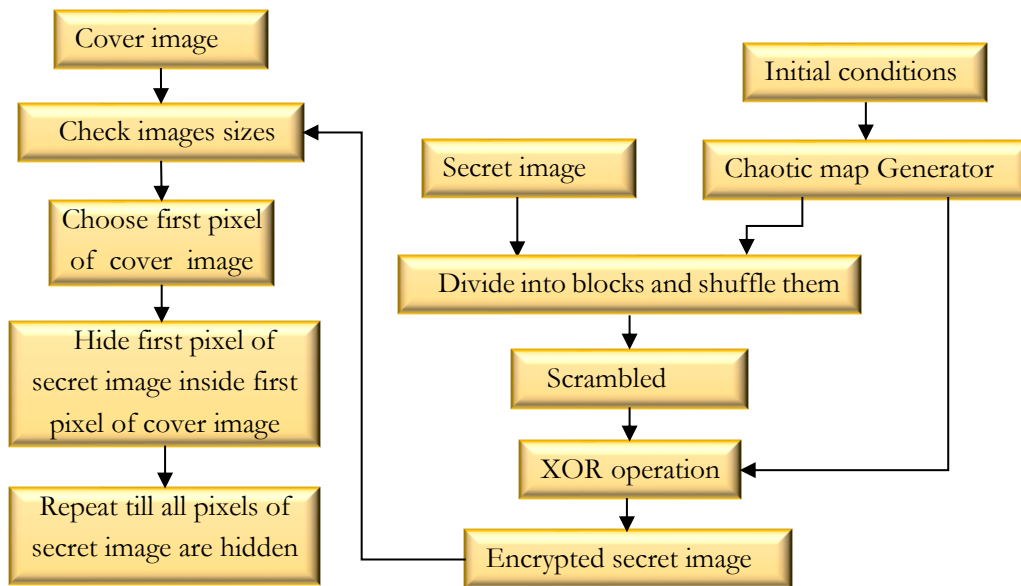


Figure 1: Block diagram of proposed steganography algorithm.

When applying LSB techniques to each byte of a 24 bit image, we can take the binary representation of the hidden data and overwrite the LSB of each byte within the cover image. If the LSB of the pixel value of cover image $C(i, j)$ is equal to the next message bit SM of secret message to be embedded, $C(i, j)$ remain unchanged; if not, set the LSB of $C(i, j)$ to SM .

4 Performance Analysis and Experimental Results

In this section, experimental results are given to demonstrate the performance of the proposed algorithm. Comparative experimental studies are also presented to show the superiority of the proposed algorithm over typical existing ones. Four standard $512 \times 512 \times 3$ colored images, namely, Airplane, Fruits, pool, and girl are used as cover images for hiding sensitive information of length 524288 bit.

4.1 Visual Attack

Visual attacks, regarded as the simplest type of steganalysis, aim at revealing the presence of hidden information through visual inspection by the naked eye. The presented algorithm is designed to be robust against visual attacks. Figure 2 presents a cover image ($512 \times 512 \times 3$ Airplane), a secret-image carrying of size (256×256), an encrypted secret image, and a stego-image carrying an encrypted secret image. A visual inspection of the cover and the stego-image does not reveal any difference between the two images.

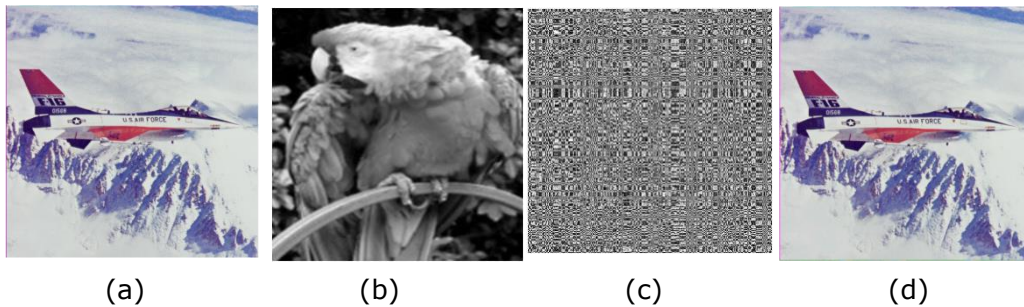


Figure 2: (a) cover image, (b) secret image, (c) encrypted secret image, (d) stego image.

4.2 Imperceptibility and Payload

For data hiding in images, hiding capacity and visual quality of the scheme play important roles. So, increasing hiding capacity adversely affects the visual quality of the stego-image. The embedding rate is the number of bits that can be embedded into one pixel, and it is measured by bits per pixel (bpp). It is known that human visual system cannot detect the distortion of a stego-image, when the peak signal to noise ratio (PSNR) is higher than 30 dB. To compare

between each of 3, 6, 8 bits per pixel, we measure PSNR for all stego-images as shown in Table 1, the highest PSNR values means the stego-image is similar to cover image.

Table 1: PSNR comparison in dB.

bpp	Airplane	Fruits	Pool	Girl
3	53.0	53.6	53.8	53.6
6	48.2	48.5	48.2	48.6
8	41.5	41.8	42.7	41.5

In Table 2, PSNR (dB) is calculated with different payload capacity of 3 bpp on a stego-image using Lena as a cover image, and the results are compared with similar steganography schemes for the same cover image.

Table 2: Comparison of the proposed algorithm to existing work in terms of PSNR (dB).

bpp	Proposed	[4]	[10]	[11]
3	53.0	37.9	37.3	37.8

4.3 Image Histogram

In Figure 3, we present the histograms of the cover image Lena and the resulting stego-image produced by our algorithm with a message of size 3 bpp, 6 bpp, and 8 bpp. It can be observed that the two histograms are very similar. This test shows a comparison between the cover image and the stego image, using the histogram as a visual comparison tool.

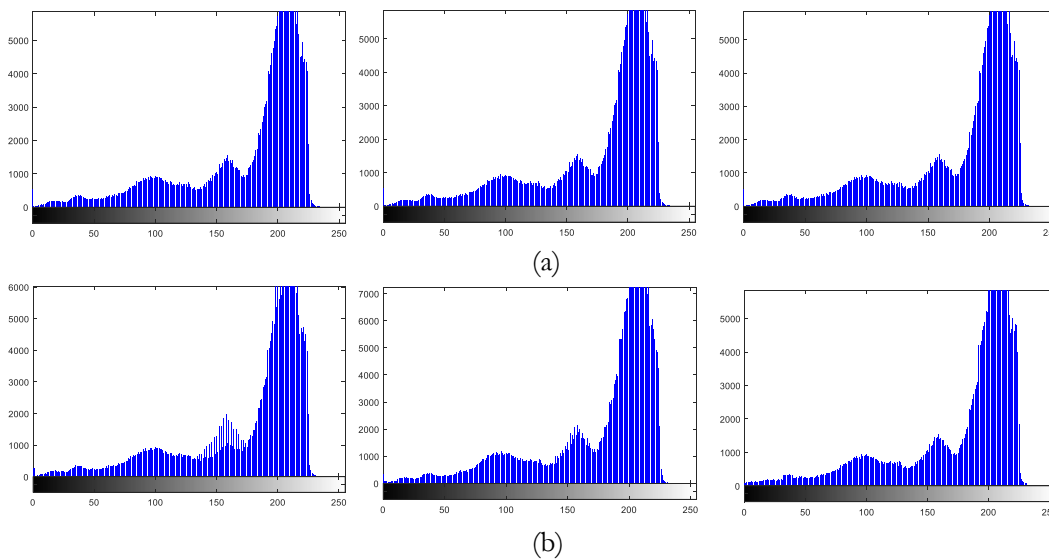


Figure 3: (a) Histogram of cover image, (b) Histogram of stego-image from left to right 3 bpp, 6 bpp, and 8 bpp.

4.4 Key Space Analysis

The key space of an encryption algorithm should be large enough to resist brute-force attacks. In the proposed algorithm, the secret key contains seven real numbers (two control parameters and four initial states). If we assume the computation precision of the computer is 10^{-15} , then the key space is about $10^{90} \approx 2^{299}$. Such a large key space can ensure a high security against brute-force attacks.

5 Conclusions

In this paper, a steganographic algorithm based on two 2-D chaotic maps has been introduced. This algorithm embeds the encrypted sensitive information using chaotic maps into the cover image according to the least significant bit technique. The LSB algorithm effectively allows the embedding of secret information at higher level frequencies, which are not visible to the human eye. The presented simulation results show the resistance of the suggested algorithm against some existing steganalytic attacks. Furthermore, the results show its advantages over some existing algorithms.

References

- [1] A. Kanso and H. S. Oun, "Steganographic algorithm based on a chaotic map," *Commun Nonlinear Sci Numer Simulat*, vol.17, pp. 3287-3302, 2012.
- [2] C. Chan and L. Cheng, "Hiding data in images by simple LSB substitution," *Pattern Recognition*, vol. 37, no. 3, pp. 469-474, 2004
- [3] D. Battikh, S. El Assad, B. Bakhache, O. Deforges, and M. Khalil, "Chaos-based spatial steganography system for Images," *International Journal of Chaotic Computing*, vol. 3, no. 1, pp. 36-44, Jun. 2014.
- [4] G. S. Yadav and A. Ojha, "Chaotic system-based secure data hiding scheme with high embedding capacity," *Computers and Electrical Engineering*, pp. 1-14, 2018.
- [5] R. El Safy, H. Zayed, and A. El Dessouki, "An adaptive steganographic technique based on integer wavelet transform," *In IEEE International conference on networking and media convergence (ICNM 2009)*, pp. 111-117, 2009.
- [6] C. Lin and P. Shiu, "High capacity data hiding scheme for DCT-based images," *J Inf Hiding Multimedia Signal Processing*, vol. 3, no. 1, pp. 220-240, 2010.
- [7] J. Fridrich and M. Goljan, and D. Rui, " Detecting LSB steganography in color and grayscale images," *IEEE Multimedia*, vol. 8, no. 4, pp. 22-28, 2001.
- [8] N. K. Pareek, V. Patidar, and K.K. Sud, "Image encryption using chaotic logistic map," *Image and Vision Computing*, vol. 24, pp. 926-934, 2006.
- [9] Y. Abandal and A. Tiedeu, "Image encryption by chaos mixing," *IET Image Processing*, vol. 10, no. 10, pp. 742-750, 2016.
- [10] Q. Wu, C. Zhu, J. Li, C. Chang, and Z. Wang, "A magic cube based information hiding scheme of large payload," *J. Inf. Secur. Appl.*, vol. 26, pp. 1-7, 2016.
- [11] Z. Eslami and J. Ahmadabadi, "Secret image sharing with authentication-chaining and dynamic embedding," *J. Syst. Softw.*, vol. 84, no. 5, pp. 803-809, 2011.

Experimental Evaluation of the Humans' Health Hazards' Potential Due to Exposure to the Microwaves' Radiations in Garaboulli City-Libya

Abdurahman Alsonosy Altawil*, Mohamed Youssef Ahmed Abou-Hussien,
Abdelbaset Karem Omran, Majdi Masoud Alrajhi

Department of Electrical and Computer Engineering, Faculty of Engineering – Garaboulli,
Elmergib University, Libya.

DOI: <https://doi.org/10.21467/proceedings.2.17>

* Corresponding author email: aaaltawil@elmergib.edu.ly

ABSTRACT

There is a high concern worldwide about the effects of the high level of energy of the transmitted electromagnetic radiations for the wireless communications on the humans' health. So, the purpose of this study is to experimentally evaluate the human health safety related to the exposure to the highest energy of the transmitted microwave radiations (highest radiation risk) at the highest operating frequency 2450 MHz of all operating frequencies (850, 900, 950, 2450 MHz) within the range of 30 MHz-3GHz of the tested AL-MADAR mobile phone base station in the population area for the first time in Garaboulli City - Libya. The specific absorption rate (SAR) value is used as a measure of the rate of absorption of microwave radiation energy in the human tissues on the basis of exposing to the highest radiation risk which is considered as the worst case scenario. The SAR values are evaluated at predetermined distances (5, 40, 80, 120 and 160 meters) by using MATLAB program. The power density and the electric field measurements of the microwaves radiation of the antenna of the selected of AL-MADAR mobile phone base station, were experimentally measured by utilizing the spectrum analyzer devise (Spectrum HF-6065), in addition to the mass density and the medium conductivity values for the investigated human tissues (eye (Sclera), brain (Grey Matter), nerve and blood) at 2450 MHz frequency. The numerical results indicate that the highest SAR value is $205.4 * 10^{-6} W/kg$ of the human blood at the shortest distance (5 meters). This SAR value is significantly lower than the international recommended safe radiation level standards. So, for the first time, these results show that the microwave equipments which use AL-MADAR network in the Garaboulli city-Libya can be considered safe on the humans' health.

Keywords: Microwaves Radiations, Specific Absorption Rate (SAR), MATLAB Program, Health Hazards & Garaboulli City-Libya.



© 2018 Copyright held by the author(s). Published by AIJR Publisher in Proceedings of First Conference for Engineering Sciences and Technology (CEST-2018), September 25-27, 2018, vol. 1.

This is an open access article under [Creative Commons Attribution-NonCommercial 4.0 International](https://creativecommons.org/licenses/by-nc/4.0/) (CC BY-NC 4.0) license, which permits any non-commercial use, distribution, adaptation, and reproduction in any medium, as long as the original work is properly cited. ISBN: 978-81-936820-5-0

1 Introduction

People nowadays commonly use several applications of the microwave communication technology which are constitutively emitting microwaves radiation such as modern mobile telephone services (text messaging ; messaging multi services (MMS) ; email ; internet access ; short range communications (infrared , Bluetooth) ; business application ; gaming and photography) , which use the cellular wireless network architecture ; whereas it's work depends on mobile phone base stations (these are also known as base transceiver stations or telecommunication structures). These telecommunication structures are multi-channel two ways radio for transmitting and receiving signals, and have antennas which produce microwaves radiation whereas they are mounted on transmission towers that need to be of at a certain height order to have a wider coverage [1]. The microwaves radiation has the potential to interact with the human biological system and could cause hazards on people's health. The microwaves radiation of all frequencies between 30MHz to 3GHz is classified as non-ionizing and can potentially lead to irreparable damages in the exposed human biological tissues [2].

On the basis of the exposure to the highest microwaves radiations (EMRs) energy (the highest radiation risk which is considered as the worst case scenario); by using the SAR measure in different human tissues, for the first time in Garaboulli City-Libya, this study is designed and conducted aiming to experimentally assess the potential radiation risks on the human health related to the exposure to the highest microwave radiation energy at the highest operating frequency 2450 MHz of all operating frequencies (850, 900, 950, 2450 MHz) which is included in the internationally recommended operating very high (VHF) and ultra high frequencies (UHF) range of 30 MHz to 3 GHz according to the stratification specified by International Telecommunication Union (ITU).

2 Materials and Methods

Firstly, due to the availability of many different designs of the mobile phone base stations that vary widely in their power, characteristics, and their potential for exposing people to the microwaves radiation [1] and secondly, based on the highest radiation risk, which is fulfilled requirement by the highest experimental values of each of the power density and the electrical field received at the population area of the tested site, the MATLAB program is used to experimentally evaluate the exposure to the highest microwaves radiation energy at the highest operating frequency 2450 MHz of all operating frequencies (850, 900, 950, 2450 MHz) , within the operating VHF and UHF range of 30 MHz to 3 GHz, of the antenna of the selected AL-MADAR mobile phone base station, which is located near Garaboulli City's bridge. This selected mobile base station uses modern mobile telephone services, and its antenna's radiation is received by the population area in tested site (Garaboli city centre).vThe selection of the highest operating frequency 2450 MHz of all operating frequencies of the tested mobile

base station was done with full consideration of the direct relationship between the calculated SAR values and the different operating frequencies.

The calculation of the SAR value which is used as the evaluating measure tool at pre determined distances (5, 40, 80, 120 and 160 meters) , was done using the correspondent information of the power density and the electric field of each investigated human tissues. The calculated SAR value is measured in watt per kilogram (W/kg).

The experimental measurements of the highest radiation energy at each earlier mentioned different distances, were done by utilizing the spectrum analyzer devise (Spectrum HF-6065), in addition to the medium conductivity (σ) values of each of the investigated human tissue [eye (Sclera), Brain(Grey Matter), nerve and blood] that have the highest values at the highest operating frequency 2450 MHz of all operating frequencies (850, 900, 950 and 2450 MHz) which is included in the internationally recommended operating VHF and UHF range of 30 MHz to 3 GHz according to the stratification published by ITU[3].

3 Theory and Calculation

This study is conducted to experimentally assess the possible health hazards on the humans due to the exposure to the highest microwaves radiation energy at the highest operating frequency 2450 MHz of all operating frequencies (850, 900, 950 and 2450 MHz), which is emitted by the selected AL-MADAR mobile phone base station that is located in Garaboulli City-Libya for the first time on the basis of considering the exposure to the highest radiation risk in the population area at the tested site; by using the SAR measure in each investigated human tissue [3, 4, 5].

3.1 Mathematical Expressions and Symbols

The MATLAB program is used to evaluate the SAR values, by applying the equation number (3) which is obtained from the equations number (1) and (2) as following:

For a sinusoidal steady state electromagnetic field, the SAR value is calculated as given in equation (1), [5];

$$SAR = (\sigma + \omega \epsilon_0 \epsilon'') \frac{E_{rms}^2}{\rho} \dots \dots \dots (1)$$

And by using the power density equation through applying the following formula [6];

$$P = \omega \epsilon_0 \epsilon'' E_{rms}^2 \dots \dots \dots (2)$$

Accordingly, the equation (1) can be expressed as following;

$$SAR = \frac{(\sigma E_{rms}^2 + P)}{\rho} \dots \dots \dots (3)$$

Where:

SAR: The evaluated specific absorption rate[watt/kilogams(W/kg)] .

E_{rms} : The measured value of the electric field[Volt/meter(V/m)] .

p : The measured value of the power density[watt/square meters(w/m^2)] .

σ : The medium conductivity[Siemen/meter(S/m)].

ρ : The mass density[Kilograms/Cubic meters(kg/m^3)] .

ϵ'' : Out of phase loss (unit less).

ϵ_0 : The vacuum permittivity[Farad/meter (F/m)].

ω : The angular frequency (radians / second).

The ρ values and σ values for each of the understudied human tissues [Eye (Sclera), Brain (Grey Matter), nerve and blood) at 2450 MHz frequency, are given in Table 1.

Table 1: Clarified the difference values of Mass density (ρ), and the medium conductivity (σ) for different parts of human body at 2450MHz frequency [3, 4].

Human Tissues	Mass Density (ρ) (kg/m^3)	Medium Conductivity(σ) (S/m)
Nerve	1075	1.0886
Brain (Grey Matter)	1045	1.8077
Eye (Sclera)	1032	2.0332
Blood	1050	2.5448

4 Results and Discussion

Table 2 shows that the maximum electrical field (V/m) and the maximum power density ($\mu W/m^2$) were detected at 5 meters distance, however the minimum electrical field (V/m) and the minimum power density ($\mu W/m^2$) were detected at 160 meters distance. It also demonstrates the calculated SAR values in the tested human tissues [Nerve, Brain (Grey Matter), Eye (Sclera), Blood] at the predetermined different distances at which all the study variables were measured.

It has been well noted in Table 1 that the Blood which has the maximum SAR value, has also the maximum Medium Conductivity(σ) of 2.5448 S/m value and the nerve which has the minimum Medium Conductivity (σ) of 1.0886 S/m value, has also the minimum SAR value.

Table 2 shows also the maximum SAR value of $205.4 \times 10^{-6} W/kg$ was measured at 5 meters distance in the blood and the minimum SAR value of $5.7 \times 10^{-6} W/kg$ was measured in the Nerve biological tissue at the distance of 160 meters.

Table 2: The measures power density, electric field values and the calculated SAR values of the investigated human tissues at 2450 MHz frequency at different distances. (*GM=Grey Matter)

Distance (m)	Electric field (V/m)	Power density ($\mu W/m^2$)	SAR ($\times 10^{-3} W/kg$)			
			Human tissue			
			Eye (Sclera)	Brain (GM*)	Nerve	Blood
5	0.291	221.2	0.1670	0.1467	0.0860	0.2054
40	0.281	210.2	0.1558	0.1368	0.0802	0.1916
80	0.192	85.94	0.0727	0.0639	0.0374	0.0894
120	0.144	55.44	0.0409	0.0359	0.0211	0.0503
160	0.075	15.21	0.0111	0.0097	0.0057	0.0136

The results given above indicate that the highest SAR value is $205.4 \times 10^{-6} W/kg$ of the blood human tissue that has been calculated at the shortest distance (5 meters) and at 2450 MHz frequency. Comparatively, this SAR's value is much lower than the international recommended safe radiation level standard's values. These standards are regulated by world authoritative bodies include the following with their correspondent safe SAR limits; $1.6 W/kg$ during 30 minutes according to the Federal Communications Commission (FCC) and $2 W/kg$ during 6 minutes according to the European recommendations.

It is important to note that the average time exposure of 30 minutes according to FCC and 6 minutes according to the European recommendations have a significance only in the cases that are exposed to the power or the electromagnetic fields which are higher than the allowed ones according to the related international standards. However, in the inhabitant residential populated areas similar to the tested site in this study, the FCC recommends not to apply the average time exposure parameter, so, the calculated SAR values which do not exceed the allowed ones according to the international standards, are considered as the allowable values to a continuous exposure for indefinite time period [7].

5 Conclusion

This study shows clearly that on the basis of the exposure to the highest microwaves radiation energy (the highest radiation risk which is considered as the worst case scenario) in the

population area at the tested site and by considering the direct relationship between the calculated SAR values and the different operating frequencies, the obtained practical results prove that microwaves radiation for all operating frequencies that are emitted by AL-MADAR wireless communication system networks in Garaboulli City-Libya can be considered safe to the people's health.

Acknowledgment

The authors are very grateful and highly thankful to all members of the developing and the investigation office in AL-MADAR Company for providing the spectrum analyzer devise (Spectrum HF-6065) and their extensive professional indispensable assistance throughout the study.

References

- [1] Girish Kumar , " *Cell Tower Radiation* ", Electrical Engineering Department ,IIT Bombay, Poway, Mumai - 400-076, December 2010. Access online on 28th August 2018 at <https://www.scribd.com/doc/44736879/Cell-Tower-Radiation-Report-sent-to-DOT-Department-of-Telecommunications>
- [2] "Exposure from mobile phones, base stations and wireless networks" A statement by the Nordic radiation safety authorities, 17 .12. 2013. Access online on 28th August 2018 at <https://www.gr.is/wp-content/media/2013/12/absolute-final-version-EMF-statement-logo.pdf>
- [3] Website of the Italian National Research Council-Institute for Applied Physics "Nello Carrara"-Florence (Italy)-2018. Access online on 28th August 2018 at <http://niremf.ifac.cnr.it/tissprop/htmlclie/htmlclie.php>
- [4] Website of the Foundation for Research information Technologies in Society (IT²IS)-Zurich Switzerland. Tissue properties→Database→Density. Access online on 28th August 2018 at <https://www.itis.ethz.ch/virtual-population/tissue-properties/database/density/>
- [5] Riadh W. Y. Habash, *Electromagnetic Fields and Radiation: Human Bioeffects and Safety*, New York, NY: Marcel Dekker, 2001. ISBN 0-8247-0677-3. Access online on 28th August 2018 at https://books.google.com.mt/books?hl=en&lr=&id=NEXgsO_y9ssC&oi=fnd&pg=PA1&ots=NgKtFf4vZR&sig=6imurgf2Ww1aGkmlif_tc3ucbaY&redir_esc=y#v=onepage&q&f=false
- [6] B.M.Tareev, "Electrical and Radio Engineering Materials-Dielectric Loss"- *MIR Publishers*, Page – 154-169. Access online on 28th August 2018 at [http://www.ursi.org/proceedings/procGA05/pdf/KP.26\(01122\).pdf](http://www.ursi.org/proceedings/procGA05/pdf/KP.26(01122).pdf)
- [7] FCC OET Bulletin No.65, 1997, Evaluating Compliance with FCC Specified Guidelines for Human Exposure to Radiofrequency Radiation. Access online on 28th August 2018 at www.fcc.gov/oet/rfsafety

Capability of Modified SIFT to Match Stereo Imagery System

Omar Abusaeeda^{1*}, Salah Naas², Nasar Aldian Shashoa³

¹ Department of Computer Networks, Faculty of Information Technology,
Azzaytuna University, Libya

^{2,3} Department of Electrical & Communication Engineering, Faculty of Engineering,
Azzaytuna University, Libya

DOI: <https://doi.org/10.21467/proceedings.2.18>

* Corresponding author email: abossada1@gmail.com

ABSTRACT

This paper presents an improved version of SIFT method for extracting invariant features from images that can be used to solve the correspondence problem between different views of an object or scene in an image. Scale invariant feature transform (SIFT) has recently gained substantial attention in the computer vision community to address the problem. Corresponding features in sequential pairs of images, at various different angular separations, were identified by applying a scale invariant feature transform (SIFT). Due to limitation in the standard SIFT; some of matches are considered false matches. Epipolar-line and disparity window criteria were introduced to enhance the performance of SIFT. Experiments revealed that considerable number of unfaithful matches were removed when new criteria are introduced. Future work will focus on improving the SIFT technique; to rectify the negative matches in order to obtain better matching result.

Keywords: SIFT, Image matching, positive matches.

1 Introduction

A typical image matching method begins with detecting points of interest, then selects a region around each point, and finally associates a descriptor with each region. Correspondences between two images may then be established by matching the descriptors of both images. SIFT is proposed by David Lowe in 2004 [1] to extract features of interest from images that can be used for reliable matching between different views of an object. The features are invariant to image scaling and rotation and partially invariant to change in 3D viewpoint and additional noise. Over recent years, SIFT has played a significant role in various computing applications such as object recognition, 3D modelling and video tracking.

Feature matching can be defined as the process of matching corresponding points between two or more images of the same scene. Feature based methods match special features of two images, such as corners or edges to produce a sparse disparity map [2,3]. This method matches



more features, rather than matching textured regions in the two images [4,5]. Feature based methods provide more precise positioning for the matching results and are more reliable than correlation-based matching when good image features can be extracted from the scene [6]. Feature based methods are widely used in wide-base stereo image matching [7,8]. Correspondences between two images is established by matching the descriptors of both images. Numerous variations exist on the computation of interest points matching. It can be traced back to the work of stereo matching using a corner detector [9,10], which was later improved by Harris and Stephens [11,12]. Consequently, the Harris corner detector has since been extensively used for various other image-matching tasks. The approach was presently expanded to match Harris corners over a large image range by using a correlation window around each corner to select likely matches. Moreover, Harris corners were used to select interest points, but rather than matching with a correlation window, they used a rotationally invariant descriptor of the local image region. This allowed the matching of features under arbitrary orientation change between the two images. Additionally, it was demonstrated that multiple feature matches could accomplish general recognition under occlusion and clutter by identifying consistent clusters of matched features [1]. The local feature approach was extended to achieve scale invariance and more distinctive features whilst being less sensitive to local image distortions such as 3D viewpoint change [13]. In recent times, there has been an inspiring body of work on extending local features matching. Most recently, there has been an impressive effort on expanding the approach of local feature descriptor [14,15]. While this method is not completely affine invariant, a different approach is used in which the local descriptor allows relative feature positions to shift extensively with only small changes in the descriptor [16]. This approach produces descriptors, which are consistently matched across a substantial range of affine distortion. It also makes the features more robust against changes in 3D viewpoint. This approach not only has the advantages of extracting more efficient feature, but it also able to identify larger numbers of features. Furthermore, Principal Components Analysis SIFT (PCA-SIFT) was introduced. This technique accepts the same input as the standard SIFT descriptor. The advantage of this approach is the size of the descriptor. It produces a more compact descriptor in comparison to standard SIFT. On the other hand, it tends to blur the edges around the objects [17]. Another local feature descriptor named, Speeded-Up Robust Features (SURF) was proposed [18]. SURF is mainly designed for real time application where the speed is the main concern. SURF performance is similar to SIFT but it is not invariant to rotation and illumination changes [5]. The choice of methods is informed by the computer vision application under consideration. It has been demonstrated recently that features identified by SIFT are highly distinctive and invariant to image scales and rotations, and partially invariant to a change in illumination [19]. It is indicated that using multiple images might help to solve some problems associated with stereo matching. However, more information may also carry the risk of increased uncertainties. Repeating features is

a common problem encountered by stereo matching algorithms that apply feature-based method for visible light images.

1.1 Repeating Features

The images in Figure 1 present a good example of repeated features, which are commonly found in stereo pairs, where Left view and Right view are the images obtained at different views. To study the effect of local similarity, consider the repeating features Object 1 and Object 2, illustrated in the two views in Figure 1.

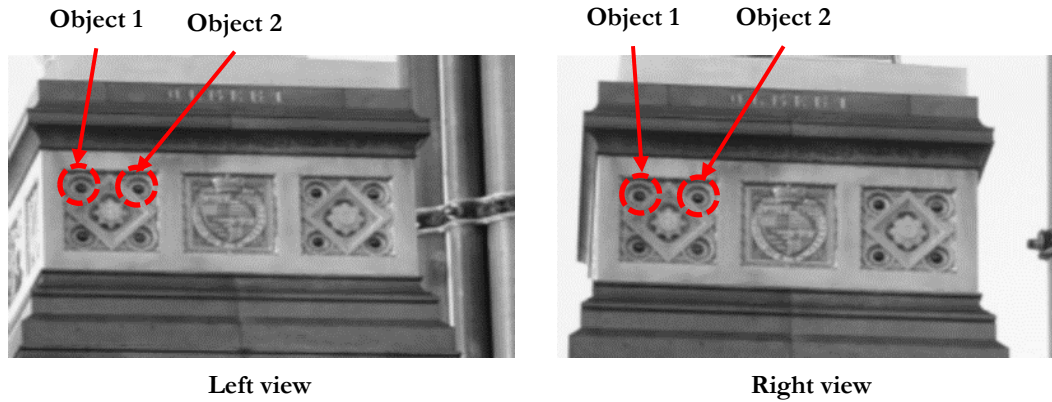


Figure 1: Repeating features extracted from two different views

By applying the stereo matching criterion on this pair of images, on one hand, and as these features are obvious and strong, the opportunity to match them is significant. On the other hand, unless special care is taken, Object 1 in the Left view would have an equal opportunity to match with Object 1, Object 2 or other similar features in the Right view. As a result, an error in matching could occur. This finding is exacerbated when considering overlapping structures commonly found in cluttered visible light images.

1.2 Keypoint Matching

The SIFT algorithm adopts the fast nearest-neighbour method to identify the best match for a particular feature from a database of features. Since the keypoint is described by its descriptor, the nearest neighbour is defined as the keypoint with minimum Euclidean distance for the invariant descriptor vector [20]. Nevertheless, numerous features from an image will not match correctly in the derived keypoints database for the reason that they were not detected in the training images. Lowe [1] mentioned to discard all matches in which the distance ratio between closest neighbour to that of the second closest neighbour is greater than 0.8. This ratio removes 90% of the false matches on the other hand it discards less than 5% of the correct matches. Even though 90% of false matched are discarded, the remaining 10% of false matches might be a problematic for a particular image application. To maximise the potential applicability of SIFT, additional boundary conditions of search for corresponding are proposed. These added criteria will tighten the support of the standard SIFT.

2 Materials and Methods

In our work, additional bounding criteria of a disparity window and an epipolar line constraint are employed. The former is defined as the intersection of the epipolar plane with the image plane, while the latter concerns the nominally zero vertical disparity. i.e. the epipolar line is along the image y-axis (vertical in the display), while the disparity window is along the image x-axis (horizontal in the display). Both criteria are shown in Figure 2.

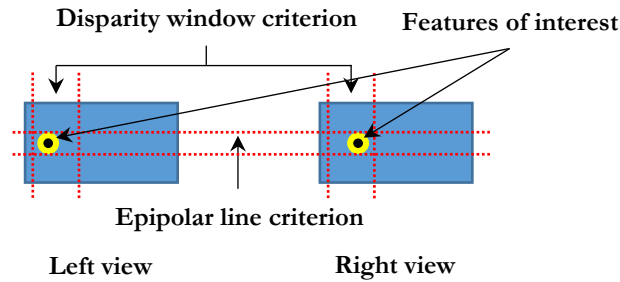


Figure 2: Two perspective views and their corresponding features of interest

Taking into account various practical fluctuations a tolerance of ± 1 pixel deviation in the y-axis coordinate position (vertical in the display) is employed to accommodate a practical epipolar line criterion [19]. To further limit the search space a disparity window criterion is introduced. The window size in pixels is determined by the angle separation between views.

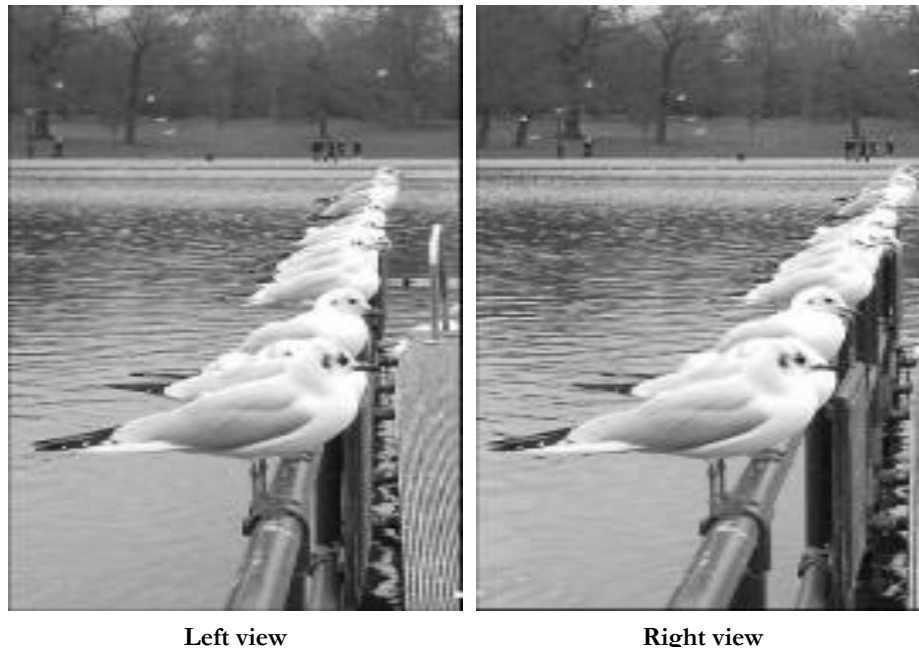


Figure 3: Corresponding pair of images employed in this study

It should be noted that for comparative purposes the new criteria are applied to corresponding pairs that have already satisfied the standard SIFT criteria. Care was taken when stereo images were selected to ensure overlapping. Repeating features were also taken into consideration to ensure that the standard SIFT is supported by the new added criteria. An example of stereo image are shown in Figure 3.

3 Results and Discussion

Matched features are categorised into two groups; negative and positive matches. The positive matches are the matches that satisfy the standard SIFT, epipolar and disparity window criteria while the negative matches satisfy the standard SIFT criterion but violate either the epipolar line or disparity window criteria. Figures 4 represents the positive matches indicated by horizontal green colour lines connecting the corresponding pairs, while the negative or erroneous matches are presented in Figure 5 and are shown as red colour lines.

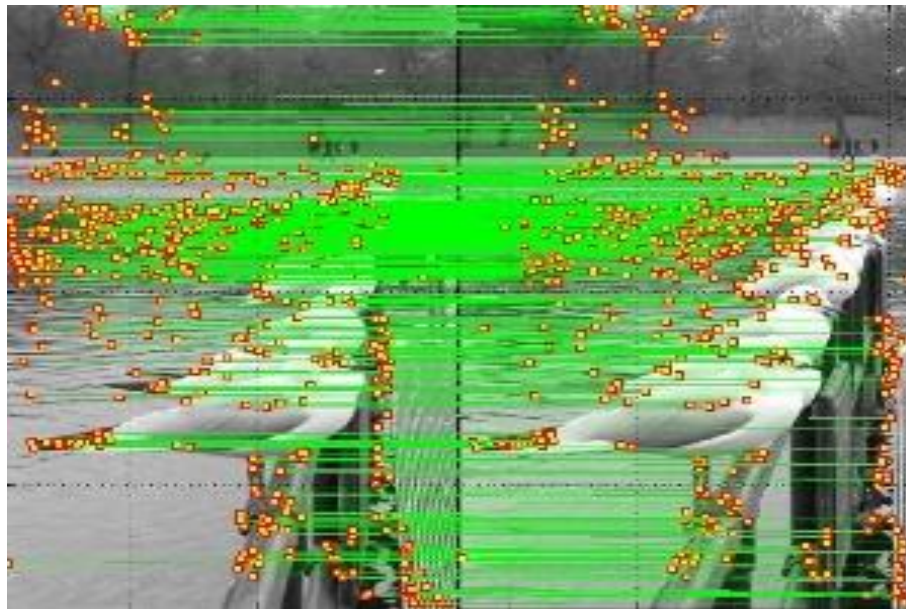


Figure 4: Proposed *matching criteria results positive matches only*

The application of the criteria tighten the support of standard SIFT. The increase in negative matches (and the corresponding decrement in positive matches) is the expected consequence of logically „ANDing“ the criteria. It is important to note that only the matches in Figure 4 (shown as green bars) which meet standard SIFT, epipolar line and disparity window criteria are considered as positive matches. The matching procedure described above has been repeated for 180 stereo pairs and the numbers of positive and negative matches for each matching criterion are presented in Figure 6.

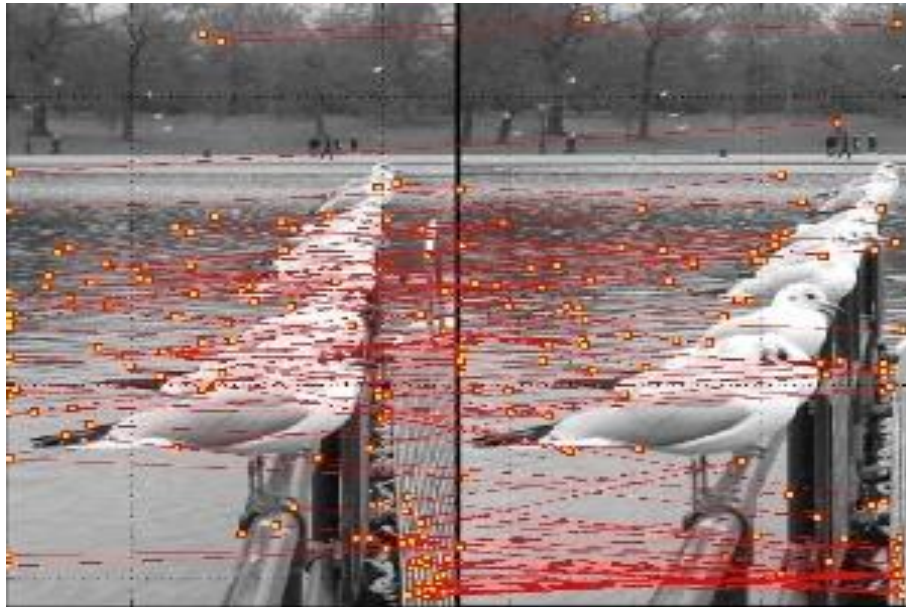


Figure 5: Proposed *matching criteria results negative matches only*

The bar chart in Figure 6 has been plotted to demonstrate the effectiveness of new criteria in rejecting incorrect matches. The first bar in black represents the average number of matches generated by the 180 stereo pairs, which corresponds to matches that have met the standard SIFT criteria.

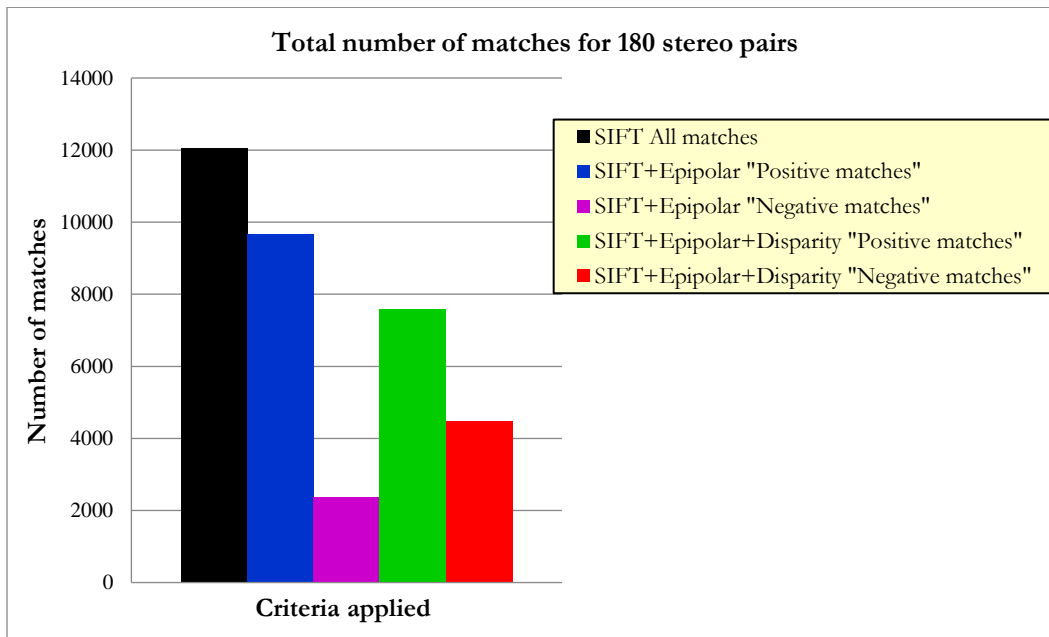


Figure 6: Total *number of matches for 180 stereo pairs*

Similarly, matches that have satisfied the epipolar line criterion, matches that have failed the epipolar line criterion, matches that have fulfilled the epipolar and disparity window criteria, and matches that have violated either or both new added criteria have been computed and plotted sequentially in the bar chart revealed in Figure 6. The proposed criteria have demonstrated that they can remove 37.2% of unfaithful matches i.e. 19.8% are attributed to the epipolar line criterion and a further 17.4% attributed to the disparity window criterion.

4 Conclusions and Future Work

The material presented in this paper assessed the performance of optimized SIFT when dealing with stereo pairs. The potential of SIFT to locate correspondences in stereo pairs is established and quantified for 180 stereo pairs. The performance of SIFT is significantly enhanced by applying two additional criteria namely; a disparity window and an epipolar line constraint. Each pair of images is analysed twice to accommodate either perspective view as the reference view. Experiments revealed that around 37% of unfaithful matches were removed. The appropriateness of the additional criteria is supported by the matching results organised in Figure 4, 5 and 6.

Solving the correspondences problem is an ill posed problem in computer vision applications. It has been established that performance of optimized SIFT significantly reduces when presented with spatially simple images. Therefore, a rigorous analysis of the SIFT parameters to increase the robustness and density of keypoints would enhance the fidelity the matching result. Also, it might be worthwhile to combine the optimized SIFT algorithm with other feature matching techniques so more keypoints are generated.

References

- [1] D.G. Lowe, "Distinctive image features from scale-invariant keypoints," *International Journal of Computer Vision*, vol. 60, no. 2, pp. 91-110, 2004.
- [2] Y. Chen and J. Z. Wang, "A region-based fuzzy feature matching approach to content-based image retrieval," *Pattern Analysis and Machine Intelligence, IEEE Transactions on*, vol. 24, pp. 1252-1267, 2002.
- [3] M. Brown, R. Szeliski and S. Winder, "Multi-image matching using multi-scale oriented patches," in *Computer Vision and Pattern Recognition, IEEE Computer Society Conference on*, vol. 1, pp. 510-517, 2005.
- [4] D. Bepalov, W. C. Regli and A. Shokoufandeh, "Local feature extraction and matching partial objects," *Comput. - Aided Des.*, vol. 38, pp. 1020-1037, 2006.
- [5] A. Baumberg, "Reliable feature matching across widely separated views," in *IEEE Computer Society Conference on Computer Vision and Pattern Recognition*, 2000.
- [6] K. Mikolajczyk and C. Schmid, "An affine invariant interest point detector," in *European Conference on Computer Vision*, vol. 4, pp. 128-142, 2002.
- [7] A. Klaus, M. Sormann and K. Karner, "Segment-based stereo matching using belief propagation and a self-adapting dissimilarity measure," *International Conference on Pattern Recognition*, vol. 18, pp. 15-18, 2006.
- [8] J. Matas, O. Chum, M. Urban and T. Pajdla, "Robust wide-baseline stereo from maximally stable extremal regions," *Image Vision Comput*, vol. 22, pp. 761-767, 2004.
- [9] K. Mikolajczyk and C. Schmid, "A performance evaluation of local descriptors," *IEEE Trans. Pattern Anal. Mach. Intell.*, pp. 1615-1630, 2005.
- [10] C. B. Perez and G. Olague, "Learning invariant region descriptor operators with genetic programming and the f-measure," in *International Conference on Pattern Recognition*, 2008, .
- [11] C. Harris, "Geometry from visual motion," 1993.
- [12] C. Harris and M. Stephens, "A combined corner and edge detector," in *Alvey Vision Conference*, pp. 50, 1988.
- [13] D. G. Lowe, "Object recognition from local scale-invariant features," in *Iccv*, pp. 1150, 1999.

-
- [14] P. Scovanner, S. Ali and M. Shah, "A 3-dimensional sift descriptor and its application to action recognition," in *Proceedings of the 15th International Conference on Multimedia*, pp. 357-360, 2007.
 - [15] P. Moreno, A. Bernardino and J. Santos-Victor, "Improving the SIFT descriptor with smooth derivative filters," *Pattern Recog. Lett.*, vol. 30, pp. 18-26, 2009.
 - [16] Z. Qi, R. Ting, F. Husheng and Z. Jinlin, "Particle Filter Object Tracking Based on Harris-SIFT Feature Matching," *Procedia Engineering*, vol. 29, pp. 924-929, 2012.
 - [17] Y. Ke and R. Sukthankar, "PCA-SIFT: A more distinctive representation for local image descriptors," in *IEEE Computer Society Conference on Computer Vision and Pattern Recognition*, 2004, .
 - [18] H. Bay, A. Ess, T. Tuytelaars and L. Van Gool, "Speeded-up robust features (SURF)," *Comput. Vision Image Understanding*, vol. 110, pp. 346-359, 2008.
 - [19] Z. Feng, B. Yang, Y. Chen, Y. Zheng and T. Xu, "Features extraction from hand images based on new detection operators," *Pattern Recognit*, 2010.
 - [20] A. Fusiello and L. Irsara, "Quasi-euclidean uncalibrated epipolar rectification," in *International Conference on Pattern Recognition (ICPR)*, 2008.

Track 2

Electrical and Electronics Engineering



© 2018 Copyright held by the author(s). Published by AIJR Publisher in Proceedings of First Conference for Engineering Sciences and Technology (CEST-2018), September 25-27, 2018, vol. 1.
This is an open access article under [Creative Commons Attribution-NonCommercial 4.0 International](https://creativecommons.org/licenses/by-nc/4.0/) (CC BY-NC 4.0) license, which permits any non-commercial use, distribution, adaptation, and reproduction in any medium, as long as the original work is properly cited. ISBN: 978-81-936820-5-0

Micro gas turbine simulation and control

Ibrahim Ahmed El-Sharif¹, Mahmoud Mansour El- Fandi²

¹Instrument department, General electrical company of Libya, GECOL, Khoms, Libya

²Electrical and electronic engineer, Faculty of engineering, Tripoli-university, Tripoli, Libya

DOI: <https://doi.org/10.21467/proceedings.2.19>

* Corresponding author email: Sssharif2004@yahoo.com

ABSTRACT

Gas turbines are widely used in power generation plants due to their compactness, fast start-stop sequences, and their applications, and...etc. A split shaft micro-turbine mechanical model is used. Three main controllers for three different loops have been designed and discussed. MATLAB/Simulink environment is used to represent the mechanical model for Micro-turbine split shaft. A speed PID controller, exhaust temperature PI controller, and mechanical & electrical power PID controller all have been designed with MATLAB/Simulink. Compensators have also been used instead of PI and PID controllers which had been used for three systems. A comparison between PI, PID controllers, and its corresponding compensator have been done through this research. At last a supervisory controller for three systems has been done. A MIMO system - Multi-Input Multi-Output -will be reduced to a SISO system - Single-Input Single-Output - during system design.

Keywords: MGT: Micro-Gas turbine, LVG: Least Value Gate, MIMO: Multi Input Multi Output

1 Introduction

Single-shaft MGT models are designed to operate at high speeds (some in excess of 100,000 revolutions per minute [RPM]) and generate electric power as high-frequency alternating current (AC). The generator output is rectified to direct current (DC) and then inverted to 60 hertz (Hz) AC for commercial use in the United States, or 50 Hz for use in countries with a 50 Hz supply. Two-shaft MGT micro-gas turbines have a turbine-driven compressor on one shaft and a separated “free” power turbine on a second shaft to power the generator. (In conventional gas turbines, this arrangement is generally used in mechanical drive service, as the free power turbine, generally via a gear box, then runs other turbo-machinery, such as compressors or pumps.) With the expansion pressure ratio split between two turbines, the power turbine on a two-shaft machine can be designed to run at lower speed with high efficiency. Split-shaft design uses a power turbine rotating at 3000 rpm and a conventional generator connected via a gearbox for speed multiplication [1]. The figure (1) illustrate a split-shaft micro-turbine as was have been chosen in this paper which consists of two main turbines



© 2018 Copyright held by the author(s). Published by AIJR Publisher in Proceedings of First Conference for Engineering Sciences and Technology (CEST-2018), September 25-27, 2018, vol. 1.

This is an open access article under [Creative Commons Attribution-NonCommercial 4.0 International](https://creativecommons.org/licenses/by-nc/4.0/) (CC BY-NC 4.0) license, which permits any non-commercial use, distribution, adaptation, and reproduction in any medium, as long as the original work is properly cited. ISBN: 978-81-936820-5-0

one for compressor driving and the other for driving conventional generator which connected with a gearbox [2]

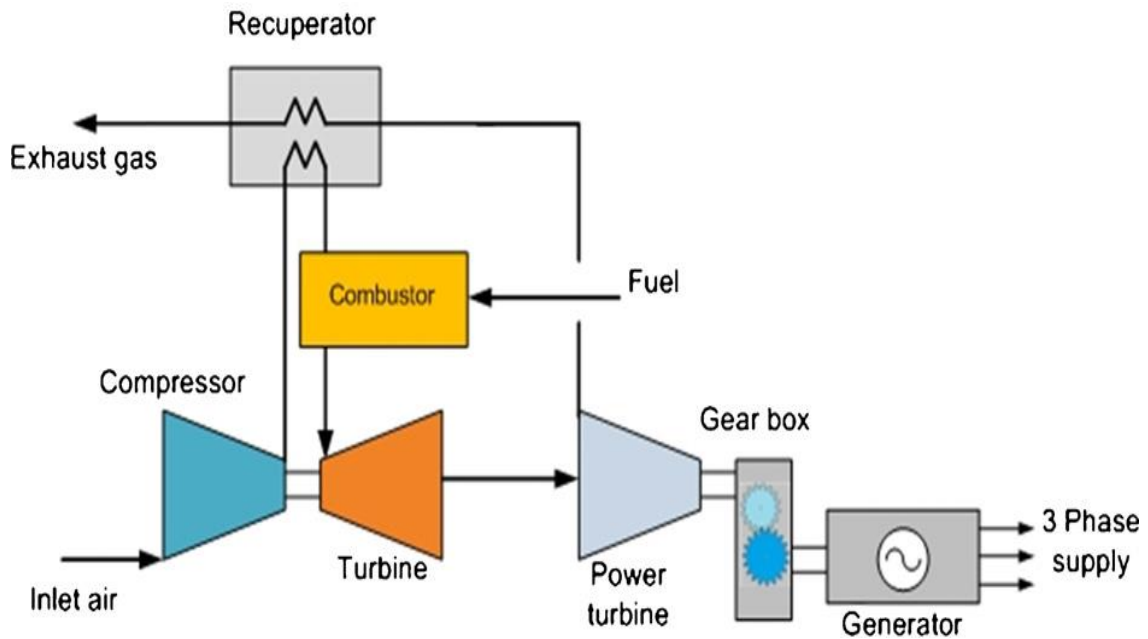


Figure1: Two-shaft MGT via a gearbox to generator

2 MIMO MGT Model with PID controller:

There are a large literature on the modelling of gas turbines, with varying level of complexity depending on the intended application. The concept of gas turbine system presented in this section is based on the paper presented by Rowen [3]. He proposed a single-shaft design, generator driven gas turbine model which includes speed control, temperature control and fuel system. This model was successfully adopted by the several authors for gas turbine simulations as well as for micro-turbine simulations with smaller time constants [4]. The three control functions of the micro-turbine are: speed control acting under part load conditions, temperature control acting as an upper output power limit, and acceleration control to prevent over speeding. The output of these control function blocks with (P_c) mechanical power control are all inserted to a least value gate (LVG), whose output is the lowest of the four inputs and results in the least amount of fuel to the compressor-turbine as shown in figure (2). This figure shows the per-unit presentation of a micro-turbine, along with its control systems [4]. Each subsystem of the micro-turbine is discussed in the following subsections.

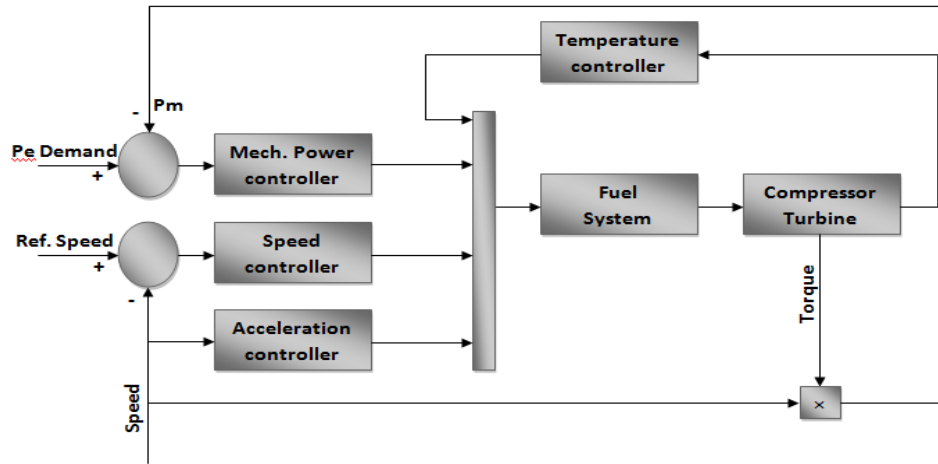


Figure 2: Micro-turbine system and its controllers

3 Speed and acceleration loop controllers.

The speed control operates on the speed error formed between a reference (one per-unit) speed and the MTG system rotor speed. It is the primary means of control for the micro-turbine under part load conditions. Speed control is usually modelled by using a lead-lag transfer function, or by a PID controller [4]. A PID controller has been used to present the speed controller, as shown in figure (3). In this figure the PID controller which has been used is maintained by changing the P,I and D parameters of the controller to reach the acceptable response on output using trial and error method as will discuss later. Acceleration control is used primarily during turbine start-up to limit the rate of the rotor acceleration prior to reaching operating speed. If the operating speed of the system is close to its rated speed, the acceleration control could be eliminated in the modelling, which is the case in this study.

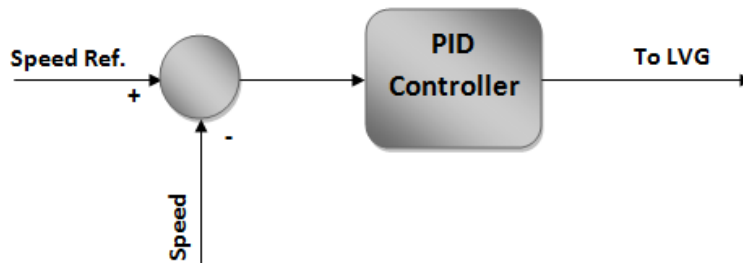


Figure3: PID speed controller

4 Fuel system.

The fuel system consists of the fuel valve and actuator. The fuel flow comes out from the fuel system results from the inertia of the fuel system actuator and the valve positioner [3]

The valve positioner transfer function is:

$$E_1 = \frac{K_{vv}}{T_v s + c} F_d$$

and the fuel system actuator transfer function is:

$$W_f = \frac{K_f}{T_f s + c} E_1$$

In equation (1) and (2), K_{vv} and (K_f) is the valve positioner (fuel system actuator) gain, T_v , T_f are the valve positioner and fuel system actuator time constants, c is a constant, F_d and E_1 are the input and outputs of the valve positioner and W_f is the fuel demand signal in p.u. The output of the LVG, V_{ce} , represents the least amount of fuel needed for that particular operating point and is an input to the fuel system. Another input to the fuel system is the per-unit turbine speed N (limited by the acceleration control). The per-unit value for V_{ce} corresponds directly to the per-unit value of the mechanical power on turbine at steady-state. The fuel flow control as a function of V_{ce} is shown below in figure (4).

The value of V_{ce} is scaled by the gain $K_3(K_3 = (1 - K_6))$, then delayed and offset by the minimum amount of fuel flow K_6 to ensure continuous combustion process in the combustion chamber. K_6 is essentially the minimum amount of fuel flow at no-load, rated speed [4].

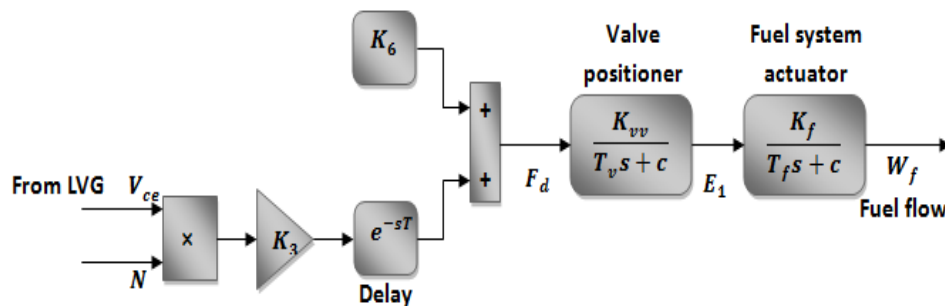


Figure4: Block diagram of the fuel system

5 Compressor-Turbine system.

The compressor-turbine is the heart of the micro-turbine and is essentially a linear, non-dynamic device (with the exception of the rotor time constant) [4]. There is a small transport

delay T_{CR} , associated with the combustion reaction time, a time lag T_{CD} , associated with the compressor discharge volume and a transport delay T_{TD} , for transport of gas from the combustion system through the turbine. The block diagram of the compressor-turbine package is shown in figure (5). In this figure both the torque and the exhaust temperature characteristics of the gas turbine are essentially linear with respect to fuel flow and turbine speed and are given by the following equations [4]:

$$\begin{aligned} &\text{Torque} \\ &= K_{HHV}(W_{f_2} - 0.23) \\ &+ 0.5(1 \\ &- N)(Nm) \end{aligned} \tag{3}$$

$$\begin{aligned} &\text{Ext. } T_x \\ &= T_R - 700(1 - W_{f_1}) \\ &+ 550(1 \\ &- N)(^{\circ}F) \end{aligned} \tag{4}$$

where K_{HHV} is a coefficient which depends on the enthalpy or higher heating value of the gas stream in the combustion chamber and T_R is the reference temperature. The K_{HHV} and the constant 0.23 in the torque expression cater for the typical power/fuel rate characteristic, which rises linearly from zero power at 23% fuel rate to the rated output at 100% fuel rate. The input to this subsystem is the p.u. fuel demand signal W_f and outputs are the p.u. turbine torque (N.M) which multiplied by the rotor speed to result the mechanical power and exhaust temperature ($^{\circ}F$). Both mechanical power and temperature signals are controlled and inserted again into the LVG.

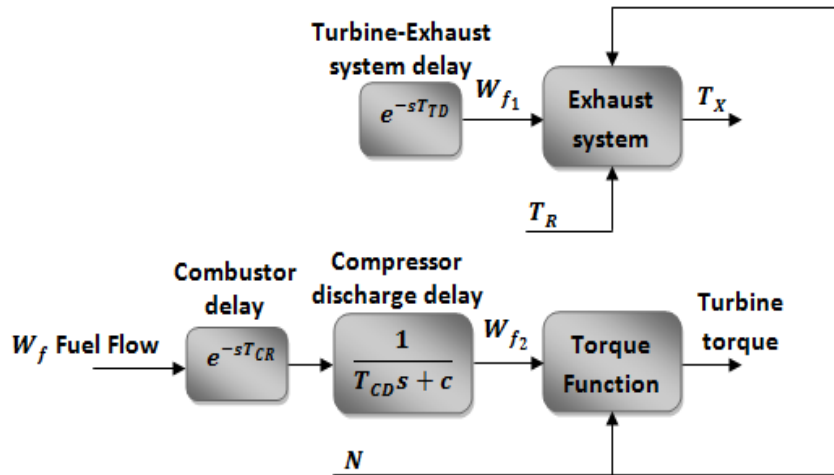
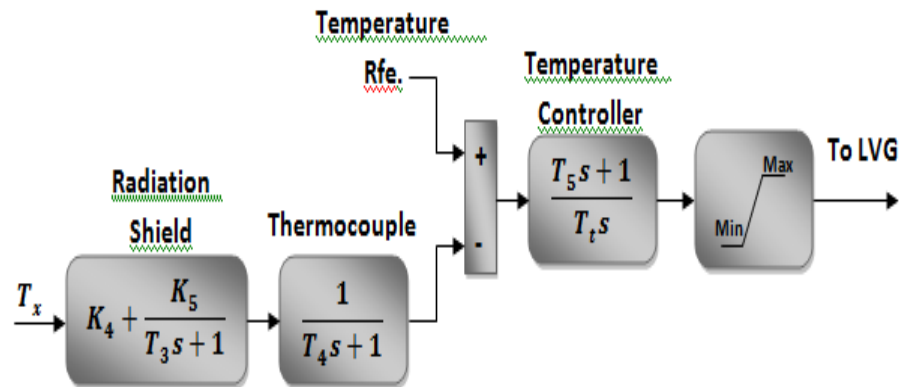


Figure5: Compressor-Turbine package of MGT

6 Temperature loop and PI controller.

Temperature control is the normal means of limiting the gas turbine output power at a predetermined firing temperature, independent of variation in ambient temperature or fuel characteristics. The fuel burned in the combustor results in turbine torque and in exhaust gas temperature. The exhaust temperature is measured using a series of thermocouples incorporating radiation shields as shown in the block diagram of the temperature controller Figure (6). In this figure, T_t is the temperature controller integration rate and T_3, T_4 are time constants associated with the radiation shield and thermocouple, respectively. K_4 and K_5 are constants associated with radiation shield and T_5 is the time constant associated with temperature controller. The output from the thermocouple is compared with a reference temperature, which is normally higher than the thermocouple output. This forces the output of the temperature control to stay on the maximum limit permitting the dominance of speed control through the LVG figure (3). When the thermocouple output exceeds the reference temperature, the difference becomes negative, and the temperature control output starts



decreasing. When this signal Figure (3) becomes lower than the speed controller output, the former value will pass through the LVG to limit the turbine's output, and the turbine operates on temperature control. The input to the temperature controller is the exhaust temperature T_x and the output is the temperature control signal to the LVG [4].

Figure6: Block diagram of temperature control system

7 The generator.

A conventional generator has been used in this study because of low speed generator to avoid the interface circuits (power electronic circuit) which used as have been said before in case of high speed generator, and also conventional generator is useful and suitable in countries where 50 Hz is mainly used. The electrical generator was modelled based on a generator swing differential equation. The swing differential equation is ascertained in terms of power [5].

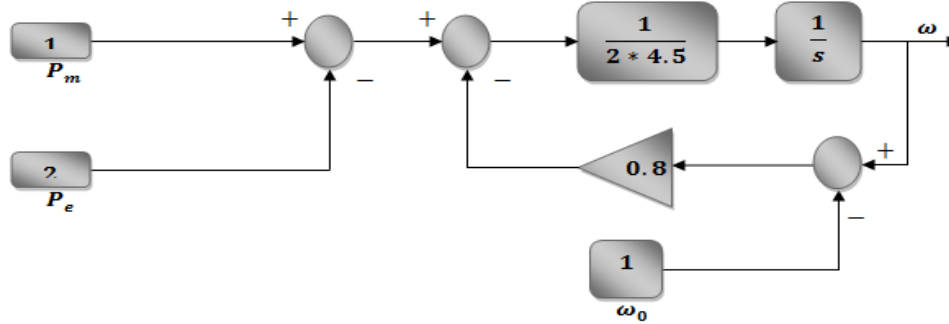


Figure7: Conventional generator

$$\begin{aligned} \frac{d\omega}{dt} &= \frac{\omega_0}{2H_{eq}} [P_m - P_e \\ &- D_{eq}(\omega \\ &- \omega_0)] \end{aligned} \quad (5)$$

Generator equation was modelled based on the assumption that losses, due to the shaft rotation are ignored [5]. The SIMULINK model representation of the electrical generator is shown in figure (7). The input as has been illustrated in figure (7) are the Mechanical power (P_m) and Electrical power (P_e) and the output was the rotor speed ω of the generator which has been inserted into the turbine as a feedback.

8 MGT loops, PID tuning, and simulation tests.

A step function has been applied as input of electrical power as set point (from zero to 0.2) p.u (Per Unit). The reference rotor speed was 1 p.u. in all simulation. The reference exhaust temperature also fixed at 950 °F. The output response results after parameters of PID maintained using trial & error method and Ziegler-Nichols method were applied. The figure (8) shows the output response of electrical power demand (P_e) and mechanical power (P_m) outputs after applying the Ziegler-Nichols method on PID controller of P_e & P_m . The parameters in figure (8) were as following :

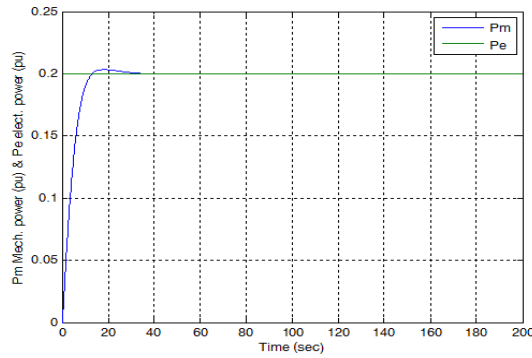


Figure8: Relationship between P_c & P_m with Ziegler-Nichols method

$T_u = 0.5$, $K_c = 12$, $K_p = 0.2 \cdot 12$, $K_i = 0.5/2 = 0.25$ and $K_d = 0.5/8 = 0.0625$

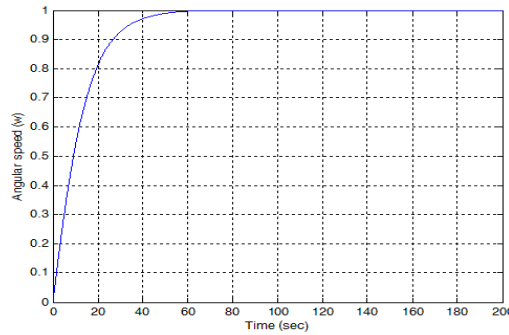


Figure9: Speed (ω) with Trial & error method.

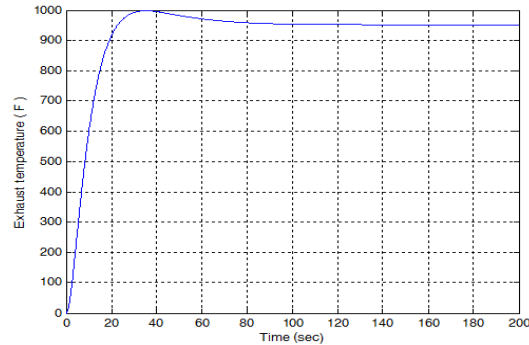


Figure10: Exhaust temperature ($^{\circ}$ F)

Ziegler-Nichols method was applied and found suitable parameter for mechanical power PID controller, whereas could not be applied with Angular speed PID controller and also in temperature PI controller. Trial & error method is the perfect method for both angular speed PID controller and temperature PI controller. Figure (9) shows the response of Angular speed PID controller using Trial & Error method. Angular speed ω (pu) PID controller using Trial & error method. PID parameter of: $K_p=1, K_i=21$ and $K_d=0.5$ $N=2$

Exhaust temperature is illustrated in figure (10) with parameter of PI controller using Trial & Error where : $P=1$ and $I=2$. Figure (11) illustrate the main structure of Micro-turbine using MATLAB/Simulink, power demand (P_e), feedback of angular speed (ω), and (TR) exhaust temperature set-point. All are represent the inputs of the Micro-turbine itself. The output of the Micro-turbine obviously are the mechanical power (P_m), rotor speed (ω), and measured exhaust temperature.

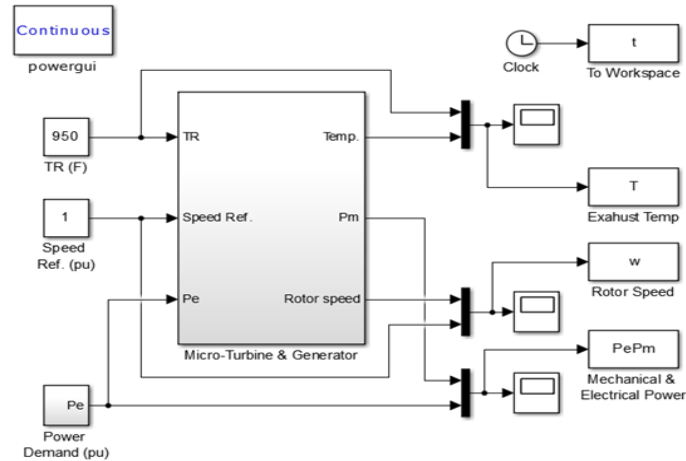


Figure11: Main structure of MGT on MATLAB/Simulink

9 Identification and model reduction of MIMO MGT with PID controller.

9.1 Mechanical & electrical power loop.

Estimation and validation of the output signal could be represented for mechanical power PID controller, angular speed PID as well and also for PI controller exhaust temperature by do several calculations the transfer function of speed loop with PID controller was as follows.

$$G_{T1} = \frac{0.08}{s^2 + 0.45s + 0.08} \quad (10)$$

To validate the response of mechanical power PID controller, figure (12) shows the actual and estimated values of that. With the same step input of both and we could obviously compare the two values to each other. The blue curve for (P_m) actual value and the red curve for (P_m) estimated value were approximately the same:

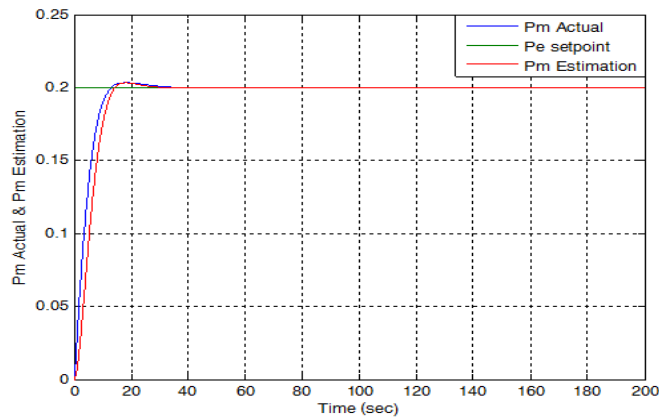


Figure12: Actual and estimation values of mech. power response.

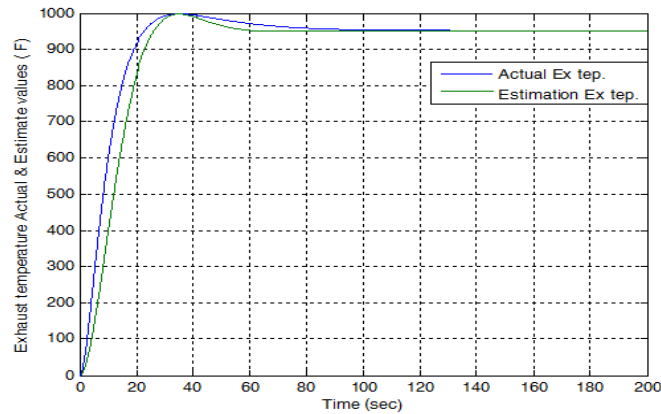


Figure13: Actual and estimation values of Exh.Tem.(°F)response.

9.2 Exhaust temperature loop.

In the same way exhaust temperature has been estimated and validated $y_{\max} = 995.3$, $y_{ss} = 950$ $t_p = 35$ sec. After several calculations has been done as above a results found were: $\zeta = 0.696$ $\omega_n^2 = 0.0156$. The transfer function of G_{T2} will be as follows:

$$G_{T2} = \frac{0.0156}{s^2 + 0.174s + 0.0156} \tag{11}$$

Figure (13) illustrate the actual (blue curve) and estimation values (green curve) of Exhaust temperature. As we can see the output response of the actual and the estimation value are approximately the same.

9.3 Rotor speed loop.

By getting values of $y = 0.6318$, $y_{ss} = 1$ $\tau = 12.56 \text{ sec}$ from the rotor speed PID controller and substituting these values in the following first order transfer function equation which represent the rotor speed as follows:

$$G_{T3} = \frac{1}{12.56 s + 1} \quad (12)$$

The figure (14) shows the actual and estimated values of rotor speed (ω) pu output response and as we could see are the same.

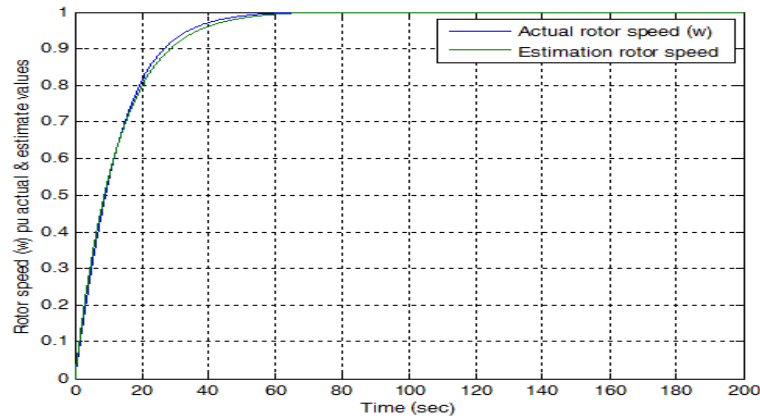


Figure14: Actual & estimated values of rotor speed(ω) output response

10 Compensators design instead of PID and PI controllers.

The design of feedback control system in industry is probably accomplished using frequency-domain more often than other method. The primary reason for the popularity of frequency-domain design is that the effects of disturbances, sensor noise, and plant uncertainties are relatively easy to visualize and assess in the frequency domain [6]. In this section PID controller in power and speed controller, also temperature PI controller will be replaced with lag compensator.

10.1 Lag Compensation For MGT Speed Controller

Mathematical model of speed controller PID for the micro-turbine which we have been discussed in chapter four, as follows :

$$P + I \left(\frac{1}{s} \right) + D \left(\frac{N}{1 + N \left(\frac{1}{s} \right)} \right) \quad (13)$$

By getting the values of P, I, D, and N from MATLAB/Simulink speed PID controller shown in figure (10) the equation (14) will be as follow:

$$PID_{(speed)} = 1 + 2\left(\frac{1}{s}\right) + \frac{1}{2}\left(\frac{2}{1 + \frac{2}{s}}\right)$$

By rearrange the equation to show the crossover frequencies of speed PID controller:

$$PID_{(speed)} = \frac{4\left(\frac{1}{4}s + 1\right)(s + 1)}{s\left(\frac{1}{2}s + 1\right)} \tag{14}$$

To replace $PID_{(speed)}$ by a appropriate compensator we must use Bode plot of speed PID controller which could be seen in the figure (15):

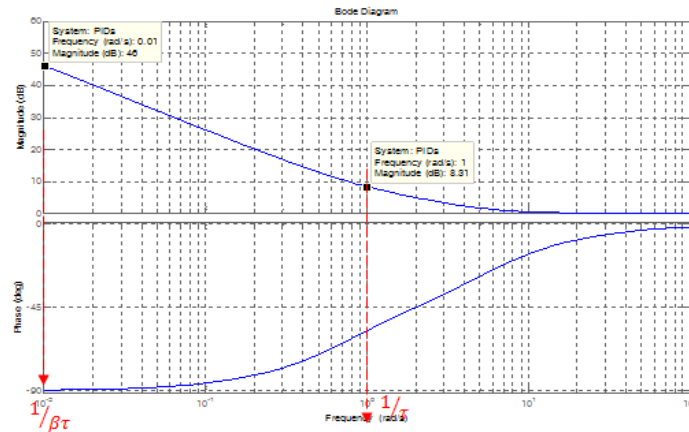


Figure15: Bode plot speed PID controller.

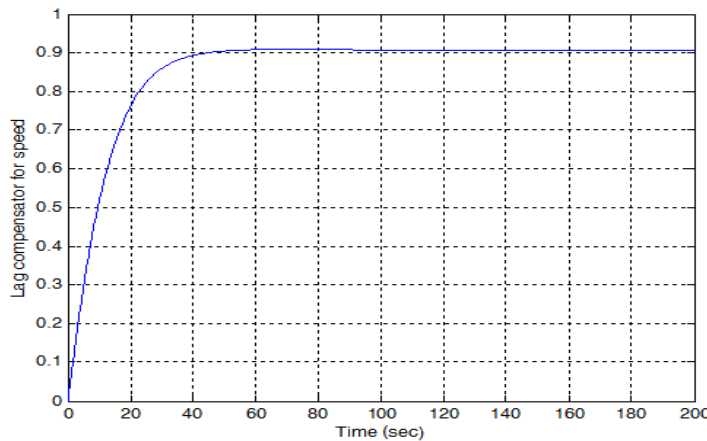


Figure16: Lag compensator response for speed loop.

As we could see the $PID_{(speed)}$ shape looks like a lag compensator with upper and lower gain crossover frequencies $\left(\frac{1}{\beta\tau}\right)$ and $\left(\frac{1}{\tau}\right)$ respectively:

$$\begin{aligned}
 D(s) &= \frac{\tau s + 1}{\beta \tau s + 1} \\
 &= \frac{s + 1}{100s + 1}
 \end{aligned}
 \tag{15}$$

as we could see the speed lag compensator response shown in figure (16) corresponding to equation (15) is acceptable except the gain which need to be increased. After increasing the lag compensator gain, equation (15) will be as follows and speed lag compensator response is then shown in figure (17). Bode plot of both PID speed controller and Lag compensator shown in figure (17) illustrate that the gain crossover frequency are nearly the same (lower is 0.01 rad/sec and the upper is 0.1 rad/sec).

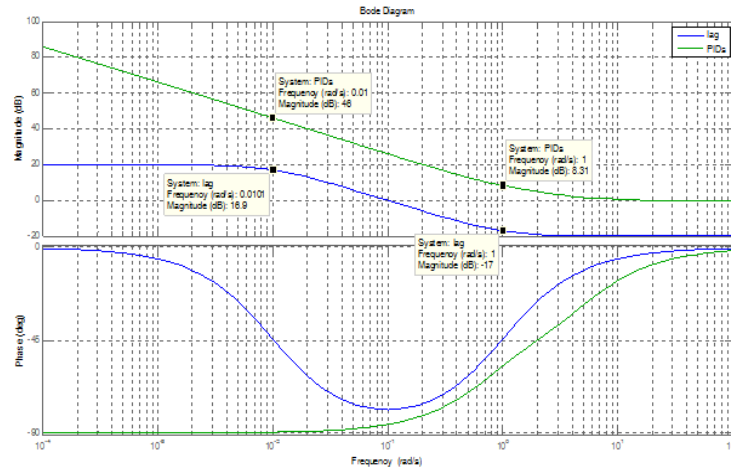


Figure17: Bode plot of lag compensator and PID for speed.

$$\begin{aligned}
 D(s) &= \frac{10s + 10}{100s + 1}
 \end{aligned}
 \tag{16}$$

10.2 Lag Compensation For MGT Mechanical Power:

As we have been done in PID speed controller a lag compensator for mechanical power is shown in figure (18)

$$\begin{aligned}
 D(s) &= \frac{\tau s + 1}{\beta \tau s + 1} \\
 &= \frac{10s + 1}{100s + 1}
 \end{aligned}
 \tag{17}$$

As we could see the mechanical power lag compensator response shown in figure (18) corresponding to equation (17) is acceptable except the gain which need to be increased. After increasing the lag compensator gain, equation (17) will be as follows and mechanical power lag compensator response is then shown in figure (19):

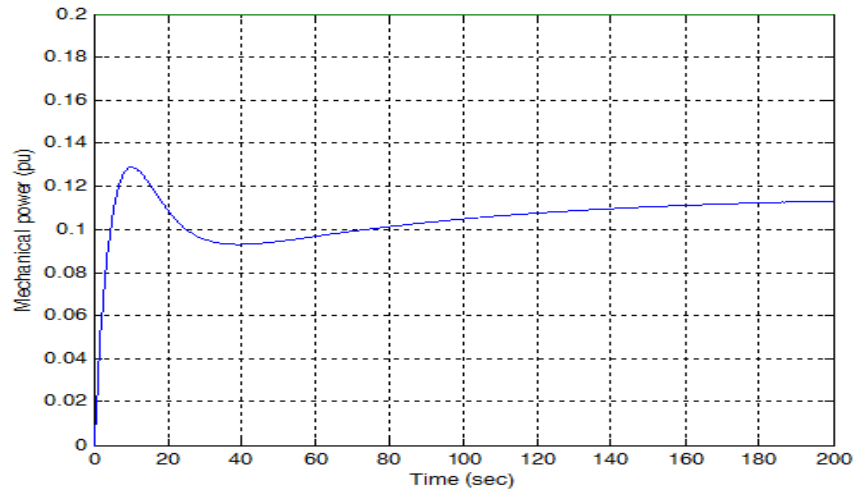


Figure18:Lag compensator response for Mech. power

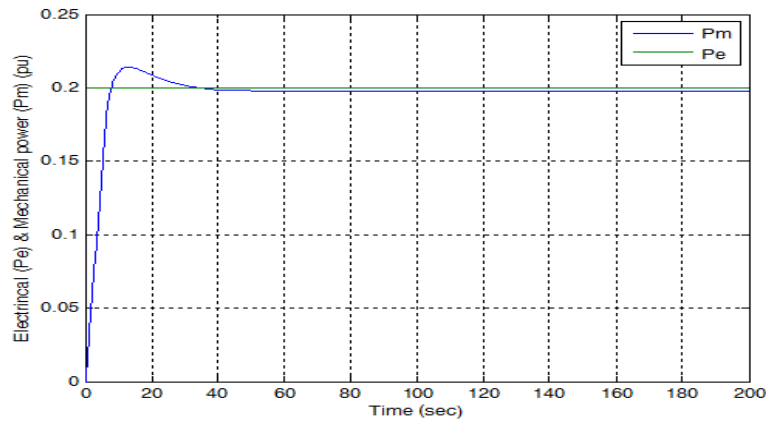


Figure19:Lag compensator response for mech. power after maintaining

$$D(s) = \frac{600s + 60}{100s + 1} \tag{18}$$

Figure (20) shows the comparison between Bode plot of the both mechanical power PID and mechanical power lag compensator which we have been gotten according to eq. (18). Bode plot of both PID mechanical power controller and Lag compensator shown in figure (20) illustrate that the gain crossover frequency are nearly the same (lower is 0.001 rad/sec and the upper is 0.1 rad/sec).

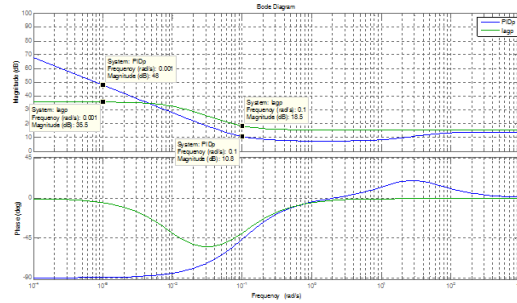


Figure20:Lag compensator response for Mech. power

10.3 Lag compensation for MGT temperature controller:

The mathematical model of Exhaust temperature PI controller for the micro-turbine which we have been discussed in section 9, as follows :

$$P + I \left(\frac{1}{s} \right)$$

By getting the values of (P) and (I) from MATLAB/Simulink Exhaust temperature PI controller shown in figure (11) the equation (19) will be as follow:

$$PI_{(Tem)} = 1 + 2 \left(\frac{1}{s} \right)$$

After getting the upper and lower gain cross over frequencies of the PI exhaust temperature controller bode plot, it was replaced with a lag compensator as in equation (20) and its response is shown in figure (21)

$$D(s) = \frac{0.5s + 1}{s + 1} = \frac{s + 2}{10s + 1} \tag{20}$$

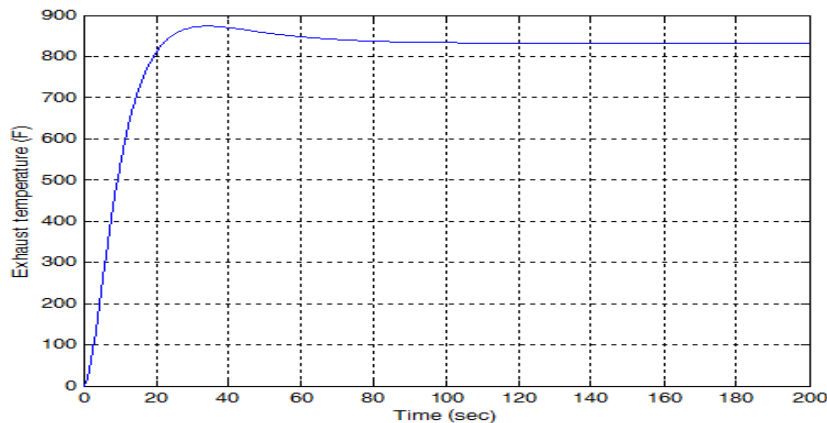


Figure21:Exh. temperature lag compensator response

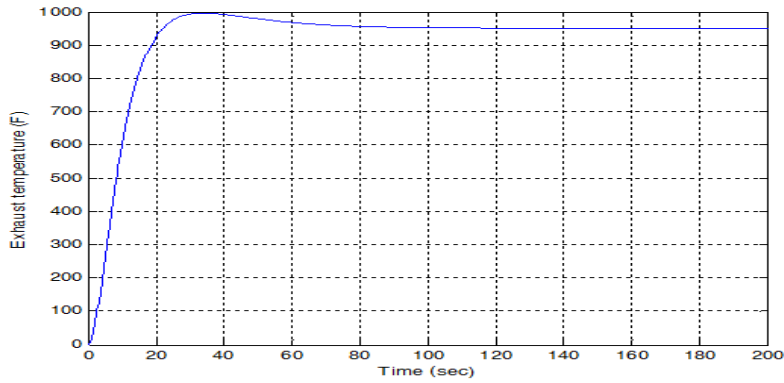


Figure22:Exh.temperaturelag compensator response after maintaining

According to fact which has (usually, as a general guideline, the upper corner frequency, $1/\tau$, of the compensator should be approximately one octave to one decade below the new gain crossover frequency ω'_g .) Taking:

$$\frac{1}{\tau} = \frac{\omega'_g}{10} = \frac{2}{10} \rightarrow \tau = 5$$

thus, the required lag compensator is:

D(s)

$$= \frac{5s + 1}{100s + 1}$$

(21)

equation(20) will be as follows and Exhaust temperature lag compensator response is then shown in figure (22).

Bode plot of both PI Exhaust temperature controller and Lag compensator shown in figure (23) illustrate that both plots are nearly the same, Notice that the sample Exh. = Exhaust and Tem. = Temperature.

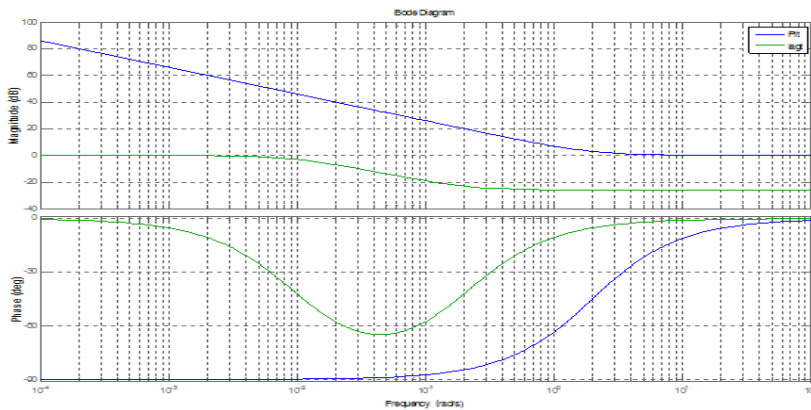


Figure23: Bode plot of lag compensator and PI for Exh.Tem.

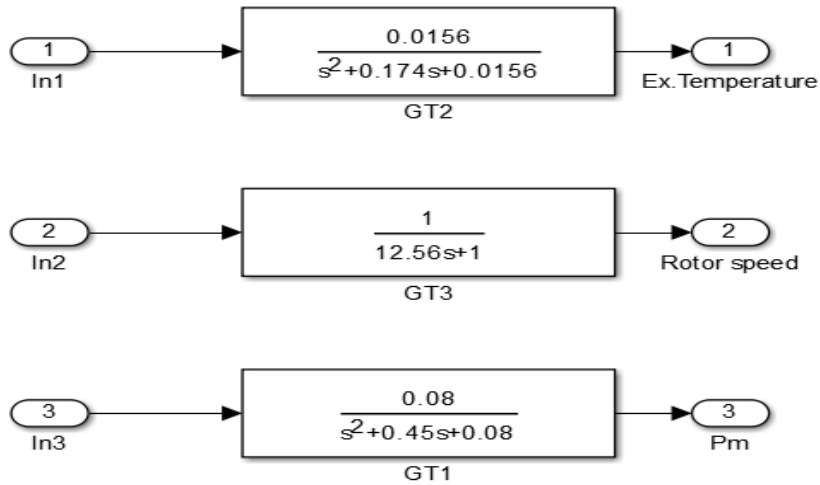


Figure24:Transfer function of power, speed and temp. systems

We could notice here that there is no interaction between the three controllers, which supervisor controller is allowable to design. The whole system is stable and could be used in industrial. Figure (24) shows the collection of three PID controllers -exhaust temperature, mechanical & electrical power and rotor speed- to build what is known of supervisor controller. The whole systems and supervisor controller itself all are shown in figure (25).

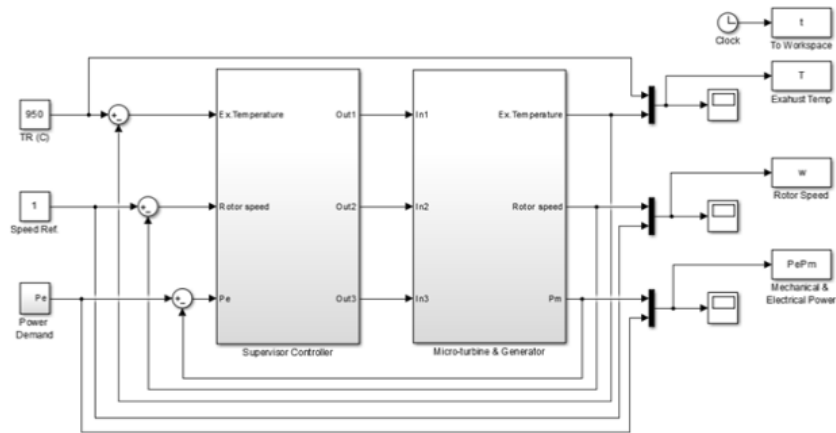


Figure25: The plant of Micro-Turbine and generator.

11 Conclusion:

The main purpose of this paper is to model, simulate, and control design of the Micro-turbine which mainly used to maintain the continuously of electrical power of the grid. The simulation

model is used to investigate the output response as well. Local controller was designed for Micro-turbine using PID controllers for both rotor speed and mechanical & electrical power systems, and a PI controller for exhaust temperature. The PID, and PI controllers tuned using Ziegler-Nichols method for Mechanical & electrical power PID controller and have been found suitable whereas, using trial & error was better for rotor speed and exhaust temperature systems, to reach an acceptable and particular output of the Micro-turbine systems. A compensators were designed for three systems -rotor speed, mechanical & electrical power, and exhaust temperature systems- instead of PID and PI controllers which have been designed before, using frequency domain with help of Bode plot reshaping. Interaction hasn't been detected between three systems. System reduction was resulted due to a MIMO (Multi-Input Multi-Output) system becomes a SISO (Single-Input Single -Output) system. Estimation and validation were both done for the PID and PI controllers. A supervisor control system was designed by collected the three IMC-based controllers and applied to the Micro-turbine. The time constant parameters were chosen to get the acceptable output responses.

References:

- [1] P.RajaSekhar, L.S Enhancement of Micro Turbine-Generator Output Voltage Quality through Application of Matrix Converter Interface uresh, ‘’, IOSR Journal of Engineering (IOSRJEN) PP 43-49 , (2013).
- [2] Larry Goldstein, Bruce Hedman, Dave Knowles, Steven I. Freedman, Richard Woods and Tom Schweizer., “Gas-fired distributed energy resource technology characterizations,” National Renewable Energy Laboratory, NREL/TP-620-34783, Nov.(2003).
- [3] W. I. Rowen, ‘Simplified mathematical representations of heavy duty gas turbines’,*J* Journal of Engineering for Power, Trans. ASME, vol. 105, no. 4,pp. 865-869, October (1983).
- [4] GodswillOfualagba, ‘The Modelling and Simulation of a Micro-turbine Generation System’, *IJSER International Journal of Scientific & Engineering Research* Volume 2, Issue 2, ISSN 2229-5518, (2012).
- [5] Emekaeusebiusomeife, ‘The impact of compressor cleaning in gas turbine engines used for oil and gas applications’, *Msc. in communication, control and digital signal processing*, (2010).
- [6] M. Gopal, ‘Control system principle and design’, McGraw-Hill companies, (2008).

Optimal Power Loss Minimization using Optimal Size and Location of Shunt Capacitors, and DG

Hesain Milad Alfrd

Department of Electrical & Computer Engineering, College of Engineering,
Elmergib University, Libya

DOI: <https://doi.org/10.21467/proceedings.2.20>

* Corresponding author email: husein.alfared@elmergib.edu.ly

ABSTRACT

One of the biggest problems that face the electric distribution network is the power losses, which could be reduced for obtaining a good voltage improvement. Two effective case studies have been used to minimize the power losses; a conventional case study which could be represented by installing Shunt Capacitors, and a modern case study which could be represented by installing Distributed generators (DG). This paper presents effective approaches, to obtain the optimal size and location of each of Shunt Capacitors, and DG, based on Newton Raphson Numerical Method. The first approach proposes load flow, and the second approach proposes optimal load flow. A Libyan distribution network was chosen for the discussion and analysis.

Keywords: Loss formula, Shunt capacitor, Distributed generation.

1 Introduction

Installation of shunt capacitors in the electrical distribution system, has many advantages for many purposes. Inductive loads such as transformers and motors cause lagging power factor which leads to a reduction in capacity, voltage levels, and increasing power losses. Optimal capacitor placement provides a network with the necessary reactive power using Tabu Search method [1]. Various techniques have been applied using capacitor allocation, and every technique has its own advantages, and defects [2]. Shunt capacitors enhance the reactive power control in addition to the system reliability and security in the distribution network. For the compensated and uncompensated networks a state-space method is used to study the reliability index [3]. Minimizing the power and energy losses using a genetic algorithm where the major objective function is to decrease the cost depending on capacitor location and reactive power support [4]. Optimal capacitor location and size to supply with the necessary compensation for the better investment required to satisfy appropriate reactive constraints based on deterministic and genetic algorithm together [5]. The improvement of the Distributed Generation technologies has a large impact on power system operation. The renewable energy sources such as solar, wind, hydro, biomass, etc., is the most important motivation for the studies including the integration of DG to the electric grid. Voltage



© 2018 Copyright held by the author(s). Published by AIJR Publisher in Proceedings of First Conference for Engineering Sciences and Technology (CEST-2018), September 25-27, 2018, vol. 1.

This is an open access article under [Creative Commons Attribution-NonCommercial 4.0 International](https://creativecommons.org/licenses/by-nc/4.0/) (CC BY-NC 4.0) license, which permits any non-commercial use, distribution, adaptation, and reproduction in any medium, as long as the original work is properly cited. ISBN: 978-81-936820-5-0

profile improvement and reducing power losses can be obtained by the installation of DG in the distribution network [6]. Essential definitions of DG and their operating constraints as well as their types, classification, and technologies [7]. DG on electric power system contributes to good power quality, voltage profile improvement, and loss reduction [8]. Hybrid PSO & HBMO algorithm is implemented in optimal placement and sizing of DG in the distribution network in order to decrease the total power losses and obtaining voltage profile enhancement [9]. Genetic Algorithm is also used for optimal size and location of DG with the purpose of supplying necessary real and reactive power to a distribution network whereas the main objective is to minimize system losses and to enhance system reliability and voltage profile [10]. Power Loss Minimization and Voltage Profile Improvement of a Distribution System Using Optimal Size and Location of DG utilized on 11 (KV) real Libyan distribution system [11]. In this paper, the optimum size and location of the shunt capacitor, and DG connected to distribution system is studied by using an optimal control theory with an excellent solution approach (Newton Raphson).

2 Materials and Methods

The Newton–Raphson (NR) method has outstanding convergence characteristics for solving non-linear algebraic systems. In comparison with the Gauss-Seidel method, a lesser range of iterations is necessary for convergence provided that, the initial values are not far away from the final solution [12].

3 Theory and Calculation

Two case studies were applied to find the optimal size and location of a shunt capacitor, and DG separately using Newton Raphson method on a power distribution system, the following Computational procedure should be done as follows:

Step 1: Run normal load flow to find the losses before the installation of the capacitor & DG.

Step 2: Run normal load flow after installing unknown shunt capacitor size on each bus.

Step 3: Find the optimal size of the shunt capacitor for each bus using Eq.(4).

Step 4: Compute the total loss using Eq. (1) after placing a shunt capacitor of the optimal size obtained in step 3.

Step 5: Run optimal load flow after installing unknown DG size on each bus.

Step 6: Find the optimal size of DG for each bus using Eq. (3).

Step 7: Compute the total loss using Eq. (1) for each bus by placing DG of optimal size obtained.

Step 8: Locate each of shunt capacitors and DG on the bus at which the loss is minimum. This is the optimum location for a shunt capacitor or DG.

Step 9: Run load flow with each of shunt capacitor and DG to get the final result.

Step 10: The voltage profile has improved after connecting a shunt capacitor and a distributed generator on the optimal location using Eq. (6).

3.1 Mathematical Expressions and Symbols

Location and size of shunt capacitor & DG units are decided in such a way that minimum system power loss and desired voltage profile are obtained. Therefore, there is a need to define the system power loss as a function of each of shunt capacitor and DG size and system bus voltages. Hence:

$$P_{loss} = \sum_{i \neq j}^m P_{line} \quad (1)$$

Where P_{loss} : is the real power loss, and m : is the number of branches in the power system.

$$P_{line(i,j)} = P_{(i)} - P_{(j)} \quad (2)$$

$$P_i = P_{DG_i} - P_{D_i} = |V_i| \sum_{j=1, j \neq i}^n |V_j| [G_{ij} \cos(\theta_i - \theta_j) + B_{ij} \sin(\theta_i - \theta_j)] \quad (3)$$

$$Q_i = Q_{DG_i} - Q_{D_i} = |V_i| \sum_{j=1, j \neq i}^n |V_j| [G_{ij} \sin(\theta_i - \theta_j) + B_{ij} \cos(\theta_i - \theta_j)] \quad (4)$$

where ' i ' is the location of the capacitor or DG unit ($i=1, 2, 3, \dots, n$) and ' n ' is the total number of bus bars in the distribution network. P_i and Q_i are net real and reactive power injection in the bus ' i ' respectively. V_i is the voltage magnitude at the bus ' i ' respectively. P_{DG_i} and Q_{DG_i} are the real and reactive power generations of DG at the bus ' i '. P_{D_i} and Q_{D_i} are the real and reactive power demand at the bus ' i '. So objective function is to minimize the power loss considering following constraints:

$$P_{loss} = \sum_{i=1}^n P_{G(i)} - \sum_{i=1}^n P_{D(i)} \quad (5)$$

Where $P_{G(i)}$ is the generated real power in the bus ' i ', and $P_{D(i)}$ is the consumed power in the bus- ' i '

Where ' n ' is a number of buses. It should highlight that enhancing the voltage profile depends upon minimizing the voltage

deviations VD as:

$$VD = \sum_{i=1}^n (|V_n - V_{ref}|)^2 \quad (6)$$

Where V_{ref} is the reference voltage that commonly equals to 1 p.u.

$$|V_{i \min}| \leq |V_i| \leq |V_{i \max}|$$

$$P_{line(i,j)} \leq P_{line(i,j) \max}$$

Proper settings for $|V_{i \min}|$ and $|V_{i \max}|$ results in better voltage profile of system.

4 Results and Discussion

A normal load flow and optimal load flow program run by Neplan (power simulation software) on a Libyan distribution network to find the optimum size and location for shunt capacitors, and distributed generation (DG). Simulations were carried out on a local distribution system,

11 kv, called Sileen Al-Bahria, in Khoms / Libya, located on an approximated area 120 km², and 78 loads.

4.1 The Consideration of Work

- 1) The data of loads obtained in currents, not in active or reactive power, measured per four months (by the general electric company of Libya).
- 2) The power factor of the loads was unknown. Hence, it considered 0.87 to calculate the active and reactive power.
- 3) The distribution system is unbalanced, which led to taking the average of the load currents, to represent the system in one line diagram per phase.
- 4) The load factor is equal to one.

4.2 Case Study I

The first case study is a normal load flow approach, which finds the optimal sizes of shunt capacitors installed at each bus, which gives the less loss according to capacitor size.

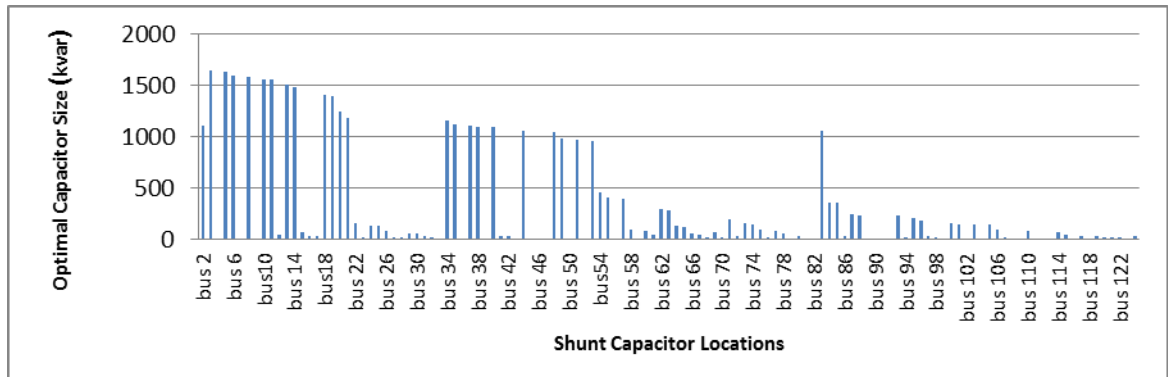


Figure 1: Optimal capacitor size for each bus bar locations

Figure 1 shows the shunt capacitor size, which is the optimal size for each bus bar location.

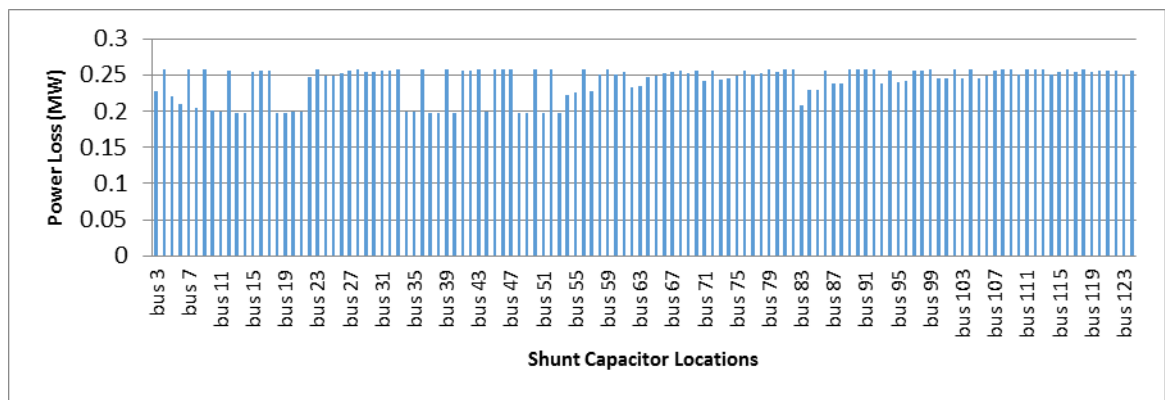


Figure 2: Power losses vs optimal shunt capacitor locations

Figure 2 shows the total losses for each optimal shunt capacitor size installed at each busbar in kvar and shows the optimal size which gives the less loss at bus 53 with total losses 0.1967 MW, and optimal capacitor size 960.5 kvar.

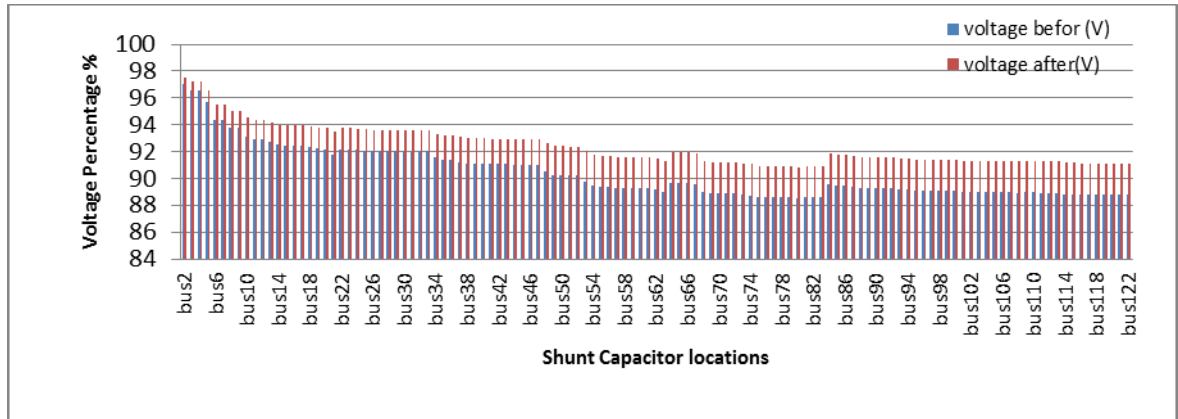


Figure 3: Voltage percentage vs shunt capacitor locations

figure 3 after connecting a shunt capacitor at bus 53 with the optimal size 960.5 kvar, shows obtaining a very good voltage improvement for each bus.

4.3 Case Study II

The second approach is an application of the optimal load flow by Newton Raphson wherein the optimal size of DG which could be found at each bus, which leads to finding the less loss in the network at all.

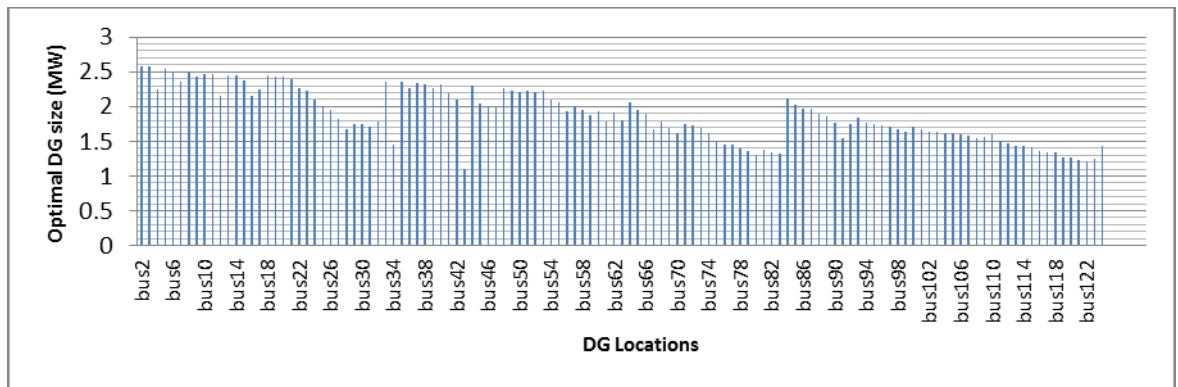


Figure 4: Optimal DG size for each bus bar location

Figure 4 shows the DG size, which is the optimal size for each bus bar location.

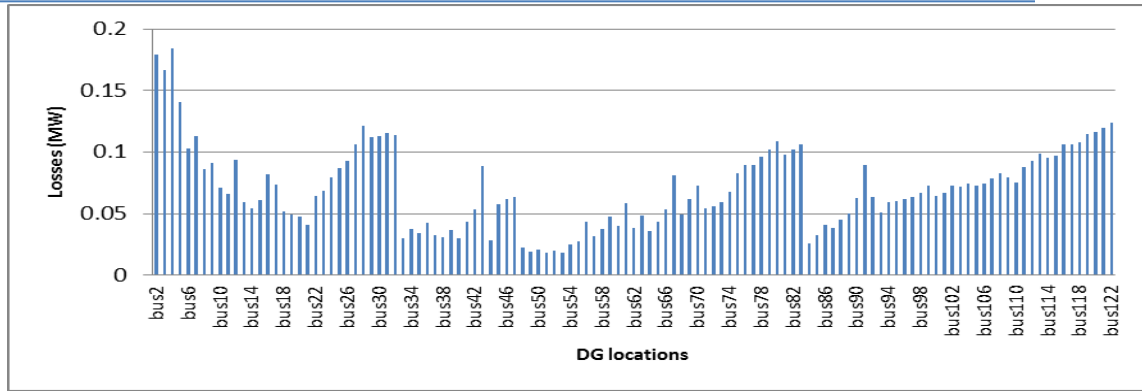


Figure 5: Power losses vs Optimal DG locations

Figure 5, which shows the total losses for each optimal DG size, installed at each busbar in MW, and shows the optimal size which gives the less loss at bus 53 with total losses 0.0292272 MW, and optimal DG size 2.218 MW.

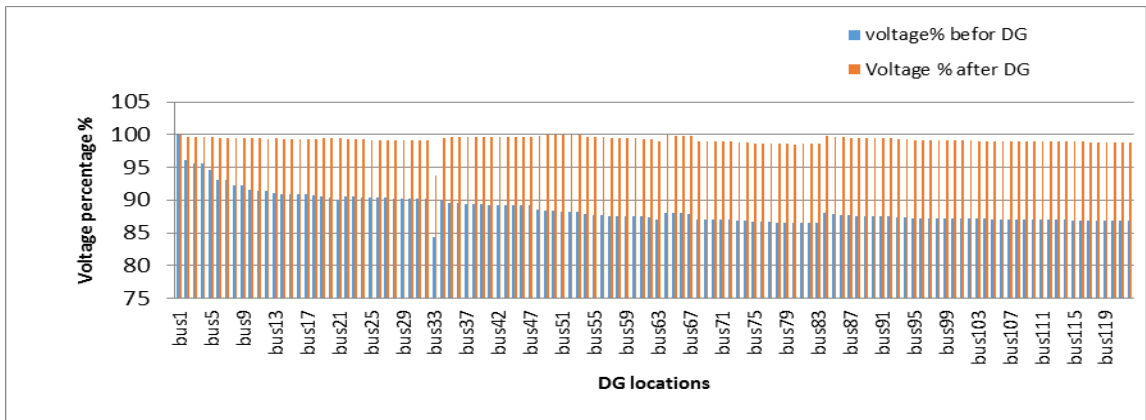


Figure 6: Voltage percentage Vs DG locations

Figure 6 after connecting a distributed generator at bus 53 with the optimal size 2.218 MW, shows obtaining a very good voltage improvement for each bus.

Comparison between the two case studies

The following table shows a comparison between the two case studies mentioned above:

Table 1: Optimal placement and sizing of DG and capacitor

Case study	Optimal bus location	Optimal size	Total Losses before	Total losses after	Power loss saving	Voltage Deviation (pu) before	Voltage Deviation (pu) after
Case I	53	960.5 kvar	0.2583 MW	0.1967 MW	0.0616 MW	1.1716	0.7327
Case II	53	2.218 MW	0.2583 MW	0.0292 MW	0.2291 MW	1.1716	0.0120

5 Conclusions

In this paper, an efficient optimization algorithm proposed for optimal size and location of shunt capacitor and DG on a Libyan distribution network . This method based on Newton Raphson has an efficient minimization of the real and reactive power losses and voltage difference to retain the voltage limits within the accepted range. Two effective case studies have been used; a conventional case study represented by installing Shunt Capacitors, and a modern case study represented by installing Distributed generators (DG). A real application on a Libyan distribution network by NEPLAN Software is applied and gave good results of loss minimization & voltage profile. A Comparison between the two case studies showed the difference between them.

6 References

- [1] R. A. Gallego, A. J. Monticelli, and R. Romero, "Optimal capacitor placement in radial distribution networks", *IEEE Trans. on Power Systems*, vol. 16, Issue 4, pp. 630- 637, 2001.
- [2] H. N. Ng, M. M. A. Salama, and A. Y. Chikhani, "Classification of capacitor allocation techniques", *IEEE Trans. on Power Delivery*, vol. 15, pp. 387-392, 2000.
- [3] Abdel hay A. Sallam, Mohamed Desouky and Hussien Desouky, "Shunt Capacitor Effect on Electrical Distribution System Reliability" *IEEE Trans on Reliability*, Vol. 43, Issue 1, pp. 170-176, March 1994.
- [4] Srinivasan Sundhararajan and Anil Pahwa, "Optimal Selection of Capacitors for Radial Distribution Systems using a Genetic Algorithm" *IEEE Transactions on Power Systems*, Vol. 9, Issue. 3, pp. 1499-1507, August 1994.
- [5] Maurizio Delfanti, Gianpietro P. Granelli, Paolo Marannino , and Mario Montagna, "Optimal Capacitor Placement Using Deterministic and Genetic Algorithms" *IEEE Transactions on power systems*, VOL. 15, Issue. 3, pp. 1041- 1046 August 2000.
- [6] T. Ackermann, G. Anderson, L. Soder, "Distributed generation: a definition" *Electric Power Systems Research*, Volume 57, Issue 3, Pages 195-20420, April 2001.
- [7] El-Khattam and M.M.A. Salama, "Distributed generation technologies, definitions, and benefits" *Electric Power Systems Research*, Volume 71, Issue 2, Pages 119-128, October 2004.
- [8] P. P. Barker, R. W. de Mello, " Determining the Impact of Distributed Generation on Power Systems: Part 1 - Radial Distribution System" *IEEE Power Engineering Society Summer Meeting*, vol. 3, pp. 1645-1656, 2000.
- [9] M. Afzalan, M. A.Taghikhani, "DG Placement and Sizing in Radial Distribution Network Using PSO&HBMO Algorithms", *Electrical Power Distribution Networks (EPDC)*, 2012 Proceedings of 17th Conference on, vol., no., pp.1-6, 2-3 May 2012.
- [10] Carmen L.T. Borges, Djalma M. Falcao, "Optimal distributed generation allocation for reliability, losses, and voltage improvement", *International Journal of Electrical Power & Energy Systems*, Volume 28, Issue 6, Pages 413-420, July 2006.
- [11] Hussein Alfared , Abdalla I. Fadel , "Power Loss Minimization and Voltage Profile Improvement of a Distribution System Using Optimal Size and Location of Distribution Generation," *Libyan conference LICEET 2018*, no. 25. March 2018.
- [12] J. C. Das, " Power System Analysis Short-Circuit Load Flow and Harmonics", Marcel Dekker, Inc.

Experimental Investigation on the Performance Evaluation of Solar Tracking Photovoltaic System

A. Kagilik*, S. Mousa, I.Enageem

Electrical and Electronic Department, Sabratha University, Sabratha, Libya

DOI: <https://doi.org/10.21467/proceedings.2.21>

* Corresponding author email: as.kagilik@gmail.com

ABSTRACT

The optimization of photovoltaic (PV) power generating system needs to be magnified by maximizing the solar radiation falling perpendicular on the PV module surface. The photovoltaic module can extract maximum power from solar irradiance by optimizing its orientation and its angle of inclination with the horizon. Therefore, it is recommended that for high efficiency and low loss of energy. PV module needs to be tilted at the correct angle. On the other hand, solar tracking system can be used to maximize the performance of the PV system, since solar tracking allows more energy to be produced because the solar array is able to remain aligned to the sun. The aim of this paper is to investigate experimentally the performance evaluation of solar tracking photovoltaic system. In this direction, an extensive experimental work at Faculty of Engineering, Sabratha-Libya to improve the output power of PV module by implementation of one axis tracking system. The project will include the design and construction of a microcontroller-based solar panel tracking system. The operation of the experimental model is based on DC motor intelligently controlled by a dedicated drive unit that moves PV panel according to the signals received from two simple but efficient light sensors. Practical comparison between fixed and tracking systems using identical PV modules is performed. It is found that the tracking system significantly improves the output power of PV module compared to the fixed PV panel under same climate conditions. Results indicated that the tracking system increases the output current by more than 60 % compared with fixed PV panel, especially at early morning hours and before the sunset hours. This demonstrates, as expected, that the tracker photovoltaic system provides more efficient performance compared to the fixed photovoltaic system.

Keywords: solar radiation, Photovoltaic system, tracking system

1 Introduction

Recently, the demand of the renewable energy such as wind energy, solar energy, etc. has been increased dramatically around the world due to reduction in existing sources of fossil fuels and the growing concern regarding environment pollution. The conversion of solar light into electrical energy represents one of the most promising and challenging energetic technologies. Today, photovoltaics is considered as highly competitive technology and its world market is



© 2018 Copyright held by the author(s). Published by AIJR Publisher in Proceedings of First Conference for Engineering Sciences and Technology (CEST-2018), September 25-27, 2018, vol. 1.

This is an open access article under [Creative Commons Attribution-NonCommercial 4.0 International](https://creativecommons.org/licenses/by-nc/4.0/) (CC BY-NC 4.0) license, which permits any non-commercial use, distribution, adaptation, and reproduction in any medium, as long as the original work is properly cited. ISBN: 978-81-936820-5-0

mainly fully developed including PV system components (mechanical/electrical). During the last decade, PV is applied at countless locations in many countries and has been implemented successfully with rapid falling installation costs and environments throughout the planet. The worldwide cumulative PV capacity reached about 303 GW by the end of 2016. During 2016, at least 75 GW PV capacity was added compared to 51 GW during 2015 with percentage increase up to 47 %. On the other hand, the global weighted average total installed cost of commissioned utility-scale (larger than 1 MW capacity) solar PV projects between 2010 and 2016 fell by 65 %, with the levelised cost of electricity (LCOE) falling by 67 % over the period. In 2016, an average LCOE of around USD 0.12 per kWh, and a range of USD 0.05 per kWh to USD 0.35 per kWh was achieved according to region [1].

The maximum solar energy extracted from the solar photons is affected by the amount of the collection of the sun radiation and the performance of PV power generating system is highly influenced by the incident solar radiation reaching the surface of the collector. Solar irradiation on PV modules varies with the modules position and the PV output power takes its maximum value when the solar radiation is perpendicular on the collector. Therefore, the optimization of PV module needs to be magnified by optimizing its orientation and its angle of inclination with the horizon. From our previous work, the strongly dependence of the maximum output power on the optimum inclination angle of the fixed PV solar module has been demonstrated and it has been found that the optimum tilt is different for each month of the year and the yearly average optimum tilt is approximately equal to the latitude of the site. Unfortunately, in spite of keeping the classical fixed PV panel in optimum position, the necessary optimum insolation for the maximum performance of PV module cannot be obtained during the whole year [2]. Thus an annually improving the output energy can be obtained by aligning the PV module with the sun such that the maximum radiation falls perpendicularly on the module surface, and the problem of loss can be avoided during the whole year.

Recent technology for optimization both the PV solar module orientation and angle of inclination and maximizing the PV performance is characterized by using the solar tracking system. Unlike the classical fixed PV panel, the function of the solar tracking device is following the sun trajectory such that the solar module is kept under optimum insolation for all positions of the sun. The sun tracking system approach must be equipped with essential features which are the azimuth tracking for adjusting the tilt angle of the surface of the PV array during changing seasons; and daily solar tracking for maximum solar radiation incidence to the PV array [3]. There are two main types of trackers, single axis and dual-axis, which usually operate using either a passive or active mechanism. It has been estimated that the tracking system increases the yield by (30 -60%) compared to stationary one. However, although the tracking systems strongly enhance the module efficiency, they increase the initial cost and complexity of the system and therefore they are still not practical solution for a small-scale application [4].

To date, the performance of photovoltaic (PV) systems with different available technologies of solar trackers have been designed and executed by many workers. In this direction, numerous methods and mathematical models have been considered to validate the design methodologies. Many measurements setup including microcontroller-based solar panel tracking system, stepper motors and drivers, light intensity sensors, voltage regulation, physical construction, and software/system operation explanation have been used to obtain the optimum PV system performance under different climate conditions. Their analyses show an increase of solar irradiation upon a tilted system, azimuth tracker system, and dual axis tracker system as compared to the horizontal system [4, 5].

The aim of this paper is to investigate experimentally the performance evaluation of a single axis solar tracking photovoltaic system under Libyan climate conditions. The measurements are performed during the whole year and the optimized tracking system for four seasons are documented. Different preliminary results are presented in a number of graphs and table for a better interpretation. The proposed tracking method in this paper has been compared with conventional fixed method and good agreement with other investigators has been demonstrated.

2 Solar Photovoltaic Tracking System

2.1 System description

The main solar tracking PV system under investigation in this work is presented. The single-axis solar tracking system consists of a PV panel rotating around a tilted shaft, under the action of a DC motor controlled with respect to the real Sun position estimated by means of two light intensity sensors. Depending on the orientation type solar trackers have a movement part based on a sun trajectory that updates the PV panel position according to the instantaneous solar irradiation. Therefore, the proposed solar tracking system was designed and executed so that specific technical requirements such as: optimum performance, operation reliability, movement simplicity are satisfied. Figure 1 shows the PV solar tracking system which designed and built in this work, while figure 2 illustrates the basic control circuit for a unipolar stepper motor or the complete hardware schematic of the system. As shown in the figures above, the solar tracking PV panels consists of moving parts and control elements, such as: PV module, DC motor, Light sensors, Limit Switch, relay and the Microcontroller. In this section, the background information on the main subsystems of the project was presented. The main part of this system is the PV module under measurements which is considered as a energy source. The second part of the system is the stepper DC motor. This motor is commonly used for precision positioning control applications and it was chosen to position the tracking sensor. The motor is characterized by brushless device, open loop positioning capability, good holding torque, excellent response characteristics and less circuit complicity.

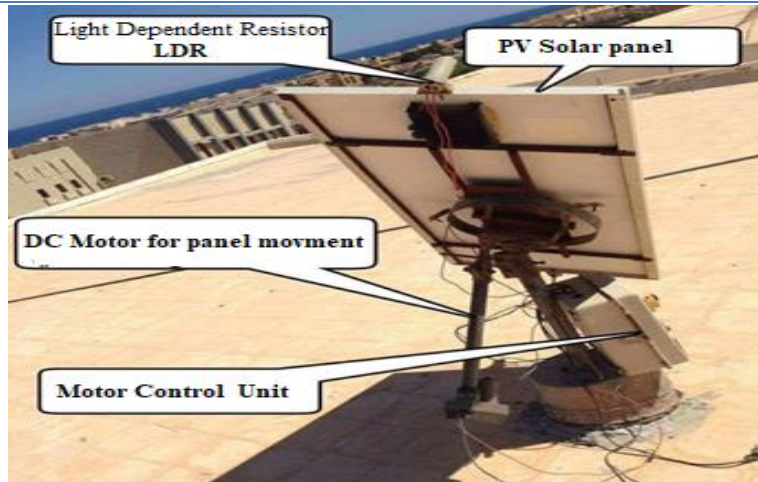


Figure 1: Solar tracking system

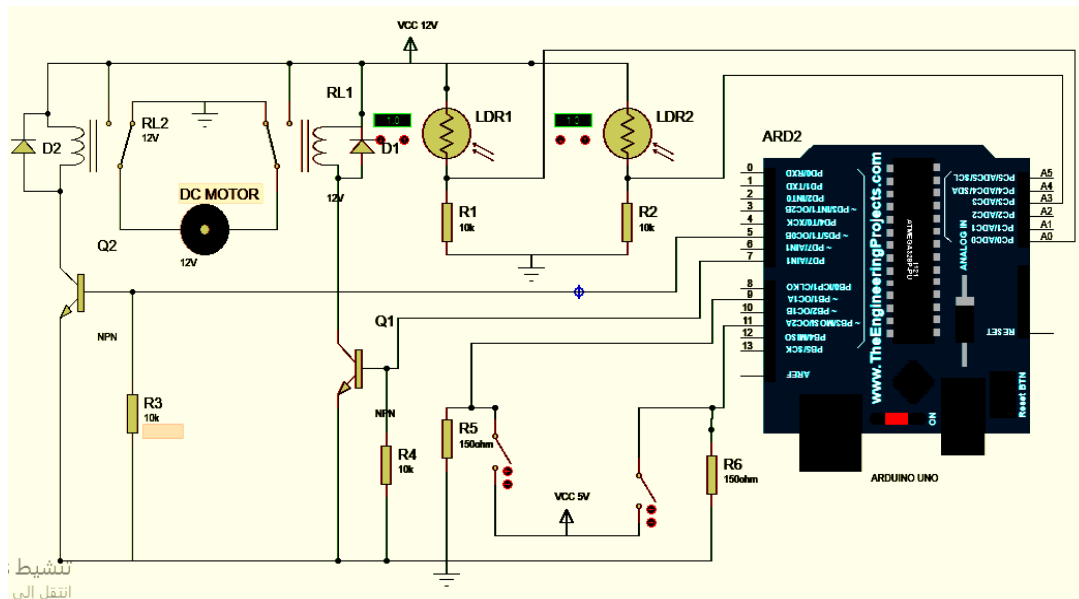


Figure 2: Hardware Schematic Diagram

The project consists of two reading of light sensor values which can control a motor to align with the greatest value which corresponds to the sun's position. Thus, these sensors allow an update of the PV panels position on a monthly or seasonal basis to obtain better PV performance and increase the global energy output of the system. Light sensors are among the most common sensor type. The simplest optical sensor is a photo resistor or Light Dependent Resistor (LDR) that the resistance of these sensors decreases with an increase in solar intensity. This is the least expensive and least complex type of light sensor.

Lastly, a microcontroller is provided to the control circuit. Since the project's focus is on embedded software control, the microcontroller is the heart of the system. The

microcontroller selected for this project is able to convert the analog photocell voltage into digital values and also provide output channels to control motor rotation. The Arduino™ MEGA2560R3 was selected as it satisfies these requirements in addition to already being provided with the class lab kit. MEGA 2560 R3 is an Arduino compatible board with Microcontroller AT Mega 328, it's based on Arduino MEGA 2560 design. All Code, shield and IDE for Arduino MEGA 2560 R3 are also valid on BUONO MEGA 2560, some visible improvement on hardware make BUONO more flexible and easier use, and it's designed for projects that require more I/O lines, more sketch memory and more RAM with 54 digital I/O pins, 16 analog inputs. The Arduino Mega 2560R3 is programmed using the Arduino Software (IDE). The Arduino Programming language is easy to learn and understand since the Arduino IDE is linked with some software's such as: Max MSP processing and MATLAB.

2.2 Algorithm for Control of Tracking System

Figure 3 shows the flowchart of the tracking system control algorithm, while figure 6 illustrates the system protocol. As can be seen, the operation of PV tracking system is based on sensor method. This programming method, using Proteus software, is to track sun's trace by using photo sensors (LDR's) that is tracked through difference in amount of light. On the other hand, the photo resistor and stepper motor theory is discussed in order to provide a better understanding as to how they relate to the solar tracker.

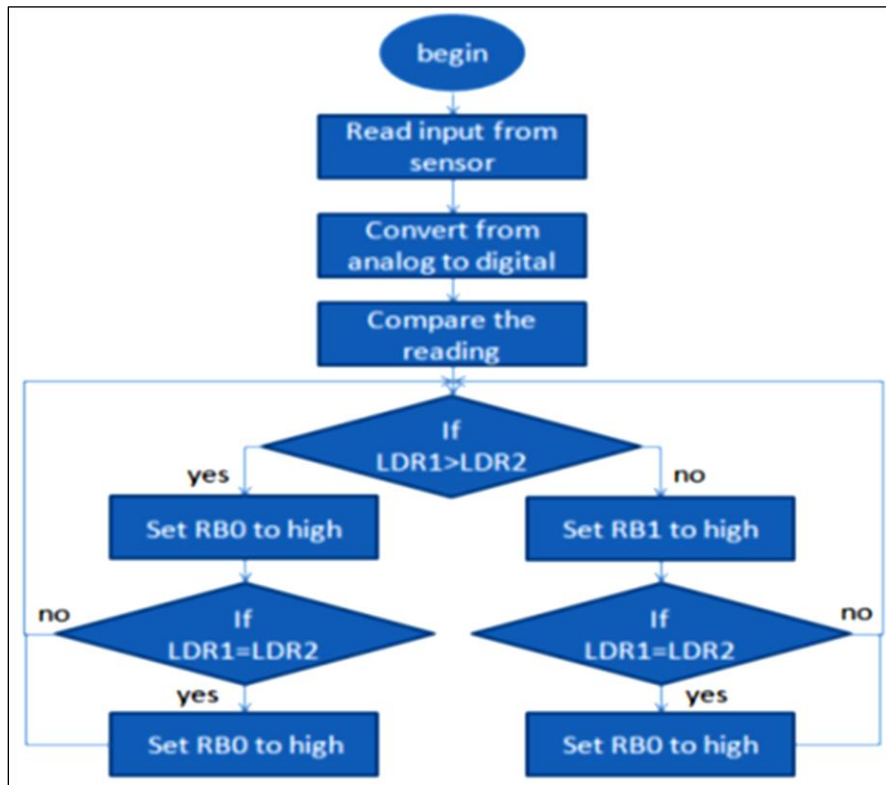


Figure 3: Flowchart of the tracking system control algorithm

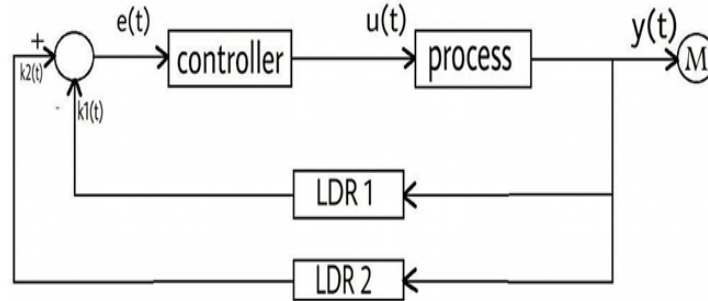


Figure 4: System control protocol

The error signal $e(t)$ is compared with the light intensity detected by the two LDRs as feedback signal. Therefore, the output error signal or the voltage difference will control to the movement direction of the PV panel, so as to bring it normally oriented to the incident sun light rays and thus to obtain a maximum conversion efficiency of light into electricity. The error signal is characterized by the difference between two sensors signals $K_1(t)$ and $K_2(t)$ through the relation given by:

$$e(t) = k_2(t) - k_1(t) \quad (1)$$

Where $k_1(t)$ and $k_2(t)$ are the first and second sensor signal, respectively. Depending on the light intensity imposed to the both sensors, there is a difference in the internal resistance value. That means when LDR1 receives much light than LDR2, then the internal resistance value of LDR1 is smaller than of LDR2 and hence this difference value will be received by the controller which works as a comparator that the output will send a signal to one of the transistors (processor) which works as On/Off switch, hence the transistor connects the current to the relay which controls the DC motor, as shown in figure 4. However, the DC motor ensures the PV panel movement according to system protocol, as follows:

$$e(t) = 0 \text{ no move} \quad (2)$$

$$e(t) > 0 \text{ right move} \quad (3)$$

$$e(t) < 0 \text{ left move} \quad (4)$$

This process will be continued during the whole day until sun set. Therefore, the controller will receive a signal from the limit switch that the DC motor will move to its original position and stops its movement until the second day, and so on. This process is also happened in a very cloudy day. In this case, the motor control unit will readjust the solar panel position until the sun shines again to continue the desired protocol, but this phenomena is rarely happened in our climate here in Libya.

3 Experimental Investigation

Experimental investigation was carried out in order to compare the performance of the solar tracking PV panel in comparison with a fixed PV panel of the same type. In this direction, an extensive experimental work at Faculty of Engineering, Sabratha-Libya was performed, to determine practically how solar PV tracking system can be optimized to extract the maximum power. Unfortunately, no long term ground global horizontal measurement stations were located near the site selected. However, it should be realized that all the data used in this work were based on the calculation of solar radiation in Sabratha city using MATLAB simulation software.

The photovoltaic performance of solar module was obtained by measuring the current–voltage characteristics under natural climate conditions. The PV modules under investigation which were installed on the roof top of Electrical Engineering Department are TE750 TOTAL poly-crystalline commercially modules with capacity of 75 W and dimension of 31x125 cm² for each module. The typical specifications of the PV solar module at STC (AM1.5, 100W/m² at 25 °C) is shown in Table I.

Table 1: Technical Data for Solar Module

Electrical characteristics	Specifications
Module type	TOTAL TE750
Number of Cells	80
Typical Peak Power (P_{max})	75W
Voltage at Peak Power (V_{mp})	17 V
Current at Peak Power (I_{mp})	4.4 A
Short Circuit Current (I_{sc})	4.7 A
Open Circuit Voltage (V_{oc})	21.6 V
Minimum Power (P_{min})	70.1 W
Minimum Pass Diode	6 A
Minimum Series Fuse Rate	8 A

Unlike the classical fixed PV panel, the mobile one driven by solar tracker is kept under optimum insolation for all positions of the Sun, boosting thus the PV conversion efficiency of the system. The experimental procedure is characterized by measuring the output current, voltage and power produced from PV module that using single axis solar tracker system that automatically searches the optimum panel position with respect to the sun is compared with 30° tilt angle fixed PV module to act as a comparison reference. It is documented from previous study that this tilt angle is found as the optimum angle for four seasons at this location [2]. However, to demonstrate that the tracking system was working in optimum conditions, a video camera has installed and observe the movement of the PV module if it can response to the sun position during the whole day. It was found that, fortunately, the system was working perfect and satisfactory results have been determined and documented.

4 Results and Discussion

Solar irradiance is one of the most important parameter for evaluation of PV system performance. Based on site metrological data (latitude and longitude) of sabratak city, where the PV module characteristics measurements were taken, a simulation of solar radiation has been performed. The calculations have been done during the whole year. For comparison, two days in summer season where the sun shine duration is more than 7 hours (at about 1000 W/m² incident power) have been chosen. Figure 5 and figure 6 illustrate the average solar irradiance (W/m²) incident on 30° tilted PV module. The calculations have been done for one day from the sun rise to sun set. As can be seen, it is found that the simulation results is in agreement with the data registered from metrological stations in Libya.

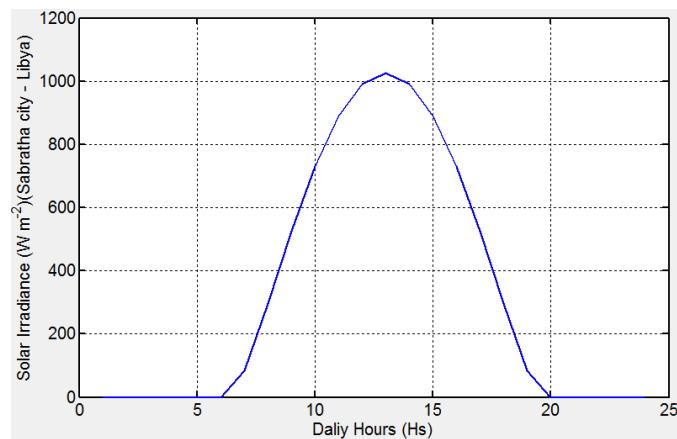


Figure 5: calculated solar radiation on tilted PV module using MATLAB simulation software (29.06.2017)

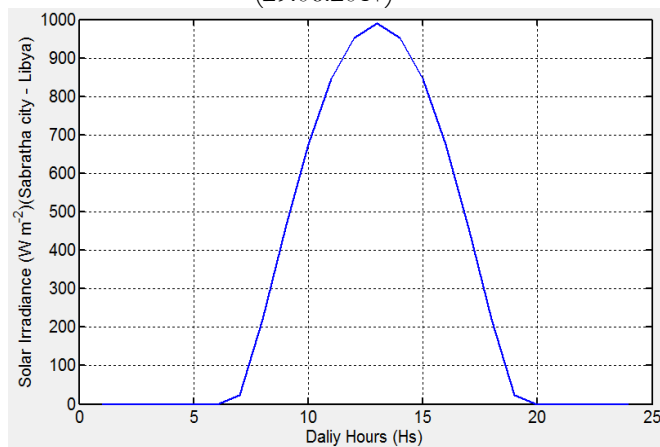


Figure 6: calculated solar radiation on tilted PV module (16.08.2017)

By measuring the current-voltage characteristics, the dependence of the photovoltaic performance on the solar irradiance has been investigated. The output power production of PV tracking module as compared to the fixed PV panel has been obtained, respectively. The

measurements have been taken during four seasons and annual analysis has been documented. Since, the short circuit current (I_{sc}) increases linearly with irradiance increasing, while the open-circuit voltage increases logarithmically with intensity, it is focused on the dependence of current on solar irradiance for both PV modules, due to the strongly dependence on radiation intensity [6]. The dependence of I_{sc} on the solar radiation for fixed and tracking modules at selected two days are shown in figures 7 and 8.

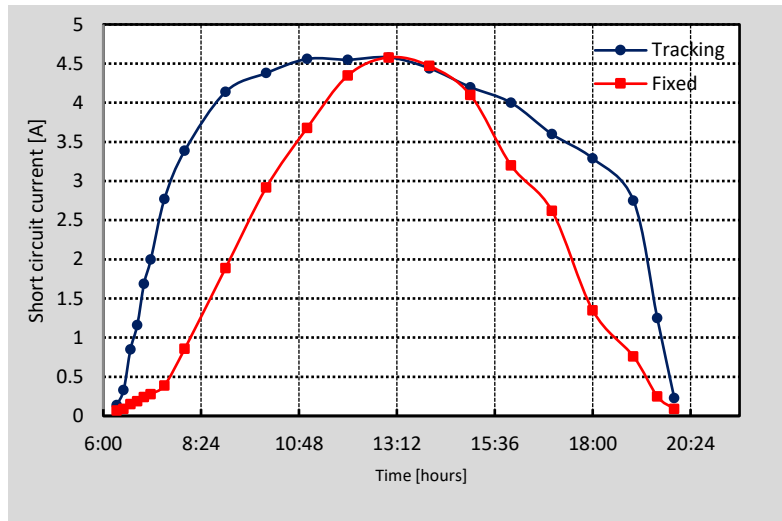


Figure 7: The dependence of the ISC on the solar irradiance (29.06.2017)

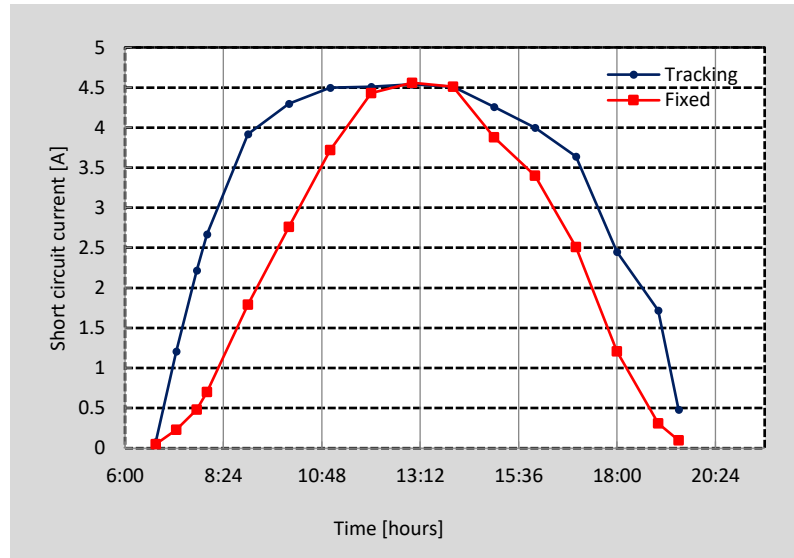


Figure 8: The dependence of ISC on the solar irradiance (16.08.2017)

As can be seen, the maximum current is obtained at the med day where the solar irradiance is maximum. On the other hand, the maximum performance obtained at optimum positions are very close to the module data specifications illustrated in table I. However, results show an increase in current of tracked panel as compared to the tilted fixed panel. This is because the maximum solar radiation is almost falling perpendicular on the tracked module surface during

the whole day, which is not possible for the fixed PV panel [7]. The tracked module achieves higher performance at the morning and evening period than the fixed PV panel, reaching up to 60% improvement at this time period due to the more light intensity absorbance. It is observed that at midday almost both panels have same output and no significant difference in current because of the same tilt angles at this time and all the systems receive almost the same amount of irradiation approximately. Finally, according to our results, it is demonstrated that the single-axis tracking panel has the highest performance compared to the other fixed PV panel.

5 Conclusions

The sun tracking has an essential advantage that provides the maximum output energy with high accuracy against any variation of incident light from the sun or climatic conditions change compare to fixed PV module due to the surface of PV module is not perpendicular toward the sun at each time. In this work, an experimental study has been made to improve the PV system output performance through maintaining the module surface in optimum position for receiving maximum solar radiation. In this direction, single-axis solar PV tracking system has been designed and executed. To demonstrate of the feasibility and effectiveness of solar tracking system, an experimental investigation has been performed.

The current–voltage characteristics of the tracked PV module have been carried out and the dependence of the short circuit current on solar irradiance has been determined. From these measurements, it has been found that there is an significant improvement in the PV module performance and an enhancement in module current of more than 60% has been obtained compared to the tilted fix PV module, specially at the morning and evening time periods. This can be explained by that the tracked module surface almost remains under perpendicular irradiance receiving maximum radiation during the whole day.

References

- [1] REN21, Renewables 2017, Global Status Report, PP. 63-71, Paris: REN21 Secretariat, ISBN 978-3-9818107-6-9.
- [2] S. Mousa, I. Najem, O. Wehida, A. Khelifa, and A. Kagilik, "Optimization of Tilt Angle for Extracting Maximum Power from Photovoltaic Modules", *Libyan International Conference on Electrical Engineering and Technologies (LICEET 2018)*, 4-6 March, 2018, Tripoli – Libya.
- [3] Bill Lane, "Solar Tracker", *EEC 517*, Department of Electrical and Computer Engineering, Cleveland State University, April 30, 2008.
- [4] Tiberiu Tudorache, Constantin Daniel Oancea, Liviu Kreindler, "Performance evaluation of a solar tracking PV panel", *U.P.B. Sci. Bull., Series C*, Vol. 74, Iss. 1, PP. 3-10, 2012, ISSN 1454-234x.
- [5] Mostafa mehrtash, Guillermo quesada, Yvan dutil, Daniel rouse, "Performance Evaluation of Sun Tracking Photovoltaic Systems in Canada", *20th Annual International Conference on Mechanical Engineering-ISME2012*, 16-18 May, 2012, School of Mechanical Eng., Shiraz University, Shiraz, Iran, ISME2012-2329.
- [6] S. Buday, "Measuring irradiance, temperature and angle of incidence effects on photovoltaic modules in Auburn Hills, Michigan", *MSc Thesis*, University of Michigan, August, 2011
- [7] S. Lakeou, E. Ososanya, B.O. Latigo, W. Mahmoud, " Design of a Low-cost Solar Tracking Photo-Voltaic (PV) Module and Wind Turbine Combination System", University of the District of Columbia.

Comparative Analysis of Electric Field and Potential Distributions over Porcelain and Glass Insulators Using Finite Element Method

Adnan S. Krzma*, Mahmoud Y. Khamaira, Maruwan Abdulsamad

Department of Electrical and Computer Engineering, Faculty of Engineering,
Elmergib University, Libya

DOI: <https://doi.org/10.21467/proceedings.2.22>

* Corresponding author email: Salamaek@Elmergib.edu.ly

ABSTRACT

This paper investigates the electrical performance of outdoor porcelain and glass insulators when subjected to an 11 kV AC voltage. The insulators are modeled in two dimensions, and the analysis of COMSOL software is used for the finite element simulations. The electric field and voltage distribution in the vicinity of the insulator surfaces were computed and examined. Comparative studies of field and equipotential lines for the insulators are presented under both dry clean and wet polluted conditions. The pollution layer over the insulator surfaces are assumed to be uniform with 0.5 mm thickness. The simulation results show that the field distribution of porcelain and glass insulators were obviously depended on the contamination conditions. The critical of high field regions on both surfaces were identified and the effect of the pollution on the electric field distribution was revealed. The results also confirmed that porcelain insulator has slightly higher field distribution near the high voltage end compared with the glass surface.

Keywords: Electric field distribution, potential distribution, finite element method, porcelain insulator, glass insulator.

1 Introduction

Outdoor high voltage insulators play an important role in the reliability of power system networks [1, 2]. Ceramic insulators have been extensively used in power transmission lines and distribution systems. In fact, insulator has crucial problems when exposed to environmental and electrical conditions. The problem of the pollution is one of the phenomena affect the insulator experienced by many utilities [3, 4]. The presence of the pollution layer on the insulating surface is quite common especially in costal and industrial areas. It is known that the performance of the dry insulator surface remains usually unchanged. But, when the polluted surface becomes wet, water films are formed on the insulating surface and noticeable leakage current flows [5]. The flow of leakage current on the insulator surface may increase



© 2018 Copyright held by the author(s). Published by AIJR Publisher in Proceedings of First Conference for Engineering Sciences and Technology (CEST-2018), September 25-27, 2018, vol. 1.

This is an open access article under [Creative Commons Attribution-NonCommercial 4.0 International](https://creativecommons.org/licenses/by-nc/4.0/) (CC BY-NC 4.0) license, which permits any non-commercial use, distribution, adaptation, and reproduction in any medium, as long as the original work is properly cited. ISBN: 978-81-936820-5-0

the probability of dry band arcing and this can eventually cause a complete flashover or degrade the insulator [6]. Therefore, field and potential distribution around the insulator are essential not only for the dry clean surface, but also for wet polluted condition. Moreover, knowing the electric field distribution along the insulator surface is very important for the detection of defects in the insulator. On this basis, computation of potential changes and field distribution is believed to provide valuable information on the state of the insulator and this may improve the reliability of the system [7].

In this paper, the performance of cap and pin ceramic insulators is investigated. The insulators are modelled based on the Finite Element Method (FEM) and a two dimension (2D) model COMSOL Multiphysics software is used for the simulation. The main purpose of the simulation was to evaluate the electrical performance of porcelain and glass surfaces under both dry clean and wet polluted conditions.

2 Insulator Profile and Computational Modeling

2.1 Insulator Profile

The insulator investigated in this study is a standard cap and pin suspension insulator rated at 11 kV. The insulating material and geometry of the insulator are shown in Figure 1.

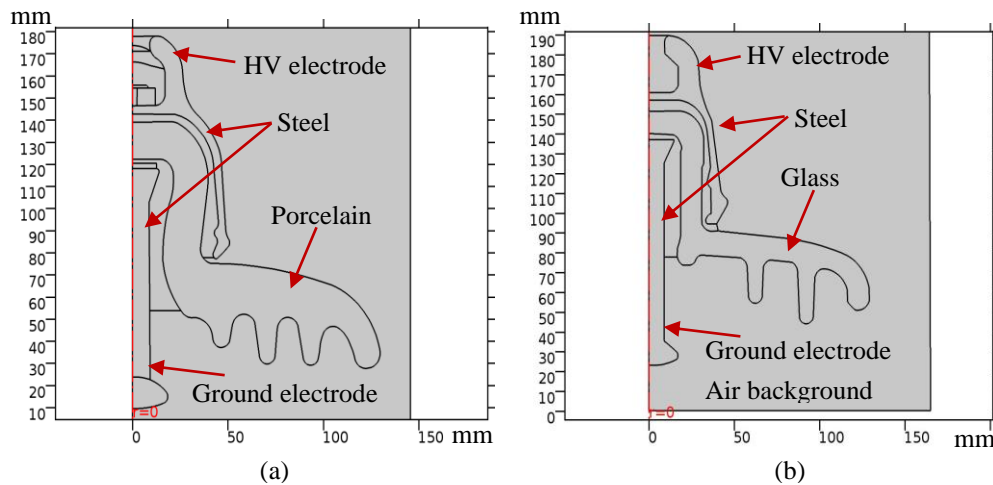
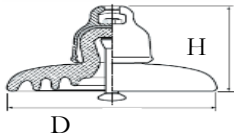



Figure 1: Cross-sectional profile of an 11 kV cap and pin insulator: (a) porcelain (b) glass

The technical dimensions of 81022 porcelain and U100BL glass profiles are summarized in Table 1, in which D is the diameter of the insulating part, H is the configuration height and L is the nominal leakage distance.

Table 1: Dimensions of 81022 porcelain and U100BL glass insulators

Profile	Material	Parameters (mm)		
		D	H	L
	Porcelain	257	146	320
	Glass	255	127	320

2.2 Material Properties

The insulators are generally comprised of two main components. The dielectric component which are porcelain and glass and the terminations which are cap and pin. The insulating housing is made of porcelain and glass materials with a relative permittivity of $\epsilon_r = 4.2$. The end fitting elements used for the high voltage and ground electrodes are made of a steel. These fittings are crimped to the dielectric to support the mechanical strength of the insulator. In this simulation, the dielectric materials of porcelain and glass were assumed to be perfect insulators with a conductivity of $1 * 10^{-14}$ S/m. The air background region surrounding the insulators was specified with appropriate conductivity of $1 * 10^{-15}$ S/m. The pollution layer along the insulator surfaces is assumed to be uniform with 1.5 mm thickness. The conductivity of the pollution layer was adopted from the laboratory with a value of $600 * 10^{-16}$ S/m and the permittivity of the layer is set to be 81 [8]. The electrical properties used for the insulator modeling are specified in Table 2.

Table 2: Dimensions of 81022 porcelain and U100BL glass insulators

Material	Relative permittivity, ϵ_r	Conductivity, σ (S/m)
Air	1.0	$1 * 10^{-15}$
Porcelain	4.2	$1 * 10^{-14}$
Glass	4.2	$1 * 10^{-14}$
Steel	1.0	$1.45 * 10^6$
Cement	2.09	$1 * 10^{-14}$
Pollution layer	81	$600 * 10^{-6}$

The high voltage (HV) terminal which represents the cap was energised with an AC voltage of 11kV at 50 Hz. This r.m.s value was subjected to the insulator under both dry clean and wet polluted conditions, according to the IEC 60507 standard [9]. The lower pin terminal was connected to the ground at 0 V. The air region surrounding the insulator is simulated effectively large to reduce its influence on the potential distribution over the insulator profile

and near to the electrodes. The outer edges of the air region are allocated with a boundary that expected zero external current and electromagnetic sources, hence demonstrating a physical system that is in isolated open space.

2.3 Finite Element Method (FEM)

The procedure for creating the 2D symmetrical model was achieved by drawing the insulator using AutoCAD tools and saved in an extension file of dxf format. The insulator was then imported to the COMSOL 5.2 Multiphysics software. The simplification of using the 2D model instead of three dimensions (3D) model is preferred. This is because it saves a significant size of memory and processing time without affecting the accuracy of the simulation results. In addition, using symmetric model, only half of the insulator structure was modelled.

After completing the stage of the structure, the model is assigned with a suitable material properties and boundaries conditions as previously described. As a part of FEM system, the entire geometry of the insulator except the end fitting regions were divided into small triangular elements as shown in Figure 2. This process is called the meshing. This meshing discretisation can enhance the accuracy of the simulation results by increasing the number of meshing elements over the insulator surface where the field intensity is found to be higher.

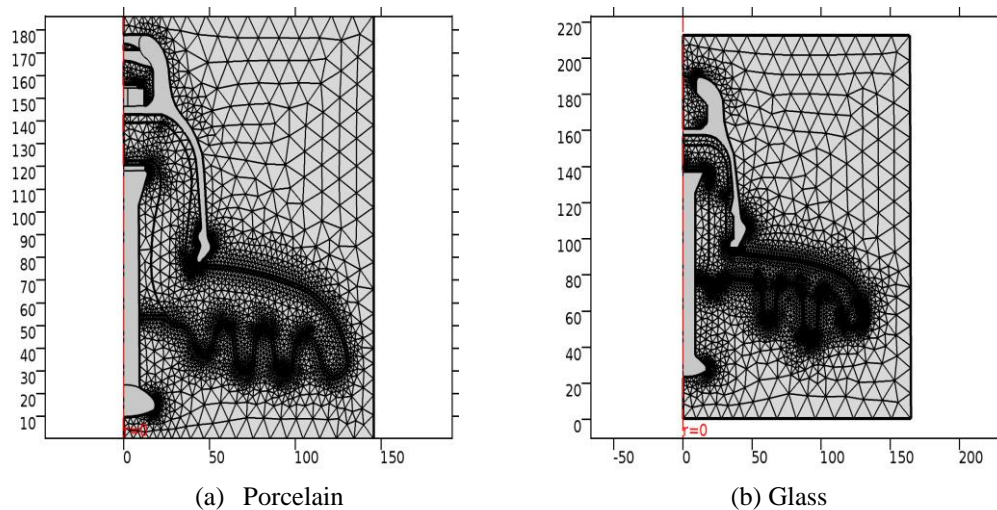


Figure 2: Meshing discretisation of insulator domain (a) Porcelain (b) Glass

The insulator model is analysed using the FEM based on Quasi-Static Electric mode, which assumes that the current changing slowly with the electromagnetic field [10]. This assumption is effective for insulator and many high voltage applications that operate at 50 Hz power frequency. The potential and field distribution are computed by solving the differential equation in the software given by equation (1).

$$-\nabla \cdot (\epsilon_0 \epsilon_r \nabla V) / \partial t - \nabla \cdot (\sigma \nabla V - J_e) = QJ \tag{1}$$

Where J_e : External current density (A/m²)

QJ : Current source (A/m³)

σ : Electric conductivity (S/m)

ϵ : Permittivity

3 Simulation Results and Discussion

3.1 Potential Distribution

The voltage distributions along the porcelain and glass insulators were computed for analysing and investigation studies. Figure 3(a) and Figure 3(b) respectively show the equipotential lines along the porcelain surface under both dry clean and wet polluted conditions. The lines are modeled at 5% voltage interval, therefore a total of 20 equipotential lines are plotted in the simulation results. The same action for voltage computation was achieved over the glass surface and Figure 3(c) and Figure 3(d) respectively observe the behaviour of the insulator under a certain conditions. As can be seen from both insulators, more than 75% of the voltage lines concentrated between the pin fitting and the first inner skirt. Over 15% of the voltage contours is concentrated nearby the cap.

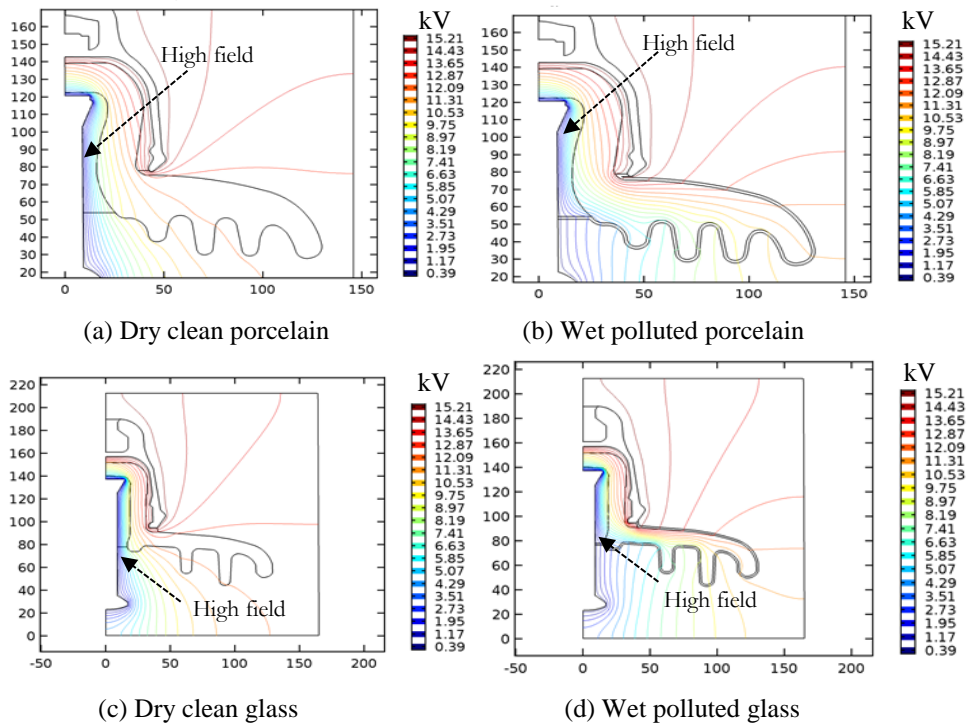
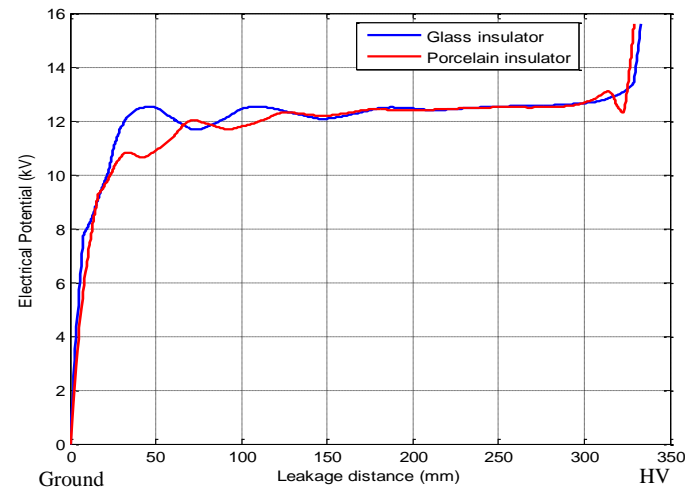
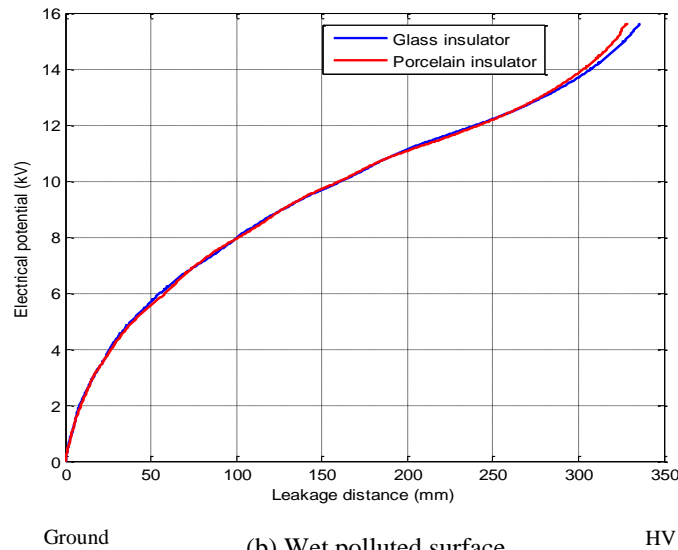


Figure 3: Equipotential contours over the surface profile of porcelain and glass insulators under dry clean and uniformly wet polluted conditions

The lines are commonly concentrated close to the end fitting regions and this may indicate to the highly field stress. When the insulator is polluted, the potential distributions are start to be uniform compared with those attained from the clean surface. This behaviour happens due to the presence of the pollution layer which helps to redistribute the potential lines widespread over the surface. The computed voltage profile along the porcelain and glass insulators under both surface conditions are shown in Figure 4. The leakage path of the insulator is measured along the surface, starting from the ground and termination at the HV end. An increase trend is observed for both graphs when shifting to the energisation end.



(a) Dry clean surface



(b) Wet polluted surface

Figure 4: Voltage profiles along the porcelain and glass insulators: (a) dry clean, and (b) wet polluted

For dry clean insulators, a steep rise in the potential is observed up to 11 kV for the porcelain and 12 kV for the glass at a surface distance of 40 mm nearby the ground end. The clean surface also shows curve undulations because of the individual lines cross the insulator at more than one points. These undulations are accompanied by electric field reveal over the insulator. For wet polluted conditions, the water droplets hit the top of the polluted surface and local variations in the resistive current can occur. This behaviour may redistribute the voltage profile and extremely high field can be initiated.

3.2 Electric Field Distribution

Figure 5 and Figure 6 show respectively the plot results of field distributions along the porcelain and glass insulators under dry clean and wet polluted surface conditions. The simulated field was represented the tangential electric field along the insulator surface. The graphs, in general, exhibit a similar tendency of field distributions along the surface profiles. Peaks can be observed in the rate of change of the tangential field at both HV and ground ends. These peaks confirmed the equipotential results concerning the high field regions. Under wet polluted condition, the tangential field attained on both surfaces was higher compared with the dry clean case. The highest field recorded was near to the metal fittings with magnitude value of 3.2 kV/cm. However, away from the metal fittings along the surface distance of the insulators, the trend of the electric field was reduced to a lower value.

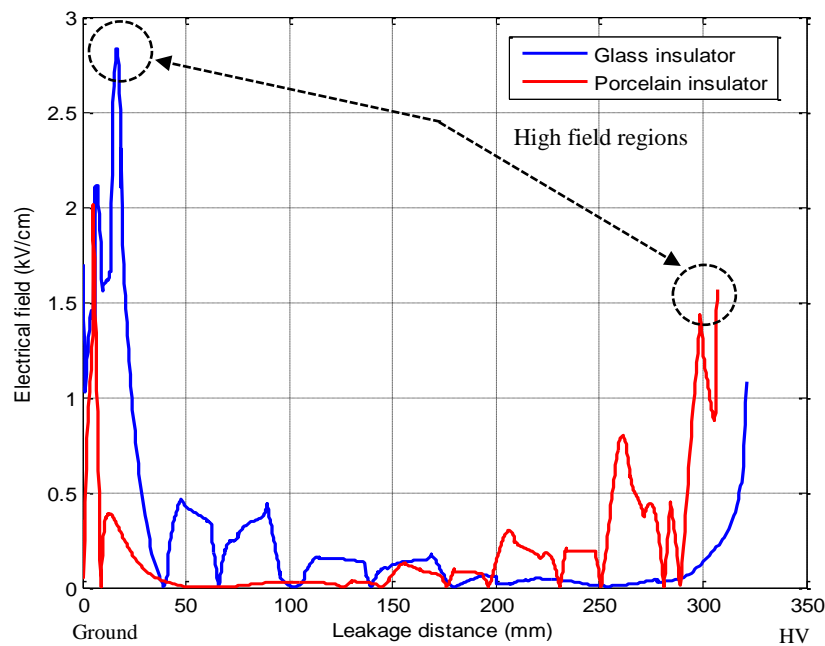


Figure 5: Field distributions over the surface of porcelain and glass insulators under dry clean condition

Porcelain insulator exhibit a significant increase in the field near to the HV terminal compared with the glass. This can be observed under both dry clean and wet polluted conditions. Therefore, the presence of the pollution layer can increase the possibility of the electric field at the insulator surface and this may lead to the surface heating and eventually to the flashover.

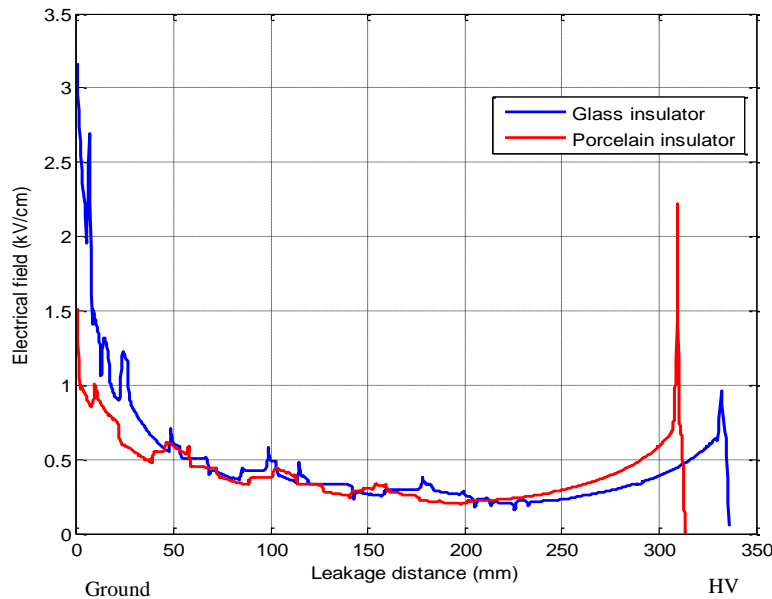


Figure 6: Field distributions over the surface of porcelain and glass insulators under wet polluted condition

4 Conclusions

The electrical performance of porcelain and glass insulators was investigated in this paper. The potential and field distributions over the insulator surfaces were studied using the Finite Element Method COMSOL Multiphysics Software. An ideal model has been adopted for an easily simulation the laboratory test conditions. The tangential field was performed on the insulator surfaces for both dry clean and wet polluted conditions. The result reveals that the highly field region was observed on the polluted insulators as expected. At the high voltage end region where is the extremely field stress, glass insulator offers better electrical performance compared with the porcelain. These all useful information might be worth to understand the insulator properties and to choose an appropriate design.

References

- [1] J. S. T. Looms. *Insulators for High Voltages*. London, United Kingdom: Peter Peregrinus Ltd, 1988, pp. 2-12.
- [2] R. S. Gorur, E. A. Cherney, and J. T. Burnham, *Outdoor Insulators*, Ravi S. Gorur, Inc., Phoenix, Arizona, USA, 1999.
- [3] S. Chakravorti and H. Steinbigler, "Boundary element studies on insulator shape and electric field around HV insulators with or without pollution," *IEEE Transactions on Dielectrics and Electrical Insulation*, vol.7, no.2,

- [4] A. S. Krzma, M. Albano, and A. Haddad, "Comparative performance of 11kV silicone rubber insulators using artificial pollution tests," in 2015 50th International Universities Power Engineering Conference (UPEC), Stoke On Trent, United Kingdom, pp. 1–6, 2015.
- [5] CIGRE Taskforce 33.04.01: "Polluted insulators: review of current knowledge," CIGRE technical brochure 158, June 2000.
- [6] A. S. Krzma, M. Albano, and A. Haddad, "Flashover influence of fog rate on the characteristics of polluted silicone rubber insulators," in 2017 52th International Universities Power Engineering Conference (UPEC), Crete, Greece, pp. 1–6, 2017.
- [7] J. L. Rasolonjanahary, L. Krahenbuhl, and A. Nicolas, "Computation of electric fields and potential on polluted insulators using a boundary element method," *IEEE Transactions on Magnetics*, vol.28, no.2, pp.1473-1476, Mar 1992.
- [8] M. Albano, A. S. Krzma, R. T. Waters, H. Griffiths, and A. Haddad, "Artificial pollution layer characterization on conventional and textured silicone-rubber insulators," in The 19th International Symposium on High Voltage Engineering (ISH), Pilsen, Czech Republic, 2015.
- [9] IEC 60507:2013, 'Artificial pollution tests on high-voltage ceramic and glass insulators to be used on a.c. systems', 3rd edition.
- [10] COMSOL Multiphysics User's Manual," ed: Version 5.2.

Long Term Peak Load Forecasting for the Libyan Network

Mahmoud Y. Khamaira *, Adnan S. Krzma, A. M. Alnass

Department of Electrical and Computer Engineering, Faculty of Engineering, Elmergib University, Libya

DOI: <https://doi.org/10.21467/proceedings.2.23>

* Corresponding author email: mykhamaira@Elmergib.edu.ly

ABSTRACT

Long term load demand forecasting is a necessary process in electric power system operation and development. It contains the accurate prediction of both magnitudes and geographical locations of electric load over the different periods of the planning horizon. Several economic implications of power utility such as economic scheduling of generating capacity, scheduling of fuel purchases, security analysis, planning of power development, maintenance scheduling and dispatching of generation units are mainly worked based on accurate load forecasting. In this paper, the peak load for seven years ahead is performed for the Libyan electric network with the simple regression method. MATLAB programming has been used for computational work. The results attained are validated with the real data obtained from the National Control Center of the General Electricity Company of Libya (GECOL).

Keywords: Long term load forecasting, Simple regression, Libyan network

1 Introduction

Global electricity demand is expected to growth by 85% in 2040 as living standards increase, economies expand and the requirement for electrification of society continues [1]. Electricity demand calculating plays a vital role in load allocation and scheduling for future generation facilities and transmission development. Load demand in a given season is subject to a range of uncertainties, comprising population growth, climate change and economic circumstances. Furthermore, historical data are significance in demand predicting. Load forecasting can be divided into three categories: short-term forecasts, medium-term forecasts and long term forecasts. Short-term forecasts are usually from one hour to one week. They play an important role in the day-to-day operations of a utility such as unit commitment, economic dispatch and load management. A short term electricity demand forecast is commonly mentioned to as an hourly load prediction. Medium-term forecasts are usually from a several weeks to a few months and even up to a one year. They are necessary in planning fuel procurement, scheduling unit maintenance and energy trading and revenue assessment for the utilities. A



© 2018 Copyright held by the author(s). Published by AIJR Publisher in Proceedings of First Conference for Engineering Sciences and Technology (CEST-2018), September 25-27, 2018, vol. 1.

This is an open access article under [Creative Commons Attribution-NonCommercial 4.0 International](https://creativecommons.org/licenses/by-nc/4.0/) (CC BY-NC 4.0) license, which permits any non-commercial use, distribution, adaptation, and reproduction in any medium, as long as the original work is properly cited. ISBN: 978-81-936820-5-0

medium-term forecast is commonly referred to as the monthly load forecast. Long-term electricity demand forecasting is a crucial part in the electric power system planning, tariff regulation and energy trading [2]. A long-term forecast is required to be valid from 5 to 25 years. This type of forecast is used to deciding on the system generation and transmission expansion plans. A long term forecast is generally known as an annual peak load [1].

This work offers an uncomplicated technique to forecast the future peak demand for the Libyan electric network. The offered technique might be useful to determine the powerful energy management strategy so as to meet the required load demand at minimum operating cost. In addition, the factors affecting load patterns are presented.

1.1 Factors Affecting Load Patterns

A large number of factors influence the load demand considerably. The effects of all these factors which affect the load need to be studied in order to improve an accurate load forecasting model.

1.2 Economic factor

Several economic factors such as the type of customers such as residential, agricultural, commercial and industrial, demographic conditions, population, GDP growth, national economic growth and social activities etc. can cause a significant variation in the load pattern. These economic factors generally affect the long-term load forecasting.

1.3 Weather Factors

Load forecasting is significantly affected by weather conditions such as temperature (dry and wet temperature), humidity, cloud coverage etc. The most essential weather factor is the temperature. The variations considerably affect the load requirement for heating in winter and air conditioning in summer. Load forecasting also affected by other factors such as humidity especially in hot and humid areas, wind speed and light intensity of the day [3].

1.4 Time and Seasonal Factors

Time factors play an important role in accurate load forecasting. It may cause a considerable change in load pattern. There are following factors;

- Seasonal variation: change of season (summer, winter, rainy and autumn), change of day light hours, change of average temperature, etc.
- Daily variation: different day time and night time consumption
- Weekly cycle: Different weekday and weekend consumption patterns
- Holidays and special days: Load pattern on holidays will be different from that of weekdays and weekend. Special days such as festive days can affect the load.

1.5 Price Factor

Load forecasting is strongly affected by electricity price. Electrical price which may have a complicated relationship with the system load, it is an important factor in load forecasting. Change in tariff may also change the load pattern.

1.6 Random Disturbances

A random disturbance happens in the power system which may disturb the load pattern considerably. The random disturbances include sudden shutdown or start of industries, wide spread strikes, marriages, special functions etc. [4].

1.7 Other Factors

In addition to all the factors listed above, the load pattern may also change due to geographical condition (urban or rural areas), type of consumers (rural or urban), home appliances sale data, television program (sports, serial etc.) etc. [3]

2 Literature Survey

Generally, long-term load demand forecasting methods can be classified in to two categories: artificial intelligence based methods and parametric methods [5]. The artificial intelligence based methods are further classified in to neural networks [6-10] support vector machines [11], genetic algorithms [12], wavelet networks [13, 14], fuzzy logics [15] and expert system [16] methods. The parametric methods are based on relating load demand to its affecting factors by a mathematical model. The model parameters are estimated using statistical techniques on historical data of load and it's affecting factors. Parametric load forecasting methods can be generally categorized under three approaches: regression methods, time series prediction methods [17]. Traditional statistical load demand forecasting techniques or parametric methods have been used in practice for a long time. These traditional methods can be combined using weighted multi-model forecasting techniques, showing adequate results in practical system. These methods cannot properly present the complex nonlinear relationships that exist between the load and factors that influence on it [18].

3 Simple Linear Regression

A regression model is a statistical procedure that allows a researcher to estimate the linear relationship that relates two or more variables. This linear relationship summarizes the amount of change in one variable that is associated with change in another variable or variables. However, the straight line connecting any two variables X (independent variable) and Y (dependent variable) can be stated algebraically as [19];

$$Y = \beta_0 + \beta_1 X + \varepsilon \quad (1)$$

where β_0 and β_1 are two unknown constants that represent the intercept and slope, known as coefficients, and ϵ is the error term. Given some estimates $\hat{\beta}_0$ and $\hat{\beta}_1$ for the model coefficients, the future values can be predicted as following;

$$\hat{y} = \hat{\beta}_0 + \hat{\beta}_1 x \tag{2}$$

where \hat{y} indicates a prediction of Y on the basis of $X = x$. The hat symbol denotes an estimated value.

Let $\hat{y} = \hat{\beta}_0 + \hat{\beta}_1 x_i$ be the prediction for Y based on the i th value of X . Then $e_i = y_i - \hat{y}_i$ represents the i th residual.

The residual sum of squares (RSS) is defined as;

$$RSS = e^2_1 + e^2_2 + \dots + e^2_n \tag{3}$$

The least squares approach chooses $\hat{\beta}_0$ and $\hat{\beta}_1$ to minimize the RSS. The minimizing values can be shown to be;

$$\hat{\beta}_1 = \frac{\sum_{i=1}^n (x_i - \bar{x})(y_i - \bar{y})}{\sum_{i=1}^n (x_i - \bar{x})^2} \tag{4}$$

$$\hat{\beta}_0 = \bar{y} - \hat{\beta}_1 \bar{x} \tag{5}$$

Where $\bar{y} = \frac{1}{n} \sum_{i=1}^n y_i$ and $\bar{x} = \frac{1}{n} \sum_{i=1}^n x_i$ are the sample means.

3.1 Assessing the Overall Accuracy of the Model

For making sure that used model is giving a good relationship between the considered variables, the Residual Standard Error (R2) can be calculated as follows [19];

$$R^2 = \frac{\text{Residual sum of squares}}{\text{Total sum of squares}} = 1 - \frac{\sum_{i=1}^n (y_i - \hat{y}_i)^2}{\sum_{i=1}^n (y_i - \bar{y})^2} \tag{7}$$

The minimum value for R^2 is 0. This would occur when there is no relationship between the two variables, so that X does not help at all in explaining the differences in values of Y . The maximum possible value for R^2 is 1. This would occur when the two variables are perfectly related, so that the observed values of Y exactly correspond with the predicted values from the regression line, and there are no prediction errors. This would mean a perfect goodness of fit.

3.2 Model Implementation

In this section, a regression model will be performed for forecasting the future peak load for the Libyan network. Data, that used to prepare the forecasted model, are as shown in the Table 1.

According to the historical data available for the peak load as shown in table 1, it is noticed that during the period (2000-2010) the growth rate is different than that in the period (2013-2017) and this due to the situation during the period (2011-2012). This difference of the growth rate that dropped from 5760 MW to 5515 MW and then jumped to 5981 MW, makes it difficult to perform a model that gives an accurate expectation, if the whole period is considered at once, therefore, the period from (2000-2017) is divided according to the growth

rate. The first period from (2000-2010), and the second one is (2013-2017), and each period is considered as a case study.

Table 1: *Historical data*

<i>Year</i>	<i>Populati on $x_i * 10^6$</i>	<i>Peak load (MW) Y_{actual}</i>
2000	4.83	2630
2001	4.93	2934
2002	5.02	3081
2003	5.12	3341
2004	5.22	3612
2005	5.32	3857
2006	5.42	4005
2007	5.53	4420
2008	5.60	4756
2009	5.74	5282
2010	5.86	5760
2011	5.97	5515
2012	6.08	5981
2013	6.20	6520
2014	6.33	6600
2015	6.45	6750
2016	6.57	7017
2017	6.70	7383

3.3 Case 1 (period 2000-2010)

In this case the historical data for the period (2000-2010) is only considered to achieve a forecasting model. The population is considered an independent variable (x_i) and the historical peak load is a dependent variable Y_i . As the regression model coefficient (β_0, β_1) can be calculated from equations 5 and 6, the forecasting model can be rewritten as following;

$$\hat{y} = -11669 + 0.0029 * x_i \quad (8)$$

From equation 7 the Residual Standard Error (R) also can be calculated;

$$R^2 = 0.996$$

Where;

\hat{y} = expected peak load

x_i = expected number of the population

As the predicated number of the population is available, the future peak load can be estimated from equation 8 as shown in the Table 2 and figure 1.

Table 2: results for case 1

<i>Year</i>	<i>$x_i * 10^6$</i>	<i>Y_{actual} (Mw)</i>	<i>\hat{y} (Mw)</i>
2000	4.83	2630	2.5133
2001	4.93	2934	2.8069
2002	5.02	3081	3.0712
2003	5.12	3341	3.3648
2004	5.22	3612	3.6584
2005	5.32	3857	3.9520
2006	5.42	4005	4.2457
2007	5.53	4420	4.5687
2008	5.60	4756	4.7742
2009	5.74	5282	5.1853
2010	5.86	5760	5.5376
2011	5.97		
2012	6.09		
2013	6.20		
2014	6.33		
2015	6.45		
2016	6.57		
2017	6.70		
2018	6.83		8386
2019	6.96		8768
2020	7.10		9179
2021	7.24		9590
2022	7.38		10001
2023	7.52		10412
2024	7.66		10823
2025	7.81		11263

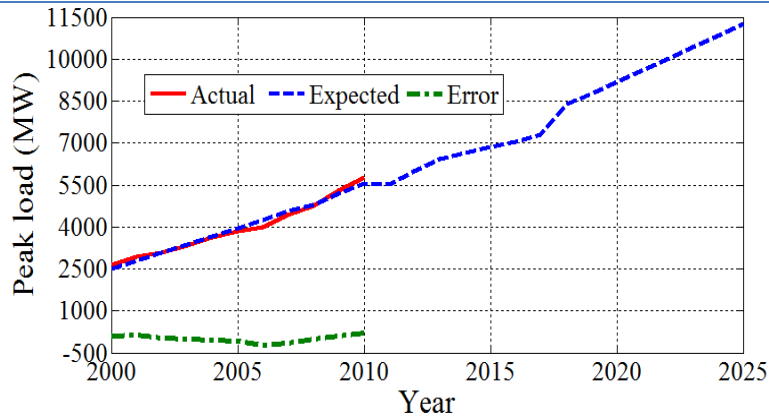


Figure 1: results for case 1

3.4 Case 2 (period 2013-2017)

In this case the historical data for the period (2013-2017) is only considered for performing a forecasting model and the same procedure that was used in the first case is done. The forecasting regression model and the R² for this case can be written as following:

$$\hat{y} = -4292.6 + 0.0017 * x_i \tag{9}$$

$$R^2 = 0.998$$

Table 3: results for case 2

<i>Year</i>	<i>x_i *10⁶</i>	<i>Y_{actual}</i> <i>(Mw)</i>	<i>ŷ (Mw)</i>
2013	6.20	6520	6.422
2014	6.33	6600	6.6466
2015	6.45	6750	6.854
2016	6.57	7017	7.0614
2017	6.70	7383	7.286
2018	6.83		7510.7
2019	6.96		7735.4
2020	7.10		7977.3
2021	7.24		8219.2
2022	7.38		8461.2
2023	7.52		8703.1
2024	7.66		8945.1
2025	7.81		9204.3

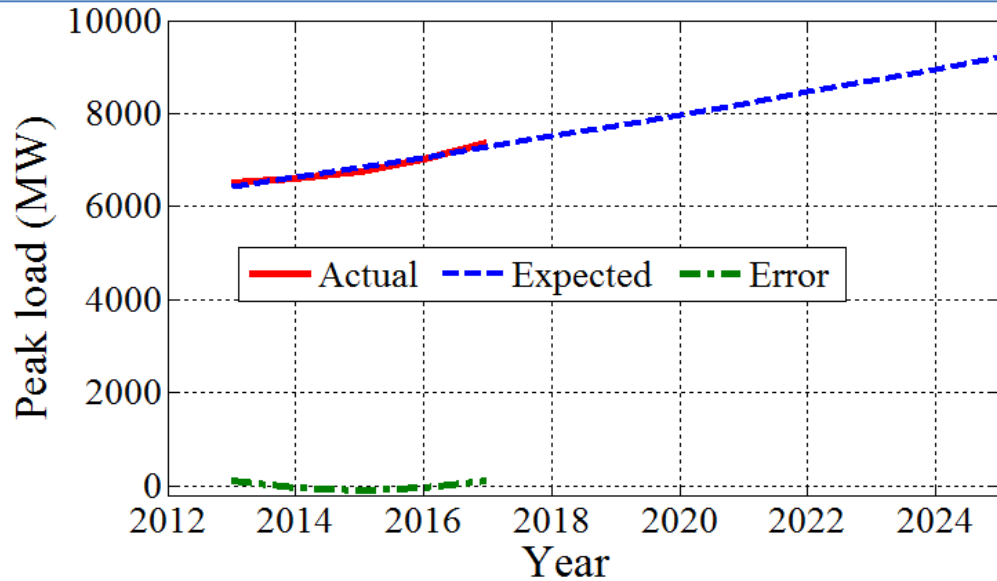


Figure 2: results for case 2

4 Discussion of Results

The simple linear regression method was applied to the peak load from 2000 to 2013. After the SLR was explained, it was used in two cases to forecast the peak load from 2018 to 2025. The results attained for case1 are summarized in the Table 1 and illustrated as graphic form in the figure 1. The data used are the annual peak loads and the population number recorded between years 2000 and 2010. It can be seen from results that the expected peak load at 2025 will be about 11263 Mw. On the other side, results for the case 2 are displayed in the Table 2 and demonstrated as graphic form in the figure 2. Data used are the annual peak loads and the population number recorded between years 2013 and 2017. It can also be also seen from the Table 2 that for case 2 the expected peak load will be around 9204.3 Mw.

5 Conclusions

Electric load predicting considers a vital part in the economic optimization and secure operation of electric power systems. It represents the first step in developing future generation, transmission, and distribution facilities. In this paper, the main factors that affect the accuracy of the load forecasts are presented and the annual peak load for seven years ahead is expected for the Libyan electric network. Results demonstrate that proposed method can be used as a good technique for long term load forecasting with minimum error.

6 Acknowledgment

The authors express their deep gratitude and thanks to engineers of the National Control Centre for the General Electricity Company of Libya for their valuable help and cooperation in this work.

References

- [1] N. Phuangpornpitak, and W. Prommee, "A Study of Load Demand Forecasting Models in Electric Power System Operation and Planning," *GMSARN International Journal* 10 (2016) 19 – 24.
- [2] Pessanha, J.F.M., and Leon, "Forecasting Long-term Electricity Demand in the Residential Sector," *Procedia Computer Science*, 2015, 55, 529-38.
- [3] G. Singh, D.S. Chauhan, A. Chandel, D. Parashar, and G. Sharma, "Factor Affecting Elements and Short term Load forecasting Based on Multiple Linear Regression Method," *International Journal of Engineering Research & Technology*, Vol. 3, Issue 12, December-2014.
- [4] Mahmoud Y. Khamaira, Adnan S. Krzma, A. M. Alnass, and I. R. Jaba, "Modeling and Forecasting Short-Term Electricity Demand for Libyan Electric Network," *The International Journal Of Engineering And Information Technology (IJEIT)*, VOL.4, NO.2, JUNE 2018.
- [5] L. Ghods, and M. Kalantar, "Different Methods of Long-Term Electric Load Demand Forecasting: A Comprehensive Review," *Iranian Journal of Electrical & Electronic Engineering*, Vol. 7, No. 4, Dec. 2011.
- [6] Al Mamun M., and Negasaka K., "Artificial neural networks applied to long-term electricity demand forecasting," *Proceedings of the Fourth International Conference on Hybrid Intelligent Systems*, pp. 204-209, Dec. 2004.
- [7] Dang Khoa T. Q., and Oanh P. T., "Application of Elman and neural wavelet network to long-term load forecasting," *ISEE Journal*, track 3, sec. B, No. 20, pp. 1-6, 2005.
- [8] Negasaka K., and Al Mamun M., "Long-term peak demand prediction of 9 Japanese power utilities using radial basis function networks," *IEEE Power Engineering Society General Meeting*, Vol. 1, pp. 315-322, 6-10 June 2004.
- [9] Taradar H. M., and Kashtiban A. M., "Application of neural networks in power systems; A review," *Transaction of Engineering, Computing and Technology*, Vol. 6, No. 1, ISSN 1305-5313, pp. 53-57, June 2005.
- [10] Kermanshahi B. S., and Iwamiya H., "Up to year 2020 load forecasting using neural nets," *Electric Power System Research*, Vol. 24, No. 9, pp. 789-797, 2002.
- [11] Pai P.-F., and Hong W. C., "Forecasting regional electricity load based on recurrent support vector machines with genetic algorithms," *Electric Power System Research*, Vol. 74, No. 3, pp. 417-425, 2005.
- [12] EL_Naggar K. M., and AL-Rumaih K. A., "Electric load forecasting using genetic based algorithm, optimal filter estimator and least error square technique: Comparative study," *Transaction of Engineering, Computing and Technology*, Vol. 6, pp. 138-142, ISSN 1305- 5313, June 2005.
- [13] Khoa T. Q., Phuong L. M., Binh P. T., and Lien N. T. H., "Application of wavelet and neural network to long-term load forecasting," *International Conference on Power System Technology*, pp. 840-844, Singapore, 21-24 November 2004.
- [14] Khoa T. Q., Phuong L. M., Binh P. T., and Lien N. T. H., "Power load forecasting algorithm based on wavelet packet analysis," *International Conference on Power System Technology*, pp. 987-990, Singapore, 21- 24 November 2004.
- [15] Faraht M. A., "Long-term industrial load forecasting and planning using neural networks technique and fuzzy interface method," *39th International Universities Power Engineering Conference, UPEC 2004*, Vol. 1, pp. 368-372, 2004.
- [16] Kandil M. S., El-Debeiky S. M., and Hasanien N. E., "The implementation of long-term forecasting strategies using a knowledge-based expert system: part-II," *Electric Power System Research*, Vol. 58, No. 1, pp. 19-25, 2001.
- [17] Al-Hamidi H. M., and Soliman S. A., "Longterm/mid-term electric load forecasting based on short-term correlation and annual growth," *Electric Power System Research*, Vol. 74, No. 3, pp. 353-361, June 2005.
- [18] Dang Khoa T. Q., and Oanh P. T., "Application of Elman and neural wavelet network to long-term load forecasting," *ISEE Journal*, track 3, sec. B, No. 20, pp. 1-6, 2005.
- [19] John O. R., Sastry G. P., and David A. D., "Applied Regression Analysis: A Research Tool," Second Edition, Springer, 1998.

THD Investigation of Hybrid Cascaded Multilevel Inverter

Alseddig Elzowawi*, Islam Saad, Mustafa Elsherif

Department of electrical and electronic engineering, Faculty of Engineering, Misurata University, Libya

DOI: <https://doi.org/10.21467/proceedings.2.24>

* Corresponding author email: Alseddig.Elzowawi@eng.misuratau.edu.ly

ABSTRACT

Hybrid cascaded multilevel (HCML) inverter is a modification of the cascaded H-bridge (CHB) inverter, where this inverter has overcome the main drawback of the CHB inverter, which is the connection of a separate DC source in each H-bridge (cell). The solution was connecting one DC source in the first cell, and capacitors in the rest of the cells. Therefore, by controlling the switches of the inverter, the voltages of the capacitors can be regulated at a certain level and the inverter can generate an alternating voltage. In this paper, two cells and three cells HCML inverters have been simulated with PLECS software and modulated with phase shift- pulse width modulation strategy (PS-PWM). This modulation scheme was implemented with C language. The modulation program considers the load current and the voltages of the capacitors as feedbacks. The two inverters have been investigated in terms of the total harmonic distortion (THD) of the voltage and current waveforms. Therefore, the effect of the load sizes and cells number was addressed. Several significant results have been obtained from this study.

Keywords: CHB inverter, HCML Inverter, PS-PWM, THD.

1 Introduction

Cascaded multilevel inverter has become the solution for many renewable energy and motor drive applications due to the considerable advantages. The simplified topology (HCML inverter) has overcome the need to connect a separate DC source in every H-bridge. Therefore, it can suit a wider range of applications in the industry sector as the cost and the size of the inverter are reduced [1, 2, 3]. A growing body of literature has investigated different aspects of this significant inverter. However, one of the major areas of study is the total harmonic distortion in the output voltage and current waveforms generated by the inverter. As the THD contents affects the power quality delivered to the load [4, 5, 6]. In [5] selective harmonic elimination pulse width modulation was suggested to modulate the considered inverters, where the THD was decreased by 10%. In this paper, the methodology used to investigate the THD content in the output waveforms was based on simulation processes. Two inverters with different cells number have been modeled and simulated with PLECS software. Thus, the number of cells and the load components (resistance and inductance) have



been considered to explore their impacts on the THD of the output voltage and the load current. Based on that, several scenarios have been studied and compared with each other to understand the effect of the above factors on the THD content.

2 Connecting the Inverters

In order to examine the effect of the load and cells number on the total harmonic distortion content in the output waveforms of the hybrid cascaded multilevel inverter, Two cells and three cells HCML inverters have been built and simulated with PLECS software. The two cells inverter has two H-bridge cells. The first cell has four IGBTs switches connected to a 100 V DC source. The second cell has four IGBTs switches connected to a capacitor. Then the load was connected in parallel with the two cells as shown in Figure 1.

Furthermore, the three cell inverter has three H-bridge cells. The first cell has four IGBTs switches connected to a 100 V DC source. However, the second and the third cells have four IGBTs switches and connected to two capacitors as depicted in Figure 2. Therefore, the capacitors will replace the DC source in the second the third cells. Hence, by regulating the voltage of the capacitors at the level of 100 V, the inverters will generate alternating voltage with maximum voltage of 200V for two cells inverter with 5-level output voltage (200, 100, 0, -100, -200), whereas, 300V for three cells inverter with 7-level output voltage (300, 200, 100, 0, -100, -200, -300). Regulation process needs a modulation scheme that can provide the proper switching states for all switches. On the other hand, it needs to synthesis the right output voltage waveform with minimum THD.

For the two cells inverter, the capacitor value was 3.5mF, the load resistance was 0.5 Ω , and the load inductance was 0.03H. However, for the three cells inverter, the two capacitors values were 4 mF, the load resistance was 1.11 Ω , and the load inductance was 0.056H. The values of these parameters were selected based on the performance of the inverters, where these values offer the best operation and output waveforms.

3 Implementing PS-PWM Strategy

Phase Shift PWM (PS-PWM) is tremendously common in the industrial applications particularly for CHB inverter. It is able to reduce the harmonics in the output, distributes the power equally between the H-bridges. PS-PWM was developed from the traditional sinusoidal PWM schemes especially for CHB inverters, where this scheme is based on multiple carriers (triangle wave carriers) compared with only one modulation signal. Each carrier is assigned to a certain H-bridge with a phase shift between the carriers.[7] Therefore, Phase shift-pulse width modulation was employed to modulate the two considered inverters. This modulation strategy was implemented in PLECS software by using C-script block. This block contains a programme written with C language, where the programme controls every process in the inverter. However, the main tasks of the C code are to generate the modulation pulses for all the switches and balance the voltages of the capacitors. Maintaining the capacitors voltages

requires measuring the voltages of the capacitors and load current and feed them back to the programme, so that the code can understand the case of the capacitors and take the decision whether to charge or discharge them depending on their voltages and the sign of the load current.

3.1 Modulating the Two Cells Inverter

The C-script block has 5 input signals, one modulation wave (sine wave) with 50 Hz and 0.8V amplitude. Two carrier waves (triangle waves) with 250 Hz and 1V amplitude, each carrier was assigned to one cell. Besides, the voltage of the capacitor was measured and fed back to the block as an input, and the load current was also measured and fed to the this block. Therefore, in order to maintain the capacitor voltage at a certain level, the C language programme has to read the values of the capacitor voltage and the load current, so that it can select the right switching states for the inverter's switches.

The two triangle carriers have a phase shift between them and that phase shift was calculated by using the following equation [8]:

$$\text{Phase shift angle } \theta_k = [(k-1)/N] \times 180 \quad (1)$$

Where:

θ_k is the phase shift angle for each cell.

k is the individual number of the cell.

N is the total number of the cells.

Therefore, the calculated phase shift angles are $\theta_{HB1} = 0^\circ$, $\theta_{HB2} = 90^\circ$. On the other hand, to enter these angles into PLECS software, they must be changed to time base on the following equation [8]:

$$\text{Phase shift time } T_k = [(k-1)/N] \times T_s / 2 \quad (2)$$

Where:

T_k is the phase shift time for each cell.

k is the individual number of the cell.

N is the total number of the cells.

T_s is the carrier frequency inverse.

Therefore, the phase shift times between the carrier signals were obtained $T_{HB1} = 0$ sec, $T_{HB2} = 0.001$ sec. Moreover, C-script block has 8 outputs, one output for every switch in the two H-bridges as can be seen in Figure 1.

3.2 Modulating the Three Cells Inverter

As this inverter has three H-bridges, so it contains one capacitor in the second and one capacitor in the third cell. Therefore, the input signals of the C-script are 7. One sine wave (50Hz, 0.8V), three triangles waves (250Hz, 1V), two feedback voltage signals of both measured capacitors voltages and one feedback load current. The phase shift between the three carriers are $\theta_{HB1} = 0^\circ$, $\theta_{HB2} = 60^\circ$, $\theta_{HB3} = 120^\circ$, while the phase shift times are $T_{HB1} = 0$ sec,

$T_{HB2} = 0.000667$ sec, $T_{HB3} = 0.00133$ sec. For the outputs, there are 12 output signals exiting the C- script, one output for every switch in the three cells, as clearly depicted in Figure 2.

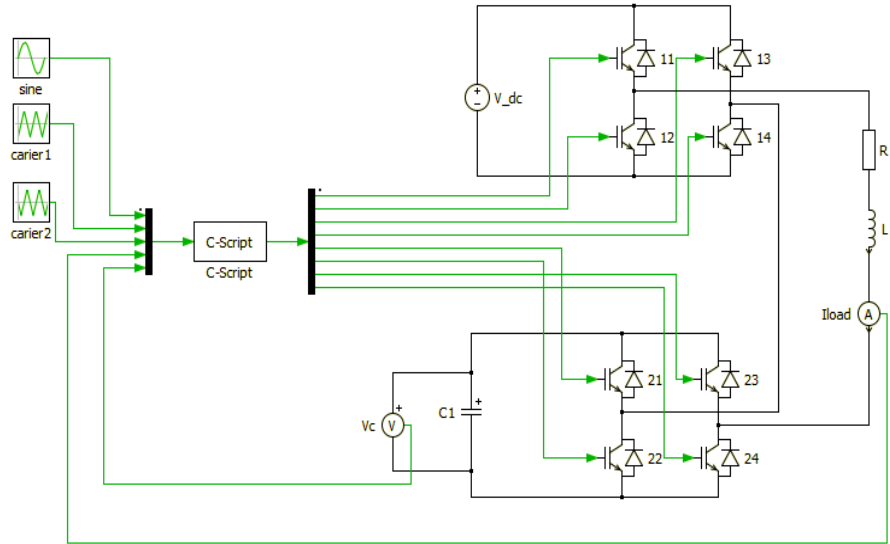


Figure 1: Two cells HCML inverter circuit

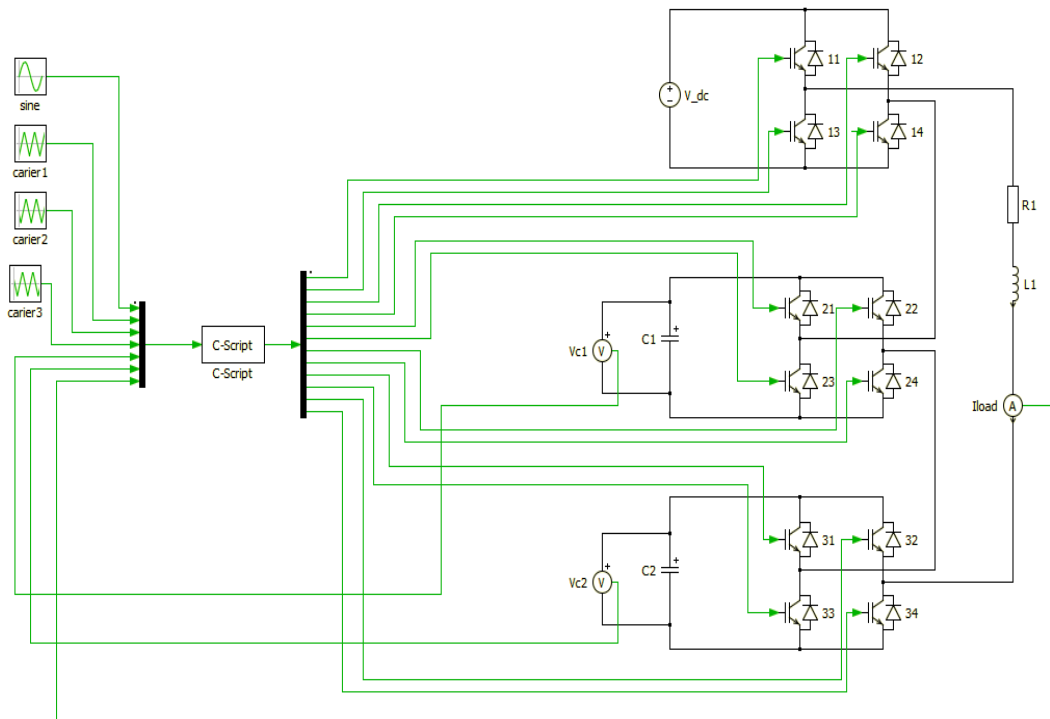


Figure 2: Three cells HCML inverter circuit

4 THD Study of the Two Inverters

In this section, the THD contents are studied in the output waveforms of the two inverters, where the inverters have been simulated under diverse resistance and inductance values. As one parameter was changing while the other was kept constant. At the same time, the THD readings of the output voltage and the load current were taken during the test at each time the parameter changes. Therefore, several THD readings have been recorded with each scenario.

4.1 THD Study under Load Resistance Effect

In this case, the impact of the load resistance on the THD was investigated. The resistance value was changed, while the other parameters of the inverter remained constant as mentioned above. Then, the THD readings were recorded as can be seen in Tables 1 and 2.

Table 1: THD readings when changing the load resistance (two cells inverter)

$R (\Omega)$	THD _v %	THD _I %
0.1	35.98	1.64
0.5	35.83	1.60
0.9	35.79	1.59
1.2	35.78	1.58
1.8	35.76	1.58
2.4	35.75	1.58
2.9	35.71	1.57

Table 2: THD readings when changing the load resistance (three cells inverter)

$R (\Omega)$	THD _v %	THD _I %
0.1	25.22	2.07
0.5	25.13	0.99
0.9	24.97	0.87
1.11	24.95	0.86
1.15	24.82	0.85
1.20	24.64	0.81
1.25	24.59	0.77

Tables 1 and 2 present the results obtained from the simulation of the first scenario, where the effect of the load resistance was examined. It can be seen from the data that the THD of the voltage is larger than that of the current. This could be due to the switching frequency of the switches and due to the smoothing effect of the load inductance for the current. Moreover,

the THD of both the output voltage and the load current were relatively decreasing with increasing the resistance value. This may be attributed to the decreasing of the load current value, which in turn reducing the discharging current from the capacitor. The data shown in tables 1 and 2 were plotted in Figures 3 and 4 respectively. These two figures confirm that clear trend of decreasing of both THDs.

On the other hand, both THDs for three cells inverter are less than that of the two cells inverter. This was caused by the higher number of cells which led to synthesize more voltage steps (7 levels) in the output voltage in the three cell inverter, thus, the output voltage became closer to the sine wave. Consequently, as the cells number increases, the output voltage will have less THD.

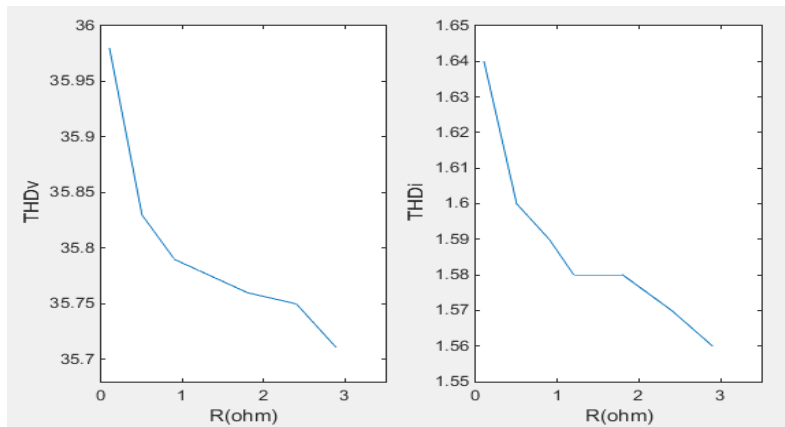


Figure 3: THD readings when load resistance changing for two cells inverter

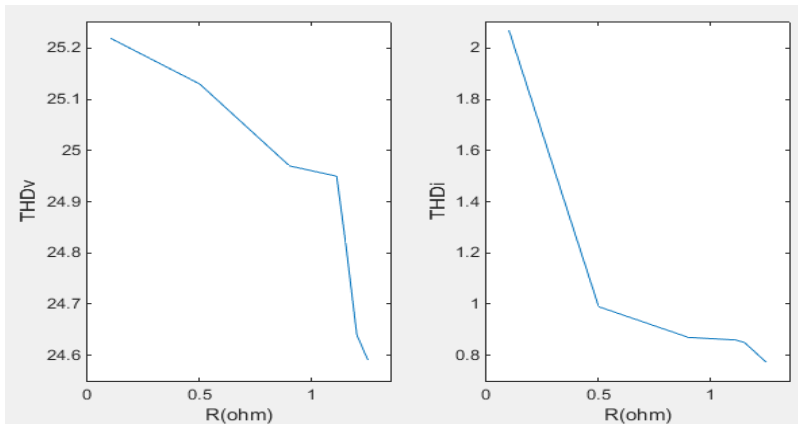


Figure 4: THD readings when load resistance changing for three cells inverter

4.2 THD Study under Load Inductance Effect

Another major factor that significantly affects the THD contents in the output waveforms, that element is the inductance of the load. Therefore, its impact was studied in this simulation scenario. The inductance value was varied while the other parameters of the inverters kept untouched. Lower and higher inductance values than that values mentioned in section 2 were tested to recognise how the load inductance influences the THD contents of the HCML inverter. A number of readings have been taken according to these values as revealed in tables 3 and 4.

Table 3: THD readings when changing the load inductance (two cells inverter)

$L (H)$	THD _v %	THD _i %
0.01	35.83	1.62
0.03	35.84	1.58
0.05	35.86	1.56
0.07	35.89	1.51
0.09	35.93	1.47
0.10	36.00	1.42
0.15	35.71	1.57

Table 4: THD readings when changing the load inductance (three cells inverter)

$L (H)$	THD _v %	THD _i %
0.01	24.49	2.57
0.035	24.63	1.04
0.056	24.95	0.96
0.09	25.08	0.89
0.12	25.11	0.81
0.15	25.17	0.74
0.20	25.21	0.63

From the tables above, it is apparent that as the inductance value was increased, the THD of the output voltage was increasing too. This could be explained by the reducing power factor as the inductance increases, where the resistance value was remained constant. However, the THD of the load current was decreasing as the inductance value was increasing, which is due to the smoothing effect of the inductance for the current. Furthermore, the THD of both the voltage and the current in the case of three cell inverter is less than that of the two cells inverter. This is similar to the result of the resistance effect. Therefore, the cells number is a vital factor that can widely improve the THD contents in the voltage and current waveforms. As a result, the cells number is an independent factor from the resistance and inductance of the load,

where as the number of cells increases, the THD content decreases. However, the cells number is limited by the size, cost and the modulating technique [9]. The data presented in table 3 and 4 were plotted as shown in Figure 5 and 6.

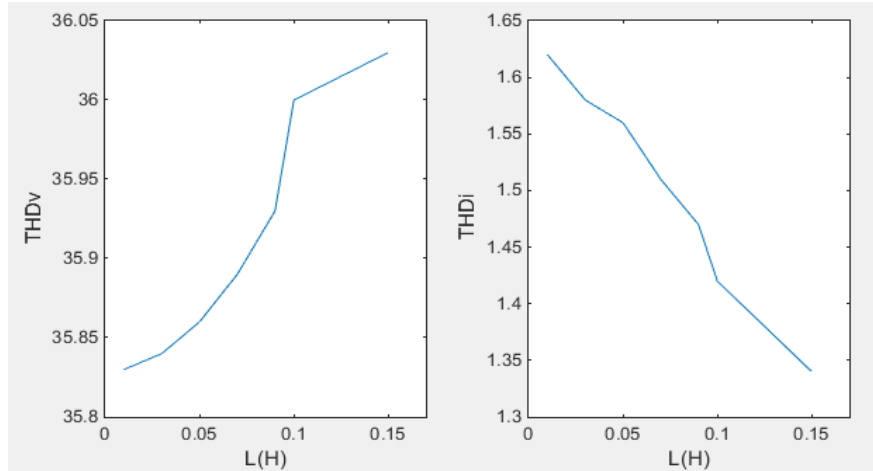


Figure 5: THD readings when load inductance changing for two cells inverter

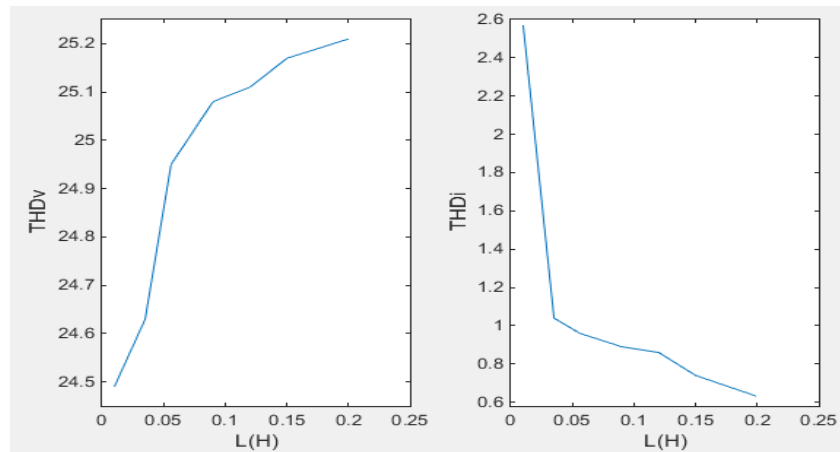


Figure 6: THD readings when load inductance changing for three cells inverter

5 Conclusions

A simulation investigation of the THD content was presented. Two cells and three cells hybrid cascaded multilevel inverters have successfully been modelled by PLECS software and simulated under various conditions. The resistance and inductance of the load have a serious impact on the THD of both the output voltage and current. For the resistance effect, it reduces the THD contents of both waveforms. However, the inductance has a different effect on both the voltage and the current. It deteriorates the voltage but improves the current. As a result, the

design of the inverter should carefully consider the load, so that the inverter can operate at a wide range of loads with minimum THD contents. The cells number as an enhancing effect of both waveforms, but, it is a limited solution when it comes to the size and the cost of the inverter. Since the number of devices will be high.

References

- [1] H. Liu, L. M. Tolbert, B. Ozpineci, and Z. Du, "Hybrid Multilevel Inverter With Single DC Source," *Midwest Symp. Circuits Syst.*, pp. 538–541, 2008.
- [2] T. A. Lipo, "A Hybrid Multilevel Inverter Topology For Drive Applications A Hybrid Multilevel Inverter Topology For Drive Applications," no. May, 2014.
- [3] L. M. Tolbert, F. Z. Peng, T. Cunningham, and J. N. Chiasson, "Charge Balance Control Schemes For Cascade Multilevel Converter In Hybrid Electric Vehicles," *IEEE Trans. Ind. Electron.*, vol. 49, no. 5, pp. 1058–1064, 2002.
- [4] N. Shrivastava and A. P. Mehta, "Survey on Harmonic Mitigation Techniques in Multilevel Inverters," vol. 3, no. 12, pp. 4307–4311, 2014.
- [5] P. Tamilvani and K. R. Valluvan, "Harmonic Mitigation in Various Levels of Multilevel Inverter with Different Loads," vol. 2, no. 9, pp. 1989–1996, 2014.
- [6] A. Papriwal and A. Mahor, "Mitigation Of Harmonics In Inverter," vol. 2, no. 9, pp. 98–105, 2012.
- [7] M. Malinowski, K. Gopakumar, J. Rodriguez, and M. A. Perez, "A Survey on Cascaded Multilevel Inverters," *Ind. Electron. IEEE Trans.*, vol. 57, no. 7, pp. 2197–2206, 2010.
- [8] J. Rodriguez *et al.*, "Multilevel Converters: An Enabling Technology for High-Power Applications," *Proc. IEEE*, vol. 97, no. 11, pp. 1786–1817, 2009.
- [9] Y.-M. Park, H.-S. Ryu, H.-W. Lee, M.-G. Jung, and S.-H. Lee, "Design of a Cascaded H-Bridge Multilevel Inverter Based on Power Electronics Building Blocks and Control for High Performance," *J. Power Electron.*, vol. 10, no. 3, pp. 262–269, 2010.

Impact of Wind Generation Location on Power System Losses

I.S.Naser

Department of Renewable Energy, College of Mining and Energy, Sebha University, Libya

DOI: <https://doi.org/10.21467/proceedings.2.25>

* Corresponding author email: ibr.naser@sebhau.edu.ly

ABSTRACT

The global environmental and renewable energy initiatives have led to an increased connection of wind generation to the electricity power networks, the increase in wind generation makes a significant impact on the power system and planning for both customers and electricity suppliers. This paper investigates the impact of wind generation location in power system losses when connected at the transmission network. The doubly-fed induction generator (DFIG) and different connection scenarios are used to investigate the impact. Finally, some conclusions that provide a better understanding of the behavior of wind generator when connected to strong bus or weak bus. The Power World Simulator is used to obtain simulated results.

Keywords: Wind generation, DFIG, Transmission network, Real system losses.

1 Introduction

The increasing interest in producing electricity using renewable resources is growing rapidly due to ability of these resources to reduce greenhouse gases [1]. In some remote areas economic factor could be a major one. One of the most prevalent and desirable technologies is wind power. Wind power has been dramatic development throughout the World especially, connected to both distribution and transmission system. Recently wind generator have been experiencing a rapid development and the size of wind turbines and wind farms are increasing, and the impact of wind generation on power system operation is more important [2]. The pattern and size of the wind turbine and generator is based on the wind characteristics. Wind generation can be divided into several types depending on the design of the rotor and generator, and wind generation can be a resource for both active and reactive power. Wind turbine generators can be modelled into two categories: a fixed speed with induction generator, and a variable speed generator in PQ or PV mode.

In general, increased wind penetration level will have the impacts on the operation of the system, and the effect is becoming increasing. These impacts could be positive or negative depend on a number of factors, including wind power penetration level, type wind generator, geographical dispersion of wind generation and the size of the electrical networks [3]. Connecting a wind generator to a network can have negative effects, such as a new loading



© 2018 Copyright held by the author(s). Published by AIJR Publisher in Proceedings of First Conference for Engineering Sciences and Technology (CEST-2018), September 25-27, 2018, vol. 1.

This is an open access article under [Creative Commons Attribution-NonCommercial 4.0 International](https://creativecommons.org/licenses/by-nc/4.0/) (CC BY-NC 4.0) license, which permits any non-commercial use, distribution, adaptation, and reproduction in any medium, as long as the original work is properly cited. ISBN: 978-81-936820-5-0

situation and changed power flow direction. Integration of a wind farm into a network can also affect the power losses and stability of the system [4]. The impact of wind generation on the distribution system has been studied and it shows that wind generation integrated on the distribution system can improve overall system voltage profile and at the same time system losses are reduced [5-6].

The objective of this paper is to investigate the impact of DFIG location based wind generation on system MWh losses in transmission system. The IEEE 30-bus system is used as a test case, simulated using the Power World Simulator, and wind penetration level is varied from 20% to 30% to assess the impact on power system MWh losses. For the studies carried out in this paper, only focus on variable speed unit (DFIG) and modelled as PV bus, this farm is operated from 0.95 PF for Q_{\max} and 0.95 PF for Q_{\min} .

2 Doubly Fed Induction Generator

This configuration consists of a wound rotor induction generator where the stator windings are directly connected to the grid and the rotor windings are connected to a back-to-back power converter. This back-to-back power converter is dimensioned for partial generator power and is able to operate bi-directionally. It uses a wound rotor induction generator with slip rings to take current into or out of the rotor winding, and variable speed operation is obtained by injecting the controllable voltage into the generator rotor at slip frequency [7].

As shown in Figure 1 the rotor winding is fed through the variable frequency power converter, typically based on two AC/DC insulated gate bipolar transistor (IGBT) based voltage source converters (VSC) linked by the DC bus. The power converter decouples the network electrical frequency from the rotor mechanical frequency, enabling the variable speed operation of the wind turbine. The voltage source converter (VSC) produces an AC voltage that is controllable in magnitude and phase, similar to the synchronous generator or synchronous compensator. The VSC commutates independently of the AC-side voltage and consequently it can be used on the load-only system. This makes the VSC useful for rotor connection, wind farm connection and so forth. Converters (C1) and (C2) in Figure 1 are used to control the doubly fed induction generator wind turbine. A number of manufacturers use converter (C1) to provide torque/speed control, together with terminal voltage or power factor control for the overall system. Converter (C2) is used to maintain the DC link voltage and provide the path for power to flow to and from the AC system at unity power factor.

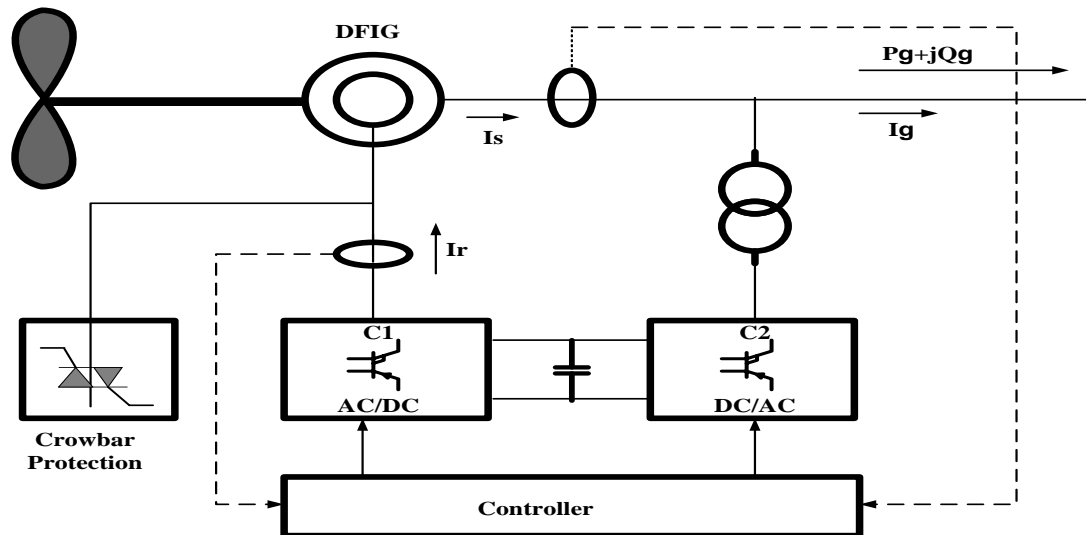


Figure 1: Typical configuration of the DFIG wind turbine

3 Doubly Fed Induction Generator Model.

Recent grid codes demand from wind farms to provide reactive output regulation, often in response to power system voltage, much as the conventional power generations. Manufacturers offer different options for var generation by DFIG based wind turbines in steady state operation. The reactive power requirements are related to the characteristics of each network. DFIG can be modelled in load flow studies as PQ or PV buses, so as to operate in power factor controlled or voltage controlled modes [8]. When the DFIG is modelled as a PQ bus, the DFIG is usually employed as a unity power factor (P.F) operation (zero reactive power output) though other (P.F) values can be specified (e.g, from 0.95 leading to 0.95 lagging). In voltage controlled mode, the DFIG is modelled as PV bus with Q limits applied. In this mode, a stator Q is varied to maintain the voltage at the point of common coupling within given reference values (in this case voltage is controlled at 1.0 p.u). For the studies carried out in this paper, only focus on variable speed unit (DFIG) and modelled as PV bus.

4 Test system and simulation results

A modified IEEE30-bus is modelled in Power World Simulator and it used as the test system [9]. The test system consists of six generators which supply power to twenty one loads through 132/33 kV substation, the modified test system is analysed using optimal power flow (OPF).

Wind farms are connected at different buses at different penetration levels of wind generation with different scenarios. For the studies carried out in this paper, only focus on variable speed unit (DFIG) and modelled as PV bus. A single-line diagram of IEEE-30 bus system is shown in Figure 2.

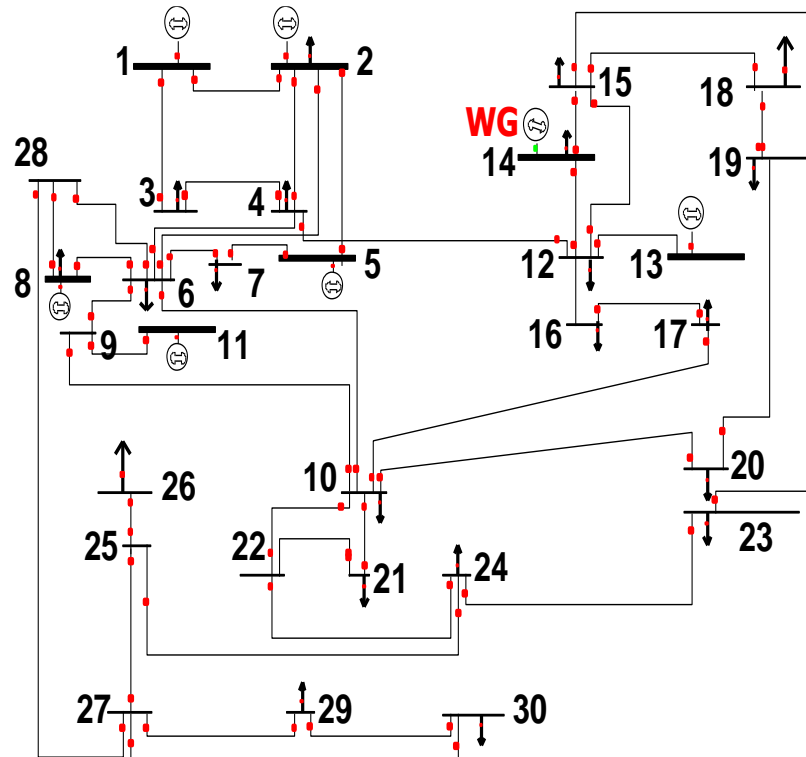


Figure 2: The modified IEEE-30 bus test system

An analysis method is used to assess a system loss that considers the time varying characteristics of the power system generation components, penetration level of wind generation, and the variable nature of wind power, using the time step option in the Power World Simulator. The analysis method has three major inputs. The wind power input is the time series values of the wind generation connected to the network in MW at one hour intervals. These data were obtained from a utility operating in the United Kingdom from a wind farm for a one day period and at one hour intervals. Table 1 shows the wind power input data for 20% and 30% penetration levels with a one day load period [10]. The input of the conventional generators is their availability considering their capacity and quantity, while the load model input is the forecasted load profile applied to the network for the evaluation of system losses.

Table 1: Wind power input data for different wind penetration with one day load period

Time (Hour)	Total Loads (MW)	20% WP (200 MW)	30% WP (300 MW)
01:00:00	283.4	24.96	55.5
02:00:00	283.4	57.7	37
03:00:00	302.5	174.5	100.5
04:00:00	302.5	162.4	8
05:00:00	358.8	104.3	91
06:00:00	358.8	45.6	275.5
07:00:00	500	119.4	165.2
08:00:00	500	190.2	5.5
09:00:00	615.5	164.4	35.7
10:00:00	615.5	143.4	167.4
11:00:00	454.6	84.7	15.3
12:00:00	454.6	54.2	110.5
13:00:00	504.3	97.9	80.7
14:00:00	504.3	200	12.5
15:00:00	745.5	157	6.5
16:00:00	745.5	123.2	285.7
17:00:00	850.1	200	300
18:00:00	850.1	96.4	7.5
19:00:00	695	130.5	0
20:00:00	695	38.2	12.4
21:00:00	450	13.5	113.6
22:00:00	450	43.8	176.3
23:00:00	314.9	30.2	165.1
00:00:00	314.9	70.1	35.9

The objective of connecting wind generation at different locations is to investigate the effect of location site on the total system MWh losses. There are three wind farm connection scenarios: a strong area at bus 28 (case 1), a weak area at bus 14 (case 2), and two locations at buses 6 and 28 as dispersion of wind generation (case3). The total system MWh losses are analysed for two different wind generation levels (20% and 30%). The results presented here are for a 24 hour period. The total system MWh losses of the network are calculated for every one hour of the simulation and are recorded. As shown in Figure 3, the value of the total system MW losses decrease with the connection of wind generation from 149.48 MW at the

peak load period in the case of no wind generation to 80.06 MW for the connection case 1 (one wind farm is connected to a strong bus 28), 84.89 MW for the connection case 3 (two wind farms are connected to buses 6 and 28) and 129.6 MW as one wind farm is connected to a weak bus 14 when the percentage of wind capacity was 20% (200 MW). It can be seen that for 20% wind penetration level, the total system real power losses are reduced significantly for both wind connection scenarios compared to the base case. From a total system real power loss point of view, a single wind farm being connected to a strong bus is a better option and will reduce the total real power losses more than other connection scenarios.

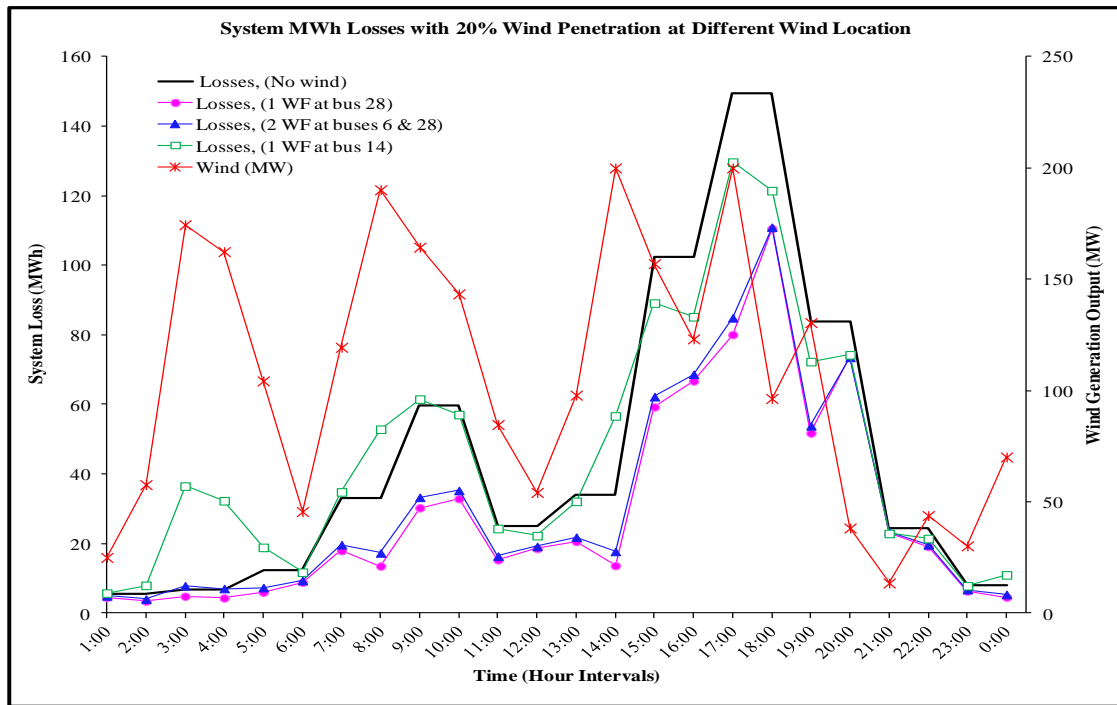


Figure 3: The total system MWh losses of IEEE-30 bus system with 20% wind penetration level, when wind farm is connected to the network at different connection scenarios.

When the wind penetration level increases from 20% to 30%, the total system MW losses are reduced more for both wind connection scenarios (for one strong location and for multiple locations) compared to the base case and when the wind generation is 30% (300 MW). The system MW losses are recorded as 59.4 MW when the wind farm is connected to the strong bus and 62 MW for 2 wind locations. The system witnesses a significant reduction in system MW losses for higher wind penetration levels as the system becomes more heavily loaded, as shown in Figure 4. However, when the wind penetration level, connected to weak bus 14, increases to 30%, the total system MW losses are increased to 166.1 MW, which is a slight

increase compared to the no wind case (149.48 MWh). This means that a higher wind penetration might increase the total system MW losses during system load ability (at the peak load) when the wind farm is connected to a weak area.

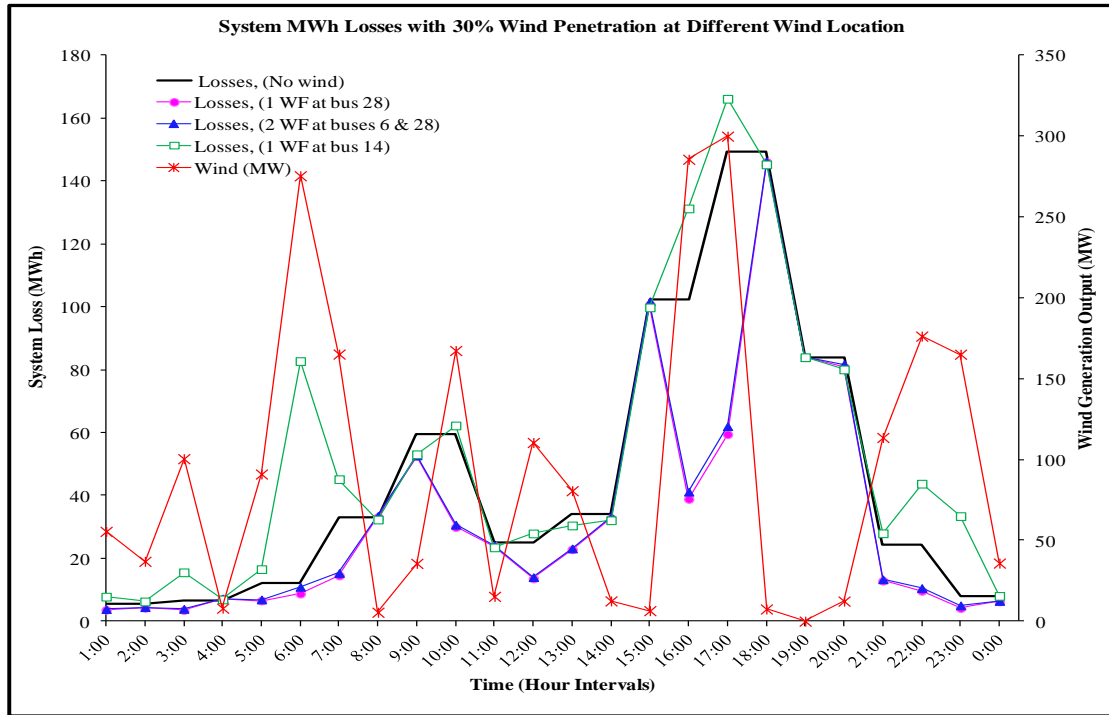


Figure 4: the total system MWh losses of IEEE-30 bus system with 30% wind penetration level, when wind farm is connected to the network at different connection scenarios.

5 Conclusions

This paper has investigated the impact of wind generation location on the total system MW losses based on system load ability in the transmission network. A DFIG based wind farm with a voltage controlled mode was integrated into an IEEE-30 bus system. Different connection scenarios of wind farms were considered; a single location (a strong bus and a weak bus) and dispersion of wind farms in two locations. Different penetration levels of wind generations were used. The results show that a single strong location for a wind farm with higher wind penetration levels can achieve a significant reduction in the total system MW losses when the system loading is high. However, the results show that total real power losses increase if the wind farm is located at a weak area with higher wind penetration levels when the system is highly loaded.

References

- [1] Federico Milano, "Assessing adequate voltage stability analysis tools for networks with high wind power penetration," IEEE DRPT Conference, 6-9 April 2008, Nanjing, China, pp.2492-2497
- [2] I.S.Naser, M.A.Alsharif, MN.Hussin, M.A. Alrmah "Evaluating the impact of wind generation on transmission network power losses", LICEET 2018, Libya
- [3] I.S. Naser, Olimpo Anaya-Lara, K. L. Lo, "Study of the Impact of Wind Generation on Voltage Stability in Transmission Networks," IEEE DRPT, The 4th International Conference on Electric Utility Deregulation and Restructuring and Power Technologies. 6th-9th July, 2011, Shandong, China
- [4] L. T. Ha, T. K. Saha, "Investigation of Power Loss and Voltage Stability Limits for Large Wind Farm Connections to a Subtransmission Network", IEEE Power Engineering Society General Meeting, Colorado, USA, June 2004.
- [5] A. P. Agalgaonkar, S.V. Kulkarni, S. A. Khaparde, "Impact of Wind Generation on Losses and Voltage Profile in a Distribution System", 86 Conference on Convergent Technologies for Asia-Pacific Region, TENCON 2003, Vol. 2, pp.775-779.
- [6] K.C Divya, P. S. Nagendra Rao, "Models for Wind Turbine Generating Systems and Their Application in Load Flow Studies", ELSEVIER, Electric Power Systems Research Vol. 76, 2006, pp. 844-856.
- [7] L. Holdsworth, X. G. Wu, J. R. Ekanayake, N. Jenkins, "Comparison of Fixed-Speed and Doubly-Fed Induction Wind Turbine during Disturbances", IEE Proceedings Part C, 150 (3), pp.343-352, 2003.
- [8] A. N. R. Ullah, T. Thiringer, "Variable Speed Wind Turbines for Power System Stability Enhancement", IEEE Transactions on Energy Conversion, Vol. 22, No. 1, pp. 52-60, March 2007.
- [9] "Power Systems Test Case Archive" available from: <http://www.ee.washington.edu/research/pstca/>
- [10] UKGDS, "United Kingdom Generic Distribution System" 2009, available from: [http://www.sedg.ac.uk/UKGDS Networks.pdf](http://www.sedg.ac.uk/UKGDS_Networks.pdf).

Antenna Elevation Control using Multiple Switched Self-Tuning Controllers Design

Ahmed M. Alnajeh ^{1*}, Othman E. Aburas ², Youssef Amer Arebi ³

¹ Department of Electrical and Computer Engineering, Applied Research and Development Center, Tripoli, Libya.

² Department of Electrical and Computer Engineering, Faculty of Engineering Alkhoms, Elmergib University, Libya.

³ Department of Electrical and Computer Engineering, Advanced Center of Technology, Tripoli, Libya.

DOI: <https://doi.org/10.21467/proceedings.2.26>

* Corresponding author email: aalnajeh@yahoo.com

ABSTRACT

Adaptive controllers have a lot of advantages over conventional ones, especially when the model of the plant to be controlled is unknown or changes with time. This paper proposes a control scheme for multiple adaptive Self-Tuning Pole-Placement controllers using both the classical technique via transfer function and the modern technique using discrete state-space. This approach enables the user to switch between the classical and modern techniques in order to control the estimated plant model on-line; the switching mechanism ensures a smooth transition amongst the two pole-placement controllers.

The performance of the proposed control scheme on the closed-loop performance of an antenna system, controlling its elevation, is demonstrated. Simulation results demonstrating the effectiveness of the switching mechanism between different controllers are presented. A Graphical User Interface is built to facilitate the controller programming and allowing the simulation of multiple adaptive controllers.

Keywords: Adaptive Self-Tuning Control, Discrete State-Space, Pole-Placement Control, Antenna Elevation Control.

1 Introduction

Control systems design techniques typically require an in-depth understanding of the plant under study and its environment. In some applications, however, the plant to be controlled is sophisticated and the involved physical processes are changeable with time and operating conditions. To deal with such situations, different approaches of adaptive control are proposed to tune the controller parameters and behavior in response to the physical processes changes [1]. Self-tuning controllers represent an important class of adaptive control since they provides systematic and flexible approaches for dealing with many difficulties including time varying parameters, non-linearity, and uncertainties. Recently, there has been increasing interest in pole-placement self-tuning controllers due to the fact that in the regulator case, they provide mechanisms to overcome the restriction to minimum phase plants of some optimal



© 2018 Copyright held by the author(s). Published by AIJR Publisher in Proceedings of First Conference for Engineering Sciences and Technology (CEST-2018), September 25-27, 2018, vol. 1.

This is an open access article under [Creative Commons Attribution-NonCommercial 4.0 International](https://creativecommons.org/licenses/by-nc/4.0/) (CC BY-NC 4.0) license, which permits any non-commercial use, distribution, adaptation, and reproduction in any medium, as long as the original work is properly cited. ISBN: 978-81-936820-5-0

controllers. In the servo case, they give the ability to directly introduce the natural angular frequency ω_n and damping ratio ζ as tuning parameters. Moreover, robustness is an essential advantage of pole-placement methods, as they simply modify the system dynamics instead of cancelling them as applied in optimal self-tuning controller [2]. However, the main drawbacks of self-tuning pole-placement controller are based on transfer function approach and also their inability to regulate steady-state error in the presence of constant disturbances. The transfer function approach depends on polynomial algorithms, which are slow to emerge [3]. In contrast, the linear algebraic tools that are required by state-space techniques are a lot more advanced and more suitable for optimal control design [1][4]. Therefore, the state-space technique is preferred over the transfer function approach, especially for multivariable and non-linear systems [5]. The main contribution of this paper is to develop a control scheme for multiple adaptive Self-Tuning Pole-Placement controllers using both the classical technique via transfer function and the modern technique using discrete state-space framework. In order to assess the performance of the proposed scheme, it is applied to single-input-single-output of an antenna model.

2 A Servomechanism for an Antenna Elevation Control

It is desired to control the elevation of an antenna designed to track a geostationary satellite as sketched in Figure 1. The antenna and drive parts have a moment of inertia J' and damping B_r arising to some extent from bearings and aerodynamic friction, but mostly from the back emf (V) of the DC-drive motor [6,7,8].

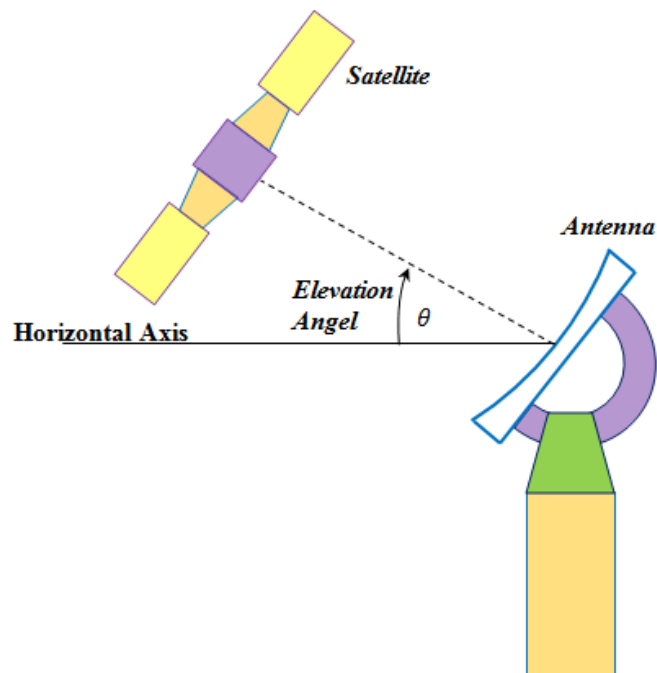


Figure 1: Schematic Diagram of Antenna System

Figure 2 shows the internal connection of DC-drive motor with the antenna system. Here, the armature inductance $L_a (H)$ is negligible because it is usually small. The continuous transfer function [7], [8] can be given by:

$$\theta(s) = \frac{a}{s(s+a)} [U(s) + \xi'(s)] \quad (1)$$

where $\xi'(s)$ is the torque disturbance due to wind, and $U(s)$ is the torque due to the DC motor.

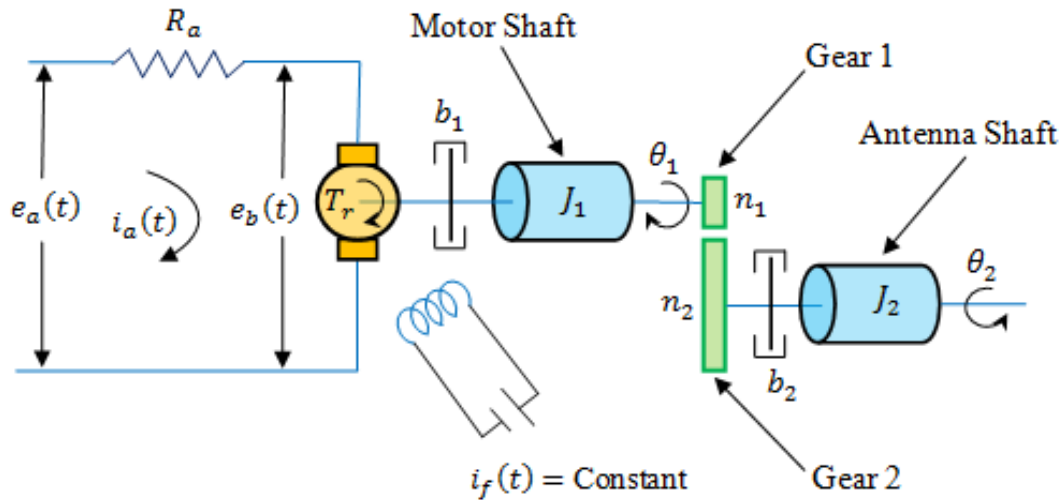


Figure 2: The Connection of DC-drive Motor with the Antenna System

The aim of the design is to measure the error between the angle of the satellite $\theta_s(t) (rad)$ and the antenna $\theta(t) (rad)$ and compute $u(t)$ so that the error e , i.e. equals to $(\theta_s(t) - \theta(t)) (rad)$, is always less than $0.001 rad$ during tracking. The geostationary satellite angle that must be followed can be adequately approximated by a fixed velocity.

$$\theta_s(t) = (0.01 rad/sec) \times t(sec).$$

The discrete model of the Antenna system can be written as:

$$\theta(z) = \frac{(aT_s - 1 + e^{-aT_s})z + (1 - e^{-aT_s} - aT_s e^{-aT_s})}{a(z-1)(z - e^{-aT_s})} [U(z) + \xi'(z)] \quad (2)$$

A discrete state-space [9] of antenna tracking control model in which the time constant $a = 0.1$, and $T_s = 1$ sec is:

$$\begin{bmatrix} X_1(t+1) \\ X_2(t+1) \end{bmatrix} = \begin{bmatrix} 0 & 1 \\ -0.9048 & 1.905 \end{bmatrix} \begin{bmatrix} X_1(t) \\ X_2(t) \end{bmatrix} + \begin{bmatrix} 0.04837 \\ 0.13895 \end{bmatrix} u(t) + \begin{bmatrix} 0.04837 \\ 0.13895 \end{bmatrix} \xi' \quad (3)$$

$$y(t) = [1 \ 0] \begin{bmatrix} X_1(t) \\ X_2(t) \end{bmatrix} \quad (4)$$

In (3), $X_1(t)$ is the position (rad) and $X_2(t)$ is the velocity (rad/sec) of the antenna.

3 Adaptive Control Algorithm

The Controlled Auto-Regressive Moving Average (CARMA) process model [10] is described as:

$$A(z^{-1})y(t) = z^{-k}B(z^{-1})u(t) + C(z^{-1})\xi'(t) \quad (5)$$

Assume that the polynomials $A(z^{-1})$ and $B(z^{-1})$ are co-prime, i.e. they do not have any common factors. Furthermore, $A(z^{-1}), C(z^{-1})$ are monic, i.e. the coefficient of the highest power is unity [11]. The classical pole-placement controller can be described by the following control-law:

$$q(z^{-1})u(t) = H(z^{-1})r(t) - F(z^{-1})y(t) \quad (6)$$

where $q(z^{-1}), F(z^{-1})$ and $H(z^{-1})$ are polynomials in the back shift operator z^{-1} .

The controller has two degrees of freedom, the first is a feed forward with the transfer operator $\frac{H(z^{-1})}{q(z^{-1})}$ and the second is a feedback with the transfer operator $\frac{F(z^{-1})}{q(z^{-1})}$. A block diagram of the closed-loop system is shown in Figure 3. The controller polynomials $H(z^{-1}), F(z^{-1})$ and $q(z^{-1})$ are designed to ensure fast output tracking of the reference signal $r(t)$.

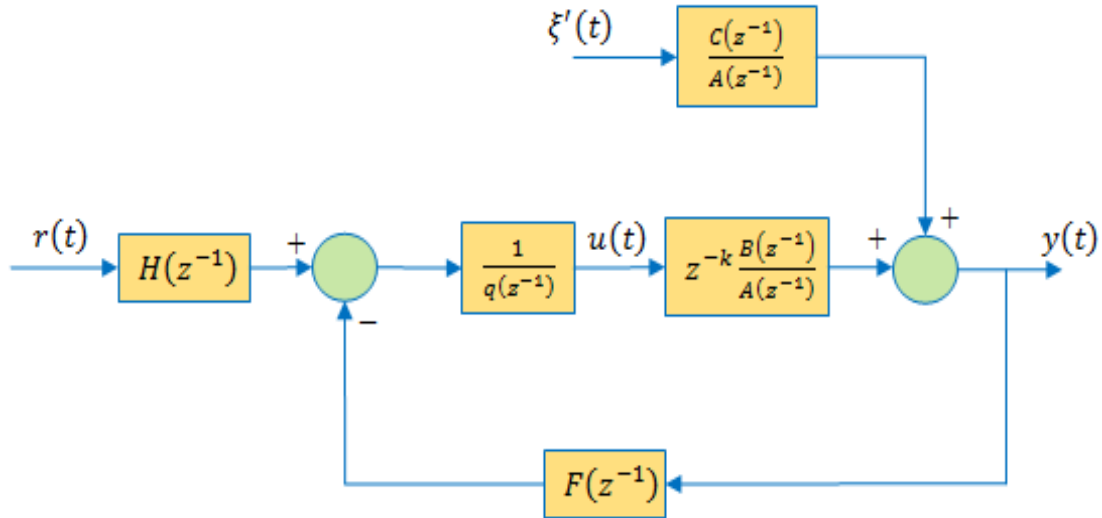


Figure 3: Classical Discrete Pole-Placement Controller

The closed-loop characteristic polynomial of the system (Diophantine equation) is [4]:

$$q(z^{-1})A(z^{-1}) + z^{-k}B(z^{-1})F(z^{-1}) = T_c(z^{-1})C(z^{-1}) \quad (7)$$

The main concept of the pole placement controller design is to specify the desired closed-loop poles polynomial $T_c(z^{-1})$ as a design parameter. By solving the Diophantine equation (7), the polynomials $q(z^{-1})$ and $F(z^{-1})$ can be obtained. The closed-loop poles polynomial

$T_c(z^{-1})$ fundamentally determines the property and the performance of the closed system [11].

The desired closed loop poles polynomial $T_c(z^{-1})$ and the controller parameters polynomials $F(z^{-1})$ and $q(z^{-1})$ are expressed in terms of z^{-1} as follows:

$$F(z^{-1}) = f_0 + f_1 z^{-1} + \dots + f_{n_a-1} z^{-n_f+1} + f_{n_f} z^{-n_f} \quad (8)$$

$$q(z^{-1}) = 1 + q_1 z^{-1} + \dots + q_{n_q-1} z^{-n_q+1} + q_{n_q} z^{-n_q} \quad (9)$$

$$T_c(z^{-1}) = 1 + t_1 z^{-1} + \dots + t_{n_t-1} z^{-n_t+1} + t_{n_t} z^{-n_t} \quad (10)$$

where, the parameters t_1 and t_2 are specified as following [11]:

$$t_1 = -2 \exp(-\zeta \omega_n T_s) \cos(T_s \omega_n \sqrt{1 - \zeta^2})$$

$$t_2 = -2 \exp(-\zeta \omega_n T_s)$$

Where ζ and ω_n are respectively the damping ratio and natural angular frequency of the second order closed loop transient response and T_s is the sampling time. In order to have a unique solution, the polynomials $F(z^{-1})$, $q(z^{-1})$ and $T_c(z^{-1})$ in the equations (8), (9), and (10) are specified as follows:

$$\left. \begin{aligned} n_q &= n_b + k - 1 \\ n_f &= n_a - 1 \\ n_t &\leq n_a + n_b + k - n_c - 1 \end{aligned} \right\} \quad (11)$$

Substituting Diophantine equation (7) into equation (6), the following equation is obtained:

$$y(t) = \frac{z^{-k} B(z^{-1}) H(z^{-1})}{T_c(z^{-1}) C(z^{-1})} r(t) + \frac{q(z^{-1})}{T_c(z^{-1})} \xi'(t) \quad (12)$$

It can be seen from equation (12) that the closed loop poles are placed at their pre-specified positions given by the desired closed loop poles polynomial $T_c(z^{-1})$ which represents the design parameter. The controller algorithm explained above can be structured as a self-tuning controller as shown in Figure 4. Where, all of the controller's parameters are calculated depending on the change in plant parameters.

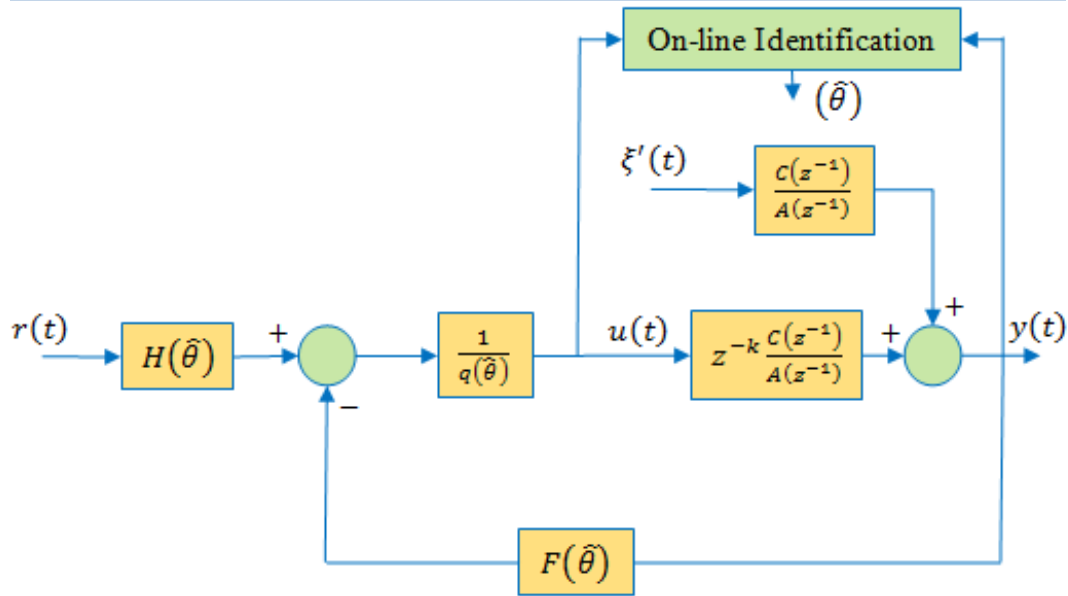


Figure 4: Classical Self-Tuning Pole-Placement Controller

The modern Self-Tuning Pole-Placement using discrete state-space control design algorithm is given in Figure 5, which is based on an on-line observer with a state feedback [6].

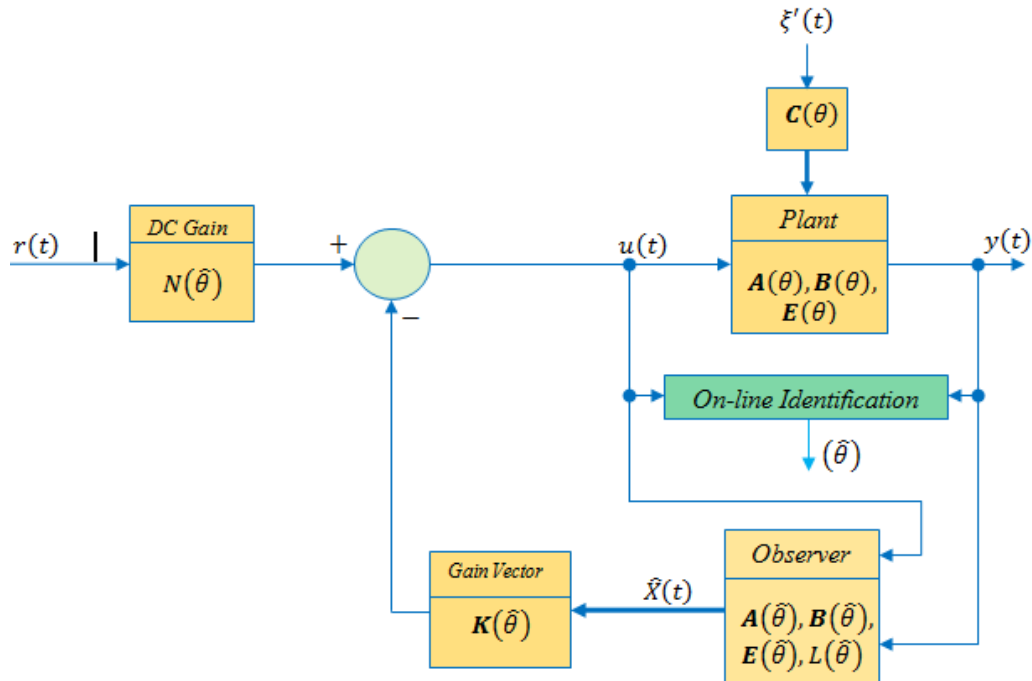


Figure 5: Shows the modern Self-Tuning pole-placement controller.

Both an on-line observer poles and the closed-loop system poles are placed based on the model parameters $\hat{\theta}$ obtained from the on-line identification scheme (RLS or ERLS

estimators). In Figure 5, the proper dc gain $\mathbf{N}(\hat{\boldsymbol{\theta}})$ is introduced on-line into the design in the presence of reference signal $\mathbf{r}(t)$ to eliminate the output steady state error. A discrete state-space model of any system can be derived and presented in discrete matrix-vector equation as follows:

$$\mathbf{X}(t+1) = \mathbf{A}\mathbf{X}(t) + \mathbf{B}\mathbf{u}(t) + \mathbf{C}\xi'(t) \quad (13)$$

$$\mathbf{y}(t) = \mathbf{E}\mathbf{X}(t) + \mathbf{b}_0\mathbf{u}(t) + \xi'(t) \quad (14)$$

The values of both control input signal $\mathbf{u}(t)$ and system output signal $\mathbf{y}(t)$ are read for every sampling instant; these values are used for on-line identification methods such as (RLS or ERLS estimators). An on-line identification method can be used to estimate plant parameters $\hat{\boldsymbol{\theta}}$ which are then used to identify state-space model as:

$$\mathbf{X}(t+1) = \mathbf{A}(\hat{\boldsymbol{\theta}})\mathbf{X}(t) + \mathbf{B}(\hat{\boldsymbol{\theta}})\mathbf{u}(t) + \mathbf{C}(\hat{\boldsymbol{\theta}})\xi'(t) \quad (15)$$

$$\mathbf{y}(t) = \mathbf{E}(\hat{\boldsymbol{\theta}})\mathbf{X}(t) \quad (16)$$

where, the estimated plant parameters $\hat{\boldsymbol{\theta}} = [-\hat{a}_1 - \hat{a}_2 \dots - \hat{a}_{n_a} \quad \hat{b}_0 \hat{b}_1 \hat{b}_2 \dots \hat{b}_{n_b} \quad \hat{c}_1 \hat{c}_2 \dots \hat{c}_{n_c}]^T$. The matrices of equations (15) and (16) can be placed in either plant framework or observer framework [7].

The transparent controllable canonical form is illustrated as follows:

$$\mathbf{X}(t+1) = \mathbf{A}_c(\hat{\boldsymbol{\theta}})\mathbf{X}(t) + \mathbf{B}_c(\hat{\boldsymbol{\theta}})\mathbf{u}(t) + \mathbf{C}_c(\hat{\boldsymbol{\theta}})\xi'(t) \quad (17)$$

$$\mathbf{y}(t) = \mathbf{E}_c(\hat{\boldsymbol{\theta}})\mathbf{X}(t) \quad (18)$$

where:

$$\mathbf{A}_c(\hat{\boldsymbol{\theta}}) = \begin{bmatrix} \mathbf{0} & \mathbf{1} & \mathbf{0} & \dots & \mathbf{0} \\ \mathbf{0} & \mathbf{0} & \mathbf{1} & \dots & \mathbf{0} \\ \vdots & \vdots & \vdots & \dots & \vdots \\ \mathbf{0} & \mathbf{0} & \mathbf{0} & \dots & \mathbf{1} \\ -\hat{a}_{n_a} & -\hat{a}_{n_a-1} & -\hat{a}_{n_a-2} & \dots & -\hat{a}_1 \end{bmatrix}, \mathbf{B}_c(\hat{\boldsymbol{\theta}}) = \begin{bmatrix} \mathbf{0} \\ \mathbf{0} \\ \vdots \\ \mathbf{1} \end{bmatrix},$$

$$\mathbf{E}_c(\hat{\boldsymbol{\theta}}) = [\hat{b}_{n_b} \quad \hat{b}_{n_b-1} \quad \dots \quad \hat{b}_1] \text{ and } \mathbf{C}_c(\hat{\boldsymbol{\theta}}) = [\hat{c}_{n_c} \quad \hat{c}_{n_c-1} \quad \dots \quad \hat{c}_1]$$

The transparent observable canonical form can be represented as:

$$\mathbf{X}(t+1) = \mathbf{A}_o(\hat{\boldsymbol{\theta}})\mathbf{X}(t) + \mathbf{B}_o(\hat{\boldsymbol{\theta}})\mathbf{u}(t) + \mathbf{C}_o(\hat{\boldsymbol{\theta}})\xi'(t) \quad (19)$$

$$\mathbf{y}(t) = \mathbf{E}_o(\hat{\boldsymbol{\theta}})\mathbf{X}(t) \quad (20)$$

Where

$$A_o(\hat{\theta}) = \begin{bmatrix} 0 & 0 & \dots & 0 & -\hat{a}_{n_a} \\ 1 & 0 & \dots & 0 & -\hat{a}_{n_a-1} \\ \vdots & \vdots & & & \vdots \\ 0 & 0 & \dots & 1 & -\hat{a}_1 \end{bmatrix}, B_o(\hat{\theta}) = \begin{bmatrix} \hat{b}_{n_b} \\ \hat{b}_{n_b-1} \\ \vdots \\ \hat{b}_1 \end{bmatrix}, C_o(\hat{\theta}) = \begin{bmatrix} \hat{c}_{n_c} \\ \hat{c}_{n_b-1} \\ \vdots \\ \hat{c}_1 \end{bmatrix} \text{ and}$$

$$E_o(\hat{\theta}) = [0 \quad 0 \quad \dots \quad 0 \quad 1]$$

The on-line controller design in discrete state-space based on one framework allows calculating a matrix $T(\hat{\theta})$ that transforms between canonical frameworks, which is given as:

$$R_c(\hat{\theta}) = [E_c(\hat{\theta}) \quad E_c(\hat{\theta}) A_c(\hat{\theta}) \quad \dots \quad E_c(\hat{\theta}) A_c^{n-1}(\hat{\theta})]$$

$$R_o^{-1}(\hat{\theta}) = \begin{bmatrix} \hat{a}_1 & \hat{a}_2 & \dots & \hat{a}_{n-1} & 1 \\ \hat{a}_2 & \dots & \hat{a}_{n-1} & 1 & 0 \\ \vdots & \vdots & 1 & 0 & 0 \\ \hat{a}_{n-1} & 1 & 0 & 0 & 0 \\ 1 & 0 & 0 & 0 & 0 \end{bmatrix}, T(\hat{\theta}) = R_o^{-1}(\hat{\theta}) \times R_c(\hat{\theta}) \quad (21)$$

where, $T(\hat{\theta})$ is the transformation matrix between transparent canonical frameworks, $R_c(\hat{\theta})$ is the observability matrix of transparent controllable canonical form and $R_o^{-1}(\hat{\theta})$ is the inverse observability matrix of transparent observable canonical form.

The estimated state vector $\hat{X}_c(t)$ of an on-line observer of transparent controllable canonical form (plane framework) can be evaluated as follows:

$$\hat{X}_c(t+1) = A_c(\hat{\theta})\hat{X}_c(t) + L_c(\hat{\theta}) \left(y(t) - E_c(\hat{\theta}) \hat{X}_c(t) \right) + B_c(\hat{\theta})u(t) \quad (22)$$

The on-line observer gain matrix $L(\hat{\theta})$ can be easily calculated by using transparent observable canonical form [7], therefore, the on-line observer gains $L(\hat{\theta})$ is transformed to transparent controllable canonical form to be used in equation (22) as follows:

$$L_c(\hat{\theta}) = T \times L_o(\hat{\theta}) = T \times \begin{bmatrix} L_{o_1}(\hat{\theta}) \\ L_{o_2}(\hat{\theta}) \\ \vdots \\ L_{o_n}(\hat{\theta}) \end{bmatrix} = T \times \begin{bmatrix} \hat{a}_{n_a} - \sigma_{o(n)} \\ \hat{a}_{n_a-1} - \sigma_{o(n-1)} \\ \vdots \\ \hat{a}_1 - \sigma_{o(1)} \end{bmatrix} = \begin{bmatrix} L_{c_1}(\hat{\theta}) \\ L_{c_2}(\hat{\theta}) \\ \vdots \\ L_{c_n}(\hat{\theta}) \end{bmatrix} \quad (23)$$

The equation of the transparent controllable canonical form gain $K_c(\hat{\theta})$ can be written as:

$$K_c(\hat{\theta}) = [K_{c_1}(\hat{\theta}) \quad , \quad K_{c_2}(\hat{\theta}) \quad \dots \quad K_{c_n}(\hat{\theta})]$$

$$= [\hat{a}_{n_a} - \alpha_{c(n)} \quad , \quad \hat{a}_{n_a-1} - \alpha_{c(n-1)} \quad \dots \quad \hat{a}_1 - \alpha_{c(1)}] \quad (24)$$

The proper dc gain N can be calculated as follows:

$$(N(\hat{\theta}))^{-1} = -E_c(\hat{\theta})(A_c(\hat{\theta}) - B_c(\hat{\theta})K_c(\hat{\theta}) - I)^{-1}B_c(\hat{\theta}) \quad (25)$$

Referring to Figure (7), the control-law can be generated as follows:

$$\mathbf{u}(\mathbf{t}) = N(\hat{\theta})\mathbf{r}(\mathbf{t}) - K_c(\hat{\theta})\hat{\mathbf{X}}_c(\mathbf{t}) \quad (26)$$

The algorithm of Self-Tuning Observer Pole-placement with Reference Signal and Proper DC Gain can be summarized as follows:

Step 1: Select the desired control-law characteristic equation $\alpha_c(\mathbf{z})$ and the desired observer characteristic equation $\sigma_o(\mathbf{z})$.

Step 2: Read the new values of $\mathbf{y}(\mathbf{t})$ and $\mathbf{u}(\mathbf{t})$.

Step 3: Estimate the process parameters $\hat{\theta}$ using recursive least squares estimator or extended recursive least squares estimator and formulate a state-space model of the plant $\{A_c(\hat{\theta}), B_c(\hat{\theta}), E_c(\hat{\theta}), C_c(\hat{\theta})\}$ using equations (17) and (18).

Step 4: Evaluate $L_c(\hat{\theta})$ using equation (23).

Step 5: Estimate the state vector $\hat{\mathbf{X}}_c(\mathbf{t})$ using equation (22).

Step 6: Calculate $K_c(\hat{\theta})$ using equation (24).

Step 7: Compute $N(\hat{\theta})$ using equation (25).

Step 8: Apply the control input signal using equation (26).

Step 2 to 8 are repeated for every sampling instant.

Both the modern self-tuning pole-placement, shown in Figure 6, and the classical controllers were programmed as multiple controller algorithms. The design provides a choice of using either classical or modern pole-placement controller on-line throughout the flick of switches (S_1, S_2). The switching (transition) decision between these different fixed structure controllers is achieved manually in order to demonstrate the feasibility of the proposed approach. Each control mode can be switched on with the flick of the switches depending on the user's choice, whereas the other controller is at standby. This design also, provides the

possibility to choose an on-line identification method such recursive least squares (RLS) or extended recursive least squares (ERLS) estimators.

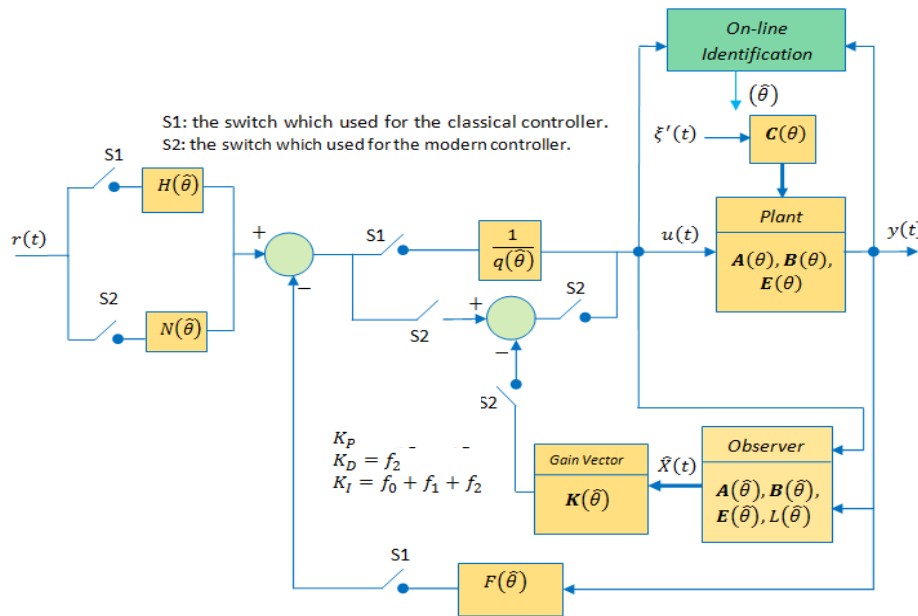


Figure 6: Multiple Self-tuning Controllers

4 Simulation Results

The main aim of developing a GUI is to simplify the control algorithms discussed in previous section so that the simulations can be carried out by users who do not even have a previous knowledge about the algorithms of self-tuning controllers. Thus, controller tuning and evaluation of the closed-loop performance can be realized interactively using the GUI in a user-friendly environment as shown in Figure 7.

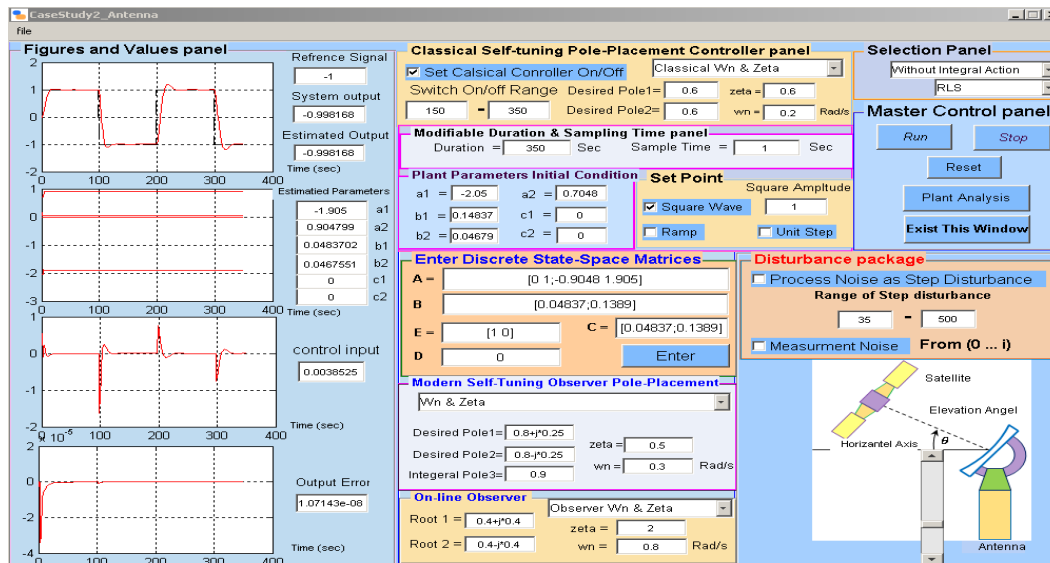


Figure 7: Multiple Controllers GUI

To study the response of the antenna output using multiple controllers, a simulation was carried out using the system described by the discrete state-space equations (8) and (9). The simulation was performed using recursive least squares estimator over 350 samples with a sample time of 1s (approximately 6 minutes) to track a rectangular signal (in dotted black line). The desired set point is a square wave signal that has peak values of 1 and -1 with a duration of 100 samples. The signal and the response using the Modern Self-Tuning Observer Pole-Placement controller is shown in the first 150 sample instants in Figure 8-a. The response of the system using the Classical Self-Tuning Pole-Placement controller is used after the 150th sample. The control input for the two cases are shown in Figure 8-b. Figures 8-a shows that these controllers are matched without any transient behaviour during switching mode.

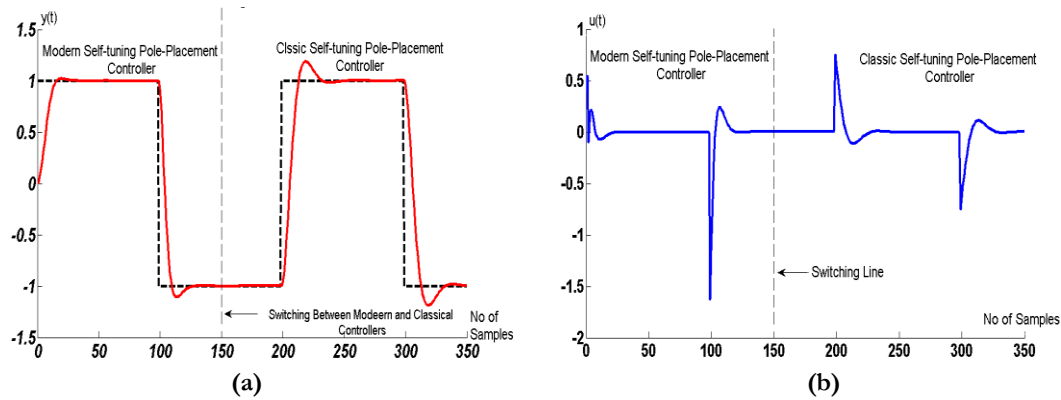


Figure 8: (a) Antenna outputs response for multiple controllers, (b) Multiple control input to the Antenna system

Another simulation was performed over 400 samples (approximately 7 minutes) using recursive least squares (RLS) estimator to track a triangular signal changes from 1 to 0 and from 0 to 1 every 100 samples instants. In this simulation, the classical self-tuning pole placement controller was switched on at 150th sampling instant, whereas the modern STOPPRI controller was used in first part of intervals as shown in Figure 8 and Figure 9.

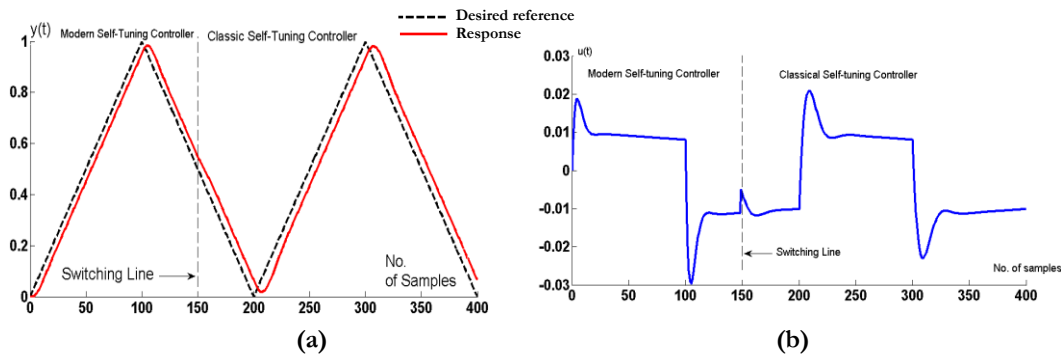


Figure 9: (a) Antenna System Output using modern and classical Controllers (b) Control Input of the Antenna System using classical and modern adaptive Controllers

In Figure 9-b, a small transient behaviour appeared at the 150th sampling instant during switching between modern and classical self-tuning controllers which does not affect the antenna response as shown in Figure 9-a and disappeared at steady-state region. 5Conclusions A multiple controller scheme incorporating an adaptive mechanism using classical transfer function technique and modern discrete state-space technique was designed the scheme was simulated with the application to antenna model controlling its elevation. This scheme enables the user to effectively switch between the classical and modern controllers. Once the desired controller is selected to be on-line, the other controller remains standby to ensure robust control performance in the presence of controller failure. Simulation testing the proposed method were carried out and shows the performance of the proposed technique.

5 Acknowledgment

The authors would like to thank Ausama Ahmed for his help in writing the manuscript.

References

- [1] A. Karl and B. Wittenmark, Adaptive Control, Courier Corporation, 2013.
- [2] D. W. Clarke, C. Mohtadi and P. S. Tuffs, "Generalized predictive control—Part I. The basic algorithm," *Automatica*, vol. 23, no. 2, pp. 137-148, 1987.
- [3] Z. Gao, "Scaling and bandwidth-parameterization based controller tuning," in *Proceedings of the American control conference*, 2006.
- [4] Narendra KS, Cheng Xiang, 2000, 'Adaptive Control of Discrete-time Systems using Multiple Models', IEEE Transaction on Automatic Control, 45, 1669-1686.
- [5] P. N. Paraskevopoulos, 2002, 'Modern control Engineering', CRC Press Taylor & Francis Group.
- [6] Gene F. Franklin, J. David Powell, Michael L. Workman, 1998, 'Digital Control of Dynamic Systems', 3rd ed., Addison-Wesley.
- [7] Katsuhiko Ogata, 1992, 'System Dynamics', 2nd ed., Prentice Hall.
- [8] Norman S. Nise, 2004, 'Control System Engineering', 4th ed., John Wiley & Sons.
- [9] M. Gopal, 2003, "Digital Control and State Variable Methods", 2nd ed., Prentice Hall.
- [10] Zhongshan Wu, 2001, 'Simulation Study And Instability Of Adaptive Control', MSc., The Department of Electrical and Computer Engineering, Louisiana State University, Louisiana, USA.
- [11] P. E. Wellstead, M. B. Zarrop, 1991, 'Self-Tuning Systems: Control and Signal Processing', John Wiley & Sons.

Control of a Three-phase Off-Grid Inverter for Photovoltaic Systems Applications

Ali M A Almaktoof, Abdulsslam M Ashoor Shaouf, Abdulbaset A Salem Wddan

Department of Electrical and Electronic, Faculty of Engineering, Sabratha University, Libya

DOI: <https://doi.org/10.21467/proceedings.2.27>

* Corresponding author email: alialmaktoof@gmail.com

ABSTRACT

This paper presented a model predictive control (MPC) strategy as used in photovoltaic (PV) systems applications to control a three-phase off-grid inverter. The PVs model was used in this study to investigate the system performance when power is supplied to a resistive-inductive load (RL-load).

The proposed strategy is to handle the output current for the three-phase, off-grid inverter with an RL-load. An assessment is given of the robustness of the control strategy under variable DC voltages, and as required for photovoltaic systems applications, by measuring the Total harmonic distortion (THD) and tracking behaviour of the reference currents; this was done for all DC voltage values. The system is tested as well with different sampling times to check the tracking behavior at designed values. The simulations and result analyses are carried out using MATLAB/Simulink to test the effectiveness and robustness of MPC for three-phase off-grid inverter with resistive-inductive load supplied by a PV system. The simulation results indicated that the proposed control algorithms achieved both high performance and a high degree of robustness in photovoltaic systems applications.

Keywords: Finite State-Model Predictive Control, three-phase off-grid inverter, photovoltaic systems.

1 Introduction

In recent years the use of renewable energy systems has become very important due to environmental concerns and the increased demand for energy [1, 2]. Renewable energy resources like solar energy can be used with maximum efficiency by utilizing appropriate power converters. As the availability of this energy resource is greatly uncertain, the power conversion system must rely on a suitable power converter and controller unit [3, 4]. The urge to increase the energy efficiency of all energy related systems in combination with the need to support emerging technologies like sustainable energy sources, promotes the development of highly efficient, high-power converters. Three-phase off-grid inverters are widely used in industrial applications and renewable energy systems [2, 5].

Model predictive control (MPC) for power converters has been researched since the early 1980s [5]. MPC requires a high number of calculations as compared to classic control methods,



© 2018 Copyright held by the author(s). Published by AIJR Publisher in Proceedings of First Conference for Engineering Sciences and Technology (CEST-2018), September 25-27, 2018, vol. 1.

This is an open access article under [Creative Commons Attribution-NonCommercial 4.0 International](https://creativecommons.org/licenses/by-nc/4.0/) (CC BY-NC 4.0) license, which permits any non-commercial use, distribution, adaptation, and reproduction in any medium, as long as the original work is properly cited. ISBN: 978-81-936820-5-0

but the fast microprocessors available today have made it possible to viably implement predictive control coupled with three-phase inverter with long prediction horizon [7]. Furthermore, MPC for power converters has distinct advantages when compared to the traditional pulse width modulation (PWM) methods [8].

Since power converters have a finite number of switching states, the MPC optimization problem can be easily formulated, simplified and reduced to the prediction of the system behaviour specifically for those possible switching states. This control method is known as a finite state-model predictive control (FS-MPC) approach. Many studies have been conducted into the successful application of FS-MPC schemes incorporated in three-phase inverters and drive applications [9-12].

The paper starts with an overview of the system description which presented in Section 2. This paper presents one of the simplest predictive control schemes, which is current control for a three-phase inverter. A simple model of the converter and the load are presented in section 3 and 4 respectively. The model predictive control of off-grid inverter is developed in Section 5. Results and discussions are presented next, followed by a conclusion in the last section of the paper.

2 System Description Overview

A three-phase off-grid inverter for the commonly renewable energy source available in Libya (solar energy) subject to model predictive control strategy is shown in Figure 1. Considering that the two switches in each inverter phase operate in a complementary mode in order to avoid short circuiting the DC source, the switching state of the power switches S_x , with $x = 1, \dots, 6$, can be represented by the switching signals S_a , S_b , and S_c defined as follows:

$$S_a = \begin{cases} 1 & \text{if } S_1 \text{ on and } S_4 \text{ off} \\ 0 & \text{if } S_1 \text{ off and } S_4 \text{ on} \end{cases} \quad (1)$$

$$S_b = \begin{cases} 1 & \text{if } S_2 \text{ on and } S_5 \text{ off} \\ 0 & \text{if } S_2 \text{ off and } S_5 \text{ on} \end{cases} \quad (2)$$

$$S_c = \begin{cases} 1 & \text{if } S_3 \text{ on and } S_6 \text{ off} \\ 0 & \text{if } S_3 \text{ off and } S_6 \text{ on} \end{cases} \quad (3)$$

These switching signals define the value of the output voltages

$$V_{aN} = S_a V_{dc} \quad (4)$$

$$V_{bN} = S_b V_{dc} \quad (5)$$

$$V_{cN} = S_c V_{dc} \quad (6)$$

Where V_{dc} is the DC source voltage.

Considering all the possible combinations of the gating signals S_a , S_b , and S_c , eight switching states and consequently eight voltage vectors are obtained (see Figure 2). In Figure 2 note that $V_0 = V_7$, resulting in a finite state of only seven different voltage vectors in the complex plane.

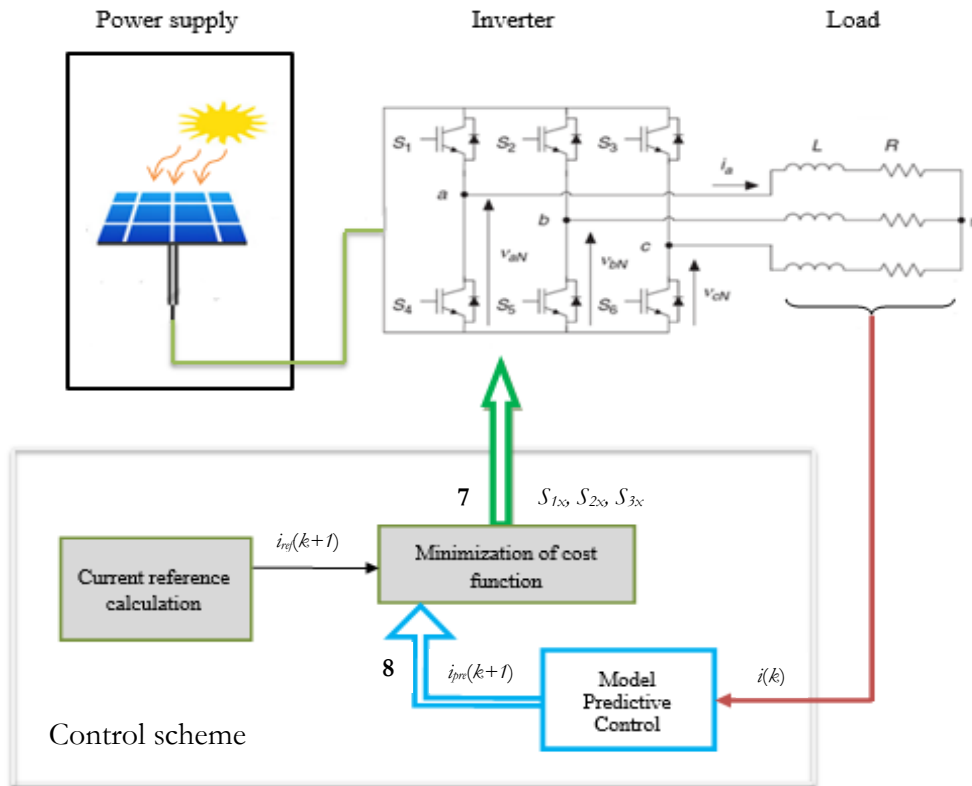


Figure 1: Inverter topology connected to the load and control block diagram

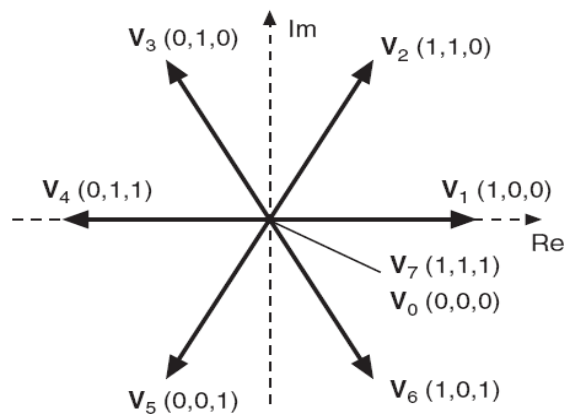


Figure 2: Voltage vectors in the complex plane.

3 Load Model

The differential equation of the load current for the inverter is applied to obtain the continuous-time state space equations of the load for each phase, the load current dynamics can be described by the vector differential equation

$$v_{DC}(t) = R_L \cdot i(t) + L_L \frac{di}{dt} \quad (7)$$

Where v is the voltage vector generated by the inverter, i is the load current vector. The load current derivative $\frac{di}{dt}$ is replaced by a forward Euler approximation [7]. That is, the derivative is approximated as follows:

$$\frac{di}{dt} \approx \frac{i(k+1) - i(k)}{T_s} \quad (8)$$

Which is substituted in (7) to obtain an expression that allows prediction of the future load current at time $k+1$, for each one of the seven values of voltage vector $v(k)$ generated by the inverter. This expression is

$$i^p(k+1) = \left(1 - \frac{RT_s}{L}\right) i(k) + \frac{T_s}{L} v(k) \quad (9)$$

Using the Clarke transformation, Clarke transformation is defined as following,

$$v_\alpha = 2/3 (Va - 0.5 Vb - 0.5 Vc) \quad (10)$$

$$v_\beta = 2/3 (0.5 \sqrt{3} Vb - 0.5 \sqrt{3} Vc) \quad (11)$$

Then, the discrete-time load model can be to:

$$\begin{pmatrix} i_\alpha(k+1) \\ i_\beta(k+1) \end{pmatrix} = \begin{pmatrix} 1 - T_s \frac{R_L}{L_L} & 0 \\ 0 & 1 - T_s \frac{R_L}{L_L} \end{pmatrix} \begin{pmatrix} i_\alpha(k) \\ i_\beta(k) \end{pmatrix} + \begin{pmatrix} \frac{T_s}{L_L} & 0 \\ 0 & \frac{T_s}{L_L} \end{pmatrix} \begin{pmatrix} v_\alpha(k) \\ v_\beta(k) \end{pmatrix}. \quad (12)$$

Equation (12) is used to predict the load current for each switching possibility.

4 Cost Function

The objective of the current control scheme is to minimize the error between the measured currents and the reference values. This requirement can be written in the form of a cost function [7, 8]. The cost function g is evaluated for each of the seven possible voltage vectors generated by this inverter to calculate the future value of the load current. The voltage vector that minimizes the cost function is selected and applied during the next sampling instant. The cost function is expressed in orthogonal coordinates and measures the error between the references and the predicted currents:

$$g = \left| i_\alpha^*(k+1) - i_\alpha^p(k+1) \right| + \left| i_\beta^*(k+1) - i_\beta^p(k+1) \right| \quad (13)$$

5 Model Predictive Control of Off-Grid Inverter

As presented early in Figure 1 a three-phase off-grid inverter for a PV system application subject to model predictive control strategy where i_{ref} represents the reference current for the predictive control, $i(k)$ is the measured variable current at time, k , and $i_{pre}(k+1)$ is the predicted current for n allowed switching states at time, $(k+1)$. The errors between the reference and predicted values are obtained to minimize the cost function, and the switching state that minimizes the cost function, is chosen. The switching signals, S , of the chosen state are then applied to the converter. To reduce the computational effort that arises from the switching possibilities (8 different switching possibilities for one prediction step), the switching state that delivers the best voltage vector among 7 voltage vectors is determined; this was illustrated in Figure 2. The optimal switching state, which is the one that minimizes the simple cost function, is selected and applied at the next sampling instance when the time is $(k+1)$. The block diagram of the different tasks performed by the predictive controller is shown earlier in Figure 1. In general, the control algorithm, can be summarized by the following steps:

- (1) Measure the load currents and DC voltage.
- (2) Initialize the value of the optimum cost function.
- (3) For all permissible switching states, predict the load currents and capacitor voltages for the next sampling instant.
- (4) Evaluate the cost function for each prediction.
- (5) Select the optimal switching state that minimizes the cost function.
- (6) Apply the new switching state.

6 Results and Discussion

The simulations and result analyses are carried out using MATLAB to test the effectiveness and robustness of FS-MPC for a three-phase, two-level off-grid inverter with resistive-inductive load supplied by a photovoltaic system as shown in Figure 1. Table 1 shows the parameters used for the simulation.

Table 1: Parameters used for the co-simulations

<i>Parameter</i>	<i>Value</i>
<i>Load resistance, R</i>	<i>10Ω</i>
<i>Load inductance, L</i>	<i>35 mH</i>
<i>DC voltage, v_{DC}</i>	<i>300 V</i>
<i>Amplitude of the reference current, i_{ref}</i>	<i>8 A</i>
<i>Sampling time, Ts</i>	<i>100 μs</i>

The control algorithm was evaluated with regard to two performance indicators: Firstly, the robustness and variability of control strategy under variable input DC voltage is done, and secondly, with different sampling time, the system is investigated.

6.1 Control strategy robustness under variable DC voltages

In this simulation the system is designed at a voltage value is 300V at sampling time $T_s = 75 \mu s$. Figure 3 shows the output current i_{α} , magnitude value of output current and output voltage v_{α} by using Fast Fourier Transform (FFT) in MATLAB/SUMLINK.

To demonstrate the stability of the proposed control method under conditions of variable DC voltages; the system has been tested when the DC voltage was changed from 125 to 600 V with $T_s = 75 \mu s$. Figure 4 shows the output currents for different values of DC voltages. It can be observed that the proposed control algorithm has the ability to follow sinusoidal reference currents despite substantially changing the DC voltage from the desired voltage except Figure 4(a). These results of the simulation are in Table 2.

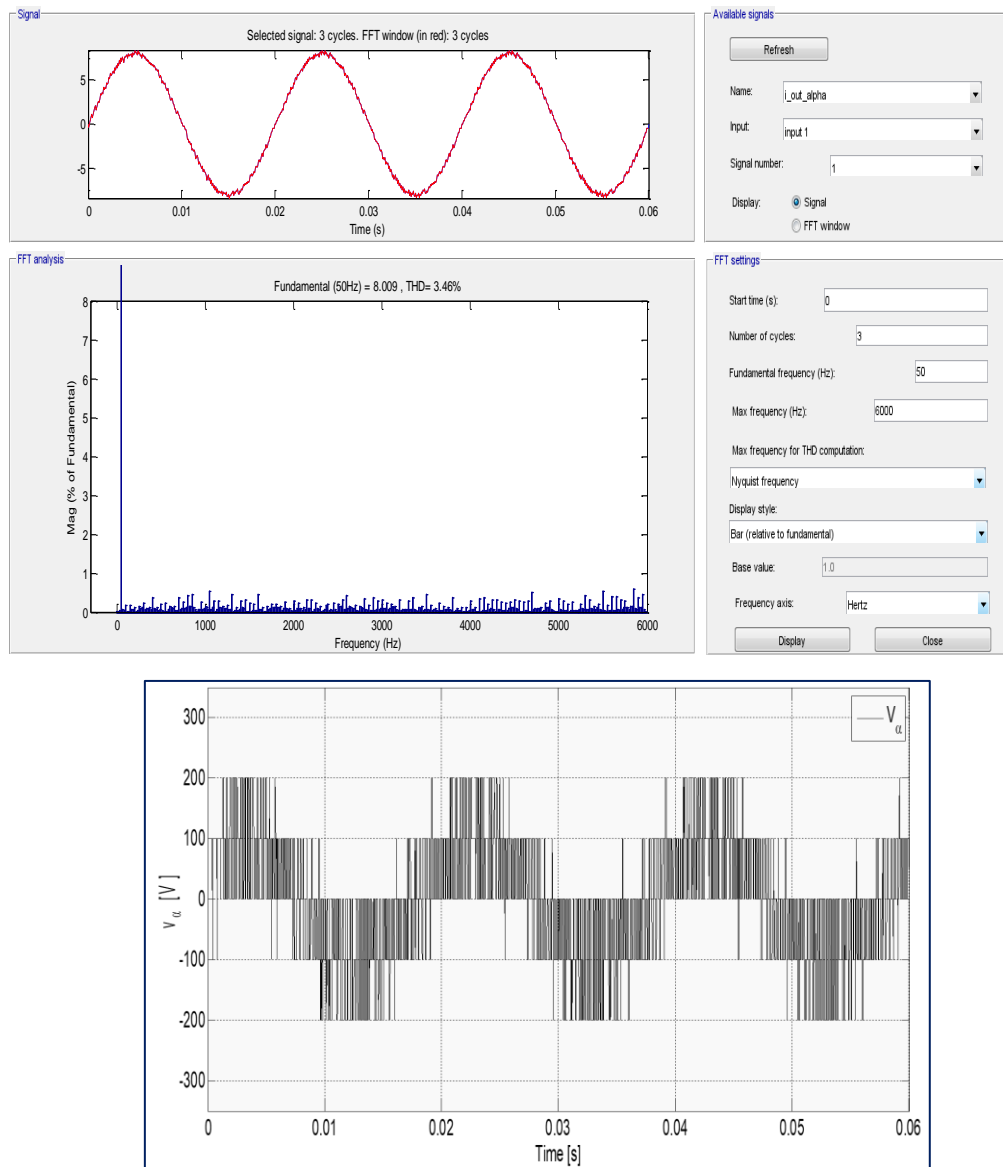


Figure 3: Output current and its magnitude value and output voltage at designed values.

Table 2: THD and output current for variable DC voltages

DC-Link value, [V]	Fund. current at 50 Hz, [A]	THD [%]
125	6.096	7.76
200	8.007	2.33
220	8.015	2.66
240	8.006	2.69
260	7.978	2.95
280	8.000	3.35
320	7.971	3.46
340	8.021	3.85
360	7.981	4.14
380	7.999	4.30
400	7.969	4.66
450	7.945	5.07
500	8.008	5.71
550	7.997	6.41
600	7.961	6.64

In Figure 4(a) is shown the output current of the DC voltage when it was set to 125V and the THD was 7.76% and the fundamental current at 50 Hz is 6.096. It is notable that the system was out of control at 125V with high THD and a high amplitude error was produced.

In Figure 4(b) is shown the results of the DC voltage when it was set to 260 V and the THD was 2.95%. Compare these results to those shown in Figure 4(c) when the DC voltage was set to 400 V and the THD 4.66%, as well as those shown in Figures 4(d) when the DC voltage was set to and 600 V and the THD was increased to 6.64%.

It is notable that voltages higher than the designed voltage value of 300 V produced a higher THD, while the amplitude of the output current was kept constant and tracked the reference current with a small error. On the other hand, for DC voltage values smaller than the designed value, a lower THD with a relatively small amplitude error was produced.

6.2 Control strategy robustness under variable DC voltages

Depending on the complexity of the controlled system, the number of calculations can be significant and will limit the minimum sampling time. In the simplest case, predictive current control, the calculation time is small, but in other schemes such as torque and flux control, the calculation time is the parameter which determines the allowed sampling time.

This simulation demonstrated the effectiveness of the proposed control method under conditions of different sampling times; in particular when the sampling time was changed from 25 to 150 μ s at the designed parameters values. Figure 4 shows the output currents for different values of sampling times. It can be observed that the proposed control algorithm has

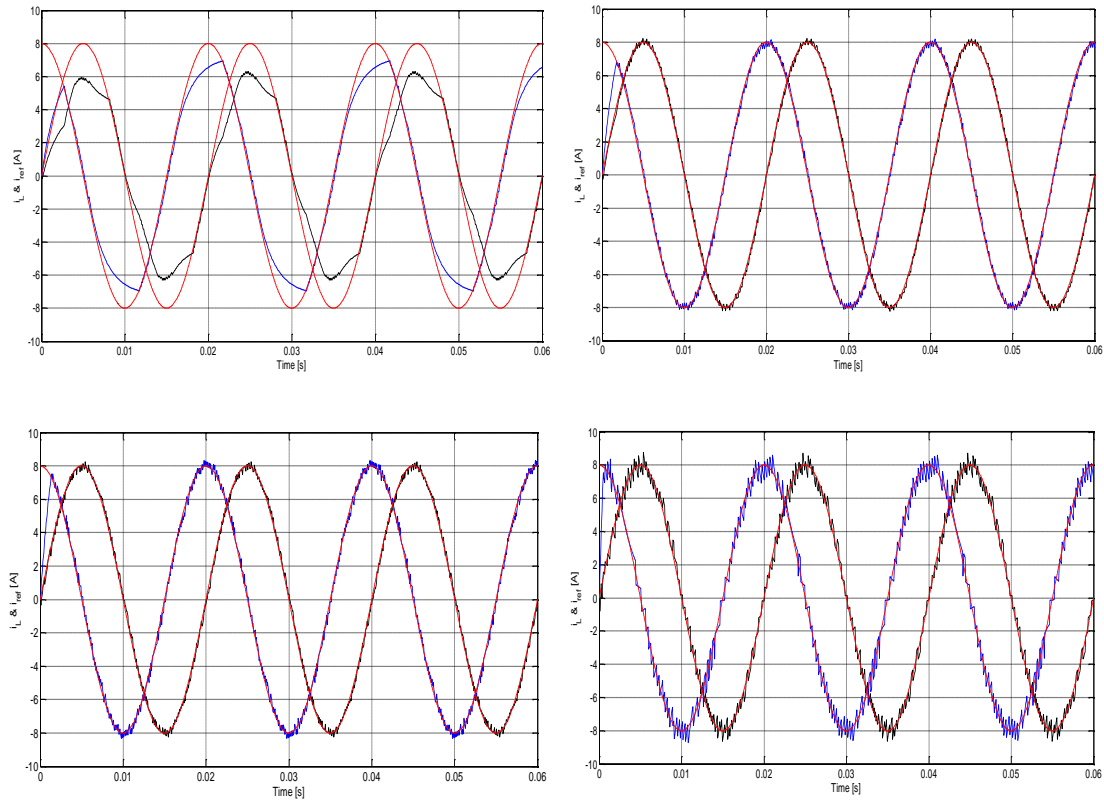


Figure 4: Output currents for different values of DC voltage at $T_s = 75 \mu s$. (a) $V_{DC} = 125V$, (b) $V_{DC} = 200V$, (c) $V_{DC} = 400V$ and (d) $V_{DC} = 600V$.

the ability to follow sinusoidal reference currents despite substantially changing the sampling time from the desired sampling time. These results of the simulation are in Table 3.

In Figure 5 is shown, the results of the output current and output voltages, where current and voltage in one phase of the load are shown in Figure 5(a) and Figure 5(b) for sampling time $T_s = 150 \mu s$ and $100 \mu s$ respectively. There is no steady state error in the current but there is a noticeable ripple. This ripple is reduced considerably when a smaller sampling time is used, as shown in Figure 5(c) and Figure 5(d) for a sampling time $T_s = 25 \mu s$ and $50 \mu s$ respectively. However, by reducing the sampling time, the switching frequency is increased as can be seen by comparing the load voltages in Figure 5.

Table 3: THD and output current for variable DC voltages

Sampling time T_s , [μs]	DC voltage, [V]	Fund. current at 50 Hz, [A]	THD [%]
25	300	7.997	1.28
50	300	7.996	2.17
75	300	8.009	3.48
100	300	8.012	4.57
125	300	7.994	5.54
150	300	8.018	6.77

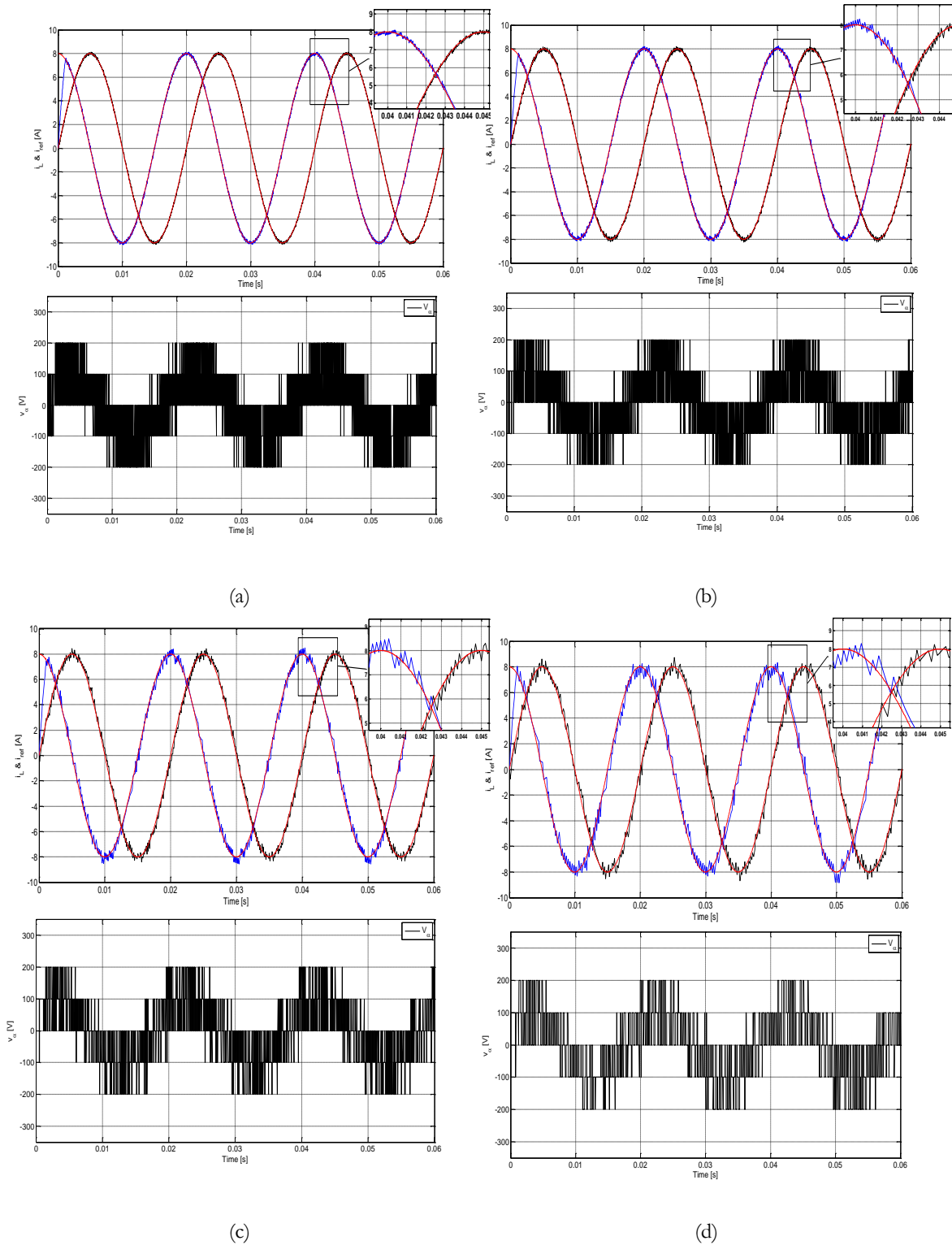


Figure 5: Output currents for different values of sampling time T_s

7 Conclusions

In this paper the MPC strategy for PV system applications has been presented to control the three-phase off-grid inverter. The PV model has been used in this paper to investigate the system performance when power is supplied to RL-load. The proposed control method does not require any kind of linear controller or modulation technique. The FS-MPC algorithm has been evaluated through simulation results. Firstly, the robustness of control strategy under variable DC for three-phase off-grid inverter for PV system application has been done in terms of the THD. Secondly, with different sampling time, the system has been investigated. The simulation results show that the predictive control method has the ability to track sinusoidal reference currents and show excellent tracking behavior with all DC voltage values. Although the theory of MPC was developed in the 1970s, its application in power converters is more recent due to the fast sampling times that are required. The fast microcontrollers available in these days have made it possible to implement the proposed control scheme to three-phase off-grid inverter for PV system application. Sampling time can critically affect the performance of a control system. selecting the best sampling time to execute the entire algorithm is depends on the switching frequency in the load voltages.

References

- [1] Siemens, 2012. Energy Sector 2012, Erlangen (Germany), www.siemens.com/energy [20 May 2018].
- [2] A. Nami & F. Zare. "Multilevel Converters in Renewable Energy Systems, Renewable Energy," T J Hammons (Ed.), ISBN: 978-953-7619-52-7, 2009. InTech, Available from: <http://www.intechopen.com/books/renewable-energy/multilevel-converters-in-renewable-energy-systems>.
- [3] E. J. Bueno, S. Cobreces, F. J. Rodríguez, A. Hernandez, & F. Espinosa, "Design of a back-to-back NPC converter interface for wind turbines with squirrel-cage induction generator," *IEEE Trans. on Energy Conversion*, Vol. 23 No.3, 2008. pp.932–45.
- [4] L. M. Tolbert & F. Z. Peng, "Multilevel Converters as a Utility Interface for Renewable Energy Systems," *IEEE Power Engineering Society Summer Meeting*, Volume 2, 16–20 2000. pp. 1271-1274. Seattle, Washington.
- [5] N. Mohan, T. M. Undeland, and W. P. Robbins, "Power Electronics: Converters, Applications and Design," (3rd edition). New York: John Wiley & Sons. 2003.
- [6] R. Kennel and D. Schroeder, "Predictive control strategy for converters," in Proc. *the third IFAC Symposium*, pp. 415–422, Lausanne, 1983.
- [7] A. M. Almaktoof, A. K. Raji and M. T. E. Kahn, "Performance Evaluation and Improvement of an FS-MPC for Two-Level VSI," *The International Conference on Electrical and Electronics Engineering, Clean Energy and Green Computing (EEECEGC 2013)*, United Arab Emirates, pp. 120–126. December 11–13, 2013.
- [8] J. Rodríguez and C. Cortés, "Predictive control of Power Converters and Electrical Drives," UK: A Johan Wiley & Sons, Ltd., 2012.
- [9] V. Yaramasu, M. Rivera, B. Wu, & J. Rodríguez, "Model Predictive Current Control of Two-Level Four-Leg Inverters—Part I: Concept, Algorithm, and Simulation Analysis," *IEEE Transactions on Industrial Electronics*, vol. 28 no. 7. July 2013, pp. 3459–3468.
- [10] H. Abu-Rub, J. Guzinski, Z. Krzeminski, & H. A. Toliyat. "Predictive current control of voltage source inverters," *IEEE Trans. on Ind. Electron*, vol. 51 no. 3, 2004. pp. 585–593.
- [11] J. Li, F. Zhuo, X. Wang, L. Wang, & S. Ni, "A grid-connected PV system with power quality improvement based on boost + dual-level fourleg inverter," in Proc. *IEEE Int. Power Electron. and Motion Control Conf.*, Wuhan, China, 2009. pp. 436–440.
- [12] R. Vargas, P. Cortés, U. Ammann, J. Rodríguez, & J. Pontt, "Predictive control of a three-phase neutral-point-clamped inverter," in *IEEE Transactions on Industrial Electronics*, vol. 54, no. 5, Oct. 2007, pp. 2697-2705.

Excimer Laser Processing of IGZO Thin Films for Transparent TFTs

Khairi. M. Abusabee^{ab*}, Khalid. M. Alajel^a, Salem. O. Elhamali^c

^aElectrical and Computer Engineering Department, Faculty of Engineering, El-Mergib University, Al-Khums, Libya

^bSchool of Science and Technology, Nottingham Trent University, Clifton Lane, Nottingham NG11 8NS, UK

^cElectrical and Computer Engineering Department, Faculty of Engineering, Al-Asmarya Islamic University, Zliten, Libya

DOI: <https://doi.org/10.21467/proceedings.2.28>

* Corresponding author email: kmabusabee@elmergib.edu.ly

ABSTRACT

The effects of post deposition annealing treatments on indium gallium zinc oxide IGZO thin films deposited by radio frequency RF magnetron sputtering at ambient temperature have been studied for application to thin film transistor TFT devices fabrication. Krypton Fluoride KrF ($\lambda = 248$ nm) excimer laser annealing ELA and low-temperature thermal annealing (150°C) has been applied to IGZO films of 30 nm and 50 nm thickness as part of the fabrication process for TFT devices. The effect of annealing pre and post patterning of the IGZO channel layers was investigated. The results indicate that single pulse ultra rapid ELA is a viable technique for processing of the channel layers to provide TFT characteristics equivalent to or even better than that produced by a 150°C annealing for one hour. ELA treatment pre-patterning resulted in TFTs demonstrating a higher ON current and on/off current ratio relative to ELA treatment post-patterning. This could be attributed to surface defects introduced by the photolithographic patterning of the IGZO channel. In comparison, the thermally treated films exhibited better performance with the post-patterning thermal treatment.

Keywords: RF magnetron sputtering, excimer laser annealing, post patterning, pre patterning, thin film transistors, IGZO.

1 Introduction

Transparent amorphous oxide semiconductors TAOS are of a great importance in display technologies and are promising candidate materials for emerging applications in flexible transparent electronics. In particular, amorphous indium gallium zinc oxide based thin film transistors (IGZO TFTs) have attracted considerable attention [1,2], and have been demonstrated as switching devices in active matrix liquid crystal displays AMLCDs, and organic light emitting diode OLEDs based display panels[3, 4].

The first functional IGZO based TFTs reported in 2004 by Nomura et al, were fabricated on flexible substrates via pulsed laser deposition PLD. These devices were investigated as an



© 2018 Copyright held by the author(s). Published by AIJR Publisher in Proceedings of First Conference for Engineering Sciences and Technology (CEST-2018), September 25-27, 2018, vol. 1.

This is an open access article under [Creative Commons Attribution-NonCommercial 4.0 International](https://creativecommons.org/licenses/by-nc/4.0/) (CC BY-NC 4.0) license, which permits any non-commercial use, distribution, adaptation, and reproduction in any medium, as long as the original work is properly cited. ISBN: 978-81-936820-5-0

alternative to amorphous silicon (a-Si) and poly silicon (poly-Si) TFTs, because of the high field effect mobility that was demonstrated in the amorphous state ($>10 \text{ cm}^2/\text{Vs}$) [1]. This mobility is attributed to the heavy metal cations with $(n-1) d^{10} ns^0$ ($n \geq 5$) electronic configuration leading to a large overlap between adjacent cations orbitals [5]. Since the first reports on IGZO TFT research, there has been an increasing interest in studying the effect of post deposition annealing as a mechanism to improve the IGZO TFTs performance and stability. It has been reported that conventional post-deposition thermal annealing at ($\sim 400^\circ\text{C}$) is an effective method to improve the IGZO TFTs performance [6], and stability [7], and reducing the tail state defects in IGZO film [5]. However, post thermal annealing at temperature higher than the maximum allowable temperature for heat resistance of plastic substrates ($\sim 150^\circ\text{C}$) is undesirable when considering low cost and flexible substrate applications. As an alternative to thermal annealing, photonic processing using lamps or laser irradiation is a method of interest for a range of thin films' applications where highly localised annealing and surface modification is imposed [8 – 12]. For example, Nakata et.al reported utilizing excimer laser annealing (ELA) to process 20 nm IGZO thin films for inverted-staggered bottom gate IGZO-TFTs deposited by RF magnetron sputtering, using two pulses from an XeCl excimer laser ($\lambda=308 \text{ nm}$) 25 ns. IGZO-TFTs irradiated at laser fluences of $130 \text{ mJ}/\text{cm}^2$ exhibited ON current more than one order of magnitude higher than that of un-annealed devices [8]. Ahn et.al fabricated bottom gate IGZO-TFT, using a 50 nm thick channel layer grown by RF magnetron sputtering at room temperature. The IGZO film was selectively laser annealed via a projection mask using an XeCl ($\lambda=308 \text{ nm}$) excimer laser in air ambient at ten pulses with a range of laser density from 0 to $250 \text{ mJ}/\text{cm}^2$. The electrical properties of the devices treated with laser energy density $130 \text{ mJ}/\text{cm}^2$ exhibited a channel mobility $21.79 \text{ cm}^2/\text{Vs}$, on/off ratio of 1.2×10^8 , threshold voltage $\sim -0.15\text{V}$. As the laser fluences increased to $130 \text{ mJ}/\text{cm}^2$ the resistivity of IGZO film decreased from $10^4 \Omega \text{ cm}$ to $3.2 \times 10^{-3} \Omega \text{ cm}$ with carrier concentration $1.3 \times 10^{20} \text{ cm}^{-3}$, and hall mobility $15 \text{ cm}^2/\text{Vs}$ [11]. It has also been reported by Zan et al [13] that Nd(YAG) laser (266 nm) or UV lamp irradiation (172 nm) suppressed the instability of IGZO TFTs, and reduced the defects in IGZO film. Lim et.al demonstrated improvement of electrical properties of bottom gate ZnO TFT devices fabricated at low temperature (200°C) [14].

For the investigation presented here, we have undertaken a comparison of low temperature (150°C) thermal processing and the application of KrF photons with single pulse irradiation to study the effects on IGZO TFTs characteristics for devices utilising low temperature deposited IGZO thin films as the TFTs active layer. We are particularly interested in when the annealing treatment is applied in the fabrication process, pre or post IGZO channel patterning, and the effect this has on the resultant characteristics.

2 Experimental procedure

2.1 Film deposition

IGZO thin films of 30 nm and 50 nm thickness were deposited by RF magnetron sputtering from a ceramic target of $\text{In}_2\text{O}_3:\text{Ga}_2\text{O}_3:\text{ZnO}$ molar ratio (1:1:1) and (purity 99.99%) onto silicon dioxide coated silicon substrates. Deposition was performed at ambient temperature (with no intentional substrate heating) across a range of sputtering conditions by varying oxygen concentrations (2% O_2/Ar , 5% O_2/Ar), and RF power (50 W, 100 W) with deposition pressure 1.33 Pa to optimise the IGZO films for use in TFT device fabrication.

2.2 Post- deposition annealing of IGZO thin films

Annealing by thermal treatment at 150°C for one hour on a hotplate was compared with excimer laser processing undertaken at ambient temperature in air using a Lambda Physik 305i 248 nm, 20 ns pulse KrF excimer laser, with a beam delivery system providing a homogenised 14 mm x 14 mm uniform irradiation at the sample plane. Processing was undertaken at fluences in the range of 0 mJ/cm^2 to 175 mJ/cm^2 ($\pm 6 \text{ mJ}/\text{cm}^2$) using single pulse irradiation. The resultant IGZO thin films are characterised by four point probe (4PP) measurements, Hall Effect, and used in TFT test devices fabrication.

2.3 IGZO-TFT fabrication

Figure.1 shows the cross section of top gate bottom contacts IGZO-TFT device fabricated on SiO_2/Si substrates as per the following process: (i) chromium (Cr) and gold (Au) deposited by evaporation for source and drain electrode contacts with thicknesses of 5 nm and 75 nm respectively and patterned by photolithography and lift off techniques; (ii) IGZO active layer deposited by RF magnetron sputtering with no intentional heating of the substrate, from an IGZO ceramic source target with $\text{In}_2\text{O}_3:\text{Ga}_2\text{O}_3:\text{ZnO}$ molar ratio of (1:1:1) 99.9% purity at RF power of 50 W, oxygen concentration 2 % O_2/Ar , at 1.33 Pa working pressure. The devices were divided into two sets. One was laser annealed before IGZO patterning, while the second set was laser annealed after IGZO patterning (in both cases, the samples were laser annealed as described in section 2.2. prior to the gate dielectric deposition). The IGZO layer was patterned via photolithography and wet etching producing IGZO channels with width (W) and length (L) of 1000 μm and 5 μm respectively. Alumina (Al_2O_3) was deposited as the gate dielectric by atomic layer deposition ALD at 120°C, and pattern by photolithography and lift off. Finally, a bilayer gate electrode of (Cr/Au, 5/75 nm) was deposited by evaporation.

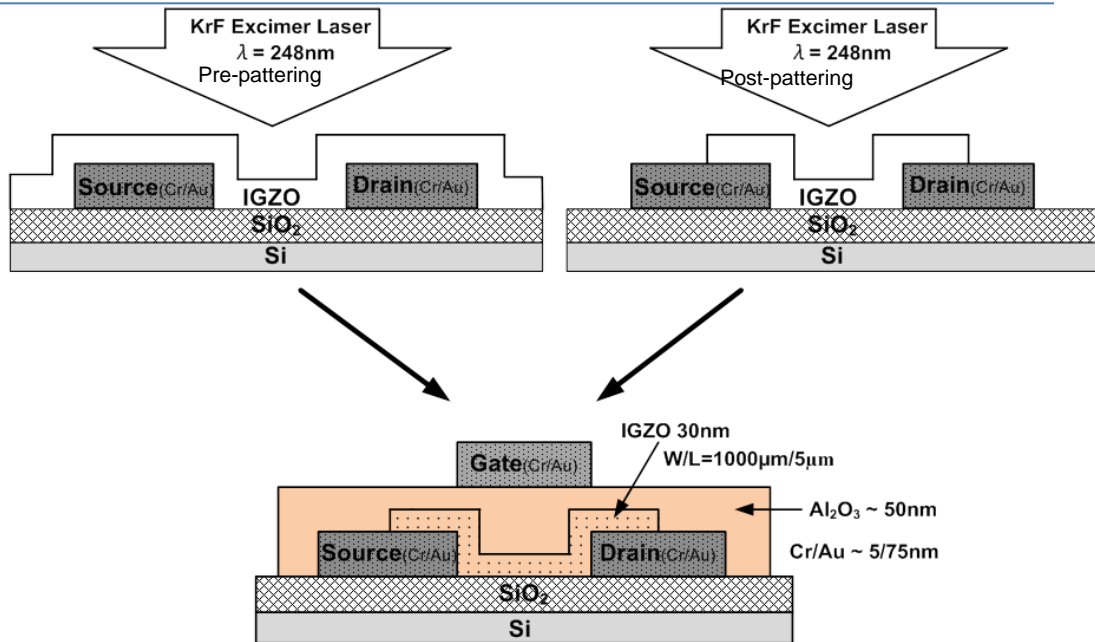


Figure 1: Schematic cross section of IGZO-TFT devices showing the concept of pre and post patterning laser anneal processing

3 Results

3.1 Electrical properties of IGZO thin films

Figure.2 illustrates the sheet resistance of IGZO films deposited at an applied RF power of 50 W and various oxygen concentrations following laser annealing at various fluences using single pulse irradiation. The as-deposited IGZO films were highly resistive and not measurable using the four point probe system (i.e. they have sheet resistances $> 5 \text{ MOhm/sq}$) for all deposition conditions examined. A measurable sheet resistance was achieved at fluences of $\geq 75 \text{ mJ/cm}^2$, with the lowest sheet resistance of 1 kOhm/sq observed at a laser fluence of 100 mJ/cm^2 for all IGZO films studied. Processing at higher fluences led to an increase in sheet resistance coincident with visible damage of the film surface at these higher fluences. Similar trends were observed with films grown at RF power 100 W.

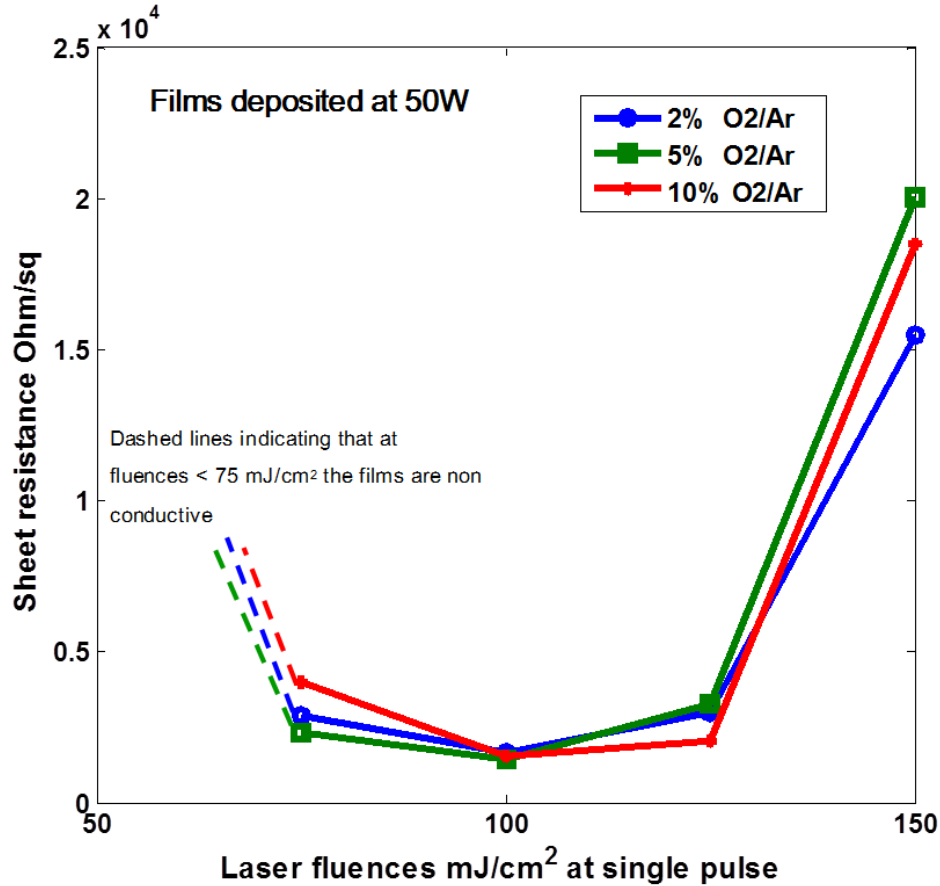


Figure 2: Sheet resistance of 30 nm thick IGZO films deposited at 50 W following laser processing irradiated at various fluences.

3.2 Hall Effect Characterisation

Figure.3 shows the electrical characteristics as determined via room temperature Hall Effect measurement of the laser processed IGZO thin films, deposited at 50 W RF power, 2%O₂/Ar, 50 nm, as a function of laser fluence. The as-deposited and samples irradiated at laser fluences of 25 mJ/cm², and 50 mJ/cm² were too resistive to be measured, consistent with the four point probe measurements. At the higher fluences investigated, of 75 mJ/cm² and 100 mJ/cm², results were obtained indicating an increase in Hall mobility at higher fluences from 11.1 cm²/Vs to 13.9 cm²/Vs. At 175 mJ/cm², however, the mobility dropped to 1.67 cm²/Vs, which again coincides with visible surface damage to the films. The drop in carriers mobility at higher fluences could be attributed to the onset of IGZO films crystallisation. The corresponding values of resistivity determined via Hall Effect measurement decreased from 5.92x10⁻² to 9.7x10⁻³ Ω.cm with fluence increasing from 75 to 125 mJ/cm² due to a steady increase in carrier concentration that is reduced at higher fluences because of samples damage.

Regarding the thermally annealed samples, they were not measurable due to their high resistance to make contacts with the Hall effect equipment. However, the thermally annealed samples were suitable as the semiconducting channel layer in TFT fabrication, the results of which are described in section 3.3. Similarly, for TFT channel layer fabrication, the laser annealing fluences that produced functional TFT test devices were the lower fluence/higher resistance films processed at $\leq 75 \text{ mJ/cm}^2$.

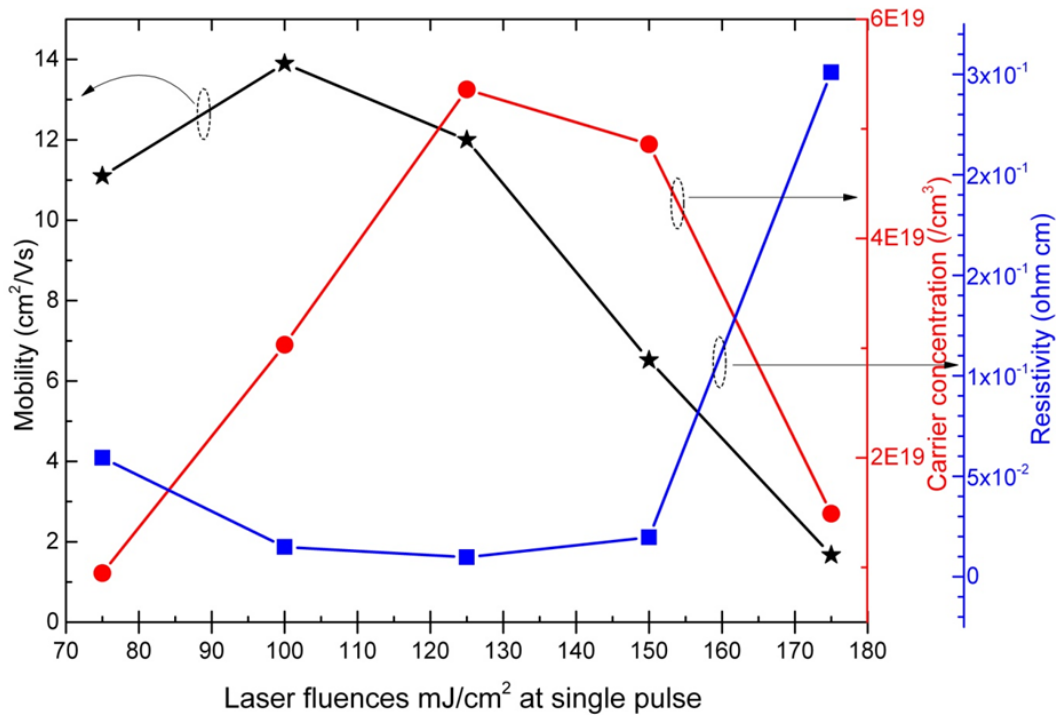


Figure3: Hall Effect characteristics, showing Hall mobility, carrier concentration, and resistivity of 50 nm thick IGZO thin films as a function of applied laser fluence.

For IGZO films with thickness of 30 nm, no Hall mobility or conductivity could be detected for as-deposited films and laser irradiated films at various fluences. The high resistivity of laser annealed 30 nm film could be linked to the surface of the film being affected by atmospheric oxygen and changing the film properties and difficulties of achieving contacts with the Hall effect system. This is still a matter for investigation. However, it was reported by Nakata et.al in a comparison study, that the dependance of Hall mobility measurements and carrier density on laser fluence of laser annealed IGZO film by XeCl excimer laser ($\lambda=308 \text{ nm}$) deposited at 20 nm where the highest Hall mobility achieved was $\sim 17 \text{ cm}^2/\text{Vs}$ at laser energy density of about 180 mJ/cm^2 [16].

3.3 Thermal annealed IGZO – TFTs result

Figure 4 shows the transfer characteristics of IGZO-TFTs with the active channel is being IGZO films of 30 nm thick. The TFTs were thermally annealed at 150 °C in an air environment for 1 hour, before and after the channel layer patterning. The results are summarised in Table 1 as compared to the non-annealed device. There was a slight improvement in electrical performance of the thermally annealed IGZO TFTs pre IGZO patterning but with an increased OFF current. Whereas, thermally annealed IGZO TFTs post IGZO patterning show significant improvement of transfer characteristics. In both cases there is a negative shift in the threshold voltage, an improvement in the ON current, and a significant improvement in the On/Off current ratio for the post pattern annealed sample. In general, for the thermally annealed devices, the improvement in performance was better when annealed post IGZO patterning. Similar result trends were observed upon repetition of this exercise.

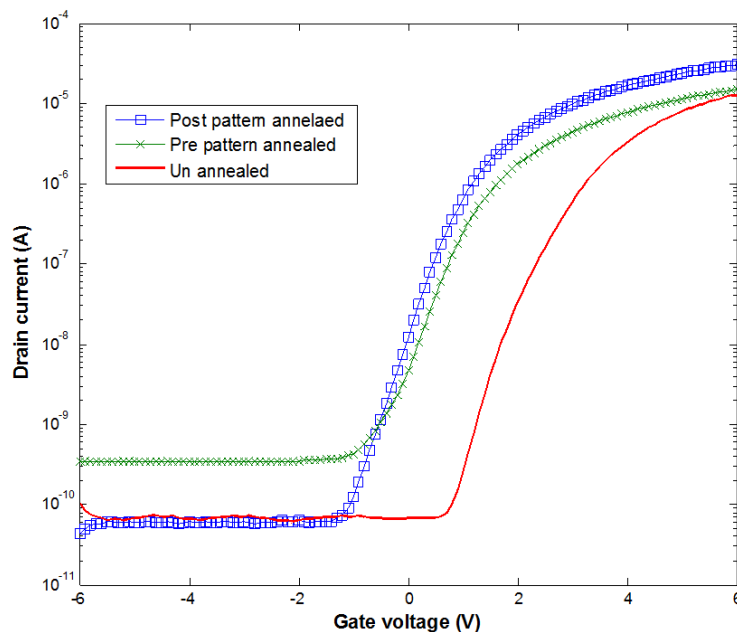


Figure 4: Transfer characteristics of IGZO-TFTs ($W/L = 1000 \mu\text{m}/5 \mu\text{m}$), $V_{DS} = 1 \text{ V}$ for samples that had been un annealed compared to samples thermal annealed at 150°C in air for 1 hour pre and post IGZO patterning.

Table 1: The effects of thermal annealing, at 150°C in air for 1 hour pre and post IGZO patterning, on IGZO –TFTs electrical properties.

Sample	V_{th} (V)	μ_{FE} (cm^2/Vs)	S (V/dec)	$I_{D \text{ Max}}$ (A)	I_{ON}/I_{OFF} ratio
Un-annealed	3.52 ± 0.14	0.14 ± 0.04	0.41 ± 0.14	1.36×10^{-5}	1.48×10^5
150°C pre patterning	1.65 ± 0.28	0.10 ± 0.03	0.64 ± 0.11	1.54×10^{-5}	7.46×10^4
150°C post patterning	1.60 ± 0.23	0.16 ± 0.09	0.52 ± 0.08	2.75×10^{-5}	0.78×10^6

Results indicated that thermal annealing at low temperature after IGZO channel layer patterning is more effective than before, which could be attributed to the effect on the interface between the IGZO layer and the dielectric layer by the photoresist heat treatment at 100°C for 1 min and 20 s, since this would be a different effect when the photoresist is heated pre and post thermal anneal.

3.4 Excimer laser annealed IGZO – TFTs result

The TFT results for the laser processed samples are shown in Figure 5 which represents the characteristics from devices fabricated on the same substrate.

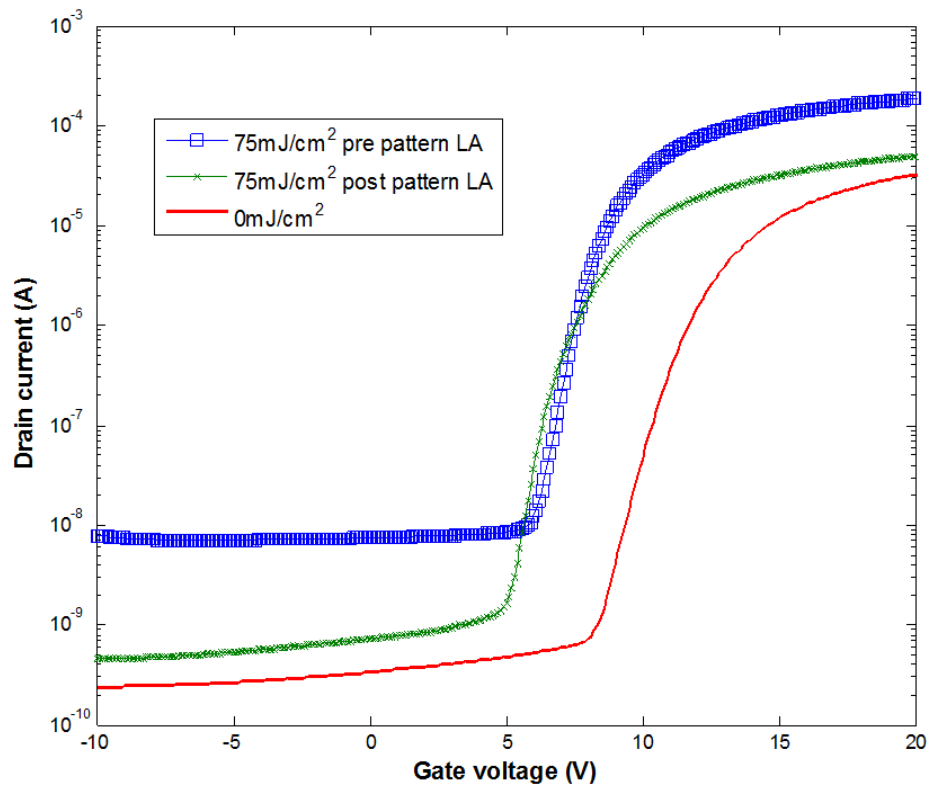


Figure 5: Transfer characteristics of IGZO-TFTs ($W/L = 1000 \mu\text{m}/5 \mu\text{m}$), $V_{DS} = 1 \text{ V}$, for samples un-annealed and laser annealed at a fluence of $75 \text{ mJ}/\text{cm}^2$ in air.

As with the thermally annealed samples, the laser treated TFTs at laser energy density of $75 \text{ mJ}/\text{cm}^2$ with single pulse show a negative shift in threshold voltage and an increase of ON current. However, devices laser annealed pre IGZO pattern demonstrate higher ON and OFF current than the devices that were laser processed post to IGZO pattern. This could be assigned to surface defects introduced during photolithographic patterning deteriorating the performance of the laser annealed TFTs. The electrical properties of these devices are summarized in Table 2.

Table 2: *Properties of IGZO –TFTs laser annealed pre and post patterning of the active layer 30 nm thick.*

Sample	V_{th} (V)	μ_{FE} (cm ² /Vs)	S (V/dec)	I_D Max (A)	I_{ON}/I_{OFF} ratio
Un- annealed	12.1±0.7	0.003±0.005	0.70±0.04	3.25x10 ⁻⁵	1.58x10 ⁵
75 mJ/cm ² pre pattern	8.15±0.5	0.64±0.69	0.71±0.07	2.00 x10 ⁻⁴	8.47x10 ⁷
75 mJ/cm ² post pattern	7.93±0.5	0.25±0.21	0.61±0.17	5.01x10 ⁻⁵	3.38x10 ⁶

Laser annealed IGZO-TFT devices with a channel layer 30 nm thick demonstrating very low field effect mobility. This is consistent with the observation that no Hall Effect measurements could be performed on 30 nm thick IGZO films at different laser energy densities, while laser processed 50 nm thick IGZO film exhibited Hall mobility as high as 13.9 cm²/Vs.

4 Discussion

A significant drop in sheet resistance of IGZO thin films deposited without intentional substrate heating as a function of laser energy density for a single pulse is observed with a strong dependence on deposition parameters. Post deposition annealing of IGZO films leads to removal of weakly bonded oxygen atoms or oxygen combination contributing to a new equilibrium changing the electrical properties of IGZO films [13, 15]. The lowest sheet resistance post laser processing was observed at deposition conditions of low deposition pressure, low oxygen concentration, and high RF power. This can be attributed to the sputtered atoms' kinetic energy and thus their surface mobility on the substrate is being controlled with the deposition parameters. Hence, the resulting film properties are dependent on the films deposition parameters [2, 5]. Upon ELA, the resistivity of IGZO films was considerably reduced and the free electron density as well as the Hall Effect mobility were effectively enhanced as a function of laser fluence. These observations could be attributed to local atomic rearrangement, the amorphous structure randomness relaxation, and trap states density reduction. The local atomic rearrangement and structure relaxation caused by ELA heating, provided that no crystallisation occurs, would enhance the overlap among ns orbitals of the contained metals leading to better carrier mobility [2, 11, 12]. The highest observed Hall effect mobility in this work was 13.9 cm²/Vs obtained by ELA with single pulse at 100 mJ/cm², which is very promising to apply laser treated IGZO to IGZO TFTs.

For IGZO-TFT devices, thermal and laser annealing IGZO channel layer patterns result enhanced electrical performance of IGZO TFTs. This is originated from induced changes in IGZO layers upon annealing including reduction of scattering or trapping defects density on the bulk IGZO or at its interface, enhanced atomic bonding, and amorphous structure relaxation leading to enhanced electrical properties of IGZO [2, 11, 12]. Laser irradiation is also expected to reduce the contact resistance between the IGZO channel layer and the source/drain electrodes due to reduction of IGZO channels resistivity and increasing the carrier concentration upon ELA. This would move the Fermi level in IGZO to higher positions towards the conduction band i.e. decreasing IGZO work function leading to better

electrical contact between IGZO layer and S/D electrodes and thus better IGZO TFTs performance [5, 11]. However, both annealing techniques resulted in negative shift in threshold voltage which could be attributed to the high defects density in the subgap density of states (DOS) pins the Fermi level, so no mobile carries. In addition, TFTs devices demonstrate high values of sub-threshold swing S which is related to trap density in the subgap. High sub-threshold swing S result in poor electrical properties such as, low speed and higher power consumption. Therefore, further investigations are needed to optimise the ELA application to IGZO TFTs fabrication using wide range of annealing parameters.

5 Conclusions

For the results presented here, the room temperature Hall Effect mobility of IGZO (50 nm thick) was effectively enhanced as the laser fluence was increased from 75 mJ/cm² to 100 mJ/cm² (single pulse) reaching values of 11.1 cm²/Vs and 13.9 cm²/Vs respectively. Laser annealing of IGZO-TFT pre IGZO channel patterns result in relatively higher ON current than post pattern while thermally annealing post IGZO pattern demonstrate higher ON current. Hence, these results demonstrate that laser annealing is a powerful technique to modify the electrical properties of IGZO films grown at room temperature for TFTs applications.

6 Acknowledgment

We would like to acknowledge the UK Technology Strategy Board for support for this work as part of the SKTP project.

References

- [1] W. S. Author, K. Nomura, H. Ohta, A. Takagi, T. Kamiya, M. Hirano and H. Hosono, "Room-temperature fabrication of transparent flexible thin-film transistors using amorphous oxide semiconductors," *Nature*, vol. 432, pp. 488-492, 2004.
- [2] H. Yabuta, M. Sano, K. Abe, T. Aiba, T. Den, H. Kumomi, K. Nomura, T. Kamiya and H. Hosono, "High-mobility thin-film transistor with amorphous InGaZnO channel fabricated by room temperature RF-magnetron sputtering," *Appl. Phys. Lett.*, vol. 89, pp. 112123, 2006.
- [3] J. Y. Kwon, K. S. Son, J. S. Jung, T. S. Kim, M. K. Ryu, K. B. Park, B. W. Yoo, J. W. Kim, Y. G. Lee and K. C. Park, "Bottom-gate gallium indium zinc oxide thin-film transistor array for high-resolution AMOLED display," *Electron Device Letters, IEEE*, vol. 29, pp. 1309-1311, 2008.
- [4] C. J. Kim, D. Kang, I. Song, J. C. Park, H. Lim, S. Kim, E. Lee, R. Chung, J. C. Lee and Y. Park, "Highly stable Ga₂O₃-In₂O₃-ZnO TFT for active-matrix organic light-emitting diode display application," in *Electron Devices Meeting, 2006. IEDM'06. International, 2006*, pp. 1-4.
- [5] H. Hosono, K. Nomura, Y. Ogo, T. Uruga and T. Kamiya, "Factors controlling electron transport properties in transparent amorphous oxide semiconductors," *J. Non Cryst. Solids*, vol. 354, pp. 2796-2800, 5/1, 2008.
- [6] K. Nomura, T. Kamiya, H. Ohta, M. Hirano, H. Hosono, "Defect passivation and homogenization of amorphous oxide thin-film transistor by wet O₂ annealing," *Appl. Phys. Lett.* 93 (2008) 192107.
- [7] K. Nomura, T. Kamiya, Y. Kikuchi, M. Hirano, H. Hosono, "Comprehensive studies on the stabilities of a-In-Ga-Zn-O based thin film transistor by constant current stress," *Thin Solid Films*, 518 (2010) 3012.
- [8] M. Nakata, K. Takechi, K. Azuma, E. Tokumitsu, H. Yamaguchi and S. Kaneko, "Improvement of InGaZnO₄ thin film transistors characteristics utilizing excimer laser annealing," *Applied Physics Express*, vol. 2, pp. 1102, 2009.

- [9] N. Mitsuru, T. Kazushige, Y. Shinya, T. Eisuke, Y. Hirotaka and K. Setsuo, " *Effects of Excimer Laser Annealing on InGaZnO₄ Thin-Film Transistors Having Different Active-Layer Thicknesses Compared with Those on Polycrystalline Silicon*, " *Jpn J Appl Phys*, 48 (2009) 115505.
- [10] Y. Yang, S. S. Yang and K. Chou, " *Characteristic Enhancement of Solution-Processed In–Ga–Zn Oxide Thin-Film Transistors by Laser Annealing*, " *Electron Device Letters*, IEEE, vol. 31, pp. 969-971, 2010.
- [11] B. Du Ahn, W. H. Jeong, H. S. Shin, D. L. Kim, H. J. Kim, J. K. Jeong, S. H. Choi and M. K. Han, " *Effect of excimer laser annealing on the performance of amorphous indium gallium zinc oxide thin-film transistors*, " *Electrochemical and Solid-State Letters*, vol. 12, pp. H430-H432, 2009
- [12] C. Tsakonas, V. Kuznetsov, W. Cranton, N. Kalfagiannis, K. Abusabee, D. Koutsogeorgis, N. Abeywickrama and P. Edwards " *Low temperature sputter-deposited ZnO films with enhanced Hall mobility using excimer laser post-processing*, " *J. Phys. D: Appl. Phys.* vol. 50, pp. 485306 (15). 2017
- [13] H. W. Zan, W. T. Chen, C. W. Chou, C. C. Tsai, C. N. Huang and H. W. Hsueh, " *Low temperature annealing with solid-state laser or UV lamp irradiation on amorphous IGZO thin-film transistors*, " *Electrochemical and Solid-State Letters*, vol. 13, pp. H144-H146, 2010.
- [14] S. Lim, J. M. Kim, D. Kim, C. Lee, J. S. Park and H. Kim, " *The Effects of UV Exposure on Plasma-Enhanced Atomic Layer Deposition ZnO Thin Film Transistor*, " *Electrochemical and Solid-State Letters*, vol. 13, pp. H151-H154, 2010.
- [15] A. Suresh, P. Gollakota, P. Wellenius, A. Dhawan and J. F. Muth, " *Transparent, high mobility InGaZnO thin films deposited by PLD*, " *Thin Solid Films*, vol. 516, pp. 1326-1329, 2008
- [16] M. Nakata, K. Takechi, S. Yamaguchi, E. Tokumitsu, H. Yamaguchi and S. Kaneko, " *Effects of excimer laser annealing on InGaZnO₄ thin-film transistors having different active-layer thicknesses compared with those on polycrystalline silicon*, " *Jpn J Appl Phys*, vol. 48, pp. 115505-115505-6, 2009.

Loss of Load Expectation of Alkhoms Generating Units

Mohamed Altaher Ben Mouhsen, Ali A. Tamtum*

Department of Electrical and Computer Engineering, Elmergib University, Libya

DOI: <https://doi.org/10.21467/proceedings.2.29>

* Corresponding author email: aamtatum@yahoo.com

ABSTRACT

AlKhoms generating power station is one of the largest stations in the Libyan generation system. It consists of eight units represent approximately 18% of the Libyan generation capacity. Hence, it is chosen to perform the reliability study presented in this paper. Generation system reliability is an important aspect in the planning for the future system capacity expansion since it provides a measurement to make sure that the total generation system capacity is sufficient to provide adequate electricity when needed. There are two approaches used for generating units reliability, deterministic and probabilistic approaches. The probabilistic approach branches into Monte Carlo simulation and analytical methods which include loss of load expectation (LOLE). The LOLE is the most widely used index in generation adequacy evaluation; it indicates the expected time for which the available generation will not be sufficient to meet the demand. In this paper, a reliability study is performed on Alkhoms generating units. Forced outage rates (FOR) is calculated, annual load data is analyzed, annual load duration curve is constructed and convolved with the generation model, and the (LOLE) is evaluated. The effect of load growth and FOR variation are also considered. A computer program is written in MATLAB as a tool for this purpose and used to construct the annual load duration curve and capacity outage probability table (COPT). the importance of this study comes from the fact that the system consists from non-identical units since the eight units has a different FOR which complicate the evaluation; as well as the fact that the binomial distribution cannot be applied directly while most published studies simplify the evaluation by grouping up identical units

Keywords: Reliability study; loss of load expectation (LOLE); Forced outage rates (FOR); Load duration curve.

1 Introduction

The fundamental aim of any power utility is to satisfy the system load and energy requirement of its customers at the lowest operating cost with an acceptable level of continuity and quality of electricity supply. In Libya, the General Electric Company of Libya (GECOL) is the power utility responsible for generation, transmission and distribution of the electric power for the whole country. The total installed capacity of the generating units was 6200MW in 2008 which is not sufficient to meet the present peak load.



Alkhoms generating station is one of the biggest stations in the Libyan generation system, it consists of eight generating units with total generating capacity of 1080 MW which represents about 18% of the Libyan gross capacity. Moreover, its data is available at the station office. Hence, it was chosen to perform this study.

Many papers throughout the world related to LOLE has been published, such as [1], in which the impact of aging characteristics of components on the calculation of reliability indices such as LOLE was described. In [2] the LOLE was evaluated for a proposed test system of six generating units is used, some units has identical FOR and identical capacities with 64 states of available capacity. In [3] a method for generation reliability assessment using intelligent systems was proposed. The effect of varying the load and failure rates on reliability indices was analysed in [4]. The relationship between LOLE and reserve margin was discussed in [5] where the peak load variation curve (DPLVC) with 365 point is used instead of load duration curve for a modified Peninsular Malaysia system consisting of 22 generating units and the LOLE was evaluated in days/year.

In [6], LOLE has been discussed for Alkhoms gas and steam units as two individual subsystems each of them consists of four identical units with 16 states of available capacity.

The object of this paper is to develop techniques to evaluate LOLE for Alkhoms generating system consisting of eight units having different capacities and different FOR with 256 states of available capacities and using a generation model based on a wide range of actual history including 2015 and 2016.

2 Generation System Reliability.

Generally; reliability can be defined as the probability of device (or system) performing its purpose adequately for the period of time intended under the operating conditions[7]. Reliability evaluation of a complete power system including generation, transmission, station and distribution facilities is an important in overall power system planning and operation[8]. Due to the enormity of the problem, reliability analysis of each level is performed independently.

Generation system reliability is concerned only to the generating units reliability, assuming that other levels are 100% reliable. The first techniques of generation system reliability were all deterministic. The most common deterministic approaches are the reserve margin and the largest set in the system[9]. Probabilistic methods can provide more meaningful information to be used in the sign and resources in planning and allocation. There are two main approaches for probabilistic evaluation of power system reliability; analytical methods and Monte Carlo simulation. Analytical techniques represent the system by mathematical methods and use direct analytical solutions to evaluate a priori reliability indices from the model, it includes loss of load expectation (LOLE), loss of energy expectation (LOEE) and frequency and duration method. Monte Carlo simulation estimates the actual random behaviour of the system[10].

The basic approach for the generating system adequacy consists of three parts as shown in Figure 1.

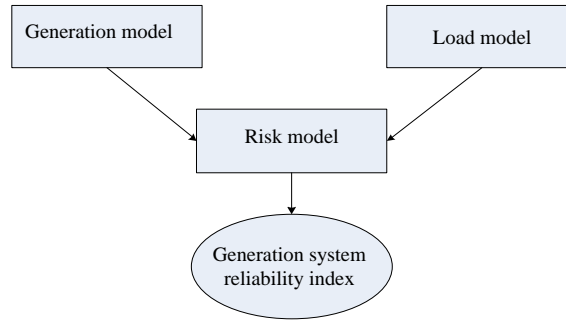


Figure 1: Generating system adequacy

The generation model and the load model are convolved to give the risk model which represent the risk of generation capacity less than load. The adequacy evaluation of the generation system consists of three steps :

- create a general capacity model based on the operating characteristics of the generating units .
- build an appropriate load model .
- combine the generation capacity model with the load model to obtain the risk model.

2.1 Generation Model (State Space Representation)

For simplicity, with no derated states considered, generating unit can be reside only in up or down (repair) state as shown in Figure 2.

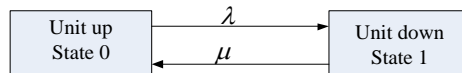


Figure 2: State space diagram of a generating unit

Where: λ is the expected failure rate.

μ is the expected repair rate.

m is the mean time to failure.

r is the mean time to repair.

T is the cycle time = $m + r$

The term unavailability (forced outage rate) can be defined as the probability of finding the unit on forced outage at a certain time in future.

$$Unavailability = U = FOR = \frac{\Sigma(down\ time)}{\Sigma(down\ time)+\Sigma(rep\ time)} \tag{1}$$

$$U = \frac{\lambda}{\lambda+\mu} = \frac{r}{r+m} \tag{2}$$

The total number of available (or unavailable) capacity states of an n units system is 2^n

2.2 Capacity Outage Probability Table (COPT)

In the analytical method, generation model is based on capacity outage probability table which lists system capacity states in increasing order of capacity outage, together with the probability of occurrence of each of these states [11].

If all units have identical capacity and FOR then the COPT can be constructed directly using binomial distribution in the following form:

$$(p + q)^n \tag{3}$$

Where: p is the availability.

q is the unavailability.

n is the number of units.

If all units haven't identical capacity but have identical FOR, binomial distribution cannot be applied directly but we should classify units in groups of tables according to their capacities and FOR and combine identical units using binomial distribution; then combine together one at a time that groups of tables. If the units have different FOR, then the expression of equation (3) becomes as follow:

$$(p_1 + q_1)(p_2 + q_2) \dots \dots \dots (p_n + q_n) \tag{4}$$

2.3 Load Model

The load model used in an analytical approach is usually either the daily peak load variation curve (DPLVC) or the load duration curve (LDC). The DPLVC includes only the peak load of each day for the period being considered, whereas the LDC includes the hourly variation of the load in this period [8]. Figure 3 shows a typical LDC.

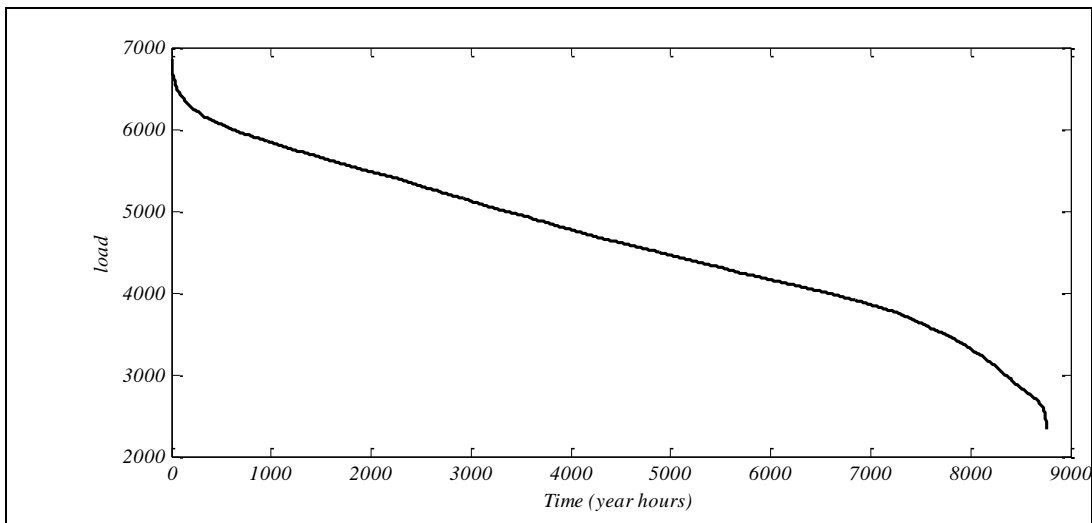


Figure 3: A typical load duration curve

3 Loss Of Load Expectation (LOLE)

The term 'capacity outage' indicates a loss of generation which may or may not result in a loss of load. This condition depends up on the generating capacity reserve margin and the system load level . A loss of load will occur only when the capability of the generating capacity remaining in service is exceeded by the system load level [11]. The LOLE indicates the expected time for which the available generation will not be sufficient to meet the demand [12]. After combining the generation capacity model with the load model ,then the loss of load expectation can be evaluated from the following formula :

$$LOLE = \sum P_k(Q_k) \cdot t_k \quad (5)$$

Where: P_k is the individual probability of capacity outage of Q_k .

Q_k is the magnitude of the outage in the system capacity outage probability table.

t_k is the number of time units in the study interval than an outage magnitude of Q_k would result in loss of load.

n is the number of states of the capacity outage probability table.

4 Numerical Results

4.1 Case study

Alkhoms generation station consisting of eight units of a total generating capacity of 1080 MW, the FOR is based on two years' operating cycle data. Table (1) illustrates the generation system data[13].

Table 1: generating system data

Unit number	Capacity (MW)	FOR
1	150	0.012
2	150	0.023
3	150	0.149
4	150	0.029
5	120	0.046
6	120	0.083
7	120	0.024
8	120	0.085

4.2 Simulation Results

Simulation is carried out using M-File/Matlab software to construct the capacity outage probability table (COPT) of 256 states of available (or unavailable) capacity, load duration curve (LDC) and evaluate the LOLE index. The capacity outage probability table is given in table (2).

Table 2: Capacity outage probability table of Alkhoms generating units

Capacity out of service (MW)	Probability	Cumulative probability
0	0.623144721257247	1.000000000000000
120	0.159660214366457	0.376855278742753
150	0.149954450175113	0.217195064376296
240	0.014299685339326	0.067240614201183
270	0.038420865720981	0.052940928861857
300	0.007994557339277	0.014520063140876
360	0.000516996133141	0.006525505801599
390	0.003441097035067	0.006008509668458
420	0.002048340770630	0.002567412633391
450	0.000152806235759	0.000519071862761
480	0.000006212499829	0.000366265627002
510	0.000124410699863	0.000360053127173
540	0.000183456026312	0.000235642427310
570	0.000039151541409	0.000052186400998
600	0.000000931712604	0.000013034859590
630	0.000001494984976	0.000012103146986
660	0.000006632737291	0.000010608162010
690	0.000003506538714	0.000003975424719
720	0.000000238720523	0.000000468886005
780	0.000000079702490	0.000000230165482
810	0.000000126776703	0.000000150462991
840	0.000000021380582	0.000000023686289
930	0.000000001523416	0.000000002305706
960	0.000000000773002	0.000000000782290
1080	0.00000000009289	0.00000000009289

The Libyan network load data of 2016 (8760 hours are only considered) with a peak load of 6861 MW is collected from GECOL, and since Alkhoms generating units represents 17.4% of the Libyan generating capacity, it is assumed that it is loaded by 17.4% of the Libyan hourly gross load, this assumption is considered because no specific unit in the Libyan generating system supplies a specific load but all units participate in the supply of Libyan gross load. The load model for the base case is the load duration curve of 2016 and the LOLE is evaluated in hours/year.

Figures 4, 5 and 6 show the LDC of the years 2016, 2017 and 2018 respectively.

Case 1 (Base case):

For the year of 2016, with a peak load of 1195 MW and the FOR of table (1), the LOLE is 1159 hours /year.

Case 2:

With an annual load growth of 6% [14] , the peak load is 1266 MW ,the LOLE of 2017 is 1893 hours /year .

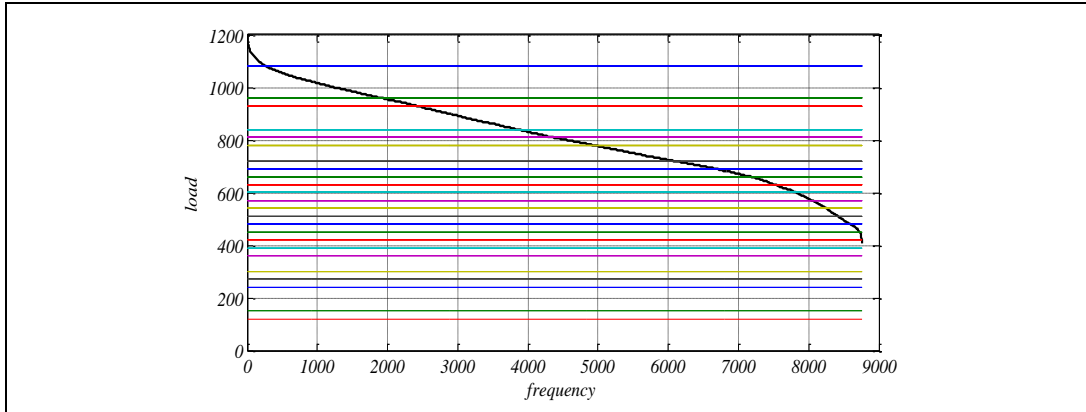


Figure 4: Load duration curve of 2016

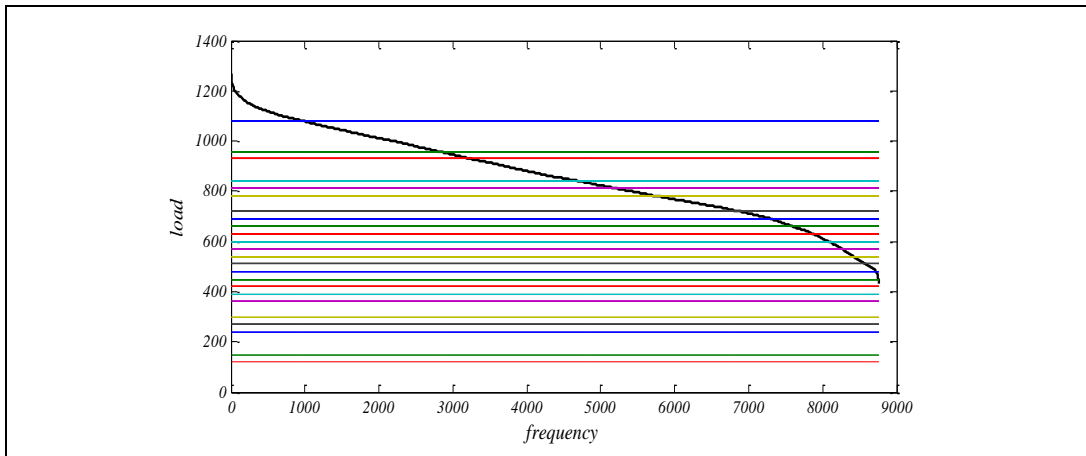


Figure 5: Load duration curve of 2017

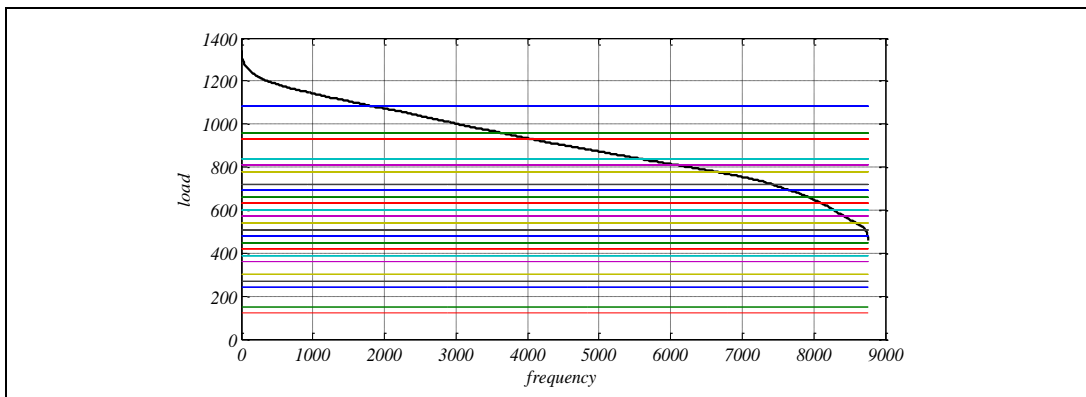


Figure 6: Load duration curve of 2018

Case 3:

With an annual load growth of 6% , the peak load is 1342.86 MW and the LOLE of 2018 is 2806 hours /year.

Case 4:

Again , for 2018 with the same assumption of case 3 , but considering a reduction of FOR of all units to 0.01,we obtain the modified COPT shown in table (3) , and the LOLE of 2018 is 2024 hrs/year.

Table 3: Capacity outage probability table of Alkhoms generating units with $FOR=0.01$

Capacity out of service (MW)	Probability	Cumulative probability
0	0.922744694427920	1.000000000000000
120	0.037282613916280	0.077255305572080
150	0.037282613916280	0.039972691655800
240	0.000564888089641	0.002690077739521
270	0.001506368239042	0.002125189649880
300	0.000564888089641	0.000618821410839
360	0.000003803960200	0.000053933321198
390	0.000022823761198	0.000050129360998
420	0.000022823761198	0.000027305599801
450	0.000003803960200	0.000004481838603
480	0.00000009605960	0.000000677878404
510	0.000000153695362	0.000000668272443
540	0.000000345814564	0.000000514577082
570	0.000000153695362	0.000000168762518
600	0.00000009605960	0.000000015067157
630	0.00000000388120	0.000000005461197
660	0.000000002328718	0.000000005073077
690	0.000000002328718	0.000000002744359
720	0.00000000388120	0.000000000415642
780	0.00000000005881	0.00000000027522
810	0.00000000015682	0.00000000021642
840	0.00000000005881	0.00000000005960
930	0.00000000000040	0.000000000000079
960	0.00000000000040	0.000000000000040
1080	0.00000000000000	0.000000000000000

5 Conclusion

Already it is known that the Libyan generation system has no reserve margin, its capacity is less than the present peak load, and it is unreliable. This paper presents a quantitative measure of the risk related to a part of Libyan generation system. The reliability study of Alkhoms generating system was performed using the available data from GECOL. The LOLE index is evaluated for different cases. Cases 1 and 2 showed that the load growth of 6% leads to

increasing LOLE by 734 hour/year (63.33 %); whereas cases 3 and 4 showed that the reduction of FOR of all units to 0.01 reduces the LOLE by 782 hour/year (27.8 %). For all cases, it is clear that the values of LOLE are very high and violates the acceptable level, this is a direct result of the high loading considered for the units of interest (17.4 % of the Libyan gross load) and dependent on the used data imported from GECOL. To overcome this bad situation, it is recommended to complete the under construction projects of the Libyan generation system to meet the present load and the future load growth.

References

- [1] Hagkwen Kim, Chanan Singh, "Reliability modeling and Simulation in power systems with aging characteristics", *IEEE transactions on power systems*, Vol.25, Issue 1, Feb. 2010, P: 21-28.
- [2] Mehdi Nikzad, Shoorangiz Shams Shamsabad Farhani, Mohammad Bigadi Tahar, Hossein Tourang, Behrang Yousefpour, "Calculation of generation system reliability index : loss of load expectation", *Life Science Journal*, 2012, 9, (4).
- [3] H.Haroonabadi, M. R. Haghifam, "Loss of load expectation assessment in deregulated power system using Monte Carlo simulation and intelligent systems", *International Journal of Smart Electrical Engineering*, Article 3, Vol.01, Issue 01, Winter 2012, Page:17-25.
- [4] C. R. Sharada Prasad, Shiddalingappa Ajjampur, Santhosh Raikar M, Prakash MN, "To study the adequacy assessment of generation system", *International Journal of advanced research in electrical, electronics and instrumentation engineering*, Vol.3, Issue 1, January 2014.
- [5] Siti Rasheeka Muhamad Zafir, Noor Miza Muhamad Razali , Tengku Juhana Tengku Hashim, "Relationship between loss of load expectation and reserve margin for optimal generation planning" , *Jurnal teknologi (Sciences &Engineering)*, 78:5-9 (2016) 27-33.
- [6] Marwan M. Alturshany , Loss of load expectation for Alkhoms gas and steam units, "B.Sc graduation project 2017 ", *Faulty Of Engineering –Elmergib University*.
- [7] Roy Billinton , Ronald N., "Reliability evaluation of engineering systems: concepts and techniques", *Plenum Publishing (New York)*, 1984 .
- [8] R. Billinton , L . Goel, "Adequacy assessment of an overall electric power system analysis", *IEEE proceeding*, Vol.139,No.1, Jan 1992 pp 57-63 .
- [9] Chanan Singh, "Power system reliability analysis", *Texas A,M University*.
- [10] Jose Faernando prada , "The value of reliability in power systems", *Massachusetts institute of technology*, Report no. EL 99- 005 WP, July 1999
- [11] Ronald N, Allan , Roy Billinton, "Probabilistic assessment of power systems", *Proceedings of the IEEE*,Vol.88 ,No.2 , PP 140 – 162 , February 2000
- [12] Roy Billinton ,Ronald N, Allan, "Reliability evaluation of power systems", *Plenum publishing (New York)*, 1984 .
- [13] *GECOL "technical reports" 2015-2016 .*
- [14] Fathi Mohamed , Haddoud Abdulnabi Haddod , Bashir Mohamed Jumaa , "Planning of Electrical Networks in GECOL", *Energy and Life magazine* , No.14 , September 2001.

Track 3

Oil and Chemical Engineering



© 2018 Copyright held by the author(s). Published by AIJR Publisher in Proceedings of First Conference for Engineering Sciences and Technology (CEST-2018), September 25-27, 2018, vol. 1.
This is an open access article under [Creative Commons Attribution-NonCommercial 4.0 International](https://creativecommons.org/licenses/by-nc/4.0/) (CC BY-NC 4.0) license, which permits any non-commercial use, distribution, adaptation, and reproduction in any medium, as long as the original work is properly cited. ISBN: 978-81-936820-5-0

Synthesis gas production with high hydrogen concentration aspen simulation

Abdalhamed A. E. Musbah^{1*}, Salah.M.Algoul², Abdalbaset M.R. Algish³, Eisa A. abdalaslam⁴

^{1,4} Chemical Engineering Department, Awlad Ali High Institute for Science and Technology, Tarhuna, Libya

² Chemical Engineering Department, The High Institute of Engineering Technology -Zliten, Libya

³ Chemical and Petroleum Department, The Higher Institute for Science and Technology, Algaraboli, Libya

DOI: <https://doi.org/10.21467/proceedings.2.30>

* Corresponding author email: almazuod@yahoo.com

ABSTRACT

There is a growing need for hydrogen and future hydrogen economy becomes high on the scientific agenda, despite the “sustainable” routes are still too expensive; however, Steam reforming of hydrocarbons is the most feasible rout. This paper focuses on the production of Synthesis gas with high hydrogen concentration via process simulation using aspen plus simulator version 2006 and methane as a feedstock; the simulation process aimed mainly to produce synthesis gas rich in hydrogen with a minimum consumption of natural gas and agents of reforming and burning. An investigation of the effects of reactor (reformer) temperature, steam to natural gas (equivalence ratio) and the oxygen ratio in air on the composition of produced gases are conducted. The combustion reactor operated over a temperature range of 500-900 °C while varying equivalence ratio from 3:1 to 3:5. The results show that the hydrogen concentration in the produced gas increased rapidly with increasing reforming temperature and the best rang is (750-850 °C) where the highest conversion was at 850°C. Low equivalence ratio 3:1 is not preferred because it results low hydrogen concentration produced in synthesis gas but equivalence ratio equal to 3:3 is preferred for synthesis process as it results complete combustion of methane present in the feed resulting higher percentage of H₂ in the produced gas. In additional, if the content of O₂ in the air used in the combustion reactor as reforming agent was increased the content of hydrogen in the produced synthesis gas increased and on the other hand the content of nitrogen which is an inert gas is decreased by approximately (7.99%). However, 70 % O₂ by volume content in the air stream ensures that the content of hydrogen (63.28%) in compared with pure oxygen gives 63.57%.

Keywords: Synthesis gas, hydrogen, simulation.

1 Introduction

The use of hydrogen for petrochemicals, fertilizers and as energy carrier in connection with renewable energy production will increase substantially in the next 5-10 years as even more



© 2018 Copyright held by the author(s). Published by AIJR Publisher in Proceedings of First Conference for Engineering Sciences and Technology (CEST-2018), September 25-27, 2018, vol. 1.

This is an open access article under [Creative Commons Attribution-NonCommercial 4.0 International](https://creativecommons.org/licenses/by-nc/4.0/) (CC BY-NC 4.0) license, which permits any non-commercial use, distribution, adaptation, and reproduction in any medium, as long as the original work is properly cited. ISBN: 978-81-936820-5-0

stringent environmental legislation is enforced, Low sulphur gasoline and diesel fuels will become mandatory and harmful emissions will be reduced drastically. Hydrogen will be required by refiners and specialty chemical manufacturers to meet the global need for cleaner products. The growing fuel cell market will be dependent on hydrogen as a primary fuel source [1]. However, the major sources of energy in the world are the traditional fossil fuels (oil, coal and natural gas) and on consequence of global economic development, especially in the recent decades led to a significant decrease in these non-renewable resources.

In addition, the increasing of energy demands will speed up the exhaustion of the finite fossil fuel, with the current proved reserves and flows, years of production left in the ground coal 148 years, oil 43 years, natural gas 61 years according to scientist's studies [2]

However, non-renewable resources of fossil fuels have led to serious energy crisis and environmental problems such as global warming pollutant emission and acid rain. Carbon dioxide is the main greenhouse gas. The major part of CO₂ emissions is due to combustion of fossil fuels. In addition, combustion of fossil fuel produces toxic gases, such as SO₂, NO_x and other pollutants [3].

For these reasons the necessity importunate to find another substitute Where many efforts have been made to explore clean energy and renewable alternatives such as biofuels and hydrogen, Hydrogen can replace the conventional fossil fuels because hydrogen overcome fossil fuel and it has the highest energy to weight ratio compared to any fuel [4].

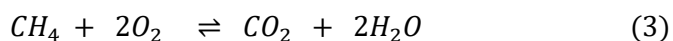
Besides using hydrogen as a source of energy, hydrogen can be used for various other purposes in different industries in hydrogenation process such as saturate compounds and crack hydrocarbons as well as in manufacturing of different chemicals like ammonia, methanol etc. [5]. Hydrogen considered as the "fuel of the future" because it is applicable to the technologies which are relating to fuel cells [6].

There are many methods to produce hydrogen but reforming natural gas is a current process of hydrogen production, economical and widely used, provides for short and medium – term energy security and environment friendly, however, producing high concentration synthesis gas is the main drawback of this process.

The reforming reactions correlated with the proprieties package for the reformer equipment are:



The combustion reaction correlated with the proprieties package for the combustor equipment is:



The equilibrium reaction correlated with the proprieties package for the all three equilibrium reactors is:



Steam reforming process involves the conversion of methane and water vapour into hydrogen and carbon monoxide the conversion is carried out at temperatures of 700 to 850 °C and pressures of 3 to 25 bars. The product contains approximately 12 % CO which can be further converted to CO₂ and H₂ through the water-gas shift reaction [7].

In this paper, a steam reforming process studied and simulated to reach the maximum hydrogen concentration in produced synthesis gas. Thus, one of the advantages of these simulations is to produce hydrogen rich fuel gas and to reduce the percentage of unwanted gas for fuel cell system and environment.

Table1: thermodynamic characteristics of the reactions presented above [8]:

	standard heat of reaction (KJ/Kgmol) at 25°C	equilibrium constant at 800°C
reaction 1	2.1X 10 ⁵	0.0313
reaction 2	1.6X 10 ⁵	0.0166
reaction 3	-8X10 ⁵	1.8X10 ¹⁷
reaction 4	-4.2X10 ⁴	4.063

The values for the proprieties of the gaseous phases implied in the reforming process were chosen from specialty literature. Table 2 shows the initial condition of the streams [9].

Table 2: the initial stoichiometric composition and conditions of first iteration simulation

component mole fraction %	natural gas	Air	Combustion steam	reforming steam
H ₂ O	-	-	1	1
CH ₄	1	-	-	-
CO	-	-	-	-
CO ₂	-	-	-	-
H ₂	-	-	-	-
N ₂	-	0.79	-	-
O ₂	-	0.21	-	-
Temperature °C	25	350	400	500
pressure atm	1	1	1	1

2 Process Description

Four reactors needed in a typical process of synthesis gas production [3]. However, the proposed simulation model requires three reactors, firstly, the Reformer: The reformer is an equilibrium reactor, in which most of the methane is reacted with steam to produce hydrogen,

carbon monoxide and carbon dioxide. The outlet gas will also contain the un-reacted methane and excess water vapour from the steam. The two reforming reactions are endothermic therefore heat must supply into the reactor to maintain the reactor temperature. The temperature of combustor feed is simulated to find the best temperature, which maximizes the reacted methane.

Secondly, the Combustor: the combustor is a conversion reactor where, the feed streams include the reformer product and an air stream. The oxygen in the air almost consumed in the combustion of the rest of unreformed methane to produce carbon monoxide and carbon dioxide. Depending on the content of oxygen in the air, the synthesis gas composition is changing.

Finally, Shift reactors: the shift reactors is an equilibrium reactor within the water-gas shift reaction occurs. In the combustor shift reactor the produced carbon monoxide is converted to carbon dioxide and more hydrogen is produced. The natural gas is reformed in a conversion reactor (Reformer) when it is combined with steam.

The proposed flow sheet of the feedstock, architecture of the model and the intermediary or final products are shown in figure 1.

3 Methodology

This conceptual model was realized in HYSYS software according with the existing technologies. The Soave Redlich kwong (SRK) equation of state has extensively used in calculating phase and reaction equilibrium. It gives good agreement with experiment so it was used to calculating the reaction equilibrium to correct the non-ideality of the gas mixture .

The synthesis gas Production was simulated using the Aspen Hysys V6.software where the following parameters simulated to find out their effects on purity and productivity of produced synthesis gas, and to increase the hydrogen produced volume fraction. These parameters are including reformer temperature, the mole ratio of natural gas to air (equivalence Ratio) used to burn it, the reforming / combustion agent (mixture steam – air with different concentration of O₂); and the volumetric composition (v/v%) of the gases resulting from the reforming / combustion process of natural gas. The process takes place at atmospheric pressure.

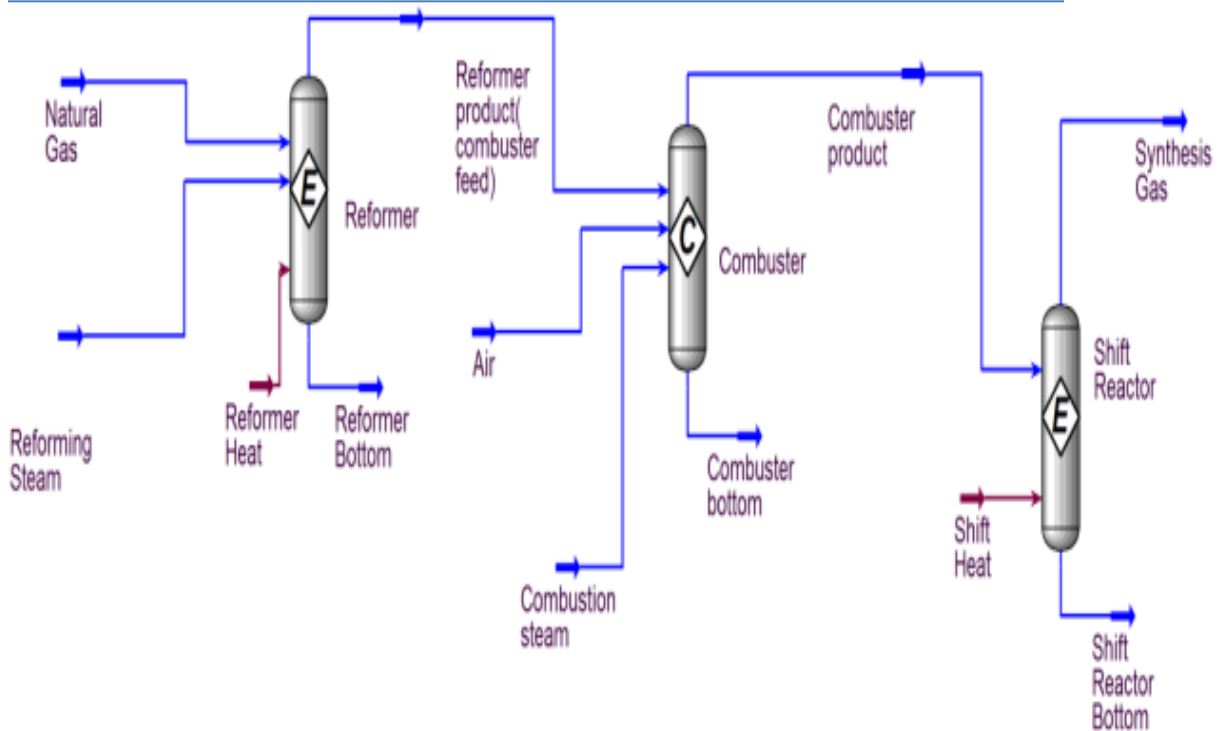


Figure 1: synthesis process flow diagram

4 Results and Discussion

To initialize the process and to run the simulation, the values for the properties of the gaseous phases implied in the reforming processes were chosen from specialty literature and shown in table 2.

4.1 Effects of varying reformer temperature on methane reforming process and produced synthesis gas composition (CO & +H₂) at constant equivalence ratio.

Form first iteration simulation for stoichiometric mole quantity of reforming process at inlet conditions it can be clearly seen that by increasing the reforming temperature the conversion of methane increased. However, the volume fraction of CO is increased and this will make the process need more shifting reaction in the third reactor to convert CO to CO₂ and H₂. For this reason the equilibrium reaction at 850 °C was chosen for the simulation where it gives highest methane

Conversion and in next reactor the produced Carbone monoxide will be eliminated.

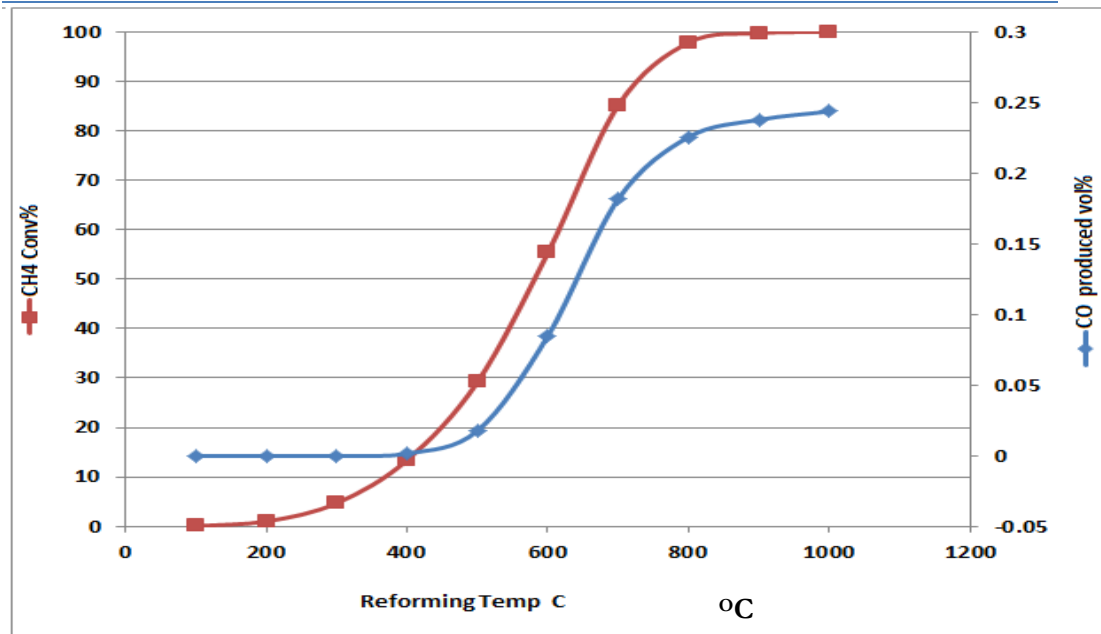


Figure 2: Reforming temperature effects on methane conversion and produced CO Vol fraction.

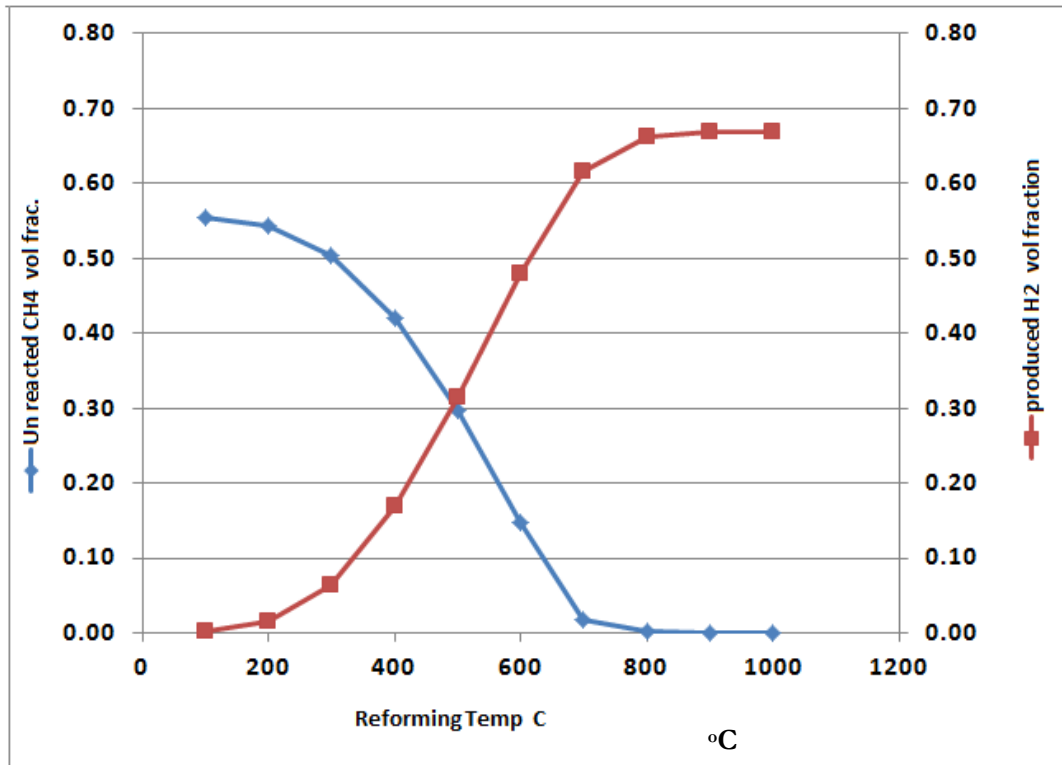


Figure3: Reforming temperature effects on produced hydrogen and unreacted methane vol fraction

From figures above, when temperature become greater than 700 °C, the volume fraction of unreacted methane approach 1 or 2 volumes present and the produced hydrogen reach the maximum value. The addition of oxygen in the second reactor serves to the purpose of ensuring that the excess of methane from the natural gas stream is consumed and since reforming reactions, is an exothermic reaction, the product gas composition is sensitive toward temperature change and it was observed that the concentration of H₂ increases with increase in temperature. Higher temperature provides more favourable condition for steam reforming of methane therefore, with increasing in temperature the concentration of methane decreases in the product gas and this is attributed to increase in concentration of hydrogen. On the other hand, the CO₂ concentration decreases with increase in temperature because higher temperature favours endothermic formation of CO from CO₂ via reverse reaction.

4.2 Effects of varying equivalence ratio (steam to methane) on produced synthesis gas composition (CO & H₂)

Equivalence ratio is the most important parameter of synthesis process. The effect of equivalence ratio on product synthesis gas composition was studied in the range 3:1 to 3:5 at 850 °C. Figure 4 shows CO₂ volume fraction is directly proportional to the equivalence ratio to specific limit. Equivalence ratio (methane to steam equal to 2 or 3) gives the highest hydrogen volume fraction, and small carbon dioxide volume produced.

With increasing in equivalence ratio, more complete synthesis process takes place producing more H₂ and this leads to decrease in concentration of CO, so less CO is produced from water gas shift reaction. However, it can increase the carbon monoxide and in this case, it needs to be eliminated in equilibrium reactor and convert it to CO₂ according to the equilibrium reaction.

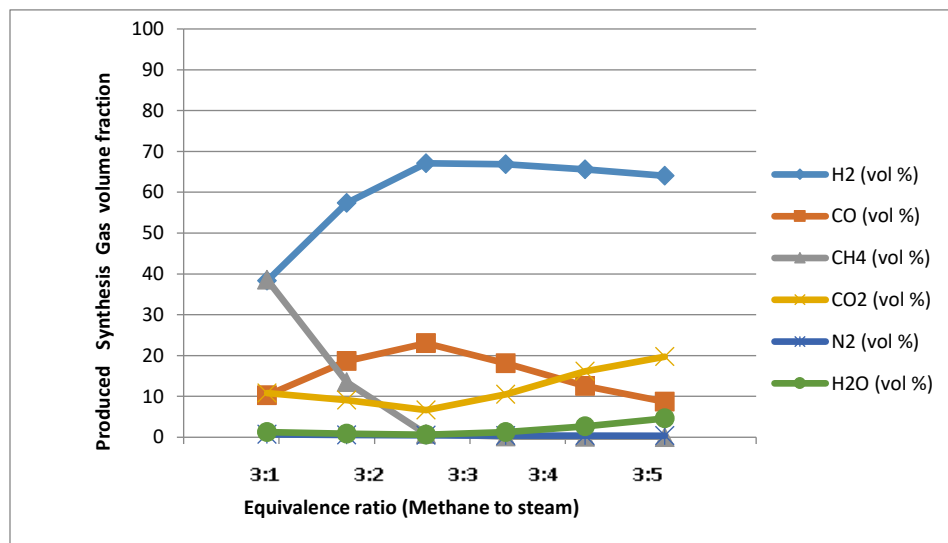


Figure 4: Simulated product gas composition (volume %) at different temperatures

4.3 Effects of varying oxygen mole fraction in air on produced synthesis gas composition at different equivalence ratio

In the conversion reactor, if the temperature in reformer reactor is less than 800 °C some amount of methane can be unconverted and in this case it needs to convert into CO₂ and H₂O via enhancing the combustion reaction. In the case of steam to methane used was 3:2 at temperature 750 °C, and air with different content in O₂ varied from 21 volumes present to 100% were used, the simulation process of the natural gas reforming gives the follow results for the ratio of Oxygen required to burnet the unreacted methane is equal to 2 : 1 stoichiometric.

If the concentration of O₂ in the air used in the second reactor, combustor reactor increased, the concentration of hydrogen in synthesis gas product will increase and as a secondary effect will decrease the concentration of nitrogen, which is an inert gas where, for a concentration of 50% O₂ it was obtained the best results of the simulation process: 63% H₂ and 4.03% N₂. It can be recommended to balance the amount of air to combust the remains unreacted CH₄ and the amount of water required in the equilibrium reactor to eliminate the unreacted methane, it recommended that it is better to carry out the reforming reaction in temperature about 850oC and the required amount of air can be cut down to become near zero, however, the results are shown in table (3), where the best equivalence ratio is 3:3.

Table3: the simulated volume fraction of produced synthesis gases

Parameters	CH ₄ Vol%	H ₂ O Vol%	CO Vol%	CO ₂ Vol%	H ₂ Vol%	N ₂ Vol%	O ₂ Vol%
equivalence ratio	3:1						
Air with 21% Vol O ₂	0.3427	0.035	0.0428	0.1334	0.3538	0.0926	0.000
Air with 50% Vol O ₂	0.3204	0.0507	0.0383	0.1691	0.3622	0.0593	0.00
Air with 70% Vol O ₂	0.3050	0.0623	0.0361	0.1930	0.3677	0.0359	0.00
Air with 100% Vol O ₂	0.2815	0.0807	0.0337	0.2284	0.3757	0.000	0.00
equivalence ratio	3:2						
Air with 21% Vol O ₂	0.1322	0.0201	0.1111	0.1329	0.5293	0.0744	0.000
Air with 50% Vol O ₂	0.1117	0.0290	0.1010	0.1707	0.5404	0.0473	0.000
Air with 70% Vol O ₂	0.0974	0.0357	0.0951	0.1955	0.5477	0.0285	0.00
Air with 100% Vol O ₂	0.0760	0.0467	0.0877	0.2313	0.5583	0.000	0.00
equivalence ratio	3:3						
Air with 21% Vol O ₂	0.0109	0.0178	0.1483	0.1331	0.6265	0.0634	0.000
Air with 50% Vol O ₂	0.0072	0.0192	0.1466	0.1409	0.6309	0.0403	0.0150
Air with 70% Vol O ₂	0.0072	0.0193	0.1470	0.1413	0.6328	0.0242	0.0281
Air with 100% Vol O ₂	0.0072	0.0194	0.1477	0.1420	0.6357	0.000	0.048
equivalence ratio	3:4						
Air with 21% Vol O ₂	0.1015	0.0132	0.1481	0.1075	0.5739	0.0558	0.000
Air with 50% Vol O ₂	0.0858	0.0186	0.1380	0.1390	0.5831	0.0354	0.000
Air with 70% Vol O ₂	0.075	0.0227	0.1318	0.1600	0.5893	0.0213	0.000
Air with 100% Vol O ₂	0.0588	0.0293	0.1233	0.1903	0.5984	0.0000	0.000

The oxygen from the air is consumed in an exothermic combustion reaction while the inert nitrogen passes through the system but if the content of oxygen in the air is raised, the effect is increasing of hydrogen content in the synthesis gas and decreasing the nitrogen content, these effects are desirable because the hydrogen is the final product and nitrogen is a useless inert gas. It gives the highest produced hydrogen volume fraction but in contrast it is clearly seen that the volume fraction of un converted carbon oxide is greater than some others, therefore, this process has a complexity that make it not easy to optimize the required amount using the simple software.

5 Conclusions

Using ASPEN PLUS simulator, a model for synthesis gas production in an atmospheric process was simulated using natural gas (Methane) as feed material. A series of simulations were carried on to investigate the effect of temperature, equivalence ratio on produced synthesis gas. The volume percentages of H₂, CO, CH₄ and CO₂ were calculated, the results showed that, the hydrogen concentration in the product gas increases rapidly with increase in temperature (750-850 °C). Low equivalence ratio 3:1 is not preferred as it results low hydrogen concentration produced in synthesis gas. However, Equivalence ratio 3:3 is preferred for synthesis process as it results complete combustion of methane present in the feed, resulting higher percentage of H₂ in the product gas. High steam to methane ratio results higher water gas shift reaction and this leads to better yield of hydrogen but much higher steam flow rates will have an opposing effect on producing higher CO produced which need higher efficient technique to be separated. In additional, if the content of O₂ in the air used to the second reactor as reforming agent was increased, the content of hydrogen in the produced synthesis gas is higher and also the content of nitrogen which is an inert gas is decreased where it reaches (7.99%). However, 70 % O₂ by volume content in the air stream ensure that, the content of hydrogen (63.28%) in compared with pure oxygen gives 63.57%.

References

- [1] Niels R. Udengaard, hydrogen production by steam reforming of hydrocarbons, Prepr. Pap. -Am. Chem. Soc., Div. Fuel Chem. 2004, 49(2), 907. El Camino Real, Suite 300. Houston, Texas 77058
- [2] E. Rytter, Method and reactor for reformation of natural gas and simultaneous production of hydrogen, 2001
- [3] M.R. Beychok, Process and environmental technology for producing SNG and liquid fuels, U.S. EPA report EPA-660/2-75-011, 1975
- [4] A. Hartstein, Hydrogen production from natural gas, 2003
- [5] M. Feidt, Energy efficiency and environment, U.P.B. Sci. Bull., Series C, Vol. 72, Iss. 1, 39-53, 2010
- [6] S.C. Amendola, M. Binder, M.T. Kelly, P.J. Petillo, S.L. Sharp-Goldman, Advances in Hydrogen Energy, 69-86, 2002. S. Gagnon, Hydrogen. Jefferson Lab., 2008
- [7] Riis T., Hagen E. F., Vie P. J. S. and Ulleberg O., Hydrogen production and storage R&D: priorities and gaps. Paris, IEA Publications, 2006
- [8] C. Basagianis, X.E. Verykos, Production of Hydrogen from Biomass via Steam Reforming of Bio-oil, Proceedings International Hydrogen Energy Congress and Exhibition IHEC 2005, Istanbul.
- [9] Nath K. and Das D., Hydrogen from biomass, Current Science, vol. 85, No. 3, (2003): pp.265-271

A Stochastic Optimisation Technique for Tuning a Continuous Stirred Tank Reactor Controllers

Yousif A. alsadiq

Chemical Engineering Department, Engineering faculty, Sirte University, Libya

DOI: <https://doi.org/10.21467/proceedings.2.31>

* Corresponding author email: ysf_826@yahoo.co.uk

ABSTRACT

A continuous stirred tank reactor mathematical model is developed based on the mass and energy balances for the reactor and heating system. A step change of the concentration is introduced and the temperature change in the reactor is measured. The objective of this paper is to comparatively study the application of PID, Generic Model Control, and Fuzzy logic controllers on the system and evaluate their performances according to the Integral of absolute error resulted. A simulated annealing algorithm is used to tune the controller's parameters. The control and simulation study has been implemented using MATLAB/SIMULINK.

Keywords: Mathematical modelling of continuous stirred tank reactor, MATLAB Simulation, PID controller, Generic Model Control, Fuzzy Logic Control, and Simulated Annealing .

1 Introduction

Continuous stirred tank reactor systems (CSTR) are the most important unit of a chemical plant used for unit operations. Basically a chemical reactor system has a complex nonlinear dynamic characteristic. There has been considerable interest in its state estimation and real time control based on mathematical modelling. However, the lack of understanding of the dynamics of the process, the highly sensitive and nonlinear behaviour of the reactor, has made it difficult to develop a suitable control strategy. An efficient control of the CSTR can be achieved only through an accurate model [1].

A PID controller represents the simplest form of controller that utilises Derivative and Integral operations on the system. PID controllers have several important functions: they have the ability to eliminate steady-state error through the integral action, and they can cope with actuator saturation, if used with anti-windup. These controllers are also effective for many control problems, particularly where there are a benign process dynamics and modest performance requirements [2]. PID controller can be represented by the following equation.

$$u(t) = K_c \left(\varepsilon(t) + \frac{1}{\tau_i} \int_0^t e(t) dt + \tau_D \frac{d\varepsilon(t)}{dt} \right) \quad (1)$$



© 2018 Copyright held by the author(s). Published by AIJR Publisher in Proceedings of First Conference for Engineering Sciences and Technology (CEST-2018), September 25-27, 2018, vol. 1.

This is an open access article under [Creative Commons Attribution-NonCommercial 4.0 International](https://creativecommons.org/licenses/by-nc/4.0/) (CC BY-NC 4.0) license, which permits any non-commercial use, distribution, adaptation, and reproduction in any medium, as long as the original work is properly cited. ISBN: 978-81-936820-5-0

Where: K_c is Proportional constant, τ_i is Time integral constant, τ_D is Derivative time constant, ε error, and u is the controller output. The need for improved process control has become obvious in recent years. Since 1987, there have been growing interest in the use of generic model control (GMC), which has been exposed to have certain robustness for a wide range of process nonlinearity against model mismatches [3]. The desired response can be obtained by incorporating two tuning parameters. More details of GMC method can be found in [4]. Consider a process described by the following equation:

$$x = f(x, u, d, t) \tag{2}$$

$$y = g(x) \tag{3}$$

Where x is the state variable, u is the manipulated variable, d is the disturbance variable t is the time, and y is the output. In general, f and g are some nonlinear functions. It follows from (2) and (3) that:

$$y = G_x f(x, u, d, t) \tag{4}$$

For a specific desired steady state value, the GMC algorithm specifies a rate of change of the output variables as:

$$\dot{y} = K_1(y_{sp} - y) - K_2 \int (y_{sp} - y) dt \tag{5}$$

In (5), two process desires are obvious. First, when the system is at a greater distance from the setpoint, then the system should travel towards the setpoint more quickly. Moreover, the longer that the system has remained offset from the setpoint, then the system should also travel towards the setpoint more quickly. The values of K_1 and K_2 are what determine the speeds. Therefore, to solve for the control, the actual output rate is set equal to the desired output rate, in other words setting (4) equal to (5), result in the following equation from which the control, u , can be solved.

$$G_x f(x, u, d, t) = K_1(y_{sp} - y) - K_2 \int (y_{sp} - y) dt \tag{6}$$

Fuzzy Logic Control has emerged as one of the most active and fruitful areas [5,6]. FLC is based on a spirit that is close to human thinking, and natural language, where the essential part of fuzzy logic is a set of linguistic control rules related by the dual concepts of fuzzy implication and compositional rules of inference [7]. FLC differs from conventional control methods, it incorporates a simple rule-based approach to solve the control problem rather than modelling the system mathematically. It also uses imprecise data, but descriptive of what must happen [8]. Figure 1, shows typical MFs of the controller. Hence the number of MFs used for variable is 3, then the number of rules required to map the input into the output is 3.

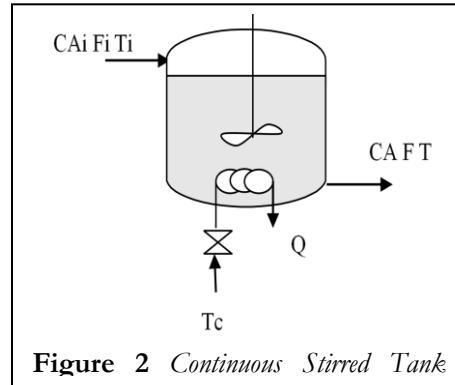
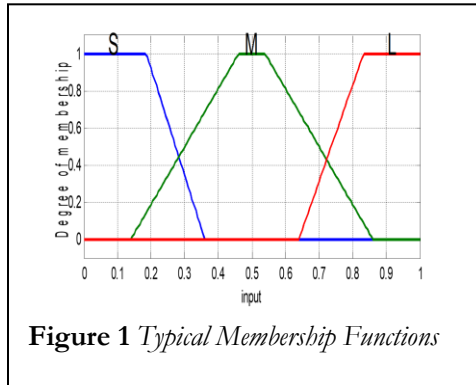
2 mathematic model of the continuous stirred tank reactor

A mathematical model of a continuous stirred tank reactor is developed depending on mass and energy balances. A summing first order irreversible exothermic reaction ($A \rightarrow B$) in a Continuous Stirred Tank Reactor as shown in Figure 2. The heat generated by the reaction is

removed using a cooling coil inside the reactor. Perfectly mixing is assumed in CSTR and the change in volume due to reaction is negligible. The reactor mass and energy equations are:

Over all mass balance

$$\frac{dV}{dt} = F_i - F \quad \text{and} \quad F_i = F \quad (7)$$



F_i, F are inlet, outlet flow, V reactor volume, t is the time, C_{Ai}, C_A inlet, outlet concentration of component A, T_i, T inlet, outlet temperature, r is reaction rate, E is activation energy, R is gas constant, k_0 is pre-exponential constant, ρ is density, C_p , specific heat capacity, H_r heat of reaction, T_c coolant temperature, and UA is a product of heat transfer coefficient and area.

Component (A) mass balance

$$\frac{dVC_A}{dt} = F_i C_{Ai} - F C_A - rV \quad (8)$$

Where r is the rate of a first order reaction

$$r = k_0 e^{\frac{-E}{RT}} C_A \quad (9)$$

and V is constant then (8) can written as:

$$\frac{dC_A}{dt} = \frac{F}{V} C_{Ai} - \frac{F}{V} C_A - k_0 e^{\frac{-E}{RT}} C_A \quad (10)$$

Heat balance

$$\frac{\rho dVC_p T}{dt} = \rho C_p F_i T_i - \rho C_p F T - H_r V C_A k_0 e^{\frac{-E}{RT}} - UA(T - T_c) \quad (11)$$

Where, V is constant, and the specific heat C_p is a function of temperature then from (8), and (11).

$$\frac{dT}{dt} = \frac{F}{V} (T_i - T) - \frac{H_r C_A k_0 e^{\frac{-E}{RT}}}{\rho C_p} - \frac{UA}{\rho C_p V} (T - T_c) \quad (12)$$

3 simulated annealing and its application to controller tuning

Simulated annealing is a global search method that is based on the analogy with the physical

annealing process of solids [9, 10, 11]. This optimisation technique has been applied to a CSTR for tuning proportional integral (PI), generic model (GMC), and Fuzzy controllers that are used to control the temperature and the concentration of the process, in MATLAB and

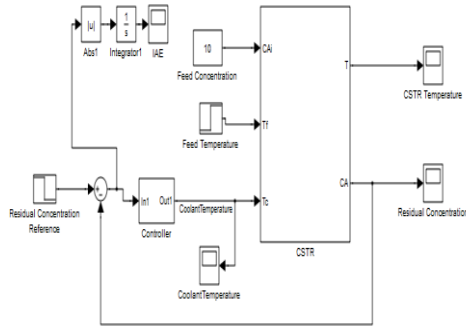


Figure 3 Feedback control system

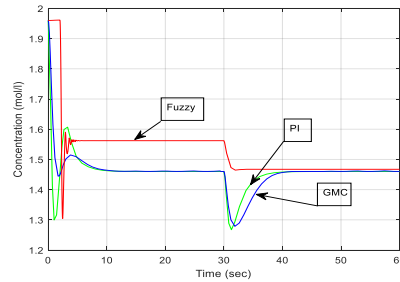


Figure 4 Concentration response of different controllers by conventional settings

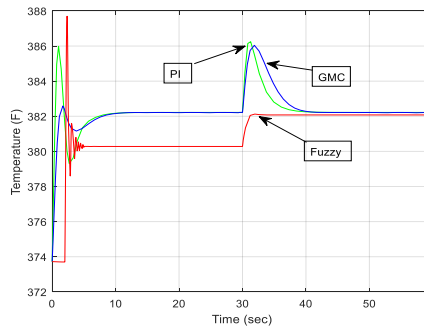


Figure 5 Temperature response of different Controllers by conventional settings

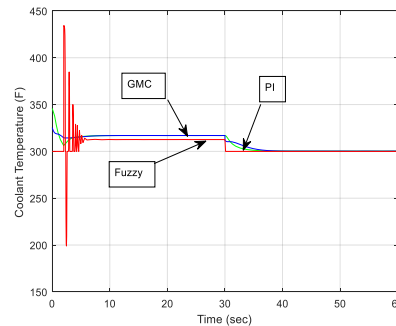


Figure 6 Coolant Temperature response for different Controllers by conventional settings

SIMULINK environment. More detail on Simulated annealing can be found in [12].

4 Simulation Results

The feedback control system can be represented in a Simulink as shown in Figure 3. The performance of the three types of controllers are illustrated below. Figures 4, 5, 6 show the results obtained by conventional settings. However, when applying the stochastic simulated annealing optimization method, the best values of the IAE obtained are 0.1791, 0.1693, 0.2048 for PI, GMC and fuzzy Controllers respectively. Where, the number of investigated solutions used for PI and GMC are 1000, while for Fuzzy controller are 3500 as there are 8 points to be tuned for both input and output membership functions. However, the best solutions were found at a simulation times 905, 655, 548 for PI, GMC, and Fuzzy controllers respectively. Figures 7,8,9,10,11, 12 and 13 depict the results obtained using (SA) algorithm.

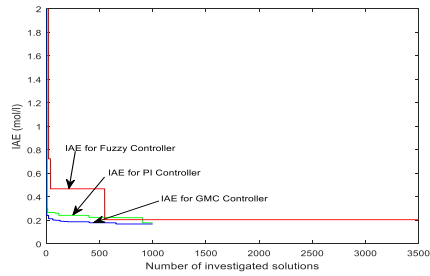


Figure. 7 IAE obtained by SA for using different controllers

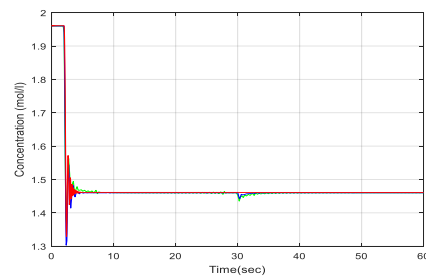


Figure 8 Concentration response of different controllers

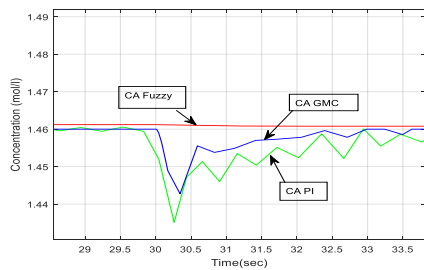


Figure 9 Enlargement of Concentration response of different controllers

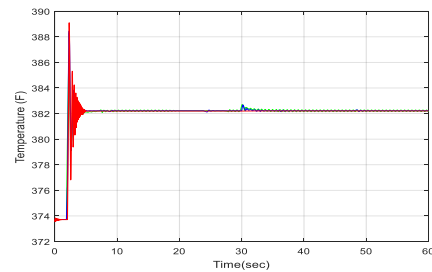


Figure 10 Temperature response of different Controllers

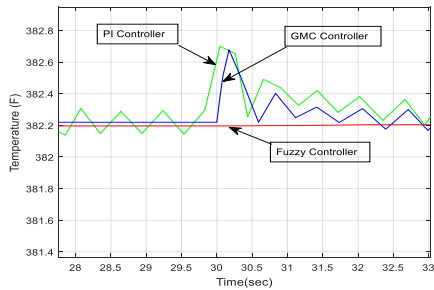


Figure 11 Enlargement of Temperature response of different Controllers

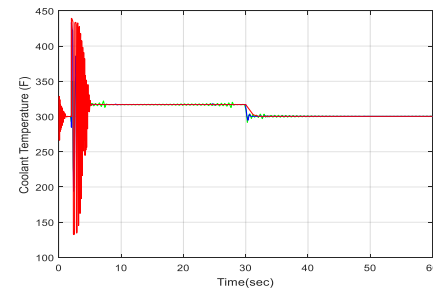


Figure 12 Coolant Temperature response for different Controllers

It is obvious that for both PI and GMC controllers an acceptable result can be achieved using conventional tuning methods, but it is very difficult to have a good membership function setting for fuzzy controller using trial and error. While, when applying simulated annealing the performance of the controllers in tracking the step change of the concentration from its initial value of 1.96 to 1.46 mol/l has been achieved. However, the controllers have the capability of eliminating the effect of the feed temperature disturbance from 300 F to 305 F on the concentration which is obvious at 30 sec as can be seen in figures 8, and 9. Moreover, it can be clearly seen in figures 10, and 12 that the Temperature and the coolant Temperature (Controller output) responses are changing according to their dependency to the concentration change,

where, it is realized that at the initial concentration value, the temperature is 373.72 F, and the coolant Temperature is 300 F. When the concentration step change introduced at time 2 sec where it has been reduced to 1.46 mol /l, the temperature value rose to 382.22 F as well as the coolant temperature that rose to 316.9 F. However, at 30 sec when the feed temperature disturbance was added, the controllers quickly overcame the disturbance and brought the temperature back to its steady state value, while the coolant temperature has dropped to 300.3 F which is the required controller value to keep the controlled parameter at its desired value. It is obvious that fuzzy controller response is a bit oscillatory at the start of the step change. Moreover, the fuzzy controller has better overcome of the feed temperature disturbance than the PI and the GMC controllers although it is a bit slower, but on other hand they are much better in eliminating the steady state error. The following table shows the results obtained when tuning the controllers using conventional methods available in MATLAB optimization toolboxes and simulated annealing optimization technique illustrated above.

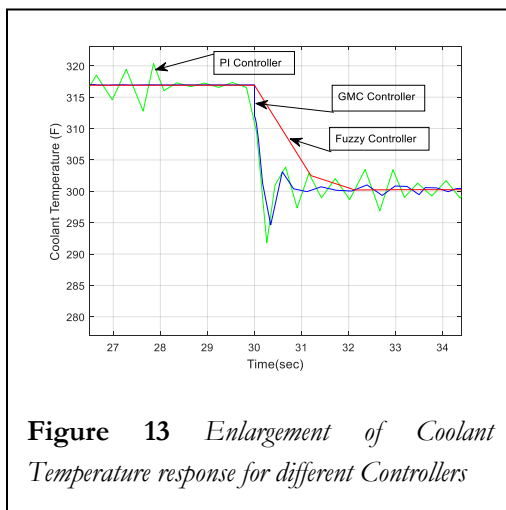


Table 1. Simulation results

<i>Using Conventional methods</i>	
<i>Controller Type</i>	<i>IAE (mol/l)</i>
<i>PI</i>	<i>1.8992</i>
<i>GMC</i>	<i>1.8606</i>
<i>Fuzzy</i>	<i>4.2093</i>
<i>Using SA algorithm</i>	
<i>PI</i>	<i>0.1791</i>
<i>GMC</i>	<i>0.1693</i>

5 Conclusion

Fuzzy Logic Controllers are nonlinear and have the influence of rejecting the disturbances better than the PI, and GMC controllers. Moreover, PI and GMC controllers have the inherent character of eliminating the steady state error which is unbeatable. The table above shows that simulated annealing is a powerful stochastic optimisation search method, where by comparing The IAE obtained using this algorithm to that obtained from conventional methods, it can be clearly seen that simulated annealing has found the best possible parameters that minimise the IAE to its minimum values which gives a better result of controller performance.

References

- [21] Suja Malar & Thyagarajan, "Modelling of Continuous Stirred Tank Reactor Using Artificial Intelligence Techniques", Department of Electrical and Electronics Engineering, PET Engineering College of India, Vol.3, pp. 145-155, (2009).
- [22] WG da Silva; PP Acarnley; JW Finch; 'Tuning of brushless dc drive speed controller with an on-line genetic algorithm', European Power Electronics Conference, Lausanne, 1999.
- [23] P. L. Lee, G. R. Sullivan. Generic model control (GMC). *Computers and Chemical Engineering*, 1988, 12(6): 573-580.
- [24] B. J. Cott, S. Macchietto. Temperature control of exothermic batch reactors using generic model control. *Industrial Engineering Chemical Research*, 1989, 28(8): 1177-1184.
- [25] CP. Coleman, D. Godbole: 'A comparison of robustness: fuzzy logic, PID, and sliding mode control', *Proceedings of the Third IEEE Conference on Fuzzy Systems*, V. 3, P. 1654 -1659, 1994
- [26] WG da Silva, PP Acarnley, and JW Finch; 'A comparison of fuzzy and conventional speed control in electric drives', European Power Electronics Conference, Lausanne, 1999.
- [27] N. Gulley, and J. S. Roger Jang, 'Fuzzy logic toolbox for use with MATLAB', The Math Workers Inc., 1995-1999.
- [28] A. Haj-Ali, H. Ying; 'Structural analysis of fuzzy controllers with nonlinear input
- [29] Prof. Song Prof. Irving;" Optimisation techniques for electrical power systems" part 2 Heuristic optimisation methods; *Power Engineering Journal*, P.151-160, June 2001
- [30] X. Yao;'A new simulated annealing algorithm', *Int. J. Computer Math.* V. 56, P.161-168, 1995.
Z. Xiaoyum, H. Yun, D. John; 'Genetic algorithms and simulated annealing for robustness analysis', *Proceedings of the American Control Conference*, V. 6, P. 3756-3760, 1997.
- [31] Z. Xiaoyum, H. Yun, D. John; 'Genetic algorithms and simulated annealing for robustness analysis', *Proceedings of the American Control Conference*, V. 6, P. 3756-3760, 1997.
- [32] Y. Alsadiq 'A Comprehensive Tuning of Distillation Column Composition Controllers using Simulated Annealing ', *Int'l Conference on Artificial Intelligence, Energy and Manufacturing Engineering (ICAEME'2014)*, P. 35- 41, June 9-10, 2014 Kuala Lumpur (Malaysia)

CO₂ Corrosion Inhibitor Assessment Using Various Measurement Techniques in oilfield

Abdelrazag Aziz

Department of Chemical and Petroleum, College of Engineering, Elmergib University, Libya
DOI: <https://doi.org/10.21467/proceedings.2.32>

* Corresponding author email: amaziz@elmergib.edu.ly

ABSTRACT

Tests and evaluation studies were conducted to select the best performance and treating rich carbon dioxide fluid composition associated with crude oil are produced. The experiments include standard electrical resistance probe for direct corrosion monitoring technique, and inspection by using an ultrasonic test to assess corrosion inhibitor.

The improvement process for chemical treatments development requires an effective strategy. The effective process for field testing inhibitor required twenty-four days to determine inhibitor performance and verifying minimum effective concentration. The standard electrical resistance probe with changeable dosage test was utilized. Ultrasonic testing one of the most widely used non-intrusive techniques is applied to measure of localized corrosion. Measurement apparatuses are adequate systems for monitoring of treatment efficiency.

Keywords: corrosion monitoring, CO₂ corrosion inhibitor, standard electrical resistance.

1 Introduction

Corrosion inhibitors are applied to decrease the rate of internal corrosion in pipelines carrying oil and gas from wells to oilfields and processing plants; even so, no single inhibitor claims all situations. The efficiency of an inhibitor is determined not only by the characteristics of the gas, crude oil and associated water of the pipeline and by the characteristics of the inhibitor itself, but the operating conditions of the oilfield (temperature, pressure, and flow rate) [1].

Because of the complication involved in evaluating corrosion inhibitors, the variety of measurement techniques to evaluate inhibitors, the costs coupled with assessing and utilizing corrosion inhibitors to decrease the rate of internal corrosion of pipelines, and the widespread utilizes of inhibitors, it is important to assess inhibitor performance and verifying minimum effective concentration that are measuring quality and quantity of inhibitors.

Knowledge of the inhibitor performance by measurement techniques has historically been used to control whether a system is protected. This requires confidence in the correlation between measurement techniques results and oilfield conditions. If the amount of corrosion inhibitors present in the oilfield is established at minimum effective concentration, then the system is considered protected and economic. As water chemistry changes, such tests need to be repeated to ensure their relevance to current oilfield conditions.



© 2018 Copyright held by the author(s). Published by AIJR Publisher in Proceedings of First Conference for Engineering Sciences and Technology (CEST-2018), September 25-27, 2018, vol. 1.

This is an open access article under [Creative Commons Attribution-NonCommercial 4.0 International](https://creativecommons.org/licenses/by-nc/4.0/) (CC BY-NC 4.0) license, which permits any non-commercial use, distribution, adaptation, and reproduction in any medium, as long as the original work is properly cited. ISBN: 978-81-936820-5-0

The study has been executed to identify dosage injected of corrosion inhibitor into the crude oil well. The well has been injected in the annulus where it should provide corrosion protection for the tubing. This well is high CO₂ producing and as such have a history of CO₂ induced pitting corrosion on the tubing found during work over. The corrosion inhibitor being injected downhole into the casing to ensure the protection of both the tubing and the flow lines of this well.

An inhibitor with an efficiency of 90% would be expected to reduce a baseline corrosion rate of 100 mpy down to 10 mpy, which may still not be acceptable based on the corrosion allowance life of oilfield infrastructures. For many conditions inhibitor efficiencies greater than 90% is achievable and desirable, but under certain severe conditions (e.g. highly turbulent flow or slug flow) an efficiency of no better than 70% may be the best attainable. Inhibition efficiency higher than 90% was achieved which is in line with the standard in oilfield [2].

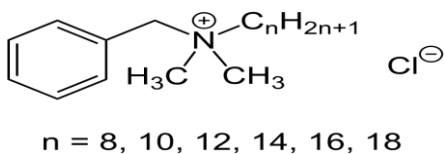
2 Chemical Composition and Functionality of Corrosion Inhibitor

Corrosion inhibitions are chemical treatments that prevent a metallic surface interact with corrosive fluids. This surface is covered to give the surface a certain level of protection. Corrosion inhibitors usually build a film of the adsorbate on the metallic surface of the adsorbent, protecting the metallic surface by creating a film. The life of the film depends on many factors, including the type of inhibitor, dissolved acidic gases, temperature, velocity, water cut, all the latter affecting the corrosive of the system. Continuous treatment is generally the preferred treatment since the concentration of inhibitor can be varied at any given time. A higher concentration of inhibitor can be applied until a film is established, and then the concentration of inhibitor can be reduced to a level enough to maintain the inhibitor film [3]. Several Corrosion inhibitors are available to prevent occurring corrosion, but the effective corrosion inhibitor used in the well is 25% of alkyl dimethyl benzyl ammonium chloride with 25% mixture of aliphatic polyamines in water solution. alkyl dimethyl benzyl ammonium chloride is a corrosion inhibitor designed for use in oil field. The product provides excellent corrosion inhibition in a wide range of environments, including hydrogen sulfide, carbon dioxide and in the presence of trace quantities of oxygen. The product is also effective in the control of bacterially induced corrosion. Physical and chemical properties have been summarized in the Table 1 [4].

Polyamine refers to a compound that consists of at least two amino groups. It is a highly charged, low molecular weight aliphatic polycation. One of the largest groups of organic corrosion inhibitors is the organic amine group. Aliphatic amines, mono-, di-, or polyamines and their salts, are all used as corrosion inhibitors. Aliphatic amines adsorb by the surface-active -NH₂ groups which forms a chemisorption bond with the metal surface. The hydrocarbon tails orient away from the metal surface toward the solution. Further protection is provided by the formation of a hydrophobic network which excludes water and aggressive ions from the metal surface. Since a lot of metal corrosion is caused by acidic compounds, the

basic organic amines can also react with the acidic compound to form an amine salt which then forms a coating on the metal thereby preventing further corrosion of the metal from occurring [5].

Table 1: Physical and chemical properties of alkyl dimethyl benzyl ammonium chloride

CAS Number	8001-54-5
Chemical name (CA)	Alkyl dimethyl benzyl ammonium chloride; Quaternary ammonium compounds
Other names	N-Alkyl-N-benzyl-N,N-dimethylammonium chloride; Benzalkonium chloride; ADBAC; BC50.
Molecular formula	$C_9 H_{13} N Cl C_n H_{2n+1}$ where $n = 8, 10, 12, 14, 16, 18$
Structural formula	 <p style="text-align: center;">$n = 8, 10, 12, 14, 16, 18$</p>
Molecular weight (g/mol)	Avg. = 359.6 g/mol
Appearance	100% is white or yellow powder; gelatinous lumps; Solution BC50 (50%) is colourless to pale yellow solutions
Density	0.98 g/cm ³
Solubility in water (% weight)	100%
Flash point	250 °C (482 °F; 523 K) (if solvent based)

The effectiveness of inhibitors depends on the chemical composition, molecular structure, and their attractions with the metal surface. Because film creation is an adsorption process, the operating conditions such as temperature and pressure are important factors for creating the film. Organic corrosion inhibitors will be attracted according to the ionic charge of the inhibitor and the ionic charge on the metallic surface [6].

3 Corrosion Rate Measurements

ER probe is generally used for the monitoring and optimization of the chemical treatment efficiency. The locations and positions where ER probes are installed is not always representative of the pipe surface. The flow conditions around probes are different from those on the pipe surface because of the geometry of these elements. The corrosion rates are generally measured on surface filmed by a corrosion inhibitor. the rate of uniform corrosion is generally low and most of the failures are caused by localized corrosion.

3.1 Corrosion Rate and Inhibition Efficiency Calculation

When measuring the ER probe, the instrument produces a linearized signal (S) that is proportional to the exposed element's total metal loss (M). The true numerical value being a function of the element thickness and geometry. In calculating metal loss (M), these geometric and dimensional factors are incorporated into the probe life (P), and the metal loss is given by [7]:

$$M = (S \times P)/1000 \quad (1)$$

Metal loss is conventionally expressed in mils (0.001 inches), as is element thickness.

Corrosion rate (C) is derived by [7]:

$$C = \frac{P \times 365 (S_2 - S_1)}{\Delta T \times 1000} \quad (2)$$

ΔT being the elapsed time in days between instrument readings S_1 and S_2 .

Efficiency of a corrosion inhibitor is to reduce corrosion rate down to an acceptable level determined by design and operational considerations. The inhibition efficiency was obtained from the corrosion rate (CR) at different concentrations of inhibitor. The efficiency of that inhibitor is thus expressed by a measure of this improvement [8]:

$$\text{Inhibitor Efficiency (\%)} = 100 \times (\text{CR}_{\text{uninhibited}} - \text{CR}_{\text{inhibited}}) / \text{CR}_{\text{uninhibited}} \quad (3)$$

where: $\text{CR}_{\text{uninhibited}}$ = corrosion rate of the uninhibited system

$\text{CR}_{\text{inhibited}}$ = corrosion rate of the inhibited system

3.2 Evaluating of Corrosion Inhibitor by Electrical Resistance Probe

Corrosion monitoring is a critical part of any oilfield corrosion control program. It should be integrated with other programs designed to optimize the process conditions, chemical injection and inspection to recognize the full potential to successfully manage oilfield operations.

Crude oil transmission pipeline system was operating between a crude oil wellhead terminal and a manifold receiving terminal over several ten miles. Pipeline system crude oil had the water cut 35 % and rich carbon dioxide. An electrical resistance probe was supported before manifold receiving terminal. A corrosion monitoring program was developed to determine if internal corrosion was a problem in the pipeline.

This field evaluation requires approximately 24 days. Figure 1 shows the experimental procedure to estimate minimum effective concentration. the performance is determined using

standard electrical resistance probes. This detailed process is designed to qualify an inhibitor formulation for field application. The inhibitor field testing protocol utilizing electrical resistance probes required 12 days to complete an incumbent baseline, 12 days to complete the test using the candidate dosage, for a total of 24 days [9]. Significant information on this technique can be found in ASTM G96 for corrosion monitoring and in NACE Publication 3D170-84.

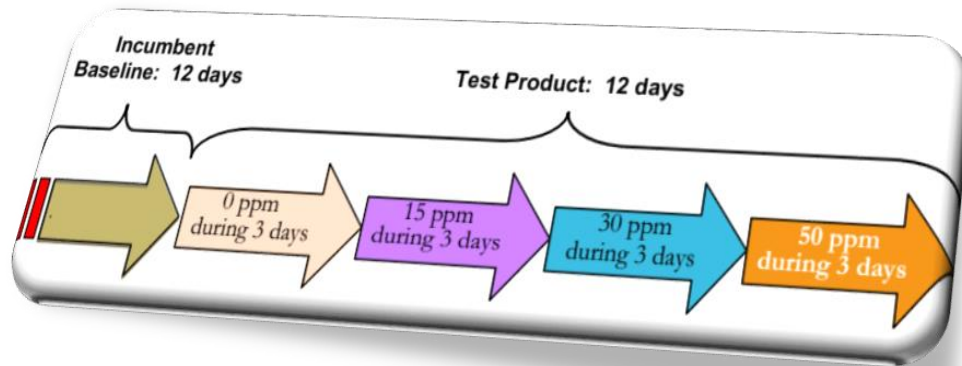


Figure 1: The experiment procedure

3.3 Ultrasonic Inspection Test

The limitations of the ER technique are that they provide representative data for general corrosion. They do not have the ability to accurately detect localized attack. The local attack rate can be over ten times the general corrosion rate. Such differences are important when trying to assess the relevance of inspection techniques such as ultrasonic tests of remaining section thickness.

Ultrasonic inspection or ultrasonic testing is applied to measure a variety of material characteristics and conditions. An ultrasonic examination is performed utilizing a device that generates an ultrasonic wave with a piezoelectric crystal at a frequency between 0.1 and 25 MHz into the piece being examined and analyses the return signal. Ultrasonic inspection has been used for decades to measure the thickness of solid objects.

Corrosion Inhibitor has been injected in annuals for approximately two years to protect the inner and outer surface of a tubing string, the flow line and the inner surface of the casing from corrosion. When the pump failed, and a workover was performed. Two lengths of the pipes were brought; both ends of the pipes were cut-out in different lengths and cut-out in half as samples.

4 Results and Discussion

4.1 The inhibitor performance and inhibition efficiency

Figures 2 present the data collected from the pipeline of the well. The slope of the metal loss data provides the corrosion rate. uninhibited segment followed by inflexion points or changes in metal loss data. This allows a better analysis of the data, especially at the lower concentrations, leading to an improved understanding of the inhibitor performance at different concentrations.

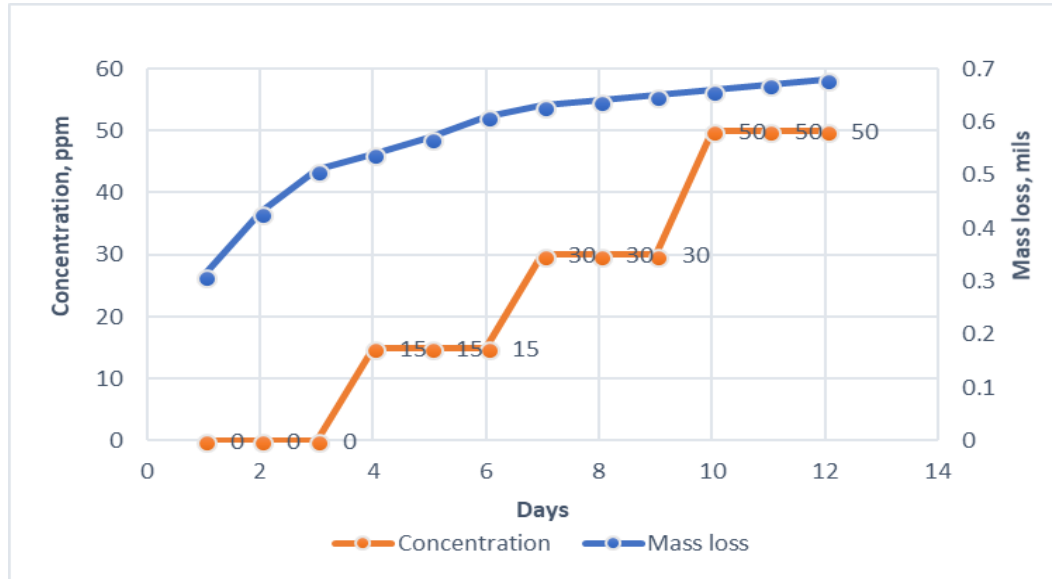


Figure 2: Metal Loss and dosage data by using electrical resistance probe

Figures 3 shows corrosion inhibitor reduced the corrosion rate considerably and the rate decreases with increase in the inhibitor concentration. The uninhibited reading at the rate of 51.1 mpy while 30 ppm concentration reduced the corrosion rates to 3.65 mpy. if the process is prone to rapid changes in corrosivity, ER probes typically may not provide accurate and reliable corrosion rate data. In some cases, namely where H_2S is present, they can be prone to error due to the presence of conductive sulfide corrosion products on the sensing element which may lead to non-conservative results. While ER data may not give reliable indications of the absolute corrosion rate, they can yield useful indications of trends and changes in corrosion activity [10].

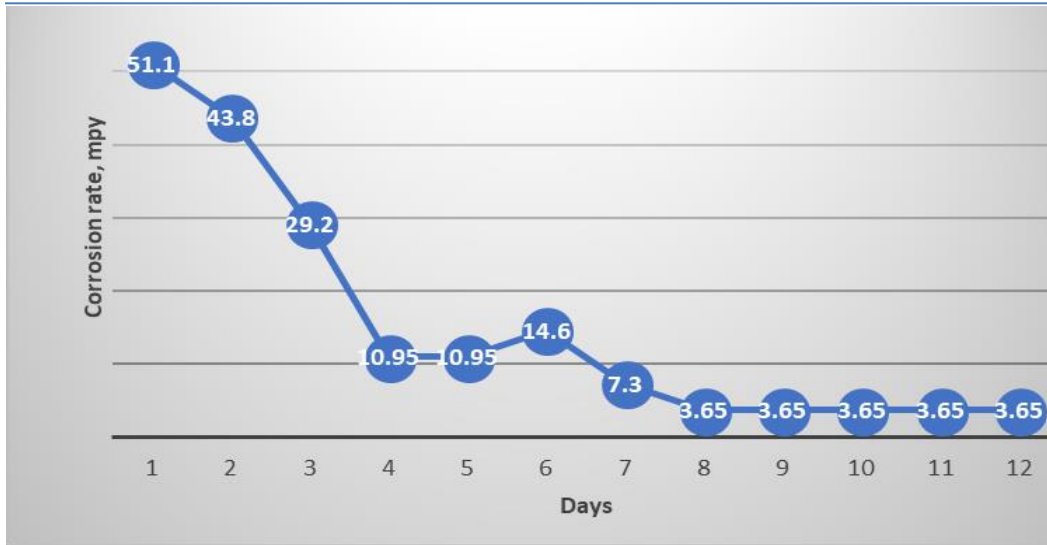


Figure 3: Corrosion rate versus time

Figure 4 shows inhibition efficiency of 93 % was observed at 30 ppm dosage. Moreover, as the concentration increases to 50 ppm, the corrosion performance was constant at the same inhibition efficiency.

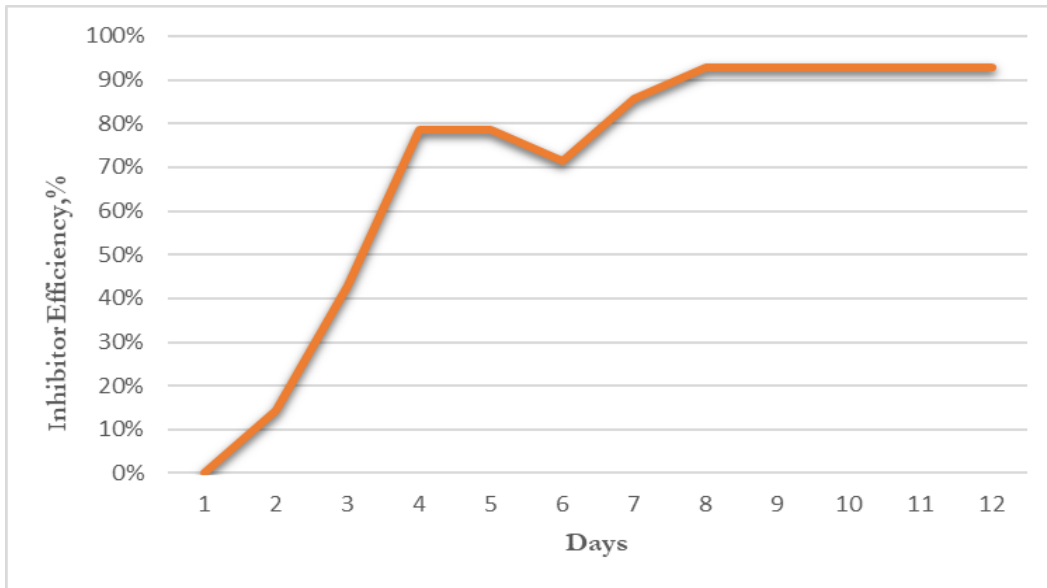


Figure 4: Inhibition efficiency versus time

4.2 localized corrosion Inspection

From the visual inspection performed on the external surface, the pipes appear to be in good condition aside from a thin layer of iron oxide scales were observed, and no signs of any

external corrosion were noted at the time of inspection. The internal surfaces of the pipes were in good condition, although the internal surfaces of the pipes were covered with a thin layer of scales. The material was made of carbon steel. All the samples a total in all 8 pieces of the pipes were ultrasonically tested and the normal wall thickness of the pipe is 6.35 mm. The results have been briefly in Table 2.

Table 2: Summary of the ultrasonic inspection test

<i>The samples</i>	Minimum Thickness, mm	Maximum Thickness, mm	Findings
<i>Sample No. 1</i>	6.7	7.3	A thin layer of scales
<i>Sample No. 2</i>	6.1	7.5	Minor internal erosion corrosion was observed
<i>Sample No. 3</i>	6.2	7.2	Minor internal erosion corrosion was observed
<i>Sample No. 4</i>	6.5	7.2	A thin layer of scales
<i>Sample No. 5</i>	6.6	7.5	A thin layer of scales
<i>Sample No. 6</i>	6.4	7.5	A thin layer of scales
<i>Sample No. 7</i>	6.2	8.2	Minor internal erosion corrosion was observed
<i>Sample No. 8</i>	6.1	7.3	Minor internal erosion corrosion was observed

5 Conclusions

The chemicals of alkyl dimethyl benzyl ammonium chloride and aliphatic polyamines have been found to be good corrosion inhibitor for the protection of the inner and outer surface of a tubing string, the flow line and the inner surface of the casing from corrosion. The corrosion inhibitor is suitable to protect oilfield infrastructures, where a three-phase and CO₂ - rich fluid combination are present.

The inspection results show that the inspected tubing samples are in good conditions. Thus, local corrosion of carbon steel is effectively decreased by corrosion inhibitor.

References

- [1] Sankara Papavinasam, R. Winston Revie, Milan Bartos, "Testing Methods and Standards for Oilfield Corrosion Inhibitors," *NACE International*, 2004, NACE-04424.
- [2] Sunday Aribo, Sunday J. Olusegun, Leonard J. Ibhadiyi, Akinlabi Oyetunji, Davies O. Folorunso, "Green inhibitors for corrosion protection in acidizing oilfield environment," *Journal of the Association of Arab Universities for Basic and Applied Sciences*, vol. 24, pp. 34-38, October 2017.
- [3] J.A. Dougherty, "Effect of Treatment Method on Corrosion Inhibitor Performance," *NACE International, Corrosion97*, Paper 97344.
- [4] https://en.wikipedia.org/wiki/Benzalkonium_chloride
- [5] Peter Kusch, Gerd Knupp, Marcus Hergarten, Marian Kozupa, Maria Majchrzak, "Identification of corrosion inhibiting long-chain primary alkyl amines by gas chromatography and gas chromatography–mass spectrometry," *International Journal of Mass Spectrometry*, no. 263, pp. 45-53, December 2006.
- [6] <http://www.corrosion-doctors.org/Inhibitors/organic.htm>
- [7] Mr. Scott Paul, PE "Report for Corrosion Inhibitor Application Tank 120-8, Valero Facility" *NACE Corrosion Specialist No. 4163*, May 2007.
- [8] Pierre R. Roberge. "Handbook of Corrosion Engineering," 1999.
- [9] Timothy H. Bieri, David Horsup, Ph.D., Melvyn Reading, Richard C. Woollam, "Corrosion Inhibitor Screening Using Rapid Response Corrosion Monitoring," *NACE International CORROSION 2006*, Paper 06692
- [10] <https://www.scribd.com/document/355728522/Corrosion-Monitoring>

Verification of the reserve of Al-Hamada oil field V-NC6 area by application of well logs.

Tariq Basher*, Essa Tabar , Ali Omran

Department of Petroleum Engineering, College of Engineering, Sirte University, Libya
DOI: <https://doi.org/10.21467/proceedings.2.33>

* Corresponding author email: tariq.alkaseh@gmail.com

ABSTRACT

The motivation behind this paper is to enrich and deepen our knowledge in the field of logging and log interpretation. The ultimate target is to have in situ assaying of a particular zone. In petroleum application this means determining the amount of oil and/or gas that is contained in the formation. The Geological structure of V- NC6 area in AL-HAMADA oil field has been studied and volumetrically estimated in seeks of the amount of hydrocarbons in the structure. To achieve this, a bunch of well logging data from different wells in V-NC6 area have been reviewed, analyzed and interpreted. Physical properties of the reservoir have been measured which include porosity and water saturation by interpretation of SP log and Induction – Electrical logs. In situ porosity has been determined by applying the Archie's equation on a real data from different resistivity tools. The average porosity of the multi pay zones structure was 14.23 % of the total volume of the reservoir 83336.3 acre ft. The second basic parameter which has been determined for in situ assaying is the saturation of the V- NC6 structure with water and hydrocarbons and they were 30% and 70% respectively. The V- NC6 area in AL-HAMADA oil field volumetrically occupied around 5.44 Million Stock tank barrels of oil.

Keywords: well logging; log interpretation; resistivity log, SP log, porosity; Water saturation.

1 Introduction

The volume of hydrocarbon reserves is a primary component of an energy company's value. Estimating that volume is a complicated, but essential and regulated, part of the resource industry's business. Geophysical methods continue to advance and are playing a more fundamental role in reservoir assessment (Hardage, 2009; PRMS-AD, 2011). To achieve this, physical properties of the reservoir have to be measured which include porosity and water saturation. Unfortunately, no one tool can give these results. Therefore, tool combinations that will measure porosity and hydrocarbons in place in the reservoir have been developed for various targets. Determining in situ properties (porosity and fluid saturation) can be done by the use of three porosity tool and resistivity tool as well. Those porosity tool that are used normally are the sonic, density and the Neutron porosity tools. A second basic parameters to be determined for in situ assaying is the saturation of the formation with hydrocarbons and



© 2018 Copyright held by the author(s). Published by AIJR Publisher in Proceedings of First Conference for Engineering Sciences and Technology (CEST-2018), September 25-27, 2018, vol. 1.

This is an open access article under [Creative Commons Attribution-NonCommercial 4.0 International](https://creativecommons.org/licenses/by-nc/4.0/) (CC BY-NC 4.0) license, which permits any non-commercial use, distribution, adaptation, and reproduction in any medium, as long as the original work is properly cited. ISBN: 978-81-936820-5-0

water. The V- NC6 area has been owned and running by the Arabian Gulf Oil Company, on November 1976 the reservoir engineers have been estimated the original hydrocarbons in place to be around 5 MM STB, and this value was economically stratified for the operator to start production from this area. In this paper we tried to redo the same job and estimate the volume of hydrocarbons occupied originally in place.

2 Materials and Methods

Al Hamadah al hamra area is located on the southern flank of the Ghadamis basin between lat 29° 00' to 29° 40' N and long 12° 35' to 13° 10' E occupying a strategic position midway between Al Qaraqaf arch to the south and centre of the basin to the north. Over 1200 ft of sediments are accumulated in the basin and range in age from Precambrian to Paleocene. While most of the lower two-thirds are clastics, the upper third is mostly marine carbonates and evaporates. Most of the lower Paleozoic units pinch out rapidly against AL Qaraqaf arch to the south in addition to their being cut off by several unconformities. These unconformities represent different erosodes during early and late Paleozoic and Mesozoic times. Large ENE-WSW trending compressional faults and folds were associated with the early Alpine progeny which were later modified with smaller N-S and NW-SE normal faults. Where; ENE – East North East and WSW – West South West

2.1 Well Location and Prospective Horizons

Based on correlation with the nearby wells, the following are the expected stratigraphic, table (1) shows tops of the interested zones in V8 –NC8 well.

Table 1 shows tops of the interested zones in V8 –NC8 well.

Lower Devonian	-2950 Ft
Do-Sandstone	- 2950 Ft.
Do-Shale	- 2969 Ft.
D1-Sandstone	- 2917 Ft.
D1 –Shale	- 3000 Ft
D2 –Sandstone	- 3019 Ft.
D2 –Shale	- 3065 Ft.
D3-Sandstone	- 3083 Ft.
Total Depth	- 3250 Ft.

3 Theory and Calculation

In this section we will show the calculation of each parameter we did use in our research and we have used real logs to interpret the data to come out with these results.

3.1 Volumetric Method:

The volumetric method requires the exactest possible data on :

- a) The thickness of the reservoir rock.
- b) Its extension.

c) Its porosity and

d) its saturation.

By a multiplication of these 4 factors we then get the original reserves in the field under reservoir conditions as in equation (1). The thickness of the pay horizon is usually obtained from downhole measurements (SP, resistance). As only the net thickness is measured

$$N = \frac{7758 * A * h * \phi * (1 - S_{wi})}{B_{oi}}$$

Where; N= Oil in place STB, A= Productive area Ft², h= net thickness Ft, ϕ = porosity %
Swi= connate water saturation %, Boi = Formation Volume Factor Rb/STB.

3.2 Volumetric Reserve Calculation:

3.2.1 Thickness (h):

The gross net pay thickness has been estimated from logs.

3.2.2 Calculation of the bulk volume of the reservoir by using ISOPACH MAP:

A net Isopach map is a map showing lines connecting points of equal net formation thickness. The bulk volume of the reservoir has been determined by using these maps. The Trapezoidal equation has been used to determine the volume of the production zones from planimeter reading.

A) Trapezoidal Equation:

$$\Delta VB_n = h/2(A_{n-1} - A_n) \dots\dots\dots(1)$$

$$BV = \{\Delta VB = h/2(A_0 + 2A_1 + 2A_2)\}$$

This equation used when

$$\frac{A_n}{A_{n-1}} \geq 0.5$$

3.2.3 Porosity (ϕ):

It is generally measured directly in the laboratory from cores or cutting and then plotted in a porosity profile these measurements are usually verified by various downhole measurements. In this paper we did use an Arche's equation to calculate the average porosity of multi strata reservoir.

$$\phi_{avg} = \frac{\sum h * \phi}{\sum h} \dots\dots\dots(2)$$

3.2.3 Water saturation (SW):

It is major factor the irreducible water saturation Swi is best established by capillary pressure measurements carried out on cores or cutting in addition to this the (archie) formula is also

useful in this respect an exact determination of the oil/water contact is usually difficult and requires experience.

a. Calculation of water saturation (SW) from SP log

The fluid saturation of a rock is the ratio of the volume of the fluid within the pores of the rock to the total pore volume. In this paper the water saturation has been calculated within two different methods; chart method and ARP'S equation method.

To estimate the water saturation of the formation must determine the R_o , R_t and R_w
Where

R_o : oil resistivity , R_t : true resistivity, R_w : water resistivity & F : formation resistivity factor

ARP'S equation method:

Compute the constant K

$$K = (60 + 1.33Tf) \dots\dots(3)$$

Where K : a termal convention constant.

Solve for R_{weq}

$$R_{weq} = R_{mf} / 10^{(-sp/k)} \dots\dots\dots(4)$$

Convert R_{weq} to R_w

If $R_{weq} < 0.12$ then use

$$R_w = (77R_{weq}) + 5/146 - (377R_{weq}) \dots\dots\dots(5)$$

If $R_{weq} > 0.12$ then use

Where; R_{weq} : Equivalent resistivity of the formation water , R_{mf} : Resistivity of the mud filtrate and SSP : static SP the maximum deflection possible for a given R_{mf}/R_w .

$$R_w = -0.58 + 10^{(0.69R_{weq} - 0.24)} \dots\dots\dots(6)$$

$$SW = \sqrt{(R_o / R_t)}$$

$$F = R_o / R_w$$

$$R_o = FR_w$$

$$S_w = \sqrt{(FR_w / R_t)} \dots\dots\dots(7)$$

b. Formation factor (F):

Archer experimentally determined that the formation factor could be determined from the porosity cementation (m) and rock texture (a)

$$\text{Thus } F = a / \phi^m \dots\dots\dots(8)$$

Though extensive use of the relationship the following values have been used with great success

$$F = \frac{R_o}{R_w} = \frac{\text{resistivity of rock saturated with fluid}}{\text{resistivity of the saturating fluid}}$$

Where ; R_m : Resistivity of the mud , R_{mf} : Resistivity of the mud filtrate, R_{mc} - Resistivity of the mud cake, and F : Formation resistivity factor

4 Results and Discussion

4.1 Estimate the total volume of the reservoir from the Isopach map:

The figure (1) is an isopach map of V-NC6 area that we used to calculate the volume of the reservoir. Table 2 shows the results of reservoir volume calculations.

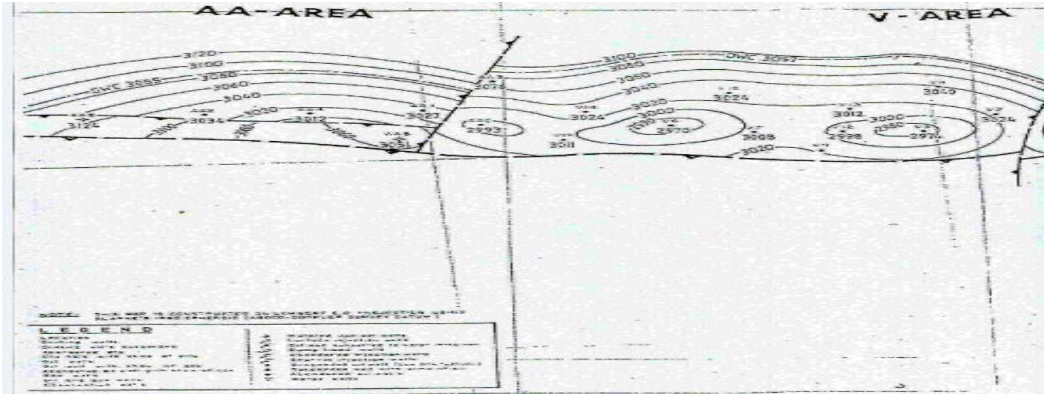


Figure (1) an isopach map of V-NC6 area of Alhamada Alhamra oil field.

Table 2 shows the results of reservoir volume calculations

Area	A (Cm ²)	A (Acre)	A _n /A _{n-1}	Method Used	ΔVP(acre.ft)
A ₀	13.77	851.123	-	-	-
A ₁	9.31	575.137	0.6757	Trapezoidal	3565.65
A ₂	5.76	355.831	0.6186	Trapezoidal	2327.42
A ₃	3.11	192.124	0.5399	Trapezoidal	1369.88
A ₄	1.7	105.019	0.5466	Trapezoidal	742.85
A ₅	0.975	60.232	0.5735	Trapezoidal	330.502

Total net pore volume (ΔVP) = 8336.302 acre.ft

4.2 Estimate the porosity of the reservoir from the well logging:

As example to calculate the porosity from well logging we estimated it from well V8. The figures 2 & 3 show the well head logs and the SP & Electrical logs of the well V8- NC6, respectively. Table 3 shows the results of the net pay thickness and porosity for each horizon of well V8.

Table 3 show the results of the net pay thickness and porosity for each horizon of well V8.

Formation	Depth (ft)	Thickness (ft)	Porosity (%)
D ₀	2950	19	0.253
D ₁	2977	23	0.141
D ₂	3019	46	0.144
D ₃	3083	67	0.153

Table 4 shows the calculation and results of the average reservoir porosity of V-NC6 area.

Well	Layer	H net (Ft.)	\emptyset %	H* \emptyset
V2	D ₀	11	0.132	1.452
	D ₁	10	0.125	1.25
	D ₂	16	0.147	2.352
	D ₃	26	0.131	3.406
V4	D ₀	14	0.15	2.1
	D ₁	18	0.139	2.5
	D ₂	32	0.15	4.8
	D ₃	20	0.146	2.92
V6	D ₀	0	0	0
	D ₁	29	0.13	3.8
	D ₂	16	0.123	1.9
	D ₃	32	0.14	4.55
V7	D ₀	0	0	0
	D ₁	17	0.13	2.21
	D ₂	29	0.154	4.54
	D ₃	15	0.164	2.46
V9	D ₀	10	0.253	2.53
	D ₁	9	0.141	1.26
	D ₂	51	0.144	7.344
	D ₃	13	0.153	1.989
V13	D ₀	0	0	0
	D ₁	16	0.088	1.45
	D ₂	18	0.142	2.55
	D ₃	0	0	0
V14	D ₀	3	0.144	0.432
	D ₁	9	0.135	1.215
	D ₂	29	0.133	3.79
	D ₃	22	0.137	3.014
V15	D ₀	0	0	0
	D ₁	30	0.148	4.514
	D ₂	0	0	0
	D ₃	0	0	0
V18	D ₀	12	0.152	1.748
	D ₁	21	0.095	1.995
	D ₂	0	0	0
	D ₃	0	0	0
Σ		630		89.729

$$\Sigma H * \emptyset = 89.729$$

$$\Sigma H = 630.5$$

$$\emptyset_{avg} = \frac{89.729}{630.5} = 0.1423 \approx 14.23 \%$$

The average reservoir porosity is 0.1423

4.3 Estimate the water saturation (Sw) from the well logging:

As example to estimate (Sw) from well logging we will estimate it from well V8:

Firstly we must find the value of (Rt) and (Rw)

-Rt from reading of the log =17.5 ohms mm

- Estimate of Rt

i- Rw with chart method at:

TD = 3250 ft , BHT =158 F, Tavg = 68 F & Rmf = 1.17 Ohm mm @ 68. The geothermal gradient = 2.769 F degree/ 100 feet.

The chart (4) has been used to estimate the formation temperature, Tf. From chart (4)

Tf=130 F

The chart (5) has been used to estimate the mud and mud filtrate resistivities.

From chart (5) Rmf@130 F = 0.6 Ohm mm

The chart (6) has been used to estimate the equivalent mud filtrate resistivity

From chart (6) Rmfeq= 0.375 Ohm mm

The chart (7) has been used to estimate the equivalent water resistivity.

From chart (7) and at SP = -70 milvolts (from log)

Rweq = 0.046 Ohm mm

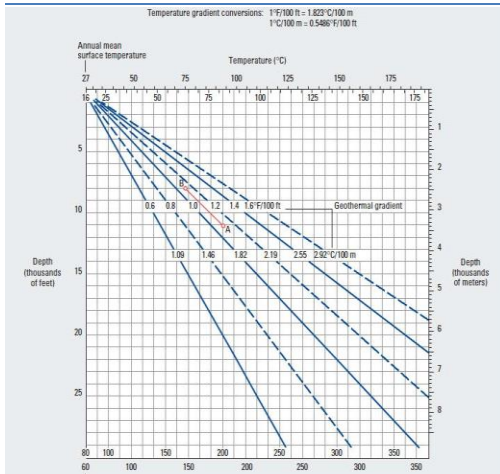
From chart (6) Rw =0.062 Ohm mm

ii- Rw with ARP'S equation at :

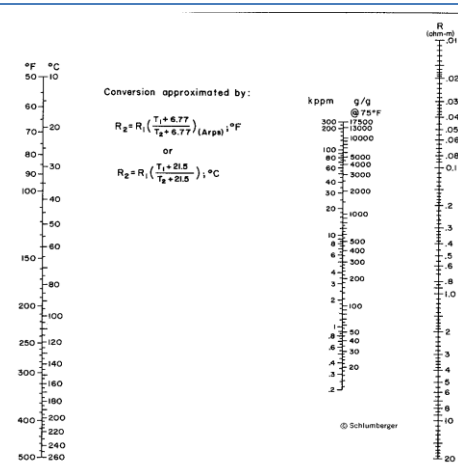
Tavg =68 F, BHT =158 F, Df = 2950 ft & Dt = 3250 ft

R1 – 1.17 @68 F and SP= -70 milvolts (from log) and T2=149.7°F

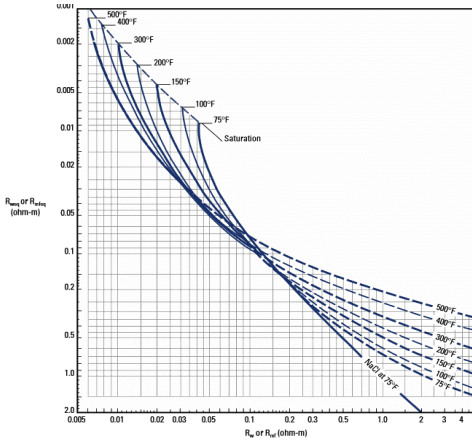
R2 (New Rmf); R2=0.5591 Ohm mm, thus (New Rmf) R2>0.1



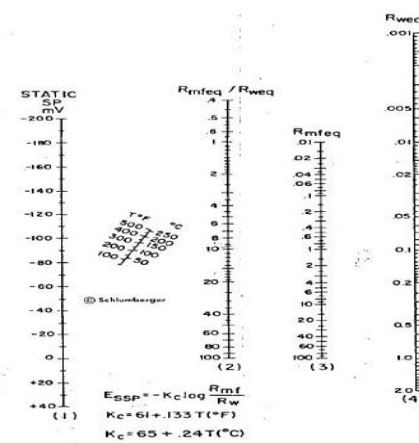
The chart (4) estimation of formation temperature, T_f .



The chart (5) to estimate the R_{mf} & R_{weq} .



The chart (6) to estimate the R_m & R_w .



The chart (7) to estimate the R_{mfq} .

iii- $R_{mfq} = 0.4752 \text{ Ohm mm}$

iv- Constant (K) = 79.91

$R_w = -0.58 + 0.7158 = 0.131 \text{ Ohm mm}$

Convert the R_w to $R_w @ T_f$; $R_w = 0.0626 \text{ Ohm mm}$

vii- To find $R_o = F * R_w$

For sand stone formation and ϕ is average porosity of well V8

$F = 31.54$, thus $R_o = 1.97447 \text{ Ohm mm}$

$S_w v8 = 0.33532 = 33.5\%$

And by applied the Arch,s equation for all the wells in the reservoir, we will estimate the average water saturation of it. Table 5 shows the application of Arch's equation for all wells on V-NC6 area.

Table 5 shows the application of Arch's equation for all wells on V-NC6 area.

Well	Layer	H net (Ft.)	$\bar{\phi}$ %	Sw %	H* $\bar{\phi}$ *Sw
V2	D ₀	11	0.132	0.201	0.2918
	D ₁	10	0.125	0.208	0.26
	D ₂	16	0.147	0.279	0.656
	D ₃	26	0.131	0.303	1.032
V4	D ₀	14	0.15	0.19	0.399
	D ₁	18	0.139	0.228	0.57
	D ₂	32	0.15	0.193	0.94
	D ₃	20	0.146	0.36	1.051
V6	D ₀	0	0	0	0
	D ₁	29	0.13	0.494	1.894
	D ₂	16	0.123	0.596	1.172
	D ₃	32	0.14	0.429	1.951
V7	D ₀	0	0	0	0
	D ₁	17	0.13	0.251	0.544
	D ₂	29	0.154	0.372	0.168
	D ₃	15	0.164	0.377	0.927
V9	D ₀	10	0.253	0.399	1.009
	D ₁	9	0.141	0.474	0.601
	D ₂	51	0.144	0.303	2.225
	D ₃	13	0.153	0.299	0.594
V13	D ₀	0	0	0	0
	D ₁	16	0.088	0.371	0.538
	D ₂	18	0.142	0.278	0.710
	D ₃	0	0	0	0
V14	D ₀	3	0.144	0.614	0.2652
	D ₁	9	0.135	0.188	0.22842
	D ₂	29	0.133	0.274	1.038
	D ₃	22	0.137	0.381	1.1483
V15	D ₀	0	0	0	0
	D ₁	30	0.148	0.238	1.0743
	D ₂	0	0	0	0
	D ₃	0	0	0	0
V18	D ₀	12	0.152	0.409	0.7149
	D ₁	21	0.095	1.097	1.09725
	D ₂	0	0	0	0
	D ₃	0	0	0	0
Σ		630			26.93079

$$\Sigma H * \bar{\phi} = 89.729 \text{ \& } \Sigma H * \bar{\phi} * Sw = 26.93079$$

$$SW_{avg} = \frac{26.93097}{89.729} = 0.30013 \approx 30 \%$$

4.4 Estimate the Original Oil in Place (OOIP) with Volumetric Equation:

$\Delta BV = 8336.3$ acre ft., porosity of the reservoir = 0.142314 , average water saturation of the reservoir = 0.300137 and the oil formation volume factor (Bo_i) = 1.165

OOIP = 5.43924×10^6 STB

5 Conclusions and Recommendations

From drilling, testing and logging results, it is concluded that V8-NC6 well proved to be one of the best oil wells in Elhamada Alhamra oil field in the “V” structure. The gross thickness of the pay zone attains 154` while the net oil sands attains about 105`. On top of the pay zone “Lower Devonian Sandstone”. The D₀ Sandstone was net at 2971` leveled with V6-NC6 well. The D₂ Sandstone was proved the thickness in the area since it attains 53` in the well V8 while its thickness is 40` in V6. It was decided to start production from D₃ sandstone at first through the perforated interval 5151`-5159` and left the other zones for future planning. It was recommended to drill a development well between the eastern and western culmination of the “V” structure I.e. between V7 and V8-NC6 wells to check the oil water contact in the D₂ sandstone unit.

6 Acknowledgment

We do thank the Arabian Gulf Oil Company for their help and support in providing the required data for this paper, as well as our staff member of Sirte University.

References

- [1] Pletcher, J.L., 2002. *Improvements to Reservoir Material-Balance Methods*. SPE, pp. 49–59
- [2] Konak, A., David, Coit, W., Alice, Smith, E., 2006. *Multi-objective optimization using genetic algorithms: a tutorial*. *Reliab Eng Syst Saf* 91 (No. 9), 992–1007.
- [3] Schulze, R.W., Riegret, Axmann, J.K., Hease, O., Rian, D.T., You, Y.L., 2002. *Evaluatory algorithms applied to history matching of complex reservoirs*. *SPE Reser Evalu Eng* 5 (2), 163–175.
- [4] Donald P. Helander – *Fundamentals of Formation Evaluation*. Copyrights © 1983 Tulsa, Oklahoma. Alfred Mayer. *Gurr –Petroleum Engineering* © Ferdinand Enke publishers Stuttgart 1976.
- [5] Craft and Hawkins- *Applied Petroleum Reservoir Engineering*, Louisiana State University 1959.
- [6] M.J. Salem & Hammuda - *Gelogy of Libya* Volumes I & II, copyright © 1991 by Tripoli University, Tripoli.

Boilers Performance Evaluation of Zuara Desalination Plant

Ali K. Muftah^{1*}, Mabruk M. Abugderah², Hakem S. Dakhel³

^{1,3}Department of Mechanical Engineering, College of Engineering, Sabratah University, Libya

²Research and Consultation Centre, Sabratah University, Sabratah, Libya

DOI: <https://doi.org/10.21467/proceedings.2.34>

* Corresponding author email: ali.alkhtabe@yahoo.com

ABSTRACT

Water is the basis of daily life and industrial development for all communities. Water desalination plants emerged as one of the most important alternatives to overcome the shortage of water resources especially in desertified countries like Libya. Boilers are the main part in thermal desalination plants which depends on steam as the working fluid to heat and evaporate the seawater. with a capacity of 80 tons/hr of superheated steam at 220°C and 15bar. Due to operating conditions, there was a decrease in steam boilers productivity and low efficiency. Heavy black smoke in chimneys was also detected. This work investigates the performance of the above mentioned boilers to determine the actual causes of these negative results by comparing the design values with different operating readings data. The results show a decrease in the efficiency of the boilers for low loading rates, which is affected by the air/fuel ratio. The deviation of this ratio from the design values leads to low efficiency and the emergence of heavy smoke in the chimneys, which causes deposits on the boiler pipes reducing the effectiveness of heat exchanger and therefore the thermal efficiency. The study also shows that the long operation suspension of the boilers in the first years of its life, due to the lack of discharge network and electricity cutoffs resulted in bad effect on the pipes conditions. The last led to the pipes deterioration resulting in water leaks and thus low boilers evaporation rates.

Keywords: desalination; boiler; thermal efficiency; air/fuel ratio.

1 Introduction

Water is the source of life used on in houses, agriculture, industry...etc. The lack and contamination of existing potable water resources led to desalination emergence as an important alternative resource to make up the shortage of demand especially in the countries that suffer from dryness. In general, there are two main types of seawater desalination technology one is the thermal or phase change processes and the other is membrane or processes without phase change. Desalination thermal processes are mostly found in countries, where fuel is quite cheap. Steam is used as the working fluid in desalination thermal type. The steam can be supplied by exhausting or bleeding steam turbines, or directly from



© 2018 Copyright held by the author(s). Published by AIJR Publisher in Proceedings of First Conference for Engineering Sciences and Technology (CEST-2018), September 25-27, 2018, vol. 1.

This is an open access article under [Creative Commons Attribution-NonCommercial 4.0 International](https://creativecommons.org/licenses/by-nc/4.0/) (CC BY-NC 4.0) license, which permits any non-commercial use, distribution, adaptation, and reproduction in any medium, as long as the original work is properly cited. ISBN: 978-81-936820-5-0

boilers. The last one has an advantage of offering the steam with the required quality and quantity.

Performance evaluation is one of the essential requirements for the conservation of energy and optimization of operating parameters of boilers. There are many studies and researches in the field of performance evaluation of boilers contributed lifting of efficient production in many factories, desalination and power plants. As per the study carried out by Pachaiyappan[1] entitled improving the boiler efficiency by optimizing the combustion air, in which the performance of the air preheater has been studied on the basis of the combustion air passing through it. The author concluded that the correct optimization of the combustion air can increase the boiler efficiency by 2-3%, and also ensures less fuel consumption. By reducing the air preheater leakage, the auxiliary power consumption is also reduced. Thus the fuel is saved which leads to a considerable amount of profit.

Bora1 and Nakkeeran[2] presented an article about the performance analysis from the efficiency estimation of coal fired boiler. This paper puts forward an effective methodology for the efficiency estimation of a coal fired boiler, in comparison with its design value and enlists some of the factors that affect the performance of a boiler and it will help to increase overall boiler efficiency and as a result, annual monetary savings of the thermal power plant. Improvement of boiler's efficiency using heat recovery and automatic combustion control system was studied by Suntivarakorna and Treedetb [3]. This research was conducted to improve the efficiency of a fire tube boiler with a fixed gate and screw conveyor for feeding fuel, the experimental result indicated that using heat recovery and fuel drying reduces by 3%wt of fuel moisture content and boiler efficiency increases by 0.41%.

As per the study carried out by Baladhiya and Doshi [4], performance evaluation and optimization of steam generating systems. The automatic controls used in modern boilers have improved the efficiency of the boiler by optimizing operating parameters required for efficient combustion process and to achieve safety in operation of fuels. Operation of boiler under optimum conditions not only helps in reducing the cost of steam generation but also helps in reducing the air pollution.

Lahijani and Supeni [5] presented a work about the evaluation of the effect of economizer on efficiency of the fire tube steam boiler. The results show the effect of using an economizer increases the feed water temperature and improves the efficiency of fire tube steam boiler.

Zuara multi effect type (MED) desalination plant is a thermal type. The first stage of the plant contains three water pipes for the boilers, with a capacity of 80 tons/hr. The produced steam has a temperature of 220°C and pressure of 15 bar. The plant was inaugurated in the beginning of 2006. At this stage the boilers thermal efficiency have exceeded 92%. Over time, due to the operating conditions of the plant, there was a decrease in steam boiler productivity and low efficiency.

The objective of this study is to compare the operation real reading data of boilers in the plant with the design values confirmed by the performance tests and detect the reasons behind the low efficiency and productivity of the plant.

2 Materials and Methods

Two types of boilers data were collected. The design data was taken from plant documents and the actual operating data (real time data) was taken from the control room of Zuara desalination plant. It is available as daily and shifts reports from the first unit start up until the last boiler shutdown. The operating reading data selected along the boilers operating life cycle with different load rates. Table (1) presents sample of design and readings data for the boiler unit1[6].

Table 1: Design and real data for different annual operating periods of boiler unit 1.

Item	Unit	Design value	Annual real data				
			2007	2009	2011	2013	2014
Feed water flow rate	t/h	80.000	68.049	72.211	75.684	72.738	70.708
Feed water temperature	°C	115.00	112.96	113.07	113.08	113.07	112.96
F.W temp. after economizer	°C	165.00	165.33	174.38	176.64	173.39	149.94
Fuel mass flow rate	kg/h	4485.2	4221.8	4595.4	4732.0	4607.5	4411.8
Boiler steam product	t/h	80.000	67.598	71.040	74.342	70.003	58.035
Steam pressure	Bar	16.00	15.00	15.03	15.00	15.08	14.79
Steam temperature	°C	233.00	219.51	219.92	222.25	221.88	220.79
Air mass flow rate	t/h	76.845	72.896	69.379	81.565	84.315	81.677
Eco. Inlet gases temp.	°C	355.00	340.92	380.64	413.54	404.9	389.67
Stack temperature	°C	150.00	159.11	177.68	185.09	194.88	169.48
Boiler operating hours/year	hr	---	2093	2857	6103	6506	4502

3 Theory and Calculation

The performance evaluation parameters of boiler, like efficiency and evaporation ratio are reduced with time due to poor combustion, as well as the heat transfer surface fouling and poor operating and maintenance conditions. Even for new boilers, some reasons such as fuel and water quality can result in poor boiler performance. Boiler efficiency tests are helpful in finding the deviation of boiler efficiency from the best or design efficiency and target problem area for corrective action. Several indicators must be identified that affect the boiler efficiency and also help to determine the reasons behind the deviation.

3.1 Boiler Efficiency η_B :

The efficiency of any equipment is generally defined as the percentage of net energy obtained from the equipment to the total energy given to the machine, regardless of the type of the energy, mechanical, thermal or chemical. There are two methods to calculate the boiler

efficiency, for direct and indirect methods. The direct method which is used in this study is easy to apply and does not require many complicated devices. The method is summarized as follows [7]:

$$\eta_{Boiler} = \frac{\dot{m}_s(h_e - h_i)}{\dot{m}_f * HV} \quad (1)$$

3.2 Boiler Evaporation Rate (B.E.R):

It is the ratio between the steam produced from the boiler and the fuel consumption, i.e. the number of kilograms of steam obtained when burning one kilogram of fuel, which expresses the performance of the boiler without paying attention to the type and quality of the steam produced or type of fuel consumed [8].

$$B. E. R = \frac{\dot{m}_s}{\dot{m}_f} \quad (2)$$

3.3 Air Fuel Ratio (A/F):

The normal way to control excess air volume (Air/Fuel ratio) is by measuring the content of the exhaust gas from the oxygen and adjusting the ratio between fuel and air to achieve the maximum air level as low as possible, while maintaining complete combustion [8].

$$A/F = \frac{\dot{m}_a}{\dot{m}_f} \quad (3)$$

3.4 Economizer Effectiveness :

The economizer is a heat exchanger used to heat feed water before entering the boiler. It can also be used to heat the combustion air. The effectiveness of the economizer is defined as the ratio of the actual heat transfer rate to the maximum possible heat transfer rate. It can be expressed as: [8]

$$\varepsilon_{Economizer} = \frac{q}{q_{max}} \quad (4)$$

$$q = \dot{m}_w C_{p_w} (T_{co} - T_{ci}) \quad (5)$$

$$q_{max} = C_{min} (T_{hi} - T_{ci}) \quad (6)$$

4 Results And Discussion

The required results were obtained by substituting the boiler operational data in the previous mathematical relationships. Some important assumptions should be taken in consideration to facilitate the access the results.

- The heating value of the heavy fuel used in the plant is constant and equal to 44084kJ/kg.K[6].
- The thermal heat capacity of feed water is constant and equal to 4.186kJ/kg.K[8]

- The thermal heat capacity of gases combustion is constant and equal to 1.17kJ/kg.K [6]
- Tables (2),(3)and (4) show the most important results obtained for the three boilers.

Table 2: Performance indicators for boiler unit 1.

<i>Performance indicators</i>	<i>Design value</i>	Results from real data				
		2007	2009	2011	2013	2014
<i>Boiler Load %</i>	100.00	84.50	88.80	92.93	87.50	72.54
<i>Boiler thermal efficiency %</i>	92.32	86.20	83.21	84.57	81.78	70.96
<i>Boiler evaporation rate</i>	17.00	16.01	15.46	15.71	15.19	13.15
<i>Air fuel ratio (A/F)</i>	16.75	17.27	15.10	17.24	18.30	18.51
<i>Economizer effectiveness%</i>	85.42	79.76	75.85	76.03	71.97	79.57

Table 3: Performance indicators for boiler unit 2.

<i>Performance indicators</i>	<i>Design value</i>	Results from real data				
		2007	2009	2011	2013	2014
<i>Boiler Load %</i>	100.00	74.79	90.75	94.04	82.79	79.50
<i>Boiler thermal efficiency %</i>	92.32	88.04	85.41	83.90	81.42	74.93
<i>Boiler evaporation rate</i>	17.00	16.35	15.87	15.59	15.13	13.89
<i>Air fuel ratio (A/F)</i>	16.75	16.95	15.32	16.27	19.06	16.98
<i>Economizer effectiveness%</i>	85.42	85.55	71.58	70.65	74.38	77.03

Table 4: Performance indicators for boiler unit 3.

<i>Performance indicators</i>	<i>Design value</i>	Results from real data				
		2007	2009	2011	2013	2014
<i>Boiler Load %</i>	100.00	77.11	89.65	87.39	88.56	80.23
<i>Boiler thermal efficiency %</i>	92.32	84.86	82.46	81.56	81.13	75.69
<i>Boiler evaporation rate</i>	17.00	15.76	15.32	15.15	15.07	14.03
<i>Air fuel ratio (A/F)</i>	16.75	16.16	16.92	16.22	16.86	17.52
<i>Economizer effectiveness%</i>	85.42	84.79	76.81	72.64	74.71	72.90

Tables (2),(3) and (4) present the performance indicators for boilers units 1,2 and 3 respectively. It can be seen that the thermal efficiency of the boilers is directly proportional to the boiler load rate. The evaporation rates are also increased by increasing the boilers loads. Figure(1) shows the affect of the loads on the boilers thermal efficiency. It is also clear that the plant in its first years of operation has not been operating with high productivity. This is also evident from the total number of boilers operating hours due to the absence of an integrated water network linking the desalination plant to the consumption areas. During this period only one boiler was operated. Even though the other boilers were periodically operated this act resulted in the deterioration of their state.

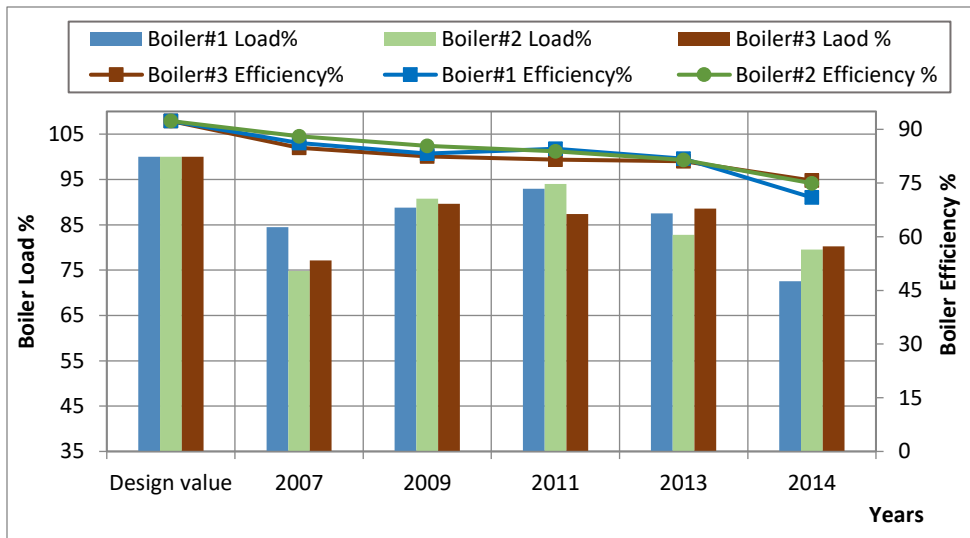


Figure1:Effect of boiler loads on boilers thermal efficiencies

The previous tables also show that the air/fuel ratio is unstable and variable in a random manner and certainly affects combustion rates. The deviation of this ratio from the design values leads to low efficiency and the emergence of heavy smoke in the chimneys, which causes deposits on the boiler pipes reducing the effectiveness of heat exchanger and the thermal efficiency especially in recent years of boilers age.

Figure (2) shows the air/fuel ratio and economizer effectiveness. The random change in the air/fuel ratio affects the combustion efficiency. The increase of air ensures complete combustion, but causes a loss of part of the thermal energy with the excess air in combustion gases. On the other hand, the lack of air quantity leads to incomplete combustion and therefore the emergence of thick black smoke in chimneys and increase the amount of this smoke, which causes the accumulation and crust on the pipes in the economizer and consequently, results in the low effectiveness of the economizer as well as a key factor in the corrosion of pipes and water leakage inside the boiler. The last was noticed through the water mass balance compared to the feed water and produced steam. This phenomenon was observed during the last years of operation of the boilers.

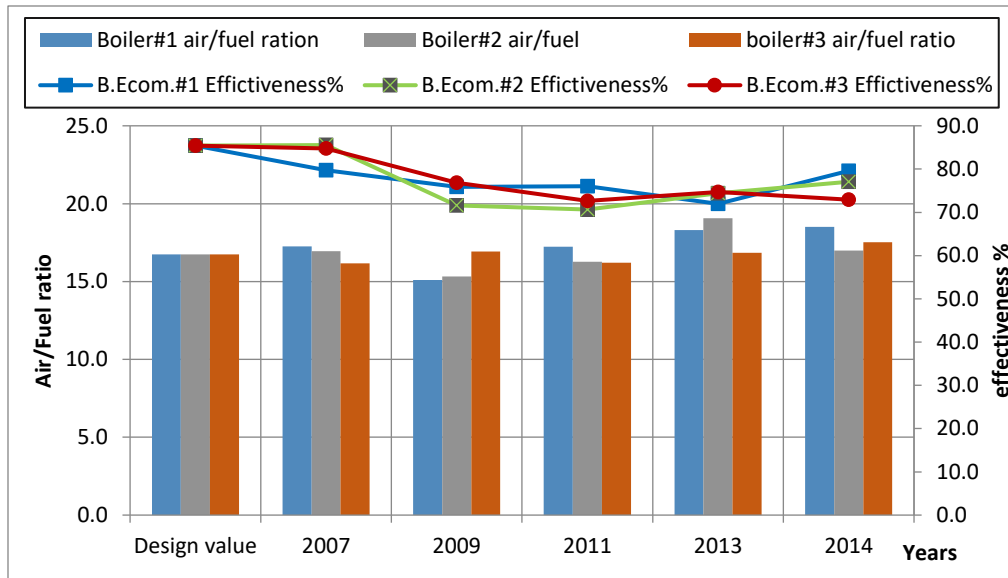


Figure 2: Air/fuel ratio and economizer effectiveness.

5 Conclusions

The boiler efficiency can be reduced by many factors. Zuara desalination boilers were exposed in the first years to long suspension period due to the absence of a network of transmission and distribution of water produced in the plant, as well as the sudden stops and frequent eruptions due to power outages in recent years. The previous problems have negative impact on the productivity of steam boilers and its efficiency and cause the corrosion for most of its parts and this lead to water leakage in the pipes. The poor mixing ratio of the air-to-fuel is a major cause of the black smoke of boilers, which due to its abundance and difficulty of disposal has affected the efficiency of the economizer and thus the performance of the boiler, So it is recommended to modify the combustion air rate of fuel in a correct ratio according to the design values as well as the use of the system of the boiler soot blower periodically and regularly according to manufactures company procedure.

6 Acknowledgment

We would like to express our sincere thanks toward Zuara Desalination Plant engineers and staff for their valuable support in the implementation of this project.

References

- [1] R. Pachaiyappan and J. Prakash, "Improving the Boiler Efficiency by Optimizing the Combustion Air", Vol.787, pp. 238-242, Access online on 24 June 2018 at <https://doi.org/10.4028/www.scientific.net/AMM78.238>
- [2] M. Bora1 and S. Nakkeeran " Performance Analysis From The Efficiency Estimation of Coal Fired Boiler", Vol.2, pp561-574, Access online on 24 June 2018 at http://www.journalijar.com/uploads/901_IJAR-3240

- [3] R. Suntivarakor and W. Treedetb "Improvement of Boiler's Efficiency Using Heat Recovery and Automatic Combustion Control System", Vol.100, pp.193-197, 2016. Access online on 26 June 2018 at <https://doi.org/10.1016/j.egypro.2016.10.164>
- [4] Baladhiya, C. S. ; Doshi, J. S."Performance evaluation and optimization of steam generating systems",Vol.10 No.1 pp.222-227, Access online on 27 June 2018 at :<http://www.researchjournal.co.in/onli..>
- [5] Ahmad M. Lahijani and Eris E. Supeni"*Evaluating the Effect of Economizer on Efficiency of the Fire Tube Steam Boiler*",Vol.07.1 pp1-4, Access online on 02 July 2018 at <https://www.researchgate.net/publication/324196534>
- [6] Manuals and performance test sheets for boilers of Zuara desalination plant, designed and constructed by SIDEM company 2005.
- [7] Amit Kumar Jain, "An Approach towards Efficient Operation of Boilers," *International Journal of Scientific & Engineering Research*, Vol. 3, pp 01-11 , Access online on 10 July 2018 at. <https://pdfs.semanticscholar.org/70f1>.
- [8] Yunus A. Cengel and Michael A. Boles, "Thermodynamics An Engineering Approach", Eight Edition. ISBN 978-0-07-339817-4
- [9] Frank P. Incropera, "Introduction to heat transfer", Sixth Edition ISBN 13 978-0470-50196-2

Estimation of Original Oil in Place for Belhedan Oil Field by Using Volumetric Method, Material Balance Equation Method, and Reservoir Simulation Method

Ali Omran Nasar^{1*}, Jibriel Abusaleem², Essa M. Tabar³

Department of Petroleum, College of Engineering, Sirte University, Libya

DOI: <https://doi.org/10.21467/proceedings.2.35>

* Corresponding author email: ali_omran95@yahoo.com

ABSTRACT

Knowing the amount of the hydrocarbon pore volume correctly is basically required to have properly design of oil and gas reservoirs. The accuracy in calculating of the hydrocarbon pore volume depends on the used method. Usually two conventional methods use to estimate the Original Oil In Place (OOIP) very quickly. These two methods are volumetric method and Material-Balance-Equation (MBE) method. However, there is another quick method that can be used to calculate (OOIP) which is reservoir simulation method. In this paper, three difference methods were used to calculate OOIP to provide Waha Oil Company with the calculated value.

Moreover, each method required sort of data; the volumetric method depends on static data. However MBE and reservoir simulation method require dynamic data of the reservoir and the area around. Usually the driving mechanism is the key point when MBE and reservoir simulation are used. The drive mechanism in studied area (Belhedan oil field) is described from the field information as a strong water drive with small gas-cap. The given field data don't have any information about the gas cap and the water dive. As a result, applying the MBE method to calculate OOIP for this case require some information about the gas cap and the aquifer. So the MBE gave a value of OOIP didn't agree with the value of OOIP that obtained from the volumetric and reservoir simulation. Lack in the information makes MBE unusable method in this case. It has been trying to solve this problem by use some correlation in calculate some parameters and ignore others. However, doing all that, the result couldn't reach any closed value that is calculated by volumetric and reservoir simulation which will explain. In the end of the paper, a prediction of well performance (well v-4) will be done from 1970 until 2020.

Keywords: Original Oil In Place, Volumetric Estimation, Material-Balance-Equation (MBE), and Reservoir Simulation Model.

1 Introduction

Knowing the amount of original oil in place is the most important parameter for reservoir engineers to make a quick decision whether the discovered area is profitable or not. There are two conventional methods and two unconventional methods use to calculate the OOIP. The two conventional methods are volumetric method and Material-Balance-Equation (MBE)



© 2018 Copyright held by the author(s). Published by AIJR Publisher in Proceedings of First Conference for Engineering Sciences and Technology (CEST-2018), September 25-27, 2018, vol. 1.

This is an open access article under [Creative Commons Attribution-NonCommercial 4.0 International](https://creativecommons.org/licenses/by-nc/4.0/) (CC BY-NC 4.0) license, which permits any non-commercial use, distribution, adaptation, and reproduction in any medium, as long as the original work is properly cited. ISBN: 978-81-936820-5-0

method, and the two unconventional methods are reservoir simulation method and decline curve analysis method⁽¹⁾. In reservoir engineer’s perspective, the most used methods in petroleum industry are volumetric method and reservoir simulation method. This is because, they are more sophisticated than the other methods to calculate OOIP. The volumetric is quick method and reservoir simulation is more accurate, for these reasons one of them usually is chosen. Among the mentioned methods this paper will focus on volumetric, MBE, and reservoir simulation.

The volumetric depends on basic data of reservoir rock and reservoir fluid properties. However, the reservoir simulation needs a lot of information starts with geological history and ends with production history additional to reservoir rock and fluid properties⁽¹⁾. On the other hand, MBE depends on combinations of fluid properties, rock properties, and production data. Since each method required different sort of data the result will be different, but which one is better this will be discussed. Moreover, each method has some advantages and disadvantages. First, volumetric is a simple method and doesn’t require a lot of information; however it is limitations the reservoir heterogeneity where the reservoir assumed is a homogenous and not accurate enough. Second, MBE depends on production data which usually are available and other reservoir properties can be obtained from laboratory experiments. However, it isn’t proper to be use when the reservoir is connected to aquifer or gas cap with no enough information about them. The reservoir simulation is quick and accurate method in calculating OOIP. The only problem can face reservoir engineers is building reservoir model that capable to produce hydrocarbon as the real reservoir. In the end, whether the calculation of initial hydrocarbon in place is made manually (volumetric – MBE) or by computer applications (reservoir simulation), the procedures are the same in principle. The three mentioned methods will be explained briefly and individually.

1.1 Volumetric Method

In a new area, usually volumetric estimation made before drilling first well, where the reservoir is assumed to be exists and there is no chance of failure. The volumetric method depends on calculation of reservoir volume which obtained of geophysical maps. There are different methods use to estimate it, like dividing the reservoir into small grid bulk or dividing the area of contour maps into pisses as show in Figure below.

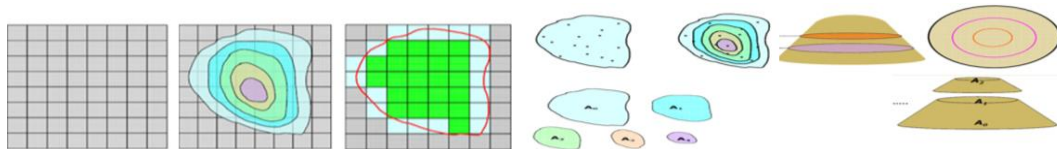


Figure 1: Methods of reservoir volume calculations⁽²⁾.

After the volume is estimated by one of the shows methods in Figure 1, it should multiple by rock porosity and fluid saturation which will result the estimation of recoverable barrels of oil

or mcf of gas. In order to convert recoverable hydrocarbon (oil or gas) to standard condition, it should be divided by its formation volume factor. The equation that uses to calculate OOIP by volumetric method can be written as:

$$OOIP = \frac{7758 Ah\phi(1 - S_{wi})}{B_{oi}} \tag{1}$$

1.2 Material Balance Equation, MBE

Material balance equation is the second method that used in this paper to estimate OOIP. Essentially, MBE depends on analyzing of production volumes, pressure condition, and fluid properties to calculate OOIP. In order to have proper understating of MBE solution assume a tank model that located at datum depth and behave like real reservoir condition that having different condition (reservoir pressure and fluid properties) as shown in Figure 2 (3). After start producing from that model, the reservoir pressure will start decrease and the oil and gas condition will change and produce new materials in the reservoir beside that some other elements will inter to the reservoir as shown in tank below.

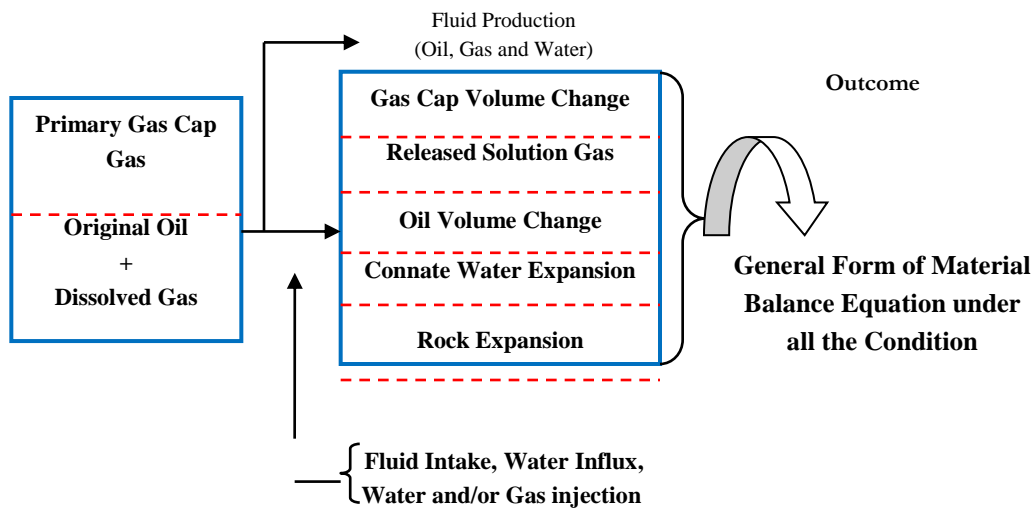


Figure 2: Tank model of reservoir under original condition and after start producing (3).

By replacing all mentioned terminologies and combine them, the general form of the material balance equation for the tank mode of above reservoir can be written as(3):

$$N = \frac{Np[Bo + (Rp - Rs)Bg] - (We - WpBw) - GinjBginj - WinjBw}{(Bo - Boi) + (Rsi - Rs)Bg + mBoi \left[\frac{Bg}{Bgi} - 1 \right] + Boi(1 + m) \left[\frac{CwS_{wi} + Cf}{1 - S_{wi}} \right] \Delta p} \tag{2}$$

The above equation is the general form MBE which uses to estimate initial hydrocarbon pore volumes, predict reservoir pressure, calculate water influx, predict future reservoir performance, and predict ultimate hydrocarbon recovery under various types of primary drive mechanisms. Furthermore, the general form of the MBE has been developed to be an equation

of straight line equation for simplicity, where some elements that are not exist in the reservoir (3). The straight-line solution method requires plotting variable group versus another variable group. Each group depends on the driving mechanism of production in which the reservoir is producing, and it is the most important tasks. Depending on the driving mechanism the solution of MBE can be taken one of the several cases: undersaturated oil reservoir case, saturated oil reservoir case, gas cap reservoir case, water drive reservoirs case, and combination drive reservoirs case(3). Since the driving mechanism of Belhedan oil fields is described as strong water drive with small cap gas, the solution of MBE as straight line equation should use either water drive case, or combination drive case. From field information the gas cap is very small and was neglected in any calculation, because there isn't enough information about it. In a water-drive reservoir mechanism, identifying the type of the aquifer and characterizing its properties are perhaps the most challenging tasks can face any reservoir engineers to calculate the amount of OOIP correctly. Havlena and Odeh solve the general form of MBE by rearrange the general form of MBE and ignores other for the purpose of simplicity by assuming no pressure maintenance comes from gas or water injection. The rearrangement of MBE equation can be written as (3):

$$N_p [B_o + (R_p - R_s) B_g] - (W_e - W_p B_w) = N \left[(B_o - B_{oi}) + (R_{si} - R_s) B_g + \left[\frac{B_g}{B_{gi}} - 1 \right] + B_{oi} (1 + m) \left[\frac{C_w S_{wi} + C_f}{1 - S_{wi}} \right] \Delta p \right] \quad (3)$$

Moreover, Havlena and Odeh had simplified the above equation to be an equation of straight line equation and shortages the number of terms to have them in equation of couple groups with different names as shown below:

$$F - W_e = N(E_o + mE_g + E_{f,w}) \quad (4)$$

In equation 4, each new symbol have different name and represent different section of the reservoir which are: F represents the reservoir volume of cumulative oil and gas produced which named as the underground withdrawal. W_e refers to the net water influx that is retained in the reservoir. E_o , E_g , $E_{f,w}$ these group presents the expansion of oil and its originally dissolved gas production, net expansion of the gas cap that occurs with the production, and the expansion of the initial water and the reduction in the pore volume respectively.

Havlena and Odeh in 1963 expressed an equation for undersaturated oil reservoir where $m=0$, and rearranging the equation 4. So the equation can be written as (4):

$$F = N(E_o + E_{f,w}) + W_e \quad (5)$$

Havlena and Odeh had further expressed equation 5 in a more condensed form as (4):

$$\frac{F}{E_o + E_{f,w}} = N + \frac{W_e}{E_o + E_{f,w}} \quad (6)$$

Dake in 1978 points out that the term $E_{f,w}$ can frequently be neglected in water-drive reservoirs. This is because water influx helps to maintain the reservoir pressure. The equation 6 cannot be solved directly to calculate the OOIP, since it is require calculating water influx first. Several water influx models can be used to calculate the water influx. One of these models is Schilthuis steady-state method, which will be use in this study. The steady-state aquifer model as proposed by Schilthuis in 1936 is given by (4):

$$W_e = C \int_0^t (P_i - P) dt = C \sum (P_i - P) \Delta t \tag{7}$$

Combining equation 6 with 7 gives a straight line equation as shown below (4):

$$\frac{F}{E_o + E_{f,w}} = N + C \frac{\sum (P_i - P) \Delta t}{E_o + E_{f,w}} \tag{8}$$

1.3 Reservoir Simulation Modelling

Usually reservoir simulation uses to find the accurate value of hydrocarbon initially in place under different conditions, and also to help reservoir engineers having a proper understanding of reservoir behaviour and making prediction which help engineers in making investment decisions. In this study, a compositional reservoir simulator has been utilized with the intention of modelling and simulating the reservoir (5). CMG (Computer Modelling Group) is the reservoir simulation that has been used. This commercial software is used in this study to determine reservoir capacities in order to maximize potential recovery and making oil prediction.

2 Data of Studied Reservoir

The data that are used in this study were obtained from Waha Oil Company. Table 1 and 2 presents basic information of reservoir fluid, rock properties, and average reservoir properties for each layer, respectively. Table 3 presents PVT data. The production data versus reservoir pressure had been clean up before it use because some data doesn't have pressure records, and it start from 1965.

Table 1: Reservoir Data Summary as of July 2013 Belhedan - Gargaf Formation (6):

Basic Reservoir Data		Average Rock & Fluid Properties	
1-Top of Pay Formation, ft	6300	8- Porosity , %	8.0
2- Datum Depth, ft	6500	9- Permeability, md	10-100
3- Total producible Wells	29	10- Water Saturation, %	33.0
4-Productive Acreage, acres	18600	11- Rock Compressibility, Psia-1	4.6*10 ⁻⁶
5- Average Net Pay, ft	190	12- Water Compressibility, Psia-1	3.3*10 ⁻⁶
6- Original BHP at Datum, Psia	3100	13-F.V.Fat Original Pressure, RB/STB	1.135
7- Reservoir Temperature, deg F	210	14- Current Reservoir Pressure, Psia	2322

Table 2: Gargaf Layers, Average Reservoir Properties above the Oil-Water Contact ⁽⁶⁾:

Gargaf Layer	Gross, ft	Net ft	Net/Gross	Porosity,%	Sw, %	HCPTh, ft
GL-1	39.7	27.0	0.68	8.5	37.6	1.43
GL-2	80.1	47.7	0.60	7.6	37.8	2.55
GL-3	75.6	37.6	0.50	6.7	36.3	1.97
GL-4	74.5	38.8	0.52	7.0	35.7	2.11
GL-5	52.9	27.0	0.51	6.8	38.9	1.37
GL-6	29.4	21.0	0.71	7.5	31.5	1.07

Table 3: PVT Data for well v42 ⁽⁶⁾:

P, Psia	V/Vsat	B _{od} , rb/stb	R _{sd} , scf/stb	μ _{od} ,cp	C _{od} 1/psi	B _o rb/STB	R _s scf/STB
478	1.0386	1.154	122			1.123	84.3
536	1.0000	1.158	133	1.29		1.127	95.0
600	0.9994	1.157			9.38E-06	1.126	
700	0.9984	1.156		1.31	1.00E-05	1.125	
800	0.9975	1.155			9.02E-06	1.124	
900	0.9966	1.154			9.03E-06	1.123	
1000	0.9956	1.153		1.35	1.00E-05	1.122	
1200	0.9938	1.151			9.06E-06	1.120	
1400	0.9921	1.149		1.39	8.57E-06	1.118	
1700	0.9896	1.146			8.42E-06	1.115	
2000	0.9871	1.143			8.44E-06	1.112	
2300	0.9846	1.140			8.46E-06	1.109	
2600	0.9823	1.138			7.80E-06	1.107	
3000	0.9794	1.134			7.40E-06	1.103	
3500	0.9757	1.130			7.58E-06	1.099	
4000	0.9722	1.126			7.20E-06	1.096	

3 Results and Discussion

The calculation of OOIP has been done by using different methods. The result of each method was compared and sent it to Waha Oil Company as it's required.

3.1 First, Volumetric Method

Estimation of OOIP has traditionally been done using volumetric method. All the data need to calculate OOIP are listed in Tables 1 and 2, which include an average value of porosity, saturation, and total net pay thickness for the six layers. Applying equation 1 the initial oil in place is calculated to be 1.29 MMMSTB as shown below.

$$OOIP = \frac{7758 Ah \phi (1 - S_{wi})}{B_{oi}} = \frac{7758 * 18600 * 190 * 0.08 * (1 - 0.33)}{1.135} = 1.294 \text{ MMMSTB}$$

It is well know that the volumetric method is a quick and an easy method of calculating OOIP. However, its result isn't that accurate when it compare with other methods, but it is satisfied method which can be use to make a quick decision when its need it.

3.2 Second, Material Balance Equation Method, MBE

The MBE method supposes to be more accurate in the results than the volumetric method, but due to the lack of information about the aquifer around the reservoir, and changing in the reservoir pressure, the MBE mightn't be the correct choice. The reservoir pressure has been changed rapidly in increasing and decreasing. The changing in the pressure is a result of opening and closing the well as it is mentioned from the company in additional to water influx. Using MBE as straight line equation in such this case which is depending basically on the reservoir pressure and production data will led for incorrect value of OOIP. Since it's a straight line equation, which is require smooth changing of reservoir pressure. In order to calculate the OOIP by MBE as straight line equation there are two important elements must be known, these elements are; reservoir type and reservoir driving mechanism. First, since the reservoir pressure in given data is higher than the bubble point pressure, the reservoir is labeled as an undersaturated oil reservoir. Second, The driving mechanism can be obtained by plotting $F/E_o + E_{f,w}$ versus N_p to see if the reservoir has water influx or not. To start calculating OOIP all the data are available except one is missing which is the oil formation volume factor, for that a correlation of plotting oil formation volume factor from the PVT experiment versus reservoir pressure as shown Figure 3.

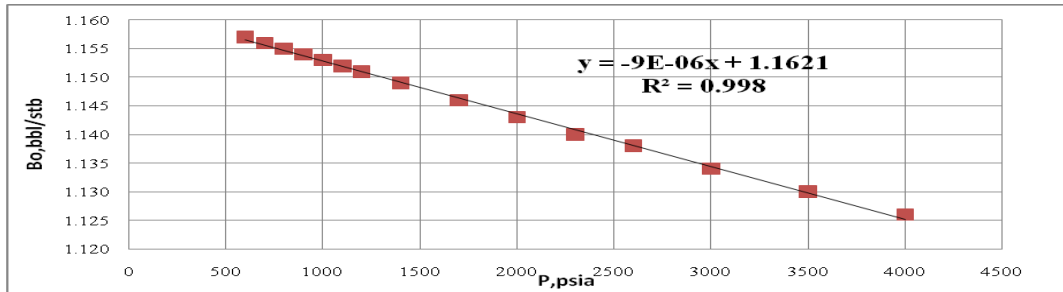


Figure 3: Curve fitting for B_o vs pressure.

From Figure 3 a straight line equation can be used to estimate B_o for any given reservoir pressure by: $B_o = -9E-06x + 1.1621$. Now calculating OOIP by using MBE can be achieve quickly since all the required data are available. After calculation by using Havlena and Odeh approach, the result of MBE as straight line equation couldn't give a correct value of OOIP since no exact straight line could be obtained as shown in Figure 4. This is return to the change in the reservoir pressure and lacking in the information about the aquifer. Such this case has been introduced by other publishers and their values were far away from the one that is calculated by other methods. The calculations are shown in Table 4a & 4b.

As a rule of thumb, the best straight line passes through the large number of points and middles the other. The OOIP from the MBE as straight line is $1E09$ which less than the value obtained from the volumetric method. Right now a decision couldn't be making whether this value is the correct or the volumetric estimation. In the end of MBE method, MBAL software for MBE method is used to see if better result can be obtained. MBAL is commonly used for modelling the dynamic reservoir effects prior to building a numerical simulator model⁽⁷⁾. As a

result, the result shows difference from MS excel sheet which gave higher value of OOIP which is 2.2 E09, it is indicate whether MBAL or excel sheet the result can never reach a closed value of the volumetric estimation.

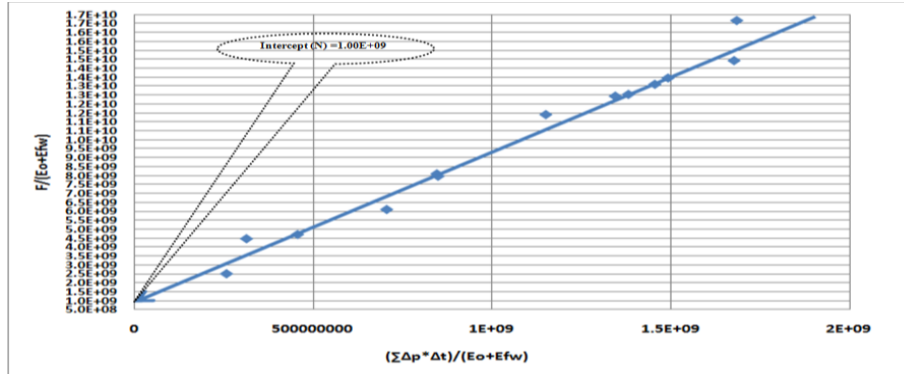


Figure 4: Plot $F/(E_o+E_{f,w})$ vs $(\sum \Delta p * \Delta t)/(E_o+E_{f,w})$ for well v42.

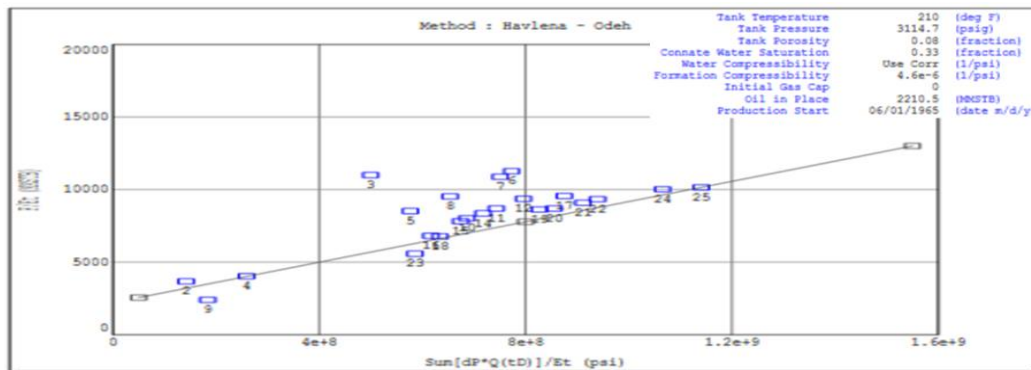


Figure 5: MBAL software result for estimation OOIP by using MBE method, analysis window⁽⁷⁾.

Table 4-a: Calculation of OOIP using MS excel of well V42⁽⁶⁾:

Date	Np	Wp	P	Bo	Δt	Δp	Eo
m/d/year	MSTB	MSTB	psia	bbbl /STB	days	psia	bbbl /STB
6/1/1965	4349.1	1.1	3079	1.1340	0	21	0
6/1/1974	12454.5	23.3	2796	1.1370	3285	304	0.001936
6/1/1976	13396.1	29.8	3032	1.1350	730	68	-0.000188
6/1/1982	16799	56.7	2727	1.1380	2190	373	0.002557
6/1/1983	17138.7	67.8	2962	1.1350	365	138	0.000442
6/1/1986	18646.1	77.6	3007	1.1350	1095	93	0.000037
6/1/1988	19583.7	108.3	2986	1.1350	365	114	0.000226
6/1/1989	20020.8	108.9	2338	1.1410	365	762	0.006058
6/1/1991	21202.9	128.9	2951	1.1360	730	149	0.000541
6/1/1992	21747.9	137.5	2982	1.1350	365	118	0.000262

6/1/1994	22570.9	147.8	3031	1.1350	365	69	-0.000179
6/1/1996	23421	191.3	2916	1.1360	730	184	0.000856
6/1/1997	24150.8	279.8	2853	1.1360	365	247	0.001423
6/1/1999	25037.8	579.6	2764	1.1370	730	336	0.002224
6/1/2000	25404.2	741.2	2935	1.1360	365	165	0.000685
6/1/2001	25770	906.9	2748	1.1370	365	352	0.002368
6/1/2002	26068.7	1023.8	2850	1.1360	365	250	0.00145
6/1/2003	26245	1060.4	2850	1.1360	365	250	0.00145
6/1/2005	26999.4	1553.9	2850	1.1360	730	250	0.00145
6/1/2006	27402.7	1922.5	2850	1.1360	365	250	0.00145
6/1/2008	28144.9	2703.3	2600	1.1390	730	500	0.0037
6/1/2009	28367	3119.8	2850	1.1360	365	250	0.00145

Table 4-b: Calculation of OOIP using MS excel of well V42 ⁽⁶⁾:

E _{fw}	E _o +E _{fw}	F	F/(E _o +E _{fw})	Δp*Δt	ΣΔp*Δt	(ΣΔp*Δt)/(E _o +E _{fw})
bbl /STB	bbl /STB	bbl	STB	Psiadays	Psiadays	Psiadays/ bbl /STB
8.61E-05	-5.25E-04	4.93E+06	-9.40E+09	0.00E+00	0.00E+00	0.00E+00
1.25E-03	3.18E-03	1.42E+07	4.46E+09	9.99E+05	9.99E+05	3.14E+08
2.79E-04	9.09E-05	1.52E+07	1.68E+11	4.96E+04	1.05E+06	1.15E+10
1.53E-03	4.09E-03	1.92E+07	4.69E+09	8.17E+05	1.87E+06	4.56E+08
5.66E-04	1.01E-03	1.95E+07	1.94E+10	5.04E+04	1.92E+06	1.90E+09
3.82E-04	4.19E-04	2.12E+07	5.08E+10	1.02E+05	2.02E+06	4.82E+09
4.68E-04	6.94E-04	2.24E+07	3.22E+10	4.16E+04	2.09E+06	3.01E+09
3.13E-03	9.18E-03	2.30E+07	2.50E+09	2.78E+05	2.37E+06	2.58E+08
6.11E-04	1.15E-03	2.42E+07	2.10E+10	1.09E+05	2.48E+06	2.15E+09
4.84E-04	7.46E-04	2.48E+07	3.33E+10	4.31E+04	2.52E+06	3.38E+09
2.83E-04	1.04E-04	2.58E+07	2.48E+11	2.52E+04	2.58E+06	2.48E+10
7.55E-04	1.61E-03	2.68E+07	1.67E+10	1.34E+05	2.71E+06	1.68E+09
1.01E-03	2.44E-03	2.78E+07	1.14E+10	9.02E+04	2.80E+06	1.15E+09
1.38E-03	3.60E-03	2.91E+07	8.08E+09	2.45E+05	3.05E+06	8.46E+08
6.77E-04	1.36E-03	2.97E+07	2.18E+10	6.02E+04	3.11E+06	2.28E+09
1.44E-03	3.81E-03	3.03E+07	7.95E+09	1.28E+05	3.23E+06	8.49E+08
1.03E-03	2.48E-03	3.08E+07	1.24E+10	9.13E+04	3.33E+06	1.34E+09
1.03E-03	2.48E-03	3.10E+07	1.25E+10	9.13E+04	3.42E+06	1.38E+09
1.03E-03	2.48E-03	3.24E+07	1.31E+10	1.83E+05	3.60E+06	1.45E+09
1.03E-03	2.48E-03	3.33E+07	1.34E+10	9.13E+04	3.69E+06	1.49E+09
2.05E-03	5.75E-03	3.50E+07	6.09E+09	3.65E+05	4.06E+06	7.05E+08
1.03E-03	2.48E-03	3.57E+07	1.44E+10	9.13E+04	4.15E+06	1.68E+09

3.3 Third, Reservoir Simulation Method

In this study, reservoir simulation software was used to calculate the initial oil in place. CMG (Computer Modelling Group) is reservoir engineering software. CMG consist of different applications which are BUIDER, IMEX, and RESULTS. The BUILDER is to build reservoir simulation model, IMEX for black oil reservoir, and RESULTS to have results graph⁽⁸⁾. As a result, a reservoir simulation model was built with 29 vertical wells. The input data for that model were obtained from Waha Oil Company as listed in Tables1, 2, and 3. In this case of field study, there is a lot of missing information, which returns to the difficulty to obtain them either from the company or from the reservoir itself. For this reason, CMG software was chosen in this study to estimate the OOIP. This simulator can generate some information which aren't available from the source. To build model there are some steps need to be followed. First, start with basic information which includes: started date, field unit, and grid number. Second, a grid system type has been used to build the area for the Belhedan reservoir. The surface area of the reservoir is 18600 acre, and consists from six layers with different reservoir properties. Third, reservoir rock and fluid used as an average value for each layer. After inserting all the required data, the reservoir model becomes ready to run and get result. Only one step still left in this model is drilling wells. A twenty nine vertical well has been drilled in the reservoir. The run was achieved and the result will be discussed acceptable. In the end, Figure 6 shows the grid top, grid thickness, reservoir porosity, permeability, net pay, water saturation, and other information as showed below.

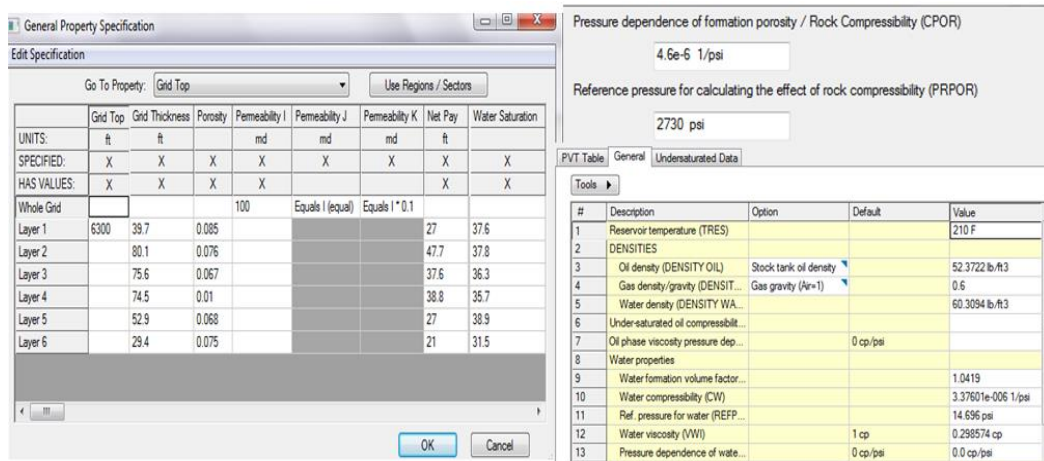


Figure 6: General property specification⁽⁸⁾

Finally, after the model has been run and the result of that model of original oil in place is highly which is 1.4 MMScf. The result of OOIP is acceptable and close to volumetric method then MBE, which make simulation has the correct value as sent it to the company for verification. Figure 7 shows the results of CMG model and oil prediction from 1965 to 2020

respectively. The prediction was done without having history matching where the well assumed producing oil from the day started until 2020.

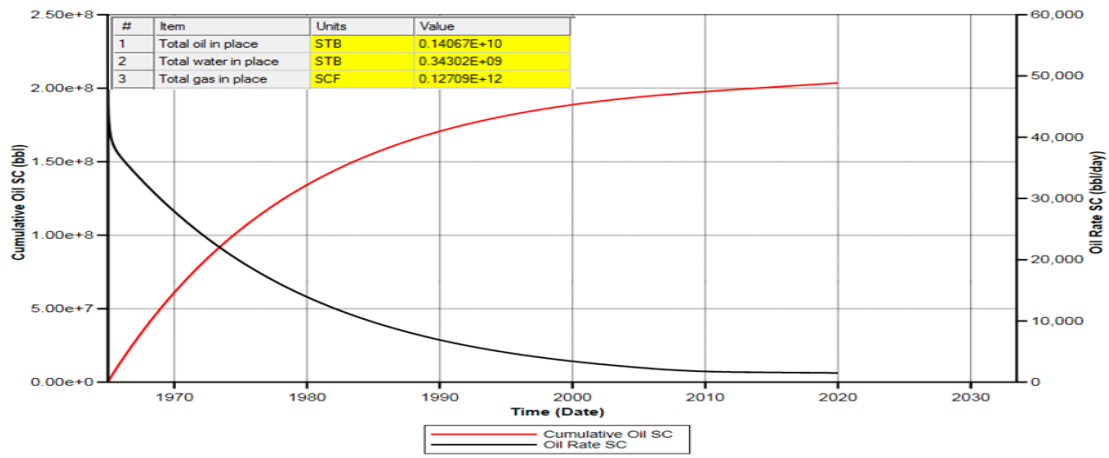


Figure 7: Result of simulation run and cumulative oil prediction and oil flow rate⁽⁸⁾

4 Conclusions

Three different methods were used to calculate the OOIP. The obtained results from these methods were different. The difference in the results between them returns to the availability of the reservoir data. The amount of OOIP that is getting from Waha Oil Company is around 1.36 MMMSTB which is close to software result and volumetric result. The diversity in the results is return for some reasons which can be summary as: First, Volumetric method is the easiest, quickest method and doesn't need much information to estimate OOIP. Second, results of MBE as straight line equation method by excel or MBAL software aren't acceptable at all, because there are some missing information about the driving mechanism that providing the energy to the reservoir. Third, Reservoir simulation method is a modern method in petroleum industry to calculate the OOIP and making prediction and history matching as well, the software is more acceptable since it generate any other information in case its missing.

5 Acknowledgment

The authors would like to express their gratitude to the Waha Oil Company for supplying the data, and to West Virginia University for providing the software used in this study.

References

- [1] B.C Craft, M. Hawkins, "Applied Petroleum Reservoir Engineering", Englewood Cliffs, NJ 07632, 1991.
- [2] Aminian, K, "Class Note of Reservoir Engineering PNGE 330", Spring 2006.
- [3] Tariq Ahmed, "Applied Reservoir Engineering, second Edition Handbook, Butterworth-Heinemann 2001.
- [4] Tariq Ahmed, Paul D. Mc Kinney, "Advanced Reservoir Engineering", Anadarko Canada Corporation, 2005.
- [5] West Virginia University, "Petroleum Engineering Department", [http:// www.wvu.edu](http://www.wvu.edu),2014.
- [6] Waha Oil Company, "Reservoir Engineering Department", January 1st 2014.
- [7] MBAL software, "West Virginia University, Petroleum Engineering Department", [http:// www.wvu.edu](http://www.wvu.edu),2014.
- [8] CMG software, "West Virginia University, Petroleum Engineering Department", [http:// www.wvu.edu](http://www.wvu.edu),2014.

Nomenclature

\emptyset = Porosity, dimensionless.	S_w = Water saturation, percentage
A = Cross section area, acre	h = Net pay thickness, ft
P_i = Initial reservoir pressure, Psi	Δp = Change in reservoir pressure = $P_i - P$, Psi
P = Average reservoir pressure, Psi	N = Initial (original) oil in place, STB
P_b = Bubble point pressure, Psi	G_p = Cumulative gas produced, scf
N_p = Cumulative oil produced, STB	R_p = Cumulative gas-oil ratio, scf/STB
W_p = Cumulative water produced, bbl	R_s = Gas solubility, scf/STB
R_{si} = Initial gas solubility, scf/STB	B_o = Oil formation volume factor, bbl/STB
B_{oi} = Initial oil formation volume factor, bbl/STB	B_g = Gas formation volume factor, bbl/scf
B_{gi} = Initial gas formation volume factor, bbl/scf	G_{inj} = Cumulative gas injected, scf
W_{inj} = Cumulative water injected, bbl	G = Initial gas-cap gas, scf
W_e = Cumulative water influx, bbl	C_f = Formation (rock) compressibility Psi^{-1}
m = Ratio of gas-cap to reservoir oil volume, bbl/bbl	C_w = Water compressibility, Psi^{-1}

Pressure Transient Analysis by Using MS. Excel Sheet and Computer Programming

Essa M. Tabar*, Ali Omran Nasar, Tariq Basher

Petroleum Engineering Department, Engineering Faculty, Sirte University, Libya

DOI: <https://doi.org/10.21467/proceedings.2.36>

* Corresponding author email: etabare4@gmail.com

ABSTRACT

Paper shows an effective using of two programs (MS Excel and computer programming) to analysis the pressure build up test data. The programs were used to determine the best infinite-reservoir acting by the relationship which between the shut-in pressure and logarithm of the shut-in time. The purpose of well test analysis is to identify the type of reservoir involved and to determine the parameters of the reservoir quantitatively. Data from one well, has been analyzed by application of modern well-test analysis techniques, such as derivative analysis and computer programming, in addition to the conventional log-log and semi-log methods, and then double check by using Type curve matching. MS Excel sheet and computer programming are using to identify: Wellbore storage effect, Middle time region “straight line”, Late time region “boundary effect”, and then calculate the permeability and skin factor. The results of two programs shows that the well is located near a sealing fault. Hence, they indicate that Horner method is the most accurate than derivative methods.

Keywords: buildup test, pressure transient, derivative method, skin factor, permeability

1 Introduction

The pressure build up test is conducted by producing a well at constant rate for some time, shutting the well in, allowing the pressure to buildup in the wellbore, and recording the pressure in the wellbore as a function of time. From these data, it is possible to estimate formation permeability and current drainage-area pressure, and to characterize damage or stimulation and reservoir heterogeneities or boundaries. The method used to analyze the pressure buildup tests can be classified into three main groups; conventional methods (Horner and MDH), pressure derivative in 1983 [1], and then double check by sing type curve matching methods. This paper present analysis of one field cases of the pressure build up test using MS Excel and computer programing (PT4).



© 2018 Copyright held by the author(s). Published by AIJR Publisher in Proceedings of First Conference for Engineering Sciences and Technology (CEST-2018), September 25-27, 2018, vol. 1.

This is an open access article under [Creative Commons Attribution-NonCommercial 4.0 International](https://creativecommons.org/licenses/by-nc/4.0/) (CC BY-NC 4.0) license, which permits any non-commercial use, distribution, adaptation, and reproduction in any medium, as long as the original work is properly cited. ISBN: 978-81-936820-5-0

During the last decade, the theory and application of pressure transient testing has tremendous improvements, and many solutions and techniques have been proposed to analysis variety of reservoirs .The purpose of analyzing well test, and production data is to determine the ability of a formation to produce reservoir fluids, where needed to do this by estimating formation properties from reservoir data. Some of the relevant properties that must be determined are permeability, skin effect, and initial reservoir pressure, in general, characterization or description of the reservoir-well system in order to evaluate well damage or stimulation, fracturing or not of the well, the existence of faults or flow barriers, the approximate shape of the drainage area of the reservoir or the change of the reservoir lithological properties [2].

For analysis purpose, pressure drawdown and build-up test data are usually separated into three regions which represent different analysis, and interpretation scenarios. The "early time region" is typically affected by wellbore storage while "middle time "region is indicative of the characteristics of the reservoir itself (transient flow), and finally, the "late time region" pertains to data affected by reservoir boundaries. A typical pressure test may not contain all three regions. It is important to note that the reservoir properties calculated from both build-up and drawdown tests represent average properties within that drainage area.

There are many graphical techniques that can be used to analyze well test data; these techniques include Cartesian, semi-log, and log-log plots of pressure and pressure drop function as shown in Figure (1). The particular analysis technique to be used depends uniquely on the reservoir to be tested. In the fact, it is important to use the log- log plot first, as an excellent diagnostic tool to identify the regions of the flow in a reservoir.

The objective of this paper to describe the reservoir well system and determine some reservoir properties for the given well by using different methods, these methods are the conventional method (Horner & MDH), derivative method. MS Excel sheet and PT4.0 program were used to evaluate this well. The analysis was used for one well in a Libyan field. The pressure of buildup data is shown in Figure 2. Properties of the well and formation are given in Table 1

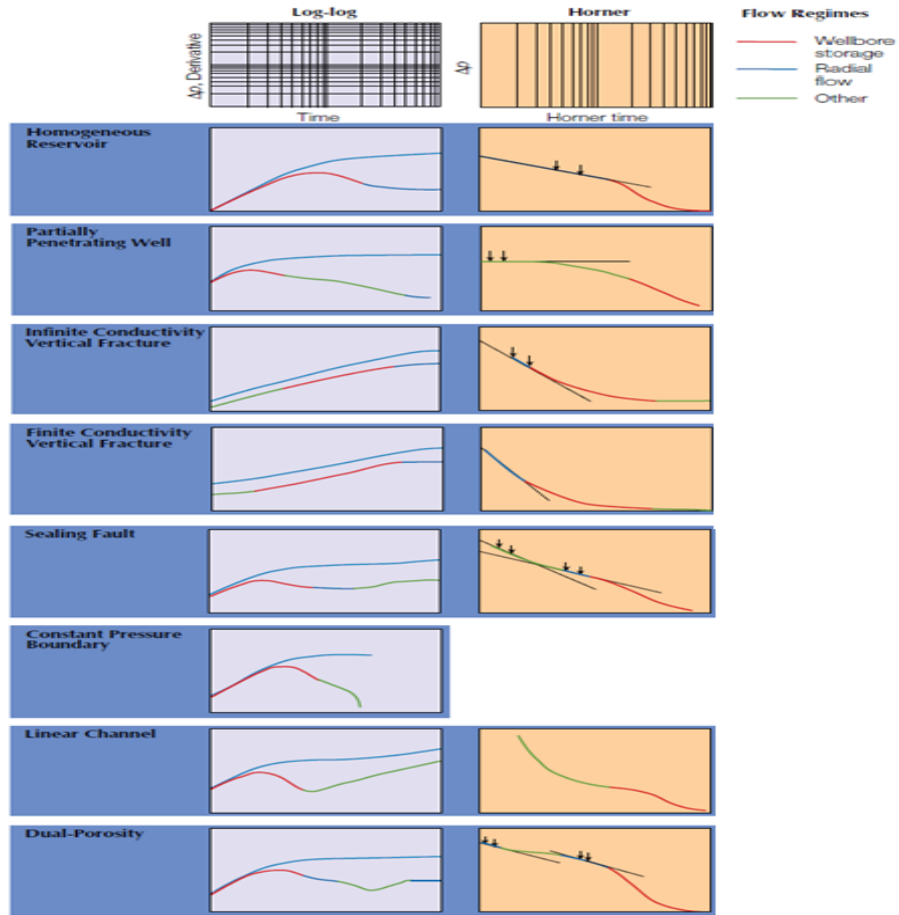


Figure 1: Log-log and semi-log plots for common reservoir systems.

Table 1: Properties of the well and formation

Property	Value
q_o (STB/D)	3540
Φ (fraction)	0.171
μ_o (cp)	0.75
C_r (psi ⁻¹)	1.27E-05
r_w (ft)	0.354
h (ft)	45.75
B_o (RB/STB)	1.3
P_{wf} (psia)	3346.50
t_p (hours)	12.5

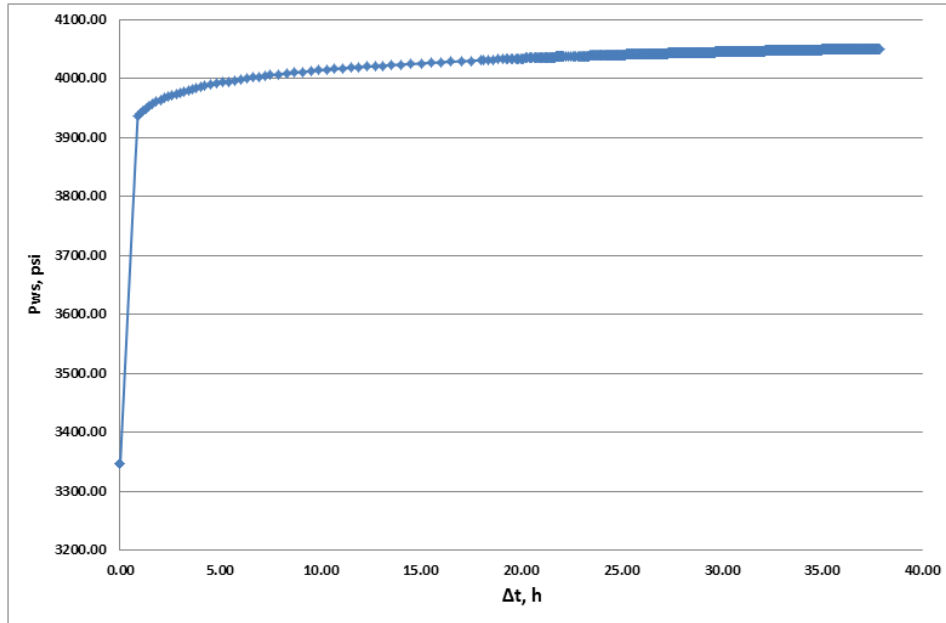


Figure 2: *Pressure buildup of the well*

2 Theories of Methods Used

2.1 Horner Method

Combining the law of conservation of mass and Darcy's law for the isothermal radial flow of fluid of small and constant compressibility toward a well in a circular reservoir, results a partial differential equation which called the Diffusivity Equation [3].

$$\frac{d^2 P}{dr^2} + \frac{1}{r} \frac{dp}{dr} = \frac{\phi \mu C_i}{0.000264k} \frac{dp}{dt} \tag{1}$$

Assuming that:

1. A well produce at a constant rate,
2. The reservoir is at uniform pressure, P_i , before production begins, and
3. The well drains an infinite area.

Solution of Eq.(1) is:

$$P = P_i + 70.6 \frac{q\beta\mu}{kh} E_i \left(\frac{-948\phi\mu C_i r^2}{kt} \right) \tag{2}$$

Where:

B = Formation volume factor, res vol./surface vol

C_t = Total compressibility, psi^{-1}

E_i = Exponential wellbore storage coefficient

h = Net formation thickness, ft.

k = Reservoir rock permeability, md

P = Reservoir pressure, psi.

P_i = Initial reservoir pressure, psi.

q = Flow rate, STB/D

r = Distance from center of wellbore, ft

t = Elapsed time, h

μ = Viscosity, cp.

\emptyset = Porosity of reservoir rock, dimensionless.

$$E_i(-x) = -\int_x^{\infty} \frac{e^{-u}}{u} du = \text{the Ei function or exponential I}$$

For $x < 0.02$, $E_i(-x)$ can be approximated with an error less than 0.6% by $Ei(-x) = \ln(1.781x)$

For $r = r_w$ the argument of the Ei function is sufficiently small after a short time that we can use the logarithmic approximation, thus, the is:

$$P_i - P_{wf} = -70.6 \frac{q\beta\mu}{kh} \left[\ln \left(\frac{1688 \phi \mu C_i r_w^2}{kt} \right) \right] \quad (3)$$

It is convenient to define a skin factor, S , in term of the properties of the equivalent altered zone:

$$S = \left(\frac{k}{k_s} - 1 \right) \ln \left(\frac{r_s}{r_w} \right) \quad (4)$$

Where:

k_s = Permeability of altered zone, md

r_s = Radius of altered zone (skin effect), ft

r_w = Wellbore radius, ft

S = Skin factor, dimensionless.

For buildup test using principle of the superposition for well has produced for time t_p at flow rate (q) before shut-in, and if we call time elapsed since shut-in Δt , the pressure drop can be modeled by Eq 5.

$$P_i - P_{ws} = -70.6 \frac{q\beta\mu}{kh} \left[\ln \left(\frac{1688\phi\mu C_t r_w^2}{k(t_p + \Delta t)} \right) - 2s \right] - 70.6 \frac{(-q)\beta\mu}{kh} \left[\ln \left(\frac{1688\phi\mu C_t r_w^2}{k\Delta t} \right) - 2s \right] \quad (5)$$

Where:

t_p : Cumulative production/most recent production rate=pseudo producing rate, h

Δt : Time elapsed since shut-in, h.

and become:

$$P_{ws} = P_i + 70.6 \frac{q\beta\mu}{kh} \ln \left[\left(\frac{t_p + \Delta t}{\Delta t} \right) \right] \quad (6a)$$

or

$$P_{ws} = P_i + 162.6 \frac{q\beta\mu}{kh} \log \left[\left(\frac{t_p + \Delta t}{\Delta t} \right) \right] \quad (6b)$$

The form of Eq 6b suggests that shut-in BHP, P_{ws} recorded during a pressure build up test should plot as straight line function of $\log [(t_p+\Delta t)/\Delta t]$. Further, the slope of (m) of this

straight line should be: $m = -162.6 \frac{q\beta\mu}{kh}$

It is convenient to use a positive number of (m) as following Equation.

$$m = 162.6 \frac{q\beta\mu}{kh} \quad (7)$$

Eq 8 uses to calculate formation permeability, k , which can be determined from a buildup test by measuring the slope m . in addition, the extrapolation of straight line to infinite shut-in

time $\left(\frac{t_p + \Delta t}{\Delta t} \right) = 1$ the pressure at this time will be original formation pressure, P_i .

$$k = 162.6 \frac{q\beta\mu}{mh} \quad (8)$$

The skin factor is obtained from Eq 9.

$$s = 1.151 \left[\left(\frac{P_{1hr} - P_{wf}}{m} \right) - \log \left(\frac{k}{\phi\mu C_t r_w^2} \right) + 3.23 \right] \quad (9)$$

Where:

P_{wf} = Flowing BHP, psi

P_{1hr} = Pressure at 1-hour shut-in time on middle time-line, psi.

2.2 Derivative method.

Five-point method was used to estimate the derivative pressure as shown in Figure 3. The following procedure used to identify the flow regimes in this study:

- Plot pressure derivative versus time on log-log plot (Diagnostic Plot).
- Identify the end of wellbore storage from unit slope line.
- Identify middle time region when zero slope straight line appears.
- Identify the late time region if there is boundary effects.

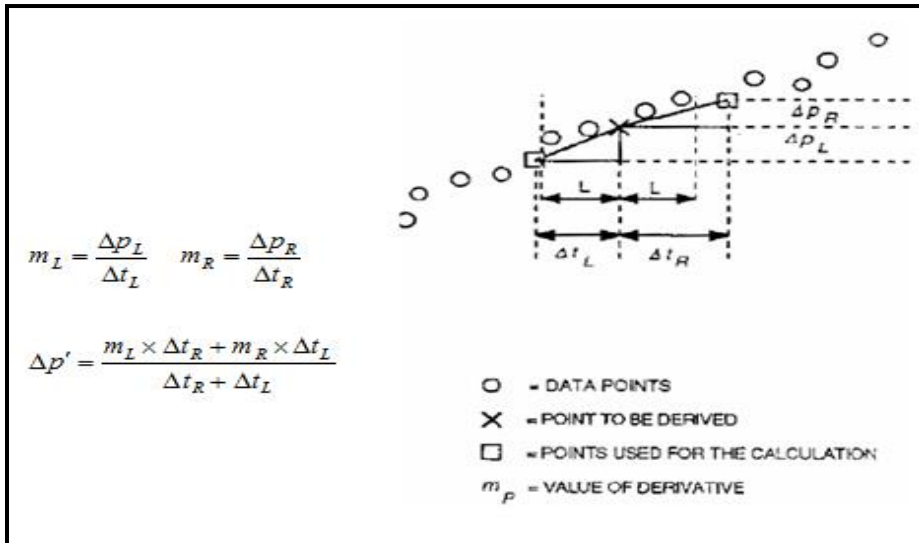


Figure 3: *Five-point method for calculating the pressure derivative* [4]

2.2.1 Determination of the pressure Derivative by MS Excel:

- 1- Plot Δp vs Δt on the log-log paper and then plot $\Delta p'$ vs Δt in the same graph, where can be calculated $\Delta P'$ from these equations:

$$m_L = \frac{\Delta p_L}{\Delta t_L} \tag{10}$$

$$m_R = \frac{\Delta p_R}{\Delta t_R} \tag{11}$$

$$\Delta p' = \frac{m_L \Delta t_R + m_R \Delta t_L}{\Delta t_R + \Delta t_L} \times \Delta t \tag{12}$$

Where:

m_L = Value of derivative in pressure derivative smoothing algorithm in left side, psi/h.

m_R = Value of derivative in pressure derivative smoothing algorithm in right side, psi/h.

$\Delta p'$ = Pressure derivative, psi/h.

Δp_L = Additional pressure change owing to presence of no flow boundary in left side, psi.

Δp_R = Pressure change in pressure derivative smoothing algorithm in right side, psi.

Δt_L = Time change in pressure derivative smoothing algorithm in left side, h.

Δt_R = Time change in pressure derivative smoothing algorithm in right side, h.

2- Estimate the formation permeability (k), skin factor (S) using the following relationship:

$$k = \frac{70.65 q \mu B}{m h} \tag{13}$$

$$S = 1.151 \left(\frac{(\Delta P)_s}{2.303 m'} - \text{Log} \left(\frac{K (\Delta t)_s}{\phi \mu C_t r_w^2} \right) + 3.227 \right) \tag{14}$$

Where:

$(\Delta p)_s$ = Pressure change coordinate during the infinite acting period, psi

$(\Delta t)_s$ = Time coordinate of a point during the infinite acting period, h.

2.3 Pressure Transient Software (PT4.0)

PT4.0 is one of the programs which used to analysis data that are obtained from drawdown and build-up tests. PT4.0 (Pressure transient (version.4)) is a full-featured system for evaluating pressure transient well tests. Using a standard Windows user interface, it implements most classical and log-log type curve methods, as well as an advanced "Adjust and Compare" technique to interactively interpret test data.

3 Calculations and Results

To illustrate the procedure, it is shown here the analysis of data of well. by using MS Excel sheet and PT4.0 software. Figure 3 shows plot of Δp ($P_{ws}-P_{wf}$) versus Δt on log-log plot, Figure 4 represents Horner semilog plot. The best straight line of first slope was found as shown in Figure 5. Figure 6 shows Horner semilog plot by using PT4.0 software MS Excel sheet was used to plot the derivative curve on log-log plot with the plot of ($P_{ws}-P_{wf}$) versus Δt as shown in Figure 7. Figure 8 shows the plotting of Derivative curve by using PT4.0 software. Permeability of the formation and the skin factor were calculated as was described in previous sections. Results of analysis data of well are shown in Table 2.

Table 2: Results of analyzing data of the well

Property	Excel Sheet		PT4.0 Program	
	Horner	Derivative	Horner	Derivative
P* (psi)	4041	-	4043.8	-
m (psi/cycle)	90.486	-	92.68	-
K (md)	135.568	171.93	132.321	109.13
Kh, (md.ft)	6202.24	7865.8	6053.68	4993
S	1.138	3.055	0.96997	-0.308

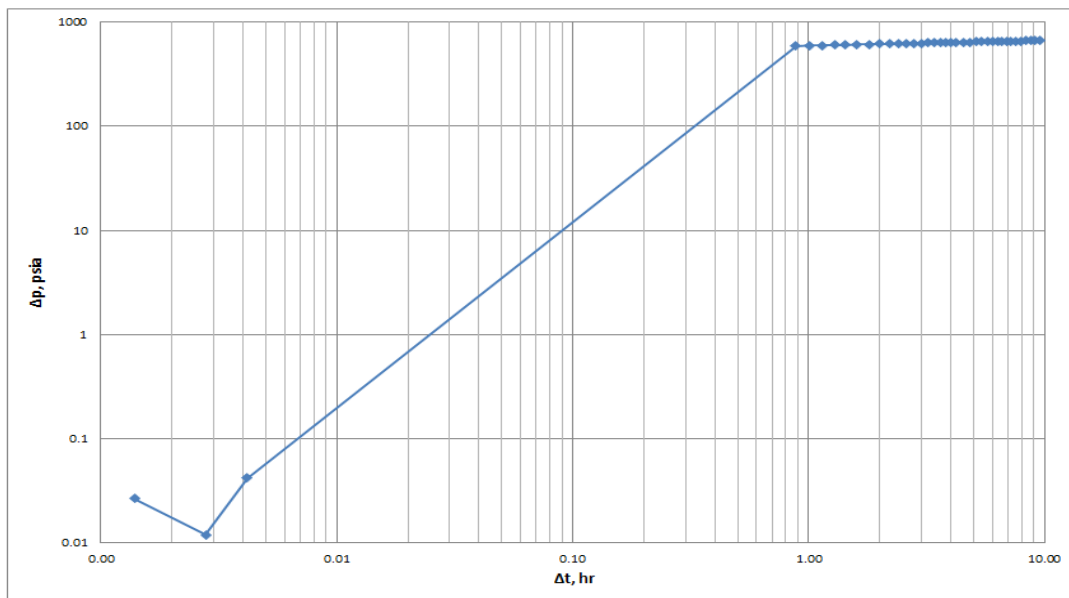


Figure 3: Δp ($P_{ws}-P_{wf}$) versus Δt on log-log plot

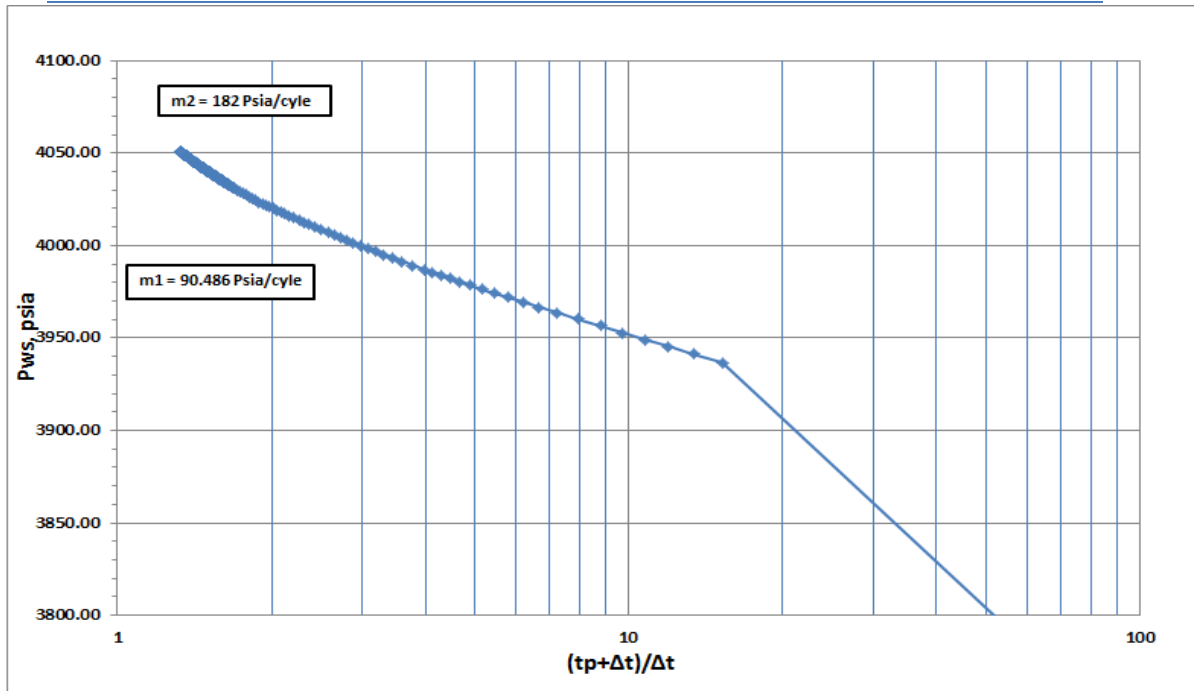


Figure 4: Horner plot of the well by using MS Excel software

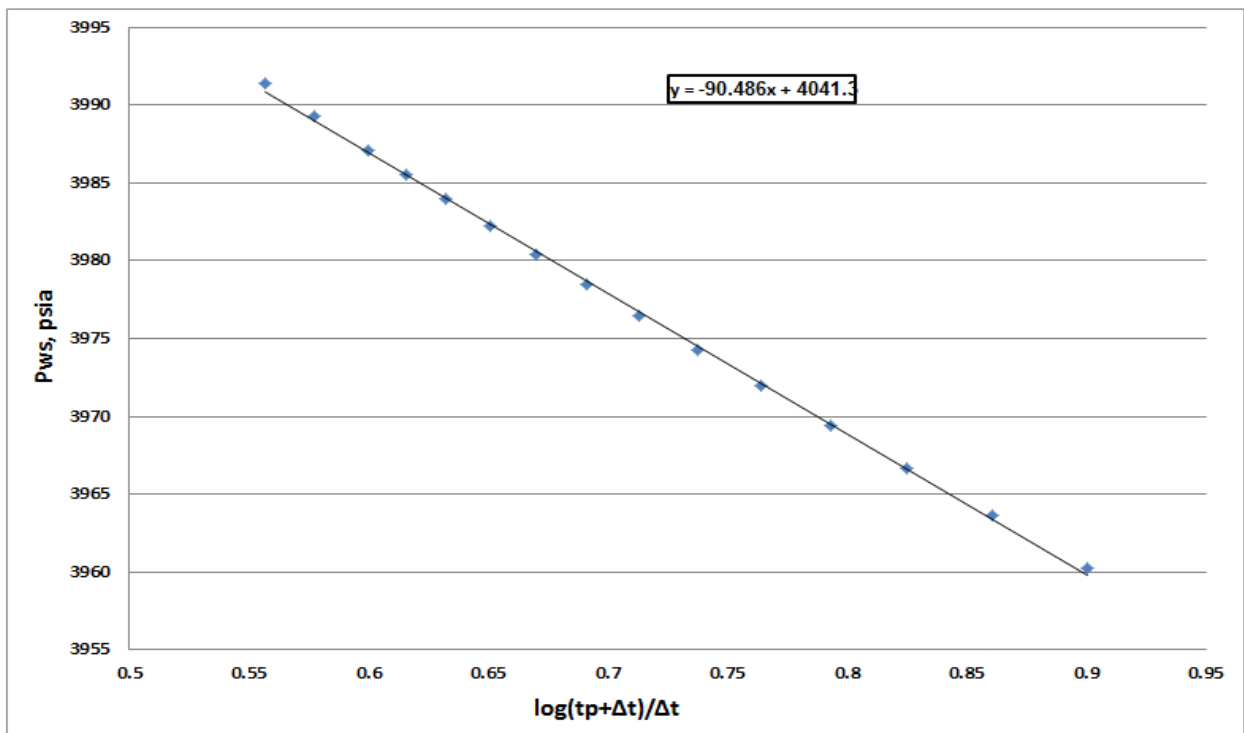


Figure 5: MTR straight line of Horner Plot

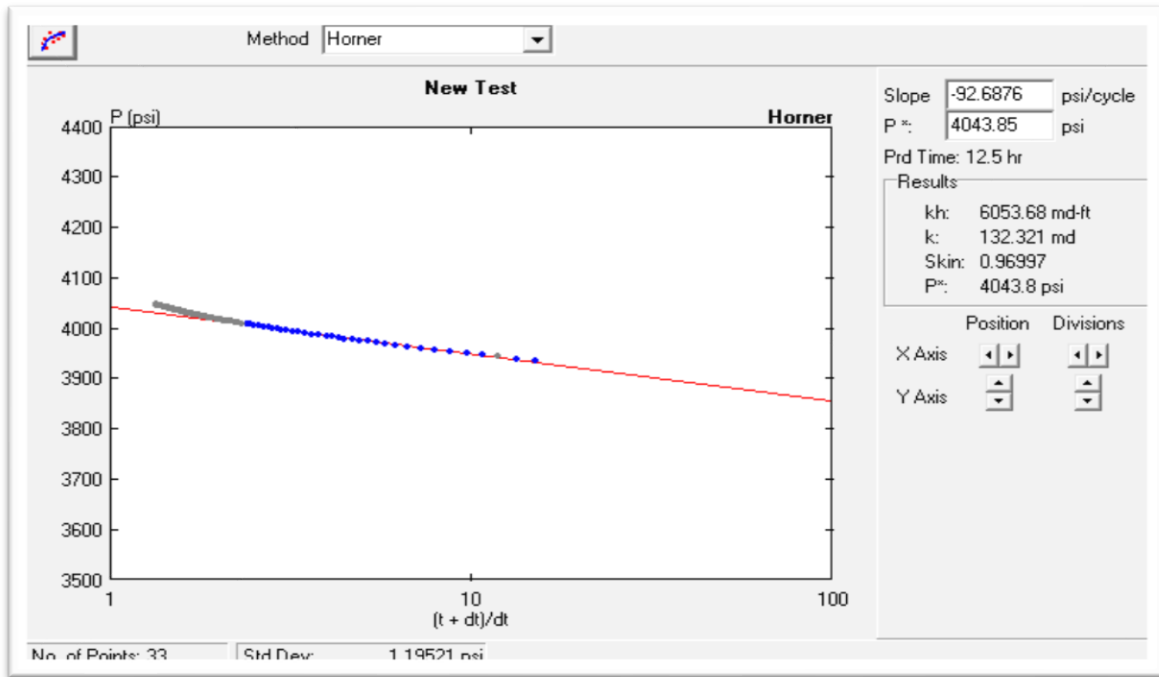


Figure 6: Horner plot for the well by using (PT4.0) software.

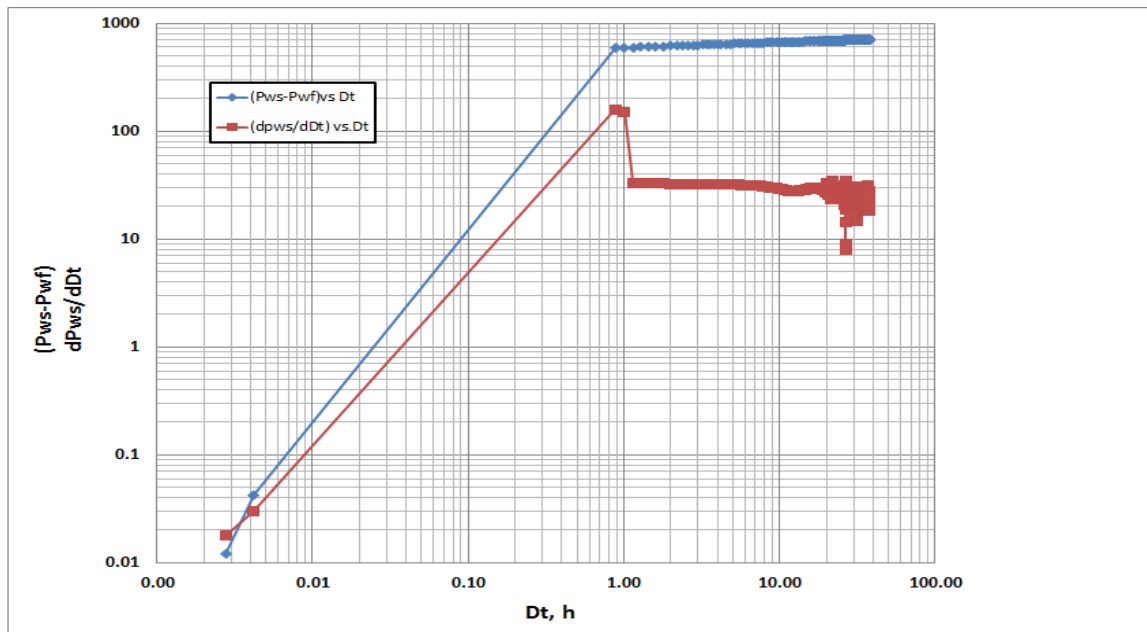


Figure 7: Derivative plot of the well by using MS Excel software

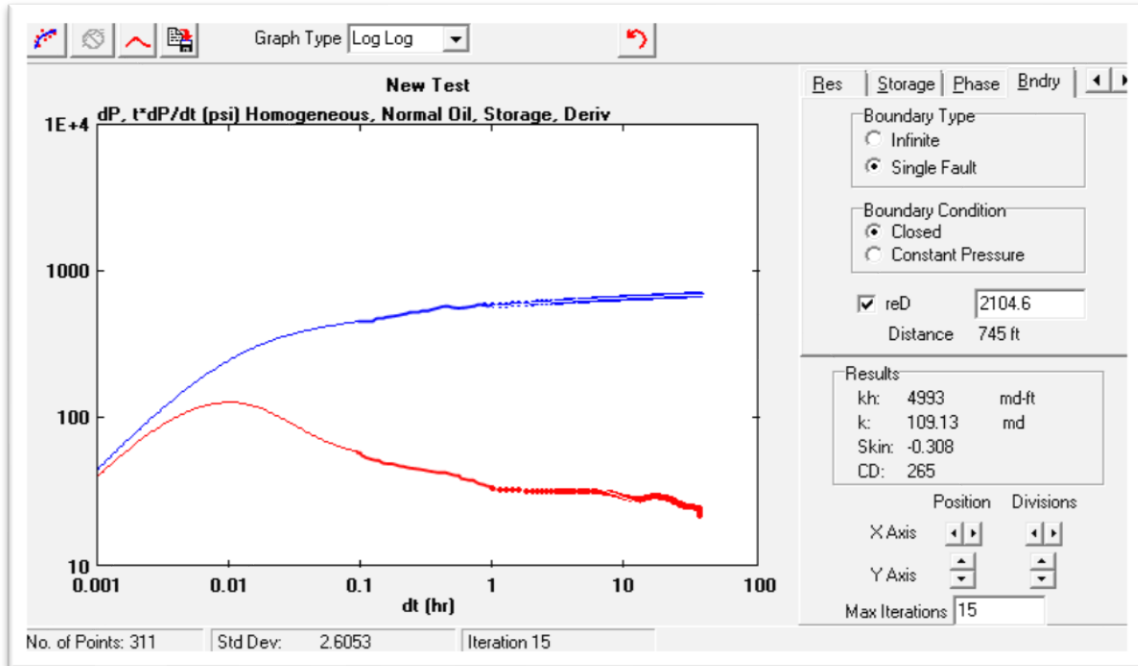


Figure 8: Derivative plot for the well by using (PT4.0) software.

4 Discussion

The paper presents a two programs that used to evaluate the pressure build up test for the well from Libyan field. MS Excel sheet and PT4.0 software were using to characterize the well, as well as estimation of formation permeability, skin factor and reservoir pressure. As shown for studied case, using of the pressure Horner curve was principle to identify the MTR of the test and to characterize the condition at the reservoir boundary. The Horner plots for both programs in Figure 4 and Figure 6 show that sealing fault has appeared by two slopes. Otherwise, the derivative curve was also used to identify the MTR and to evaluate the reservoir condition and the sealing fault has not appeared clearly because the period of buildup test (37hrs) was small as shown in Figure 7 and 8. Table 2 shows the results of Horner and derivative methods by using both programs MS Excel and PT4.0 software. As the results, formation permeability by both programs are agree to each other and reservoir pressure as well. The skin factor of the well indicates that the zone around the well has small damage by using Horner plot for both programs while derivative plot gives positive value of skin factor

by using MS Excel and negative value by using PT4.0 software. According to the results of the studied case which indicate that Horner method is the more accurate than derivative methods.

5 Conclusion

This paper presents a simple procedure to analyze the pressure buildup test using MS Excel and PT4.0 software. Sealing fault was appeared clearly in Horner plot by two slopes whereas derivative plot, the second slope was not presented clearly. Horner plot of MS Excel software gives appreciate results to PT4.0. whereas the derivative method gives not that much different results between both of programs. Results of the studied case indicates that Horner method is more accurate than method of direct derivative method. For the future, hopefully, there will be more cooperation between oil and gas governmental/international companies and PE in Sirte University, therefore to provide us the commercial petroleum simulators to develop models according to field data which help us to increase the knowledge of academic research and develop the student in academic and field study. Hence, using directly the modern programs in well testing will save time and provides reliable parameter values.

References:

- [1] D. Bourdet, T. M. Whittle, A A Douglas, and Y. M. Pirard: "A new Set of Type Curves Simplifies Well Test Analysis," *World Oil, May 1983, pp95*
- [2] R. C . Earlougher, "Advances in Well Test Analysis," *Society of Petroleum Engineers, Dallas, TX, 1977.*
- [3] D. R. Horner, "Pressure Buildup in Wells" *Proceedings of Third World Petroleum Congress, E. J. Brill, Leiden, November 1951, p503.*
- [4] J. Lee, and R. A. Wattenbarger, "Gas Reservoir Engineering", *SPE Textbook Series vol. 5, TX:., (1996).*

Evaluation of Corrosion Resistance of Mild Steel and Aluminium Using Anodic Inhibitor Method and Passivity

Ali Ramadan Elkais* and Dr Mohamed K Zambri

^{1,2} Department of Chemical and Petroleum Engineering, Faculty of Engineering, El-Mergib University, Libya

DOI: <https://doi.org/10.21467/proceedings.2.37>

* Corresponding author email: elkaisali@gmail.com

ABSTRACT

Mild steel and Aluminium considered from the metals that commonly used in engineering applications with a high proportion of up to 85%. On the other hand, due to the weakness of its resistance to corrosion environments different methods of corrosion protection are required to increase the resistance level particularly in the marine and acidic environments, where this give the significance of this study to be presented. **This** research involves studying the effect of some different corrosion resistance of mild steel and Aluminium by applying anodic inhibitor of mild steel (Sodium Dichromate and Potassium dichromate) in sea water environment and Aluminium by using passive film of Al_2O_3 in acidic environment (Hydrochloric acid HCL and Nitric acid HNO_3). An experimental work has been done and evaluation of corrosion resistance have been measured from weight loss during different period of time.

Keywords: Corrosion, Corrosion environment, Mild steel, Aluminum, passivity, inhibitor, Anodic

1 Introduction

There are many protection methods and measures have been used and considered to prevent or control corrosion process of metals and using the inhibitors was one of these methods. The inhibitor substance has been defined as the substance which can be added to a corrosive environment to decrease the rate of corrosion can occur due to this environment [1 - 3]. Inhibitor sources can be extracts (organic) , chemical solutions (Inorganic), Fig (1) illustrates the classification of inhibitors. In addition, the mechanism of how these substances minimize the corrosion rate can be summarized as these substances form a very thin film on the metal surface in different ways that can affect directly on the environment's corrosivity rate [4]. Anodic inhibitors which also can be called "*passivation inhibitors*" that work on minimizing the anode reaction and gradually cause blocking the anode reaction and supporting occurring the natural reaction of passivation metal surface to produce a very thin layer (film) adsorbed on the metal surface and protecting it from corrosion [6].



© 2018 Copyright held by the author(s). Published by AIJR Publisher in Proceedings of First Conference for Engineering Sciences and Technology (CEST-2018), September 25-27, 2018, vol. 1.

This is an open access article under [Creative Commons Attribution-NonCommercial 4.0 International](https://creativecommons.org/licenses/by-nc/4.0/) (CC BY-NC 4.0) license, which permits any non-commercial use, distribution, adaptation, and reproduction in any medium, as long as the original work is properly cited. ISBN: 978-81-936820-5-0

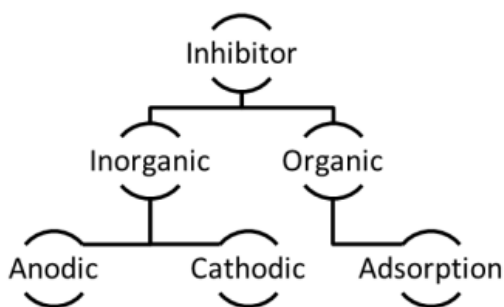
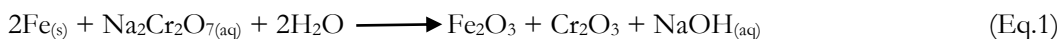


Figure (1): The classification of inhibitors [4]

2 Materials selection and Methods

In this work two metals were tested and different protection methods were applied on each of them. **The first** metal was Mild steel and chemical inhibitor was used to protect the metal from corrosion and sodium dichromate solution was used as coating material which historical been considered as very active inhibitor [5]. When the metal exposed to this chemical solution for a certain of time (in this work 48 hours) a very thin layer from iron oxide and chromium oxide was produced (Eq. 1) where this layer works to protect the mild steel surface from corrosion by isolating it from surrounding environment (sea water & atmosphere).



The second metal was Aluminium and has been protected experimentally also by an oxide layer produced on the metal surface in different way (*passivation inhibitor*). This experiment is to prove that not all environments can produce the protection layer even they are have the same classifications (e.g. acids). In this work an Aluminium bar was exposed to different environments (HCL & HNO₃) and an Aluminium oxide layer was produced from the reaction between the Nitric acid and aluminium surface to protect the metal from the corrosive environment.

3 Experimental work and results

3.1 Mild steel protection

In this experiment a sample of mild steel has been used to test the ability of a specific chemical inhibitor (Sodium dichromate Solution) to protect the metal surface from corrosion in two different environments (sea water & atmosphere). Sodium dichromate solution was prepared in two concentrations which are 0.1M and 0.5M and the following point were applied and considered:

- The sample of mild steel was polished, prepared, and weighted, W_1 (Fig. 2).

- Immerse the sample in sodium dichromate solutions (0.1M & 0.5M) for a period of time (1 – 3 days). Figure 3 shows the protection layer of chrome oxide.
- After 1 day remove the sample from solutions and record the total weight, W_2 .
- Calculate the weight of coating layer ($W_2 - W_1$).
- Immerse the coated sample in the corrosive environment (sea water) for 24 hours.
- Remove the sample from sea water and record the total weight, W_3 .
- Calculate the weight loss ($W_2 - W_3$).
- Repeat the above steps for the other period of time, environment and time of coating with recording the results for each case.



Figure 2: Prepared sample of mild steel.



Figure 3: Coated sample of mild steel

To make sure that the coating substance gives the aim that used to, the mild steel has been exposed to the same corrosive environment without applying the coating substance on the surface to produce the protection layer, Figure (4) shows the affected uncoated sample of mild steel before and after the sample exposed and immersed in sea water for 5 days . Figure (5) shows a coated sample of mild steel also before and after immersed in sea water for 5 days. The results obtained for different conditions are illustrated in tables 1 – 3:



Figure (4): Uncoated sample of mild steel immersed in sea water for 5 days



Figure (5): Coated sample of mild steel immersed in sea water for 5 days

Table (1): Corrosion of mild steel without protection

Samples	Weight of sample, gm	Time of exposure in sea water, hrs	Weight loss gm / cm ²
1	26.7253	24	0.00295
2	27.1127	48	0.03333
3	26.7285	72	0.03809
4	26.8365	96	0.04095

Table (2): Protection of mild steel by 0.1M sodium dichromate in sea water and air

Environment	Sample weight, gm	Coating layer, gm	Weight loss	Exposure time
Sea water	26.5045	0.0006	0.0005	24 hrs
Atmosphere	26.3992	0.0007	0.00045	7 days

Table (2): Protection of mild steel by 0.5M sodium dichromate in sea water and air

Environment	Sample weight, gm	Coating layer, gm	Weight loss	Exposure time
Sea water	26.0047	0.0031	0.0010	24 hrs
Atmosphere	25.8415	0.0016	0.0004	5 days

3.2 Aluminium protection (*Passivation*)

The Aluminum metal has been considered one of the metals that have the ability to form an oxide layer on the surface comes from the reaction between the environment and the metal surface and this layer works to protect the metal from corrosion [6]. Therefore, to evaluate this property for the Aluminum metal, an aluminum samples were immersed in acids solutions (10%v/v HCL and 10% v/v HNO₃). An oxide layer was formed from the reaction between the Aluminum and Nitric acid where this reaction occurs due to the availability of oxygen atoms in nitric acid. On the other hand, in case of HCL acid this oxide layer could not be formed due to the lake of oxygen in the reaction environment and a reaction of consuming the aluminum was occurred producing aluminum chloride and hydrogen gas (Eq. 2) and this later comes from consuming the electrons resulted from the aluminum to convert the hydrogen ion to hydrogen gas on the aluminum metal surface (Eq. 3). This was clear from monitoring the concentration of hydrogen ion in the reaction solution and the change in PH value. The results of this monitoring was recorded and presented in table 4. Figure (6) shows the different between two samples of Aluminum where the corroded one immersed in HCL and the protected one immersed in Nitric acid.



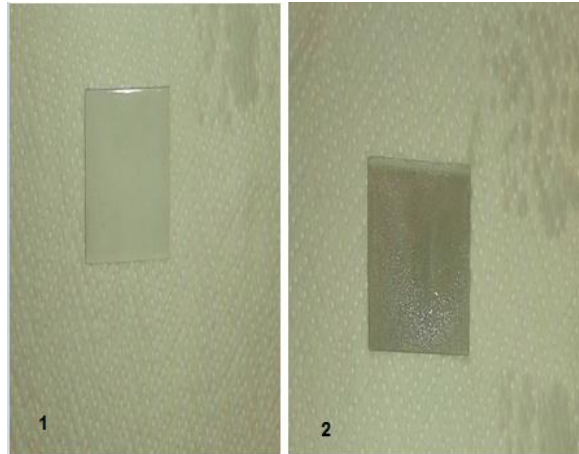


Figure 6: Aluminum sample (1) protected (HNO₃) Aluminum sample (2) corroded (HCL)

Table 4: Concentration monitoring of hydrogen ion and pH at 20 °C

Days	HCL, 10% v/v		HNO ₃ , 10% v/v	
	H ⁺ Conc. mv	pH	H ⁺ Conc. mv	pH
1	271	2.89	324	1.70
2	245	4.01	321	2.24
3	175	4.40	285	2.14
4	156	5.40	294	2.13
5	130	5.51	263	2.59
6	106	5.80	266	2.57
7	101	6.90	255	2.62
Weight loss in HCL acid solution = 0.9116 gm after 7 days				
Weight loss in Nitric acid solution = 0.1361 gm after 7 days				

In the table it was clear that the pH change with time due to the change in concentration of hydrogen ion in hydrochloric acid solution which comes from the passive layer of protection not formed. On the other hand, there was a slight change in the concentration of hydrogen ion in nitric acid because of the formation of protection passive layer. Figure 7 and Figure 8 prove that decreasing the concentration of hydrogen ion leads to increase the pH of HCL acid solution. In addition, there was a slight decrease in the concentration of hydrogen ion in nitric acid led to also a slight increase in pH because of the protection layer.

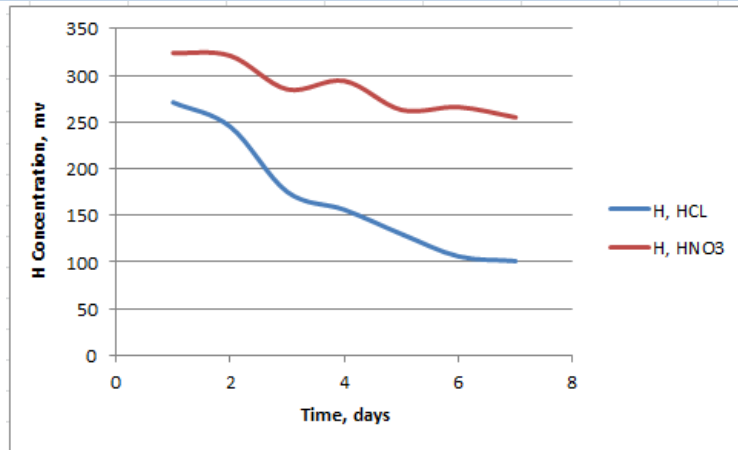


Figure 7: Monitoring of hydrogen ion concentration in HCL & HNO₃ solutions

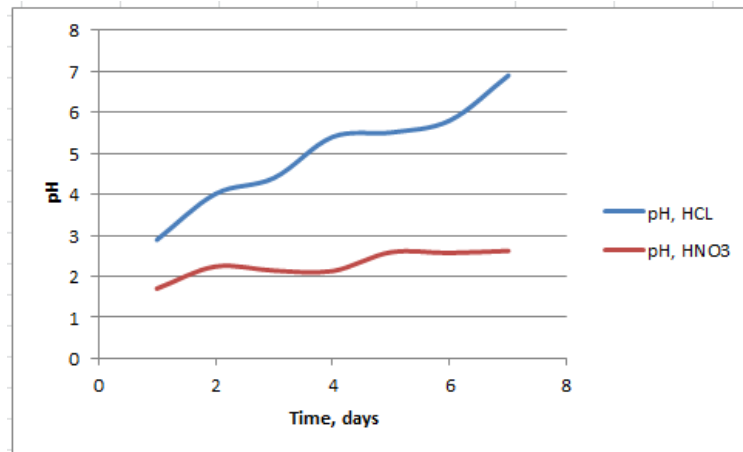


Figure 8: Monitoring of PH in HCL & HNO₃ solutions

4 Conclusions

The results obtained confirmed that the chemical solution of sodium dichromate can be successfully used as chemical inhibitor to protect the mild steel in sea water and atmosphere. Moreover, the most important result achieved in this work that the passive film (protection layer) cannot be formed for all metals and corrosive environments because of the dependency on the reaction between the metal surface and environment.

5 Acknowledgment

The authors are thankful to the Chemical & petroleum Engineering Department, Engineering Faculty, El-Mergib University, Khums Libya, for providing laboratory facilities to complete the research.

References

- [1] P. R. Roberge, "Handbook of Corrosion Engineering", *New York: Mc Graw Hill Hand-Book*, 1999

-
- [2] Edrah S., Elkais A., Zambri M. (2016) Anticorrosion of Mild Steel in Sea Water at different temperatures by using green inhibitors "Posidonia oceanica" "*1st International Conference on Chemical, Petroleum, and Gas Engineering*" at Al-Mergib University, Faculty of Engineering, department of Chemical and petroleum engineering 20 -22 / 2016.
- [3] Taleb H. Ibrahim and Mohamed Abou Zour " Corrosion Inhibition of Mild Steel using Fig Leaves Extract in Hydrochloric Acid Solution" *Int. J. Electrochem. Sci.* 6 (2011) 6442 – 6455.
- [4] Camila G. Dariva and Alexandre F. "Corrosion Inhibitors – Principles, Mechanisms and Applications", *Journal of INTECH (Open Science / Open minds)*, 2014, Access online on 01/04/2018 at <http://dx.doi.org/10.5772/57255>.
- [5] B. E. Roethell, and G. L. Cox, "Prevention of Corrosion of Metals by Sodium Dichromate as Affected by Salt Concentrations and Temperature" *Industrial & Engineering Chemistry*", 1931, 23 (10), pp 1084–1090
- [6] Firas F. Sayyid, Ali M. Ali, and Wadhah A. Tawfek, " Evaluation of Corrosion Resistance of Medium Carbon Steel using different Protection Methods" *Journal of Engineering and Technology*, 2012, Vol 30, Issue 7

Optimum Deposition of Tungsten Oxide on Titania Nanotubular Arrays and Study the Photoactivity of Nano-Composite Photoanode

Asma Mustafa Husin Milad^{1*}, Soud Saad Awitil², Mohammad B. Kassim³, Wan Ramli Wan Daud⁴

^{1,2} Department of Chemical & Petroleum Engineering, College of Engineering, Elmergib University, Libya

³ School of Chemical Sciences and Food Technology, Faculty of Science and Technology, UKM, Bangi, Malaysia

⁴ Department of Chemical & Process Engineering, Faculty of Engineering & Built Environment, UKM, Bangi, Malaysia

DOI: <https://doi.org/10.21467/proceedings.2.38>

* Corresponding author email: asma.aga2009@gmail.com

ABSTRACT

The novelty of this research works in the two-step formation of tungsten oxide (WO₃)-loaded TiO₂ nanotube arrays composite film by study the optimum conditions of electrodeposition of WO₃ nanoparticles on TiO₂ nanotubes arrays based on their photo-activity performance. The W have been incorporated from a sodium tungstate-based aqueous electrolyte containing from 0.2 M sodium tungstate (Na₂WO₄) with addition of 0.13 M hydrogen peroxide (30%) and drops from H₂SO₄ up to get pH = 1; it accumulates to form a self independent structure of WO₃ on the surface of the nanotubes. WO₃ was deposited for several times intervals at room temperature and annealed at 350 °C for 30 minutes. TiO₂ nanotubes (TNTA) were successfully grown by anodizing of titanium foil (Ti) in organic (98% vol., ethylene glycol, 2 vol.% Di water and 0.5 wt% ammonium fluoride and acidic (0.5M phosphoric acid and 0.14M sodium fluoride) electrolyte. The possible growth of TiO₂ nanotubes in the applied potential at 20V for 45 minutes was investigated. It were found such electrochemical condition resulted in formation of nanotube with average diameter 50 & 120 nm and the length 3.5 & 0.6 μm for organic and acidic electrolytes respectively. The anodized samples were annealed at 500 °C in N₂ gas for 3 hours. The structural, morphology and composition of TiO₂ nanotubes and WO₃/TiO₂ nanotube were characterized with XRD, FESEM and EDX. FESEM results of the nanotubular arrays showed uniform arrays of titania nanotubular and showed. EDX results showed trace of tungsten has been incorporated into TiO₂. The influences of tungsten content on the photocurrent densities of WO₃/TiO₂ nanotubular photoanodes were investigated by recording current-potential profiles. The preliminary results indicated that the WO₃/TiO₂ produced showed good photocurrent densities due to the behavior of W⁶⁺ ions which allows to electron traps that suppress electron-hole recombination and exploit the lower band gap of material to produce a water splitting process by increasing the charge separation and extending the energy range of photo-excitation for the system.

Keywords: Titanium oxide nanotubular arrays (TNT), Anodization, tungsten oxide (WO₃), electrodeposition, photoelectrochemical measurements.



© 2018 Copyright held by the author(s). Published by AIJR Publisher in Proceedings of First Conference for Engineering Sciences and Technology (CEST-2018), September 25-27, 2018, vol. 1.

This is an open access article under [Creative Commons Attribution-NonCommercial 4.0 International](https://creativecommons.org/licenses/by-nc/4.0/) (CC BY-NC 4.0) license, which permits any non-commercial use, distribution, adaptation, and reproduction in any medium, as long as the original work is properly cited. ISBN: 978-81-936820-5-0

1 Introduction

Hydrogen is an attractive alternative source of energy because it is renewable if collected through the splitting of water, burns cleanly (producing only H₂O), and could deliver energy in the same method as fossil fuels, via combustion or electricity through the use of fuel cells. Generated hydrogen through the splitting of water is a very desirable alternative fuel for the following reasons: sunlight is a plentiful and renewable energy source [1]; the hydrogen generating device has no moving parts, therefore maintenance is minimal; and the associated infrastructure is simple [2]. Photoelectrochemical reaction for water splitting is a process in which water is split into hydrogen (H₂) and oxygen (O₂) on the surface of a specific type of photoactive material, namely titania (TiO₂) semiconductor [3, 4]. The photocatalytic splitting of water using oxide semiconductors is initiated by the direct absorption of a photon, which creates separated electrons and holes in the energy band gap of the material [5]. During the past few decades, significant efforts have been made to search for a low cost and efficient photoelectrochemical cell (PEC). An ideal PEC cell needs to have an optimum band gap with the right band positions for both its CB and VB. In addition, it needs to be readily available, non-toxic and stable in an aqueous solution. Moreover, this material has to have a high absorption and good photon-to-electron conversion efficiency. So far, no single material has been found that meets all the criteria above for a cheap and efficient PEC cell. Most of the existing materials suffer from either stability issues or low photon-to-electron conversion efficiency. TiO₂ has high band gap level which has a potential for water splitting under UV-light, but it cannot absorb visible light and hence, suffer from low light absorption efficiency. An anatase TiO₂ shows fewer recombination reactions due to the indirect band gap and hence, produces better photocatalytic activity compared to rutile that has a direct band gap. Moreover, other oxide such as WO₃ has low band gap level of 2.2-2.8 eV [6] has good absorbance in visible light but it has insufficient CB or VB edge for water reduction and oxidation; it can absorb the blue region of the solar spectrum up to ca. 500 nm. Recently, WO₃ was considered as a new photoanode material or mixture material with TiO₂ for water splitting because WO₃ can offer relatively small band gap and has high stability in an aqueous solution. Although WO₃ has shown great potential such as photo-oxidation of water with visible light and has high photocurrent levels with nanocrystals, the quantum yield is still low [7, 8]. In this work, strategies were centred on controlling the structure or the chemical composition of the TiO₂ nanotube arrays composite (TNNTA). The electrochemical anodization is the simplest method of fabricating TNNTA from a titanium foil. The 1-D nanostructures offer highly efficient charge transport channels longitudinally. Various efforts have been made to employ mixed WO₃/TiO₂ systems to enhance the efficiency of electrochromic effects in aqueous solution [9, 10]. Whereas, the enhancement of the photocatalytic performances of TiO₂ was possible since WO₃ can serve as an electron accepting species [11]. However, WO₃/TiO₂ or WO_x/TiO₂ were mainly prepared by different methods as physical mixing [12], multi-step

grafting of ammonium tungstate [13, 14], improved sol–gel method, co-precipitation [15], hydrothermal method [16] and electrodeposition [17], where WO_3 or WO_x only covered the surface of TiO_2 with low amounts in most situations. The ability of WO_x-TiO_2 to be excited by visible light and degrade the dyes were confirmed by several researchers, where Li et al. (2001) proven that the photoactivity of WO_x-TiO_2 was significantly higher than that of pure TiO_2 and an optimal content of WO_x in TiO_2 was found to be 3% for WO_x in TiO_2 was the highest rate of methylene blue (MB) photodegradation [18]. The most related researches about WO_3/TiO_2 were summarized in Table 1.

Table 1: Summary of previous researches about Tungsten trioxide on TNTA

	Synthesis Method	Significant Findings	Ref
$WO_3/TNTA$ nanocomposite	Electrochemical deposition	The maximum conversion efficiency of 0.87% was obtained for $WO_3/TNTA$ nano-composite. H_2 and O_2 gases were collected during the photoreaction were had the volume ratio of 2.2:1 volume ratio.	[19]
W-Doped TNTA	A direct anodization	Showed that photocurrent densities of 3 wt% W-doped TNTA which were obtained were 0.25 mA/cm ² at 1 V bias, which is much higher than that of the undoped sample.	[20]
$WO_3/TNTA$ nanocomposite	A facile hydrothermal method	Exhibited enhanced photocatalytic activity toward Rhodamine B (RhB) degradation when compared with pure TNTA and P25. The optimum percentage of WO_3 decorated on TNTA for the improvement of photocatalytic properties is 5 wt. %.	[21]
WO_3-TNTA	A sol–gel template technique	Samples exhibited a strong photoresponse in the visible region and a low PL emission. High efficiency of 2,3-dichlorophenol degradation was obtained under visible light.	[22]
W doped TNTA	An anodization of Ti–W alloys	The content of 9 at% WO_3 in photoresponse experiments is most beneficial, in long term experiments a higher efficiency is observed for the 0.2 at% W content.. This demonstrates that under optimized WO_3 doping conditions a lasting visible light activation of TiO_2 nanotubes can be achieved.	[23]
W-TNTA	A radio-frequency (RF) sputtering	The effect of W on the photoelectrochemical properties of TNTA was due to W atoms which occupy the substitutional position within the vacancies of TNTA. Found the W-TNTA system plays important roles in efficient electron transfers due to the reduction in e^-/h^+ recombination.	[24]
WO_3-TNTA	A wet impregnation	A maximum photocurrent of 2.1 mA/cm ² with a photoconversion efficiency of 5.1% was obtained, which is approximately twice higher than that of pure TiO_2 nanotubes. The findings were mainly attributed to higher charge carrier separation, which minimized the recombination losses and enhanced the transportation of photo-induced electrons in this binary hybrid photoelectrode.	[25]
WO_3-TNTA	A wet impregnation	A low content of WO_3 species successfully diffused into the TiO_2 lattice and formed W–O–Ti bonds, which significantly promoted effective charge separation by trapping photo-induced electrons from TiO_2 . The photocurrent density, photoconversion efficiency, STH efficiency, and H_2 generation of the resultant hybrid nanotubes were increased.	[26]
WO_3-TNTA	A wet impregnation	In PEC studies, high-crystallinity anatase-phase WTNs exhibited a higher photocurrent density (2.4 mA/cm ²) than WTNs of amorphous or polycrystalline phases.	[27]
WO_3/TiO_2 heterojunction	Liquid phase deposition	TiO_2 film provides an excellent platform for WO_3 deposition. WO_3 expands the absorption band edge of TiO_2 film to visible light region. WO_3/TiO_2 heterojunction film shows high photoelectrocatalytic activity.	[28]
WO_3-loaded TiO_2 nanotube	Tungsten as the cathode	WO_3 -loaded TiO_2 nanotube arrays with the highest aspect ratio, geometric surface area factor and at% of tungsten exhibited the more favorable photocatalytic degradation of MO dye under UV light irradiation	[29]

As a result, the main focus of this work is to enhance the photocurrent density of TNTA and increased its ability to generate hydrogen by deposition of WO_3 nanoparticles and to form a highly efficient nanocomposite structure. As well, the optimum conditions of electrodeposition of WO_3 on TNTA to get the best photocurrent of TNTA semiconductors in PEC. A full investigation of the intrinsic material properties of the resulted samples was performed, which included crystallinity, morphology, and electronic absorption spectrum, by FESEM, X-ray diffraction (XRD) and UV-VIS diffuse reflectance. Finally the optimised photoelectrodes were investigation by measuring photocurrents enhancement via PEC measurements.

2 Materials and Methods

Short TiO_2 nanotubular array (STNTA) was prepared by anodizing a Ti-foil in **an acidic electrolyte** [30] containing 0.5M *ortho*-phosphoric acid and 0.14M sodium fluoride at pH 2 under constant stirring and the voltage profile. Similarly, a much longer titania nanotubes were synthesized in accordance with the procedures reported by [31]) which required the anodization of T-foil in an organic electrolyte consisting of ethylene glycol (EG) with 2% vol. DI water and 0.3 wt% of NH_4F at pH 5.9. The post-treatment process of the TNTA prepared above involved annealing, which is a vital step for the transformation of the amorphous state of titanium oxide into anatase crystals. Prior to annealing, the surface of the anodized samples was cleaned with deionized water to remove ionic residues, and the samples were dried under N_2 flow at 100 °C for 12 hr. The TNTA samples were loaded in to a muffle furnace in a ceramic boat and were annealed at 500 °C for 3 hr in N_2 flow. The temperature was increased at a rate of 5 °C/min. The synthetic procedures for making Tungsten Oxide/TNTA were improved from previously reported work through few modifications such as deposition bath compositions, calcination temperature and electrodes configurations as summarized in Table 2. However, Figure 1 shows the cyclic voltammetry scan of TNTA in deposition electrolyte, whereas, the cyclic voltammogram suggested that the electrodeposition potential of about -0.38 V which is similar to the reported potential for W(IV) reduction to W(0) [32].

Table 2 Electrodeposition and calcinations conditions of tungsten oxide on TNTA electrodes.

Electrodeposition Bath	Deposition Temperature	Electrodes Configuration	Calcination Conditions	Ref.
<ul style="list-style-type: none"> • 0.2M of Sodium tungstate (Na_2WO_4, 99%, Merck) • 0.13M of Hydrogen Peroxide Solution (H_2O_2, 30%, Sigma-Aldrich)₂ and • drops of Sulfuric acid (H_2SO_4, 70%, Merck) 	23-25 °C	Anode: Long-TNTA (LTNTA) & Short-TNTA (STNTA) Cathode:Pt Reference: Ag/AgCl	350 °C for 30 min in purified air	Krasnov and Kolbasov [33]

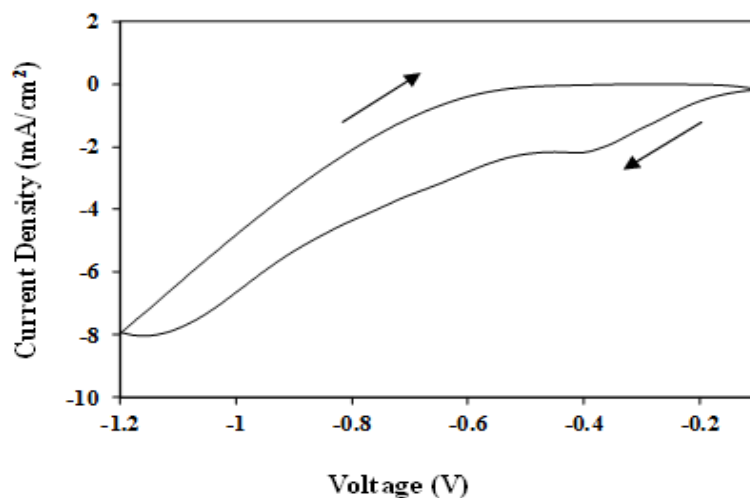


Figure 1: Cyclic voltammogram of TNTA electrode in 0.2M Na_2WO_4 , 0.13M H_2O_2 electrolyte.

The synthesized photoanodes were characterized by field emission scanning electron microscope (FESEM), energy dispersive X-ray (EDX), X-ray photoelectron spectrometer (XPS), X-ray diffraction (XRD) and ultraviolet and visible light (UV-VIS) spectroscopy. Photoelectrochemical data of the photoanodes were collected by using the in-house PEC system [34, 35] and the results were discussed in comparison with TNTA.

3 Results and Discussion

Figure 2 and Figure 3 show the morphology (FESEM top-view) of the STNTA and LTNTA with WO_3 deposit, respectively. It can be seen that TiO_2 tubes are covered with a very thin layer of WO_3 started to form and became much thicker as the deposition period became longer (Figure 2c and 3c). However, in most cases the surface area shows open and nicely decorated tubes with small individual WO_3 nanoparticles (diameter of ~ 5 nm) was visible for 5 minutes deposition period and became larger (agglomeration) as the deposition time getting longer until a thick layer was formed as shown in Figure 2e & f and 3f. The EDX result is represented and it clearly indicates that W is present (Table 3) in the particles.

Table 3: Elemental Composition of WO_3 /TNTA at different deposition periods.

Deposition Time (min)	Elemental content (Atomic %)							
	WO_3 /STNTA				WO_3 /LTNTA			
	Ti	O	C	W	Ti	O	C	W
1	35.38	64.57	-	0.04	41.69	51.08	7.13	0.11
5	37.96	61.88	-	0.16	37.07	59.09	3.61	0.23
10	38.69	61.05	-	0.26	28.89	57.02	13.82	0.28
15	57.41	42.19	-	0.40	26.55	55.32	17.68	0.45
30	51.26	47.73	-	1.01	30.72	59.61	9.01	0.66
45	32.60	60.58	-	6.823	26.45	65.04	5.77	2.74

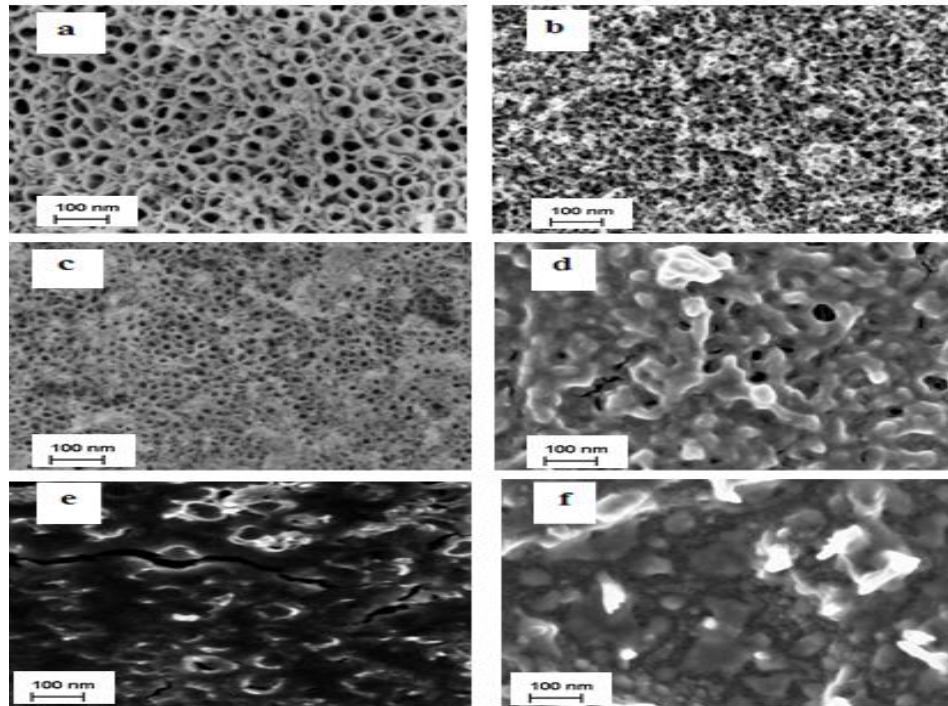


Figure 2: FESEM top view of WO₃/STNTA at variety deposition time: (a) 1, (b) 5, (c) 10, (d) 15, (e) 30, and (f) 45 minutes.

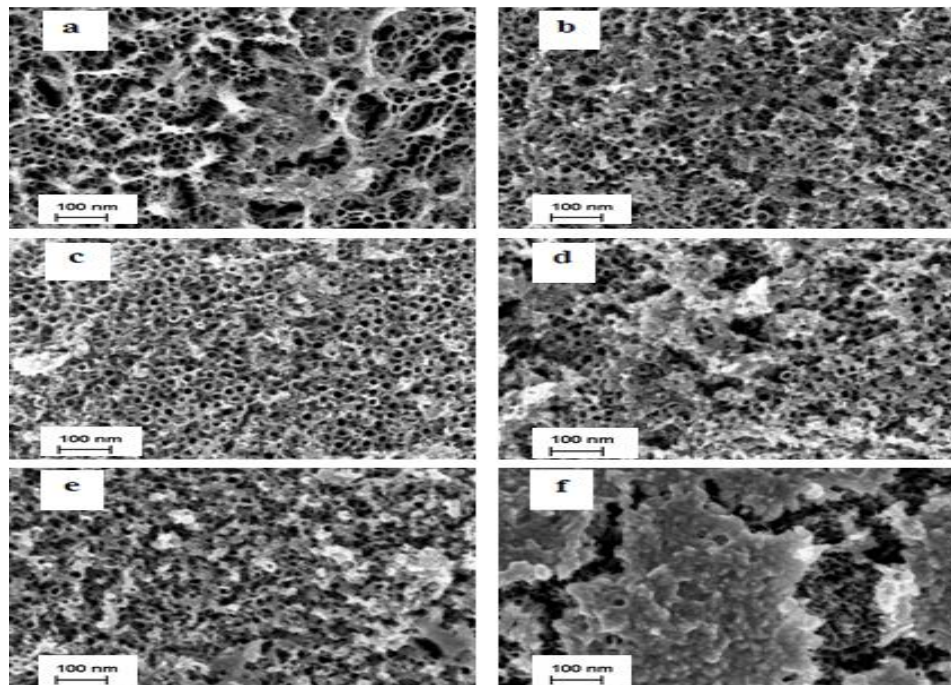


Figure 3: FESEM top view of WO₃/LTNTA at selection deposition time: (a) 1, (b) 5, (c) 10, (d) 15, (e) 30, and (f) 45 minutes.

For WO_3 -TNTA nanocomposite electrode, the content existences of deposited WO_3 nanoparticles on short and long TNTA were studied by XRD measurement. The XRD patterns for WO_3 -STNTA and WO_3 -LTNTA are depicted in Figure 4a & b, respectively. Previous investigations on bulk WO_3 have reported the following phase transformation sequence upon heating: triclinic (δ - WO_3) (-30°C) \rightarrow monoclinic (γ - WO_3) (330°C) \rightarrow orthorhombic (β - WO_3) (740°C) \rightarrow tetragonal (α - WO_3) [36]. In this work, the XRD patterns (Figure 4a & b) show diffraction signals for the monoclinic WO_3 under the conditions (JCPDS No.83-950), indicating a desirable crystallinity was formed in the nanocomposite sample after calcinations at 350°C [37]. As shown in Figure 4a & b, there was no new diffraction peak can be ascribed to the crystal phase of $\text{W}_x\text{Ti}_{1-x}\text{O}_2$ for the calcination temperatures used in this study which can be concluded that no reaction between oxides. The nanocomposite show sharp diffraction peaks at 34.0° (202), 49.0° (004), and 55.3° (024), for WO_3 /LTNTA's XRD spectrum which were similar to those detected by Lai and Sreekantan [25].

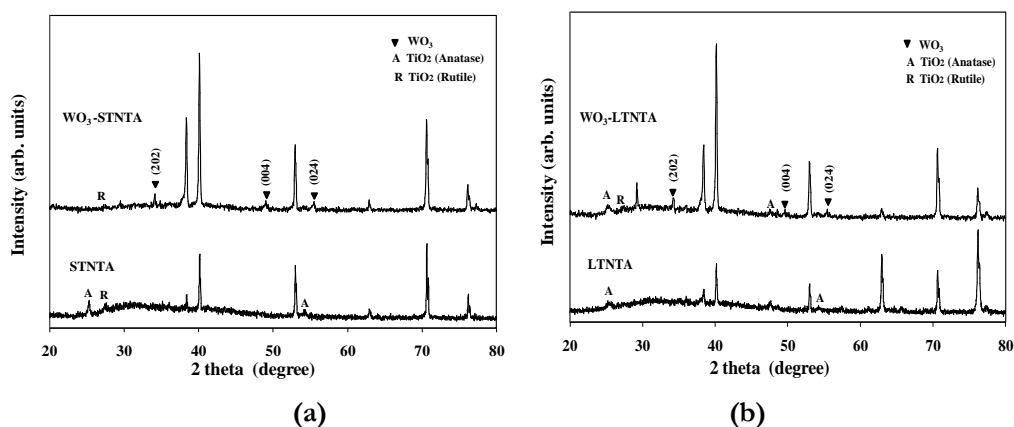


Figure 4: X-ray diffraction patterns of (a) WO_3 /STNTA and (b) WO_3 /LTNTA.

However, the peak at 30° was unknown. The XRD profiles of WO_3 /LTNTA became stronger and sharper than WO_3 /STNTA because most of the deposited WO_3 nanoparticles were formed on the surface of the LTNTA (due to smaller tube diameter) but the particles were deposited in the tubes and on the surface (due to big diameter) of the STNTA. The reflectance ($R\%$) of WO_3 /TNTA nanocomposites were measured using UV-VIS spectroscopy, and the reflectance spectra are shown in Figure 5. The transmittances were almost zero due to the Ti base. The intensity of the reflectance depends on the morphology and amount of metal oxide formed on the surface. Besides absorption by the deposited nanoparticles, the detected scattering of light was very weak due to the morphological structure of tubes which absorbs the scattering light. The fluctuation of reflectance was strong in 1- WO_3 /TNTA samples in the visible region (400 to 800 nm) for one min deposition period as shown in Figure 6. This is due to the small amount of WO_3 content. The WO_3 /TNAs with different WO_3 contents were used as photoelectrodes in PEC water-splitting cell for evaluation of their photocurrent densities production. The photocurrent density-voltage response was plotted under 100 W/m^2 illuminations. The corresponding experimental results are presented in Figure 6a & b for

WO_3/TNTA and WO_3/LTNTA respectively for different deposition periods. The maximum photocurrent densities of 0.3 and 0.37 mA/cm^2 were observed at 1 V vs. SCE in the 10- WO_3/STNTA and 15- WO_3/LTNTA with 0.16 and 0.45 at% of W content respectively, which is relatively higher compared with that of the pure STNTA and LTNTA (0.06 and 0.32 mA/cm^2 at 1 V vs. SCE, respectively). The WO_3/STNTA prepared by deposition for 1, 5, 15, 30 and 45 min exhibited decreased photocurrent densities of approximately 0.1, 0.18, 0.17, 0.14 and 0.12 mA/cm^2 at 1 V vs. SCE, respectively. It is noted that WO_3/LTNTA photoanodes which were deposited for 1, 5, 10, 30 and 45 min produced photocurrent densities about 0.19, 0.26, 0.33, 0.22 and 0.09 mA/cm^2 at 1 V vs. SCE, respectively. These results clearly showed the significant effects of different WO_3 contents in the TNTA on the PEC performances. The resultant photocurrent densities of WO_3/STNTA increased linearly as shown in Figure 6a. Moreover in Figure 6b, the photocurrent densities of WO_3/LTNTA at 1, 15 and 45 min deposition periods were mostly constant, and the other curves were increased slightly in logarithmic shape.

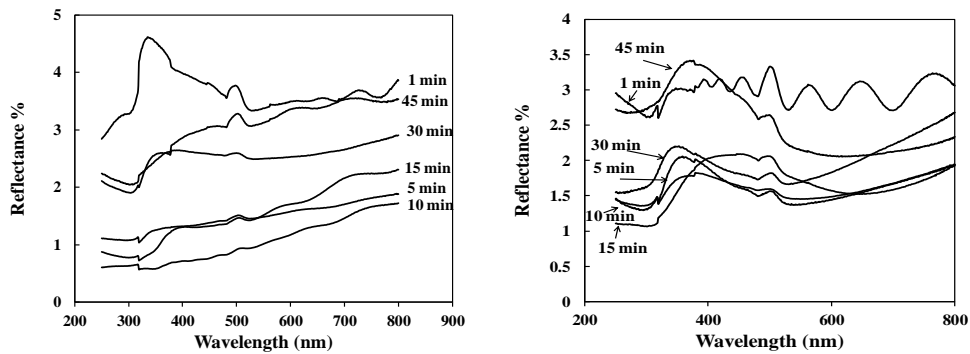


Figure 5: Reflectance spectra of WO_3/STNTA (left) and WO_3/LTNTA (right) at various deposition periods.

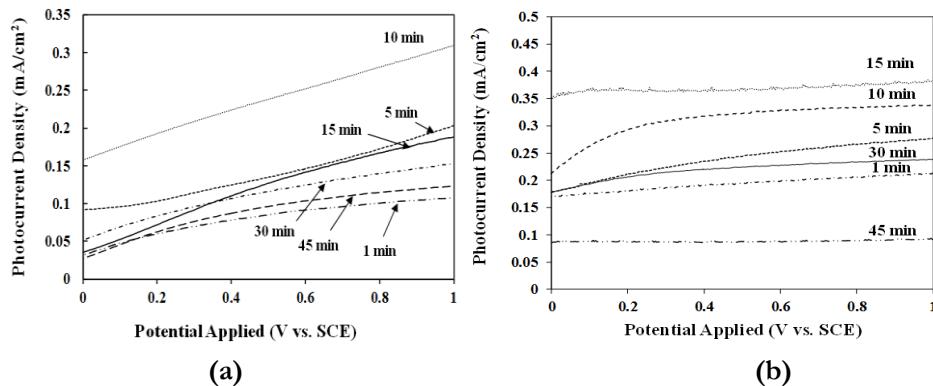


Figure 6: Photocurrent density as a function of measured potential (vs. SCE) for a) WO_3/STNTA and b) WO_3/LTNTA photoelectrodes deposited at different deposition period under light illumination.

Figure 7 was illustrated the predicted mechanism of electrons movement in WO_3/TNTA photoelectrodes. Composite WO_3 and TNTA materials have shown a favorable electron injection from the CB of TNTA to that of WO_3 and hole transfer between VBs in the opposite direction, which reduces e^-/h^+ recombination in both semiconductors. The CB of WO_3 is not negative enough for water reduction, some modifications are needed to achieve H_2 evolution. Also WO_3/TNTAs have a higher UV response compared to WO_3 materials. This is improvement could be attributed in part to better absorption and better transport due to the organized nanostructures. In addition, the electron transfer from TNTA to WO_3 results in a wide electron-hole separation, which could improve the IPCE values as well

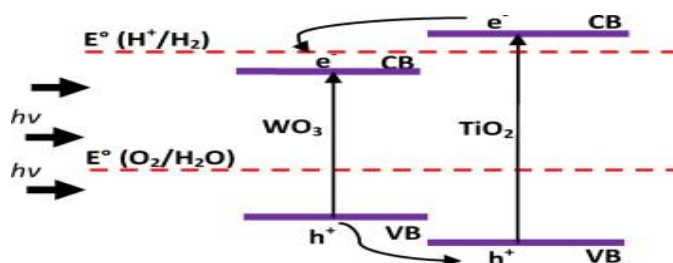


Figure 7: Schematic diagram showing the energy band position and the electron transfer direction for WO_3/TNTA nanocomposite electrode after being excited by light.

4 Conclusion

This work was focused on the synthesis, characterization, PEC testing of hetero-nanocomposite TNTA semiconductors with WO_3 nanoparticles. However, getting the best performance for the photoelectrochemical testings for electrodes were quite difficult since it was influenced by the stability and the ability of the electrodes to produce photocurrent. However, short and long TNTA synthesized by anodization of Ti-foil in two types of electrolytes (acidic and organic) lead to synthesis two different morphologies of TNTA. Subsequently, Metal oxides nanoparticles (WO_3) which has a small band gap were deposited on TNTA individually from sodium tungstate aqueous solution at room temperature. The morphologies of deposited WO_3 on TNTA varied depending on deposition periods and crystal type. Similarly, the content of WO_3 on TNTA increased upon electrodeposition period according to EDX results. Likewise, for WO_3/STNTA and WO_3/LTNTA the maximum photocurrent were 0.3 mA at 10 minutes and 0.37 mA at 15 minutes, respectively.

5 Acknowledgment

The authors express their sincere thanks to Universiti Kebangsaan Malaysia for allowing this work to use the UKM-GUP-BTT-07-30-190, UKM-OUP-TK-16-73/2010 and UKM-OUP-TK-16-73/2011 research grants. A.M.H. Milad thanks the Elmergib University.

References

- [1] M. Gratzel. "Photoelectrochemical cells". *Nature*, vol. 414, pp. 338-344. 2001

-
- [2] H. Wang and J. P. Lewis. "Second-generation photocatalytic materials: aniondoped TiO₂". *Journal of Physics: Condensed Matter*, vol. 18, pp. 421-434. 2006
- [3] A. Fujishima and K. Honda. "Electrochemical photolysis of water at a semiconductor electrode". *Nature*, vol. 238, pp. 37-38. 1972
- [4] O. Khaselev and J. A. Turner. "A monolithic photovoltaic-photoelectrochemical device for hydrogen production via water splitting". *Science*, vol. 280, pp. 425-427. 1998
- [5] A. J. Bard and M. A. Fox. "Artificial Photosynthesis: Solar Splitting of Water to Hydrogen and Oxygen". *Accounts of Chemical Research*, vol. 28, pp. 141-145. 1995
- [6] M. Spichiger-Ulmann and J. Augustynski. "Aging effects in n-type semiconducting WO₃ films". *Journal of Applied Physics*, vol. 54, pp. 6061-6064. 1983
- [7] W. Erbs; J. Desilvestro; E. Borgarello; and M. Gratzel. "Visible-light-induced oxygen generation from aqueous dispersions of tungsten(VI) oxide". *Journal of Physical Chemistry B*, vol. 88, pp. 4401-4006. 1984
- [8] H. Ali; N. Ismail; M. S. Amin; and M. Mekewi. "Decoration of vertically aligned TiO₂ nanotube arrays with WO₃ particles for hydrogen fuel production". *Frontiers in Energy*, vol. 12, pp. 249-258. 2018
- [9] I. Shiyonovakaya and M. Hepel. "Bicomponent WO₃/TiO₂ Films as Photoelectrodes". *Journal of Electrochemical Society*, vol. 146, pp. 243-249. 1999
- [10] S. Higashimoto; N. Kitahata; K. Mori; and M. Azuma. "Photo-electrochemical properties of amorphous WO₃ supported on TiO₂ hybrid catalysts". *Catalysis Letters*, vol. 101, pp. 49-51. 2005
- [11] H. Tada; A. Kokubu; M. Iwasaki; and S. Ito. "Deactivation of the TiO₂ photocatalyst by coupling with WO₃ and the electrochemically assisted high photocatalytic activity of WO₃". *Langmuir*, vol. 20, pp. 4665-4670. 2004
- [12] C. S. Fu; C. Lei; G. Shen; and C. G. Yu. "The preparation of coupled WO₃/TiO₂ photocatalyst by ball milling". *Powder Technology*, vol. 160, pp. 198-202. 2005
- [13] J. Engweiler; J. Harf; and A. Baiker. "WO_x/TiO₂ catalysts prepared by grafting of tungsten alkoxides: Morphological properties and catalytic behavior in the selective reduction of NO by NH₃". *Journal of Catalysis*, vol. 159, pp. 259-269. 1996
- [14] S. Eibl; B. C. Gates; and H. Knözinger. "Structure of WO_x/ZrO₂ Catalysts Prepared from Hydrous Titanium Oxide Hydroxide: Influence of Preparation Parameters". *Langmuir*, vol. 17, pp. 107-115. 2001
- [15] H. M. Yang; R. R. Shi; K. Zhang; Y. Hu; A. Tang; and X. Li. "Synthesis of WO₃/TiO₂ nanocomposites via sol-gel method". *Journal of Alloys and Compounds*, vol. 398, pp. 200-202. 2005
- [16] D. Ke; H. Liu; T. Peng; X. Liu; and K. Dai. "Preparation and photocatalytic activity of WO₃/TiO₂ nanocomposite particles". *Materials Letters*, vol. 62, pp. 447-450. 2008
- [17] P. K. Shin and A. C. C. Tseung. "Study of Electrodeposited Tungsten Trioxide Thin Films". *Journal of Materials Chemistry*, vol. 2, pp. 1141-1148. 1992
- [18] X. Z. Li; F. B. Li; C. L. Yang; and W. K. Ge. "Photocatalytic activity of WO_x-TiO₂ under visible light irradiation". *Journal of Photochemistry and Photobiology A: Chemistry*, vol. 141, pp. 209-217. 2001
- [19] J. H. Park; O. O. Park; and S. Kim. "Photoelectrochemical water splitting at titanium dioxide nanotubes coated with tungsten trioxide". *Applied Physics Letters*, vol. 89, pp. 163106-163109 2006b
- [20] J. Zhao; X. Wang; Y. Kang; X. Xu; and Y. Li. "Photoelectrochemical Activities of W-Doped Titania Nanotube Arrays Fabricated by Anodization". *IEEE Photonics Technology Letters*, vol. 20, pp. 1213-1215. 2008
- [21] M. Xiao; L. Wang; X. Huang; Y. Wu; and Z. Dang. "Synthesis and characterization of WO₃/titanate nanocomposite with enhanced photocatalytic properties". *Journal of Alloys and Compounds*, vol. 470, pp. 486-491. 2009
- [22] E.-l. Yang; J.-j. Shi; H.-c. Liang; and W.-k. Cheuk. "Coaxial WO₃/TiO₂ nanotubes/nanorods with high visible light activity for the photodegradation of 2,3-dichlorophenol". *Chemical Engineering Journal*, vol. 174, pp. 539-545. 2011
-

- [23] C. Das; I. Paramasivam; N. Liu; and P. Schmuki. "Photoelectrochemical and photocatalytic activity of tungsten doped TiO₂ nanotube layers in the near visible region". *Electrochimica Acta*, vol. 56, pp. 10557-10561. 2011
- [24] C. W. Lai and S. Sreekantan. "Visible light photoelectrochemical performance of W-loaded TiO₂ nanotube arrays: structural properties". *Journal of Nanoscience and Nanotechnology*, vol. 12, pp. 3170-4. 2012
- [25] C. W. Lai and S. Sreekantan. "Incorporation of WO₃ species into TiO₂ nanotubes via wet impregnation and their water-splitting performance". *Electrochimica Acta*, vol. 87, pp. 294–302. 2013a
- [26] C. W. Lai and S. Sreekantan. "Preparation of hybrid WO₃-TiO₂ nanotube photoelectrodes using anodization and wet impregnation: Improved water-splitting hydrogen generation performance". *International Journal of Hydrogen Energy*, vol. 38, pp. 2156-2166. 2013b
- [27] C. W. Lai and S. Sreekantan. "Effect of heat treatment on WO₃-loaded TiO₂ nanotubes for hydrogen generation via enhanced water splitting". *Materials Science in Semiconductor Processing*, vol. 16, pp. 947-954. 2013c
- [28] M. Zhang; C. Yang; W. Pu; Y. Tan; K. Yang; and J. Zhang. "Liquid phase deposition of WO₃/TiO₂ heterojunction films with high photoelectrocatalytic activity under visible light irradiation". *Electrochimica Acta*, vol. 148, pp. 180-186. 2014
- [29] W. H. Lee; C. W. Lai; and S. B. A. Hamid. "One-Step Formation of WO₃-Loaded TiO₂ Nanotubes Composite Film for High Photocatalytic Performance". *Materials*, vol. 8, pp. 2139-2153. 2015
- [30] V. K. Mahajan; S. K. Mohapatra; and M. Misra. "Stability of TiO₂ nanotube arrays in photoelectrochemical studies". *International Journal of Hydrogen Energy*, vol. 33, pp. 5369-5374. 2008
- [31] Z. B. Xie; S. Adams; and D. J. Blackwood. "Effects of anodization parameters on the formation of titania nanotubes in ethylene glycol". *Electrochimica Acta*, vol. 56, pp. 905-912. 2010
- [32] F. ShafiaHoor; V. S. Murulidharan; M. F. Ahmed; and S. M. Mayanna. "Study In The Electrochemical Behavior Of Wo3-Pt Coating: A Cyclic Voltammetric Approach". *IOSR Journal of Applied Chemistry (IOSRJAC)*, vol. 1, pp. 09-14. 2012
- [33] Y. S. Krasnov and G. Y. Kolbasov. "Electrochromism and reversible changes in the position of fundamental absorption edge in cathodically deposited amorphous WO₃". *Electrochimica Acta*, vol. 49, pp. 2425-2433. 2004
- [34] L. J. Minggu; W. R. Wan Daud; and M. B. Kassim. "An overview of photocells and photoreactors for photoelectrochemical water splitting". *International Journal of Hydrogen Energy*, vol. 35, pp. 5233-5244. 2010
- [35] K. Shankar; K. Tep; G. K. Mor; and C. A. Grimes. "An electrochemical strategy to incorporate nitrogen in nanostructured TiO₂ thin films: modification of bandgap and photoelectrochemical properties". *Journal of Physic D*, vol. 39, pp. 2361-2366. 2006
- [36] T. Vogt; P. Woodward; and B. Hunter. "The high-temperature phases of WO₃". *Journal of Solid State Chemistry*, vol. 144, pp. 209-215. 1999
- [37] W. Li; J. Li; X. Wang; J. Ma; and Q. Chen. "Photoelectrochemical and physical properties of WO₃ films obtained by the polymeric precursor method". *International Journal of Hydrogen Energy*, vol. 35, pp. 13137-13145. 2010

Modeling the Effect of CO₂ on Thermodynamic Behavior of CO₂/Libyan Natural Gas Mixture

Almadi A. Alhwaige*, Ali S. Ebshish, Salem M. Abdusalam, Ahmed M. Bshish

Department of Chemical and Petroleum Engineering, College of Engineering, Elmergib University, Alkhoms, Libya

DOI: <https://doi.org/10.21467/proceedings.2.39>

* Corresponding author email: aaa148@case.edu

ABSTRACT

A great challenge has been done for utilization of natural gas (NG) for potential applications at various operating conditions. Accurate thermo-physical properties of NG play an important role in design and processing of NG systems. Among of these properties, compressibility factor, density, and viscosity of gas mixtures provide the feasibility of a given process. Carbon dioxide (CO₂) is present in large quantities that produced from NG reservoirs. Understanding the effect of CO₂ on thermodynamic properties of Libyan NG is important for developing the next generation of modern applications. The major thermodynamic properties considered in the present study were compressibility factor, density, and viscosity. The objective of this work is to investigate the effect of CO₂ content on properties of Libyan NG using theoretical calculations. MATLAB logarithms were developed to predict the thermo-physical properties of Libyan NG with different CO₂ concentrations. The effect of CO₂ on thermodynamic behavior of NG mixture under different conditions of pressure and temperature was studied using the Redlich Kwong equation of state (RK-EoS). CO₂ concentration has a great impact on the CO₂/NG mixture properties. The results revealed that the compressibility factor of CO₂/NG mixture is inversely proportional with the CO₂ concentration; however, as CO₂ content increases the gas mixture density increases.

Keywords: Libyan natural gas; Carbon dioxide; Thermodynamic Properties; z-factor; Gas density; Viscosity of gas mixture.

1 Introduction

Since many decades, the world depends strongly on the natural gas (NG) as a major source for energy supply. The main challenge for using this energy for wide different applications is how to utilize and process the NG from its reservoir to the place where the energy needed. The key role in designing and processing of NG system is to identify its accurate thermo-physical properties. The most important gas mixture properties in the design calculations are compressibility factor, viscosity and density of the gas mixture [1-4].

In particular, compressibility factor is a measure of the gas deviation from perfect behavior and is defined as the ratio of the real gas volume to the ideal volume [1,2]. In simple way, the



© 2018 Copyright held by the author(s). Published by AIJR Publisher in Proceedings of First Conference for Engineering Sciences and Technology (CEST-2018), September 25-27, 2018, vol. 1.

This is an open access article under [Creative Commons Attribution-NonCommercial 4.0 International](https://creativecommons.org/licenses/by-nc/4.0/) (CC BY-NC 4.0) license, which permits any non-commercial use, distribution, adaptation, and reproduction in any medium, as long as the original work is properly cited. ISBN: 978-81-936820-5-0

density is equal to number of molecules multiply molecular weight over the occupied volume. The viscosity is the fluid (Liquid or Gas) property of resistance to flow and may be thought of as a measure of fluid friction [2].

Viscosity and density are essential physical quantities to describe the statics and dynamics behaviors of gas mixtures. These properties only can describe more than half of the fluid properties [2]. Gathering density and viscosity data on a NG gives manufacturers the ability to predict how it behaves in the real world. Availability of these properties provide analog for good concentration of NG transportation systems and contribute for excellent design processes with high production [4].

In the most cases, NG often contains some amounts of heavier hydrocarbons and non-hydrocarbons (impurities), which have a significant contribution to change the thermodynamic behavior of the NG [3]. In case of enhanced oil recovery (EOR) process, carbon dioxide (CO₂) is widely used as injected gas to the gas-oil reservoirs for increasing the reservoir pressure. The injected CO₂ will mix with the NG/oil; therefore, the thermodynamic properties of these products are directly affected due to the change of CO₂ concentration in the products. Hence, effect of CO₂ on densities and viscosities of gas mixtures is considered very important [5].

Generally, the thermodynamic properties are obtained experimentally and theoretically. Equations of state (EoSs) and empirical correlations are considered the common methods to predict thermodynamic behaviors of NG when unavailable experimental data. In addition, analytical methods are more attractive than experimental work because experiments are expensive, time consuming, and sometimes are not applicable [6,7]. Previously, we reported a study for fitting the equations of state for predicting the thermodynamic properties of Libyan NG mixture [1]. The results revealed that the Redlich Kwong cubic equation of state (RK-EoS) provides a better fit to Standing and Katz chart (K-Z). Therefore, in this study, Redlich Kwong (RK) was used as the model for predicting the NG properties. The objective of the present work is to investigate the effect of CO₂ composition on the viscosity and density of the Libyan NG mixture at different range of temperatures and pressures.

2 Theory

Cubic equations of state (EoSs) are the simplest models that predicting the PVT behavior of fluids (liquid and gases) with a broad range of temperatures and pressures. Many forms of equations of state have been used to predict NG compressibility factor (z-factor) and consequently the other gas properties such as viscosity and density [1].

The general form of the cubic equation of states is given in Eq.1. The solution of this equation provides three different complex roots for molar volume. However, the disadvantage of this form is that it can be solved only by trial and error method. However, it was difficult of guessing the initial value of molar volume for the trial and error method. Therefore, the modern form of the equations of state have been obtained by replacing the molar volume

parameter with z-factor according to the relationship that is given in Eq.2. Eq. 3 shows the final version of the general form of the modern EoSs. Table 1 illustrates the parameters that presented in Eq.3 belong to the most widely used EoSs [1].

$$V = \frac{RT}{P} + b - \frac{a(T)}{P} \frac{V - b}{(V + \epsilon b)(V + \sigma b)} \quad (1)$$

$$V = \frac{ZRT}{P} \quad (2)$$

$$Z = 1 + \beta - q\beta \frac{Z - \beta}{(Z + \epsilon\beta)(Z + \sigma\beta)} \quad (3)$$

$$\beta = \Omega \frac{P_r}{T_r} \quad (4)$$

$$q = \frac{\Psi \alpha(T_r)}{\Omega T_r} \quad (5)$$

Where P_r and T_r are reduced pressure and temperature of pure components, respectively. The expression $\alpha(T_r)$ is a function in T_r and ω . The numerical assignments for parameters ϵ , σ , Ω , ω and Ψ are depending on the type of EoS as shown in Table 1.

Table 1: Parameters assignments for generic EoS.

E.O.S.	$\alpha(T_r)$	Σ	ϵ	Ω	Ψ	Z_c
VdW	1	0	0	1/8	27/64	3/8
RK	$T_r^{-1/2}$	1	0	0.08664	0.42748	1/3
SRK	$\alpha_{\text{SRK}}(T_r; \omega)$	1	0	0.08664	0.42748	1/3
PR	$\alpha_{\text{SRK}}(T_r; \omega)$	$1 + \sqrt{2}$	$1 - \sqrt{2}$	0.07779	0.45724	0.30740
$\alpha_{\text{SRK}}(T_r; \omega) = \left[1 + (0.480 + 1.574\omega - 0.176\omega^2)(1 - T_r^{1/2}) \right]^2$ $\alpha_{\text{PR}}(T_r; \omega) = \left[1 + (0.37464 + 1.54226\omega - 0.26992\omega^2)(1 - T_r^{1/2}) \right]^2$						

The gas density (ρ_g) and viscosity (μ_g) of gas mixtures are defined as given in the following relations.

$$\rho_g = \frac{pM_g}{ZRT} \quad (6)$$

$$\mu_g = 1 * 10^{-4} k_v \text{EXP} \left[x_v \left(\frac{\rho_g}{62.4} \right)^{y_g} \right] \quad (7)$$

$$k_v = \frac{(9.4 + 0.02M_g)T^{1.5}}{209 + 19M_g + T} \tag{8}$$

$$x_v = 3.5 + \frac{986}{T} + 0.01M_g \tag{9}$$

Where, ρ_g is the density of the gas mixture in g/cm^3 , μ_g is the viscosity in ϕ , M_g is the molecular weight of gas mixture, R is the universal gas constant, γ_g is the specific gravity for gas, and x_v is the parameter used to calculate γ_g .

3 Methodology

In this work, the thermodynamic properties of compressibility factor, viscosity and density of Libyan NG were theoretically predicted. Table 2 list the used the data of Libyan NG, which was obtained from Milletah Oil and Gas (MOG) Company. Matlab logarithm of Redlich Kwong equation (RK-EoS) was launched for predicting the z-factor, viscosity, and density of NG mixtures with different CO₂ compositions at various values of reduced temperatures and reduced pressures.

Table 2 The composition of gas mixture.

Component	Formula	Composition %
Hydrogen Sulphide	H ₂ S	01.27
Carbon Dioxide	CO ₂	15.65*
Nitrogen	N ₂	04.59
Methane	C ₁	70.06
Ethane	C ₂	04.40
Propane	C ₃	01.76
i-Butane	i-C ₄	00.40
n-Butane	n-C ₄	00.67
i-Pentane	i-C ₅	00.30
n-Pentane	n-C ₅	00.30
n-Hexane	n-C ₆	00.29
n-Heptane	n-C ₇	01.80
n-Octane	n-C ₈	00.08
n-Nonane	n-C ₉₊	00.02
Water	H ₂ O	02.00

*In this study, the CO₂ composition was changed, but the composition ratios of the other gases mentained constants.

In the initial step, the critical temperature (T_c) and critical pressure (P_c) for gas mixture were calculated using Eqs.10 and 11, respectively. Then, the reduced temperature (T_r) and reduced pressure (P_r) were evaluated using Eqs. 12 and 13, respectively.

$$T_C = \sum_{i=1}^n T_{ci} y_i \quad (10)$$

$$P_C = \sum_{i=1}^n P_{ci} y_i \quad (11)$$

$$T_r = \frac{T}{T_c} \quad (12)$$

$$P_r = \frac{P}{P_c} \quad (13)$$

Where P_{ci} and T_{ci} are the critical pressure and critical temperature of pure component i , respectively; y_i is the mole fraction of component i . T_r and P_r are reduced temperature and reduced pressure, respectively. T_c and P_c are critical temperature and critical pressure of the gas mixture, respectively.

The second step, the compressibility factor (Z) was estimated using RK-EoS as given in Eq. 3. RK-EoS was found the best EoSs for prediction the compressibility factor of the Libyan gas mixture [1]. Finally, the density and viscosity of the gas mixture were predicted using Eqs. 6, and 7 respectively.

Since the main objective of this study is to investigate the effect of CO₂ composition in the NG properties, the composition of CO₂ in the gas mixture was varied from 10 % to 50%. Besides, the densities and viscosities of these gas mixtures were evaluated at different temperatures and pressures.

4 Results and Discussion

4.1 Compressibility Factor

The compressibility factor as a function of reduced pressure and reduced temperature has been computed using Redlich Kwong equation of state (RK-EoS). The predicted results using RK-EoS were compared with the z -factor that previously obtained from Standing-Katz (S-K) chart and the results are shown in Figure 1.

The properties were evaluated at different reduced pressure ranging from 1 to 13, and at reduced temperatures of 1.5, 2, and 3. The S-K chart was used as a reference chart to examine the reliability of using RK-EoS in predicting the compressibility factor. As clearly seen from Figure 1, the behaviour of the compressibility factor that obtained using RK-EoS is in a good agreement with that obtained by S-K chart. As previously reported by Salem and his co-workers [1], among of the equations of state, RK-EoS showed the best fit to S-K chart to describe the Libyan NG behavior. Therefore, the RK-EoS was selected in this study for predicting the further thermodynamic properties of the gas mixture.

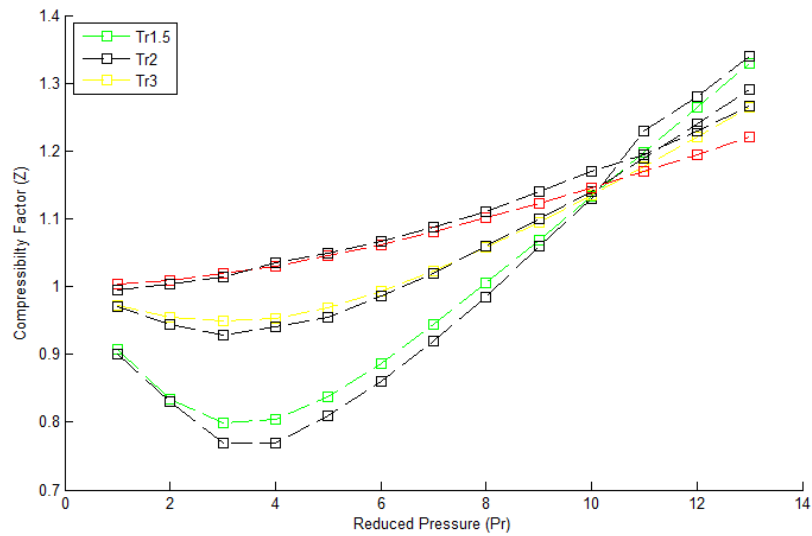


Figure 1 Effect of reduced temperature on the compressibility factor at various pressures: RK-EoS in coloured lines and S-K in Black lined [1].

4.2 Effect of CO₂ Concentration on the Viscosity of Gas Mixture

Viscosity of NG mixture is very important quantity for knowing how the production and transportation processes are designed. Pressure and temperature have great influence on the viscosity behavior of NG mixture. Viscosity of the gas mixture is evaluated using Eq.7 by applying the z-factor that obtained from RK-EoS. The composition of CO₂ in the gas mixture has been varied from 10% to 50% and for each case the viscosity was calculated. Figure 2 shows the viscosity of the NG mixtures with different CO₂ compositions at different reduced temperatures.

As seen in Figure 2, the results indicated that the viscosity of gas mixture increase with an increase in the amount of CO₂. This finding is very important to take in account because the design of the production and transportation process strongly depends on determination of accurate value of viscosity. In addition, the results demonstrate that the viscosity of gas mixture is proportional with the reduced pressure. For example, at Tr = 1.25, the viscosity of the gas mixture was increased from 1 to 2.5 cp with an increase in the reduced pressure from 4 to 8. This seems to be quite logic because the viscosity dependent with the density, which is increased with the system pressure. Furthermore, it is clearly that all cases predicted that the viscosity have nonlinear relationship with the reduced pressure at the low values; however, it became nearly linear at high values of reduced pressure. Therefore, there is no effect of the reduced pressure at high reduced pressure values. On the other hand, the viscosity has inverse relationship with reduced temperature. Figure 3, displays the viscosity of gas as a function in the reduced temperatures at CO₂ composition of 0.1565. The results indicated that the viscosity has linearly proportional relationship at low reduced temperatures; however, it increases nonlinearly at high reduced temperature.

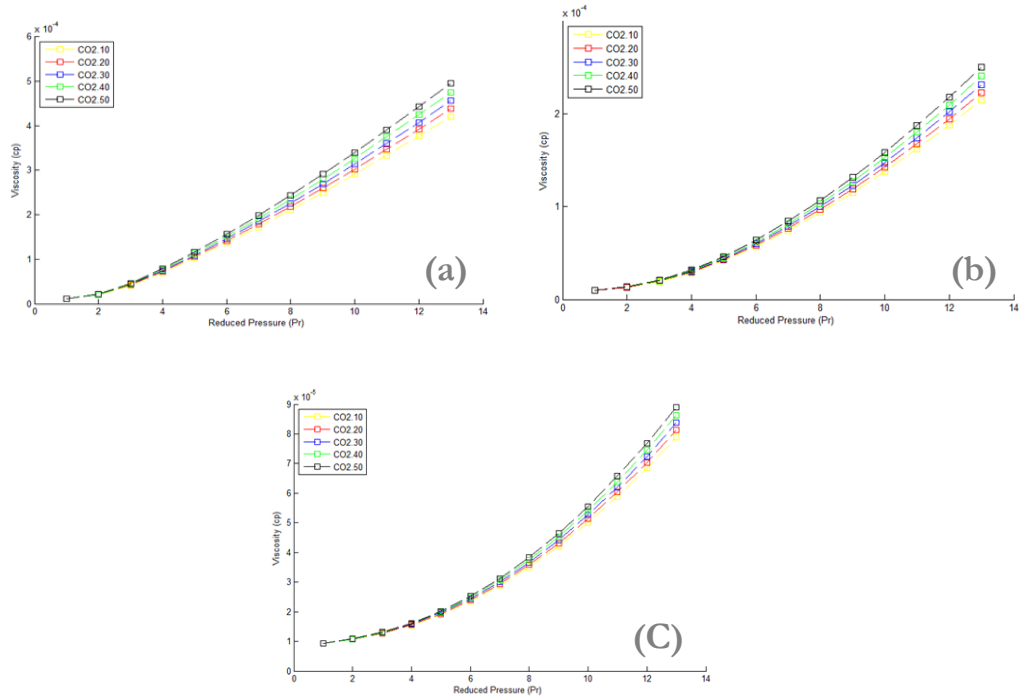


Figure 2 the effect of CO₂ on the viscosity of natural gas mixture at different reduced temperatures; **(a)** at $T_r = 1.25$, **(b)** at $T_r = 1.5$, and **(c)** at $T_r = 2$.

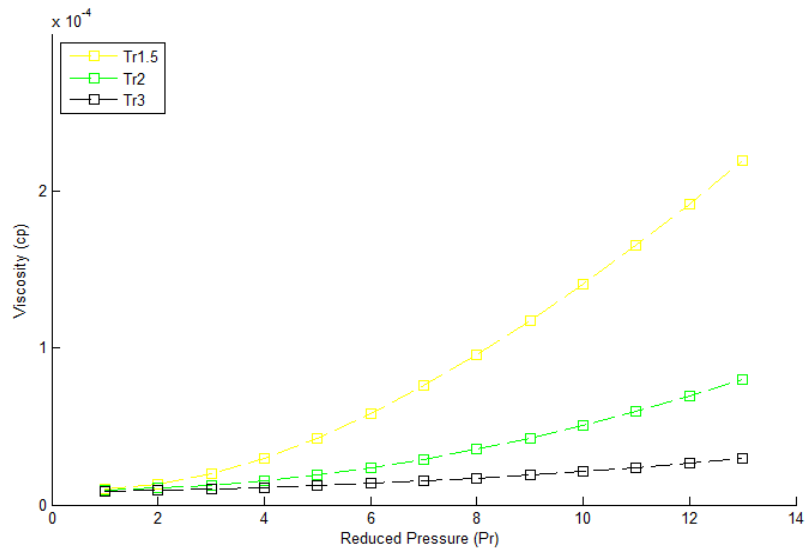


Figure 3 The viscosity of MOG gas mixture versus reduced pressure at different reduced temperatures.

4.3 Effect of CO₂ Composition on the Density of Gas Mixture

In this part, the density of the gas mixture has been evaluated using Eq.6 with z-factor values obtained from RK-EoS. Figure 4 shows the effect of CO₂ composition on the density of the gas mixture at different reduced pressures and reduced temperatures. As seen in Figure 4, the density of the gas mixture doesn't remarkably change with varying CO₂ concentration in gas mixture. In addition, the behaviour of the gas density seems to be identical at all values of CO₂ compositions. However, the numerical values of the densities indicate that there is a slight increase in the gas density with increase the concentration of CO₂.

Furthermore, Figure 4 shows that the gas density increases notably with increasing reduced pressure, especially at high reduced temperature. At low reduced temperature, the density was sharply increased at beginning and then, it became increased gradually to reach equilibrium. However, the density values increased linearly with reduced pressure. Figure 5 shows the effect of reduced temperature on the gas mixture at fixed CO₂ composition of 0.1565. The results showed that the density has an inverse relation with the reduced temperatures. For instant, the density values were read 5, 7, and 12 g/cm³ for decreasing the reduced temperature as 1.25, 2.0, 3.0, respectively.

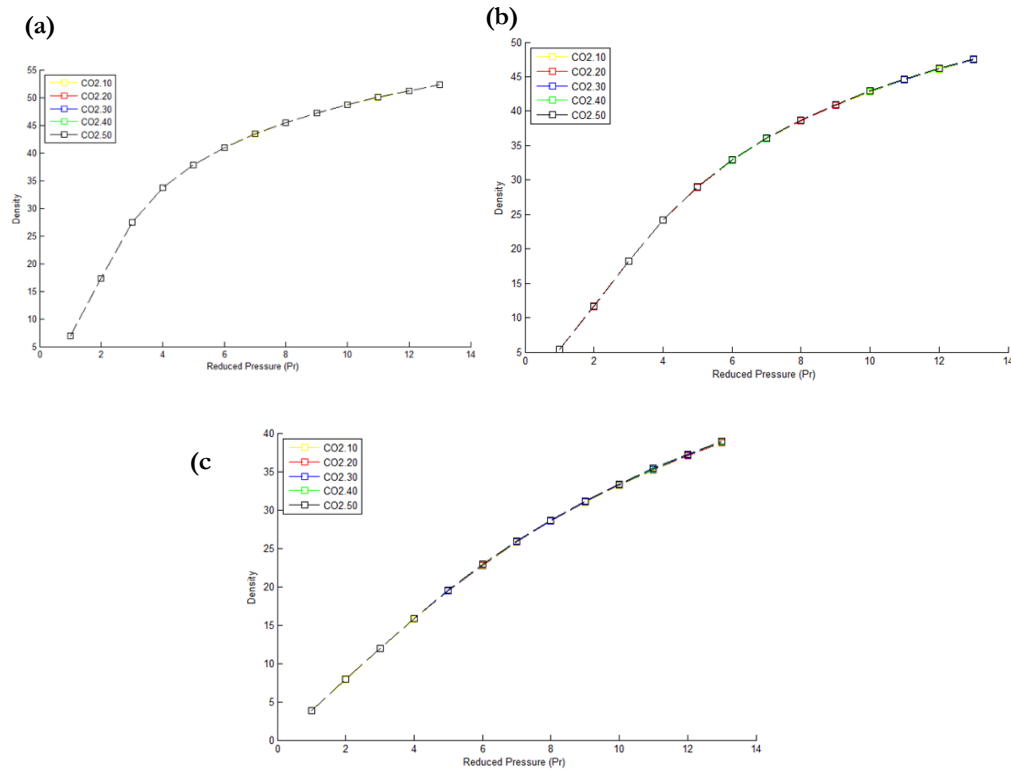


Figure 4 the effect of CO₂ Concentration on the density of natural gas mixture at different reduced temperatures; (a) at $T_r = 1.25$, (b) at $T_r = 1.5$, (c) at $T_r = 2$.

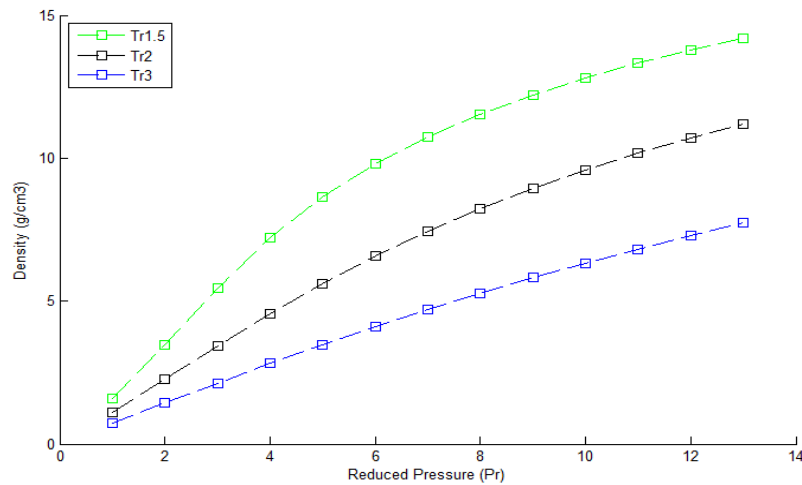


Figure 5 The density of MOG gas versus reduced pressure at different reduced temperatures.

5 Conclusions

Prediction of thermodynamic properties of Libyan NG under diverse conditions is very important in designing and processing of NG system. Among of these properties, density and viscosity have significant contribution to describe more than half of the other properties belong to gas mixtures. Redlich Kwong equation of state (RK-EoS) was used in this work to investigate the effect of CO₂ composition in the Libyan NG mixture of MOG on its viscosity and density. The data of NG mixture with different compositions of CO₂ was correlated to RK-EoS to obtain the compressibility factor of the gas over a range of reduced pressures from 1 to 14 and reduced temperatures from 1.5 to 3. Then, the z-factor obtained from RK-EoS was used to predict the viscosity and density of the mixture over mentioned conditions. The results showed that the increase of CO₂ content in the gas mixture leads to an increase in the viscosity. It also revealed that the density of the mixture is slightly increased with the increase in the CO₂ content. This finding is very useful to gas manufacturers for better design of gas piping and storage system. Moreover, this study demonstrated that the viscosity and density are increased with increase of the applied pressure. Nonetheless, the results showed that the density and viscosity are inversely proportional to the operating temperatures.

References

- [1] Salem M. A.; Ahmed M. B.; Ali S. E.; Almahdi A. A. Simulation of Thermodynamic properties of natural gas Mixture feedstock of mellitah gas plant, 1st International Conference on Chemical, Petroleum, and Gas Engineering (ICCPGE-2016), December 20-22, 2016; Alkhoms, Libya, 2016, 1, 229-235 (<http://iccpge.elmergib.edu.ly/iccpgePapers/281.pdf>).
- [2] Viswanathan A. Viscosities of natural gases at high pressures and high temperatures, Master Thesis, Petroleum Engineering, Texas University 2007. (<http://oaktrust.library.tamu.edu/bitstream/handle/1969.1/5823/etd-tamu-2007A-PETE-Viswana.pdf?sequence=1>)

- [3] Fayazi A.; Arabloo M.; Mohammadi A. H. Efficient estimation of natural gas compressibility factor using a rigorous method. *J. Natural Gas Sci. Eng.*, 2014, 16, 8-17 (<https://doi.org/10.1016/j.jngse.2013.10.004>).
- [4] Wetenhall B.; Race J. M.; Downie M. J., The effect of CO₂ purity on the development of pipeline networks for carbon capture and storage schemes, *International J. Greenhouse Gas Control* 2014, 30, 197–211. (<http://dx.doi.org/10.1016/j.ijggc.2014.09.016>).
- [5] Moshfeghian M. Impact of CO₂ on natural gas density, 2018. (http://www.petroskills.com/blog/entry/00_totm/apr18-fac-impact-of-co2-on-natural-gas-density#.Wusq0vkzwc)
- [6] Kumar, N. Compressibility factor for natural and sour reservoir gases by correlations and cubic equations of state, M.Sc. Thesis, 2004 Texas Tech University (<http://hdl.handle.net/2346/1370>) or (<https://ttu-ir.tdl.org/ttu-ir/handle/2346/1370>).
- [7] Heidaryan E.; Salar abadi A.; Moghadasi J. A novel correlation approach for prediction of natural gas compressibility factor, *J. Natural Gas Chemistry*, 2010, 19, 189–192 ([https://doi.org/10.1016/S1003-9953\(09\)60050-5](https://doi.org/10.1016/S1003-9953(09)60050-5)).

**Second Volume of this Proceedings
is Published in “AIJR Proceedings”
Series 4, 2018**

at

<https://doi.org/10.21467/proceedings.4>

AIJR Proceedings Series

A scientific conference explores the developments of scientific research in the field of applied engineering sciences, technologies, material science, environmental and engineering management, in order to support inter-disciplinary work. CEST-2018 was organized by Faculty of Engineering Garaboulli, and Faculty of Engineering, Al-khoms, Libya.

First Conference for
Engineering Sciences and
Technology

CEST-2018

Volume 1

AiJR

To learn more about
AIJR Publisher
Please visit us at: www.aijr.in

